Technical Report
TR-21-07
December 2022

Post-closure safety for the final repository for spent nuclear fuel at Forsmark

Radionuclide transport report, PSAR version

SVENSK KÄRNBRÄNSLEHANTERING AB

SWEDISH NUCLEAR FUEL
AND WASTE MANAGEMENT CO

Box 3091, SE-169 03 Solna
Phone +46 8 459 84 00
skb.se

ISSN 1404-0344
SKB TR-21-07
ID 1918122
December 2022

Post-closure safety for the final repository for spent nuclear fuel at Forsmark

Radionuclide transport report, PSAR version

Svensk Kärnbränslehantering AB

This report is published on www.skb.se

Summary

The post-closure safety assessment for the final repository for spent nuclear fuel at Forsmark, version PSAR, is documented in a main report and main references. This is one of the main references, which describes calculations of radionuclide release and transport for the repository and compares the resulting radiological doses to applicable regulatory limits. Release and transport in several additional cases that help illustrate barrier function are also described. Site characteristics and processes affecting release and transport are also described.

The dominant processes responsible for geosphere radionuclide transport include advection through networks of fractures, diffusion in intact host rock adjacent to fractures, ion exchange and surface complexation reactions on mineral surfaces within the host rock, radionuclide decay and in-growth of daughter radionuclides, and radionuclide sorption onto clay colloids that may be generated in the buffer material under some conditions. A comprehensive strategy for representing flow in fractures and engineered features of the repository was developed in the SR-Site project. The outputs of that flow modelling activity, which represent inputs to the transport modelling described here, are advective travel times and flow-related transport resistance parameters for individual transport pathways and flow rates at individual deposition holes. Model uncertainties related to the representation of flow are addressed by considering multiple conceptual models of the discrete fracture network based on different degrees of correlation between fracture transmissivity and length. Multiple realisations of the discrete fracture network are included to address uncertainties associated with the stochastic generation of fracture networks. Steady flow and chemical conditions for the present day are used in the transport calculations; variant simulations and screening analyses allowing transient flow and chemical conditions demonstrate that the steady approximation is an adequate representation. Sorption processes are represented by equilibrium sorption partitioning coefficients with appropriately defined probability distributions instead of detailed modelling of ion-exchange and surface-complexation reactions.

Two scenarios for which canister failures and subsequent radionuclide release cannot be ruled out are identified. The two scenarios are failure of the copper canister by corrosion and by earthquake-induced shear movements in fractures intersecting the canister positions. Two additional hypothetical scenarios (a growing pinhole failure and failure due to isostatic load) are also analysed to illustrate barrier functions although the analyses discussed in the PSAR main report led to the conclusion that the canister failure modes associated with these scenarios can be ruled out. Important near-field processes are dependent on the release scenario, but generally include dissolution of the fuel matrix and corrosion of structural parts of the fuel assemblies and control rods, precipitation/dissolution of secondary radionuclide-bearing minerals, and sorption onto clay buffer and backfill material. Diffusion in the buffer material is the primary transport mechanism if the buffer material remains in place; otherwise, advection is the primary transport mechanism in the near field.

Probabilistic calculations of radionuclide release and transport demonstrate that the mean releases from the engineered barrier system give rise to doses below the dose corresponding to the regulatory risk limit. The dose-equivalent releases are also significantly below estimates of dose corresponding to background concentrations of uranium and radium. The releases are small because the geosphere and engineered barrier system protect the canisters by providing favourable hydrological and geochemical environments, thus resulting in small probability of failure for a few canisters and negligible probability of failure for the vast majority of canisters. In the shear-failure scenario, sorption on buffer material also attenuates radionuclide release.

Radionuclide release from the engineered barrier system is further attenuated by the geosphere. The geosphere attenuation is approximately a factor of 3 for the corrosion scenario (central case conditions). The attenuation is relatively modest in the central corrosion case because the canisters that are most likely to fail are associated with flow paths with modest retention. Geosphere attenuation is stronger for variant modelling cases that result in larger releases from the engineered barrier system. Thus, in addition to protecting the canisters and limiting releases, the geosphere also reduces uncertainty in the estimated doses by attenuating the dose for variant cases that have larger release from the engineered barrier system. For all probabilistic cases considered, the mean annual effective dose is at least an order of magnitude smaller than the dose corresponding to the risk limit. For the central corrosion

case, the peak of the mean annual effective dose is estimated to be 0.2 μSv/year. For comparison, the dose corresponding to the risk limit is approximately 14 μSv/year and the dose corresponding to typical background radiation is approximately 1 000 μSv/year.

Sorption to mobile clay colloids is an uncertain process that is handled pessimistically by neglecting a range of potential mitigating processes. When this process is included, the geosphere is not a significant barrier to radionuclide transport for the brief periods in which high colloid concentrations are possible. However, these periods are brief and the small near-field release rates are sufficient to keep dose-equivalent releases below the dose corresponding to the risk limit.

Results of simplified analytical models are in good agreement with results obtained with the numerical models. The agreement enhances confidence in the dose equivalent release calculations presented here for two reasons. First, the comparison provides an important quality assurance check on the numerical modelling of dose equivalent releases. Second, it demonstrates that potential doses are controlled by relatively simple processes that are straightforward to understand and model.

Sammanfattning

Säkerhetsanalysen PSAR görs för att analysera säkerheten efter förslutning för ett geologiskt förvar i Forsmark. Analysen ligger till grund för SKB:s ansökan om att uppföra ett slutförvar för använt kärnbränsle i Forsmark. Resultatet av säkerhetsanalysen dokumenteras i PSAR:s huvudrapport och huvudreferenser samt i stödjande rapporter. Den här rapporten utgör en av huvudreferenserna och beskriver beräkningar av frigörelse och transport av radionuklider för förvaret i Forsmark och jämför beräknad radiologisk dos med den dos som motsvarar myndigheternas riskkriterium. Frigörelse och transport beskrivs också för flera beräkningsfall som hjälp för att illustrera betydelsen av enskilda barriärer och barriärfunktioner. Dessutom beskrivs platskaraktäristik och processer som påverkar frigörelse och transport.

De viktigaste processerna som påverkar radionuklidtransporten i geosfären är advektion genom nätverk av sprickor, diffusion i intakt bergmatris intill sprickor, jonbytes- och ytkomplexeringsreaktioner på mineralytor i bergmatrisen, radioaktivt sönderfall och inväxt av dotternuklider. En omfattande strategi för att modellera vattenflöde i sprickor och tekniska barriärer utvecklades i SR-Site. Utdata från vattenflödesmodelleringen i form av advektiv gångtid och flödesrelaterade tranportmotståndsparametrar för individuella transportvägar och flödeshastigheter i individuella deponeringshål används som indata till transportmodelleringen. Modellosäkerheter relaterade till beräkningen av vattenflödet omhändertas genom att beakta flera konceptuella modeller av det diskreta spricknätverket baserat på olika grad av korrelation mellan spricktransmissivitet och sprickstorlek. Flera realiseringar av det diskreta spricknätverket har använts för att beakta osäkerheten till följd av den stokastiska genereringen av spricknätverken. Konstant flöde och konstanta kemiska förhållanden motsvarande dagens situation används huvudsakligen i transportberäkningarna. Variationsfall samt beräkningar med varierande flöde och kemiska förhållanden visar att approximationen med konstanta förhållanden är adekvat. Sorptionsprocesser representeras med jämviktssorptionskoefficienter med lämpligt definierade sannolikhetsfördelningar i stället för detaljerad modellering av jonbytes- och ytkomplexeringsreaktioner.

Två scenarier identifieras för vilka det inte kan uteslutas att kapselns isolering går förlorad och att radionuklider frigörs. De två scenarierna är korrosion av kopparkapseln och kapselskador till följd av jordskalvsinducerade skjuvrörelser i sprickor som korsar kapselpositionen. Två hypotetiska restscenarier (växande initialt pinnhål och skada på grund av isostatisk last) analyseras också för att belysa barriärernas funktion, även om analysen som beskrivs i PSAR:s huvudrapport leder till slutsatsen att dessa båda kapselskador kan uteslutas. Viktiga närzonsprocesser är scenarioberoende, men generellt omfattar de upplösning av bränslematrisen och korrosion av metall i bränsleboxarna och i styrstavar, utfällning/upplösning av sekundära mineraler som innehåller radionuklider samt sorption på bentoniten i buffert och tunnelåterfyllning. Diffusion i buffertmaterialet är den primära transportmekanismen, om buffertmaterialet är kvar, annars är advektion den primära transportmekanismen i närzonen.

Probabilistiska beräkningar av frigörelse och transport av radionuklider visar att medelutsläppet från de tekniska barriärerna är lägre än den dos som motsvarar myndigheternas riskkriterium. Utsläppet är också betydligt lägre än dosen från bakgrundskoncentrationer av uran och radium. De låga utsläppen beror på att geosfären och de tekniska barriärerna skyddar kapslarna genom att tillhandahålla en gynnsam hydrologisk och geokemisk miljö, som resulterar i en låg sannolikhet för skador på ett fåtal kapslar och försumbar sannolikhet för skador på en majoritet av kapslarna. I skjuvscenariot bidrar också sorption på buffertmaterial till en dämpning av radionuklidutsläppet.

Radionuklidfrigörelsen från de tekniska barriärerna dämpas ytterligare av geosfären, vilket medför en minskning med ungefär en faktor tre för korrosionsscenariot (centralfallet). Dämpningen är relativt begränsad i det centrala korrosionsfallet på grund av att de kapslar som har högst sannolikhet att skadas är sammankopplade med flödesvägar med ringa retention. Geosfärens dämpning är större för beräkningsfall som resulterar i högre utsläpp från de tekniska barriärerna. Förutom att skydda kapslarna och begränsa utsläppen, reducerar geosfären alltså också osäkerheter i de uppskattade doserna genom att dämpa dosen mer för de fall som har högre utsläpp från de tekniska barriärerna. För alla probabilistiska fall som beaktats är den effektiva årliga medeldosen åtminstone en storleksordning lägre än dosen som motsvarar SSM:s riskkriterium. För det centrala korrosionsfallet är den

högsta årliga effektiva dosen beräknad till 0,2 µSv/år. Som jämförelse är dosen som motsvarar riskkriteriet ungefär 14 µSv/år och dosen som motsvarar typisk bakgrundsstrålning omkring 1 000 µSv/år.

Sorption på mobila lerkolloider är en process av osäker omfattning som hanteras pessimistiskt genom att försumma ett antal för säkerheten gynnsamma delprocesser. Då denna process inkluderas, är geosfären inte en signifikant barriär mot radionuklidtransport under de kortvariga perioder då höga kolloidkoncentrationer är möjliga. Dessa perioder är dock kortvariga och utsläppstakten från närzonen är tillräckligt låg för att hålla dosekvivalenta utsläpp under dosen som motsvarar myndigheternas riskkriterium.

Resultat av beräkningar med förenklade analytiska modeller stämmer väl överens med resultat från de numeriska modellerna. Överrensstämmelsen stärker tilltron till de dosekvivalenta utsläppsberäkningarna av två anledningar. Dels ger jämförelsen en viktig kvalitetskontroll av den numeriska modelleringen av dosekvivalenta utsläpp och dels visar den att potentiella doser kontrolleras av relativt enkla processer som är okomplicerade att förstå och modellera.

Contents

1 Introduction

This report presents radionuclide transport calculations for the assessment of post-closure safety in SKB's Preliminary Safety Assessment Report (PSAR) for a final repository for spent nuclear fuel at Forsmark. In order to start the construction of the final repository, SKB is required, under the Act on Nuclear Activities, to obtain an approval of the PSAR, see further Chapter 1 of the **Post-closure safety report**.[1] As described in Section 2.5.12 of the **Post-closure safety report**, the present report is one of 16 main references for the **Post-closure safety report** and is there referred to as the **Radionuclide transport report**.[2]

Calculations of radionuclide release, transport and dose consequences for different scenarios and cases are important components of the assessment of post-closure safety. This report quantitatively describes such calculations for all scenarios contributing to the calculated risk for the proposed repository and compares the resulting radiological annual doses to applicable regulatory limits. The report also summarises transport assessments for residual scenarios that were selected to illustrate performance of the repository barrier systems.

An 11-step methodology is applied for the PSAR post-closure safety assessment (Figure 2-2 of the **Post-closure safety report**). This report focuses on Step 9, Analyses of Selected Scenarios with Respect to Isolation and Retardation. In addition, transport-related aspects of Step 2a, Description of Initial Site State and Step 7, Definition and Analyses of Reference Evolution are also described.

Several scenarios that have the potential to cause radionuclide mobilisation and release from the engineered barrier system are identified in Chapter 12 of the **Post-closure safety report**. The current report analyses consequences of the two scenarios identified as the most risk significant: canister failure due to corrosion and canister failure due to shear load. In the 'canister failure due to corrosion' scenario (called briefly the corrosion scenario below) canisters fail as a result of enhanced corrosion due to advective conditions in the deposition hole following the loss of buffer through erosion. In the 'canister failure due to shear load' scenario, canisters fail due to earthquake-induced secondary shear movement along fractures intersecting the canister positions. Details of the two scenarios are discussed in the **Post-closure safety report**. In addition, several residual scenarios that help understand barrier functions of the repository are also analysed.

In addition to the analyses of selected scenarios, this report also briefly summarises site characteristics that affect radionuclide transport. Further, several radionuclide transport/retention processes that are not explicitly included in the PSAR but require further analyses are discussed.

Some aspects of radionuclide transport are discussed in the **Post-closure safety report** and are not discussed here, including dose to non-human biota, risk summation, and gas-phase transport.

The present report is an update of the corresponding report for SKB's previous safety assessment SR-Site (SKB 2010d). Large parts of the previous report are left unchanged. The report also contains the following additional material:

Chapter 7 Complementary calculations for the safety assessment PSAR

Appendix J Safety assessment PSAR – Updated scoping calculations on the depletion of fracture calcite under fresh water infiltration at Forsmark

Appendix K Safety assessment PSAR – Updated calculations on penetration of dilute water

Appendix L Safety assessment PSAR – Input data

Appendix M Safety assessment PSAR – Comparison of PSAR and SR-Site results

[1] To improve readability, abbreviated names in bold font are used here to refer to the PSAR **Post-closure safety report** and its main references. Full report names are provided in the reference list, and in Table 1-1.

[2] The present report is published some time before the submission of the PSAR. In case the need for any changes of the contents of this report arises between its publication and the submission of the PSAR, a report of these changes will be provided in the PSAR.

The results shown in Chapter 4–6 have not been updated since the SR-Site assessment. Instead, in Appendix M, results of recalculations of selected SR-Site cases are compared to the corresponding calculations using updated input data for the PSAR as given in Appendix L. In Appendix M it is concluded that the differences in results are sufficiently limited that the conclusions drawn from the results of the SR-Site radionuclide transport calculations are still valid with updated input data for the PSAR. It is also noted that the demonstration of compliance with SSM's risk criterion in the **Post-closure safety report** is based on the updated PSAR results given in Appendix M, and not on the SR-Site results.

In Appendices J and K, new analyses and calculations related to the penetration of dilute water along recharge pathways are presented. Specifically, in Appendix J effects of calcite depletion and rock mineral weathering along a recharge path are assessed, while in Appendix K dilute water penetration calculations along recharge pathways are presented. The analyses and results of these two appendices are not further discussed in the present report but are used in the assessment of canister failure in the **Post-closure safety report**. The motivation for including the two appendices in the present report is that they strongly relate to the solute transport discipline.

Table 1-1. Abbreviated report names used in this report and their full references.

Abbreviation used when referenced in this report	Full reference, as given in the reference list
Buffer, backfill and closure process report	**Buffer, backfill and closure process report, 2022.** Post-closure safety for the final repository for spent nuclear fuel at Forsmark – Buffer, backfill and closure process report, PSAR version. SKB TR-21-03, Svensk Kärnbränslehantering AB.
Canister production report	**Canister production report, 2022.** Produktionsrapport Kapsel. SKBdoc 1407944 ver 2.0, Svensk Kärnbränslehantering AB. (In Swedish.) (Internal document.)
Climate report	**Climate report, 2020.** Post-closure safety for the final repository for spent nuclear fuel at Forsmark – Climate and climate related issues, PSAR version. SKB TR-20-12, Svensk Kärnbränslehantering AB.
Data report	**Data report, 2022.** Post-closure safety for the final repository for spent nuclear fuel at Forsmark – Data report, PSAR version. TR-21-06, Svensk Kärnbränslehantering AB.
Fuel and canister process report	**Fuel and canister process report. 2022.** Fuel and canister process report for the final repository for spent nuclear fuel at Forsmark – PSAR version. SKB TR-21-02, Svensk Kärnbränslehantering AB.
Geosphere process report	**Geosphere process report, 2022.** Post-closure safety for the final repository for spent nuclear fuel at Forsmark – Geosphere process report, PSAR version. SKB TR-21-04, Svensk Kärnbränslehantering AB.
Model summary report	**Model summary report, SKB 2022.** Post-closure safety for the final repository for spent nuclear fuel at Forsmark – Model summary report, PSAR version. SKB TR-21-05, Svensk Kärnbränslehantering AB.
Post-closure safety report	**Post-closure safety report, 2022.** Post-closure safety for the final repository for spent nuclear fuel at Forsmark – Main report, PSAR version. SKB TR-21-01, Svensk Kärnbränslehantering AB.
Spent fuel report	**Spent fuel report, 2021.** Använt kärnbränsle att hantera i KBS-3-systemet. SKBdoc 1380282 ver 3.0, Svensk Kärnbränslehantering AB. (In Swedish.) (Internal document.)

2 Processes and site characteristics affecting transport

This chapter has not been updated since the SR-Site assessment (SKB 2010d), with the exception of the new Section 2.2.3. In a few places, references in the SR-Site version were made to the main references of the SR-Site assessment, the references written in bold. It has been verified that the PSAR versions of the corresponding reports are equally valid as references in these cases. The references in bold, therefore, refer to the PSAR versions.

The migration of solutes through fractured rock is dependent on a number of processes and variables. These are outlined in the **Geosphere process report** and can generally be categorised as being either geological (i.e. relating to microstructural properties of the rock), hydrogeological (i.e. relating to flow), or hydrochemical in nature (i.e. relating to groundwater chemistry). Although the migration of solutes can also be related to a broader class of reactive transport processes governing groundwater composition, in this chapter the focus is primarily on features and processes of importance for the transport of radionuclides from canister positions in the repository to the biosphere.

In this context, geological factors of importance relate primarily to the existence of a hydraulically connected fracture system traversing the repository volume as well as the flow-wetted surface and microporous structures both immediately adjacent to fracture surfaces and within the deep rock matrix. Although there is considerable overlap in the ontological description of features and processes that are considered geological and those categorised as being hydrogeological, both are important for the overall description of radionuclide transport processes. Hydrochemical features include the groundwater chemistry parameters that govern the solubilities of radionuclides and influence the chemical reactions of nuclides with geological materials lining flowpaths through the near field, far field, and biosphere. Hydrochemical features, although more precisely differentiated than geological or hydrogeological entities in this description, are still strongly dependent on the couplings between geology, flow and chemical reactions involving other non-nuclide groundwater chemical constituents. The following sections give an overview of the main features.

2.1 Flow

Groundwater flow is a primary control on radionuclide migration in the subsurface. The groundwater flow system at Forsmark has been studied extensively and is described in detail in Section 10.3.6 of the **Post-closure safety report** and supporting documents. At present, flow at Forsmark is primarily vertically upward from the repository to a shallow bedrock aquifer associated with large, nearly horizontal fractures/sheet joints because of the effects of a local topography-driven flow cell, then horizontally in the shallow bedrock aquifer to discharge locations at topographic lows (Follin 2008).

The existence of flow in fractured rock, its spatial distribution, and temporal variability are strongly governed by the geological characteristics of the site and hydraulic boundary conditions. In some situations, flow may be relatively evenly distributed throughout the available flow space, although in-situ observations suggest (e.g. Abelin et al. 1991a, b, 1994) that it is more likely to be channelised to varying degrees. Channelised flow can arise spontaneously on the level of regional fault structures and more local scale heterogeneous fracture networks where water flow preferentially follows the path of least resistance in connected hydraulic features. A comprehensive modelling approach is used to represent the effects of such channelling at Forsmark. The modelling approach uses a combination of discrete fracture network (DFN), continuous porous medium (CPM), and equivalent continuum porous medium (ECPM) models. The latter class of models represents flow in fractured rock by upscaling a DFN representation to a CPM representation. Models of flow during the temperate period use nested DFN/ECPM models with explicit CPM representation of tunnels, boreholes and near-surface soil layers. Modelling of flow during the glacial and periglacial periods has been carried out using ECPM representations without explicit representation of the repository engineered features.

Regardless of how the flow modelling is carried out, flow-related input to transport calculations is limited to three parameters: equivalent flow rate at the canister (Q_{eq}), the advective travel time (t_w), and the flow-related transport resistance (F). Definitions for these "flow triplet" parameters may be found in Joyce et al. (2010).

The flow triplets vary spatially and by realisation of the stochastically generated DFN. The Q_{eq} varies by canister location, release path (see Section 3.3), and DFN realisations. The t_w and F parameters are properties of the flowpath connecting a near-field release location to a geosphere discharge location. Thus, a unique pair of t_w and F is required for each combination of DFN realisation, canister location, near-field release path, and flow path through the geosphere. Depending on the transport code being used (3.6), spatial variability of t_w and F along the flow path may also be represented (e.g. element by element in a finite element representation of the flow). Cumulative distributions of F for different realisations of the hydrological model are found in Joyce et al. (2010). Within each realisation, the F values associated with different deposition holes span a large range.

The flow and transport modelling approach used represents spatial variability and channelling phenomena down to the level of individual fractures. Channelling phenomena can occur at even smaller scales because of physical features such as enlarged fracture intersections or within-fracture variability in fracture aperture. Channelling at the sub-fracture scale is not represented. Technical bases for neglecting within-fracture channelling are discussed in Section 2.1.1 and Appendix A.

Future glacial cycles are expected to have significant effect on groundwater flow (**Climate report**). For most of the transport scenarios analysed here and in the **Post-closure safety report**, these effects are ignored and steady temperate-period flow and chemical conditions are assumed. Selected modelling cases presented later in this report are used to assess the impacts of climate variability and show that the temperate-period results provide a reasonable approximation to peak mean annual dose. Section 2.1.2 describes how flow evolution on a glacial cycle is represented in those selected modelling cases.

2.1.1 Spatial variability and the nature of channelised flow

On the scale of single fractures, the existence of a heterogeneous transmissivity field may result in the merging of flow lines in high velocity regions of the fractures. Owing to the limited spatial extent of these regions, this merging may decrease the F of certain parts of the fracture relative to the estimate representing the average flow smeared evenly over the whole fracture surface. As shown by Cvetkovic et al. (1999) increasing amounts of fracture-scale heterogeneity results in a broadening of the F and t_w distribution and an increasing statistical average of these variables. Although an increasing average implies enhanced retardation, this does not apply to the fast flowpaths in the fracture, which are of most relevance for safety assessment calculations. When considering the fracture as a whole, broadening of the F and t_w distributions implies both a greater frequency of fast flowpaths together with a greater frequency of slow flowpaths at the expense of middling flowpaths. Furthermore, this does not consider the location or extent of the solute source nor the setting in which individual fractures reside (i.e. in a heterogeneous three dimensional network of connected structures). For this reason it is important to not only consider heterogeneity on the level of individual fractures, but also effects arising on the larger scale of the fracture network itself which also includes consideration of hydraulic boundary conditions and source term locations relevant for the solute transport under consideration.

Calculations made by Painter (2006) indicate that internal variability in transport aperture and transmissivity has only a minor effect on the estimated F and the t_w provided the internal variability is not greater than the fracture-to-fracture variability. One cause of the insensitivity is a "choke-point effect" caused by the fact that fluid can enter and leave a fracture only on limited areas, thereby constraining the flowpath geometries. The overall effect of fracture-to-fracture transmissivity variability and hydraulic connectivity are referred to collectively as network scale effects in this report. In cases where the network scale variability was less than the internal fracture variability, more severe channelling resulted in a greater frequency of fast flowpaths with reduced F. Although these calculations were made for non-contacting fractures, similar results are likely for fractures with asperity contacts since the flow naturally tends to seek out the path of least resistance. This does not necessarily mean that flow channelling is unimportant but merely that the effect in many cases may be weak in relation to the impact of network scale stochastic variability.

The problem remains, however, how to adequately account for flow channelling in safety assessment calculations when it is not possible to make large scale hydrogeological simulations with sufficiently well resolved spatial variability (i.e. on the level of individual fractures) to adequately capture important flow channelling phenomena. Since the flow in sparse, heterogeneous fracture networks tends to be governed by network scale effects, the issue essentially boils down to estimating the effective flow-wetted surface that channelised flow makes contact with in individual fractures. In the previous SR-Can safety assessment (SKB 2006a) this was handled by a heuristic assumption that the F value should be pessimistically reduced by a factor of ten relative to that estimated based on average fracture transmissivities and the assumption of flow contact with entire fracture surfaces. This was not based on any specific quantitative reasoning, but primarily on subjective expert judgement under the assumption that the bulk of the flow might only contact about 10 % of the total fracture surface area.

In the SR-Site and PSAR safety assessments, the F value is not reduced by a factor of ten as was done previously since this is considered to be an unnecessarily pessimistic assumption for three reasons. First, fracture-to-fracture variability is generally larger than within-fracture variability in aperture. Second, fluid can only enter and leave fractures on limited area, significantly constraining the meander of flowlines (Painter 2006). Third, substantial portions of the non-contacting fracture surface area outside of the dominant flow channels may still be accessible by diffusion within the fracture pore space and thus provide additional surface area for radionuclides to interact with the rock matrix. While this type of transverse dispersion can usually be neglected on the timescale of tracer tests performed in fractured rock, it is of great significance at safety assessment timescales where rates of diffusive mass transfer can become commensurate with the rate of advective transport. On balance this means that non-scaled F ranges can often be assumed for transport calculations even in the presence of significantly channelised flow without introducing large errors provided a set of reasonable conditions can be fulfilled. Calculations detailing the conditions under which this assumption is considered reasonable are presented in Appendix A.

2.1.2 Evolution of flow over a glacial cycle

Understanding of climate evolution at the Forsmark site is described in detail in the **Climate report**. Future glacial cycles will have a significant effect on groundwater flow and chemistry. For most of the transport scenarios analysed here and in the **Post-closure safety report**, these effects are ignored and steady temperate-period flow and chemical conditions are assumed. Selected modelling cases presented later in this report are used to assess the impacts of climate variability and show that the temperate-period results provide a reasonable approximation to peak mean annual dose.

In those selected modelling cases that include unsteady conditions, a pessimistic abstraction of the groundwater flow field evolution is used in place of the full details of the flow and chemical evolution during a glacial cycle. A simplification of the glacial cycle is developed in the **Climate report** to support the abstraction, see Figure 2-1. The simplified cycle has two temperate periods, three periglacial periods, two glacial periods, and two submerged periods in the 120 kyr cycle. It is noted that the summed percentages of each climate period coincides with the corresponding percentages for the original, non-simplified cycle. In the abstraction, the cycle repeats 8 times in the 1 million year assessment period of interest. Table 2-1 provides times for each flow change in the first 120 kyr cycle.

Detailed simulations of transient flow during a glacial cycle have been undertaken (Vidstrand et al. 2010). These simulations show that both the direction and magnitude of groundwater flow are affected by the glacial cycle. As an alternative to representing the full details of transient groundwater flow fields in the transport simulations, a pessimistic bounding abstraction is developed. The abstraction includes changes in flow magnitude, but uses pathlines from the temperate period (Joyce et al. 2010) and ignores changes in flow direction. This abstraction is pessimistic because it greatly overestimates the vertical component of the flow velocity compared with detailed simulations (Vidstrand et al. 2010), and also ignores lengthening of the flow paths that may occur during some of the climate periods.

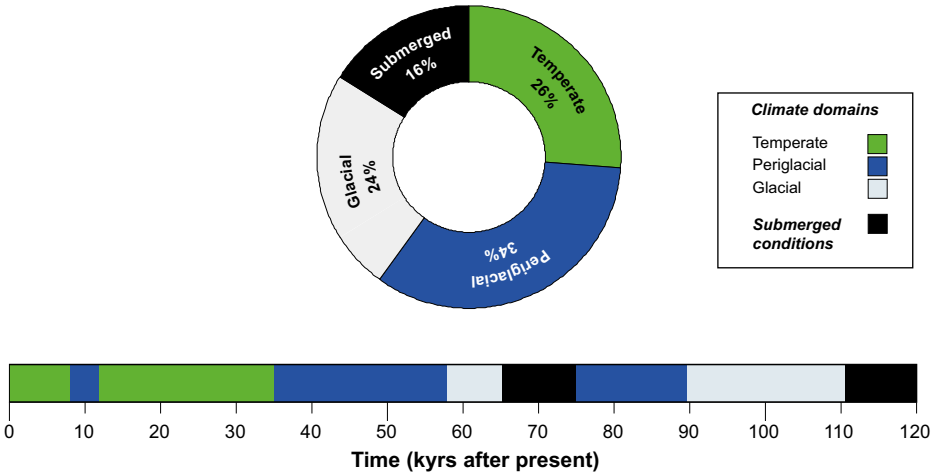

Figure 2-1. *Simplified glacial cycle for use in the geosphere transport assessment (modified from* ***Climate report****, Figure 4-37).*

Table 2-1. Duration of each climate period in the simplified 120 kyr cycle (Climate report, Table 4-7). The percentage of each accumulated period is also indicated.

Period	Calendar time (kyrs)	Duration (kyrs)	Accumulated duration (kyrs)
Temperate	0–8	8	8
Periglacial	8–12	4	4
Temperate	12–35	23	8 + 23 = 31 (26 %)
Periglacial	35–58	23	4 + 23 = 27
Glacial	58–65	7	7
Submerged	65–75	10	10
Periglacial	75–89	14	27 + 14 = 41 (34 %)
Glacial	89–111	22	7 + 22 = 29 (24 %)
Submerged	111–120	9	10 + 9 = 19 (16 %)

The glacial periods summarised in Figure 2-1 and Table 2-1 need to be further subdivided into advancing, glacial maximum, and retreating phases because the groundwater velocity will be very different in these three phases. For the advancing ice sheet, it takes 366 years for the ice sheet to move between ice front locations I and IV, see Vidstrand et al. (2010) for details. For the retreating ice sheet it takes 61 years to move between ice front locations IV and I. As an approximation, it is judged that when the ice front is beyond these ice front locations, the influence of the ice front on the repository will be small, i.e., conditions close to periglacial or submerged will prevail. However, even beyond these times, there is some influence, even if not comparable to the peak, see Figure 2-2, which shows the Darcy flux at repository depth within the repository footprint (measurement locality 2 in Vidstrand et al. 2010). Specifically, during the ice advance, the increase in Darcy flux relative to temperate conditions prevails approximately for 2,000 years. It is decided to represent the glacial advancing period as having duration of 1,800 years, which is much longer than the time to move between ice front locations I and IV, but slightly shorter than the time 2,000 years. The more rapid retreating phase is modelled as having duration of 300 years; i.e., the ratio in duration between advance and retreat phases is maintained. It is also noted that the increase in Darcy flux during the advancing phase is smaller than during the retreating phase. This is due to the fact that the advancing phase is characterised by permafrost in front of the ice sheet, whereas the retreating ice sheet is warm based such that no permafrost is present, see Vidstrand et al. (2010) for details.

Flow scaling factors for each climate domain are obtained from the calculated Darcy flux distributions at deposition hole locations in the super-regional groundwater flow model of Vidstrand et al. (2010). In Figure 6-18 of Vidstrand et al. (2010), the maximum, median, and minimum Darcy flux distributions are shown normalised by the temperate period value. The normalised median values from Figure 6-18 of Vidstrand et al. (2010) and the duration of each flow epoch from Table 2-1 are used to obtain time-

dependent flow factors (Figure 2-3). In developing the flow factors, the glacial state with a 2-km tongue of permafrost was assumed for the glacial advancing period, and the glacial state without permafrost was assumed for the glacial retreating phase. The latter assumption is regarded as slightly pessimistic because the fluxes in the glacial case without permafrost of Vidstrand et al. (2010) were developed for an advancing ice sheet but applied here for a retreating ice sheet. In the far-field calculations with MARFA, the t_w and F for the temperate period are inversely scaled by the values in Figure 2-3 to obtain corresponding values for other stages in the glacial cycle.

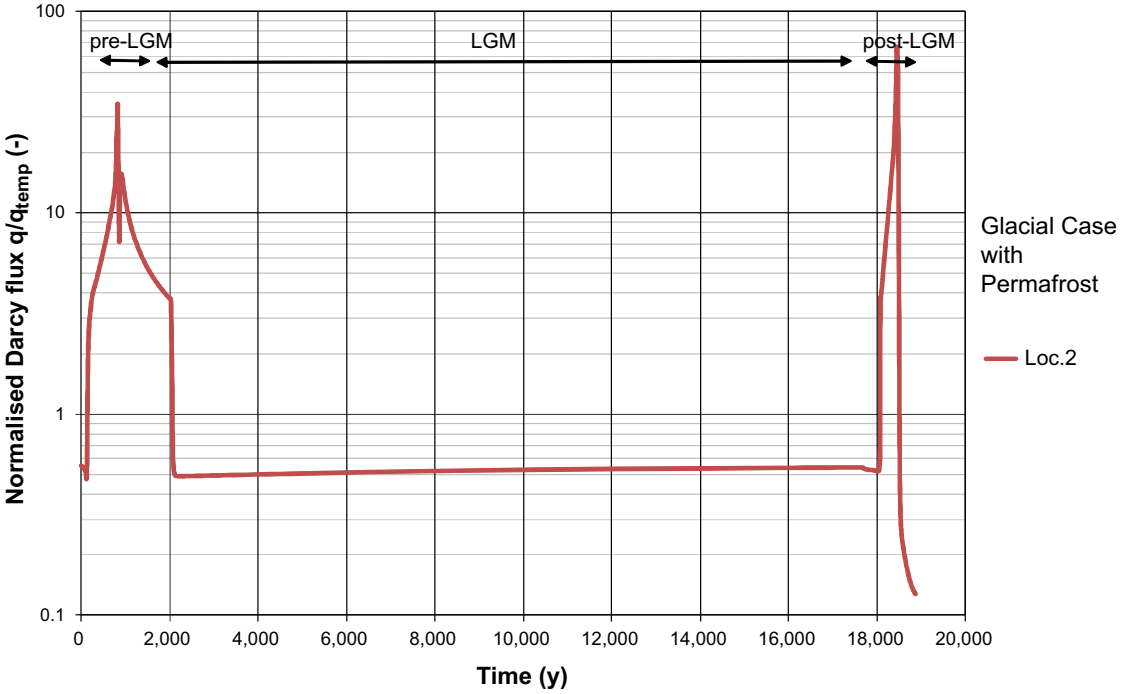

Figure 2-2. *Change in Darcy flux relative to the temperate period as the ice sheet advances and retreats over the repository location. Figure is modified after Figure G-12 (Appendix G) of Vidstrand et al. (2010).*

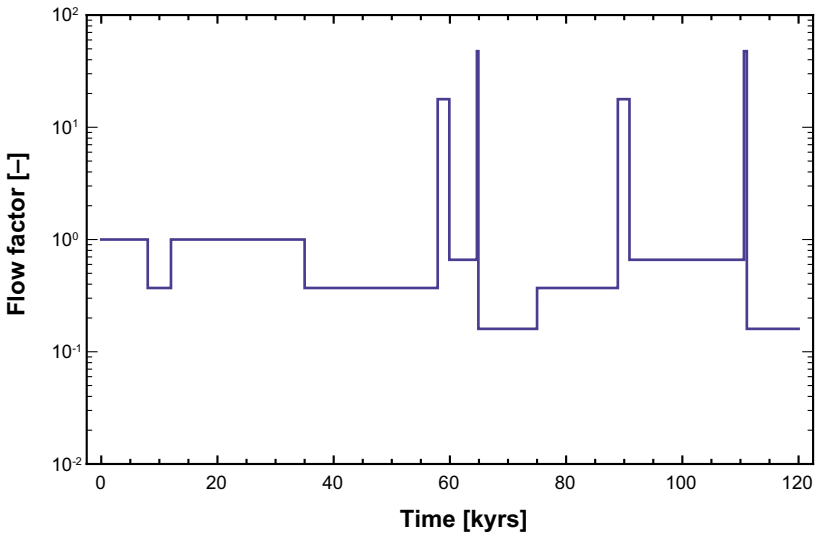

Figure 2-3. *Flow scaling factors for one glacial cycle (of eight during 1 million years) for use in far-field radionuclide transport simulations. The spikes at the end of the two glacial periods have duration of 300 years (not resolved on this scale). The scaling factor is defined relative to the Darcy flux in the temperate period and is used to adjust both advective travel time and flow-related transport resistance.*

2.2 Chemistry

A broad overview of chemical processes of relevance for the safety assessment is given in the **Geosphere process report**. In this section, chemical processes of specific importance for radionuclide migration in the far field are described. The chemical composition of groundwater and the reactions between aqueous solutes is of great importance for understanding the sorption processes that give rise to the transport retardation effects modelled.

Although the partitioning of nuclides between the aqueous and surface sorbed phases is treated in a simple fashion using a linear isotherm (K_d) approach, it is important to remember that the conditional K_d value is simply the ratio of immobilised and dissolved solute that is specific for a particular solid phase composition, water chemistry, and solute concentration and does not rely on any particular mechanistic argumentation regarding underlying sorption processes. Here, the term sorption is used to describe adsorption processes involving ion-exchange and surface complexation. Ion-exchange refers to the electrostatic interactions of dissolved solutes with permanently charged sites of minerals, usually phyllosilicates. Surface complexation, however, refers to the interactions of dissolved solutes with surface reactive groups on mineral surfaces. Inner sphere surface complexation involves covalent bonding of solutes to these reactive groups, whereas outer-sphere surface complexation refers to the electrostatic interaction of solutes with the reactive groups.

By their very nature, surface reactive groups are sensitive to the groundwater composition, in particular pH, and the relative abundance of binding sites is therefore strongly dependent on groundwater chemistry. Nuclides sorbed by way of ion-exchange or outer sphere surface complexation are sensitive to ionic strength since the electrostatic interactions are weak and they can easily be displaced by competing solutes. Nuclides that form inner sphere surface complexes are typically considered less sensitive to ionic strength on account of their stronger bonds with the surface.

Direct and indirect competitive effects involving other dissolved species in groundwater influence sorption of nuclides. Direct effects involve the presence of other groundwater solutes that, owing to their much higher concentration, compete against nuclides for a limited number of sorption sites even if they sorb less strongly than the migrating nuclide. Reactive ligands in solution such as carbonate and hydroxyl ion also compete with sorption sites to bind radionuclides in the form of aqueous complexes. This is an example of an indirect competive effect. In general the free concentration of a solute makes up a variable part of the total dissolved concentration of a substance. The distribution of a nuclide between its various complexed forms (i.e. its speciation) has a strong influence on the overall magnitude of sorption.

There are a number of different ligands present in groundwater that may influence the speciation of radionuclides. Chief among these are hydroxyl ions (involved in hydrolysis), carbonate, and to a lesser extent chloride. Depending on redox conditions, the presence of sulphate or sulphide may also play a role in radionuclide speciation. Certain nuclides are highly sensitive to redox potential and can switch between largely immobile forms under reducing conditions to relatively more mobile forms under oxidising conditions. The redox potential at which a transition is thermodynamically possible from reduced to oxidised forms is also influenced by pH and carbonate concentration.

The two key variables that govern a large portion of radionuclide speciation are the pH and carbonate concentration (or equivalent partial pressure of carbon dioxide). These are considered to be of primary relevance for the sorption of many of the radionuclides, particularly those that sorb by way of a surface complexation mechanism. For solutes that sorb principally by ion-exchange or outer-sphere surface complexation, the concentration of competing solutes given by the total dissolved solids (TDS) or ionic strength is a key variable influencing sorption. Redox speciation is considered separately owing to the overwhelmingly strong control that it exerts on the mobility of certain radionuclides (principally, U, Np, Tc, and Pu).

2.2.1 Spatial variability of groundwater chemistry

The spatial distribution of groundwater composition at different times in the temperate phase of repository evolution is shown in Figure 2-4 for 2 000 years, and in Figure 2-5 for 9 000 years.

2.2.2 Evolution of groundwater chemistry over a glacial cycle

The evolution of groundwater chemistry over time is described in some detail in the **Post-closure safety report** and only a brief overview of the most salient features is given here. Over a glacial cycle the changes in groundwater chemistry are driven by different processes: infiltration of meteoric water in combination with land uplift during the temperate period (*interglacial*), alternating pulses of dilute, glacial melt water and deep saline groundwater during the glacial advance and retreat (*periglacial*), and nearly stagnant conditions when a stable ice sheet exists over the repository. During various parts of the glacial phase, permafrost may also extend to a significant depth in the rock and prevent the flow of water.

The temperate period is characterised by a slow freshening of the groundwater surrounding the repository over many thousands of years under the influence of infiltrating meteoric water. During this period, the groundwater evolves towards lower pH levels and higher carbonate concentrations. This is also likely to result in a steady increase in the redox potential over time. The intruding meteoric water displaces saline water in the fracture system and mixes by diffusive exchange with stagnant water in the rock matrix.

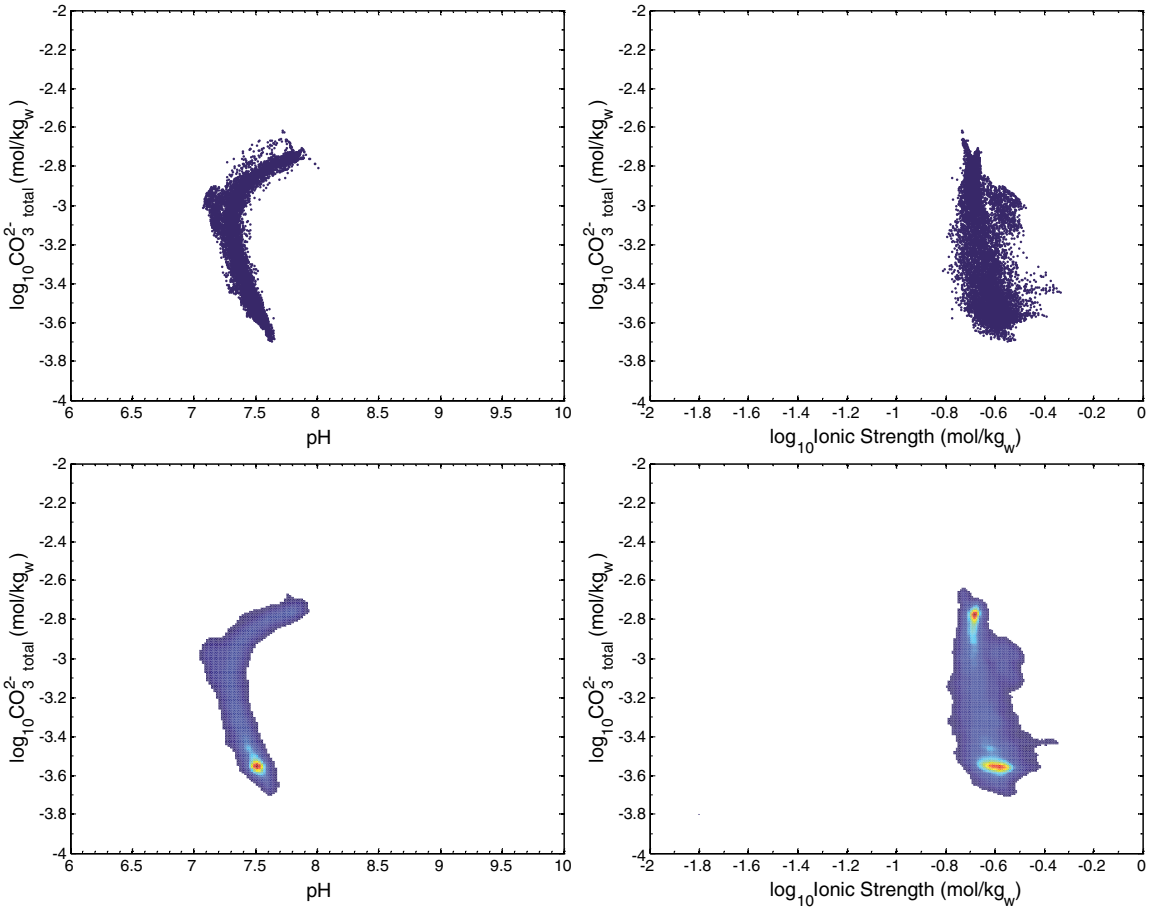

Figure 2-4. *Distribution of groundwater compositions at 2 000 years in the temperate phase of repository evolution. Data are given for total carbonate versus pH (left hand side), and total carbonate vs. ionic strength (corresponding to the data calculated by Salas et al. (2010) and stored on SKB's trac database). The data are visualised in scatterplot form (top) and as a smoothed 2D histogram (bottom).*

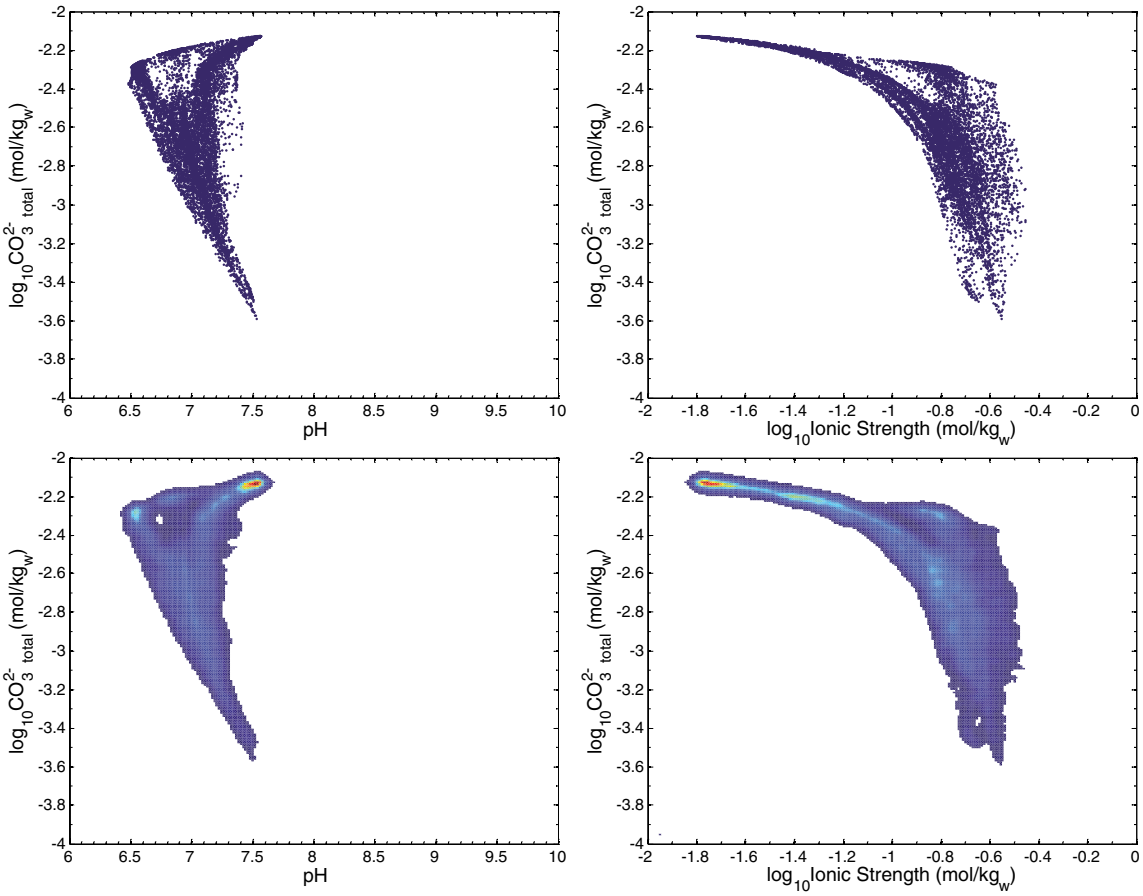

Figure 2-5. *Distribution of groundwater compositions at 9 000 years in the temperate phase of repository evolution. Data are given for total carbonate versus pH (left hand side), and total carbonate vs. ionic strength (corresponding to the data calculated by Salas et al. (2010) and stored on SKB's trac database). The data are visualised in scatterplot form (top) and as a smoothed 2D histogram (bottom).*

During the ice-front advance, the large hydraulic gradient near the advancing front of the ice margin results in dilute glacial meltwater being forced to great depth in the rock before exiting downstream of the advancing front although still short of the repository location. The meltwater comes in part from water under the ice itself held in a liquid state by isostatic pressure and partly from water draining from the surface of the ice through moulins near the ice margin. The disturbance in hydrogeological conditions displaces the existing saline water in the fracture system forcing it downwards and forwards. This results in saline upconing of deep brine groundwater to shallower depths in the repository vicinity. As the ice margin approaches and passes over the repository, the flows are partly reversed and melt-water may penetrate the repository environment. Since the hydraulic connectivity of the fracture system and conductivity of the rock is very heterogeneous, some recharge flowpaths experience very large and rapid changes in groundwater chemistry, whereas others are hardly affected. Generally it is the flowpaths characterised by high Darcy fluxes and low F values that experience the greatest changes.

After the ice margin has passed, the flow gradually decreases until at some point nearly stagnant conditions are achieved owing to the extremely low hydraulic gradients under the main part of the ice sheet and the influence of permafrost, which reduces inflows to the groundwater system. The large mass of ice on top of the land mass simultaneously pushes down on the crust, which has an influence on hydraulic conductivity of the rock. During this phase of the repository evolution, flows are much reduced relative to the temperate phase and flowpaths are longer to the discharge locations downstream of the ice front. Salt stored in the rock matrix begins to diffuse back out into the diluted fracture water and slowly restores salinity in the fracture system.

As the ice front begins to retreat, a similar sequence of processes is set in motion although in reverse. In this case, the newly re-established saline groundwater in the fracture system is rapidly flushed out by the forced intrusion of meltwater in the vicinity of the ice front. After the retreating ice front passes

over the repository location, additional episodes of saline upconing may occur. After the ice front has retreated even further, the saline conditions typical of the temperate period becomes slowly re-established. At this time, the isostatic load of the ice will depress the crust and result in the repository site being inundated with marine water and under sea level.

The subsequent uplift of the crust due to glacial rebound will slowly change the shoreline location and topographic elevation of the land relative to the sea. The slowly changing topographical conditions and shoreline results in the repository eventually becoming an inland location. The slowly evolving hydrogeological situation then results in a gradual freshening of groundwater in the repository environment due to infiltrating meteoric water and a return to temperate conditions.

Although this paints a broad picture of the main sequence of events characterising an individual glacial cycle, it is important to also consider that such cycles can be expected to reoccur with a predetermined periodicity and possibly deepening intensity with time as described in the **Climate report**. There may also be transients (e.g. stadial and interstadial periods) and shorter glacial/interglacial periods over the total 120 ka timespan of the full glacial cycle. In the radionuclide transport calculations, however, a much simpler tableau of glacial evolution is considered as indicated in Figure 2-1.

2.2.3 Impact of elevated pH conditions

The uncertainties in the chemical evolution of groundwater are implicitly considered in the derivation of K_d values for radionuclides, which is discussed in the context of the salinity and redox potential (Eh) of the groundwater (Crawford 2010). Parts of the geosphere, however, may experience an altered pH level relative to the site investigation data owing to the use of large quantities of cement in the repository including rock reinforcements and plugs (Bath 2012). This altered state relative to the initial conditions may persist for very long periods as the cement phases degrade slowly. To demonstrate qualitatively the effect of alkaline leachate from cementitious construction materials on K_d values and radionuclide retention, a supplementary study has been carried out in Crawford (2014). The performed calculations indicate that the presence of construction materials such as cement in the repository should not have a significant impact on far-field dose rates provided the high pH (> 10) plume has only a limited spatial persistence along discharge paths associated with leaking canisters. The conclusion is further supported by that canister failures are expected only after about one hundred thousand years and then only at high flow locations. It is quite unlikely that elevated pH conditions would persist at such locations so long after repository closure.

The study does not analyse the effect of local use of cement in the expected flow pattern, but a more pessimistic approach has been used instead. In the rock where high Silica cement or ordinary Portland cement (OPC) has been used, there may be local changes in the retardation, for example for some of the most important and dose-contributing radionuclides in the far-field. The local effects are depending on where in the rock the cement is used, the dissolution of the cement and the flow pattern in the fractured rocks. Previous studies have shown that water with potential high pH from the solution of OPC does not reach down to repository depth in any major extent (Sidborn et al. 2014, Molinero et al. 2016).

2.3 Background levels of naturally occurring radionuclides

A number of nuclides belonging to naturally occurring U-series decay chains are present in the groundwater at Forsmark. To place in context the mean annual effective doses calculated later in this report, it is useful to have an estimate of the corresponding dose from the naturally occurring radionuclides.

Activities of U-238, U-234, Th-230, Ra-226, and Rn-222 (belonging to the U-238 decay chain) have been measured during the site investigations as well as Th-232, Ra-228, Th-228 (belonging to the Th-232 decay chain), and U-235 (Laaksoharju et al. 2008). If one excludes Rn-222, the largest contributors to the natural background activity in Forsmark groundwater are Ra-226, U-238, and U-234. These nuclides are shown in Figure 2-6 as a function of sampling depth. Generally, it is found that Ra-226 activities are greatest at depth with a slight decrease towards the surface. The opposite behaviour is observed for U with the lowest activities found at depth with a steady increase

towards the surface. Both these trends are in broad qualitative agreement with the understanding of groundwater chemistry at the site. The groundwater activity of Ra, for example, is well correlated with TDS (more so with Ca concentration) indicating a geochemical control by way of ion-exchange or possibly solid solution involving calcite. Barite, which forms solid solutions with Ra, does not appear to be present in significant amounts in Forsmark fracture minerals, an observation which is consistent with the only weak correlation between dissolved Ba and Ra concentrations at the site. The decreasing trend of U activities with depth appears to be coupled to the decreasing redox potential and carbonate concentration at increasing depths. Most sampled groundwaters at Forsmark have a U-234/U-238 isotope ratio between 2–3 (Sandström et al. 2008).

Assuming that the arithmetic average of sampled nuclide activities can be taken to be approximately representative of the situation existing at 2000 AD in the corrosion scenario (central case), a comparative estimate of far-field release rates arising from these naturally occurring nuclides can be made. The release rate (Bq/yr) of naturally occurring nuclides can be estimated by multiplying the arithmetic average of the measured groundwater activities (Bq/m^3) with the discharge flux v_{ex} (m^3/m^{2}yr) and surface area a_{ex} (m^2) for release:

$$N_i \approx \overline{A}_i \cdot v_{ex} \cdot a_{ex} \qquad 2\text{-}1$$

Since the naturally occurring background of dissolved nuclides is not restricted to the local or even the regional scale model area, the total release rate depends on the landscape surface area assumed to make the calculation. In order to make a relevant comparison with the anthropogenic dose rates, some reference area needs to be assumed. For the purposes of the safety assessment, the most appropriate reference area is the predicted area for hypothetical nuclide release from the repository. The particle tracking calculations used to estimate surface exit locations in the central case are used to estimate this area in this analysis. The surface exit locations at 2000 AD for all realisations of the hydrogeological semi-correlated case (cf. Table 4-1) are shown in Figure 2-7. The relevant surface area was estimated by binning the particle release locations into a 2D histogram with 40 m × 40 m cells and calculating the area of occupied cells.

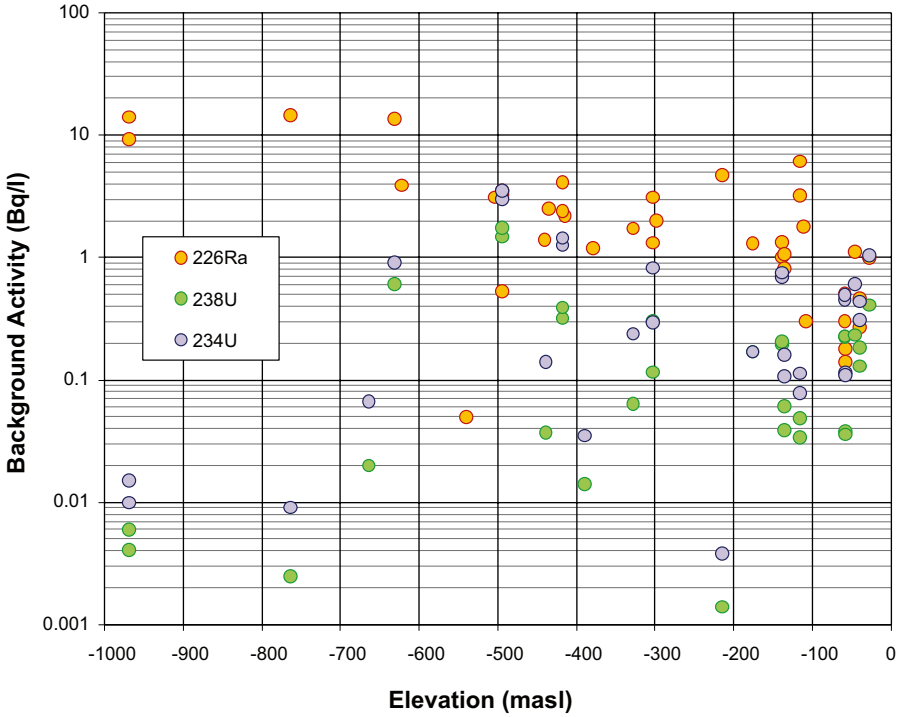

Figure 2-6. *Typical background activities of the main naturally occurring radionuclides of interest in groundwater at the Forsmark site (Laaksoharju et al. 2008) (numerical values are taken from the SKB SIMON database). Rn-222 is neglected on account of its gaseous form and consequent rapid dilution in the biosphere (it is also neglected in the calculation of far-field dose rates owing to its low relative contribution to radiological risk).*

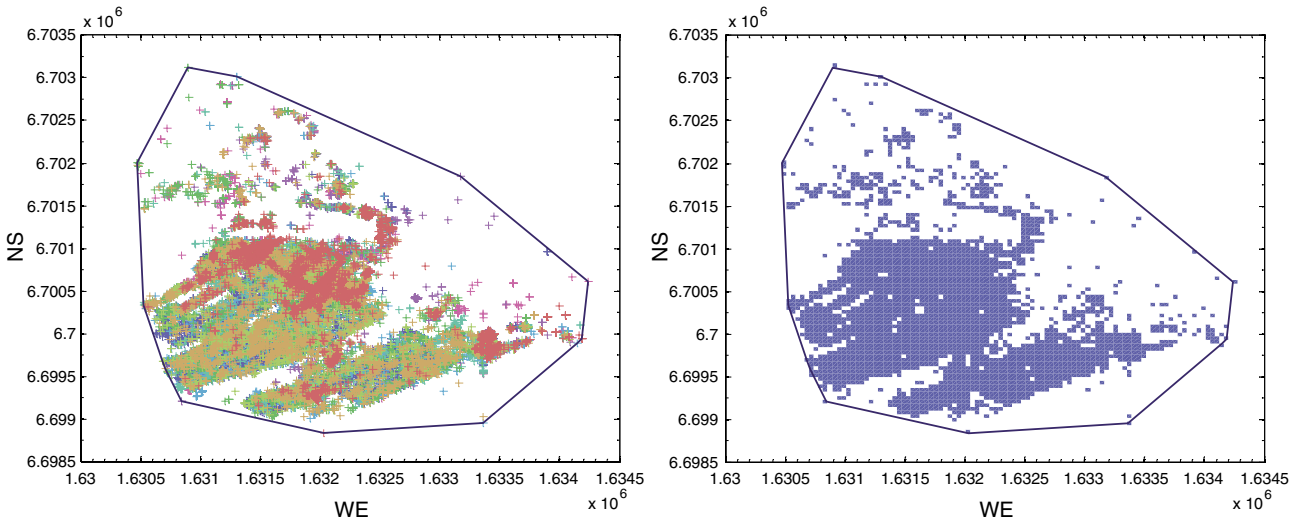

Figure 2-7. *Particle exit locations at 2000 AD for all realisations of the hydrogeological semi-correlated case (left). The approximate footprint of particle release locations for all simulations taken together as an ensemble is also shown (right) where particles are sorted into a 2D histogram of 40 m × 40 m cells. The convex hull of the full set of release locations is also shown as a reference (blue outline).*

The arithmetic mean of the groundwater activity is deemed an appropriate measure of groundwater activity since the total release of nuclides represents a summation of groundwater activities originating from many different flowpaths. In accordance with this, the standard error of the mean activity is deemed the relevant measure of uncertainty. The individual realisations of the hydrogeological model, however, may be considered as all equally valid with regard to estimated release area. This means that the variance of the estimated area between realisations must be treated as a data uncertainty rather than a measure of variability, given that in reality there should be only one true value of the release area for a given set of boundary conditions.

Since the release area estimate is based on only a limited number of realisations, it is necessary to calculate an expanded range of uncertainty that explicitly takes the limited sample size into account. If it is assumed that the uncertainty of the estimated area can be modelled as a lognormally distributed variable, then the correct form of the expanded uncertainty range is given by the student-t distribution. A lognormal measure of the uncertainty is considered appropriate in this case since the variation of the particle release area between realisations is sufficiently large that it would imply negative areas if treated as a normally distributed uncertainty. Based on nine realisations of the hydrogeological model, the release area and its expanded uncertainty range are therefore estimated to be $(1.9 \pm 1.7) \times 10^6$ m^2. If, on the other hand, the ensemble of particle release locations from all realisations were to be considered together, the estimated release area would be 4.1×10^6 m^2.

The average groundwater discharge in a 5×5 km area surrounding the Forsmark site is given by Follin et al. (2007) as roughly 2.6 mm/yr at an elevation of –100 m. This, however, is only a very approximate estimate since the upward discharge varies with depth and one ideally would need to consider that the discharge rate to the surface consists of water originating from different depths representing different advective recharge histories and most likely different hydrochemical compositions (see Figure 2-8). A large proportion of the upwards flow in the upper 100 m, for example, derives from local flow cells that do not necessarily penetrate very deeply into the bedrock and therefore may not carry representative amounts of naturally occurring nuclides. Based on the depth dependent discharge fluxes calculated by Follin et al. (2007), less than 1 % of the upward water flux at an elevation of –100 m originates from repository depth and only about 13 % originates from elevations less than –200 m. Water sampled at elevations above –100 m is generally more dilute than groundwaters sampled at greater depths owing to the larger turnover of water in the shallower flow cells. Assuming, however, that the average groundwater activity measured at the site and depicted in Figure 2-6 is reasonably representative of the upwelling groundwater at an elevation of about –100 m then an approximate order of magnitude estimate of the natural background nuclide flux can be made. This assumes that none of the naturally occurring activity originating from shallow flow cells contributes in a meaningful way to the overall nuclide flux.

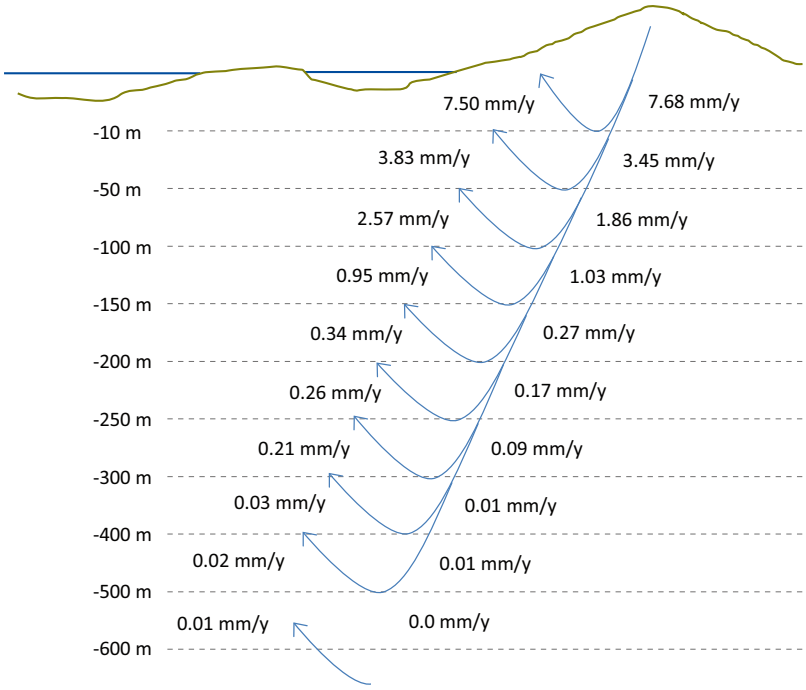

Figure 2-8. *Average vertical groundwater fluxes over a 5 km × 5 km surface area at different elevations at the Forsmark site as calculated by Follin et al. (2007). Since the surface discharge represents a mix of groundwaters with different advective histories, the upward flux at –100 m is chosen arbitrarily as being approximately representative of water carrying the average nuclide activity based on the data in Figure 2-6.*

Table 2-2 gives the mean groundwater activity (Bq/m^3), the estimated mean flux (Bq/m^{2}yr), and estimated mean release of natural background activity (Bq/yr) calculated for U-238, U-234, and Ra-226 at the Forsmark site. Since the mean release (Equation 2-1) is equal to the product of several variables with either normal or lognormally distributed uncertainties, it also has a lognormal uncertainty distribution. The estimated mean release and associated confidence interval given in Table 2-2 implicitly assumes this.

Table 2-2. Summary of natural background activities of naturally occurring radionuclides (U-238, U-234, and Ra-226) estimated flux to the surface, and total release rate within the same release footprint as the semi-correlated case far-field transport calculations.

		Mean activity (Bq/m^3)	Mean flux (Bq/m^{2}yr)	Mean release (Bq/yr)
U-238	Mean CI (95 %)	94.1 ± 31.5 47 – 169	$(2.42 \pm 0.81) \times 10^{-1}$ 0.12 – 0.43	$(4.7 \pm 4.6) \times 10^{5}$ 5.73×10^{4} – 1.68×10^{6}
U-234	Mean CI (95 %)	243 ± 78 125 – 429	$(6.24 \pm 2.02) \times 10^{-1}$ 0.32 – 1.1	$(1.21 \pm 1.18) \times 10^{6}$ 1.52×10^{5} – 4.31×10^{6}
Ra-226	Mean CI (95 %)	1 530 ± 325 995 – 2 260	3.94 ± 0.84 2.56 – 5.81	$(7.61 \pm 7.02) \times 10^{6}$ 1.18×10^{6} – 2.62×10^{7}

2.4 Transport and retention processes

The migration of radionuclides in fractured rock is controlled by a variety of processes including advection and dispersion in water flowing through fractures, diffusion in the water in the pore space of the rock matrix, sorption processes, mineral precipitation/dissolution reactions, and interactions with colloids (**Geosphere process report**). The **Geosphere process report** further identifies the dominant mechanisms as advection/dispersion in flowing water in fractures, diffusion in the water-filled pore space of the rock matrix, and sorption onto mineral grains. These processes are generally

modelled using the advection dispersion equation in the fractures coupled with a Fickian model for matrix diffusion and a linear model for sorption in the rock matrix. Similar processes govern the movement of radionuclides out of the canisters and through the buffer material with the main difference being that precipitation/dissolution may be important within the canister for some radionuclides. Generally, these modelling simplifications of what is in reality a complex, coupled reactive transport process are justified on the basis that the transported radionuclides are extremely dilute, trace components within the groundwater (**Geosphere process report**). However, a few neglected processes require some additional discussion, which is given in the following subsections.

2.4.1 Non-linear sorption processes

A number of different non-linearities can influence the retardation of transported radionuclides. The most direct effect is intrinsic non-linearity where sorptivity is limited by the finite number of binding sites available for sorption. This is most frequently formalised in the Langmuir isotherm where the amount of solute sorbed as a proportion of the aqueous concentration decreases with increasing surface loading up to a maximum monolayer sorption capacity. Where there are multiple surface sites with different reactive characteristics and maximum sorption capacities, the Freundlich isotherm is sometimes used as an approximation. Multicomponent, Langmuirian non-linear behaviour also arises where there is competition between different groundwater constituents for a limited number of binding sites. These types of intrinsic non-linearities are explicitly represented in thermodynamic models of ion exchange and surface complexation.

In many cases, the concentrations of migrating radionuclides are sufficiently low that intrinsic non-linearities do not need to be considered and conditional K_d values appropriate for extremely dilute nuclide concentrations can be assumed. This is frequently the case for radionuclides with strong solubility controls governing the near-field source term. In these cases, although retention in the immediate vicinity of the source may feature strongly non-linear characteristics a transition to approximately linear behaviour is expected after a short migration distance as the release is diluted by the retarded advective transport. The retardation effect achieved over the bulk of the subsequent migration path can then be characterised by approximately linear sorption over the relevant concentration range, all other things being equal.

Even when nuclide concentrations are not dilute, the conditional K_d value may be considered effectively constant if the approximately static background concentration of naturally occurring isotopes establishes the appropriate region of the non-linear sorption isotherm where the conditional K_d value is evaluated. This is particularly relevant for radioelements such as Cs, Ra, U, Sr, Th, and to a lesser extent the naturally occurring rare earth counterparts of the trivalent actinides and lanthanides. Provided the transported concentration of anthropogenic nuclides does not exceed the background levels, the assumption of sorption linearity is an acceptable approximation.

Intrinsic non-linearity is considered relatively straightforward to handle since it is always possible to establish a relevant concentration range over which a conditional K_d value can be defined that pessimistically overpredicts radiological consequences. More important non-linearities, however, relate to the impact of variable groundwater chemistry on the magnitude of the conditional K_d value. Selection of an appropriate K_d value therefore requires careful consideration of the ranges of groundwater chemistry that might be encountered and their spatial and temporal variability. As outlined in Crawford (2010) the K_d data supplied are associated with large uncertainties. A large proportion of this uncertainty relates to variable or uncertain contact solution compositions used in laboratory sorption measurements and how these relate to projected groundwater compositions.

At present it is not possible to quantitatively relate changes in sorptivity with evolving groundwater chemistry for many of the safety relevant nuclides. This is largely due to the lack of sufficiently detailed, multidimensional data sets of unambiguous sorption data for granitic rock types. Also, at any given time the concentration of major groundwater constituents can vary by two or more orders of magnitude throughout the repository volume. As outlined in Section 2.2.1 and 2.2.2 the spatially variable groundwater compositional profile also evolves over time under the influence of the prevailing hydrogeological boundary conditions. Fast flowpaths featuring low F values can be expected to exhibit greater temporal changes in chemical composition than slower flowpaths featuring higher F values. Since groundwater chemistry is not resolved on the level of individual flowpaths through the rock,

a detailed knowledge of how groundwater composition influences the conditional K_d value would not necessarily give narrower bounds of uncertainty for radionuclide transport and it is only possible to speculate on the average impact of changing groundwater compositions throughout the repository volume as a whole. More detailed discussion concerning the neglect of non-linear sorption processes and its justification for the purposes of the safety assessment in the presence of evolving groundwater chemistry can be found in Crawford (2010).

2.4.2 Precipitation and dissolution in the far field

Although precipitation and dissolution processes are considered to be of central importance for determining the source terms for solubility limited nuclides in the spent fuel canisters, these processes are typically disregarded in the far-field transport modelling. Over long time scales it is conceivable that pure phase precipitates of solubility limited nuclides will form outside the canister deposition holes in the near field. The further mobilisation of these nuclide enrichment zones along a migration path is limited by the groundwater flow and solubility equilibria governing the aqueous concentration of the nuclide in contact with the pure phase. For the redox sensitive radioelements, U in particular, the groundwater redox buffering effect arising from the presence of the enrichment zone itself may result in self-limiting transport dynamics which could conceivably give rise to roll front behaviour not dissimilar to that observed in some natural analogues. Immediately downstream of such mineralisations, however, the concentration of the nuclide will be diluted to below the solubility limit by various other retention processes and no longer controlled by pure phase solubility equilibrium. In these locations, the aqueous concentration will instead be governed by solid solutions with fracture filling minerals (discussed in Section 2.4.3) as well as ion exchange and surface complexation with fracture minerals. These processes may be considered to occur in addition to the diffusion and sorption on rock matrix microsurfaces assumed in transport calculations. This is a particularly relevant consideration if the abundance of potential co-precipitating fracture minerals along a flowpath is such that they have a lower overall retention capacity than the sorptive surfaces that can be effectively equilibrated in the rock matrix on the timescale of transport (as the scoping calculations detailed in Appendix B indeed suggest).

The retardation effect that these retention processes impose on the migrating nuclide causes further dilution of the nuclide until it reaches a concentration whereby sorption can be regarded as approximately linear both within the rock matrix and the advective pore space. This hierarchy of retardation processes and the continuous transition from highly non-linear sorption to approximately linear behaviour over a short distance from the repository is one of the main justifications for the assumption of intrinsically linear sorptivity in the far field as already outlined in Section 2.4.1. In an overwhelming majority of studied cases, the natural analogues used to support understanding of radionuclide migration behaviour in the near field and far field exhibit these characteristics outlined above (i.e. a hierarchy of processes active in different parts of the geosphere with increasing distance from the spent fuel analogue). Specific examples of these used in support of the corrosion scenario are discussed in more detail in the **Post-closure safety report**.

The background concentrations of naturally occurring nuclides and non-active counterparts of anthropogenic radioelements, however, in many cases may be governed by solubility equilibria (in particular, U and Th). Deep within the rock matrix, recoil processes due to U-series radioactive decay lead to the accumulation of various U, Th, and Ra isotopes in the pore water until secular equilibrium is attained. Microprecipitates of secondary U(IV) and Th(IV) phases are likely to govern U and Th concentrations in the aqueous phase deep inside the rock matrix. On the other hand, and assuming that solid solution forming minerals such as calcite and barite are absent from the rock matrix, the pore water concentration of Ra is likely to be governed by ion-exchange sorption. Porewater concentrations of rare earth element (REE) counterparts of the trivalent lanthanides and actinides are unlikely to be pure phase solubility limited owing to their extremely low concentrations. The background concentrations of these solutes are therefore largely expected to reflect the effect of surface complexation sorption involving mineral surfaces in the rock matrix.

In the immediate vicinity of fracture surfaces, solubility limiting phases may be absent in which case the formation of solid solutions with ferric oxyhydroxides and hematite as well as ion-exchange/surface complexation sorption will instead control U and Th availability (concentrations of REE are also expected to be influenced by this). Near the fracture surfaces, however, the interplay between redox

buffering due to the weathering of ferrous minerals and the redox potential of flowing groundwater (together with the groundwater pH and pCO_2) govern the redox status of the predominant form of U in the groundwater. Amongst the redox sensitive radionuclides, U is particularly sensitive to groundwater composition and there is considerable evidence from U-series disequilibrium that U has been mobilised as U(VI) and re-deposited as relatively immobile U(IV) many times in the Forsmark fracture system over geological timescales (≥ 1 Ma) (Sandström et al. 2008).

The solubility equilibria governing the aqueous phase concentrations of U and Th deep within the rock matrix coupled with additional surface reactive processes and matrix diffusion near and at the fracture surfaces sets the relevant groundwater concentration range for conditional K_d evaluation even though precipitation and dissolution of these solutes is not directly modelled in far-field transport calculations.

2.4.3 Sorptive interactions with fracture minerals

Secondary minerals in the form of fracture coatings lining the advective flow space are expected to sorb migrating nuclides (both naturally occurring and anthropogenic). Although the term sorption has been used consistently throughout the PSAR reports to refer specifically to ion exchange and surface complexation, the description is extended here to also include surface reactions involving solid solutions with minerals such as calcite, barite, and ferric oxides. There are many different types of minerals present in fracture coatings at the Forsmark site. The most important of these from a perspective of potential nuclide retention, are calcite, hematite, chlorite, and other clay minerals (referred to here as a group although including illite, smectites, and various mixed layer clays).

Chlorite and clay minerals are expected to sorb nuclides by ion exchange and surface complexation interactions whereas calcite and hematite can additionally form solid solutions with migrating nuclides. Although precipitation/dissolution equilibrium is typically neglected in safety assessment on account of the extremely low concentration of transported nuclides (outlined already in Section 2.4.2), solid solutions are extremely relevant for far-field transport processes in the geosphere on account of the fact that, unlike pure phase equilibria, such processes are active already at very low nuclide concentrations.

Generally, the retention processes involving fracture-filling minerals are considered to give an additional transport retardation effect over and above that estimated by the customary handling of retardation by matrix diffusion and sorption on rock matrix microsurfaces. For the central case where static groundwater compositions and flow trajectories are assumed, it is pessimistic to neglect these additional retardation processes because they only serve to lower far-field doses. Throughout the glacial cycle, however, groundwater chemistry is expected to change and in certain situations the neglect of the additional retention processes in the fracture minerals could potentially have negative radiological consequences for the far-field doses. This has been handled by screening calculations of possible changes in solute retention on fracture filling materials as a function of evolving groundwater chemistry, as discussed in Section 2.4.4.

2.4.4 Consequences of neglected retention processes and temporal changes in groundwater chemistry

The neglect of sorption on fracture minerals lining the advective pore space is generally expected to be a cautious assumption given that retention is relatively stronger in the fracture minerals than in the rock matrix. If fracture surface retention processes were to be included in the safety assessment modelling this would give additional retardation of the early breakthrough of transported radionuclides. The fracture minerals that would be expected to contribute most to the enhanced retardation are chlorite and other clay minerals, calcite, and (although to a lesser extent due to low abundance) hematite.

Since the quantity of such minerals lining the fracture space is limited, however, the retention capacity is small and only significant for flowpaths where the retardation effect arising due to matrix diffusion and sorption on rock matrix microsurfaces is weak. On account of the fracture minerals being distributed in a thin layer that is in direct contact with the flowing water, equilibrium sorption can be reasonably assumed for ion-exchange and surface complexation reactions on the timescale of transport.

Based on the statistical abundances of fracture minerals hosted in flow-bearing fractures at Forsmark (Löfgren and Sidborn 2010a), estimates have been made of the additional retardation effect arising due to equilibrium sorption on fracture minerals. On average, there are about 6–14 g of calcite, 2–5 g of chlorite, and 1–2 g of clay minerals per square metre of fracture area in typical flow bearing fractures at Forsmark. Given that the matrix retardation is approximately proportional to the square of the F, the additional retardation due to sorption on fracture minerals is mostly negligible for flowpaths featuring F values greater than 10^4–10^5 yr/m. Although only an estimate, this range may be considered to be an approximately representative transition region that depends additionally on the strength of sorption both in the rock matrix and on fracture minerals. For flowpaths featuring very low F values, on the other hand, nuclide retention on fracture minerals is expected to have a much larger impact on the overall transport retardation (for details see Appendix B). For this reason, the neglect of fracture mineral retention processes is considered a pessimistic assumption in the radionuclide transport modelling.

This reasoning assumes, however, that the evolving groundwater composition does not change in such a way that might lead to a sudden pulse-like release of surface sorbed nuclides under elevated flow conditions, which might occur periodically during a glacial cycle. In a model without explicit consideration of fracture mineral retention, nuclides are sequestered to a greater extent in the rock matrix rather than in association with the fracture minerals where they might be more easily mobilised. For some nuclides this might lead to far-field dose rates being underestimated.

In order to address this issue, consideration has been given to the potential for remobilisation to occur during the glacial IIa (saline upconing) and IVa (glacial meltwater penetration) time domains. These events are thought to be representative of the largest deviations expected from the conditions established during the temperate phase of repository evolution, which comprises the central case. These time domains are also characterised by significantly higher flowrates and lower F values than the temperate phase hydrogeological conditions. Cross plots of the main hydrochemical parameters influencing sorption are shown in Figure 2-9 as an aid to understanding relative changes in sorptivity of nuclides at different times in response to evolving groundwater chemistry.

Here, the impact of changing groundwater chemistry is considered simultaneously for phyllosilicate fracture minerals (i.e. chlorite and clay) and the rock matrix since the primary sorption mechanisms of ion-exchange and surface complexation are the same in each case. A change in groundwater composition, for example, that gives rise to a decrease in rock matrix sorptivity might also be reasonably inferred to give a similar although not necessarily proportionate decrease in sorptivity for fracture filling minerals that feature similar sorption mechanisms.

Fracture calcite, on the other hand, must be considered separately since it may form solid solutions with migrating nuclides. Since calcite does not typically occur within the rock matrix itself, this process is not considered to be a relevant mechanism of nuclide retention in the rock matrix and is therefore not modelled. In order to properly account for the full range of retention processes that might occur in association with fracture minerals, however, one would therefore also need to consider the possible role of solid solution formation with calcite (and possibly barite in the case of Ra-226). For this reason, detailed scoping calculations have been made on the impact of evolving groundwater chemistry on retention by solid solution (see Appendix B).

Since the different sorption mechanisms respond in different ways to evolving groundwater chemistry, they are each considered separately in the following discussions. The overall impact of changing groundwater chemistry on far-field dose rates, however, needs careful consideration of all relevant sorption mechanisms simultaneously in the context of the prevailing hydrogeological situation. This must also be considered in the context of the inventory of nuclides that are actually sorbed by fracture minerals relative to that sequestered in the rock matrix. Since the fracture minerals have a limited capacity for nuclide retention relative to the rock matrix, the impact of remobilisation is generally not expected to be large even in cases where it might be reasonably expected to occur.

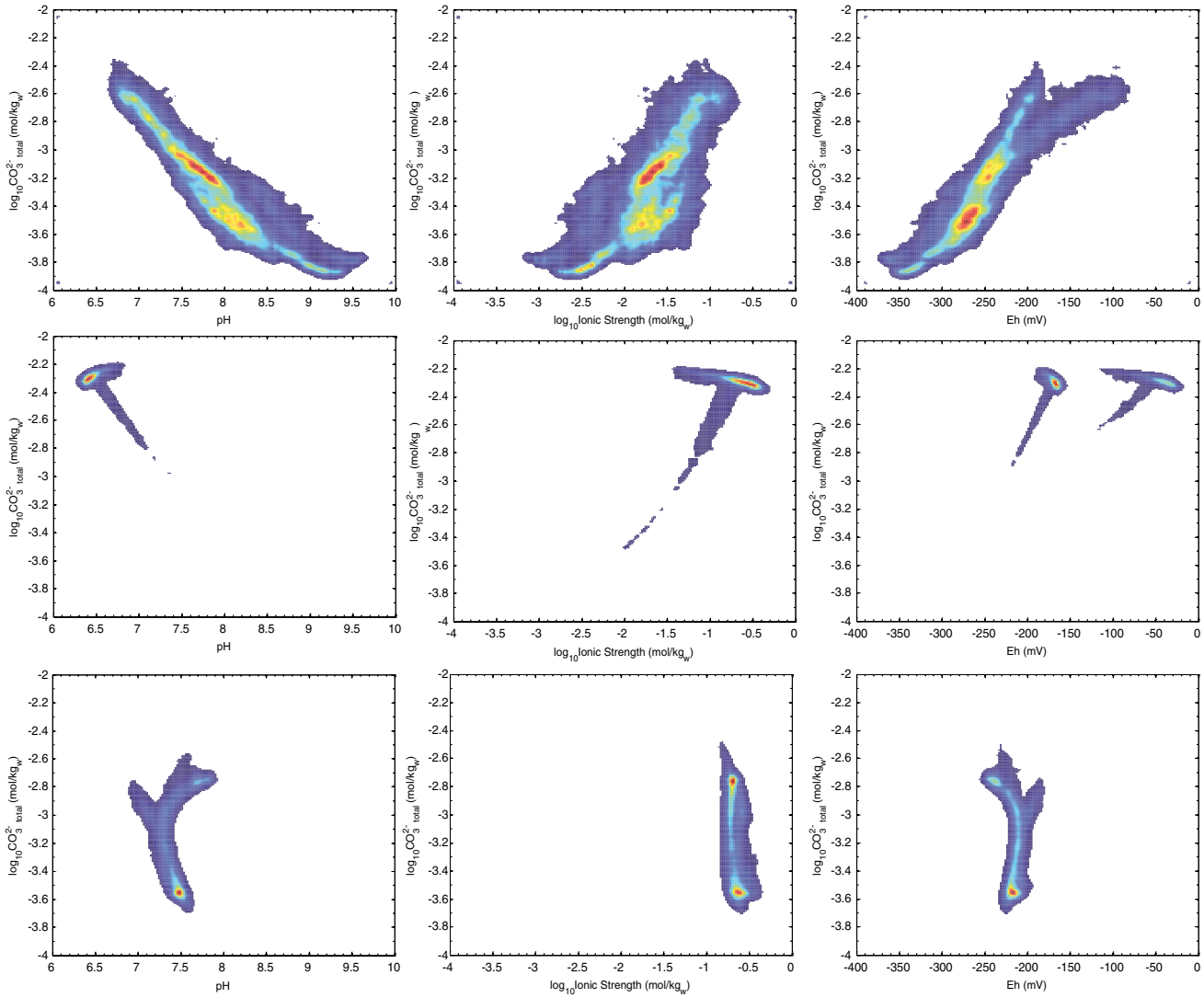

Figure 2-9. *Comparative plots of groundwater master variables influencing sorption. Data are shown for the hydrochemical reference case at 3 000 years (bottom row), glacial IIa case (centre row), and glacial IVa cases (top row) in the form of 2D histogram plots (log_{10} space). In each case the total carbonate concentration is plotted versus pH (left), ionic strength (centre), and Eh (right). The plots correspond to the data calculated by Salas et al. (2010) and stored on SKB's trac database.*

Impact of evolving groundwater chemistry on ion-exchanging nuclides

For nuclides that sorb by an ion-exchange mechanism (or whose sorption is otherwise strongly influenced by ionic strength), K_d values are chosen to reflect the most unfavourable groundwater compositions expected. The groundwater compositions existing at 2 000–3 000 years during the temperate time domain represent the peak groundwater salinity. Since sorption of these nuclides is negatively affected by elevated ionic strength, the hydrochemical conditions existing at this time are therefore used as a basis for the recommended rock matrix K_d values in the central case. For these particular solutes (Cs, Sr, and Ra), groundwater chemistry transfer factors are calculated with the aid of a simplified ion-exchange model to account for ionic strength effects during this time domain (Crawford 2010). In the case of Ni, which exhibits a weak ionic strength dependency, groundwater chemistry correction factors are calculated on the basis of a power law regression model relating apparent K_d with ionic strength. Although slightly higher peak salinities are expected during the glacial IIa domain, this only occurs during brief transient periods and is not considered representative of the conditions prevailing during most of the repository evolution.

The correction implied by the chemistry transfer factor is very small relative to the level of overall uncertainty in the uncorrected K_d data sets. Counterintuitively, the solutes that are most strongly influenced by ionic strength on account of their weak sorptivity are also given smaller correction factors than more strongly sorbing solutes that are less affected by ionic strength. This is due to the larger underlying data uncertainty in the case of the more weakly sorbing solutes which tends to drown out the systematic trends that can be quantitatively related to evolving groundwater salinity. This should not be taken to mean that ionic strength is less important for the weakly sorbing solutes, but rather that the effect is more difficult to quantify for weakly sorbing solutes relative to the more strongly sorbing solutes.

It must also be remembered that since the changes in groundwater composition are not resolved on the level of individual migration paths, extrapolation to the groundwater situations existing at different times must consider the statistical distribution of spatially variable groundwater compositions throughout the entire repository volume which, in itself, introduces additional statistical dispersion in the calculation of K_d uncertainty ranges. It is therefore important when discussing the impact of evolving groundwater chemistry to distinguish between the true impact of ionic strength on the sorption process as it actually occurs from the impact that is statistically quantifiable for modelling purposes. Changes in groundwater salinity are therefore likely to have a much more profound local impact on sorptivity than has been quantified in the K_d recommendation. Since the K_d data are recommended for relatively saline conditions, this means that the strength of sorption will be pessimistically underestimated during the bulk of repository evolution.

Higher salinities encountered during the glacial IIa domain could result in a mobilisation of nuclides that are sensitive to ionic strength and give far-field dose rates higher than predicted by the transport modelling. Essentially, this would mean that radionuclide mass flux during the low-salinity phases of repository groundwater evolution would be overestimated and the radionuclide mass flux during the transitory saline glacial IIa phase would be underestimated. The nuclide most strongly influenced by this (and which has the largest potential impact on far-field dose rates) is Ra-226. However, the landscape dose conversion factor for Ra-226 is almost 3 orders of magnitude lower during the glacial periods compared with the interglacial period (Avila et al. 2010), thus easily overwhelming any potential effects of underestimating salinity during the glacial IIa period.

Although not strictly considered to be an ion-exchanging solute, Ni-59 might also be affected by evolving salinity on account of its apparent sensitivity to ionic strength. Given that Ni-59 contributes much less to far-field dose rates, however, any variation in sorptive retention due to evolving groundwater composition is not expected to make a meaningful contribution to the overall picture of risk. Moreover, the landscape dose factor for Ni-59 is more than 3 orders of magnitude smaller during the glacial period as compared with the interglacial period (Avila et al. 2010).

During the glacial IVa period, decreased groundwater ionic strength would typically result in enhanced sorptivity both in the fracture minerals and in the rock matrix, which is pessimistically neglected.

Impact of evolving groundwater chemistry on surface-complexing nuclides

For nuclides that sorb by way of a surface complexation mechanism, it was judged not feasible at this time to make quantitative predictions of how changing groundwater chemistry might affect the magnitude of sorption. This is largely due to a lack of suitable mechanistic models describing the sorption of nuclides in association with granitic rock. At the same time, it is acknowledged that relatively sophisticated surface complexation models do indeed exist for sorption of nuclides in association with fracture filling minerals such as illite and smectite. Similarly to the quantification of ionic strength effects, however, even a very detailed mechanistic model would be unlikely to give a much reduced span of K_d uncertainty owing to the large spatial variability of groundwater compositions existing throughout the repository volume at any given time. In spite of this, it is still possible to make a relatively detailed qualitative account of how changes in groundwater chemistry might affect sorptivity based upon the well-known behaviour of model systems comprised of single minerals.

For surface complexing nuclides, groundwater pH, carbonate concentration (or pCO_2), and redox potential (Eh) are considered to be the most important master variables influencing sorption. In general, lower pH levels and higher carbonate concentrations are expected to result in reduced sorptivity of cationic nuclides by way of changes in the relative abundance of negatively charged surface binding sites as well as increased aqueous phase complexation by carbonate. For anionic nuclides one would generally expect the opposite behaviour with regard to pH changes (although this mostly concerns hematite, which has a relatively high point of zero charge). In most cases, however, the sorption of anions is negligible owing to a higher abundance of negative surface charge at prevailing groundwater pH and because their sorption is also subject to competition from other anionic groundwater constituents.

Redox potential also has a very strong influence on the predominant state of the redox sensitive nuclides that mostly sorb by surface complexation mechanisms. Higher Eh can imply a transition from relatively immobile reduced forms to more mobile oxidised forms that, in some cases, could imply the possibility of remobilisation during the glacial IVa period. Carbonate also plays an important role in redox speciation by altering the threshold at which transitions between predominantly reduced and oxidised forms can take place. Of the redox sensitive solutes, Pu and Np are not expected to be influenced by this on account of the Eh being well below their respective thresholds for transition from reduced to oxidised speciation for all conceivable groundwater situations predicted during the glacial cycle. U and Tc, on the other hand, may experience a transition to predominantly oxidised speciation during the glacial IVa period. The predominant redox speciation of U, however, is sufficiently uncertain even during the temperate time period that both oxidised and reduced speciation cases are propagated. This is due to the fact that the Eh and carbonate concentration ranges predicted during the temperate phase are such that the predominance of the U(IV) form cannot be strictly guaranteed at all times throughout the repository volume.

Although less mobile, the reduced U(IV) form is considered to be the more pessimistic assumption in the central case since it represents a more concentrated secondary source of the Ra-226 daughter nuclide. As already noted for Ra-226, any changes in the relative sorptivity of U which might give rise to remobilisation must also be considered in the context of the lower landscape dose factors during the periods of remobilisation. For this reason remobilisation scenarios affecting U transport in the far field are not considered to be of great significance to the overall picture of radiological risk. Notwithstanding this, however, sensitivity calculations are made with low U sorptivity as a variant of the central corrosion case in Section 4.5.4 and to assess the possible role of periodic transitions to low U sorptivity during the full glacial cycle in Section 4.5.7.

It should also be noted that the ranges of uncertainty recommended for K_d data implicitly include the full range of spatial and temporal variability expected in groundwater compositions. Although this means that nuclide dose rates are likely to be pessimistically overestimated during the temperate time domain, this does not necessarily inform the discussion of possible remobilisation of nuclides due to changing groundwater chemistry during the glacial IIa and IVa periods. Based on the relative trends of pH and carbonate concentration depicted in Figure 2-9, however, a decrease in sorptivity is expected during the glacial IIa domain on account of higher carbonate concentrations and reduced pH relative to the temperate time period. Groundwater conditions during the glacial IVa domain are more heterogeneous with a much broader range of pH and carbonate concentrations than are predicted to exist during the temperate time domain. On average, however, the carbonate concentration is higher although the pH is also slightly higher implying a mixed impact on sorptivity.

Impact of evolving groundwater chemistry on retention by solid solution

In Appendix B, detailed scoping calculations have been made with the aim of approximately quantifying retention by solid solution during the temperate time domain as well as likely impacts that changes in groundwater chemistry might bring about. In these calculations, the retention of nuclides as solid solutions in association with calcite (and barite in the case of Ra-226) has been cast in a conditionally constant K_d framework. Although there are known situations in which a conditionally constant K_d description may not be an appropriate means of modelling transport retardation by solid solution, the

approach is justified for the purpose of making scoping calculations through the application of a series of simplifying assumptions that are considered reasonable for the physicochemical boundary conditions describing the geosphere environment. Although only a small number of solutes (Ra, Am, Ni, U(IV), U(VI)) representing a range of different sorption chemistries are considered in the calculations, more general conclusions concerning impacts on the retardation of other nuclides may then be drawn by invoking appropriate geochemical analogies. In order to be consistent with the corresponding discussion for retention by ion-exchange and surface complexation, equivalent K_d values are derived for the groundwater compositions existing at 3 000 years in the temperate time domain as a hydrochemical reference case.

The scoping calculations indicate that equilibrium retention by solid solutions with calcite varies considerably amongst the different nuclides studied. In some cases the retention capacity is of similar magnitude (Am and Ni) or larger (Ra) than that of the chlorite and clay minerals, although in other cases the retention by solid solution is estimated to be considerably smaller than that of the chlorite and clay minerals (U(IV) and U(VI)). Groundwater chemistry correction factors defined in a similar fashion to that outlined previously for ion-exchanging nuclides indicate that retention is generally higher under most of the glacial cycle relative to the hydrochemical reference case with the exception of the glacial IIa time domain where retention by calcite solid solution appears to decrease slightly relative to the hydrochemical reference case. On the other hand, retention appears to be significantly enhanced during the glacial IVa time domain, which suggests that remobilisation scenarios are unlikely for solid solutions involving calcite. The considerable increase in retention by calcite during glacial IVa also suggests that possible decreases in sorptivity predicted for the surface complexing nuclides in association with chlorite and other clay minerals may be at least partially offset in some cases. This would certainly appear to be the case for trivalent actinides and lanthanides by way of geochemical analogy with Am.

Although barite has not been identified in quantifiable amounts in the fracture system at Forsmark its presence might be reasonably inferred from the only slight oversaturation of barite apparent in the groundwater compositions measured at the site (Crawford 2010). Calculations indicate that as little as 1 mg/m^2 of barite would be sufficient to represent a larger retention capacity for Ra than that of the other fracture minerals. Calculation of chemistry correction factors for radiobarite indicate that retention of Ra is considerably reduced during the glacial IIa and IVa time domains relative to the hydrochemical reference case. If barite were the only mineral likely to form solid solutions with Ra, this would imply the potential for remobilisation during the glacial IIa and IVa periods. Interestingly, the decrease in retention by barite is offset by a corresponding increase in retention by calcite and the chlorite/clay mineral group during the glacial IVa period. If the amount of barite is much less than about 1 mg/m^2, the net effect would be an increase in retention during glacial IVa although still a slight decrease in retention during glacial IIa. As already noted, however, the landscape dose conversion factors are significantly lower during the glacial periods. The radiological consequences of remobilisation scenarios of anthropogenic Ra-226 therefore appear to be minor.

Although equilibrium sorption on fracture minerals can generally be assumed for ion-exchange and surface complexation sorption mechanisms, this is not necessarily always the case for solid solution retention processes on account of the kinetic effects related to the uptake process. In the scoping calculations, both equilibrium sorption and kinetically limited modes of solute uptake are therefore considered. It is concluded, however, that there is sufficient uncertainty concerning rates and actual mechanisms of kinetic rates of solute uptake at this time that the notion of equilibrium sorption by solid solution formation is not a prudent assumption for safety assessment modelling. The retention of radionuclides as solid solutions in association with calcite or barite may therefore be significantly less than that estimated on the basis of the equilibrium assumption.

2.5 Summary of geosphere non-flow related data

The movement of solutes through fractured rock depends on several parameters, which are discussed in detail in the **Data report** and supporting documents. Parameters related to the rock matrix – the effective diffusivity, diffusion available porosity, and sorption partitioning coefficient – are summarised briefly here. These data are site specific, depending on the geological settings and groundwater composition.

Commonly, a homogenous distribution of minerals in the rock is considered and hence the rock matrix parameters are constant. However, the effect of rock matrix mineral alterations and fracture-filling minerals on radionuclide retention by matrix diffusion is discussed in Löfgren and Crawford (2014) and in Crawford and Löfgren (2019). In these works, flowpaths in the rock matrix are assumed to encounter a number of different rock volumes with differing matrix retention properties conceptualised as a discretely layered rock matrix including fracture coatings. It is demonstrated that the inclusion of this type of greater variability in matrix diffusion parameters generally gives rise to additional transport retention and hence reduces the peak far-field dose. Therefore, the simplified conceptualisation used, where flow paths are in practice surrounded by undisturbed rock, is pessimistic.

Flow-related parameters are specific to the modelling case addressed. Data for the flow triplet parameters (Q_{eq}, t_w, F) are therefore discussed on a case-by-case basis where appropriate in Chapters 3 to 6. Near-field parameters related to the properties of buffer and backfill material can be found in the **Data report** and supporting documents. Other parameters related to the conceptualisation of radionuclide release and conversion of radionuclide mass discharge to a radiological dose rate are discussed in the following chapter.

2.5.1 Diffusion-available porosity

The diffusion available porosity is discussed in the **Data report**. Based on consideration of the dominant rock type in the repository volume, a flowpath average porosity of 0.18 % is recommended for use in radionuclide transport calculations. This recommended value is reduced relative to the measured laboratory value to account for the possible biasing effect of mechanical damage incurred during drilling and core extraction. The applied scaling factor of 0.8 is based on comparison of water saturation porosities with microcrack volume (porosity) measurements made in triaxial compression tests using site-specific rock samples.

2.5.2 Effective diffusivity

The handling of effective diffusivity and data used is discussed in the **Data report**. Based on the analysis documented there, a flowpath average effective diffusivity is recommended for use in transport calculations. For the purposes of the safety assessment, the effective diffusivity recommended for cations and neutral species is assumed to have a lognormally distributed uncertainty with the following characteristics:

$$\log_{10} D_e = -13.7 \pm 0.25 \qquad 2\text{-}2$$

For anionic radionuclides, the recommended distribution is:

$$\log_{10} D_e = -14.2 \pm 0.25 \qquad 2\text{-}3$$

It should be noted that the standard error of the estimate given in Equations 2-2 and 2-3 relate to uncertainty rather than spatial variability and the estimates are considered to be already averaged. The uncertainties associated with the formation factor and effective diffusivity estimates are shown to be too small to impact the radionuclide transport modelling to any significant degree (Löfgren 2014, 2015, Crawford and Löfgren 2019). Since radionuclides may be present in a number of different speciated forms depending on groundwater chemistry, there is the possibility that cationic, anionic and neutral forms may exist contemporaneously. Because the safety assessment codes only allow for the assignment of a single effective diffusivity per nuclide this means that a judgement must be made for which effective diffusivity is to be used. Table 2-3 summarises the assumed speciation of different elements and redox species of importance for the safety assessment.

Table 2-3. Dominant speciated forms estimated for elements and redox states at pH 8 and for saline groundwater (5 190 mg/l Cl^-, 22 mg/l HCO^{3-}) approximately representative of current conditions at repository depth. Carbonate complexed forms may take on greater significance in groundwater of more meteoric character. In situations where there is doubt concerning the most likely speciation, the anionic form might be considered a more cautious choice.

Element	Dominant species	Status
Cs(I)	Cs^+	Cation
Ra(II)	Ra^{2+}	Cation
Sr(II)	Sr^{2+}	Cation
Eu(III)	$EuCO_3^+$	Cation
Ho(III)	$HoCO_3^+$	Cation
Sm(III)	$SmCO_3^+$	Cation
Ac(III)	$AcCO_3^+$	Cation
Am(III)	$AmCO_3^+$	Cation
Cm(III)	$CmCO_3^+$	Cation
Np(IV)	$Np(OH)_4$	Neutral
Np(V)	NpO_2^+, $NpO_2CO_3^-$	Cation/Anion (carbonate dependent)
Pa(IV)	$Pa(OH)_4$	Neutral
Pa(V)	$PaO_2(OH)$	Neutral
Pu(III)	$PuOH^{2+}$, Pu^{3+}	Cation
Pu(IV)	$Pu(OH)_4$	Neutral
Pu(V)	PuO_2^+	Cation
Pu(VI)	$PuO_2(CO_3)_2^{2-}$, PuO_2CO_3	Anion
Th(IV)	$Th(OH)_3CO_3^-$	Anion
U(IV)	$U(OH)_4$	Neutral
U(VI)	$UO_2(CO_3)_3^{4-}$, $UO_2(CO_3)_2^{2-}$	Anion
Ni(II)	Ni^{2+}, $NiCl^+$	Cation
Zr(IV)	$Zr(OH)_5^-$	Anion
Ag(I)	$AgCl_2^-$, $AgCl_4^{3-}$, $AgCl_3^{2-}$	Anion
Cd(II)	$CdCl^+$, Cd^{2+}, $CdCl_2$	Cation
Pb(II)	$PbCO_3$, $PbCl^+$, $PbOH^+$, Pb^{2+}	Cation
Pd(II)	$Pd(OH)_2$	Neutral
Mo(VI)	MoO_4^{2-}	Anion
Nb(V)	NbO_3^-, $Nb(OH)_5$	Anion
Tc(IV)	$TcO(OH)_2$	Neutral
Tc(VII)	TcO_4^-	Anion
C(IV)	HCO_3^{3-}	Anion
C(-IV)	CH_4 (or organic acids)	Neutral
Cl(-I)	Cl^-	Anion
I(-I)	I^-	Anion
Se(-II)	HSe^-	Anion
Se(IV)	$HSeO_3^-$, SeO_3^{2-}	Anion
Se(VI)	SeO_4^{2-}	Anion
Sn(IV)	$Sn(OH)_2$	Neutral

2.5.3 Rock matrix sorptivity

The recommended K_d data are based in part on site specific data obtained during the Forsmark and Laxemar site investigations, and in part on data contained in the open scientific literature. These data are documented in Crawford (2010) and the **Data report**. The data are corrected to account for biases due to differences in sorptive surface area and cation exchange capacity (CEC) of the crushed rock types used in laboratory investigations relative to the intact site specific rock assumed as a reference material for transport calculations (Forsmark metagranite).

In the small number of cases (Cs, Sr, Ra, Ni) where an ionic strength dependency has been quantified, data have been selected for the most unfavourable groundwater compositions expected which corresponds to roughly 2 000–3 000 years in the temperate case (Salas et al. 2010). Generally, the overall uncertainty of the underlying data sets dominate and the correction implied by temporal changes in groundwater composition gives rise to only very small differences in the recommended values. Although salinity is slightly less on average at 3 000 years than 2 000 years, the difference is sufficiently small as to be statistically insignificant for the estimation of corrected K_d values. For elements where it is not feasible to quantitatively estimate the impact of spatially and temporally variable groundwater composition on sorptivity, K_d data representing a range of contact water compositions are combined to give an uncertainty range that is thought to reasonably represent the diversity of hydrochemical conditions expected. The conditional K_d values recommended for use in safety assessment in most cases represent a relatively large span of contact water compositions and experimental conditions. Although there may be some bias in the sampled parameter space for certain nuclides, the recommended data capture as much of the groundwater compositional uncertainty as is reasonably possible to achieve. In many cases it is likely that the uncertainty distributions represent a broader parameter space than is predicted for the used groundwater compositions.

Recommended data for geosphere transport calculations

Sorption K_d data recommended for use in radionuclide migration calculations in the geosphere are summarised in Table 2-4. The data are given in the form of lognormal distributions characterised by a mean (μ) and standard deviation (σ) and implicitly include the combined impact of uncertainty as well as spatial and temporal variability. The median of the K_d uncertainty distribution may be taken to be the best estimate value for central case deterministic calculations. Since uncertainty rather than variability is expected to make the dominant contribution to the statistical dispersion of the recommended K_d data ranges it is not possible to estimate a meaningful flowpath average for the geosphere. For stochastic simulations, it was recommended that the lognormal distributions be sampled uniformly between the 2.5 % and 97.5 % percentiles specified as the lower and upper K_d limits in the table.

K_d values are given for the predominant redox species considered most likely for the groundwater compositions existing during the temperate phase of groundwater evolution. For all redox sensitive nuclides except U, the reduced species is predominant. Pu is assumed to be present in the trivalent state even though a mixed Pu(III,IV) state is possible. Since Pu(III) is assigned a slightly lower K_d interval than Pu(IV), this may be considered cautious with regard to model parameterisation. At later times during the temperate phase, reduced U(IV) speciation cannot be guaranteed and it is likely that U(VI) is predominant in parts of the repository environment. Owing to this uncertainty, both U(IV) and U(VI) cases have been propagated forward in the transport calculations. For times greater than 9 000 y in the temperate case, the trend to increasing carbonate concentration and decreasing Eh owing to infiltration of meteoric water may give more weakly reducing conditions, although this is principally an issue for U redox speciation.

Table 2-4. Recommended sorption partitioning coefficient, K_d values. The predominant species for redox sensitive elements are highlighted in bold text. Values are given for the best estimate (median), parameters for the lognormal distribution (μ and σ), as well as lower and upper limits corresponding to the 2.5 % and 97.5 % percentiles, respectively.

Radionuclide (Redox State)	Best estimate K_d (m^3/kg)	$\log_{10}K_d - \mu$	$\log_{10}K_d - \sigma$	Lower K_d limit (m^3/kg)	Upper K_d limit (m^3/kg)
Ac(III)	1.48×10^{-2}	–1.83	0.72	5.74×10^{-4}	3.83×10^{-1}
Ag(I)	3.49×10^{-4}	–3.46	0.51	3.46×10^{-5}	3.52×10^{-3}
Am(III)	1.48×10^{-2}	–1.83	0.72	5.74×10^{-4}	3.83×10^{-1}
C, HCO_3^-	0.0	–	–	0.0	0.0
C, CH_4	0.0	–	–	0.0	0.0
C, $-CO_2H$	0.0	–	–	0.0	0.0
Cd(II)	1.10×10^{-3}	–2.96	0.65	5.97×10^{-5}	2.04×10^{-2}
Cl(-I)	0.0	–	–	0.0	0.0
Cm(III)	1.48×10^{-2}	–1.83	0.72	5.74×10^{-4}	3.83×10^{-1}
Cs(I)	3.49×10^{-4}	–3.46	0.51	3.46×10^{-5}	3.52×10^{-3}
Eu(III)	1.48×10^{-2}	–1.83	0.72	5.74×10^{-4}	3.83×10^{-1}
H(I)	0.0	–	–	0.0	0.0
Ho(III)	1.48×10^{-2}	–1.83	0.72	5.74×10^{-4}	3.83×10^{-1}
I(-I)	0.0	–	–	0.0	0.0
Mo(VI)	0.0	–	–	0.0	0.0
Nb(V)	1.98×10^{-2}	–1.70	0.64	1.11×10^{-3}	3.53×10^{-1}
Ni(II)	1.10×10^{-3}	–2.96	0.65	5.97×10^{-5}	2.04×10^{-2}
Np(IV)	5.29×10^{-2}	–1.28	0.65	2.84×10^{-3}	9.84×10^{-1}
Np(V)	4.13×10^{-4}	–3.38	0.74	1.48×10^{-5}	1.15×10^{-2}
Pa(IV)	5.92×10^{-2}	–1.23	0.48	6.76×10^{-3}	5.18×10^{-1}
Pa(V)	5.92×10^{-2}	–1.23	0.48	6.76×10^{-3}	5.18×10^{-1}
Pb(II)	2.52×10^{-2}	–1.60	0.56	2.05×10^{-3}	3.10×10^{-1}
Pd(II)	5.20×10^{-2}	–1.28	0.83	1.22×10^{-3}	2.21
Pu(III)	1.48×10^{-2}	–1.83	0.72	5.74×10^{-4}	3.83×10^{-1}
Pu(IV)	5.29×10^{-2}	–1.28	0.65	2.84×10^{-3}	9.84×10^{-1}
Pu(V)	9.14×10^{-3}	–2.04	0.60	6.19×10^{-4}	1.35×10^{-1}
Pu(VI)	9.14×10^{-3}	–2.04	0.60	6.19×10^{-4}	1.35×10^{-1}
Ra(II)	2.42×10^{-4}	–3.62	0.41	3.87×10^{-5}	1.51×10^{-3}
S(-II)	0.0	–	–	0.0	0.0
Se(-II)	2.95×10^{-4}	–3.53	0.55	2.50×10^{-5}	3.48×10^{-3}
Se(IV)	2.95×10^{-4}	–3.53	0.55	2.50×10^{-5}	3.48×10^{-3}
Se(VI)	2.95×10^{-4}	–3.53	0.55	2.50×10^{-5}	3.48×10^{-3}
Sm(III)	1.48×10^{-2}	–1.83	0.72	5.74×10^{-4}	3.83×10^{-1}
Sn(IV)	1.59×10^{-1}	–0.80	0.28	4.51×10^{-2}	5.58×10^{-1}
Sr(II)	3.42×10^{-6}	–5.47	0.99	3.84×10^{-8}	3.05×10^{-4}
Tc(IV)	5.29×10^{-2}	–1.28	0.65	2.84×10^{-3}	9.84×10^{-1}
Tc(VII)	0.0	–	–	0.0	0.0
Th(IV)	5.29×10^{-2}	–1.28	0.65	2.84×10^{-3}	9.84×10^{-1}
U(IV)	5.29×10^{-2}	–1.28	0.65	2.84×10^{-3}	9.84×10^{-1}
U(VI)	1.06×10^{-4}	–3.97	0.66	5.53×10^{-6}	2.05×10^{-3}
Zr(IV)	2.13×10^{-2}	–1.67	0.35	4.48×10^{-3}	1.02×10^{-1}

3 Conceptualisation of transport processes and conditions within the repository and its environs

This chapter has not been updated since the SR-Site assessment (SKB 2010d), with the exception of the addition of recent references as concerns verification of the MARFA code in Section 3.6.3 and the new Section 3.7.3. Changes in modelling details and updated input data for the PSAR are given in Appendix L. In a few places, references in the SR-Site version were made to the main references of the SR-Site assessment, the references written in bold. It has been verified that the PSAR versions of the corresponding reports are equally valid as references in these cases. The references in bold, therefore, refer to the PSAR versions.

The three hydrogeological models (semi-correlated, uncorrelated and fully correlated) described by Joyce et al. (2010) form the base for the calculations. The hydrogeological calculations are performed for different climate conditions. Temperate conditions at the time 2000 AD are assumed to provide adequate representations of near-field and far-field conditions at Forsmark for the purpose of estimating radionuclide release and transport. This approximation is relaxed in a few selected variant modelling cases to evaluate its adequacy.

The EFPC criterion has been applied for most of the calculation cases, i.e. canister positions intersected by fractures that also intersect the entire tunnel perimeter have been discarded. This means that those deposition holes have been filtered from the results of the transport calculations.

3.1 Selection of radionuclides

The selection of radionuclides is based on radiotoxicity, inventory, half-life and shared solubility. The selection is further described in Appendix D. Some of the selected, short-lived nuclides were omitted in cases where they would have decayed to insignificance at the time of the start of the calculation.

The following 23 fission and activation products were selected: Ag-108m, C-14, Cd-113m, Cl-36, Cs-135, Cs-137, Eu-152, H-3, Ho-166m, I-129, Mo-93, Nb-93m, Nb-94, Ni-59, Ni-63, Pd-107, Se-79, Sm-151, Sn-121m, Sn-126, Sr-90, Tc-99 and Zr-93.

The following 22 decay chain nuclides (ordered by chain) were selected: Pu-240, U-236, Th-232, Cm-245, Am-241, Np-237, U-233, Th-229, Cm-246, Am-242m, Pu-242, Pu-238, U-238, U-234, Th-230, Ra-226, Pb-210, Am-243, Pu-239, U-235, Pa-231 and Ac-227. Some nuclides with short half-lives in comparison to their progeny were only included by adding their initial inventory to that of their progen. This applies to e.g. Cm-244, Pu-241, Cm-243 and Pa-233.

3.2 Radionuclide release from the fuel

The following contributions to the outward transport from the fuel can be distinguished:

- The instantaneously accessible fraction of radionuclides, IRF, that is assumed to rapidly dissolve in the water void volume and be subsequently released from the canister. This gives rise to a pulse of uncertain duration, the uncertainty stemming from e.g. uncertainties in the detailed development of the canister failure through which the IRF is made accessible.
- A contribution from the corrosion of metal parts in the fuel assemblies and the congruent release of radionuclides embedded in the metal parts. These inventories are collectively called the corrosion release fraction, abbreviated CRF.
- A contribution from fuel dissolution and the congruent release of radionuclides embedded in the fuel matrix.
- Elemental solubilities as a limit for radionuclide release. If the solubility limit is reached, the concentration of the dissolved nuclide in the water does not increase further.

3.2.1 Release of instantaneous release fraction

As soon as a continuous water pathway has been formed the instant release fraction of the inventory dissolves in the water in the canister void.

In the corrosion scenario the IRF is assumed to rapidly dissolve and be subsequently flushed from the canister. Since these nuclides are in general non-sorbing and since the flow related retardation properties in the geosphere are poor for the flow paths associated with the deposition positions in question, they are generally released as pulses of durations of tens of years from the geosphere to the biosphere. The release of the IRF is calculated separately, see Section 4.1.3.

3.2.2 Release of activation products in metal parts

The inventory of activation products in the metal parts of the fuel assemblies has normally been assigned to the instantaneously accessible fraction (for example in SR-Can, SKB 2006a), since it has been considered unnecessary to develop a model for the metal parts as nuclides in these are dispersed during transport through the near field and far field. However, in the corrosion scenario this assumption would lead to unrealistically high peaks in the releases of e.g. Ni-59 and Nb-94. Therefore, corrosion of metal parts of the fuel assemblies is included in the near-field model, with corrosion rates given in Section 3.2 in both SKB (2010b) and the **Data report**. The fraction of the inventory for which corrosion of metal parts determines the release rate is called the corrosion release fraction, CRF. The CRF is given in Section 3.2 in both SKB (2010b) and the **Data report**, in the same manner as other fractions of the inventory.

3.3 Near-field transport and retention

After failure the canister is not assumed to provide any transport resistance except in the growing pinhole scenario.

There is no transport resistance at all in the near field in the corrosion scenario. The release is assumed to occur with the water flow in the deposition hole.

In all scenarios, but the corrosion scenario, the nuclides are sorbed with varying efficiency in the buffer and the diffusion and sorption properties determine the time for diffusion through the buffer to the rock at release path Q1, i.e. a fracture intersecting the deposition hole. In the shear load scenario the shear is assumed to increase the fracture transmissivity significantly. The Q_{eq} value for the intersecting fracture is, therefore, assumed to be sufficiently high that it does not contribute to the transport resistance in the near field. In the two hypothetical residual scenarios, isostatic load and growing pinhole, the limited flow in the fractures intersecting the deposition hole contributes to the transport resistance through the Q_{eq} value. Thermally induced spalling is assumed to have occurred in the wall of the deposition hole. This implies, that the transport resistance at the interface at Q1 is lower than if spalling is not included.

In the growing pinhole scenario two additional exits from the near field are included: an excavation damaged zone, EDZ, in the floor of the deposition tunnel (if such a zone is assumed to exist), Q2, and a fracture intersecting the deposition tunnel, Q3. The radionuclide transport is assumed to occur by diffusion in the buffer and backfill in the deposition hole and by diffusion and advection in the deposition tunnel. The nuclides are sorbed with varying efficiency in the buffer and backfill and the water flow, the diffusion and sorption properties in the backfill determine the time for diffusion through the buffer and backfill to the rock at release paths Q1, Q2 and Q3. The advective flow in the deposition tunnel and the boundary conditions for the near field at Q1, Q2 and Q3 are determined in the hydrogeological calculations. In the section describing the near-field model COMP23 (Section 3.6.1) more details are given and in Figure 3-1 the modelled system in the pinhole scenario including the three release paths Q1, Q2 and Q3 is shown. A detailed description of the discretisation, diffusion resistances and boundary conditions used in COMP23 in the different scenarios is given in Appendix G.

3.4 Geosphere transport and retention

The solute transport in the geosphere is conceptualised to occur by advective flow along discrete migration paths where retention is caused by matrix diffusion and equilibrium sorption on rock matrix microsurfaces (**Geosphere process report**). For modelling purposes these processes are assumed to be reversible and linear thereby implying a Fickian formulation of matrix diffusion characterised by an effective diffusivity, D_e, that can vary spatially along a flowpath depending upon the local microstructural properties of the rock. The effective diffusivity of specific solutes in the rock depends upon the geometric structure and connectivity of the rock matrix porosity, which is conceptualised to consist of both microfractures and grain boundary porosity. The handling of effective diffusivity and data used are discussed in the **Data report**.

In a similar fashion, the sorptive properties of the rock are modelled based on the assumption of a constant linear partitioning coefficient, K_d, which also can vary spatially along a flowpath depending on the local mineralogy of the rock and porewater chemistry. The residence time distribution of a solute subject to advective transport and retardation by matrix diffusion and linear sorption is a function of the master variables D_e, K_d and F. The diffusive mass transfer to the rock matrix is furthermore assumed to be one-dimensional and perpendicular to the advective flowpath along which the radionuclide is transported.

3.5 Biosphere representation

The biosphere is mainly represented by multiplying the radionuclide releases from the near field or from the geosphere by an appropriate dose conversion factor (LDF).

The so obtained doses, or, in the case of the near field, dose equivalent releases, are the main calculation end-points in the consequence calculations presented in this report. The conversion to dose is done to obtain a convenient measure of the impact of the releases, where also a total measure is obtained as the summed dose.

For the shear load scenario with early failure the use of LDF values overestimates the doses in this time perspective since i) the LDF is a pessimistic upper bound on releases occurring continuously over an entire interglacial period taking into account accumulation whereas a large part of the interglacial period has elapsed without any releases when the repository is sealed and ii) it is not meaningful to use the LDF concept for a radionuclide that decays to insignificance over an interglacial period, since the concept is based on a continuous releases over the period.

Basic Landscape Dose Conversion Factors (LDF)

The Basic Landscape Dose Conversion Factors, LDF, have been used for estimating doses for scenarios characterised by nearly constant release rates during a long-term period. The LDF values are therefore derived from simulations using constant unit release rates during the whole simulation period. LDF values are calculated for the different climate conditions, e.g. interglacial, periglacial, glacial and submerged. The used values are the maximum values (over time and objects) obtained from the transient modelling. For all radionuclide transport cases the values for interglacial conditions are used, except in the cases assessing influence of varying climate where also values for periglacial, glacial and submerged conditions are used. The highest doses from a constant release rate from the repository are expected under temperate conditions when humans are exposed to radionuclides that have accumulated in a wetland that has been converted to arable land, and when contaminated well water is utilised by human inhabitants and livestock. Hence, the LDFs for the interglacial period are the maximum values applicable during the reference glacial cycle. The interglacial period, i.e. the period from deglaciation to the onset of periglacial conditions, cf. Figure 4-36 in the **Climate report**, is represented by climate conditions similar to those of today and is, in accordance with the reference glacial cycle, assumed to prevail for 18 400 years (i.e. from –9000 BC to 9400 AD) and include both submerged and temperate conditions. The LDF values used include the influence of exposure from a well. The details of how the LDF values have been derived are given in the **Post-closure safety report**, Section 13.2 and in Avila et al. (2010). The interglacial-period LDF values used are given in Table 3-7; see the **Data report** for LDF values for other climate domains.

Dose Conversion Factors for pulse releases (LDF pulse)

In the corrosion scenario the instant release fraction, IRF, are generally released as pulses of durations of tens of years from the geosphere to the biosphere, see further 4.1.3. The basic LDF values (previous section) are not applicable for pulse releases, since the former are derived from simulations with a constant release rate during long-term periods, whereas pulse releases will, by definition, take place during a relatively short time period. Hence, the derivation of LDF pulse values has been done by performing simulations for a release of 1Bq to the landscape during a short time period. The duration of the release period has been varied from 1 to 1 000 years and simulations have been carried out for pulse releases occurring at different times within an interglacial period. Studies of the effect of the starting time of the releases and the duration of the pulse have shown very little influence of these factors in the derived Dose Conversion Factors. In Table 3-7 values of the LDF pulse are presented for those radionuclides that occur in pulse releases. The values are the maximum annual effective doses calculated for 1-year pulses released at 9000 BC, 3500 AD and 9400 AD.

Distributed LDF

There are also a few cases, calculated for illustrative purposes, see Section 6.2.3 and Section 6.5, where a large number of canisters are assumed to fail. In such cases, LDF values calculated for a release spread over the landscape objects according to the distribution of release locations over time during the modelled interglacial period are applied, rather than the basic LDF values where the landscape object yielding the highest dose is pessimistically used to represent the biosphere. These LDF values are referred to as distributed LDF.

Time dependent biosphere

In a few cases of relatively early releases, the basic LDF values would represent an overestimation of the dose consequences, again since a steady state release situation is far from established. In some of these cases, time dependent releases are transferred to the same biosphere model as used for the derivation of LDF values and a time dependent dose, taking into account both the temporal variation of the release and the development of the landscape, is obtained.

3.6 Models used

Calculations of radionuclide release and transport rely on three primary computer codes COMP23, FARF31 and MARFA. The codes are described in Section 3.6.1, 3.6.2 and 3.6.3, respectively. The codes are further described in the **Model summary report**. In addition, all three codes require information derived from groundwater velocity fields calculated by the ConnectFlow code (Joyce et al. 2010). A summary of the transport model chain is given in Section 3.6.4.

In addition to the numerical codes an analytical model for both near-field and far-field calculations is used. A short description of the model is given in Section 3.6.5 and a more detailed description is given in the **Model summary report**.

3.6.1 COMP23

COMP23 (Romero 1995, Cliffe and Kelly 2006, Kelly and Cliffe 2006) is a compartment code used for radionuclide migration calculations in the near field (the canister and the engineered systems). The code was initially developed as NUCTRAN (Romero 1995) and was subsequently incorporated into the SKB safety assessment calculation framework Proper as the submodel COMP23. Proper is a collection of codes used for migration and consequence calculations through the near field, the far field and the biosphere and uses standardised methods to transfer data and results between the different submodels. An implementation of the COMP23 model written in Matlab/Simulink is used for the near-field migration calculations. This implementation of COMP23 is also called Compulink (Vahlund and Hermansson 2006).

COMP23 has been used by SKB in the SR 95 (SKB 1995), the SR 97 (Lindgren and Lindström 1999, SKB 1999), SR-Can interim (SKB 2004) and the SR-Can (SKB 2006a) assessments of a final repository of the KBS-3 type. A closely related code, NUCTRAN/NUCFLOW, (which originate from the same source but allows for multiple sources opposed to COMP23 which only handles single sources) was used in the SAFE assessment of the SFR repository for operational waste (Lindgren et al. 2001).

COMP23 models processes related to radionuclide release and transport in the canister interior, the buffer and the deposition tunnel backfill. These incorporate the processes radioactive decay, metal corrosion (modelled as a constant metal corrosion rate), fuel dissolution, dissolution of gap inventory (modelled as an instantaneous release), speciation of radionuclides (i.e. dissolution/precipitation of nuclides with shared elemental solubilities), diffusion and sorption in the buffer and advection, diffusion and sorption in the deposition tunnel backfill. It also handles the release of radionuclides to different exit paths from the near field.

COMP23 is a multiple-path model that calculates transient nuclide transport in the near field of a repository by use of a network of coupled resistances and capacitances in analogy with an electrical circuit network. Analytical solutions, instead of fine discretisation, at sensitive zones, for example at the exit point of a small canister hole and at the entrance to fractures, are embedded to enhance calculation speed.

Figure 3-1 shows the canister, deposition hole and the deposition tunnel backfill and how these are modelled by COMP23 in the growing pinhole scenario. Three exits from the near field are included: a fracture intersecting the deposition hole at the vertical position of the canister lid, denoted Q1, an excavation damaged zone, EDZ, in the floor of the deposition tunnel (if such a zone is assumed to exist), Q2, and a fracture intersecting the deposition tunnel, Q3. In the hydrogeological modelling, the number of fractures intersecting a deposition hole and the properties of these fractures are determined statistically based on the DFN description of the rock. If more than one fracture intersects a deposition hole, the transport capacity of the several fractures are added and pessimistically assigned to the single fracture, Q1, modelled by COMP23. The equivalent flow rate through Q2 is also calculated as an integral part of the hydrogeological modelling. The flow rate in the deposition tunnel and the distance to the nearest Q3 fracture through which radionuclides are released to the geosphere from the tunnel are given by the hydrogeological modelling. Transport by advection and diffusion in the tunnel is included in the near-field simulations and the computational domain is extended in the downstream direction to include the Q3 fracture. All needed results from the hydrogeological modelling are transferred to COMP23 through the ptb-files from ConnectFlow.

Effects of spalling in deposition holes are treated by a modification of the equivalent flow rates for the transport path Q1, see Appendix G.

Advective conditions in the buffer, as in the corrosion scenario, are simply treated by equating the outflux from the canister interior compartment with the release to Q1. The release paths Q2 and Q3 are not modelled when advective conditions are assumed in the buffer since releases to Q1 completely dominate over those to Q2 and Q3 for such cases.

Further details of the discretisation, diffusion resistances and boundary conditions used in the different scenarios are described in Appendix G.

3.6.2 FARF31

FARF31 (Norman and Kjellbert 1990, Lindgren et al. 2002, Elert et al. 2004) is a code used for radionuclide migration calculations in the far field, i.e. the geosphere.

FARF31 has been employed already in earlier assessments, e.g. SR 97 (Lindgren and Lindström 1999) and SR-Can (SKB 2006a).

FARF31 is based on a model with a one-dimensional advection-dispersion equation along a, possibly curved, stream tube coupled to a pure diffusion equation in the direction perpendicular to the centroid of the stream tube, for a number of radionuclides. Chain decay and in-growth are included in the model. The concept of a stream tube can be compared to the combined effect of a large number of individual fractures all sharing the same inlet and outlet.

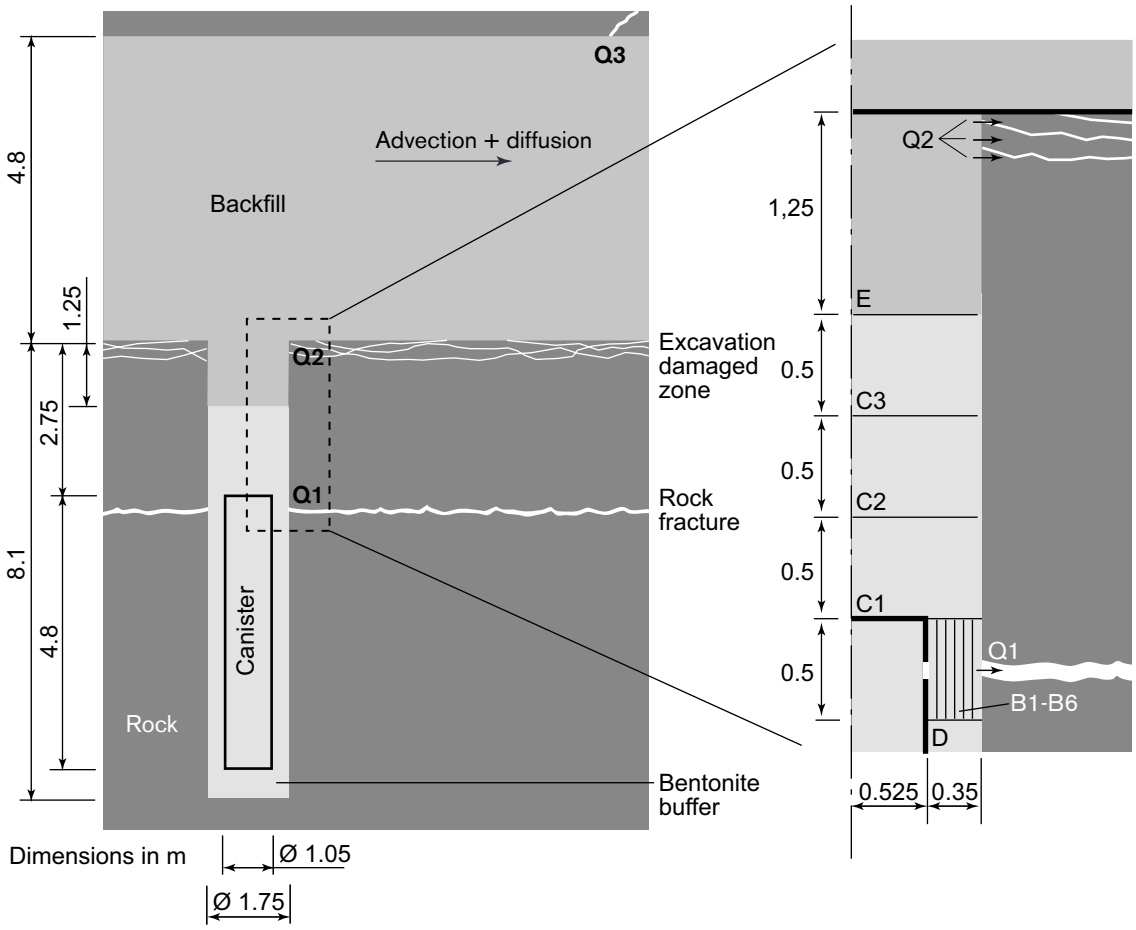

Figure 3-1. *COMP23 model, for the growing pinhole scenario, with details of its model representation as compartments B1–B6, C1–C3, D and E. The transport paths Q1, Q2 and Q3 to a fracture intersecting the deposition hole, to the excavation damaged zone, and to a fracture intersecting the deposition tunnel, respectively, are also shown.*

The governing equations are solved in the Laplace domain using the advective travel time in the longitudinal direction as the independent variable to obtain a unit response function, which is subsequently convoluted with the input function to obtain the output function. A detailed description of the solution method can be found in Norman and Kjellbert (1990).

It is noted that the equations are expressed in terms of accumulated travel time rather than distance along the flow path. This feature makes it easy to calculate travel times in a stand-alone groundwater flow model, and subsequently radionuclide transport in a decoupled fashion.

FARF31 was originally developed to be used with a groundwater flow model adopting a continuum representation of the rock. Groundwater flow is primarily modelled through a discrete fracture network (DFN) where individual fractures are represented explicitly. Here, the conceptualisation of a migration path is slightly different than in a continuum-based groundwater flow model. Rather than macroscopic stream-tubes encompassing both rock and flow paths, the equation now describes flow paths through the actual open pore space, i.e., through the connected fracture network. However, the governing equations are identical for the two conceptualisations. The entities calculated in the DFN-based groundwater flow models are the advective travel time (t_w) and flow-related transport resistance (F) along flow paths.

3.6.3 MARFA

The computer code MARFA (Painter and Mancillas 2009) uses a particle-based Monte Carlo method to simulate the transport of radionuclides in fractured or unfractured geologic media. MARFA was specifically designed to integrate with the safety assessment workflow used by SKB. Version 3.2.2 and earlier versions accept pathline trajectories from the ConnectFlow code (Serco 2008) in the form of ConnectFlow ptv-files. The pathline trajectories represent transport pathways. MARFA then solves radionuclide transport along the pathways using a time-domain particle method. With this method, particles are advanced along a pathway using deterministic spatial displacements and random transit times for each step. Testing and experience with the code demonstrate that the code is computationally efficient and extremely robust. Limited and unlimited matrix diffusion, equilibrium sorption, longitudinal dispersion, decay, and in-growth are represented. MARFA supports full spatial variability for all pathway properties, decay chains of any length, and full temporal variability in radionuclide source strength. The code reports radionuclide release rates (breakthrough) at the pathway endpoints. The functionality of MARFA for stochastic rock properties in a single segmented flowpath is not used.

MARFA Version 3.2.2 was used in SR-Site. Verification tests for this version are described in the MARFA Version 3.2.2 User's Manual (Painter and Mancillas 2009). Additional comparisons between MARFA and FARF31 were also undertaken to provide further confidence in the MARFA results for SR-Site parameter ranges (Appendix C). Verification of MARFA Version 5.0 is fully documented in Painter et al. (2020), and further verification cases are presented in Painter (2013) and in Crawford and Löfgren (2019).

Note that in a stochastic framework with multiple realisations, COMP23 and FARF31 must be executed once for each realisation, but MARFA need to be run only once with parameters for all pathway realisations as input. With multiple pathway realisations, MARFA calculates an ensemble mean breakthrough. The Monte Carlo nature of the algorithm ensures that an unbiased statistical estimate of the ensemble mean is obtained even when too few particles are used to accurately calculate breakthrough for each pathway realisation. Moreover, the statistical uncertainty in the ensemble mean is greatly reduced relative to that of individual realisations, a property of the method with significant advantages in terms of computational efficiency.

3.6.4 Summary of the transport model chain

Model linkages and data flows differ somewhat depending on whether far-field transport is modelled with MARFA or FARF31. Data flows and model linkages for FARF31 and MARFA are shown in Figure 3-2and Figure 3-3, respectively.

FARF31, with its integrated description of the transport pathway, requires only global information about each pathway from ConnectFlow. The required information – the F and t_w along each pathway – is contained in ConnectFlow ptb-files. The ptb-files also contain the third component of the so-called flow triplets, the equivalent flow rate Q_{eq} at the canister. Q_{eq} is required by COMP23.

MARFA accommodates a spatially resolved (segmented) description of the transport pathway and thus accepts ConnectFlow ptv-files, which contain F and t_w parameters and a rocktype descriptor for each segment in each segmented pathway.

MARFA and FARF31 both calculate radionuclide release rates in terms of moles of radionuclides per time per each realisation. These release rates are then converted to effective doses by simply multiplying with the Dose Conversion Factors (LDFs) and averaged to get mean annual releases. A description of the work done for developing the LDFs is provided in Avila et al. (2010).

The potential role of bentonite colloids in facilitating transport of certain radionuclides is addressed in variant modelling cases using MARFA. For those variants, the data flow shown in Figure 3-3 is modified slightly. Specifically, in the colloid-facilitated transport variant, the output of COMP23 is further processed to partition radionuclides between colloid-associated and dissolved states. The model for that partitioning process is described later in this report. The implementation of the partitioning model is not through compiled software but relies on Mathematica™ scripts.

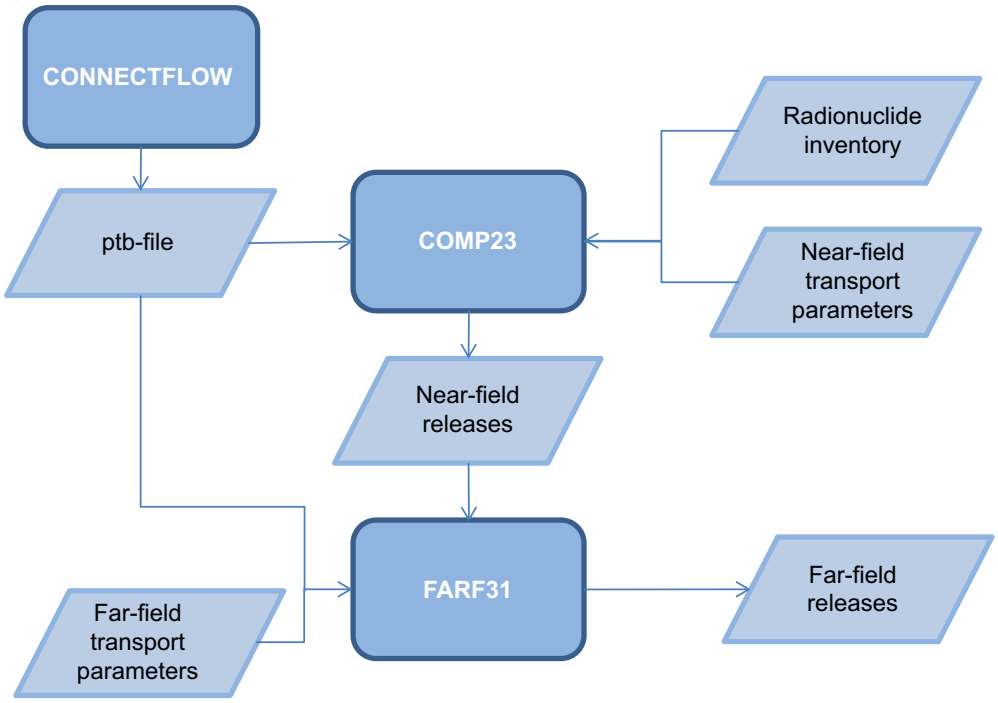

Figure 3-2. *Model linkages and data flows for radionuclide transport simulations using FARF31.*

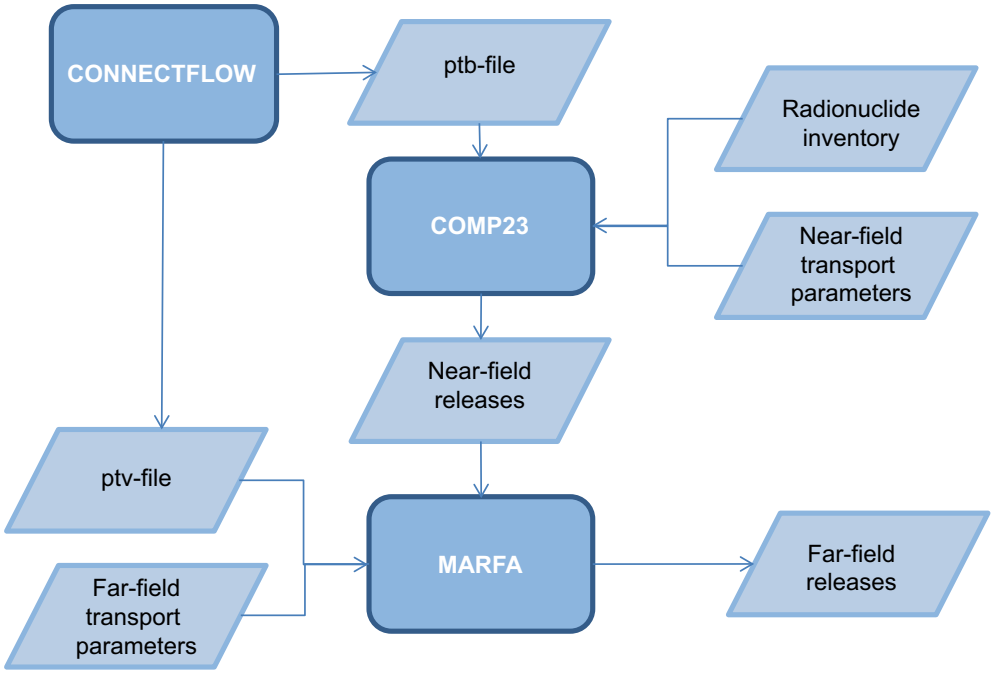

Figure 3-3. *Model linkages and data flows for radionuclide transport simulations using MARFA.*

3.6.5 Analytical models

Analytical simplified versions of the near-field and far-field transport models have been developed (Hedin 2002b). These models use the same input data as the corresponding numerical models and doses are calculated using the same LDF values as in the numerical approach. The models may be executed probabilistically and yield results in good agreement with the deterministic and probabilistic calculation cases in the SR 97 assessment (Hedin 2002b, SKB 2004). In the SR-Can assessment they were shown to be in good agreement for the corrosion scenario, for the shear load scenario and for

releases from a pinhole failure of the canister (SKB 2006a). A single realisation with the analytical models executes in around 0.1 second on a 2 GHz Personal Computer, making them well suited for probabilistic calculations. The corresponding calculation time for the numerical models is of the order of 10 seconds.

The analytical models have been benchmarked against the numerical models for several calculation cases in this report. The roles of the analytical models are to i) quickly and preliminarily evaluate calculation cases to be used in the planning of the transport calculations, ii) serve as one of several quality assurance measures of the numerical calculations by identifying potential differences in results obtained with the analytical and numerical models and seeking explanations for these (are they due to modelling errors or to differences in the nature of the models?), and iii) demonstrating an understanding of the nature of the models facilitated by the simple nature of the analytic models.

3.6.6 Input data to the transport models

Detailed discussions of data sources and data qualification methods can be found in the **Data report**. Unless otherwise noted, parameter values required in the radionuclide transport calculations are taken from the **Data report**. Specific sections of the **Data report** relevant to radionuclide transport calculations are as follows: parameters required to model spent fuel mobilisation are discussed in Chapter 3; buffer and backfill data required to model radionuclide migration in the near field are described in Section 5.3; flow related and non-flow related migration properties are found in Section 6.7 and 6.8, respectively; landscape dose factors are discussed in Section 7.2. Additional discussions of parameters and parameter summaries are also provided in this report, as needed, to facilitate a self-contained reading.

For some modelling cases, input parameters are required that are outside the scope of the **Data report**. Input parameters required for those cases are documented here. The specific parameters are colloid concentrations for modelling cases that consider colloid-facilitated transport (Sections 4.5.6 and 4.5.8) and flow scaling factors for cases that considered the effects of unsteady flow (Sections 4.5.7 and 4.5.8). In addition, one set of modelling cases (Section 6.4) that used a hypothetical residual scenario to illustrate certain barrier functions of the geosphere was completed before SR-Site data were finalised. Assumed parameters for those modelling cases are summarised in Appendix H.

3.7 Summary of all data used

Hydrogeological data related to flow and transport, obtained from the modelling reported in Joyce et al. (2010) are transferred to the calculations through the ptb/ptv-files. Three fracture size/transmissivity correlation functions are considered yielding three variants of the hydrogeological DFN model. Several cases/realisations are available for each variant of the hydrogeological model, see Table 3-1. The ptb-files and ptv-files are archived at SKB, see Table 3-8. All hydrogeological cases used in the radionuclide release calculations are for the time 2000 AD.

Almost all data are qualified in the **Data report** and therefore is only a short summary of the input given in this section. Table 3-2 gives a summary of the data used. Input data used in the PSAR are given in Appendix L.

The numerical dose estimates are dependent on the radionuclide inventory assumed. Sensitivity to the assumed inventory and implications of using an average inventory in the calculations are discussed in detail in Appendix E. The inventories for most nuclides that contribute significantly to dose vary by less than a factor of 1.5. The exception is Ag-108m, which has negligible inventory in BWR canisters and a PWR inventory that is a factor of 4 higher than the assumed average. However, Ag-108m contributes significantly to the total dose only in the shear failure case with early failure and in hypothetical cases used to illustrate barrier function. Most of the dose-contributing radionuclides are single radionuclides and hence the doses are directly scaled to the inventories. Although the dose from Ra-226 is dependent of the inventories of its precursor radionuclides, U-238, Pu-238, U-234 and Th-230, none of those radionuclides differ more than a factor of two between different canisters.

Table 3-1. Hydogeological realisations used in the radionuclide transport calculations (Joyce et al. 2010).

Hydrogeological DFN model	Realisations
Semi-correlated model	Base case and 10 additional realisations at 2000 AD
	Crown space
	No EDZ
	EDZ with transmissivity of 10^{-7} m^2/s
	EDZ with transmissivity of 10^{-6} m^2/s
Uncorrelated model	Base case and 5 additional realisations
Fully correlated model	Base case and 5 additional realisations

Table 3-2. Input data for the probabilistic calculations for the corrosion, shear load, isostatic load and pinhole scenarios. Input data used in the PSAR are given in Appendix L.

Parameter name	Parameter	Unit	Data	NF/ FF	Data report section and symbol
HALFLIFE	Half-life	yr	Constants	NF/ FF	3.1[a)] $t_{½}$
FPC, EFPC	Criteria for exclusion of deposition holes		Corrosion: Used to select deposition holes, given in ptb-files Shear load: Not used Isostatic load: Same as corrosion Pinhole: Same as corrosion	NF/ FF	
Near-field geometry			See Appendix G, Table G-1	NF	
Number of failed canisters			See each case	NF	
INVENTORY	Radionuclide inventory	mol	Constant. Data for average canister calculated from all fuel assemblies	NF	3.1[a)]
FDMC	Fuel conversion time	yr	Log-triangular (10^6, 10^7,10^8 yr)	NF	3.3
IRF	Instant release fraction of inventory	–	Data for average canister. Normal distributions for Cl, Cs, I, Se. Triangular distributions for Sr, Ni, Nb, Mo Tc, Pd, Sn. 100 % for H, Ag. Single value for Cd	NF	3.2[a)] *IRF*
CRF	Corrosion release fraction of inventory	–	Data for average canister. Double triangular distributions for C, Cl, Ni, Se, Mo, Zr, Tc, Sn-121m, U-233. 100 % for Nb-94. Single value for Nb-93m	NF	3.2[a)] *CRF*
TCORR	Corrosion time	yr	Log-triangular (10^2, 10^3, 10^4 yr)	NF	3.2 t_{corr}
TFAILURE	Time for failure	yr	Corrosion: As calculated with the corrosion model, see each case. Shear load: See each case Isostatic load: 10 000 years and 100 000 years (postulated) Pinhole: Initial failure (postulated)	NF	
TDELAY	Delay time for onset of radionuclide transport [c)]	yr	Corrosion: 0 years Shear load: 100 years Isostatic load: 0 years Pinhole: 1 000 years	NF	4.2 t_{delay}
TLARGE	Time for large canister defect	yr	Corrosion: Same as time for failure Shear load: Same as time for failure Isostatic load: Same as time for failure Pinhole: 10 000 yr (postulated)	NF	4.2 t_{large}
ADELAY, ALARGE	Canister defect sizes	m	Corrosion: Unlimited at the time for failure Shear load: Unlimited at the time for failure Isostatic load: Unlimited at the time for failure Pinhole: Between onset and TLARGE: 2 mm radius penetrating pinhole. After TLARGE: Unlimited.	NF	4.2 r_{defect}

Parameter name	Parameter	Unit	Data	NF/ FF	Data report section and symbol
CSOL	Solubility limits	mol/m^3	Calculated distributions based on distributions of several groundwater compositions, see Appendix F Corrosion: Not used (except in one alternative case “including solubility limits in the near field”) Shear load: Calculated distributions Isostatic load: Calculated distributions Pinhole: Calculated distributions	NF	3.4
KDB	Buffer sorption partitioning coefficients	m^3/kg	Corrosion: Not used Shear load: Log triangular distributions Isostatic load: Log triangular distributions Pinhole: Log triangular distributions	NF	5.3 K_d
DEB	Buffer effective diffusivities	m^2/s	Corrosion: Not used Shear load: Distributions Isostatic load: Distributions Pinhole: Distributions	NF	5.3 D_e
EPSB	Buffer porosities (diffusion available porosity)	–	Corrosion: Not used Shear load: Anions: Triangular (0.13, 0.18, 0.24) Minor changes in the **Data report** Cations: Triangular (0.43, 0.44, 0.47) Minor changes in the **Data report** Isostatic load: Same as shear load Pinhole: Same as shear load	NF	5.3 ε
RHO for material 2	Buffer density (density of the solid particles)	kg/m^3	Corrosion: Not used Shear load: Constant = 2780 kg/m^3 Isostatic load: Constant = 2780 kg/m^3 Pinhole: Constant = 2780 kg/m^3	NF	5.1 ρ_s
KDBF	Backfill sorption partitioning coefficients	m^3/kg	Corrosion: Not used Shear load: Not used Isostatic load: Log triangular distributions Pinhole: Log triangular distributions	NF	5.3 K_d
DEBF	Backfill effective diffusivities	m^2/s	Corrosion: Not used Shear load: Not used Isostatic load: Log triangular distributions Pinhole: Log triangular distributions	NF	5.3 D_e
EPSBF	Backfill porosity (diffusion available porosity)	–	Corrosion: Not used Shear load: Not used Isostatic load: Anions: Triangular (0.13, 0.18, 0.26) Cations: Triangular (0.44, 0.46, 0.48) Pinhole: Same as isostatic load	NF	5.3 ε
RHO for material 3	Backfill density (density of the solid particles)	kg/m^3	Corrosion: Not used Shear load: Not used Isostatic load: Constant = 2780 kg/m^3 Pinhole: Constant = 2780 kg/m^3	NF	5.1 ρ_s
QEQ_1	Equivalent flow from deposition hole to fracture(s) intersecting deposition hole	m^3/yr	Corrosion: Not used Shear load: 1 m^3/yr Isostatic load: Given in ptb-files (QEQ) Pinhole: Given in ptb-files (QEQ)	NF	6.7 Q_{eq1}
QEQ_2	Equivalent flow to EDZ	m^3/yr	Corrosion: Not used Shear load: Not used Isostatic load: Given in ptb-files (QEQ) Pinhole: Given in ptb-files (QEQ)	NF	6.7 Q_{eq2}
QEQ_3	Equivalent flow to fractures intersecting deposition tunnel	m^3/yr	Corrosion: Not used Shear load: Not used Isostatic load: Given in ptb-files (QEQR) Pinhole: Given in ptb-files (QEQR)	NF	6.7 Q_{eq3}

Parameter name	Parameter	Unit	Data	NF/ FF	Data report section and symbol
LR_TUN_3	Path length to the first fracture in tunnel	m	Corrosion: Not used Shear load: Not used Isostatic load: Given in ptb-files (LR_TUN) Pinhole: Given in ptb-files (LR_TUN)	NF	
TRAPP_3* LR_TUN_3/ TR_TUN_3	Darcy flux in the deposi-tion tunnel (Porosity*Path length/travel time)	m/yr	Corrosion: Not used Shear load: Not used Isostatic load: Calculated from porosity (TRAPP), path length (LR_TUN) and travel time (TR_TUN) given in ptb-files Pinhole: Same as isostatic load	NF	
U0_1	Darcy flux at deposition hole	m^3/m^2,yr	Corrosion: Used to calculate the flow in the deposition hole, given in ptb-files (U0) Shear load: Not used Isostatic load: Used for spalling, given in ptb-files (U0) Pinhole: Used for spalling, given in ptb-files (U0)	NF	6.7 *q/U0*
FLEN	Length of largest fracture intersecting deposition hole	m	Corrosion: Not used Shear load: Not used Isostatic load: Used for spalling, given in ptb-files (FLEN) Pinhole: Used for spalling, given in ptb-files (FLEN)	NF	
Wzone	Width of spalling zone	m	Corrosion: Not used Shear load: Not used Isostatic load: Used for spalling, Constant = 0.5 m Pinhole: Used for spalling, Constant = 0.5 m	NF	6.5 W_{zone}
Lzone	Length of spalling zone	m	Corrosion: Not used Shear load: Not used Isostatic load: Used for spalling, Constant = 8 m Pinhole: Used for spalling, Constant = 8 m	NF	6.5 L_{zone}
Dzone	Thickness of spalling zone	m	Corrosion: Not used Shear load: Not used Isostatic load: Used for spalling, Constant = 0.1 m Pinhole: Used for spalling, Constant = 0.1 m	NF	6.5 d_{zone}
Epszone	Porosity of spalling zone	–	Corrosion: Not used Shear load: Not used Isostatic load: Used for spalling, Constant = 0.02 Pinhole: Used for spalling, Constant = 0.02	NF	6.5 ε_{zone}
Dp	Diffusion coef-ficient in spalling zone (damaged zone)	m^2/s	Corrosion: Not used Shear load: Not used Isostatic load: Used for spalling, Constant = 10^{-11} m^2/s. Calculated from $Dp=Dw/\tau^2$ according to Neretnieks et al. (2010). τ is given in the **Data report**. Pinhole: same as isostatic load	NF	6.5
RHO for material 1	Water density	kg/m^3	Constant = 1 000 kg/m^3	NF	
Dw	Diffusivity in water	m^2/s	Corrosion: Not used Shear load: Not used Isostatic load: Constant = 10^{-9} m^2/s. Used for calculation of the diffusivity in spalling zone Pinhole: Constant = 10^{-9} m^2/s. Used for calculation of the resistance in the hole in the pinhole scenario and for calculation of the diffusivity in spalling zone	NF	6.8 D_w

Parameter name	Parameter	Unit	Data	NF/ FF	Data report section and symbol
KDR	Rock sorption partitioning coefficients	m^3/kg	Corrosion: Truncated log-normal distributions Shear load: Not used Isostatic load: Truncated log-normal distributions Pinhole: Truncated log-normal distributions	FF	6.8 K_d
DER	Rock effective diffusivities	m^2/s	Corrosion: Log normal distributions, mean values anions: 2.1×10^{-7} m^2/yr, cations: 6.6×10^{-7} m^2/yr Shear load: Not used Isostatic load: Same as corrosion Pinhole: Same as corrosion	FF	6.8 D_e
EPSR	Rock porosities (diffusion available porosity)	–	Corrosion: Constant = 0.0018 Shear load: Not used Isostatic load: Constant = 0.0018 Pinhole: Constant = 0.0018	FF	6.8 ε
	Rock density (solid density)	kg/m^3	Corrosion: Constant = 2700 kg/m^3 Shear load: Not used Isostatic load: Constant = 2700 kg/m^3 Pinhole: Constant = 2700 kg/m^3	FF	6.4 ρ
F_1, F_2, F_3	Rock flow-related transport resistance for paths beginning at Q1, Q2 and Q3	yr/m	Corrosion: Given in ptb-files (F) Shear load: Not used Isostatic load: Given in ptb-files (F) Pinhole: Given in ptb-files (F)	FF	6.7 F
TW_1, TW_2, TW_3	Rock advective travel time for paths beginning at Q1, Q2 and Q3	yr	Corrosion: Given in ptb-files (TW) Shear load: Not used Isostatic load: Given in ptb-files (TW) Pinhole: Given in ptb-files (TW)	FF	6.7 t_w
PE	Rock Peclet number	–	Corrosion: Constant = 10 Shear load: Not used Isostatic load: Constant = 10 Pinhole: Constant = 10	FF	6.7 Pe
DPEN	Max. penetration depth in rock matrix	m	Corrosion: Constant = 12.5 Shear load: Not used Isostatic load: Constant = 12.5 Pinhole: Constant = 12.5	FF	6.7 L_D
LDF	Biosphere LDF factors	Sv/y per Bq/y	Constant. Calculated LDF values, see Table 3-7.	FF	7.2 *LDF*
KDC	Colloid sorption coefficients	m^3/kg	Corrosion: Only used in calculations including colloids Buffer sorption coefficients, KDB, are used Shear load: Not used Isostatic load: Not used Pinhole: Not used	FF	
	Concentration of suspended colloids	kg/m^3	Corrosion: Only used in calculations including colloids 10 mg/litre and 10 g/litre Shear load: Not used Isostatic load: Not used Pinhole: Not used	FF	

a) Values for SR-Site are given in the corresponding section of the SR-Site data report (SKB 2010b).
b) Only used in PSAR.
c) Time between canister failure and the establishment of a continuous water pathway from the fuel to the exterior of the canister.

3.7.1 Probabilistic input data

The software @risk (the risk analysis add-in for excel, Palisade Corporation) was used to generate input data to the transport calculations when the **Data report** recommended a distribution. Also correlations recommended in the **Data report** were used. In all simulations Latin hypercube was used as the sampling type and 6 916 iterations were run. The simulation results were transferred to Matlab files (.mat files) and these files were always used as input to COMP23 and FARF31. Each line number in the .mat files forms a unique set of input data for a single calculation and in this section it is called a realisation.

The variants of the corrosion case, including cases addressing best available technique (BAT), had different numbers of realisations depending on how many possible failure times the case was holding. Each failure time was iterated 50 times (see Section 4.4.4 about convergence) so the total number of realisations in each case was the number of failure times multiplied by 50. The input files containing 6 916 realisations were always used starting from realisation 1 in the input file and ending at the realisation number. For corrosion variants with less than 6 916 realisations the procedure is not fully consistent with Latin hypercube sampling, i.e. the advantage of the Latin hypercube is not fully used. However, this is not expected to create any biases. In a few corrosion variants, the number of realisations was greater than 6 916 and in these calculations the input datasets were re-run from the beginning as many times as needed to calculate up to the realisation number in demand. Again, this procedure is not fully consistent with Latin hypercube sampling but is not expected to create biases in the results.

All variants of the shear load cases were run with exactly 6 916 realisations except for the SR-Site case with a failure at 100 000 years, which was run with 1 000 realisations. This case had an input data set with 1 000 simulations sampled by Latin hypercube.

All variants of the isostatic load case and the pinhole cases were run with exactly 6 916 realisations, i.e. the optimal spread of data sampled by Latin hypercube is used.

3.7.2 Deterministic input data

The deterministic input data set consists of median values from the probabilistic input data sets of 6 916 iterations, see Table 3-3 and Table 3-4. All variables were the same in all different calculation cases except for the transport parameters (U0, QEQ, FLEN, TW, F, TRAPP, LR_TUN and TR_TUN). These parameters change with the hydrogeological case for the shear cases, the isostatic load cases and the pinhole cases. The semi-correlated base case is used for the shear load, isostatic load, the base case and the no spalling case of the pinhole scenario. The rest of the pinhole cases had specific hydrogeological cases.

Near-field transport parameters are median values after excluding the special cases of OKFLAG = 1, FPC > 0 and EFPC > 4, see Table 3-5. The only exception is in the shear load scenario where QEQ always is assumed to be high and set to 1 m3/yr both in the probabilistic and deterministic calculations. OKFLAG = 1 represents paths where the particle failed to start due to no fracture or low velocity. Excluding FPC > 0 means that deposition holes are excluded due to background fractures or deformation zone fractures. Excluding EFPC > 4 means that canister positions intersected by fractures that also intersect the entire tunnel perimeter have been discarded.

The far-field transport parameters are median values after excluding OKFLAG = 1, 2, 3 and 4, FPC > 0 and EFPC > 4, see Table 3-6. OKFLAG 2, 3, 4 indicates that the particle tracing in the hydrogeological calculations failed to compleate.

For the corrosion scenario the transport parameters change with the hydrogeological case and the results from the erosion/corrosion model and the parameters used in the deterministic calculations are always those connected to the earliest failure time, see Section 4.3.

The LDF-values used for both deterministic and probabilistic calculations are given in Table 3-7.

Table 3-3. Median values of D_e, K_d and ε used in the deterministic near-field and far-field calculations. ε rock is not in the table since it is constant, 1.80×10^{-3} (–), for all nuclides. Input data used in the PSAR are given in Appendix L.

	D_e buffer (m^2/yr)	D_e backfill (m^2/yr)	D_e rock (m^2/yr)	K_d buffer (m^3/kg)	K_d backfill (m^3/kg)	K_d rock (m^3/kg)	ε buffer (–)	ε backfill (–)
Ac-227	4.20×10^{-3}	5.00×10^{-3}	6.30×10^{-7}	5.20	5.20	1.5×10^{-2}	0.45	0.46
Ag-108m	4.20×10^{-3}	5.00×10^{-3}	6.30×10^{-7}	0.00	0.00	3.5×10^{-4}	0.45	0.46
Am-241	4.20×10^{-3}	5.00×10^{-3}	6.30×10^{-7}	2.50×10^{1}	2.50×10^{1}	1.5×10^{-2}	0.45	0.46
Am-242m	4.20×10^{-3}	5.00×10^{-3}	6.30×10^{-7}	2.50×10^{1}	2.50×10^{1}	1.5×10^{-2}	0.45	0.46
Am-243	4.20×10^{-3}	5.00×10^{-3}	6.30×10^{-7}	2.50×10^{1}	2.50×10^{1}	1.5×10^{-2}	0.45	0.46
C-14	4.20×10^{-3}	5.00×10^{-3}	6.30×10^{-7}	0.00	0.00	0.0	0.45	0.46
Cd-113m	4.20×10^{-3}	5.00×10^{-3}	6.30×10^{-7}	6.60×10^{-2}	6.60×10^{-2}	1.1×10^{-3}	0.45	0.46
Cl-36	2.50×10^{-4}	3.10×10^{-4}	2.00×10^{-7}	0.00	0.00	0.0	0.18	0.19
Cm-245	4.20×10^{-3}	5.00×10^{-3}	6.30×10^{-7}	2.50×10^{1}	2.50×10^{1}	1.5×10^{-2}	0.45	0.46
Cm-246	4.20×10^{-3}	5.00×10^{-3}	6.30×10^{-7}	2.50×10^{1}	2.50×10^{1}	1.5×10^{-2}	0.45	0.46
Cs-135	8.40×10^{-3}	9.90×10^{-3}	6.30×10^{-7}	3.10×10^{-2}	3.10×10^{-2}	3.5×10^{-4}	0.45	0.46
Cs-137	8.40×10^{-3}	9.90×10^{-3}	6.30×10^{-7}	3.10×10^{-2}	3.10×10^{-2}	3.5×10^{-4}	0.45	0.46
Eu-152	4.20×10^{-3}	5.00×10^{-3}	6.30×10^{-7}	5.20	5.20	1.5×10^{-2}	0.45	0.46
H-3	4.20×10^{-3}	5.00×10^{-3}	6.30×10^{-7}	0.00	0.00	0.0	0.45	0.46
Ho-166m	4.20×10^{-3}	5.00×10^{-3}	6.30×10^{-7}	5.20	5.20	1.5×10^{-2}	0.45	0.46
I-129	2.50×10^{-4}	3.10×10^{-4}	2.00×10^{-7}	0.00	0.00	0.0	0.18	0.19
Mo-93	2.50×10^{-4}	3.10×10^{-4}	2.00×10^{-7}	0.00	0.00	0.0	0.18	0.19
Nb-93m	4.20×10^{-3}	5.00×10^{-3}	6.30×10^{-7}	3.10	3.10	2.0×10^{-2}	0.45	0.46
Nb-94	4.20×10^{-3}	5.00×10^{-3}	6.30×10^{-7}	3.10	3.10	2.0×10^{-2}	0.45	0.46
Ni-59	4.20×10^{-3}	5.00×10^{-3}	6.30×10^{-7}	6.60×10^{-2}	6.60×10^{-2}	1.1×10^{-3}	0.45	0.46
Ni-63	4.20×10^{-3}	5.00×10^{-3}	6.30×10^{-7}	6.60×10^{-2}	6.60×10^{-2}	1.1×10^{-3}	0.45	0.46
Np-237	4.20×10^{-3}	5.00×10^{-3}	6.30×10^{-7}	3.90×10^{1}	3.90×10^{1}	5.3×10^{-2}	0.45	0.46
Pa-231	4.20×10^{-3}	5.00×10^{-3}	6.30×10^{-7}	3.10	3.10	5.9×10^{-2}	0.45	0.46
Pb-210	4.20×10^{-3}	5.00×10^{-3}	6.30×10^{-7}	4.90×10^{1}	4.90×10^{1}	2.5×10^{-2}	0.45	0.46
Pd-107	4.20×10^{-3}	5.00×10^{-3}	6.30×10^{-7}	5.10	5.10	5.2×10^{-2}	0.45	0.46
Pu-238	4.20×10^{-3}	5.00×10^{-3}	6.30×10^{-7}	3.90×10^{1}	3.90×10^{1}	1.5×10^{-2}	0.45	0.46
Pu-239	4.20×10^{-3}	5.00×10^{-3}	6.30×10^{-7}	3.90×10^{1}	3.90×10^{1}	1.5×10^{-2}	0.45	0.46
Pu-240	4.20×10^{-3}	5.00×10^{-3}	6.30×10^{-7}	3.90×10^{1}	3.90×10^{1}	1.5×10^{-2}	0.45	0.46
Pu-242	4.20×10^{-3}	5.00×10^{-3}	6.30×10^{-7}	3.90×10^{1}	3.90×10^{1}	1.5×10^{-2}	0.45	0.46
Ra-226	4.20×10^{-3}	5.00×10^{-3}	6.30×10^{-7}	1.10×10^{-3}	1.10×10^{-3}	2.4×10^{-4}	0.45	0.46
Se-79	2.50×10^{-4}	3.10×10^{-4}	2.00×10^{-7}	0.00	0.00	3.0×10^{-4}	0.18	0.19
Sm-151	4.20×10^{-3}	5.00×10^{-3}	6.30×10^{-7}	5.20	5.20	1.5×10^{-2}	0.45	0.46
Sn-121m	4.20×10^{-3}	5.00×10^{-3}	6.30×10^{-7}	3.90×10^{1}	3.90×10^{1}	1.6×10^{-1}	0.45	0.46
Sn-126	4.20×10^{-3}	5.00×10^{-3}	6.30×10^{-7}	3.90×10^{1}	3.90×10^{1}	1.6×10^{-1}	0.45	0.46
Sr-90	4.20×10^{-3}	5.00×10^{-3}	6.30×10^{-7}	1.10×10^{-3}	1.10×10^{-3}	3.4×10^{-6}	0.45	0.46
Tc-99	4.20×10^{-3}	5.00×10^{-3}	6.30×10^{-7}	3.90×10^{1}	3.90×10^{1}	5.3×10^{-2}	0.45	0.46
Th-229	4.20×10^{-3}	5.00×10^{-3}	6.30×10^{-7}	3.90×10^{1}	3.90×10^{1}	5.3×10^{-2}	0.45	0.46
Th-230	4.20×10^{-3}	5.00×10^{-3}	6.30×10^{-7}	3.90×10^{1}	3.90×10^{1}	5.3×10^{-2}	0.45	0.46
Th-232	4.20×10^{-3}	5.00×10^{-3}	6.30×10^{-7}	3.90×10^{1}	3.90×10^{1}	5.3×10^{-2}	0.45	0.46
U-233	4.20×10^{-3}	5.00×10^{-3}	6.30×10^{-7}	3.90×10^{1}	3.90×10^{1}	5.3×10^{-2}	0.45	0.46
U-234	4.20×10^{-3}	5.00×10^{-3}	6.30×10^{-7}	3.90×10^{1}	3.90×10^{1}	5.3×10^{-2}	0.45	0.46
U-235	4.20×10^{-3}	5.00×10^{-3}	6.30×10^{-7}	3.90×10^{1}	3.90×10^{1}	5.3×10^{-2}	0.45	0.46
U-236	4.20×10^{-3}	5.00×10^{-3}	6.30×10^{-7}	3.90×10^{1}	3.90×10^{1}	5.3×10^{-2}	0.45	0.46
U-238	4.20×10^{-3}	5.00×10^{-3}	6.30×10^{-7}	3.90×10^{1}	3.90×10^{1}	5.3×10^{-2}	0.45	0.46
Zr-93	4.20×10^{-3}	5.00×10^{-3}	6.30×10^{-7}	4.70	4.70	2.1×10^{-2}	0.45	0.46

Table 3-4. Median values of solubilities (temperate conditions, see Appendix F), IRF and CRF used in the deterministic near-field and far-field calculations. If IRF+CRF is greater than one CRF is 1-IRF. The solubility, CSOL, 1.00×10^{17} corresponds to unlimited solubility. Input data used in the PSAR are given in Appendix L.

	CSOL (mol/dm^3)	IRF (–)	CRF (–)
Ac-227	1.00×10^{17}	0.00	0.00
Ag-108m	1.10×10^{-5}	1.00	0.00
Am-241	2.50×10^{-6}	0.00	0.00
Am-242m	2.50×10^{-6}	0.00	0.00
Am-243	2.50×10^{-6}	0.00	0.00
C-14	1.00×10^{17}	9.20×10^{-2}	6.40×10^{-1}
Cd-113m	1.00×10^{17}	1.00	0.00
Cl-36	1.00×10^{17}	8.60×10^{-2}	1.50×10^{-2}
Cm-245	2.60×10^{-6}	0.00	0.00
Cm-246	2.60×10^{-6}	0.00	0.00
Cs-135	1.00×10^{17}	2.90×10^{-2}	0.00
Cs-137	1.00×10^{17}	2.90×10^{-2}	0.00
Eu-152	1.00×10^{17}	0.00	0.00
H-3	1.00×10^{17}	1.00	0.00
Ho-166m	4.10×10^{-6}	0.00	0.00
I-129	1.00×10^{17}	2.90×10^{-2}	0.00
Mo-93	1.00×10^{17}	1.20×10^{-2}	8.10×10^{-1}
Nb-93m	4.90×10^{-5}	1.70×10^{-2}	1.00
Nb-94	4.90×10^{-5}	1.80×10^{-2}	1.00
Ni-59	3.00×10^{-4}	1.20×10^{-2}	9.60×10^{-1}
Ni-63	3.00×10^{-4}	1.20×10^{-2}	9.70×10^{-1}
Np-237	1.00×10^{-9}	0.00	0.00
Pa-231	3.30×10^{-7}	0.00	0.00
Pb-210	1.70×10^{-6}	0.00	0.00
Pd-107	3.90×10^{-6}	2.00×10^{-3}	0.00
Pu-238	4.80×10^{-6}	0.00	0.00
Pu-239	4.80×10^{-6}	0.00	0.00
Pu-240	4.80×10^{-6}	0.00	0.00
Pu-242	4.80×10^{-6}	0.00	0.00
Ra-226	9.10×10^{-7}	0.00	0.00
Se-79	6.70×10^{-9}	4.20×10^{-3}	1.30×10^{-4}
Sm-151	1.10×10^{-7}	0.00	0.00
Sn-121m	9.00×10^{-8}	1.90×10^{-4}	5.20×10^{-1}
Sn-126	9.00×10^{-8}	3.00×10^{-4}	0.00
Sr-90	3.70×10^{-3}	2.50×10^{-3}	0.00
Tc-99	3.80×10^{-9}	2.00×10^{-3}	6.10×10^{-5}
Th-229	2.60×10^{-9}	0.00	0.00
Th-230	2.60×10^{-9}	0.00	0.00
Th-232	2.60×10^{-9}	0.00	0.00
U-233	9.50×10^{-10}	0.00	2.50×10^{-1}
U-234	9.50×10^{-10}	0.00	0.00
U-235	9.50×10^{-10}	0.00	0.00
U-236	9.50×10^{-10}	0.00	0.00
U-238	9.50×10^{-10}	0.00	0.00
Zr-93	1.80×10^{-8}	9.20×10^{-6}	1.30×10^{-1}

Table 3-5. Median values of transport parameters used as input data in the deterministic near-field calculations.

	Isostatic load, pinhole base case and no spalling	Pinhole Crown space	Pinhole no EDZ	Pinhole max EDZ 6	Pinhole max EDZ 7
U0_1 (m/yr)	7.00×10^{-6}	6.7×10^{-6}	5.00×10^{-6}	6.90×10^{-6}	6.50×10^{-6}
QEQ_1 (m^3/yr)	4.20×10^{-6}	4.2×10^{-6}	4.50×10^{-6}	4.30×10^{-6}	4.20×10^{-6}
FLEN (m)	6.00	6.20	1.60×10^{1}	5.90	6.00
TW_1 (yr)	2.10×10^{2}	1.20×10^{2}	4.70×10^{2}	1.30×10^{2}	1.60×10^{2}
F_1 (yr/m)	5.50×10^{6}	3.20×10^{6}	4.90×10^{7}	2.60×10^{6}	3.80×10^{6}
QEQ_2 (m^3/yr)	9.30×10^{-5}	9.50×10^{-5}	0.00	6.00×10^{-4}	2.20×10^{-4}
TW_2 (yr)	1.90×10^{2}	9.50×10^{1}	0.00	1.10×10^{2}	1.40×10^{2}
F_2 (yr/m)	3.50×10^{6}	1.2×10^{6}	0.00	9.20×10^{5}	1.60×10^{6}
QEQR_3 (m^3/yr)	1.20×10^{-4}	2.70×10^{-4}	2.00×10^{-5}	8.40×10^{-4}	3.30×10^{-4}
TW_3 (yr)	1.70×10^{2}	8.00×10^{1}	2.90×10^{2}	1.10×10^{2}	1.40×10^{2}
F_3 (yr/m)	2.40×10^{6}	6.00×10^{5}	1.10×10^{7}	6.30×10^{5}	1.30×10^{6}
TRAPP_3 (m)	4.50×10^{-1}	1.00	4.50×10^{-1}	4.50×10^{-1}	4.50×10^{-1}
LR_TUN_3 (m)	5.10	118	1.80×10^{1}	5.00	5.30
TR_TUN_3 (yr)	2.00×10^{5}	890	1.20×10^{6}	2.60×10^{5}	2.40×10^{5}

Table 3-6. Median values of transport parameters used as input data in the deterministic far-field calculations.

	Isostatic load, pinhole base case and no spalling	Pinhole Crown space	Pinhole no EDZ	Pinhole max EDZ 6	Pinhole max EDZ 7
TW_1 (yr)	1.80×10^{2}	9.20×10^{1}	2.10×10^{2}	1.06×10^{2}	1.35×10^{2}
F_1 (yr/m)	4.00×10^{6}	2.20×10^{6}	1.20×10^{7}	1.68×10^{6}	2.57×10^{6}
TW_2 (yr)	1.60×10^{2}	7.90×10^{1}	1.00×10^{-21}	9.70×10^{1}	1.27×10^{2}
F_2 (yr/m)	2.30×10^{6}	7.50×10^{5}	1.00×10^{-21}	6.19×10^{5}	1.12×10^{6}
TW_3 (yr)	1.50×10^{2}	6.30×10^{1}	2.00×10^{2}	9.60×10^{1}	1.26×10^{2}
F_3 (yr/m)	1.90×10^{6}	3.20×10^{5}	5.10×10^{6}	5.08×10^{5}	1.01×10^{6}

Table 3-7. Basic Landscape Dose Factors (Sv/yr per Bq/yr), Dose Conversion Factors for pulse releases and distributed Dose Conversion Factors (Avila et al. 2010, Kautsky 2012). Input data used in the PSAR are given in Appendix L.

Radionuclide	Basic LDF (Sv/yr per Bq/yr)	LDF pulse (Sv/yr per Bq)	Distributed LDF (Sv/yr per Bq/yr)
Ag-108m	7.05×10^{-13}	5.08×10^{-16}	7.99×10^{-14}
Ac-227	1.30×10^{-11}		
Am-241	1.46×10^{-12}		7.34×10^{-13}
Am-243	1.53×10^{-12}		7.57×10^{-13}
C-14	5.44×10^{-12}		9.48×10^{-13}
Cl-36	5.84×10^{-13}	4.29×10^{-15}	1.86×10^{-13}
Cm-244	8.74×10^{-13}		4.41×10^{-13}
Cm-245	1.58×10^{-12}		7.78×10^{-13}
Cm-246	1.55×10^{-12}		7.75×10^{-13}
Cs-135	3.96×10^{-14}	1.84×10^{-16}	1.16×10^{-14}
Cs-137	1.20×10^{-13}		6.03×10^{-14}
Ho-166m	5.90×10^{-14}		1.15×10^{-14}
I-129	6.46×10^{-10}	5.56×10^{-14}	5.96×10^{-11}
Nb-94	4.00×10^{-12}	3.18×10^{-16}	2.29×10^{-13}
Ni-59	7.39×10^{-14}	9.67×10^{-18}	6.57×10^{-15}
Ni-63	1.21×10^{-15}		5.88×10^{-16}
Np-237	4.83×10^{-11}		2.48×10^{-11}
Pa-231	8.10×10^{-12}		2.94×10^{-12}
Pb-210	5.07×10^{-12}		2.56×10^{-12}
Pd-107	6.73×10^{-15}		2.00×10^{-15}
Po-210	8.86×10^{-12}		4.47×10^{-12}
Pu-239	1.94×10^{-12}		1.00×10^{-12}
Pu-240	1.88×10^{-12}		9.54×10^{-13}
Pu-242	1.89×10^{-12}		1.03×10^{-12}
Ra-226	3.75×10^{-12}		1.40×10^{-12}
Se-79	1.21×10^{-9}	9.70×10^{-14}	1.50×10^{-10}
Sm-151	7.16×10^{-16}		3.61×10^{-16}
Sn-126	2.47×10^{-11}	2.31×10^{-15}	2.58×10^{-12}
Sr-90	2.19×10^{-13}		1.10×10^{-13}
Tc-99	8.98×10^{-13}	2.81×10^{-15}	2.03×10^{-13}
Th-229	3.61×10^{-12}		1.80×10^{-12}
Th-230	1.31×10^{-11}		3.48×10^{-12}
Th-232	1.72×10^{-12}		8.51×10^{-13}
U-233	2.50×10^{-12}		4.24×10^{-13}
U-234	3.62×10^{-12}		5.19×10^{-13}
U-235	2.76×10^{-12}		4.41×10^{-13}
U-236	1.85×10^{-12}		3.37×10^{-13}
U-238	1.85×10^{-12}		3.30×10^{-13}
Zr-93	2.77×10^{-14}		6.35×10^{-15}

3.7.3 QA-related issues

All erroneous data and data changed at a late stage, identified for the SR-Site and described in the SR-Site radionuclide transport report (SKB 2010d, Section 3.7.3), have been updated and used in the PSAR, see Appendix L.

During the work and final control of data according to the quality assurance plan described in Section 2.9 of the **Post-closure safety report**, it was identified that a basic LDF for Rn-222 of 5.20×10^{-14} instead of 5.10×10^{-14} is used in the calculations. This implies that the dose consequences of Rn-222 are overestimated by 2 % in the PSAR results.

Used scripts, input data and main results are archived at SKB, see Table 3-8.

Table 3-8. List of scripts, input data and main results are archived at SKB (Internal documents, access might be given on request).

SKBdoc, version	Title	Issuer, year
1256019 ver 1.0	Hydrogeological model data and results – Forsmark	SKB, 2010
1260107 ver 1.0	Supporting calculations related to radionuclide transport	SKB, 2010
1260295 ver 1.0	Results from radionuclide transport calculations with COMP23 and FARF31	SKB, 2010
1260297 ver 1.0	Scripts and input data used for radionuclide transport calculations with COMP23	SKB, 2010
1265612 ver 1.0	Scripts and data used for Analytical erosion corrosion calculations	SKB, 2010
1266150 ver 1.0	Radionuclide transport calculations with MARFA	SKB, 2010
1929341 ver 1.0	Radionuclide transport calculations for the PSAR	SKB, 2021

4 Canister failure due to corrosion

4.1 Introduction

The results shown in this chapter have not been updated since the SR-Site assessment (SKB 2010d), with the exception of some minor notes in Section 4.5.7. Instead, in Appendix M, results of recalculation of selected cases in the SR-Site corrosion scenario are compared to the corresponding calculations using updated input data for the PSAR. The aim is to demonstrate that the differences in results are sufficiently limited that the conclusions drawn from the results of the SR-Site radionuclide transport calculations are still valid with updated input data for the PSAR. The updated input data for the PSAR are given in Appendix L. Also, calculations are performed in the PSAR to analyse the impact of irregular fuels. This is described in Section 7.1.

In a few places, references in the SR-Site version were made to the main references of the SR-Site assessment, the references written in bold. It has been verified that the PSAR versions of the corresponding reports are equally valid as references in these cases. The references in bold, therefore, refer to the PSAR versions.

In the 'canister failure due to corrosion' scenario (called briefly the corrosion scenario below) canisters fail as a result of enhanced corrosion due to advective conditions in the deposition hole following the loss of buffer through erosion.

For this failure mode, both the canister and the buffer are bypassed, and the rock retention is small since substantial copper corrosion after buffer erosion only occurs in deposition holes with high flow rates, which in general are associated with flow paths to the surface of low geosphere retention.

4.1.1 Evolution of the canister after canister failure

According to the analysis of copper corrosion for advective conditions, a band, 0.35 m high and covering half the circumference of the canister, is assumed to be evenly corroded (SKB 2010a). This means that when penetration occurs, a large amount of damage must be assumed in the copper shell.

The time required to penetrate the cast iron insert is pessimistically neglected since it is difficult to estimate a reasonable development for this process for this failure mode. Also, because penetration of the copper shell in general occurs after several hundred thousand years for the few canisters exposed to the highest corrosion rates, the additional time to penetrate the cast iron insert is of less importance.

Once the copper canister and the cast iron insert have failed, the void in the insert is assumed to be rapidly filled with water due to the high flow rate and the lack of transport resistances in the absence of the buffer and with a large amount of damage also to the cast iron insert.

4.1.2 Radionuclide release

Advective conditions in the buffer must be assumed also for the consequence calculations for the corrosion scenario. There is no buffer hindering the outward transport of radionuclides meaning that this is controlled by the flow rate through the deposition hole, q (m^3/yr). The following three contributions to the outward transport can be distinguished.

- The instantaneously accessible fraction of radionuclides, IRF, that is assumed to rapidly dissolve in the water in the void volume and be subsequently flushed from the canister. This gives rise to a pulse of uncertain duration, the uncertainty stemming from e.g. uncertainties in the detailed development of the canister failure through which the IRF is made accessible. The treatment of the IRF pulse is further described below.
- A contribution from the corrosion of metal parts in the fuel assemblies and the congruent release of radionuclides embedded in the metal parts. These inventories are collectively called the corrosion release fraction, abbreviated CRF.

- A contribution from fuel dissolution and the congruent release of radionuclides embedded in the fuel matrix.

In a case where the buffer is severely eroded, a colloid filter (**Buffer, backfill and closure process report**) cannot be guaranteed. This means that the use of elemental solubilities as a limit for radionuclide release could be questioned, since it cannot be excluded that the solid particles formed by various radionuclides reaching saturation would leave the canister and migrate further. In this case, however, this is of minor concern, since the flow through the deposition hole is often too high for solid phases to precipitate (with the exception of uranium). This is demonstrated in Section 4.5.2 below by analysing a case where solubility limits are included.

The release into the fracture is thus controlled by the corrosion rate and the fuel dissolution rate, with two exceptions:

1. For uranium, a concentration limit is still an effective constraint on release, due to the large amount of U-238 present in the fuel. This limits the near-field releases of uranium isotopes, but also leads to increased near-field releases of Th-230, Th-229 and Pa-231 generated by the re-precipitated U-234, U-233 and U-235, respectively.
2. It cannot be excluded that co-precipitation processes and sorption/immobilisation in the remaining bentonite in the deposition hole could confine Th-230 to the near field. If this is the case, its daughter nuclide, the considerably more mobile Ra-226, would be released. The so generated Ra-226 is assumed to be released to the flowing groundwater in the fracture intersecting the deposition hole. This causes higher releases of Ra-226, since there is a contribution not only directly from the fuel dissolution, but also from the confined Th-230. Since Ra-226 is often the main contributor to dose, this also causes higher total doses. Sorption of thorium in the near field is thus assumed. The effect of disregarding thorium sorption is analysed as a separate calculation case.

Furthermore, as the flow rate in the intersecting fracture is high, the retention in the rock is in general limited for these deposition holes.

A description of the discretisation and boundary condition used in COMP23 is given in Appendix G, Section G.6.

Radionuclide release due to gas-phase transport is not considered in transport calculations here but is discussed in the **Post-closure safety report**, Section 13.8.

4.1.3 IRF-pulse

The fraction of the inventory assumed to be instantaneously released from the fuel upon water contact is expected to be released to the geosphere in a matter of years in the corrosion scenario, since the flow rates at the deposition positions with the eroded buffer and failed canister are high, see further Table 4-3 below. Since these nuclides are in general non-sorbing and since the flow related retardation properties in the geosphere are poor for the flow paths associated with the deposition positions in question, they are generally released as pulses of durations of tens of years from the geosphere to the biosphere. In this case, the basic LDF values would yield overly pessimistic estimates of doses. Therefore, the calculations for the IRF are made separately. There are two reasons to calculate them separately; one is the fact that the calculated basic LDF-values are not developed for peak releases as described in Section 3.5 and the other is that it is not meaningful to present many sharp peaks (up to almost 2 000 in one of the probabilistic cases) in a figure.

A number of nuclides with an IRF, and with half-lives up to 10 000 years (e.g. Sr-90, Cs-137, Ag-108m and C-14,), were excluded from the analysis of the corrosion cases since they would decay to insignificance before a failure would occur.

Tc-99

The release of the IRF part of Tc-99 has been calculated in two different ways for the near field and for the far field. For the near field the dose equivalent release is calculated in the same way as for all other IRF nuclides. The far-field pulse release is modelled with the far-field transport model since sorption in the geosphere is considerable for Tc-99. To obtain the far-field annual effective dose the IRF of Tc-99 was included in a separate calculation with COMP23 and transferred to the FARF31 calculations. This means that the far-field annual effective dose of all Tc-99 (the IRF and non IRF parts) is available when the figures for the far-field release are plotted, however the mean annual effective dose is lower than 10^{-3} μSv for all corrosion cases and therefore not visible in the figures.

Deterministic calculations

Deterministic calculations of the IRF-pulse from I-129, Se-79, Cs-135, Ni-59, Cl-36, Sn-126 and Nb-94 are calculated as follows. The total dose associated with a pulse release, $D_{TotPulse}$, is calculated by taking the IRF inventory at 100 000 years multiplied by the pulse LDF-values, given in Table 3-7, to yield a total peak dose from the pulse release for one canister. The IRF inventory could be taken at the actual failure time for the different cases, but this would not affect the result much since these nuclides are long-lived in comparison to the failure times.

Note that it is also pessimistic to apply the pulse LDF approach because the maximum dose for a given mass released to the biosphere is obtained when the entire mass is released at once, noting that the LDF pulse values are by definition taken for the point in time in the landscape development where the consequences are maximal.

Probabilistic calculations

The IRF pulses in the probabilistic cases are shown to give negligible contribution to the mean dose, by applying the treatment for the central corrosion case, see Section 4.4.2. Therefore, the IRF-pulse releases are not reported for the other cases. However, they are considered in the account of risk dilution reported in the **Post-closure safety report**, Section 13.9.

4.2 Summary of calculation cases

There are three hydrogeological models (semi-correlated, uncorrelated and fully correlated), described by Joyce et al. (2010) and summarised in the **Data report**, Section 6.7, that form the base for the calculation cases. In Figure 4-1, the hydrogeological models are indicated with blue boxes.

Three erosion/corrosionvariants (erosion/corrosion model, initial advection and no advection, orange boxes in Figure 4-1) are included, yielding together with the three hydrogeological models a total of nine combinations to consider in the derivation of calculation cases for radionuclide transport and dose. Of these, the three ‘no advection’ variants are not further treated as they do not lead to canister failures. A *central corrosion case* based on the ‘Erosion/corrosion model’ (specific for SR-Site and PSAR) was identified as the one on which assessments of radionuclide transport and dose should primarily be made. In addition, the variant with initial advection was studied. The green boxes in Figure 4-1 indicate all the calculation cases for radionuclide transport and dose. The cases are reported in the same order as in the figure.

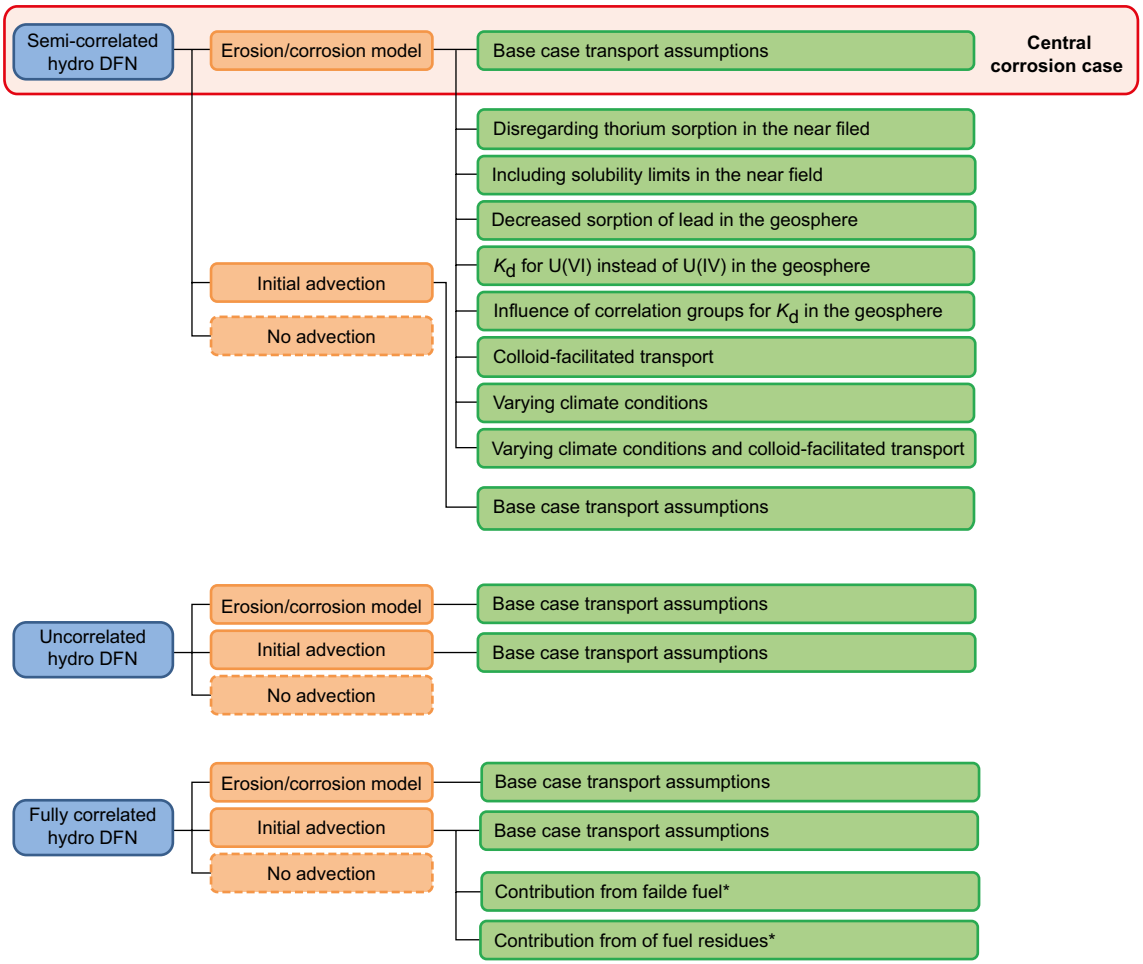

Figure 4-1. *Overview of calculation cases for the corrosion scenario. Blue boxes indicate hydrogeological DFN models, orange boxes indicate erosion/corrosion variants and green boxes indicate the transport conditions defining the calculation cases for radionuclide transport and dose. The calculation cases are presented in the same order as in this figure. * Case only calculated in the PSAR.*

The *central corrosion case* consists of the semi-correlated hydrogeological DFN-model, the erosion model and base case transport assumptions. The following sensitivity cases of alternative transport conditions are analysed for the central corrosion case:

- a case disregarding thorium sorption in the near field,
- a case including solubility limits in the near field,
- a case with decreased sorption of lead in the geosphere,
- a case with K_d for U(VI) instead of U(IV) in the geosphere,
- a case assessing the influence of correlation groups for K_d in the geosphere,
- cases with colloid facilitated transport in the geosphere,
- a case with varying climate conditions,
- a case with varying climate conditions and colloid facilitated transport in the geosphere.

By combining one of the hydrogeological models with one of the erosion/corosion variants five additional corrosion cases are identified. These calculation cases are analysed with the base case transport assumption.

4.3 Input data specific for the corrosion scenario

Most of the input data used in the corrosion scenario are given in Section 3.7 that summarises data for all scenarios. In this section more details regarding the used hydrogeological calculations and failure times are given.

The failure times are obtained as output from the erosion/corrosion calculations reported in SKB (2010a) and the results are available in SKBdoc, see Table 3-8. The input to those calculations is qualified in the **Data report**.

Several realisations of each of the three variants of the hydrogeological DFN model are propagated to the corrosion scenario, see Table 4-1. In all calculations for this scenario, deposition positions are rejected according to the EFPC criterion (canister positions intersected by fractures that also intersect the entire tunnel perimeter have been discarded) in the output from the hydrogeological modelling. In the central corrosion case, data from the 10 realisations of the semi-correlated DFN model are used.

Table 4-1. Hydrogeological realisations used in the corrosion scenario (Joyce et al. 2010).

Hydrogeological DFN model	Realisations
Semi-correlated model	Base case and 10 additional realisations
Uncorrelated model	Base case and 5 additional realisations
Fully correlated model	Base case and 5 additional realisations

The corrosion case is based on data for only the few deposition holes that experience canister failure due to corrosion. This means that all deposition holes of relevance experience a high flow rate and in general also a low flow-related rock transport resistance, since these properties are strongly correlated. It is noted that the calculated hydraulic and transport properties of these deposition holes are from the extreme tails of distributions derived from a complex hydrogeological model with stochastic components (the generated fracture network). For the deterministic calculations of the corrosion scenario the parameters used are those connected to the earliest failure time; these parameters are summarised in Table 4-2. For probabilistic calculations, the ten realisations of the semi-correlated model variant are used in order to obtain more reliable representations of these tails, see Table 4-3. For the uncorrelated and fully correlated DFN model variants, for which consequences are analysed in Section 4.6 and 4.7, the five available realisations are used.

Table 4-2. Data for the deposition holes where the first canister fails, used in deterministic calculations for SR-Site (corresponding data for PSAR are given in Appendix L Table L-22).

Hydrogeological model; Erosion/corrosion model	Time of failure (yr)	Rock transport resistance, F (yr/m)	Advective travel time, t_w (yr)	Advective flow through deposition hole, q (m^3/yr)
Semi-correlated; SR-Site	114 485	53 660	6	0.733
Uncorrelated; SR-Site	97 815	5 757 000	292	0.641
Fully correlated; SR-Site	99 700	45 600	12	0.626
Semi-correlated; Initial advection	44 049	53 660	6	0.733
Uncorrelated; Initial advection	47 107	5 757 000	292	0.641
Fully correlated; Initial advection	47 657	45 600	12	0.626

Table 4-3. Data for the deposition holes where canisters fail due to corrosion for the ten realisations of the semi-correlated DFN model used in probabilistic calculations for SR-Site (corresponding data for PSAR are given in Appendix L Table L-23). Sorted by ascending time of failure.

Time of failure (yr)	Rock transport resistance, F (yr/m)	Advective travel time, t_w (yr)	Advective flow through deposition hole, q (m^3/yr)
114 485	53 660	6	0.733
122 557	564 900	61	0.557
132 155	14 510	23	0.267
157 452	26 260	7	0.358
157 805	642 100	78	0.316
179 621	87 820	14	0.251
201 037	89 910	17	0.144
230 828	818 600	38	0.148
305 884	33 970	16	0.082
313 807	33 140 000	2 501	0.079
361 884	2 184 000	124	0.083
377 494	38 170	14	0.095
391 981	24 220 000	2 021	0.060
402 471	157 900	19	0.086
442 257	155 100	19	0.075
471 801	163 400	29	0.067
480 309	25 290 000	2 070	0.047
504 166	53 660	6	0.733
521 967	24 830 000	1 994	0.042
526 759	116 600	241	0.050
531 274	53 660	6	0.733
569 225	53 660	6	0.733
569 701	564 900	61	0.557
595 478	53 660	6	0.733
600 806	564 900	61	0.557
612 248	471 800	31	0.048
612 252	53 660	6	0.733
644 354	564 900	61	0.557
652 328	211 100	20	0.044
674 477	564 900	61	0.557
693 725	564 900	61	0.557
705 692	1 710 000	99	0.033
714 768	26 260	7	0.358
750 814	642 100	78	0.316
753 537	26 260	7	0.358
777 848	14 510	23	0.267
792 067	642 100	78	0.316
803 247	11 330	20	0.035
807 815	26 260	7	0.358
822 765	14 510	23	0.267
845 022	87 820	14	0.251
845 360	26 260	7	0.358
849 820	642 100	78	0.316
869 351	26 260	7	0.358
885 650	14 510	23	0.267
889 770	642 100	78	0.316
891 310	87 820	14	0.251
893 681	53 660	6	0.733
901 874	9 083 000	601	0.026
915 297	642 100	78	0.316
918 487	2 008 000	135	0.024
929 149	14 510	23	0.267
941 008	61 400	18	0.032
956 114	87 820	14	0.251
956 944	14 510	23	0.267
978 463	3 845 000	91	0.033

4.4 Central corrosion case

4.4.1 Deterministic calculations

Hydrogeological case:	Semi-correlated, ten realisations
Erosion/corrosion model:	SR-Site model
Failure time:	114 485 years
Number of failed canisters:	1
Solubility limits:	No
Thorium sorption in near field:	Yes (modelled as low solubility limit)
Number of realisations:	1
Number of nuclides:	37

A deterministic calculation of the central corrosion case is performed for a canister taken from the realisation with the earliest failure time of the analysed realisations (114 485 years after deposition) with corresponding geosphere transport data, i.e. data used to calculate the corrosion time are from the same hydrogeological calculation as the geosphere transport data. Advection occurs in the buffer void and the dose equivalent releases are primarily determined by the fuel dissolution rate set to 10^{-7}/yr. The contributions from the instantly released fraction of nuclides, IRF, are calculated separately.

Table 4-4 shows peak annual doses from the pulse releases from the instantly released fraction, IRF. The IRF inventory at 100 000 years has been multiplied by the pulse LDF-values given in Table 3-7.

Figure 4-2 shows the near-field releases converted to doses through multiplying the release rate by the LDF-value. As mentioned in Section 3.5, the conversion to dose is done to obtain a convenient metric of release consequence that can also be summed to obtain a metric that considers all nuclides.

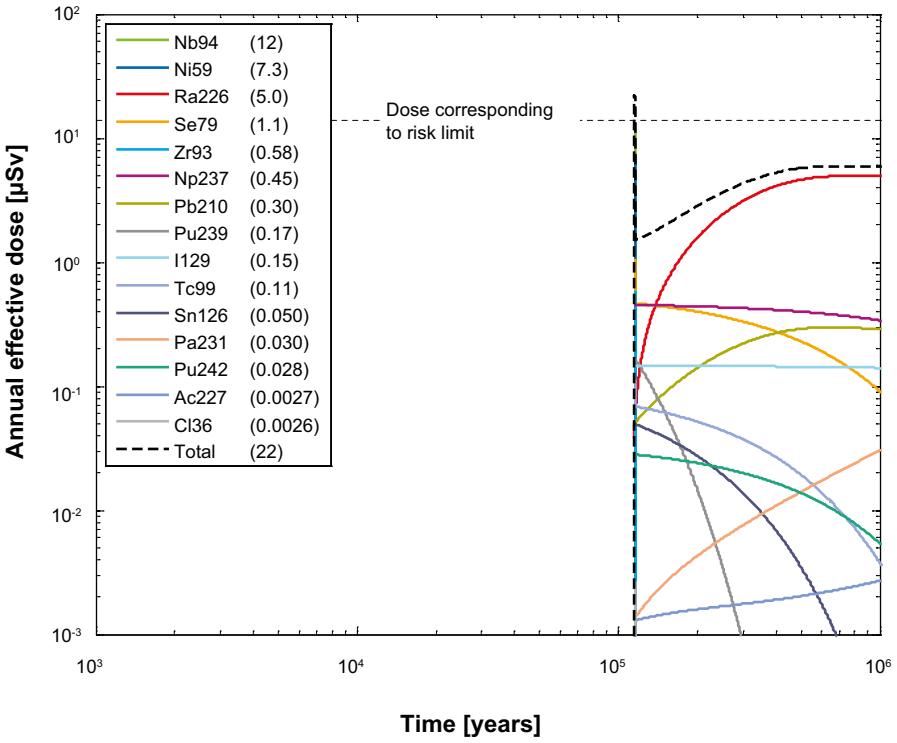

Figure 4-2. *Near-field dose equivalent release for a deterministic calculation of the central corrosion case. The legend is sorted by peak (in the one-million year period) of the annual effective dose. The values in brackets are peak dose in units of µSv. The curves for Nb-94 and Ni-59 are hidden under the curve showing the total dose equivalent release.*

Table 4-4. Peak annual dose from the pulse releases from the instantly released fraction, IRF, for a deterministic calculation of the central corrosion case. The dose is calculated at 100 000 years.

Nuclide	Peak annual dose (μSv)
I-129	3.82
Se-79	1.72
Cs-135	0.21
Cl-36	0.12
Nb-94	0.026
Sn-126	0.019
Ni-59	0.012
Tc-99	6.81[a)]

[a)] The peak annual dose for Tc-99 is only valid for the near field.

The dose equivalent releases from the geosphere are shown in Figure 4-3.

The dose equivalent release from the near field is dominated by Tc-99 (as IRF-pulse), Nb-94 and Ni-59. The peak contributions from Nb-94 and Ni-59 are due to the relatively fast release of the part of these nuclides embedded in the metal in the fuel assemblies. The time for metal corrosion is short (log-triangular 10^2, 10^3, 10^4 yr) compared to the time scale for the release. The doses caused by releases from the far field are dominated by I-129 (as IRF-pulse), Ra-226 and Se-79 (as IRF pulse). The far-field pulse release for Tc-99 is modelled with the far-field transport model since sorption in the geosphere is considerable for Tc-99. The pulse release of Tc-99 is thus included in the results shown in Figure 4-3.

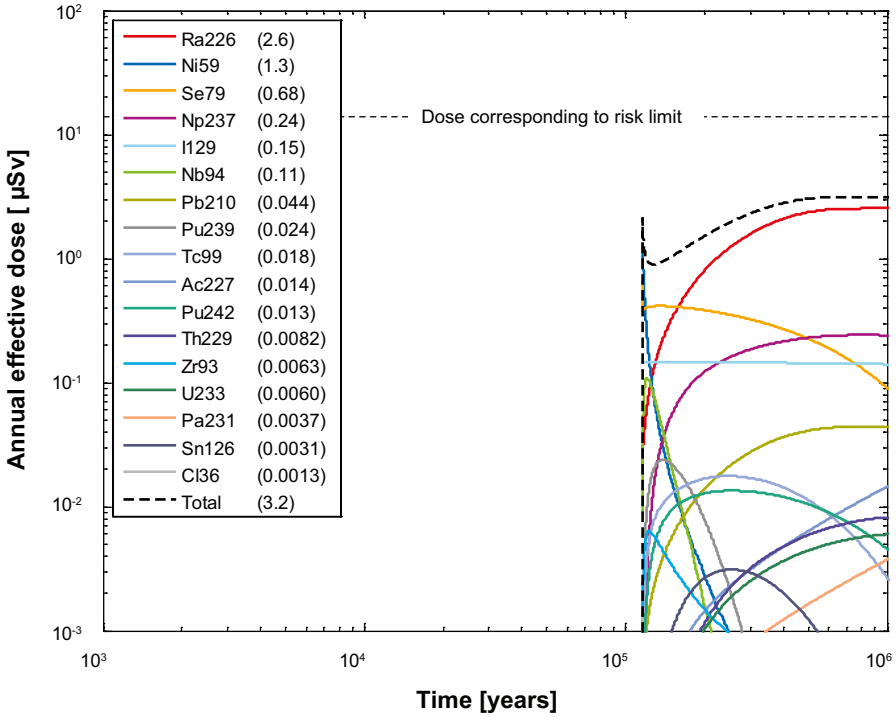

Figure 4-3. *Far-field annual effective dose for a deterministic calculation of the central corrosion case. The legend is sorted by peak (in the one-million year period) of the annual effective dose. The values in brackets are peak dose in units of μSv.*

4.4.2 Probabilistic calculations

Hydrogeological case:	Semi-correlated, ten realisations
Erosion/corrosion model:	SR-Site model
Failure time:	56 times according to Table 4-3
Mean number of failed canisters:	0.12
Solubility limits:	No
Thorium sorption in near field:	Yes (modelled as low solubility limit)
Number of realisations:	50 per canister failure time
Number of nuclides:	37

A probabilistic calculation of the central corrosion case is performed with failure times and geosphere transport data from the ten realisations of the semi-correlated DFN model, see Table 4-3. The mean number of failed canisters, 0.12, is an outcome of the corrosion calculations (SKB 2010a). The contributions from the instantly released fraction of nuclides, IRF, are calculated separately.

The contribution from the IRF pulse in the probabilistically calculated mean dose is treated as follows. The probability of canister failure, p_{Fail}, is determined for each 100 000 year interval from the calculated distribution of canister failure times for the central corrosion case. The total probability until one million years is the sum of all p_{Fail}, i.e. 0.12 for the central corrosion case. The width of the dose curves in the biosphere is typically 1 000 years. The likelihood that an exposure due to a pulse release, p_{Expo}, is present at a given point in time during the 100 000 year interval is thus $10^{-2} \cdot p_{Fail}$. (The likelihood of overlaps between pulses is very small due to the low probabilities.) The total dose associated with a pulse release $D_{TotPulse}$ is determined at the start of each 100 000 year interval (in the same way as described for the deteministic case). The probabilistically calculated mean dose is then obtained as the probability of exposure multiplied with the total dose associated with the pulse release ($p_{Expo} \cdot D_{TotPuls}$). The result of this procedure for the central corrosion case is shown in Table 4-5. As seen in the table, the highest mean dose is around 1×10^{-3} µSv, i.e. more than four orders of magnitude below the dose corresponding to the risk limit. The pulse releases thus give negligible contributions to the probabilistically calculated mean dose. It is also noted that this treatment assumes that temperate conditions are prevailing. Including probabilities of periglacial and glacial climate conditions would reduce the mean dose further. The IRF pulse of Tc-99 is modelled with the far-field transport model since sorption in the geosphere is considerable for Tc-99. The pulse release of Tc-99 is thus included in the results shown in Figure 4-5.

Figure 4-4 shows near-field dose equivalent releases and Figure 4-5 shows the corresponding far-field dose equivalent releases. The failure times are reflected as distinct features in the release curves, in particular for the near field. The pulse like features are due to release controlled by corrosion of the metal parts of the fuel assemblies (e.g. Ni-59). The metal corrosion times (ranging between 100 and 10 000 years) are such that the releases appear as pulses on the time scale of the dose curves. The first releases occur after around 110 000 years when the first canister fails.

Table 4-5. Calculation of the total mean dose from release of the instant release fraction, IRF, in the central corrosion case.

Time interval [yr]	p_{Fail}	p_{Expo}	$D_{TotPulse}$ [µSv]	Mean dose [µSv]
0–100 000	0	0	0	0
100 000–200 000	1.25×10^{-2}	1.25×10^{-4}	5.92	7.4×10^{-4}
200 000–300 000	4.17×10^{-3}	4.17×10^{-5}	5.54	2.3×10^{-4}
300 000–400 000	1.04×10^{-2}	1.04×10^{-4}	5.25	5.5×10^{-4}
400 000–500 000	8.33×10^{-3}	8.33×10^{-5}	5.01	4.2×10^{-4}
500 000–600 000	1.46×10^{-2}	1.46×10^{-4}	4.81	7.0×10^{-4}
600 000–700 000	1.46×10^{-2}	1.46×10^{-4}	4.64	6.8×10^{-4}
700 000–800 000	1.25×10^{-2}	1.25×10^{-4}	4.49	5.6×10^{-4}
800 000–900 000	2.29×10^{-2}	2.29×10^{-4}	4.37	1.0×10^{-3}
900 000–1 000 000	1.67×10^{-2}	1.67×10^{-4}	4.26	7.1×10^{-4}

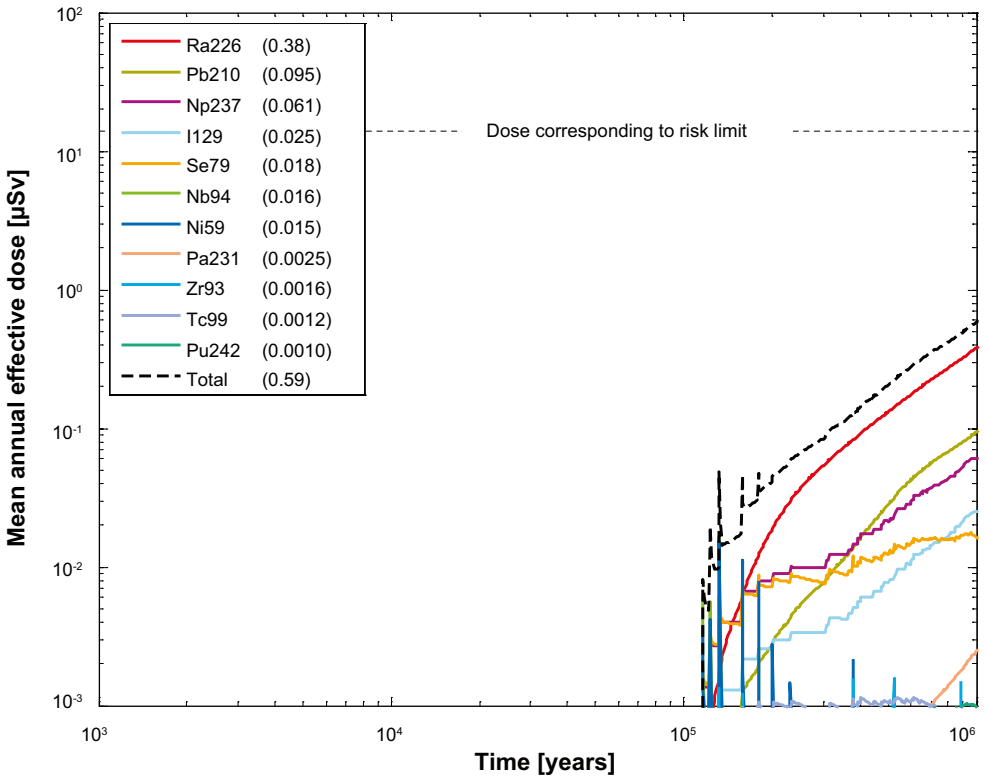

Figure 4-4. *Near-field dose equivalent release for a probabilistic calculation of the central corrosion case. The average mean of failed canisters is 0.12. The legend is sorted by peak (in the one-million year period) of the mean annual effective dose. The values in brackets are peak dose in units of µSv.*

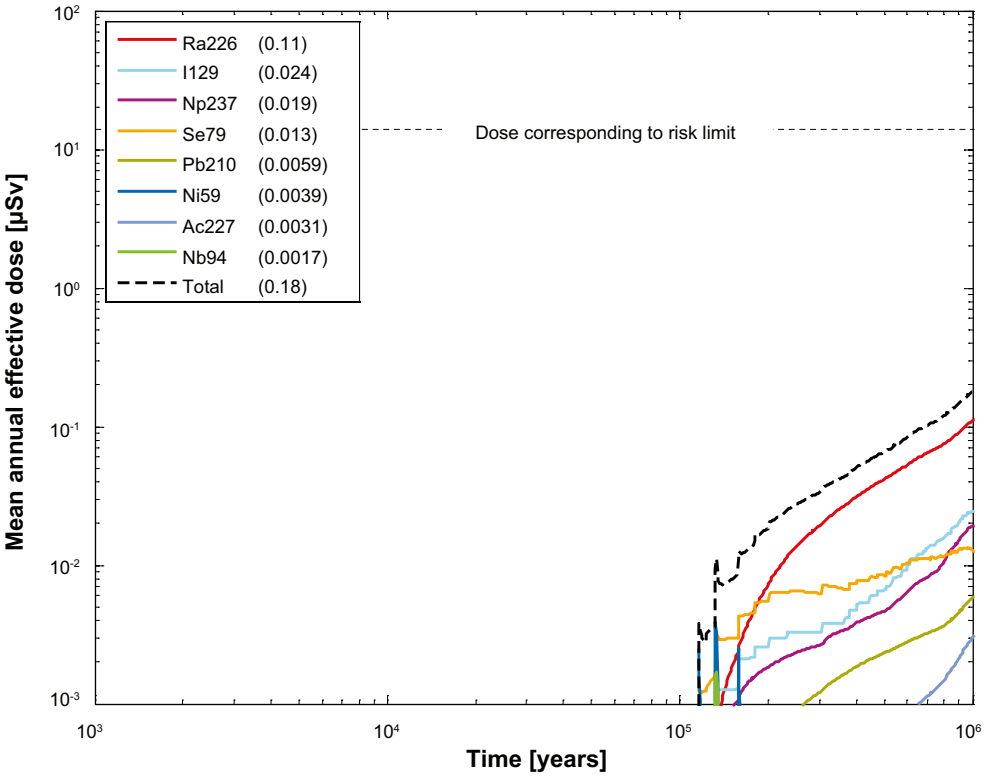

Figure 4-5. *Far-field mean annual effective dose for a probabilistic calculation of the central corrosion case. The legend is sorted by peak (in the one-million year period) of the mean annual effective dose. The values in brackets are peak dose in units of µSv.*

The doses caused by releases from the near field are dominated by Ra-226. Much of the Ra-226 released from the near field is transmitted through the geosphere since the failed canisters are located in deposition holes intersected by large, highly transmissive fractures with low retention. The release of Ra-226 from the geosphere is almost exclusively due to Ra released from the near field and not to in-growth in the geosphere. This, in turn, is related to the fact that the parent nuclide Th-230 is assumed to be confined to the near field. Despite the fast release in the far field the dose from Pb-210 decrease significantly due to its short half-life (22 years). The far field also significantly influences nuclides controlled by corrosion with pulse like releases in the near field, for example Ni-59. For Tc-99 the geosphere retention is significant and the dose is below 10^{-3} µSv/yr.

Some statistics for the far-field release are shown in Figure 4-6. Note that these are derived only for the realisations of the failure times where failures actually occur in the corrosion calculations. Since the mean number of failed canisters is about 0.12, the most likely outcome of the corrosion calculations is zero failures. This is not reflected in the percentiles in Figure 4-6, other than for the mean value. Taking this into account would bring the 99th and 95th percentiles closer to the mean.

4.4.3 Sensitivity analysis

Introduction

This section presents results of sensitivity analyses of the results of the dose calculations, i.e. the sensitivity of the uncertainty in calculated dose to uncertainties in the input parameters is analysed. All analyses concern the probabilistic calculation of the central corrosion case.

It is of interest to determine i) the variables that correlate with the dose over the entire dose range and ii) the parameter values that are related to high and low doses. Ra-226 dominates the dose in most of the realisations in the central corrosion case and it is thus of particular interest to clarify sensitivities of the Ra-226 dose to input parameters.

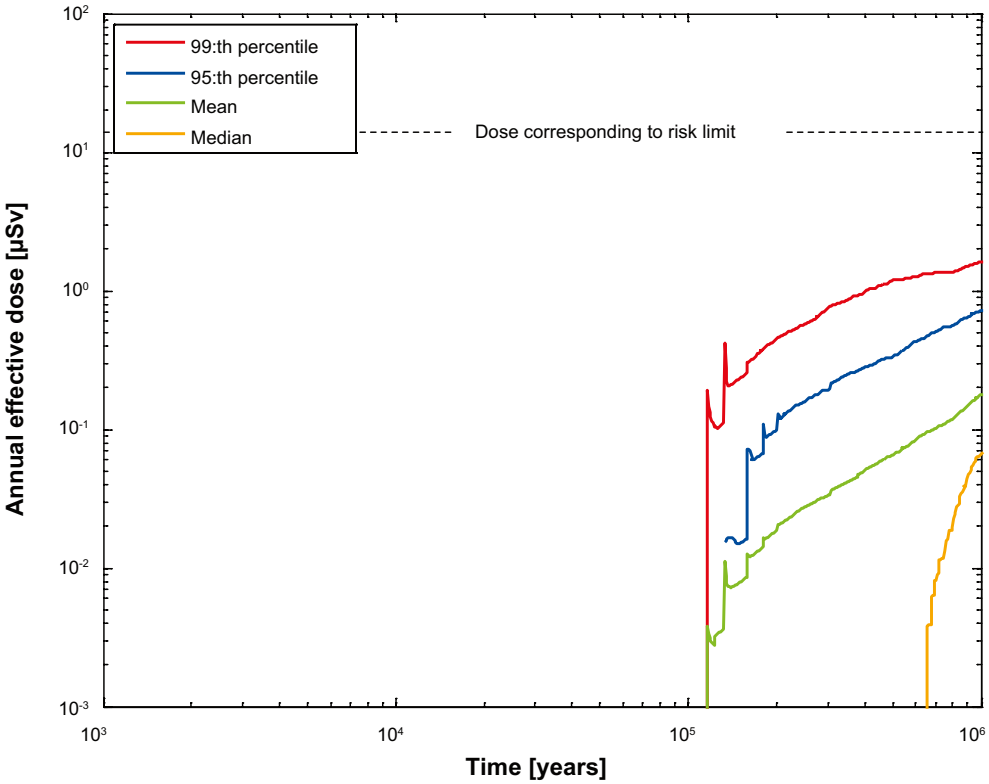

Figure 4-6. *Far-field annual effective dose (mean, median, 95th and 99th percentiles) for the probabilistic calculation of the central corrosion case.*

Global sensitivity analysis

The first purpose is thus to perform a so-called global sensitivity analysis, i.e. to identify the input parameters that have the greatest influence on the spread of the results. The contribution to output spread depends on both the spread of the input parameter and the model's sensitivity to variations in that particular input parameter. A range of methods for this type of sensitivity analysis exists (Saltelli et al. 2000). Several studies and reviews have demonstrated that standardised rank regression is a suitable method for sensitivity analysis of non-linear systems where the calculation end point is a monotonic function of the input variables (Saltelli et al. 1993, Helton 1993, Hamby 1994, Iman and Conover 1979). This applies to the present non-linear and monotonic system (Hedin 2003), and the standardised rank regression coefficient (SRRC) is, therefore, used for identifying the most important variables contributing to dose uncertainty.

A standardised rank regression analysis of the total dose at 10^6 years on the input variables yields, in descending order, the fuel dissolution rate D_{Fuel}, the flow-related transport resistance along the geosphere flow path, F, and the failure time $t_{Failure}$ as the input parameters most affecting dose results, see Figure 4-7. Regressing on Ra-226 dose at 10^6 years yields a similar result due to the dominance of Ra-226. The ranking of the two most important variables is switched in this case. This switching of the ranking is consistent with the fact that the fuel dissolution rate, D_{Fuel}, affects all nuclides whereas the F parameter only affects sorbing nuclides. Thus, F is relatively more important for the Ra-226 dose than for the total dose, which is in some of the realisations dominated by the non-sorbing I-129. It is also noted that the three variables F, t_w (advective travel time) and $t_{Failure}$ are correlated, meaning that their significance is not necessarily as high as indicated by the SRRC method. This is further investigated with a tailored regression model, as descibed below. Standardised rank regression analysis on maximum of total dose over time yields an almost identical result as regressing on total dose at one million years (not shown in the figure). However, regressing on e.g. peak Ni-59 equivalent dose from the near field (not shown in the figure) identifies also the corrosion release rate, *CRR*, as a sensitive input variable. *CRR* is proportional to 1/TCORR. This sensitivity to *CRR* is consistent with the fact that in some realisations of the central corrosion case, the peak dose due to Ni-59 occurs shortly after canister failure and is then caused by the releases congruent with the corrosion of the metal parts of the fuel assemblies.

Main risk contributors

The standardised rank regression analysis identifies the variables that co-vary with the dependent variable, the total dose, over the entire dose range. To determine the variables that are related to the highest doses, a conditional mean value analysis (Hedin 2002a) was carried out. Here, the subsets of input parameter values related to the top percentile of the dose are selected. For each such subset, the mean value of the logarithmically transformed data was determined for each parameter and compared to the corresponding mean value of the entire input distribution. A dimensionless, normalised measure, α99, is obtained by dividing the difference between the two mean values by the standard deviation of the entire distribution.

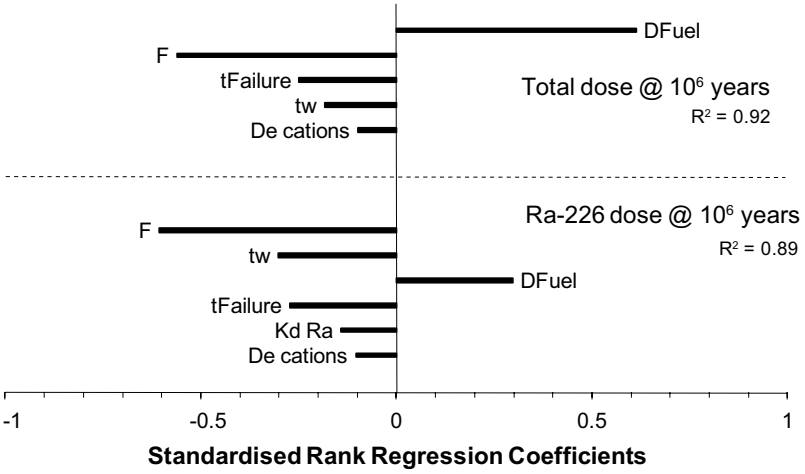

Figure 4-7. *Results of standardised rank regression for the central corrosion case. Regressing on total dose at 10^6 years and on Ra-226 dose at 10^6 years yields similar results due to the dominance of Ra-226.*

The so determined conditional mean value identifies variables that take on significantly different values in the top percentile realisations compared to the entire dose distribution. In descending order, the $t_{Failure}$, D_{Fuel}, F and t_w parameters were identified as most significant, see Figure 4-8. Similarly, α1-values, relating to the lowest percentile of the dose distribution were determined. Also, α99−α1 values were determined to distinguish extreme outcomes from others. The highest ranking variables were, in descending order, D_{Fuel}, F, t_w (t_w is strongly correlated to F) and $t_{Failure}$.

Tailored regression model

The understanding and mathematical formulation of the transport models used in the dose calculations can be utilised to further explain the results. The release rate of Ra-226 is determined by the amount of its parent nuclide, Th-230, liberated from the fuel matrix and subsequently assumed to sorb in the near field. This amount is proportional to the product of the fuel dissolution rate, D_{Fuel}, and the time, t, elapsed between the canister failure and the point in time for which the dose is calculated, i.e. it is proportional to $D_{Fuel} \cdot t$. In the studied case $t = 10^6 - t_{Failure}$. It can further be shown that the released Ra-226 is transported through the geosphere with a certain transmission efficiency, θ, that in its full expression depends in a complex way on all the uncertain parameters relating to geosphere transport, see e.g. Hedin (2002b). However, it can also be demonstrated that most of the variability of θ is captured by the simpler expression (Hedin 2003):

$$\theta \propto \exp\left(-cF^{0.5}\left(K_d D_e\right)^{0.25}\right) \qquad 4\text{-}1$$

where c is a positive constant determined by well known properties like the density of the rock and the half-life of Ra-226. This suggests that the Ra-226 dose varies according to:

$$\log\left(DoseRa226\right) = Constant + \log\left(D_{Fuel} t\right) - cF^{0.5}\left(K_d D_e\right)^{0.25} \qquad 4\text{-}2$$

and that a tailored regression model according to the above expression could be successful in explaining the calculated results. Figure 4-9 shows how such a regression model is able to predict the calculated results when successively more terms are included in the model. As seen in the figure, the agreement when all terms are included is good, with an R^2-value of 0.99.

These expressions also reveal combinations of input variables of importance. Obviously, combinations of high D_{Fuel} and t values and combinations of low values of the three factors occurring in the exponent of the first expression favour high doses. This result also illustrates that the variable t_w, identified as important for the Ra-226 dose by the SRRC method above is not needed to explain the Ra-226 dose. It is concluded that t_w is identified in the SRRC method only since it is correlated to the F parameter. (This can be further analysed through use of partial rank correlations in the SRRC method.)

A *partition plot*, Figure 4-10, showing how high and low dose results relate to the variable groups $D_{Fuel} \cdot t$ and $F^{0.5}(K_d \cdot D_e)^{0.25}$ confirms the explanatory power of these variable groups.

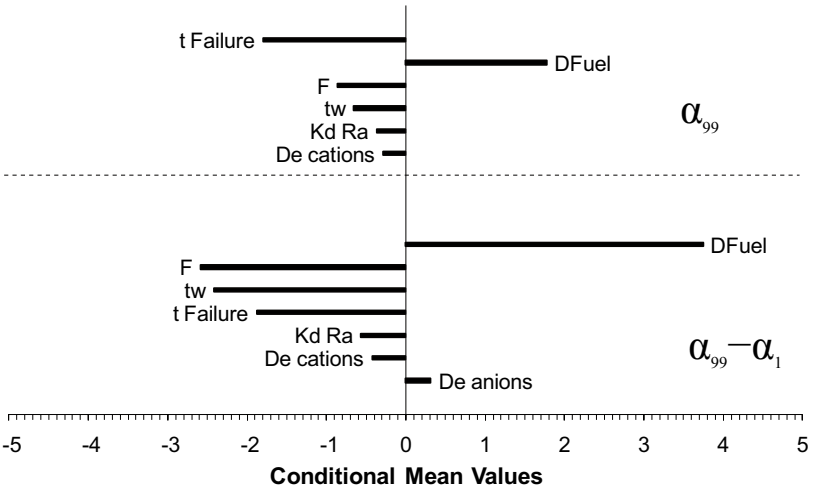

Figure 4-8. *Conditional mean values for the central corrosion case.*

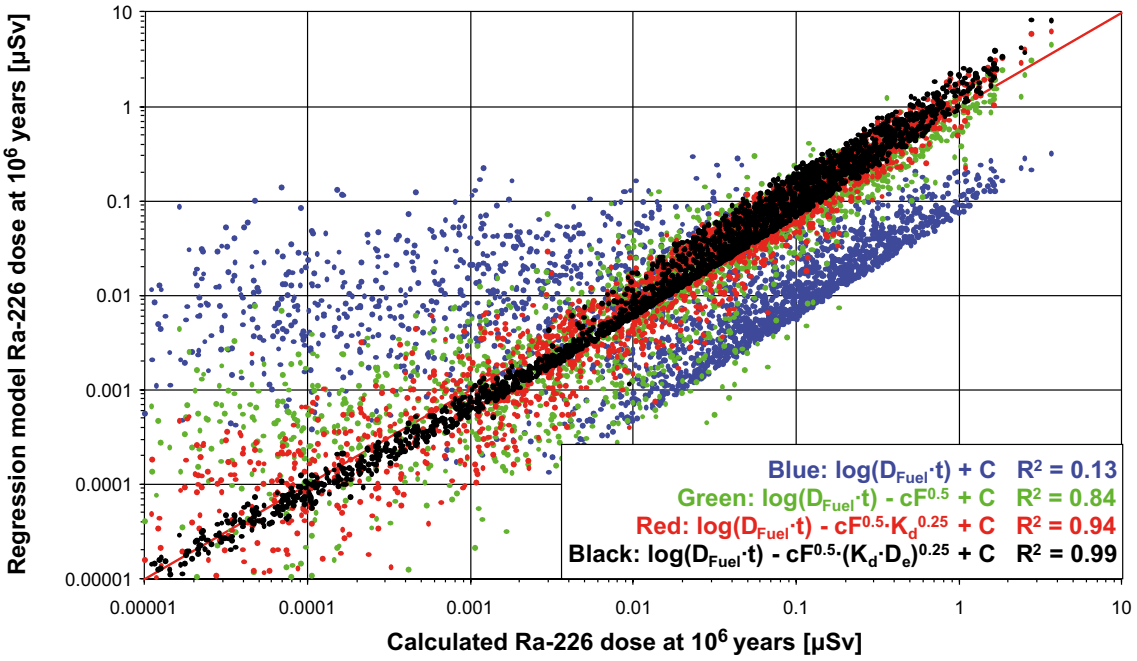

Figure 4-9. *Four tailored regression models, including successively more variables, for the Ra-226 dose at one million years for the central corrosion case.*

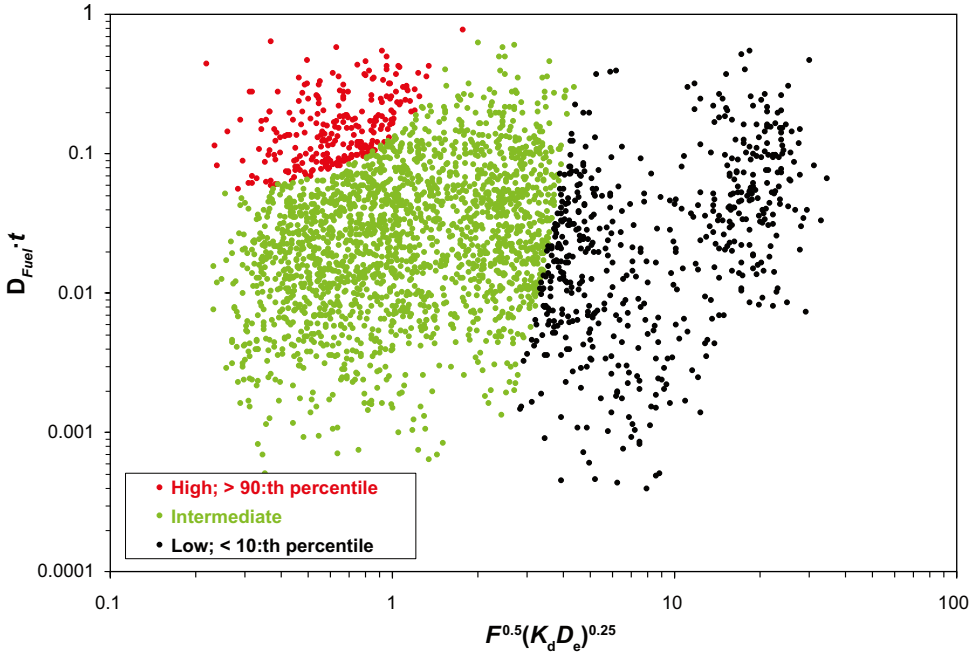

Figure 4-10. *Partition plot demonstrating how the two groups of variables on the axes relate to high and low dose results for Ra-226 for the central corrosion case.*

Conclusions

The above analyses show that relatively simple methods can identify the uncertain input parameters to which the probabilistic result is most sensitive. That sensitivities can be identified with relatively simple methods is in part due to the nature of the conceptualisation of the calculation cases in the corrosion scenario, where the buffer is omitted and the near-field release is essentially controlled only by the fuel dissolution rate.

The fuel dissolution rate, D_{Fuel}, and the geosphere flow-related transport resistance, F, emerge generally as the uncertain input parameters to which the result is most sensitive. The uncertainty in corrosion release rate, CRR, has a significant impact on the result of near-field releases immediately after failure for nuclides that are released congruently with metal corrosion.

It is also noted that a number of different assumptions regarding transport conditions are analysed in Section 4.5, where it is found that the sensitivity to these assumptions is low, see Figure 4-58 and Figure 4-59. Similar results are expected for all corrosion variants since they differ from the central corrosion case only through somewhat altered input distributions for the failure times and the hydrogeological transport parameters.

4.4.4 Issues related to the probabilistic nature of the calculations

Convergence

The number of canister failure times varies significantly in the different corrosion cases (from 56 in the central corrosion case to 1 964 in a case that does not use best available technique BAT). Data in the **Data report** have distributions and these have been used to make input files to COMP23 and FARF31 for probabilistic calculations, see Section 3.7.1. To assure a correct use of the probabilistic data, each canister failure time needs to be run several times with different sets of input (realisations). In Figure 4-11 the near-field and far-field releases of Ni-59, in the central corrosion case, are shown for different numbers of realisations per canister failure time. Both curves converge rapidly; 50 realisations were judged to be adequate and this value was used for all the corrosion cases. The choice of 50 realisations provides sufficient accuracy in the statistics without excessive total calculation times.

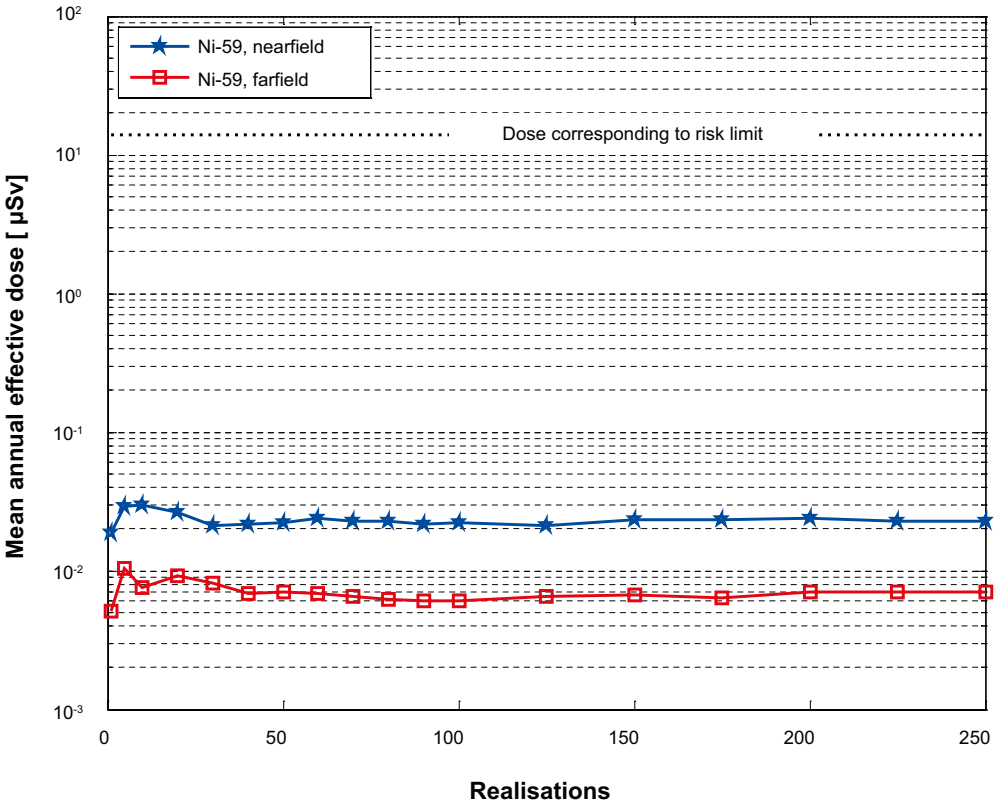

Figure 4-11. *Mean annual effective dose for Ni-59 as a function of the number of realisations in the central corrosion case.*

Risk dilution

The issue of risk dilution is discussed in the methodology Section 2.6.2 in the **Post-closure safety report** and needs to be addressed for the corrosion scenario. Doses are accounted for as a continuous contribution and as a relatively short pulse contribution.

In all probabilistic cases of the corrosion scenario, a fixed number of canisters, depending on the case studied, were assumed to fail at a set of fixed times. Thus, this factor cannot give rise to risk dilution. Regarding the pulse releases, these are given as peak doses for an assumed, single release of the entire IRF inventory and can thus not give rise to risk dilution.

The continuous contributions have, for a fixed failure time, an initial peak of limited duration followed by an increasing dose that generally grows beyond the value of the initial peak. Because this means that the maximum dose occurs at the end of the one million year assessment time, risk dilution is not an issue for the continuous contributions; the maximum risk is experienced by the same hypothetical generation living at the end of the assessment period irrespective of failure time. This is verified by comparing the peak-of-the-mean value (0.177 μSv/yr) to the mean-of-the-peaks value (0.179 μSv/yr) for the central corrosion case.

Risk dilution, including a treatment of the pulse releases, is further discussed in Section 13.9 in the **Post-closure safety report**.

4.5 Alternative cases based on the semi-correlated hydrogeological DFN model

In order to assess the sensitivity of the results to various assumptions, a set of alternative cases based on the semi-correlated hydrogeological DFN model have been undertaken.

4.5.1 Disregarding thorium sorption in the near field

Deterministic calculations

Hydrogeological case:	Semi-correlated, ten realisations
Erosion/corrosion model:	SR-Site model
Failure time:	114 485 years
Number of failed canisters:	1
Solubility limits:	No
Thorium sorption in near field:	No
Number of realisations:	1
Number of nuclides:	37

A deterministic calculation of the central corrosion case disregarding thorium sorption in the near field is performed to assess the sensitivity of the release of primarily Ra-226 due to alternative transport conditions for thorium.

The calculation of the IRF-pulses for the deterministic central corrosion case is also valid for the case disregarding thorium sorption in the near field. Hence, Table 4-4 shows the peak annual doses from the pulse releases from the instantly released fraction, IRF.

Figure 4-12 and Figure 4-13 show the deterministic near-field and far-field dose equivalent releases, respectively, for the central corrosion case when disregarding thorium sorption in the near field. The dose from thorium is obviously higher in this case compared to the central corrosion case. The dose caused by the release of the dose-dominating Ra-226 is lower in this case compared to the central corrosion case, showing that the assumption of thorium sorption in the near field made in the central corrosion case is pessimistic.

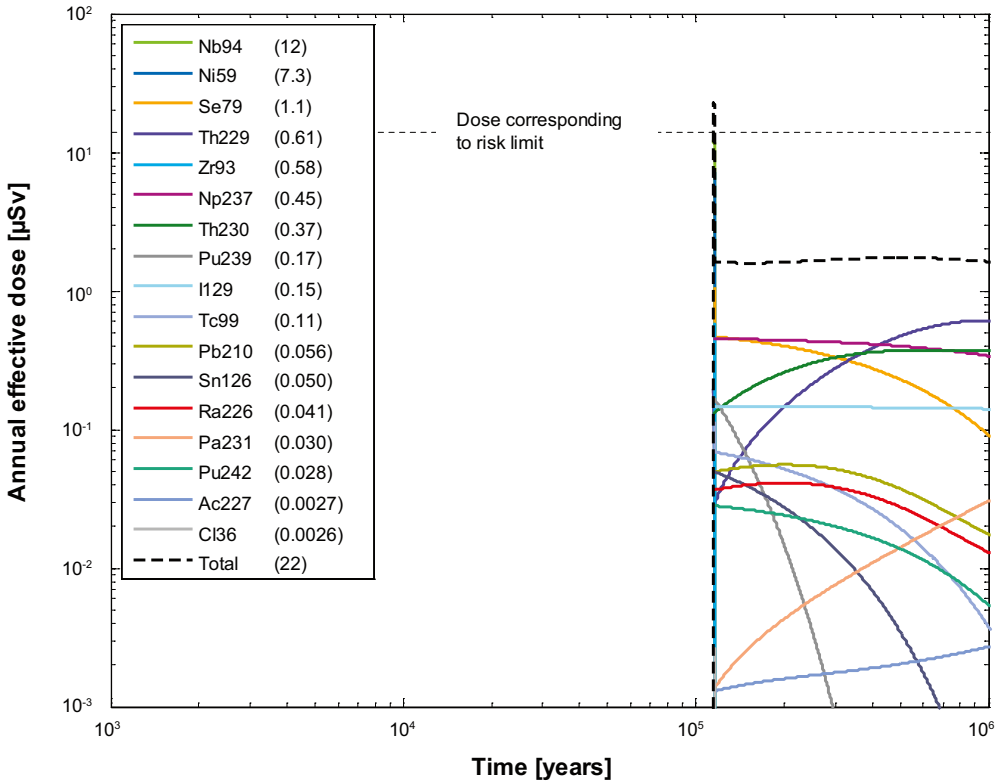

Figure 4-12. *Near-field dose equivalent release for a deterministic calculation of the central corrosion case, disregarding thorium sorption in the near field. The legend is sorted by peak (in the one-million year period) of the annual effective dose. The values in brackets are peak dose in units of µSv.*

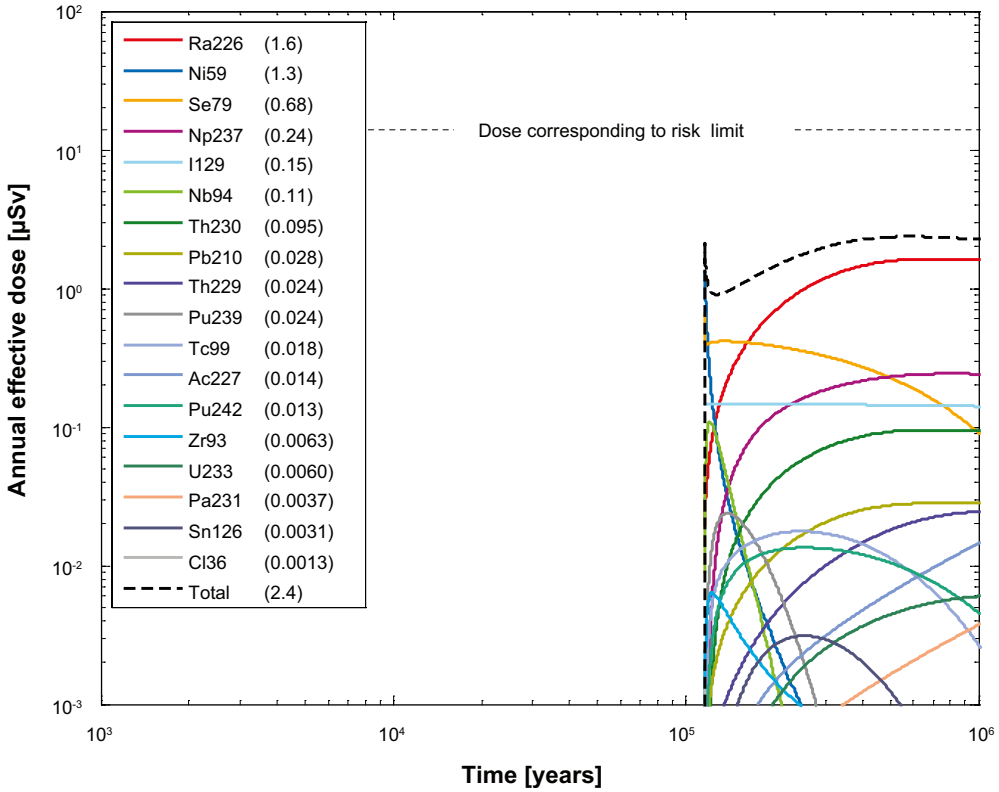

Figure 4-13. *Far-field annual effective dose for a deterministic calculation of the central corrosion case, disregarding thorium sorption in the near field. The legend is sorted by peak (in the one-million year period) of the annual effective dose. The values in brackets are peak dose in units of µSv.*

Probabilistic calculations

Hydrogeological case:	Semi-correlated, ten realisations
Erosion/corrosion model:	SR-Site model
Failure time:	56 times according to Table 4-3
Mean number of failed canisters:	0.12
Solubility limits:	No
Thorium sorption in near field:	No
Number of realisations:	50 per canister failure time
Number of nuclides:	37

The contributions from the instantly released fraction of nuclides, IRF, are not included in the calculations except for Tc-99 that is included in the far-field calculations. The results for the IRF presented for the central corrosion case is judged to be enough to conclude that their contribution is negligible also in this case, see Section 4.4.2.

Figure 4-14 and Figure 4-15 show near-field and far-field dose equivalent releases, respectively, for the central corrosion case when disregarding thorium sorption in the near field. Doses caused by release of Ra-226 and the total dose are both lower than in the central case, showing that the assumption of thorium sorption in the near field made in the central corrosion case is pessimistic.

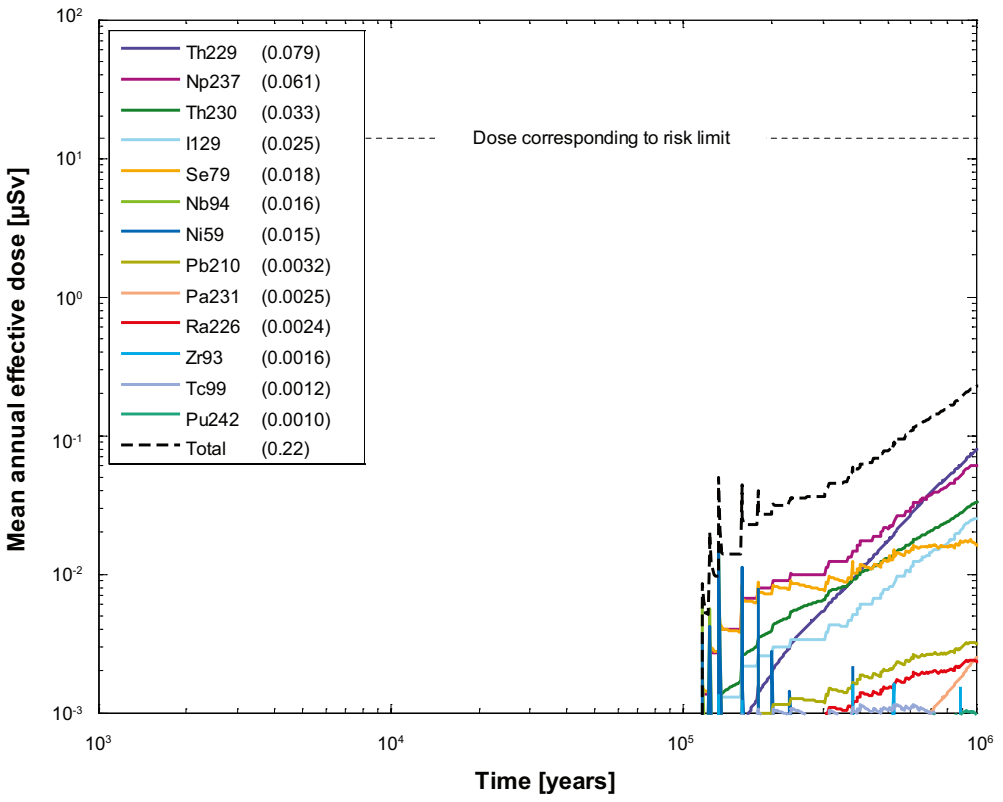

Figure 4-14. *Near-field dose equivalent release for the probabilistic central corrosion case, disregarding thorium sorption in the near field. The legend is sorted by peak (in the one-million year period) of the mean annual effective dose. The values in brackets are peak dose in units of µSv.*

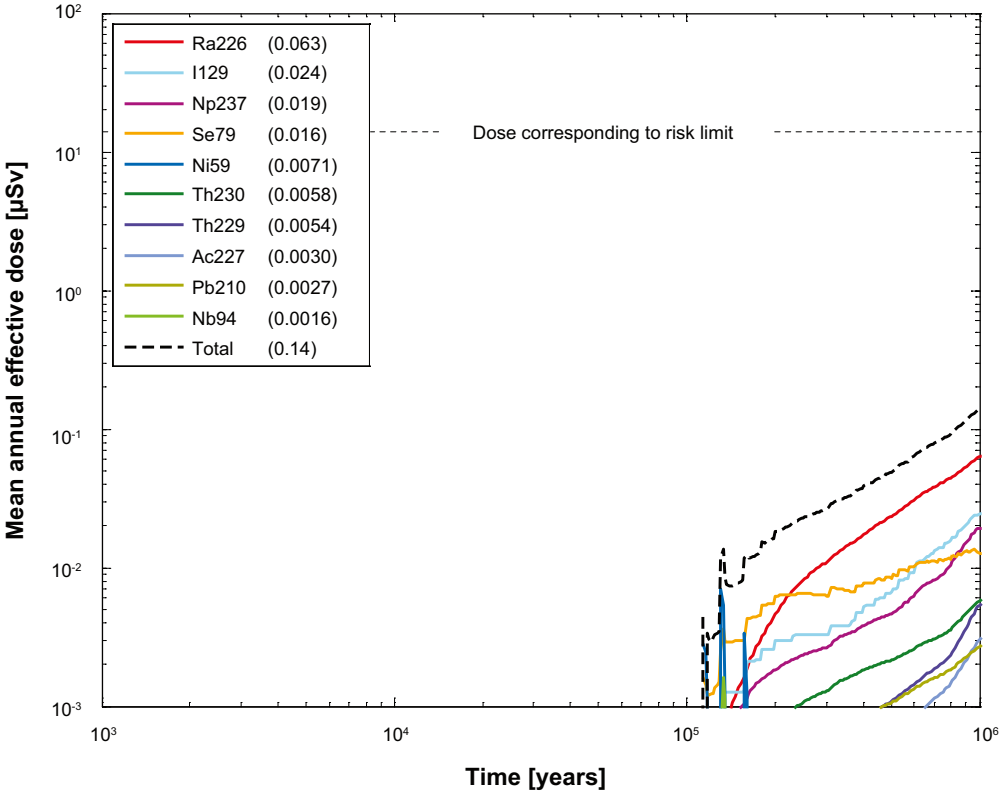

Figure 4-15. *Far-field mean annual effective dose for the probabilistic central corrosion case, disregarding thorium sorption in the near field. The legend is sorted by peak (in the one-million year period) of the mean annual effective dose. The values in brackets are peak dose in units of µSv.*

4.5.2 Including solubility limits in the near field

Deterministic calculations

Hydrogeological case:	Semi-correlated, ten realisations
Erosion/corrosion model:	SR-Site model
Failure time:	114 485 years
Number of failed canisters:	1
Solubility limits:	Yes
Thorium sorption in near field:	Yes (modelled as low solubility limit)
Number of realisations:	1
Number of nuclides:	37

The calculation of the IRF-pulses for the deterministic central corrosion case is also valid when including solubility limits in the near field. Hence, Table 4-4 shows the peak annual doses from the pulse releases from the instantly released fraction, IRF.

Figure 4-16 and Figure 4-17 show the deterministic near-field and far-field dose equivalent releases, respectively, for the central corrosion case when including solubility limits in the near field. The constant level of the doses caused by release of Np-237 and Zr-93 in Figure 4-16 indicate that they reach their solubility limits and hence the doses from these two nuclides are lower than in the central corrosion case. The total dose is the same as in the deterministic calculation of the central corrosion case.

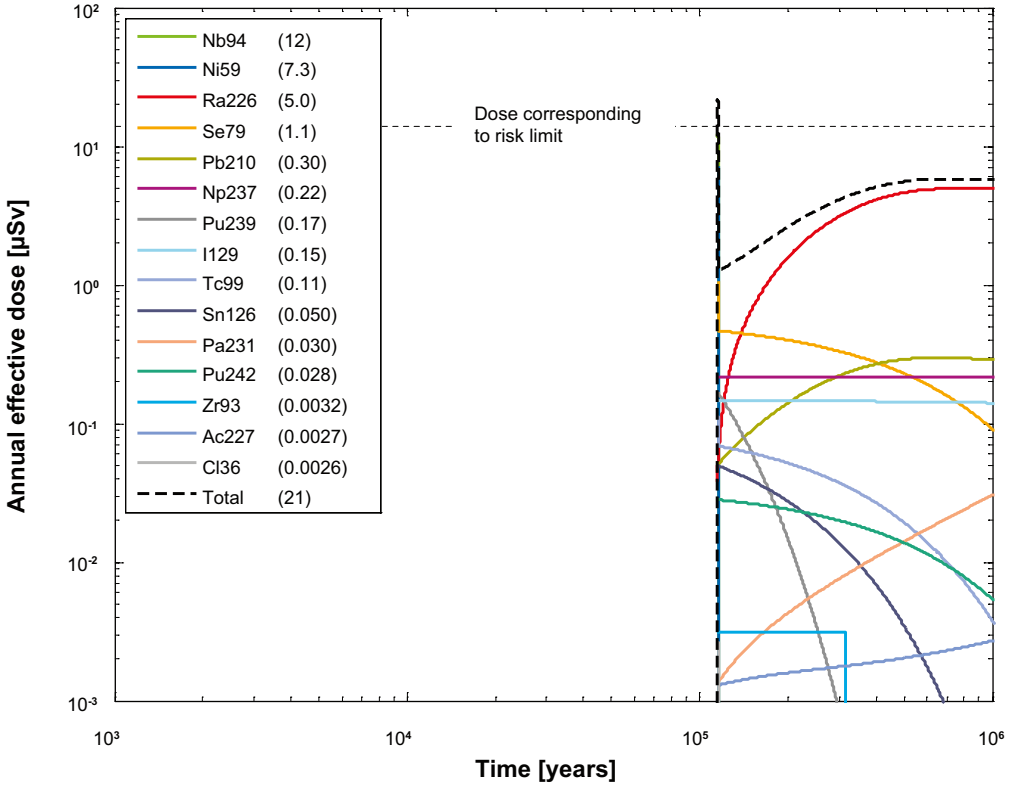

Figure 4-16. *Near-field dose equivalent release for a deterministic calculation of the central corrosion case, including solubility limits in the near field. The legend is sorted by peak (in the one-million year period) of the annual effective dose. The values in brackets are peak dose in units of µSv.*

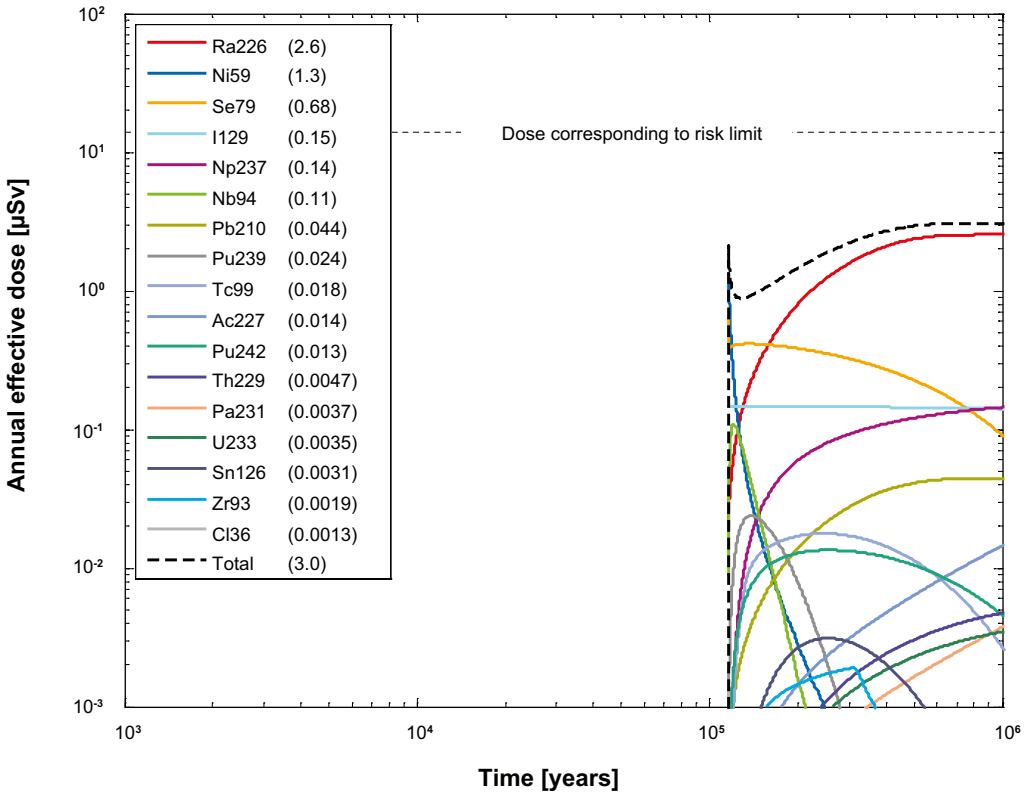

Figure 4-17. *Far-field annual effective dose for a deterministic calculation of the central corrosion case, including solubility limits in the near field. The legend is sorted by peak (in the one-million year period) of the annual effective dose. The values in brackets are peak dose in units of µSv.*

Probabilistic calculations

Hydrogeological case:	Semi-correlated, ten realisations
Erosion/corrosion model:	SR-Site model
Failure time:	56 times according to Table 4-3
Mean number of failed canisters:	0.12
Solubility limits:	Yes
Thorium sorption in near field:	Yes (modelled as low solubility limit)
Number of realisations:	50 per canister failure time
Number of nuclides:	37

The contributions from the instantly released fraction of nuclides, IRF, are not included in the calculations except for Tc-99 that is included in the far-field calculations. The results for the IRF presented for the central corrosion case are judged to be sufficient to conclude that their contribution is negligible also in this case, see Section 4.4.2.

Figure 4-18 and Figure 4-19 show near-field and far-field dose equivalent releases, respectively, for the central corrosion case when including solubility limits in the near field. The near-field dose caused by release of Pb-210 is considerably higher than for the central corrosion case. This is due to Ra-226 reaching the solubility limit in some realisations and when Ra-226 is confined to the canister interior it generates Pb-210. The far-field doses are, however, similar to those of the central corrosion case. Pb-210 decays considerably in the geosphere because of its short half-life.

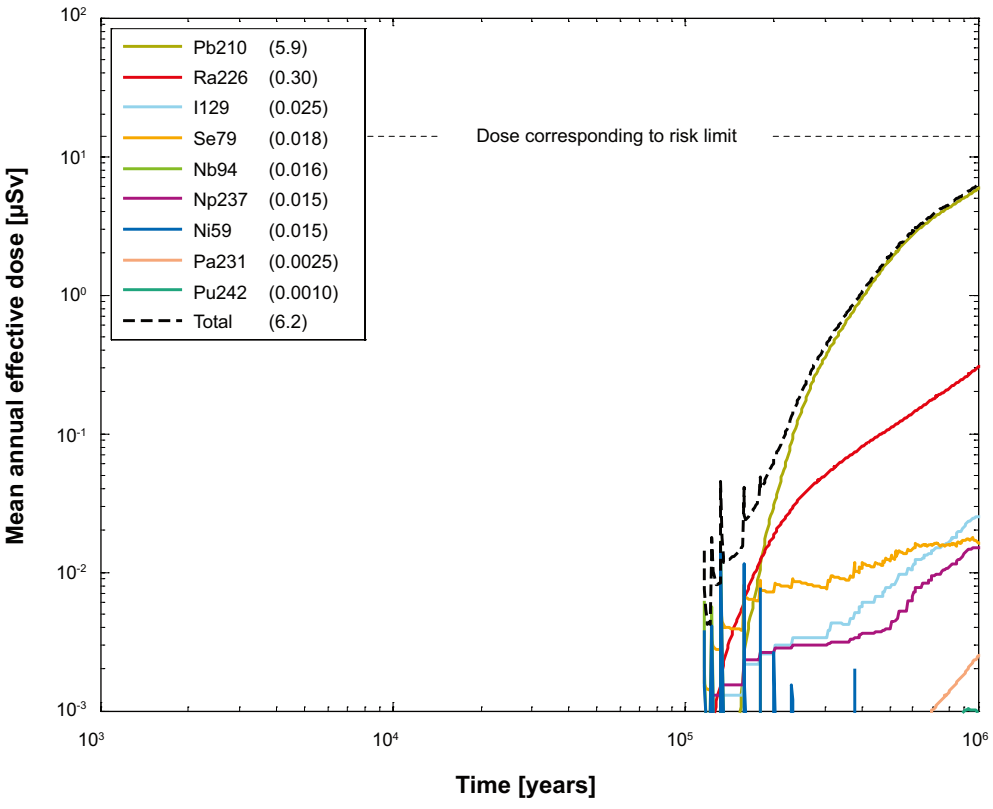

Figure 4-18. *Near-field dose equivalent release for the probabilistic central corrosion case, including solubility limits in the near field. The legend is sorted by peak (in the one-million year period) of the mean annual effective dose. The values in brackets are peak dose in units of µSv.*

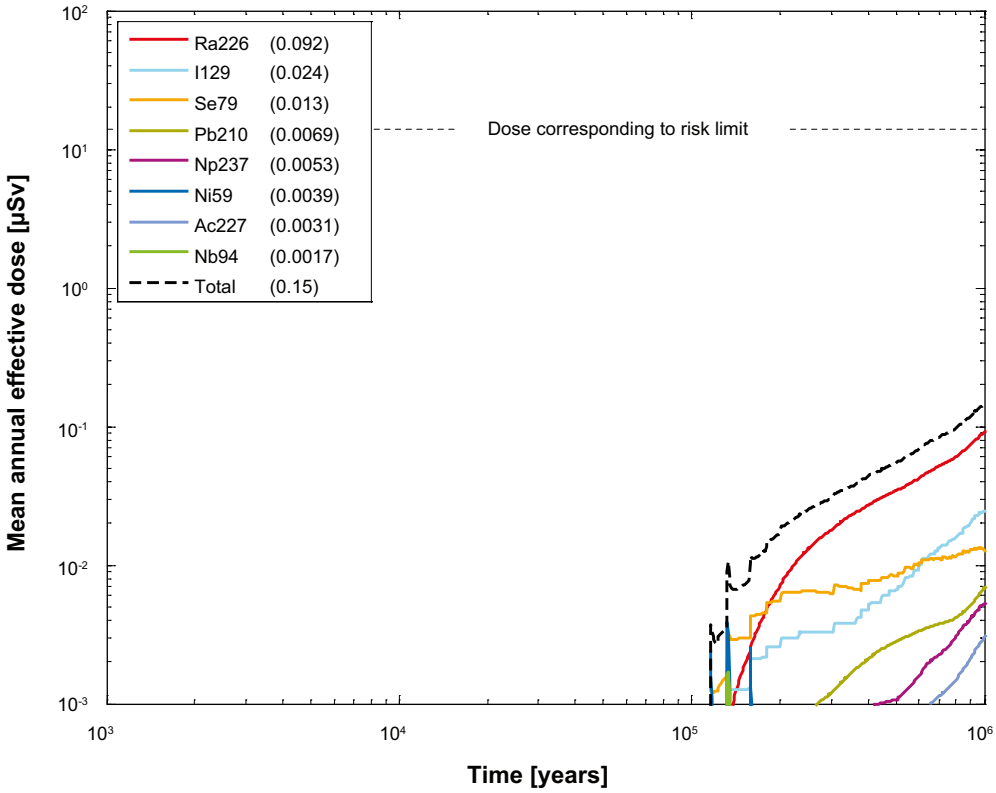

Figure 4-19. *Far-field mean annual effective dose for the probabilistic central corrosion case, including solubility limits in the near field. The legend is sorted by peak (in the one-million year period) of the mean annual effective dose. The values in brackets are peak dose in units of µSv.*

4.5.3 Decreased sorption of lead in the geosphere

In the Bedrock K_d data report (Crawford 2010, Section 5.2.6) it is stated: "Due to the uncertainties outlined above, a case could be made for the use of the geochemical analogue Ni(II) as a sensitivity case study in place of the data ranges given for Pb(II). It is possible, however, that the use of the Ni(II) analogue is overly pessimistic since Ni sorption appears to be more strongly influenced by ionic strength. This may be attributable to the larger first hydrolysis constant for Pb(II) which also implies stronger binding for inner sphere surface complexation. In this regard, the K_d for Pb(II) sorption is expected on theoretical grounds to be larger than that for Ni(II)." This consideration of decreased sorption of Pb(II) has been addressed in a deterministic calculation and is presented in Figure 4-20.

In comparison with the results from the deterministic calculation for the central corrosion case, Figure 4-3, the increase in the effective dose from Pb-210 is almost 20 times. However, the increase in the total dose is only 20 %.

4.5.4 K_d for U(VI) instead of U(IV) in the geosphere

All far-field calculations are done with K_d values for U(IV). According to Crawford (2010) and also described in Section 2.4.4, it cannot always be guaranteed that U(IV) is the dominant redox species in the repository volume. Therefore, the **Data report** recommends calculations with both U(IV) and U(VI). This statement only influences the K_d values in the rock.

Figure 4-21 shows the far-field effective dose for a probabilistic calculation of the central corrosion case with K_d values for U(VI). Compared to the central corrosion case with K_d values for U(IV), Figure 4-5, the doses from the uranium isotopes are increased but no other nuclides are affected. The increase in release of the uranium isotopes is not high enough to affect the total dose. U-233, which increases almost 9 times to 0.0022 µSv, is the only uranium isotope that becomes high enough to be seen in the main part of the figures in this report as they have a limit down to 0.001 µSv.

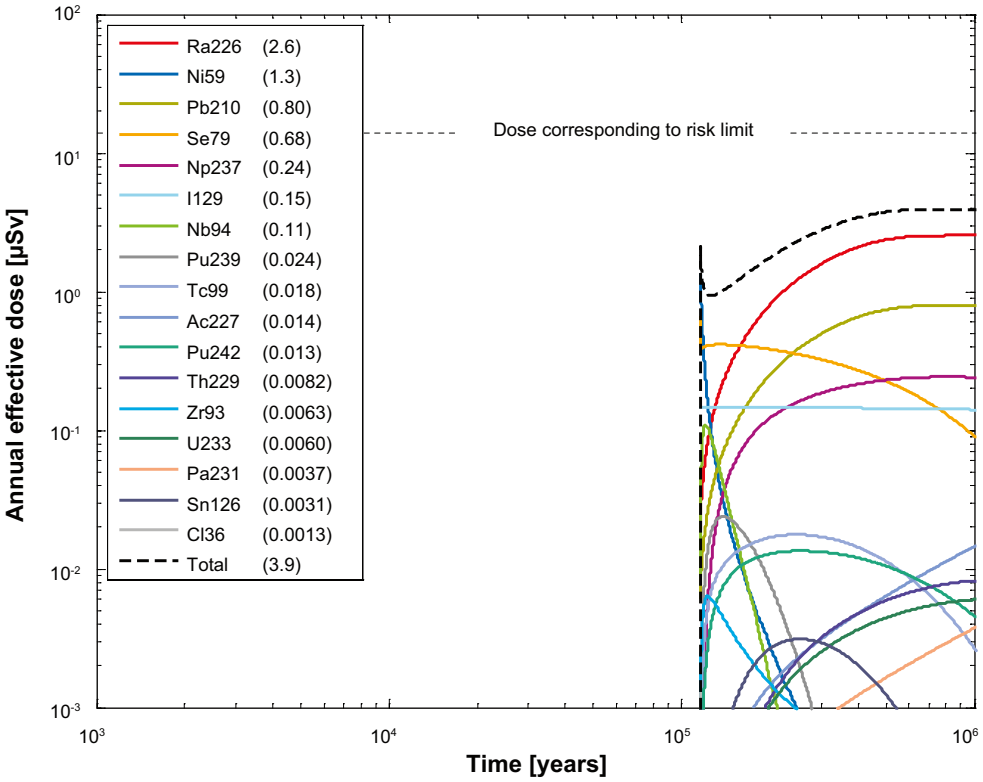

Figure 4-20. *Far-field annual effective dose for a deterministic calculation of the central corrosion case with decreased K_d for lead in the geosphere. The legend is sorted by peak (in the one-million year period) of the annual effective dose. The values in brackets are peak dose in units of µSv.*

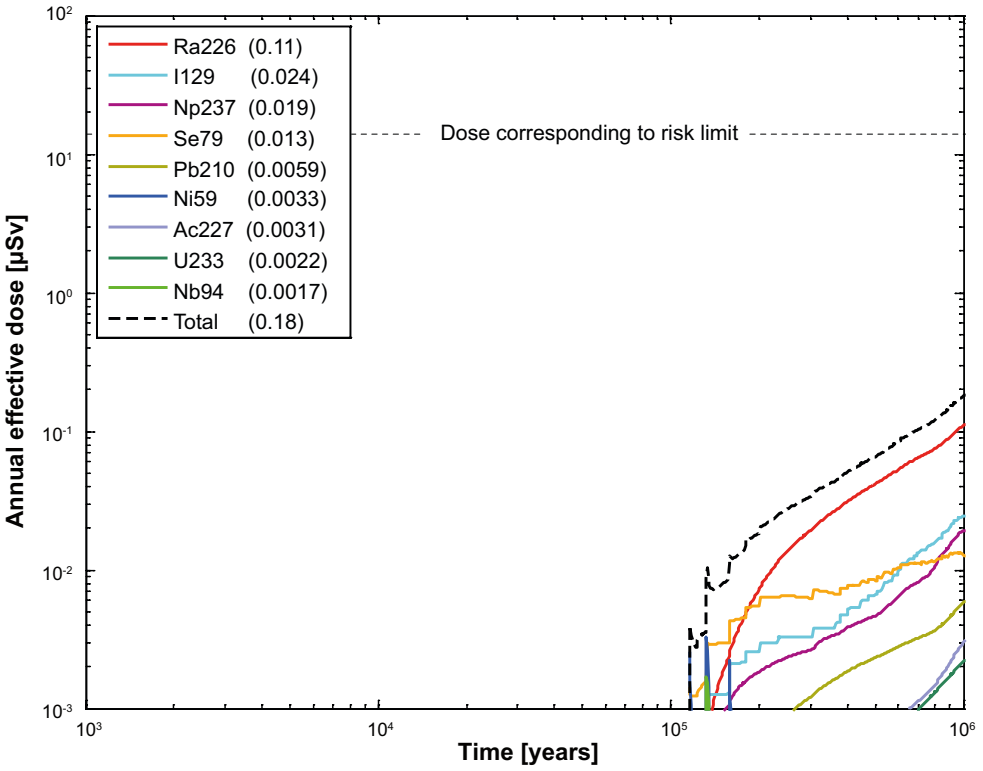

Figure 4-21. *Far-field annual effective dose for a probabilistic calculation of the central corrosion case with K_d values for U(VI). The legend is sorted by peak (in the one-million year period) of the mean annual effective dose. The values in brackets are peak dose in units of µSv.*

Figure 4-22 shows a detailed comparison between far-field effective doses from the uranium isotopes for the central corrosion case calculated with K_d values for U(IV) and U(VI). Due to the very low releases of uranium, the limits on the y-axis have been changed in this figure.

4.5.5 Influence of correlation groups for K_d in the geosphere

All calculations are done with five correlation groups for K_d in rock, according to the data report for the SR-Can assessment (SKB 2006b). Late in the SR-Site process, when most of the calculations were done, the correlation groups were changed from five to two. The purpose of the calculations presented in this section is to investigate whether the change has any considerable influence on the releases from the far field.

Four cases are used to investigate the influence of correlation groups for K_d in rock. In all cases in this investigation the same releases from the near field, the probabilistic calculation of the central corrosion case, is used as input to the FARF31 calculation. The other input parameter that may influence the far-field releases is D_e for rock. D_e is always fully correlated in SR-Site and in all calculation cases in this comparison except for the case with no correlations, where D_e also is uncorrelated. The following four cases are calculated:

- without any correlation groups,
- fully correlated case, i.e. one correlation group,
- two correlation groups, (according to the **Data report**)
- five correlation groups (according to the data report for SR-Can (SKB 2006b).

It is not possible to see any differences between the four cases, see Figure 4-23. The conclusion is that the correlation groups have negligible influence on the results. Hence, no corrections have been done to the calculations due to the change in correlation groups for K_d. In addition it is concluded that the influence of correlations for D_e is negligible.

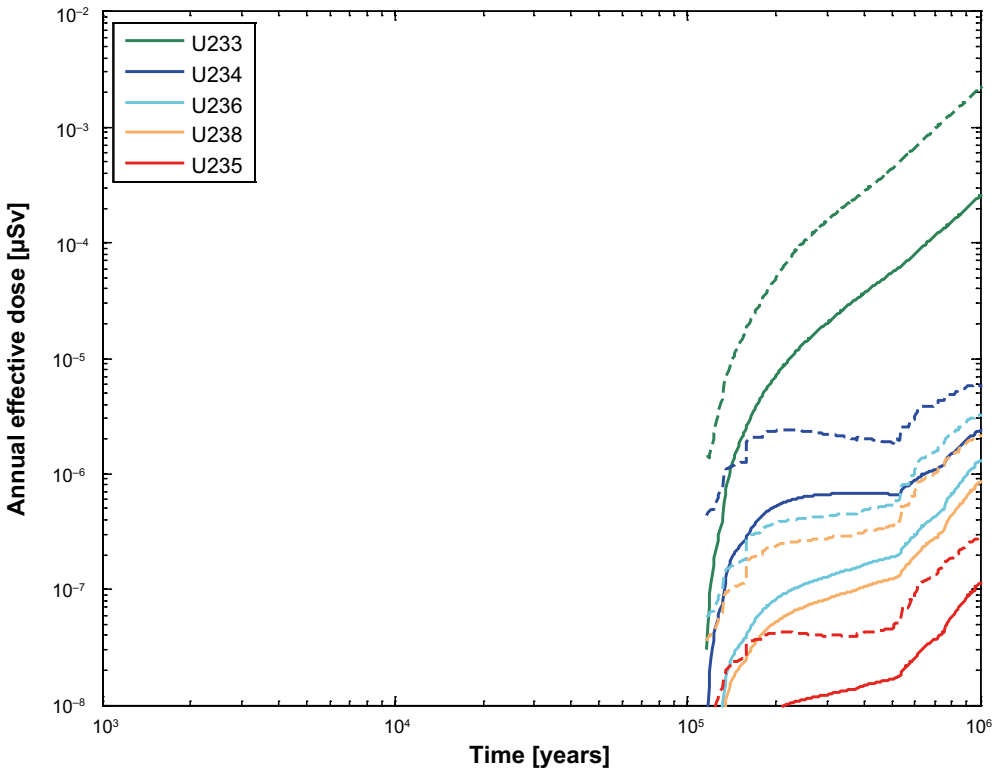

Figure 4-22. *Comparison between far-field annual effective doses from the uranium isotopes for probabilistic calculations of the central corrosion case with K_d values for U(IV) (solid lines) and U(VI) (dotted lines). Observe the change in y-axis limits.*

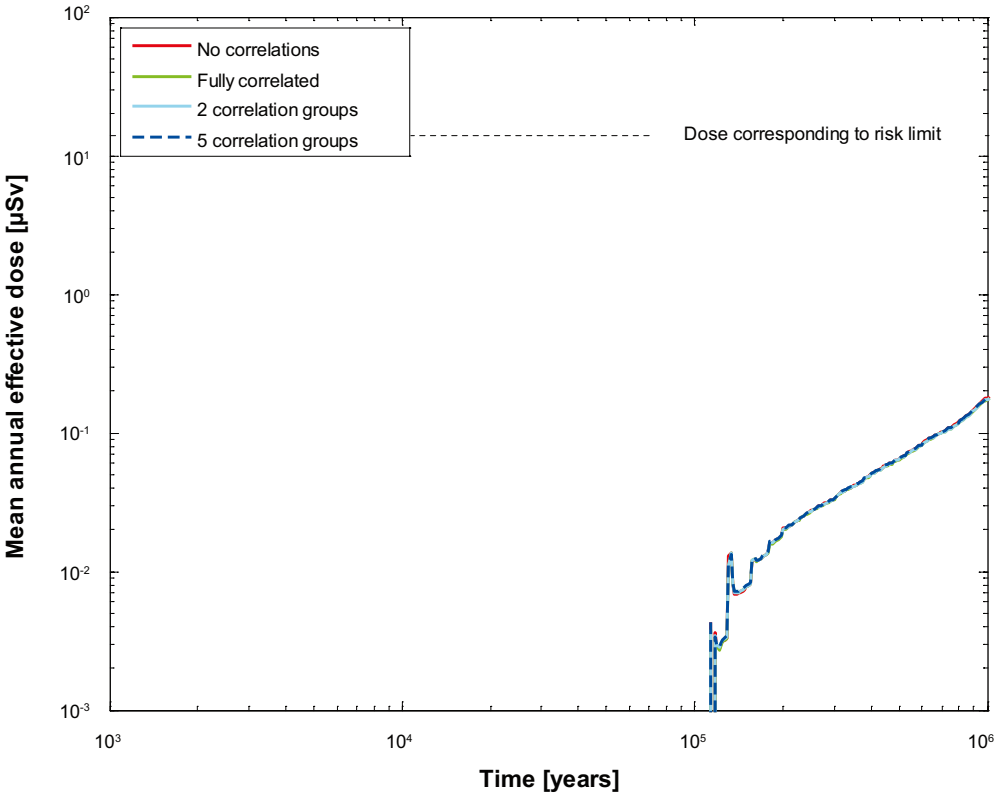

Figure 4-23. *Far-field mean annual effective dose for probabilistic calculations of the central corrosion case with different correlations for K_d and D_e for rock.*

4.5.6 Colloid-facilitated transport

The presence of bentonite material in tunnel backfill and borehole buffer is expected to result in bentonite colloids in the groundwater near deposition holes and along the geosphere transport pathways. Radionuclides that have a strong affinity for bentonite will sorb onto bentonite colloids and may be transported through the geosphere with reduced interaction with the rock matrix, i.e., with a reduced retention. Colloid facilitated transport involves a complicated combination of processes, many of which can mitigate the transport. Mitigating processes include colloid retardation in fractures, physical filtration (straining) of colloids in fractures, colloid flocculation and sedimentation, saturation of sorption sites on colloids, and competition for sites on colloids. These processes are uncertain or involve uncertain parameters that are difficult to quantify in short duration experiments. Rather than attempting to develop detailed process models for colloid-facilitated transport, potential mitigating processes are ignored so as to place an upper bound on the possible effect. Ignoring these potential mitigating processes and taking into consideration that sorption of radionuclides onto bentonite is understood to be a reversible process on the time scale of geosphere transport (**Buffer, backfill and closure process report**), the effect of colloids in facilitating transport may be modelled through the introduction of effective transport parameters as described in Appendix I for reversible sorption. The effective parameters depend on the colloid concentration and on the equilibrium partitioning coefficient for sorption onto colloids.

Colloid concentrations that can be stably supported are highly sensitive to groundwater chemistry. It has been determined (Wold 2010) that 10 mg/l is a reasonably pessimistic value for colloid concentrations for typical groundwater chemistries. However, this value may be higher during brief periods when dilute glacial melt water enters the geosphere. A value of 10 g/l has been determined to be a pessimistic value for colloid concentrations in very dilute waters (**Buffer, backfill and closure process report**).

The partitioning coefficient for sorption onto bentonite colloids K_c may be related to the same parameter for sorption onto bentonite buffer material K_d as $K_c = \gamma K_d$ where γ is a ratio of specific surface areas for colloidal and bulk bentonite. Given that bentonite is a fine-grained material and that equilibrium

partitioning coefficients for bentonite are typically measured using colloidal suspensions with particle sizes less than 1 µm, $\gamma \approx 1$ is a reasonable assumption. Thus, K_c distributions were taken from the **Data report**, Section 5.3.

Using the MARFA transport code and the effective parameters derived in Appendix I for reversible sorption, the effects of colloids are demonstrated in Figure 4-24. Except for the effects of colloids, this modelling case is identical to the central corrosion base case in Section 4.4.2. The dark blue curve is near-field mean-annual release expressed as an effective dose, the black curve is the far-field mean-annual effective dose without colloids. The green and pink curves are the far-field doses with colloid concentrations of 10 mg/l and 10 g/l, respectively.

4.5.7 Varying climate conditions

MARFA simulations are undertaken to address the corrosion scenario for a case with unsteady flow caused by climate evolution. In this analysis only the magnitude of the groundwater flow changes, not its direction, as a function of the prevailing climate (climate domains). In a supplementary study by Selroos et al. (2013), both groundwater flow magnitude and direction are considered variable as a function of climate (the same climate sequence as in SR-Site). This study indicates that multiple glacial cycles imply a large dilution of transported radionuclides. Furthermore, it is shown that only a small proportion of transported nuclides discharge from the geosphere during the period when the ice retreats and groundwater flows are high (SKB 2013a).

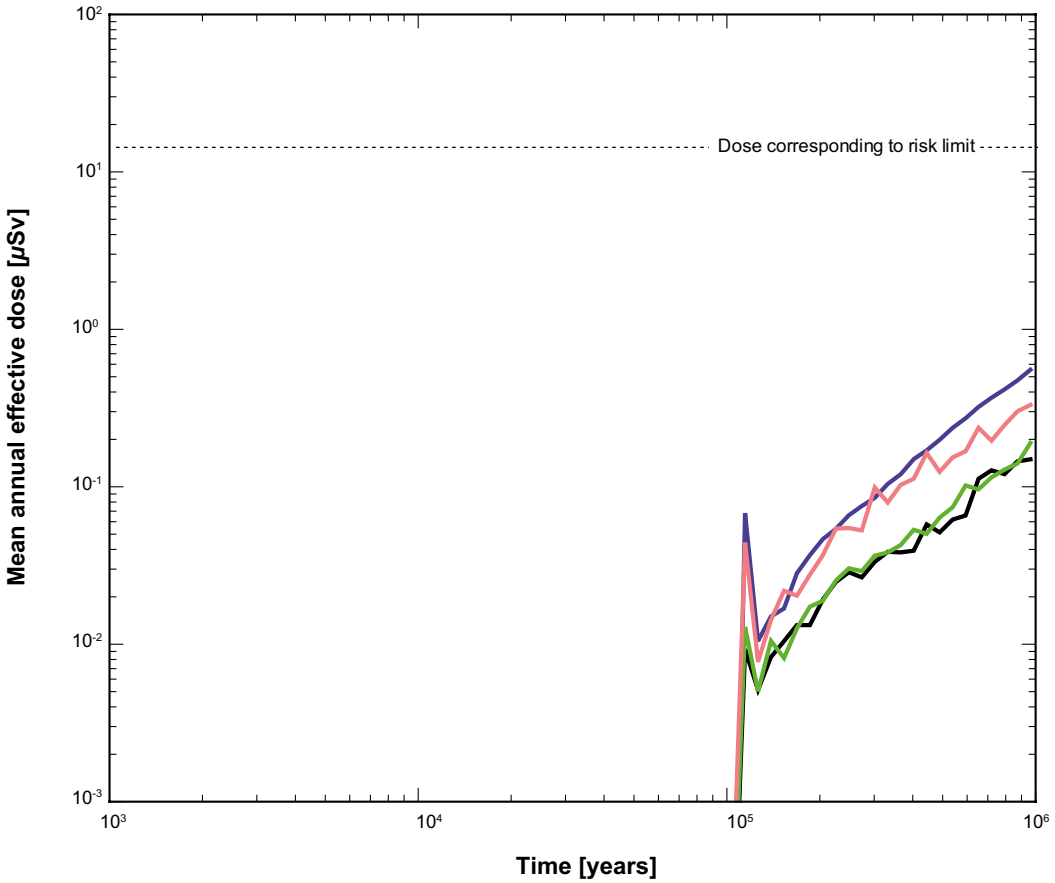

Figure 4-24. *Mean annual effective dose for the probabilistic central corrosion case, with and without the effects of bentonite colloids in facilitating transport (reversible sorption). The black, green, and pink curves are far-field dose with colloid concentrations of 0 mg/l, 10 mg/l, and 10 g/l, respectively. The dark blue curve is the near-field dose equivalent release.*

The transport simulations are identical to the central corrosion case described in Section 4.4.2 except for the use of the flow scaling factors shown in Figure 2-3 and the use of sorption K_d-values for oxidising conditions for the redox sensitive elements during ice front passages (i.e., during the time periods when flow scaling factors are 20 and 50, respectively). In addition, different dose conversion factors (LDFs) are applied for different periods in the glacial cycle. The near-field release calculations used as input to the MARFA simulations do not take into consideration the changes in flow. This simplification is based on the fact that releases of radioelements that are not solubility limited will be limited by the rate of waste-form dissolution, which is independent of flow rate.

Mean annual effective dose versus time for this case is show in Figure 4-25. Also shown is the case without flow changes, i.e., with temperate flow throughout the assessment period. The results are based on 2 800 realisations where both near-field and far-field parameters follow distributions, as described in Section 3.7.1.

The results in Figure 4-25 indicate that the flow, K_d and LDF changes collectively cause a slight increase in peak dose. However, the main effect is the sharp downward spikes in dose during the time of glacial approach and retreat. Although the radionuclide discharge to the biosphere is increased sharply during these periods due to changes in flow and, more importantly, changes in K_d for redox-sensitive radionuclides, this increase is more than compensated by the greatly reduced LDF factors during these periods.

The results without flow changes can also be compared to the corresponding case calculated using FARF31, see Section 4.4.2, showing very similar total dose results.

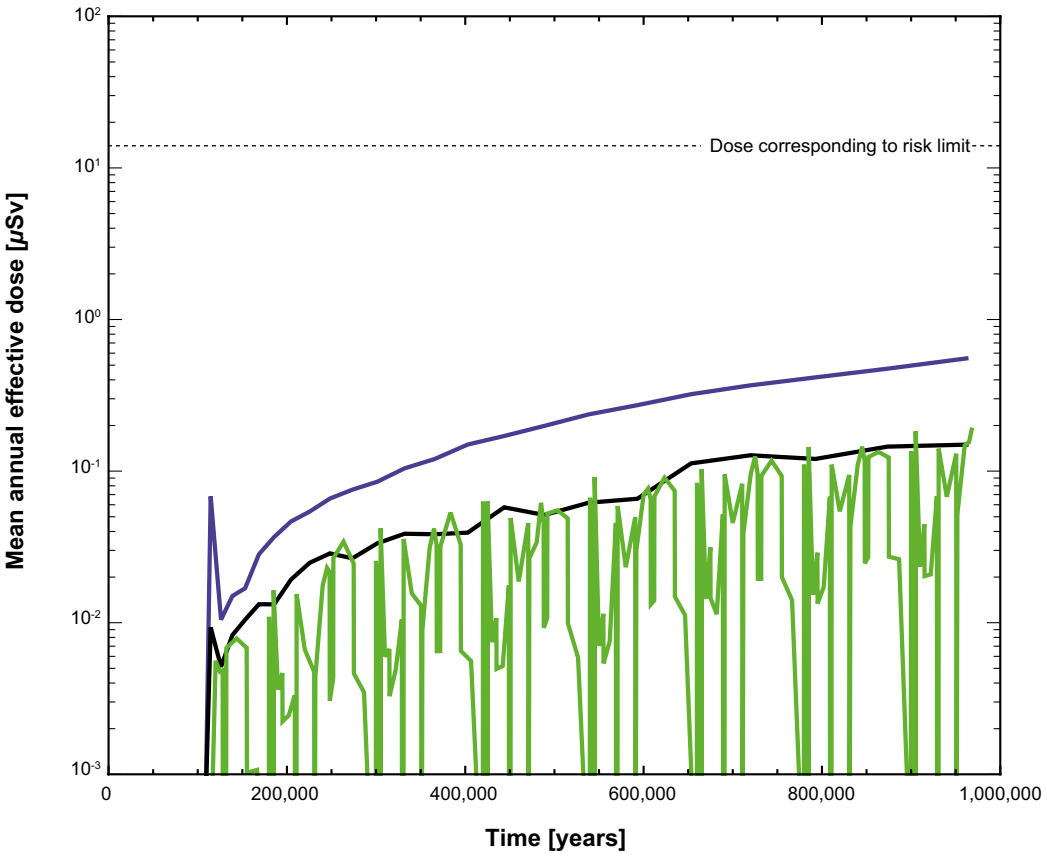

Figure 4-25. *Far-field annual effective dose (green curve) for a probabilistic calculation of the central corrosion case with varying climate conditions. For comparison the near-field dose equivalent release (blue curve) and also the far-field dose (black curve) without flow changes are given.*

4.5.8 Varying climate conditions and colloid-facilitated transport

MARFA calculations are undertaken to evaluate the simultaneous effects of varying climate conditions and colloid-facilitated transport. The simulations are identical to those in Section 4.5.7 except for that the colloid facilitated transport model of Section 4.5.6 is used. As has been noted, 10 mg/l has been determined to be a reasonable value for colloid concentration except during periods where dilute groundwater is expected to contact clay minerals in buffer and backfill. During the periods of dilute groundwater 10 g/l is used for the colloid concentration.

Results for a case with colloid concentration held constant at a high value of 10 g/l is shown in Figure 4-26. By comparing with Figure 4-25 it can be seen that colloids enhance transport over the colloid-free case and that the far-field dose approaches the near-field dose during the temperate period. Mean annual dose is not significant increased in the other periods because the LDF factors are lower then.

Results for a case with varying colloid concentration is shown in Figure 4-27. In this case, the colloid concentration is 10 g/l during periods of dilute groundwater and 10 mg/l otherwise. Dilute groundwaters are assumed to exist during the brief periods of glacial retreat/advance and also during the second halves of the glacial maximum and temperate periods (**Climate report**). Results are similar to those of Figure 4-26 except that the period of colloid-enhanced dose is limited to the second half of the temperate period.

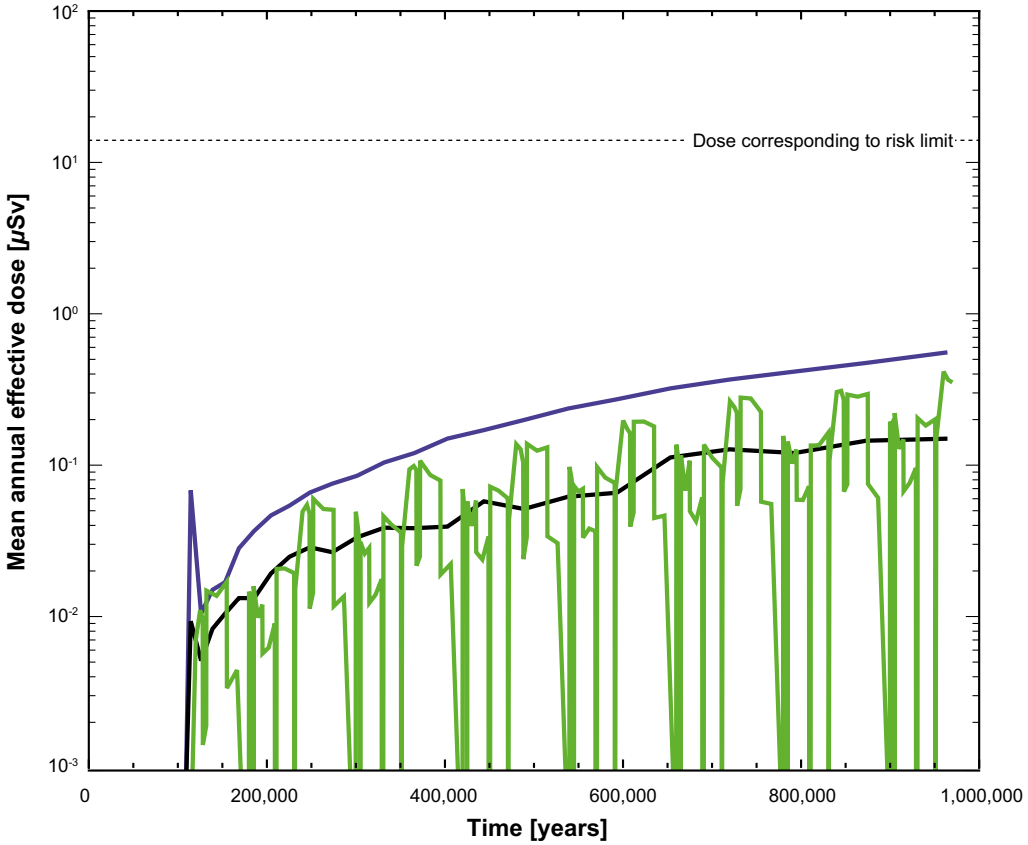

Figure 4-26. *Far-field annual effective dose (green curve) for a probabilistic calculation of the central corrosion case with varying climate conditions and colloid-facilitated transport (reversible sorption). For comparison the near-field dose (blue curve) is given. The colloid concentration is constant in this case and has a value of 10 g/l.*

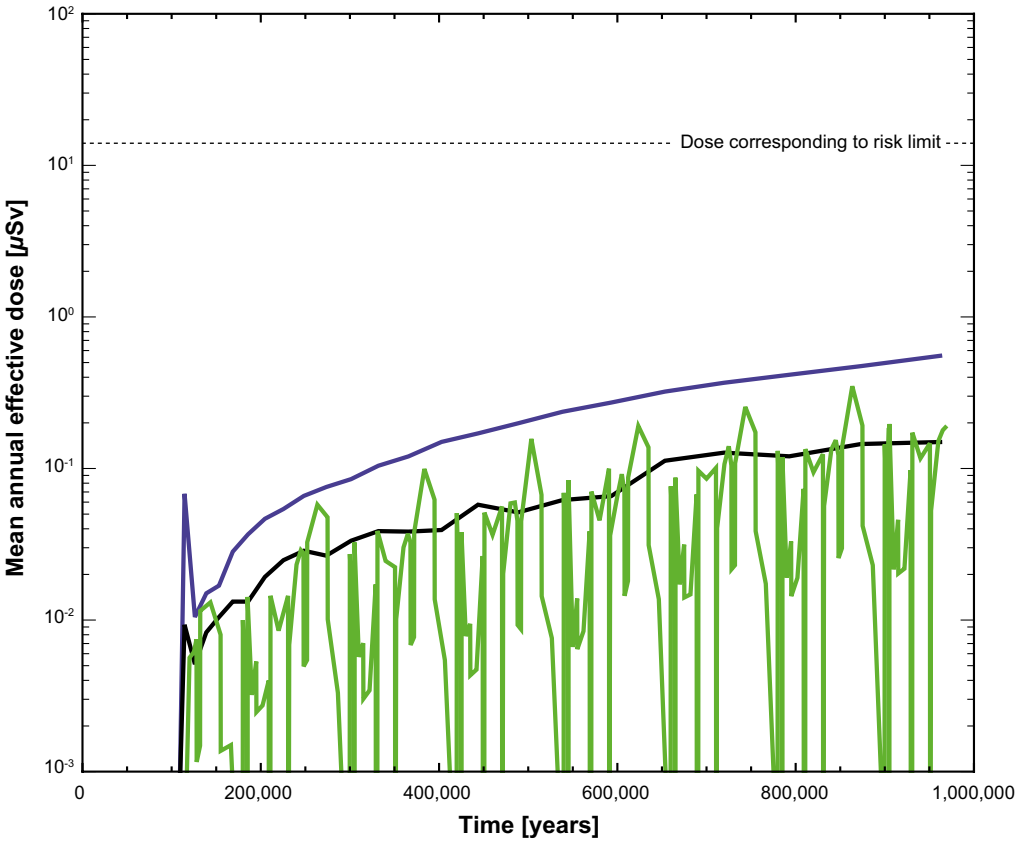

Figure 4-27. *Far-field annual effective dose (green curve) for a probabilistic calculation of the central corrosion case with varying climate conditions and colloid-facilitated transport (reversible sorption). For comparison the near-field dose (blue curve) is given.*

4.5.9 Initial advection

Deterministic calculations

Hydrogeological case:	Semi-correlated, ten realisations
Erosion/corrosion model:	Initial advection
Failure time:	44 049 years, according to Table 4-2
Number of failed canisters:	1
Solubility limits:	No
Thorium sorption in near field:	Yes (modelled as low solubility limit)
Number of realisations:	1
Number of nuclides:	37

A deterministic calculation of the semi-correlated case with initial advection is performed for a canister taken from the realisation with the earliest failure time of the analysed realisations, (44 049 years after deposition) with corresponding geosphere transport data, i.e. data used to calculate the corrosion time are from the same hydrogeological calculation as the geosphere transport data. Advection occurs in the buffer void and the dose equivalent releases are primarily determined by the fuel dissolution rate set to 10^{-7}/yr. Table 4-4 shows the peak annual doses from the pulse releases from the instantly released fraction, IRF.

Figure 4-28 and Figure 4-29 show the deterministic near-field and far-field dose equivalent releases, respectively, for the semi-correlated case with initial advection. Note that the peak in Figure 4-28 reaches outside the figure (doses larger than 100 μSv) but the real maximum doses are given in brackets in the figure legend. Doses from the near field are dominated by releases of Nb-94 and Ni-59 shortly after canister failure and by Ra-226 in the longer term. Doses from the far field are dominated by releases of Ra-226.

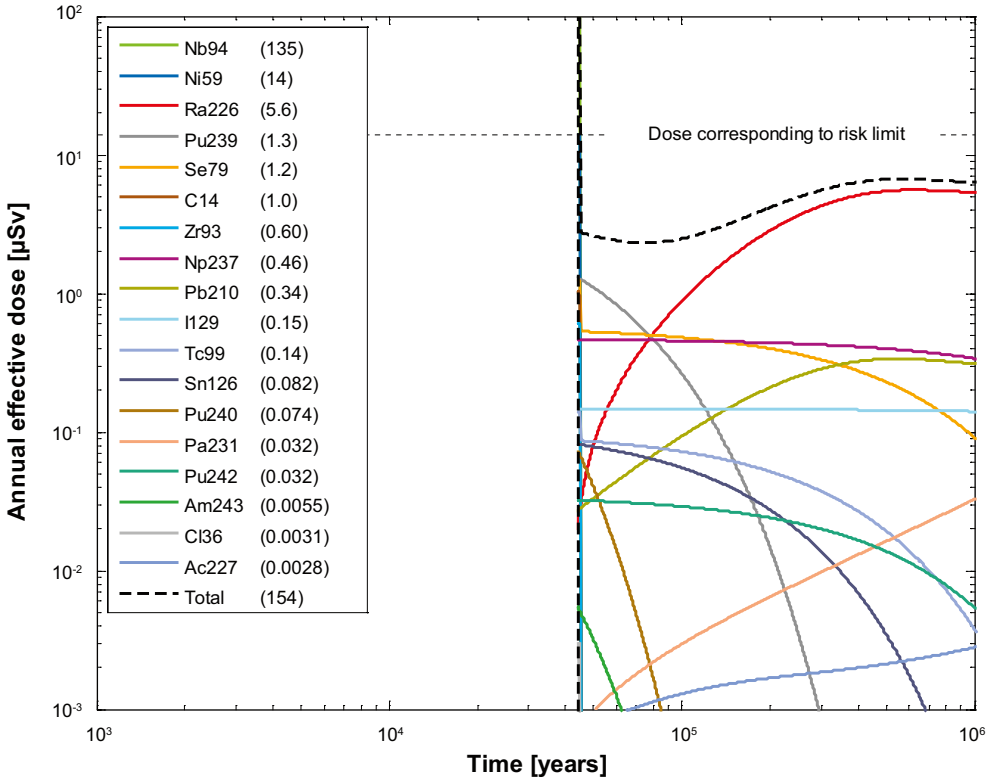

Figure 4-28. *Near-field dose equivalent release for a deterministic calculation of the central corrosion case, with initial advection in the erosion/corrosion model. The legend is sorted by peak (in the one-million year period) of the annual effective dose. The values in brackets are peak dose in units of µSv. Note that the dose equivalent release for Nb-94 is 135 µSv/year, i.e. above the limit of the y-axis.*

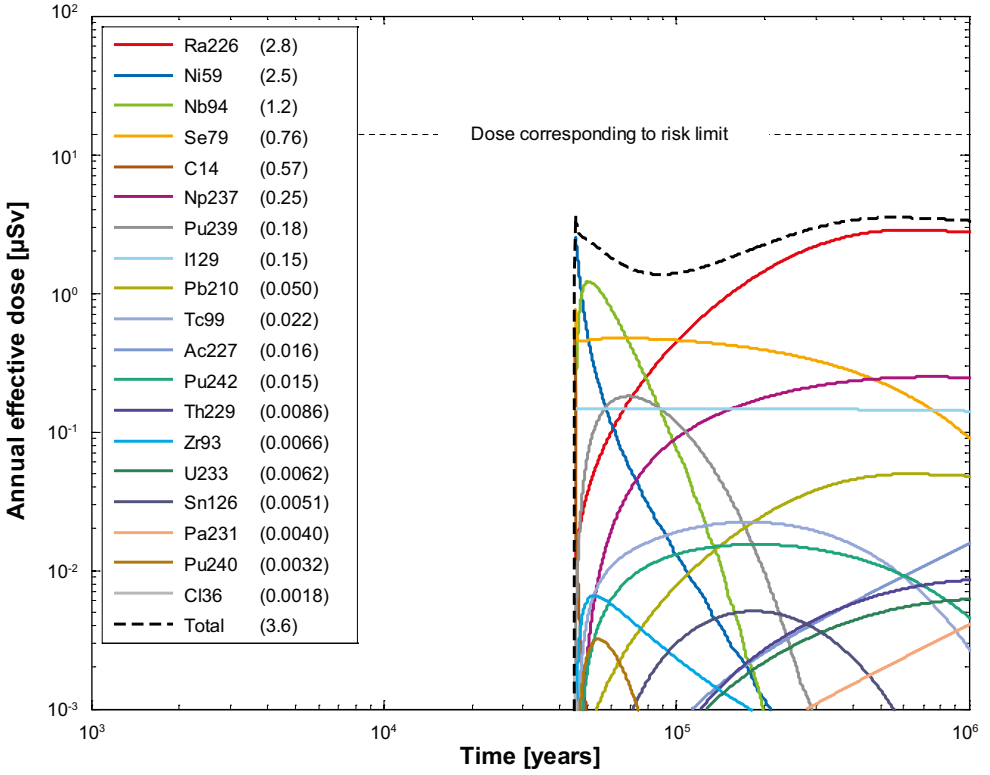

Figure 4-29. *Far-field annual effective dose for a deterministic calculation of the central corrosion case, with initial advection in the erosion/corrosion model. The legend is sorted by peak (in the one-million year period) of the annual effective dose. The values in brackets are peak dose in units of µSv.*

Probabilistic calculations

Hydrogeological case:	Semi-correlated, ten realisations
Erosion/corrosion model:	Initial advection
Failure time:	84 times according to the erosion/corrosion calculations
Mean number of failed canisters:	0.17
Solubility limits:	No
Thorium sorption in near field:	Yes (modelled as low solubility limit)
Number of realisations:	50 per canister failure time
Number of nuclides:	37

A probabilistic calculation of the semi-correlated case with initial advection is performed with failure times and geosphere transport data from the ten realisations of the semi-correlated DFN model and failure times from the corrosion calculations with initial advection. The contributions from the instantly released fraction of nuclides, IRF, are not included in the calculations except for Tc-99 that is included in the far-field calculations. The results for the IRF presented for the central corrosion case are judged to be sufficient to conclude that their contribution is negligible also in this case, see Section 4.4.2.

Figure 4-30 and Figure 4-31 show the near-field and far-field dose equivalent releases, respectively, for the semi-correlated case with initial advection. The total dose in the longer term is about 1.5 times higher than in the central corrosion case and is dominating by Ra-226.

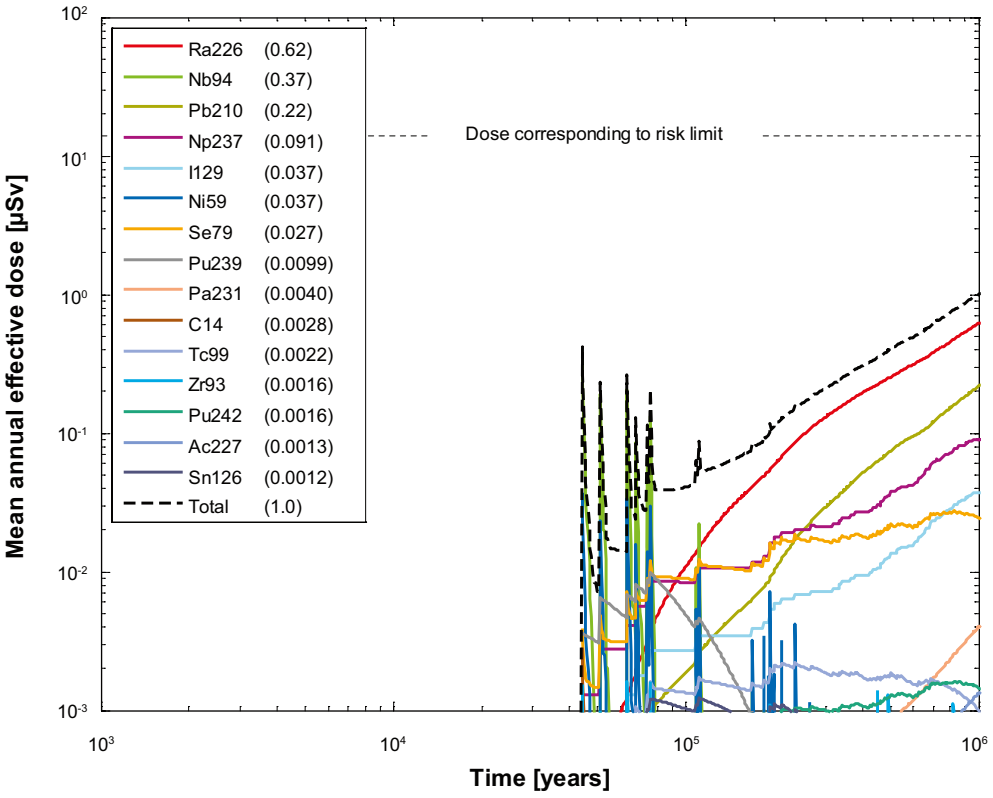

Figure 4-30. *Near-field dose equivalent release for a probabilistic calculation of the central corrosion case, with initial advection in the erosion/corrosion model. The legend is sorted by peak (in the one-million year period) of the mean annual effective dose. The values in brackets are peak dose in units of µSv.*

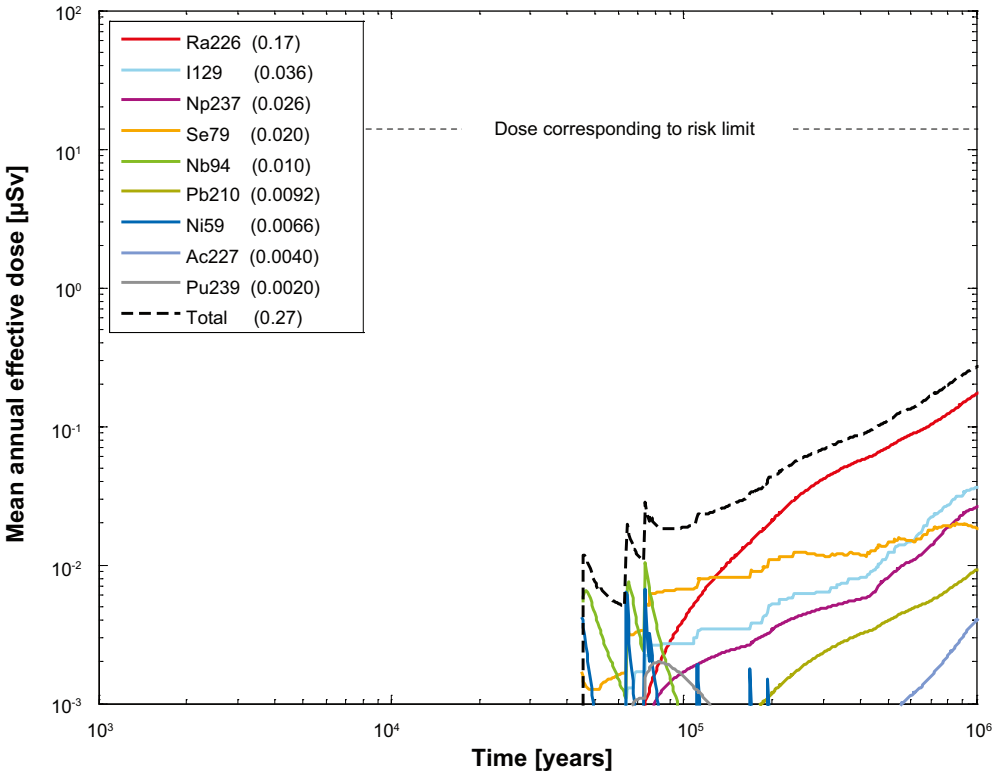

Figure 4-31. *Far-field mean annual effective dose for a probabilistic calculation of the central corrosion case, with initial advection in the erosion/corrosion model. The legend is sorted by peak (in the one-million year period) of the mean annual effective dose. The values in brackets are peak dose in units of µSv.*

4.6 Uncorrelated hydrogeological DFN model

4.6.1 Base case transport assumptions

Deterministic calculations

Hydrogeological case:	Uncorrelated, five realisations
Erosion/corrosion model:	SR-Site model
Failure time:	97 815 years, according to Table 4-2
Number of failed canisters:	1
Solubility limits:	No
Thorium sorption in near field:	Yes (modelled as low solubility limit)
Number of realisations:	1
Number of nuclides:	37

A deterministic calculation of the uncorrelated case is performed for a canister taken from the realisations with the earliest failure time of the analysed realisation (97 815 years after deposition) with corresponding geosphere transport data, i.e. data used to calculate the corrosion time are from the same hydrogeological calculation as the geosphere transport data. Advection occurs in the buffer void and the dose equivalent releases are primarily determined by the fuel dissolution rate set to 10^{-7}/yr. Table 4-4 shows the peak annual doses from the pulse releases from the instantly released fraction, IRF.

Figure 4-32 and Figure 4-33 show the deterministic near-field and far-field dose equivalent releases, respectively, for the uncorrelated case. Doses caused by Nb-94 and Ni-59 are dominating the releases from the near field and I-129 is dominating the far-field releases. The low releases of Ra-226 from the far field is an effect of the high F value, see Table 4-2.

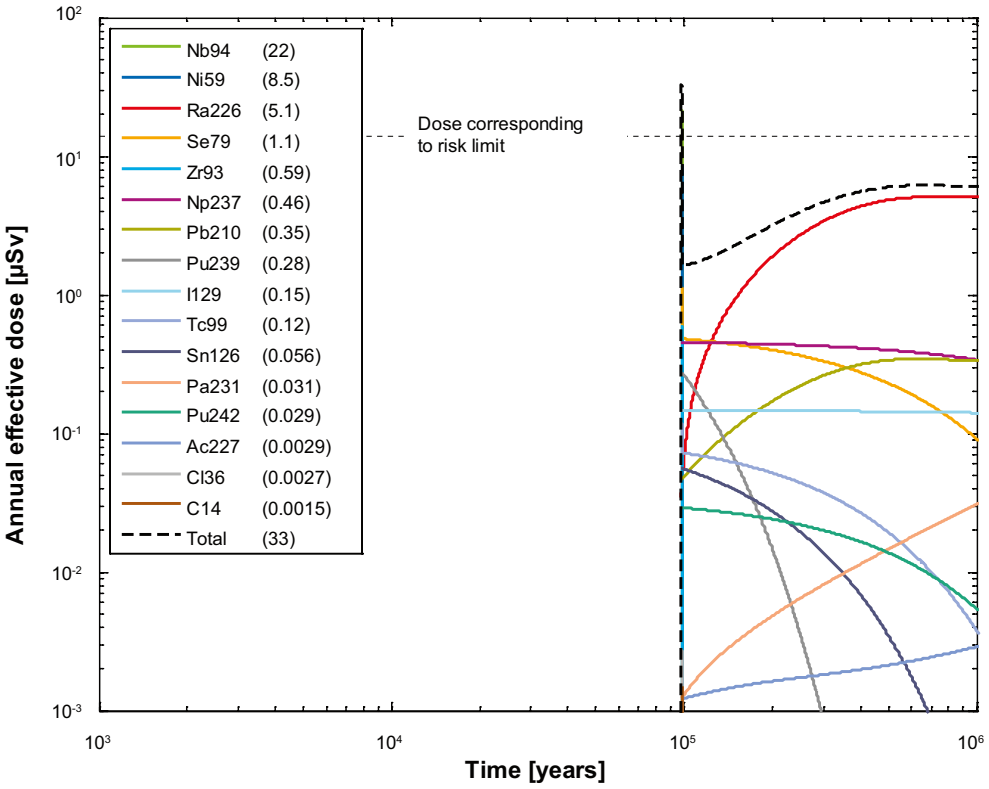

Figure 4-32. *Near-field dose equivalent release for a deterministic calculation of the corrosion scenario, with hydrogeological data from the uncorrelated model. The legend is sorted by peak (in the one-million year period) of the annual effective dose. The values in brackets are peak dose in units of µSv.*

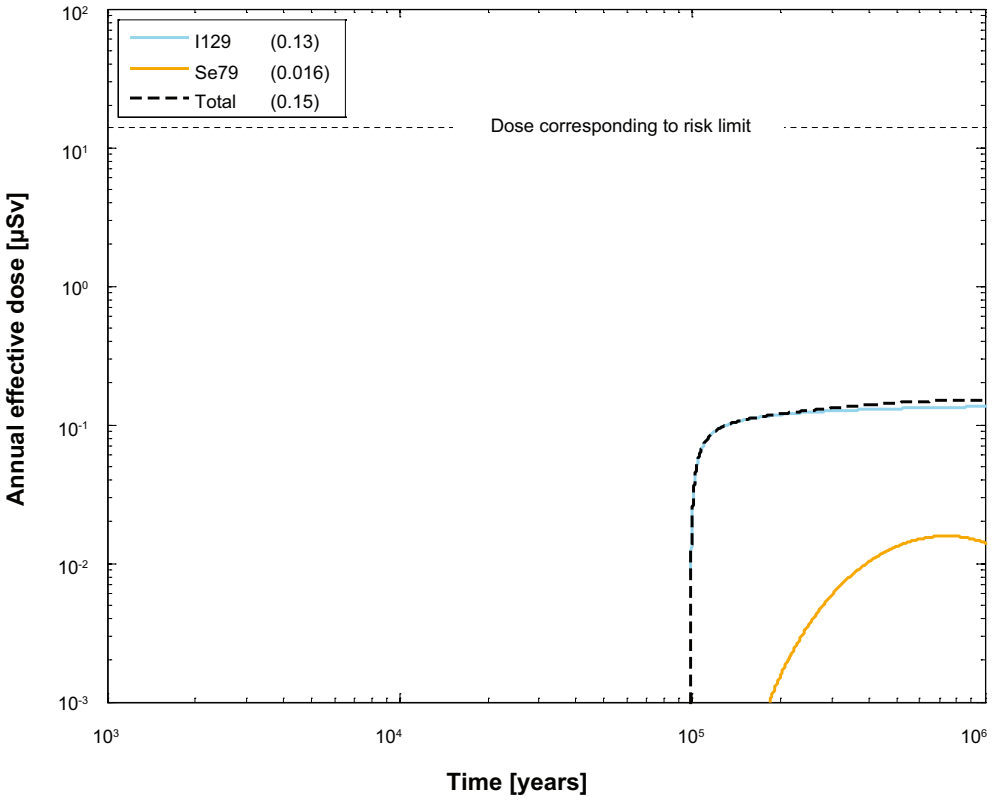

Figure 4-33. *Far-field annual effective dose for a deterministic calculation of the corrosion scenario, with hydrogeological data from the uncorrelated model. The legend is sorted by peak (in the one-million year period) of the annual effective dose. The values in brackets are peak dose in units of µSv.*

Probabilistic calculations

Hydrogeological case:	Uncorrelated, five realisations
Erosion/corrosion model:	SR-Site model
Failure time:	154 times according to the erosion/corrosion calculations
Mean number of failed canisters:	0.65
Solubility limits:	No
Thorium sorption in near field:	Yes (modelled as low solubility limit)
Number of realisations:	50 per canister failure time
Number of nuclides:	37

A probabilistic calculation of the uncorrelated case is performed with failure times and geosphere transport data from the five realisations of the uncorrelated DFN model. The contributions from the instantly released fraction of nuclides, IRF, are not included in the calculations except for Tc-99 that is included in the far-field calculations. The results for the IRF presented for the central corrosion case are judged to be sufficient to conclude that their contribution is negligible also in this case, see Section 4.4.2.

Figure 4-34 and Figure 4-35 show the near-field and far-field dose equivalent releases, respectively, for the uncorrelated case. The total doses from the near field and far field are about 5 times higher and 2.5 times higher, respectively, compared to the central corrosion case, and are dominated by the Ra-226 release.

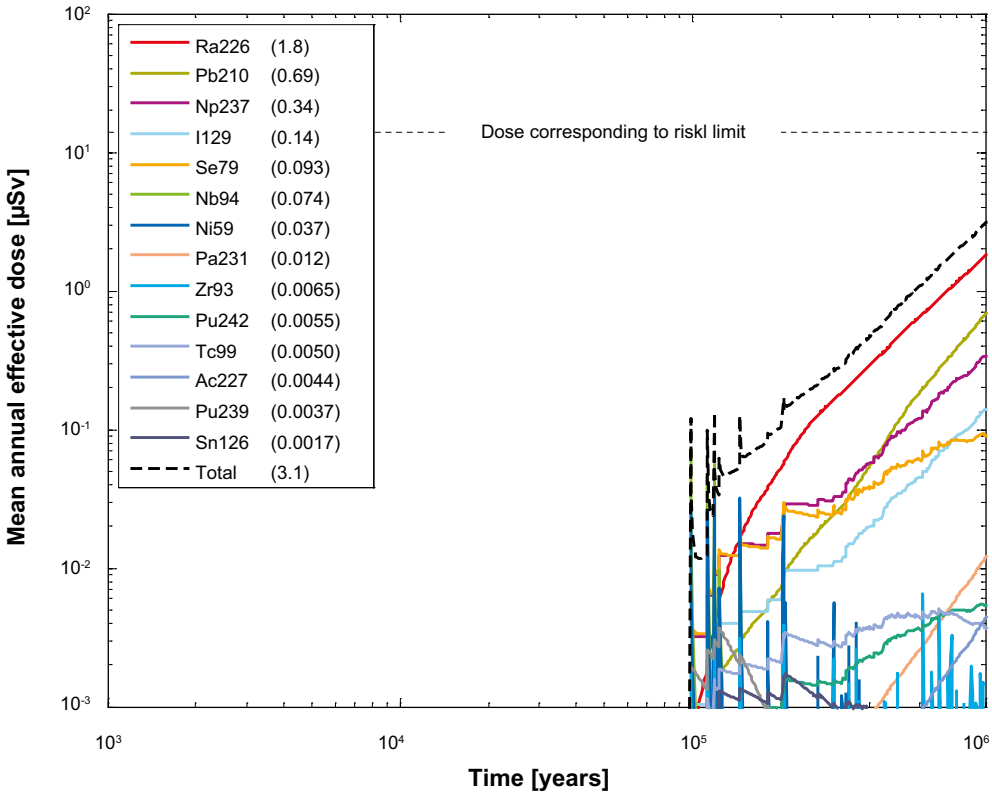

Figure 4-34. *Near-field dose equivalent release for the probabilistic calculation of the corrosion scenario, with hydrogeological data from the uncorrelated model. The legend is sorted by peak (in the one-million year period) of the mean annual effective dose. The values in brackets are peak dose in units of µSv.*

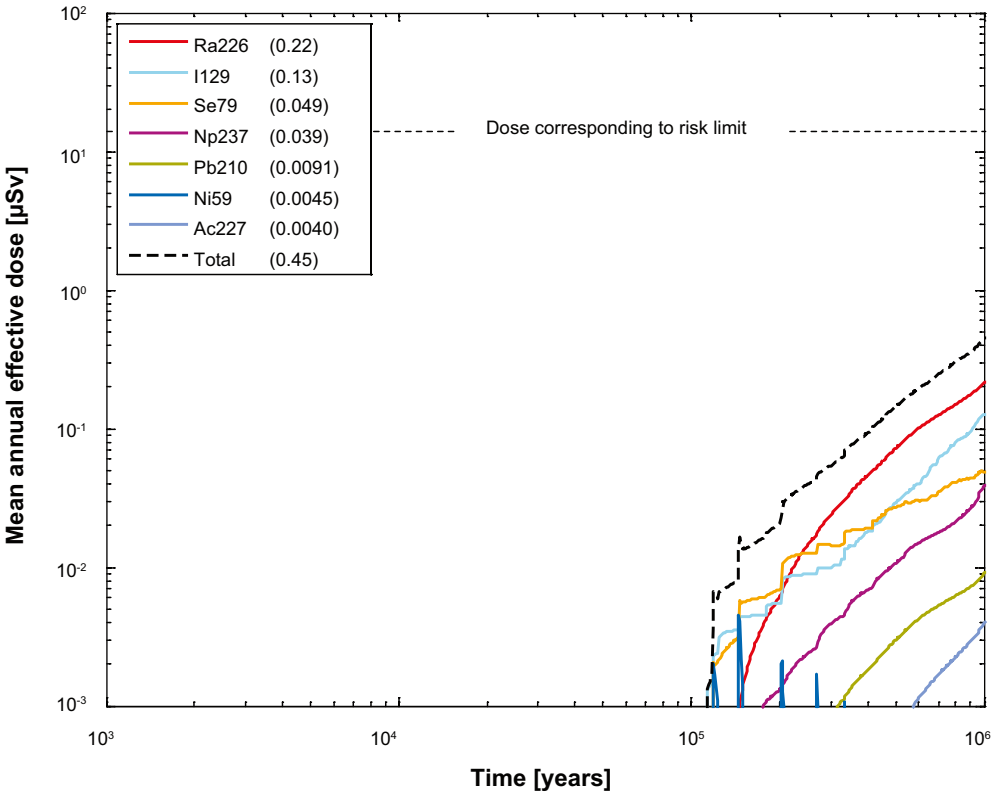

Figure 4-35. *Far-field mean annual effective dose for the probabilistic calculation of the corrosion scenario, with hydrogeological data from the uncorrelated model. The legend is sorted by peak (in the one-million year period) of the mean annual effective dose. The values in brackets are peak dose in units of µSv.*

4.6.2 Initial advection

Deterministic calculations

Hydrogeological case:	Uncorrelated, five realisations
Erosion/corrosion model:	Initial advection
Failure time:	47 107 years, according to Table 4-2
Number of failed canisters:	1
Solubility limits:	No
Thorium sorption in near field:	Yes (modelled as low solubility limit)
Number of realisations:	1
Number of nuclides:	37

A deterministic calculation of the uncorrelated case with initial advection is performed for a canister taken from the realisation with the earliest failure time of the analysed realisations (47 107 years after deposition) with corresponding geosphere transport data, i.e. data used to calculate the corrosion time are from the same hydrogeological calculation as the geosphere transport data. Advection occurs in the buffer void and the dose equivalent releases are primarily determined by the fuel dissolution rate set to 10^{-7}/yr. Table 4-4 shows the peak annual doses from the pulse releases from the instantly released fraction, IRF.

Figure 4-36 and Figure 4-37 show the deterministic near-field and far-field dose equivalent releases, respectively, for the uncorrelated case with initial advection. Note that the peak in Figure 4-36 reaches outside the figure (doses larger than 100 µSv) but the real maximum doses are given in brackets in the figure legend. Doses from the near field are dominated by releases of Nb-94 and Ni-59 shortly after canister failure and by Ra-226 in the longer term. Releases of I-129 are dominating the doses from the far field. The high F value, see Table 4-2, implies that the far-field releases of Ra-226 are low.

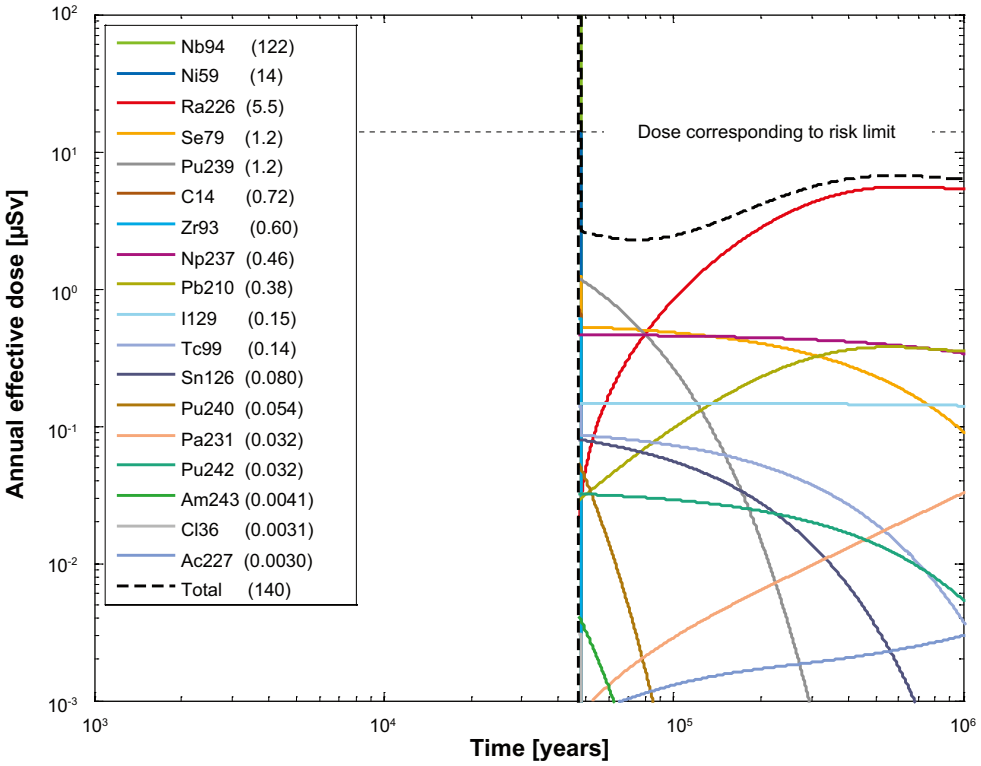

Figure 4-36. *Near-field dose equivalent release for a deterministic calculation of the corrosion scenario, with hydrogeological data from the uncorrelated model and initial advection in the erosion/corrosion model. The legend is sorted by peak (in the one-million year period) of the annual effective dose. The values in brackets are peak dose in units of µSv. Note that the dose equivalent release for Nb-94 is 122 µSv/year, i.e. above the end of the y-axis.*

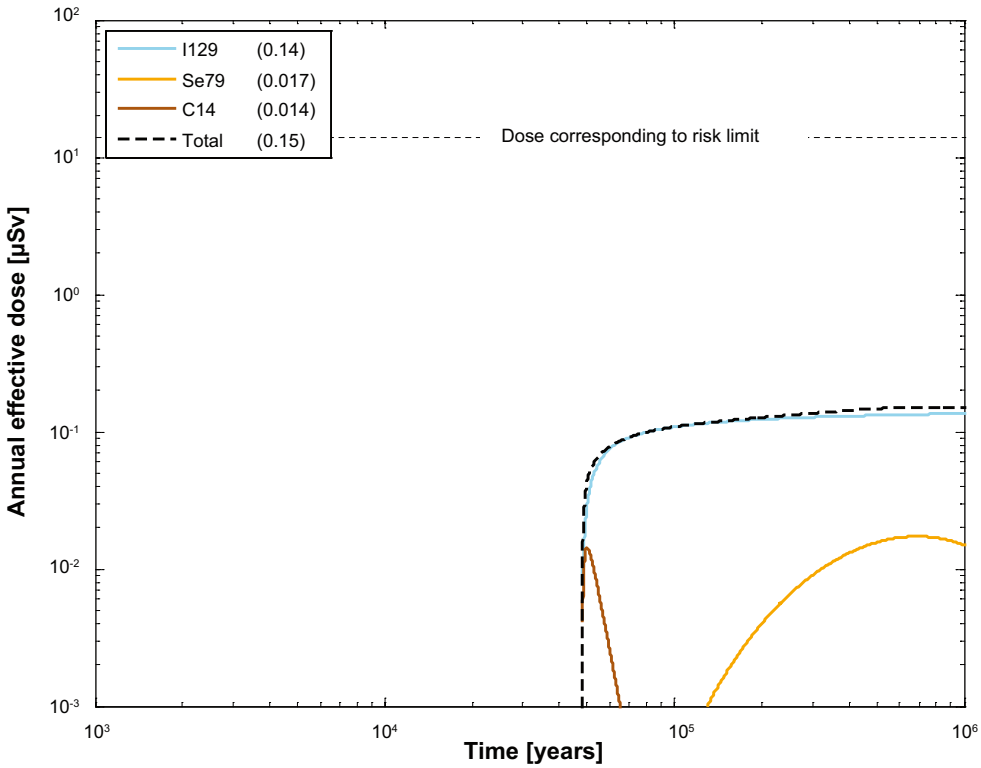

Figure 4-37. *Far-field annual effective dose for a deterministic calculation of the corrosion scenario, with hydrogeological data from the uncorrelated model and initial advection in the erosion/corrosion model. The legend is sorted by peak (in the one-million year period) of the annual effective dose. The values in brackets are peak dose in units of µSv.*

Probabilistic calculations

Hydrogeological case:	Uncorrelated, five realisations
Erosion/corrosion model:	Initial advection
Failure time:	289 times according to the erosion/corrosion calculations
Mean number of failed canisters:	1.22
Solubility limits:	No
Thorium sorption in near field:	Yes (modelled as low solubility limit)
Number of realisations:	50 per canister failure time
Number of nuclides:	37

A probabilistic calculation of the uncorrelated case with initial advection is performed with failure times and geosphere transport data from the five realisations of the uncorrelated DFN model. The mean number of failed canisters is 1.22. The contributions from the instantly released fraction of nuclides, IRF, are not included in the calculations except for Tc-99 that is included in the far-field calculations. The results for the IRF presented for the central corrosion case is judged to be enough to conclude that their contribution is negligible also in this case, see Section 4.4.2.

Figure 4-38 and Figure 4-39 show the near-field and far-field dose equivalent releases, respectively, for the uncorrelated case with initial advection. Doses from the near field are dominated by releases of Ra-226 and Pb-210 and from the far field by Ra-226 and I-129. The total doses from the near-field and the far-field are about 12 times higher and 5 times higher, respectively, compared to the central corrosion case.

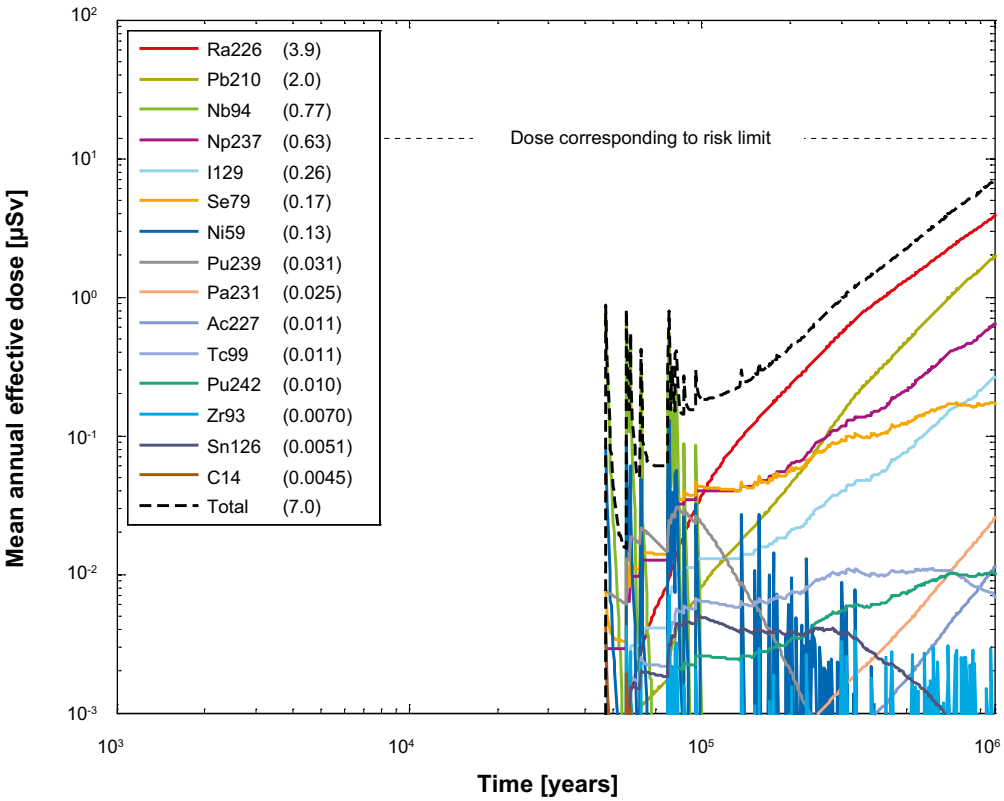

Figure 4-38. *Near-field dose equivalent release for the probabilistic calculation of the corrosion scenario, with hydrogeological data from the uncorrelated model and initial advection in the erosion/corrosion model. The legend is sorted by peak (in the one-million year period) of the mean annual effective dose. The values in brackets are peak dose in units of µSv.*

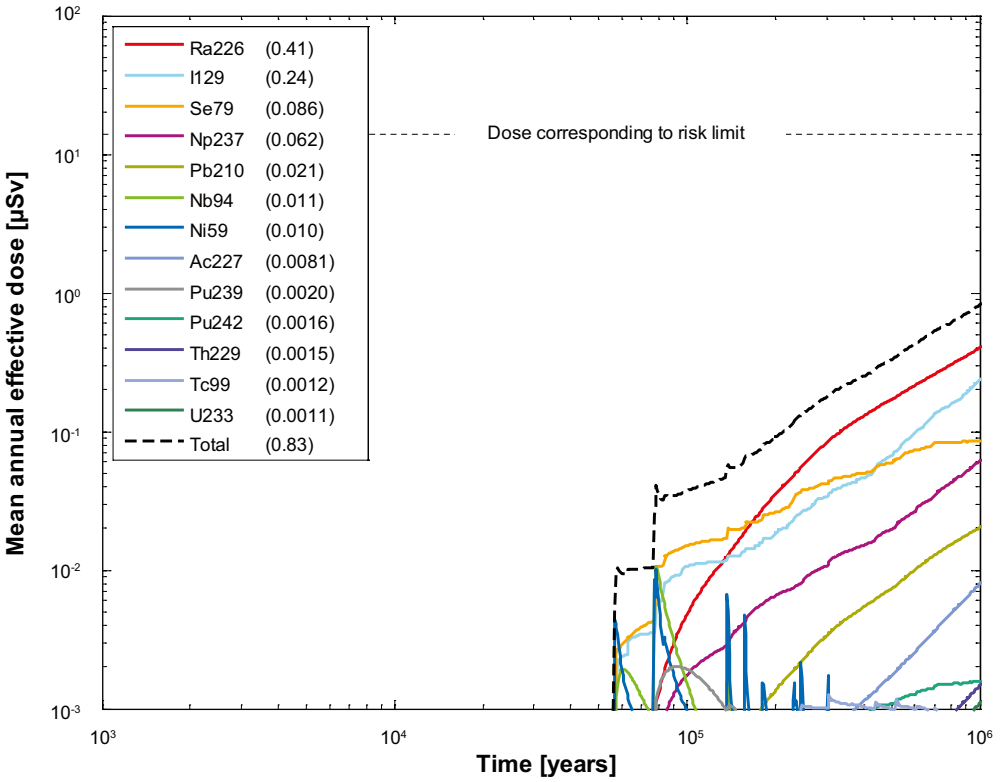

Figure 4-39. *Far-field mean annual effective dose for the probabilistic calculation of the corrosion scenario, with hydrogeological data from the uncorrelated model and initial advection in the erosion/corrosion model. The legend is sorted by peak (in the one-million year period) of the mean annual effective dose. The values in brackets are peak dose in units of µSv.*

4.7 Fully correlated hydrogeological DFN model

4.7.1 Base case transport assumptions

Deterministic calculations

Hydrogeological case:	Fully correlated, five realisations
Erosion/corrosion model:	SR-Site model
Failure time:	99 700 years, according to Table 4-2
Number of failed canisters:	1
Solubility limits:	No
Thorium sorption in near field:	Yes (modelled as low solubility limit)
Number of realisations:	1
Number of nuclides:	37

A deterministic calculation of the fully correlated case is performed for a canister taken from the realisation with the earliest failure time of the analysed realisations (99 700 years after deposition) with corresponding geosphere transport data, i.e. data used to calculate the corrosion time are from the same hydrogeological calculation as the geosphere transport data. Advection occurs in the buffer void and the dose equivalent releases are primarily determined by the fuel dissolution rate set to 10^{-7}/yr. Table 4-4 shows the peak annual doses from the pulse releases from the instantly released fraction, IRF.

Figure 4-40 and Figure 4-41 show the deterministic near-field and far-field dose equivalent releases, respectively, for the fully correlated case. Doses caused by Nb-94 and Ni-59 are dominating the releases from the near field shortly after canister failure and releases of Ra-226 are dominating in the longer term in the near filed as well as in the far field.

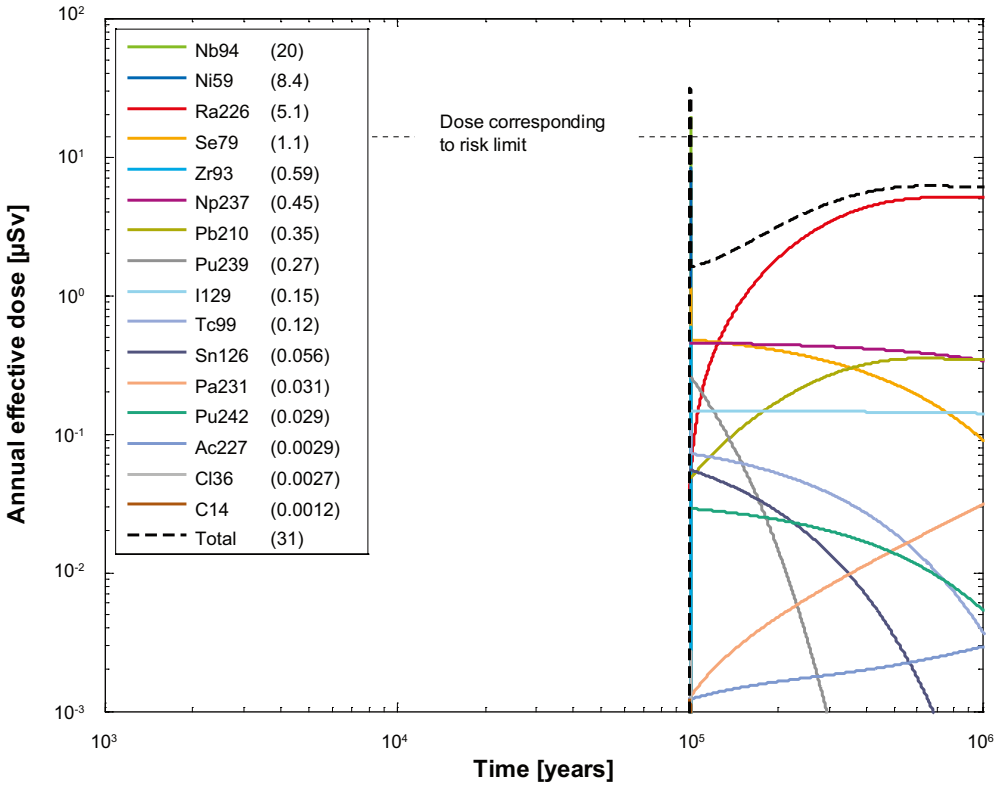

Figure 4-40. *Near-field dose equivalent release for a deterministic calculation of the corrosion scenario, with hydrogeological data from the fully correlated model. The legend is sorted by peak (in the one-million year period) of the annual effective dose. The values in brackets are peak dose in units of µSv.*

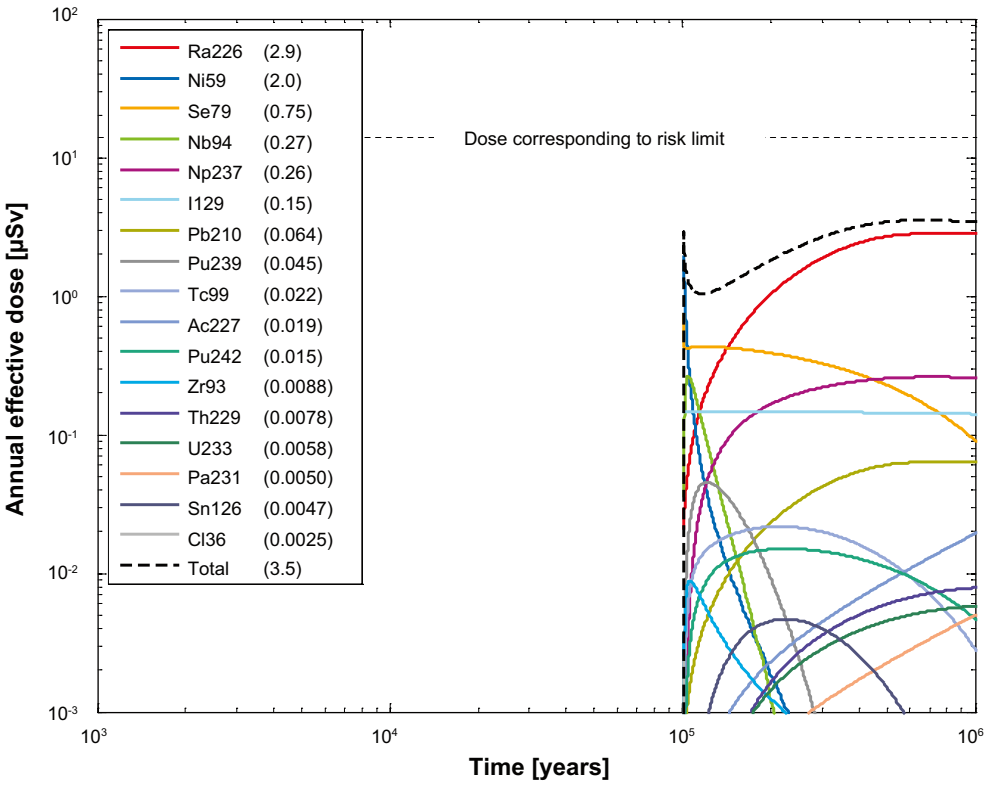

Figure 4-41. *Far-field annual effective dose for a deterministic calculation of the corrosion scenario, with hydrogeological data from the fully correlated model. The legend is sorted by peak (in the one-million year period) of the annual effective dose. The values in brackets are peak dose in units of µSv.*

Probabilistic calculations

Hydrogeological case:	Fully correlated, five realisations
Erosion/corrosion model:	SR-Site model
Failure time:	132 times according to the erosion/corrosion calculations
Mean number of failed canisters:	0.57
Solubility limits:	No
Thorium sorption in near field:	Yes (modelled as low solubility limit)
Number of realisations:	50 per canister failure time
Number of nuclides:	37

A probabilistic calculation of the fully correlated case was performed with failure times and geosphere transport data from the five realisations of the uncorrelated DFN model and the erosion/corrosion calculations in SKBdoc, see Table 3-8. The mean number of failed canisters is 0.57. The contributions from the instantly released fraction of nuclides, IRF, are not included in the calculations except for Tc-99 that is included in the far-field calculations. The results for the IRF presented for the central corrosion case are judged to be sufficient to conclude that their contribution is negligible also in this case, see Section 4.4.2.

Figure 4-42 and Figure 4-43 show the near-field and far-field dose equivalent releases, respectively, for the fully correlated case. The near-field doses are dominated by Ra-226 and are about 5 times higher than in the central corrosion case. The far-field doses are dominated by Ra-226 and I-129 and are about 3.5 times higher than in the central corrosion case.

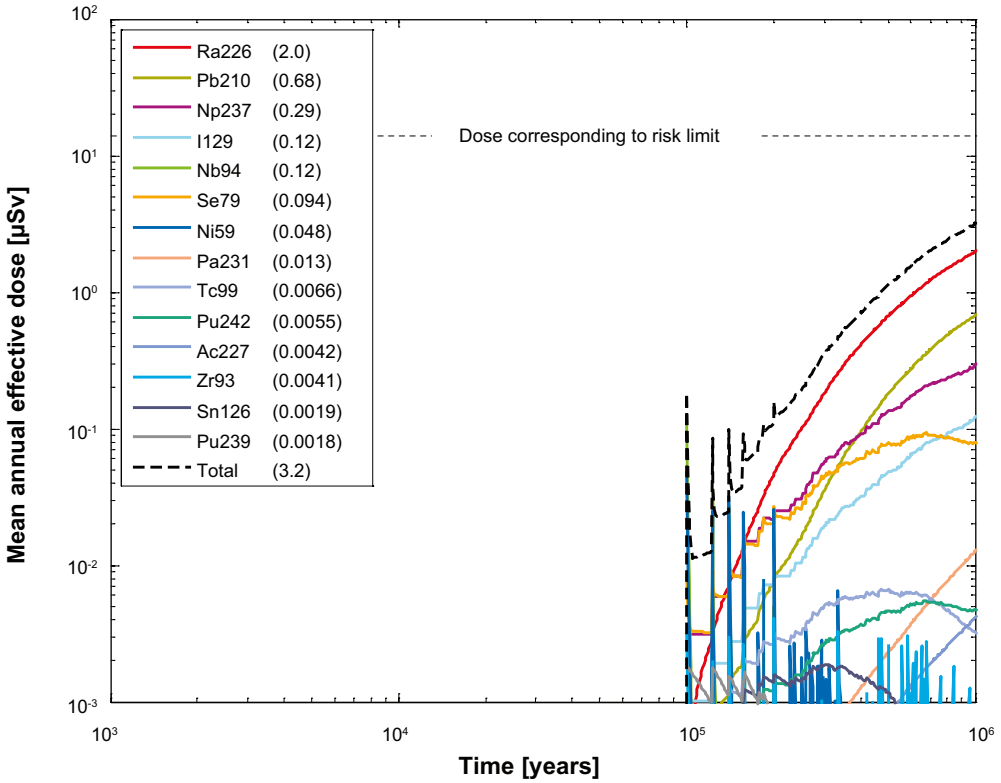

Figure 4-42. *Near-field dose equivalent release for the probabilistic calculation of the corrosion scenario, with hydrogeological data from the fully correlated model. The legend is sorted by peak (in the one-million year period) of the mean annual effective dose. The values in brackets are peak dose in units of µSv.*

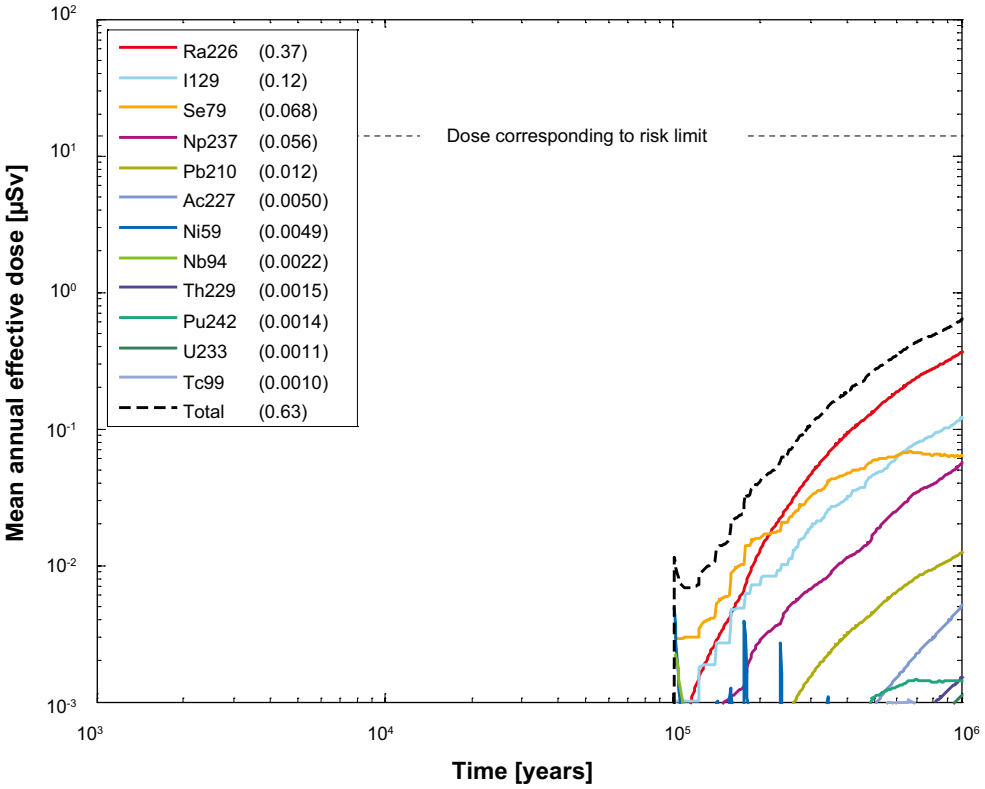

Figure 4-43. *Far-field mean annual effective dose for the probabilistic calculation of the corrosion scenario, with hydrogeological data from the fully correlated model. The legend is sorted by peak (in the one-million year period) of the mean annual effective dose. The values in brackets are peak dose in units of µSv.*

4.7.2 Initial advection

Deterministic calculations

Hydrogeological case:	Fully correlated, five realisations
Erosion/corrosion model:	Initial advection
Failure time:	47 657 years, according to Table 4-2
Number of failed canisters:	1
Solubility limits:	No
Thorium sorption in near field:	Yes (modelled as low solubility limit)
Number of realisations:	1
Number of nuclides:	37

A deterministic calculation of the fully correlated case with initial advection is performed for a canister taken from the realisation with the earliest failure time of the analysed realisations (47 657 years after deposition) with corresponding geosphere transport data, i.e. data used to calculate the corrosion time are from the same hydrogeological calculation as the geosphere transport data. Advection occurs in the buffer void and the dose equivalent releases are primarily determined by the fuel dissolution rate set to 10^{-7}/yr. Table 4-4 shows the peak annual doses from the pulse releases from the instantly released fraction, IRF.

Figure 4-44 and Figure 4-45 show the deterministic near-field and far-field dose equivalent releases, respectively, for the fully correlated case with initial advection. Note that the peak in Figure 4-44 reaches outside the figure (doses larger than 100 µSv) but the real maximum doses are given in brackets in the figure legend. Doses from the near field are dominated by releases of Nb-94 and Ni-59 shortly after canister failure and by Ra-226 in the longer term. The same nuclides are dominating the doses from the far field.

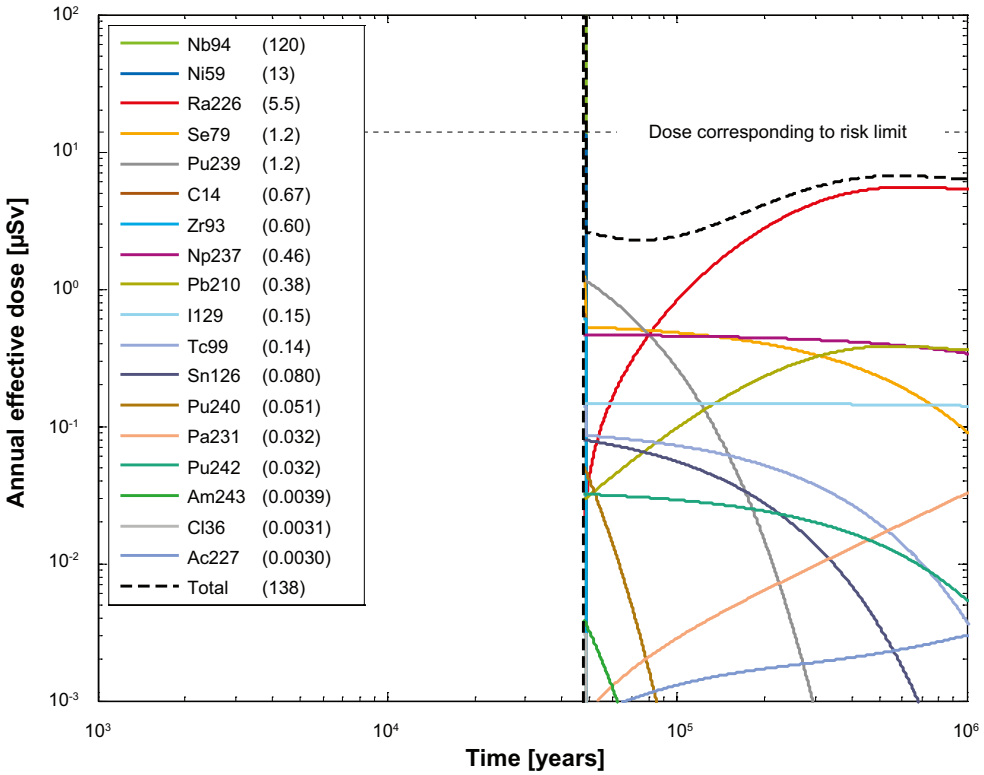

Figure 4-44. *Near-field dose equivalent release for a deterministic calculation of the corrosion scenario, with hydrogeological data from the fully correlated model and initial advection in the erosion/corrosion model. The legend is sorted by peak (in the one-million year period) of the annual effective dose. The values in brackets are peak dose in units of µSv. Note that the dose equivalent release forNb-94 is 120 µSv/year, i.e. above the limit of the y-axis.*

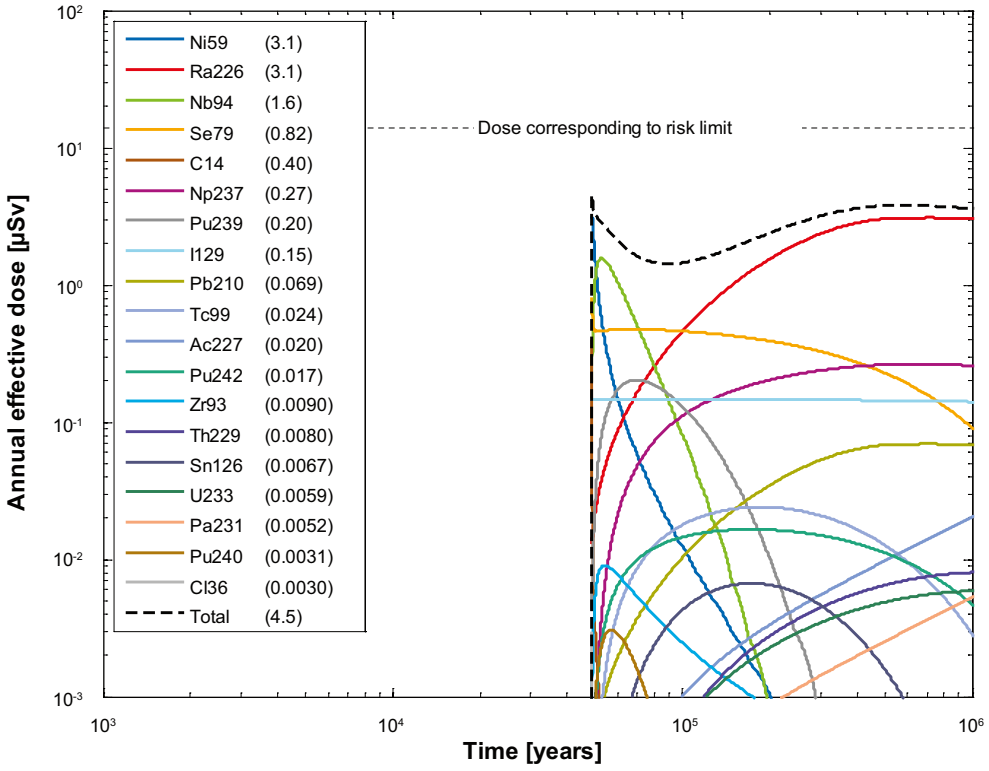

Figure 4-45. *Far-field annual effective dose for a deterministic calculation of the corrosion scenario, with hydrogeological data from the fully correlated model and initial advection in the erosion/corrosion model. The legend is sorted by peak (in the one-million year period) of the annual effective dose. The values in brackets are peak dose in units of µSv.*

Probabilistic calculations

Hydrogeological case:	Fully correlated, five realisations
Erosion/corrosion model:	Initial advection
Failure time:	200 times according to the erosion/corrosion calculations
Mean number of failed canisters:	0.86
Solubility limits:	No
Thorium sorption in near field:	Yes (modelled as low solubility limit)
Number of realisations:	50 per canister failure time
Number of nuclides:	37

A probabilistic calculation of the fully correlated case with initial advection was performed with failure times and geosphere transport data from the five realisations of the uncorrelated DFN model and the erosion/corrosion calculations in SKBdoc, see Table 3-8. The mean number of failed canisters is 0.86. The contributions from the instantly released fraction of nuclides, IRF, are not included in the calculations except for Tc-99 that is included in the far-field calculations. The results for the IRF presented for the central corrosion case are judged to be sufficient to conclude that their contribution is negligible also in this case, see Section 4.4.2.

Figure 4-46 and Figure 4-47 show the near-field and far-field dose equivalent releases, respectively, for the fully correlated case with initial advection. Both near-and far-field doses are dominated by releases of Ra-226 and the total doses are about 10 times higher and 5 times higher, respectively, compared to the central corrosion case.

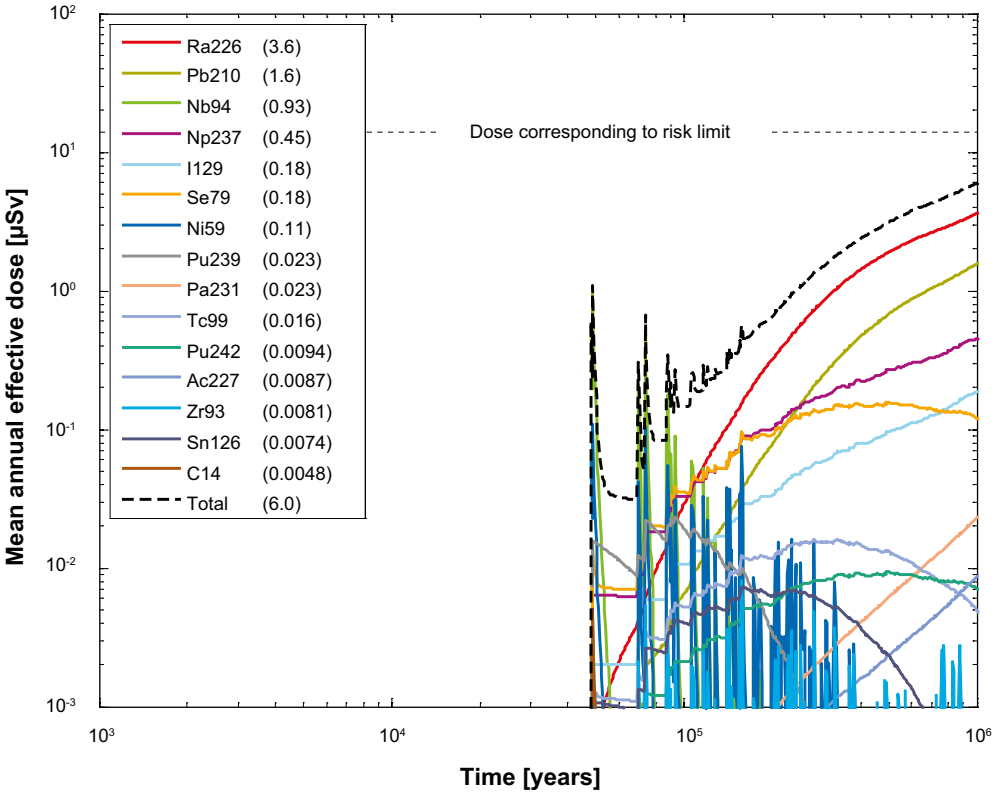

Figure 4-46. *Near-field dose equivalent release for the probabilistic calculation of the corrosion scenario, with hydrogeological data from the fully correlated model and initial advection in the erosion/corrosion model. The legend is sorted by peak (in the one-million year period) of the mean annual effective dose. The values in brackets are peak dose in units of µSv.*

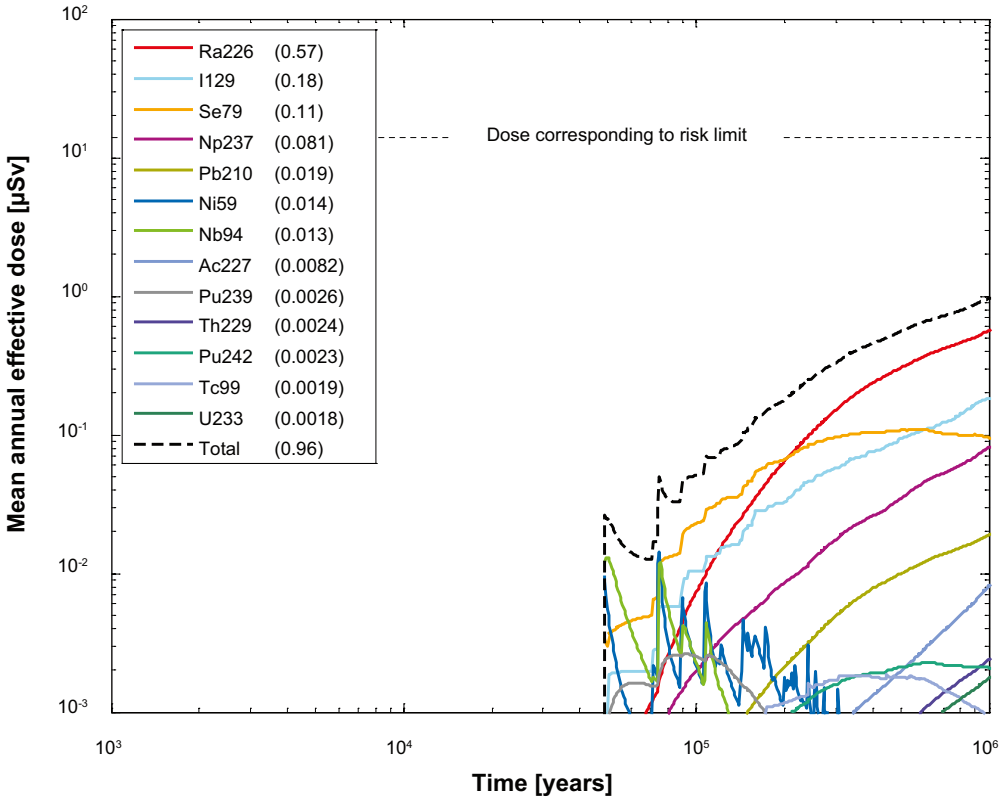

Figure 4-47. *Far-field mean annual effective dose for the probabilistic calculation of the corrosion scenario, with hydrogeological data from the fully correlated model and initial advection in the corrosion model. The legend is sorted by peak (in the one-million year period) of the mean annual effective dose. The values in brackets are peak dose in units of µSv.*

4.8 Cases addressing best available technique (BAT)

According to Swedish legislation, a licence application for a final repository needs to address the issues of best available technique (BAT). Factors considered in this section are:

- Alternative copper shell thickness, 25 mm and 100 mm, respectively.
- Alternative deposition hole rejection criteria.

These factors are implemented in the corrosion calculations and analysed as BAT-cases. The BAT cases are variant cases that do not use best available technique.

Alternative copper shell thickness

Hydrogeological case:	Semi-correlated, ten realisations
Erosion/corrosion models:	SR-Site model
Failure time:	107 times (25 mm)
	21 times (100 mm)
Mean number of failed canisters:	0.22 (25 mm)
	0.044 (100 mm)
Solubility limits:	No
Thorium sorption in near field:	Yes (modelled as low solubility limit)
Number of realisations:	50 per canister failure time
Number of nuclides:	37

Two probabilistic calculations of the corrosion case were performed with transport data from the ten realisations of the semi-correlated DFN model and corrosion model for copper thicknesses of 25 mm and 100 mm. In the reference design is the copper thickness 50 mm. The mean number of failed canisters is 0.22 and 0.044 for copper thickness of 25 mm and 100 mm, respectively. The contributions from the instantly released fraction of nuclides, IRF, are not included in the calculations.

Figure 4-48 and Figure 4-49 show the near- and far-field total dose equivalent releases, respectively, for corrosion cases with copper thicknesses of 25 mm, 50 mm (central corrosion case) and 100 mm. Doses both from the near-field and the far-field become about two times lower if the thickness of the copper shell is doubled.

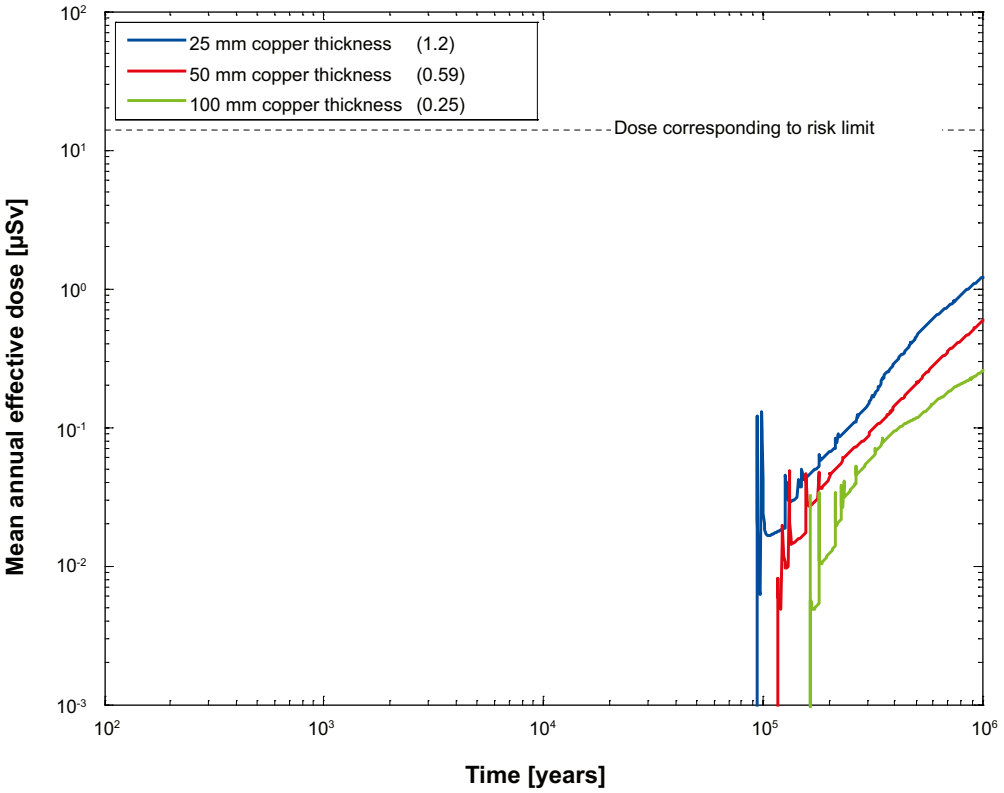

Figure 4-48. *Near-field dose equivalent releases for probabilistic calculations of the cases with a copper thickness of 25 mm, 50 mm (central corrosion case) and 100 mm. The legend is sorted by peak (in the one-million year period) of the mean annual effective dose. The values in brackets are peak dose in units of µSv.*

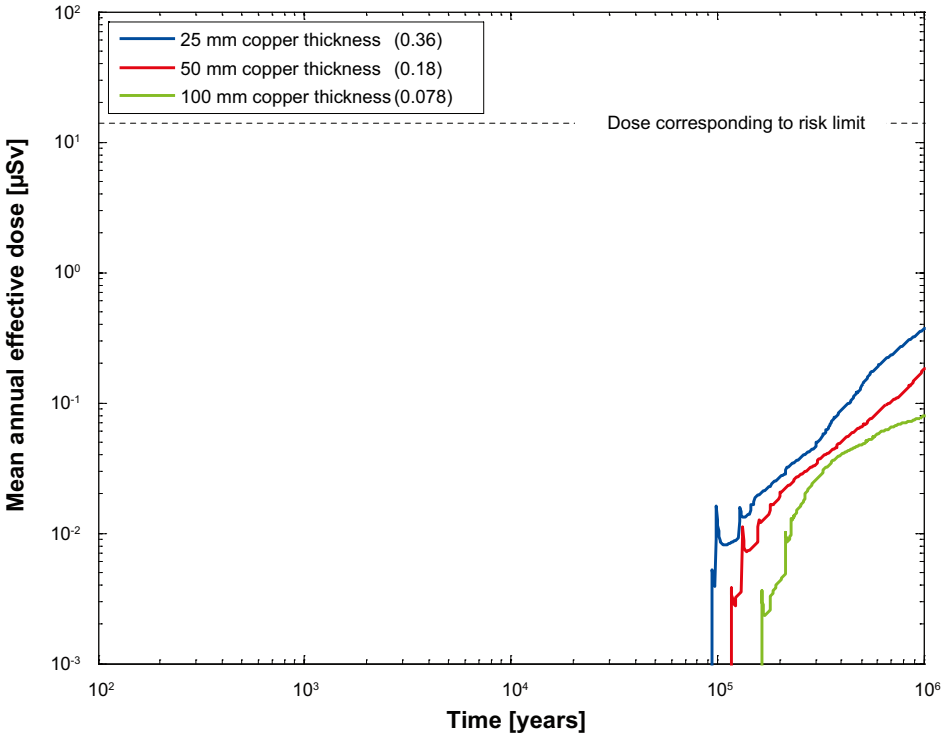

Figure 4-49. *Far-field mean annual effective dose for the probabilistic calculations of the cases with a copper thickness of 25 mm, 50 mm (central corrosion case) and 100 mm. The legend is sorted by peak (in the one-million year period) of the mean annual effective dose. The values in brackets are peak dose in units of µSv.*

Alternative deposition hole rejection criteria

Hydrogeological case:	Semi-correlated, ten realisations
Erosion/corrosion models:	SR-Site model
Failure time:	126 times (no T/L-filtering)
	1 964 times (neither T/L- nor EFPC-filtering)
Mean number of failed canisters:	0.26 (no T/L-filtering)
	3.7 (neither T/L- nor EFPC-filtering)
Solubility limits:	No
Thorium sorption in near field:	Yes (modelled as low solubility limit)
Number of realisations:	50 per canister failure time
Number of nuclides:	37

The groundwater flow around and through deposition holes have a large impact on both the loss of bentonite which may potentially lead to advective conditions and on the rate of corrosion by sulphide in the groundwater. Applying the EFPC criterion means to avoid deposition holes with high groundwater flow and it has been applied to all calculations. Furthermore, an additional deposition hole rejection criterion related to the combination of a high transmissivity and length of the intersecting fracture (T/L-filtering) was assumed in all the calculations.

Two probabilistic calculations of the corrosion case were performed with transport data from the ten realisations of the semi-correlated DFN model, without T/L-filtering and without both T/L-filtering and EFPC-filtering. The mean number of failed canisters is 0.26 and 3.7 for no T/L-filtering and neither T/L- nor EFPC-filtering, respectively. The contributions from the instantly released fraction of nuclides, IRF, are not included in the calculations.

Figure 4-50 and Figure 4-51 show the near- and far-field total dose equivalent releases, respectively, for corrosion cases with no T/L-filtering, neither T/L- nor EFPC-filtering and the central corrosion case (T/L- and EFPC-filtering). Dose from the far field increases 67 times for the case without T/L- nor EFPC-filtering compared to the central corrosion case.

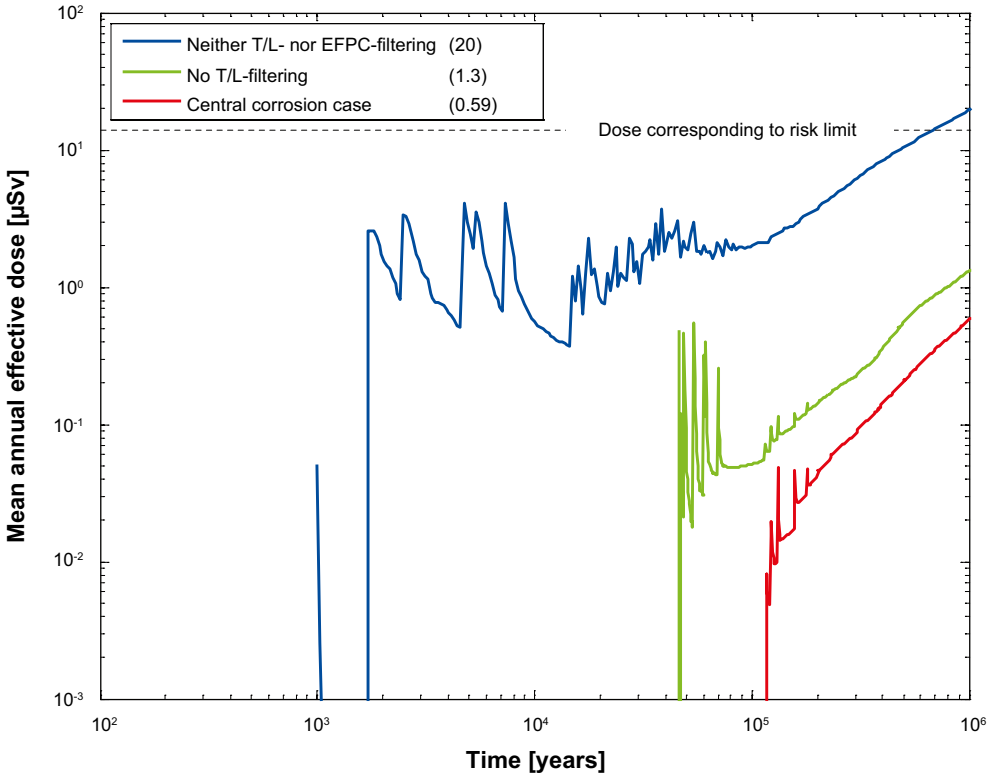

Figure 4-50. *Near-field dose equivalent release for the probabilistic calculations of the cases with no T/L-filtering, neither T/L- nor EFPC-filtering and the central corrosion case (T/L- and EFPC-filtering). The legend is sorted by peak (in the one-million year period) of the mean annual effective dose. The values in brackets are peak dose in units of µSv.*

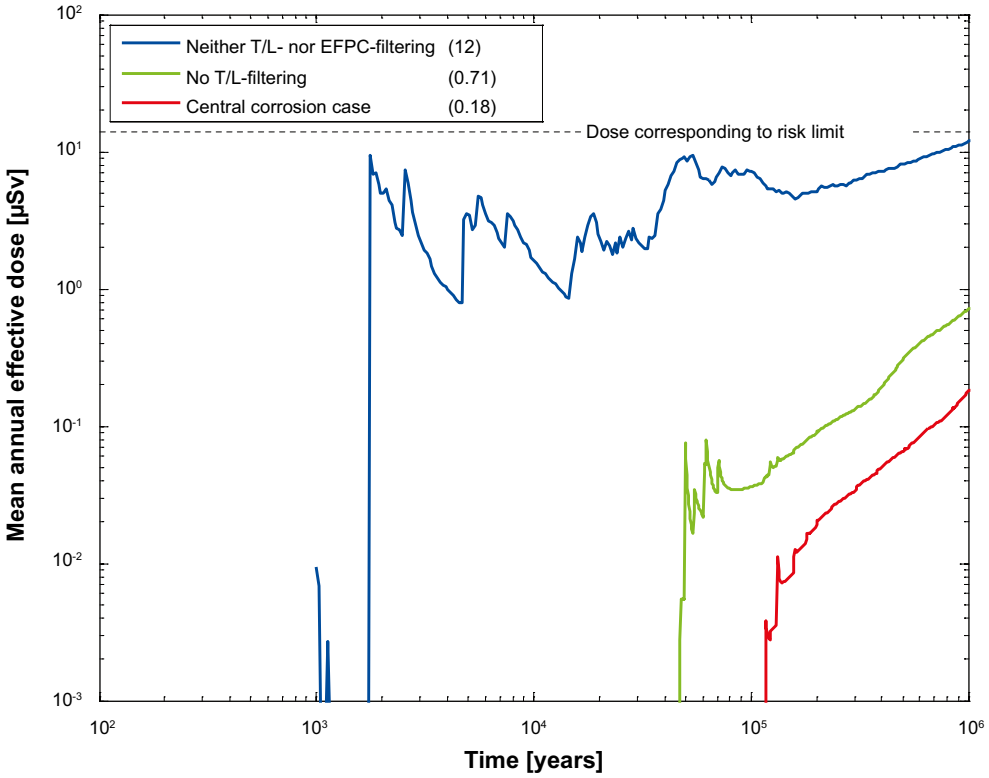

Figure 4-51. *Far-field mean annual effective dose for the probabilistic calculations of the cases with no T/L-filtering, neither T/L- nor EFPC-filtering and the central corrosion case (T/L- and EFPC-filtering). The legend is sorted by peak (in the one-million year period) of the mean annual effective dose. The values in brackets are peak dose in units of µSv.*

4.9 Alternative safety indicators for the central corrosion case

Four alternative indicators to risk are used: release of activity from the geosphere, radiotoxicity flux from the geosphere, concentrations of radionuclides in ecosystems and natural geosphere fluxes of radionuclides. The following reference values are used when evaluating these indicators.

- The Finnish activity release constraints. These constraints are strictly applicable only in the Finnish regulatory context, but are nevertheless deemed useful as reference values.
- The reference value for radiotoxicity flux from the geosphere suggested by the EU SPIN project.
- Measured concentrations of naturally occurring radionuclides in ecosystems at the Forsmark site or other, comparable sites. Not further described here, see the **Post-closure safety report,** Section 13.5.8.
- Naturally occurring fluxes of radionuclides at the site.

4.9.1 Finnish activity release constraints

The Finnish Radiation and Nuclear Safety Authority STUK has issued activity release constraints to the environment (STUK 2001).

These nuclide specific constraints are defined for long-lived radionuclides only. The effects of their short-lived progeny have been taken into consideration in the constraints defined for the long-lived parents. The nuclide-specific release rate constraints are:

- 0.03 GBq/yr for the long-lived α-emitting isotopes of Ra, Th, Pa, Pu, Am and Cm,
- 0.1 GBq/yr for Se-79, I-129, and Np-237,
- 0.3 GBq/yr for C-14, Cl-36, Cs-135, and the long-lived isotopes of U,
- 1 GBq/yr for Nb-94 and Sn-126,
- 3 GBq/yr for Tc-99,
- 10 GBq/yr for Zr-93,
- 30 GBq/yr for Ni-59,
- 100 GBq/yr for Pd-107 and Sm-151.

The constraints apply to activity releases that arise from the expected evolution scenarios and that may enter the environment after several thousands of years, whereas dose rate constraints are applied in the shorter term. In applying the above constraints, the activity releases can be averaged over 1 000 years at the most. The sum of the ratios between the nuclide-specific activity releases and the respective constraints shall be less than one. It should be noted that the Finnish regulator has derived these constraints partly based on a set of reference biospheres considered possible in the future at the planned disposal site, Olkiluoto at the coast of the Baltic Sea, and partly on natural fluxes of radionuclides established for similar environments. The reference values of the Finnish regulatory guide are thus not directly applicable for other disposal concepts and sites (EU 2002). However, both the disposal concept and the sites considered in Sweden are similar to those for which the Finnish activity release constraints have been developed.

Figure 4-52 shows the result of applying this activity constraint to releases calculated for the central corrosion case. The releases from the geosphere are around two orders of magnitude lower than the STUK constraint.

The pulses from IRF are not included in these calculations. But applying that the activity releases can be averaged over 1 000 years, implies that the release of the IRF give a negligible contribution to the calculated total activity release.

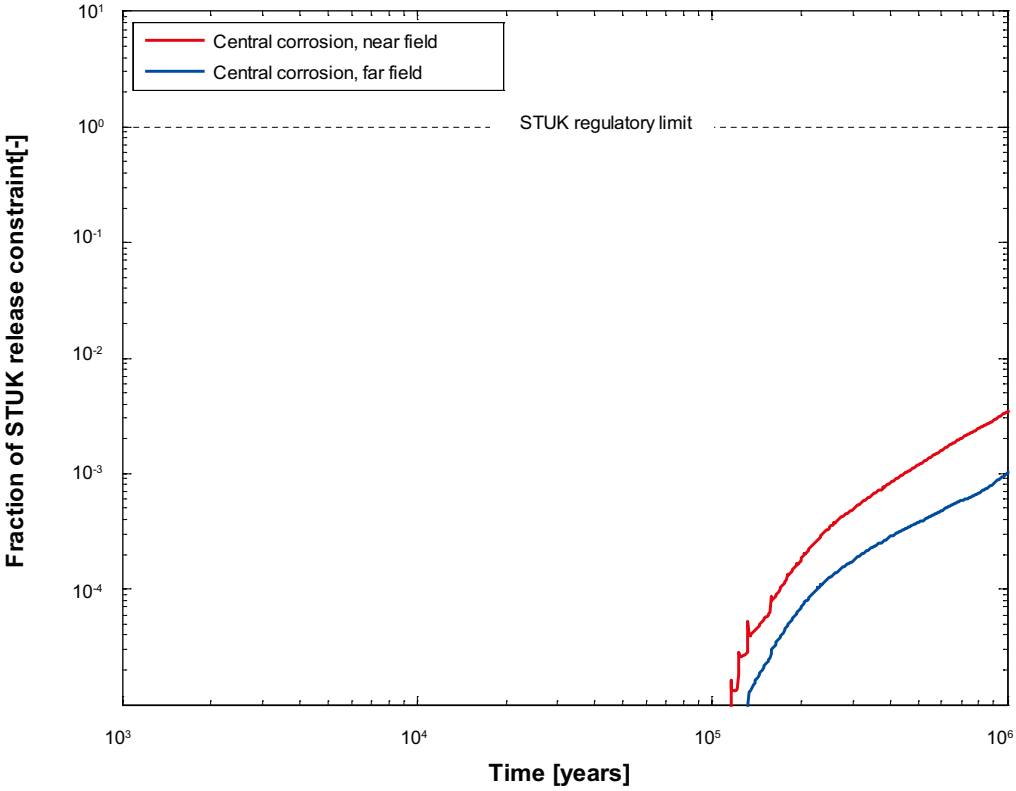

Figure 4-52. *Releases as a fraction of the activity release constraint index adopted by the Finnish regulator.*

4.9.2 Radiotoxicity flux from the geosphere – EU SPIN Project

An EU project (EU 2002) concludes that two alternative indicators could preferably be used to complement the dose indicator. These are:

- Radiotoxicity concentration in biosphere water: preference for medium time frames, i.e. several thousand to several tens of thousands of years.
- Radiotoxicity flux from the geosphere: preference for later time frames.

The project also reports on reference values that could tentatively be used for comparisons to calculated concentrations and fluxes of radionuclides from the repository. Regarding radiotoxicity flux from the geosphere, an indicative reference value of 60 Sv/yr for a typical area of 200 km^2 was suggested. The SPIN reference value was calculated from natural activity flux (Bq/year) converting to radiotoxicity flux by using ingestion dose coefficients from ICRP72 (ICRP 1996). It was assumed that each daughter is in secular equilibrium with its parent, i.e. the dose coefficients of the daughter nuclides (half-life >1 day) are added to the studied nuclide. For further details see the SPIN project report (EU 2002).

The same approach was used on the central corrosion case. The release rate (Bq/yr) is converted to a radiotoxicity flux (Sv/yr) using the ICRP72 ingestion dose coefficients (Sv/Bq) (ICRP 1996) (the same values as reported by EU (EU 1996) and also by IAEA (IAEA 1996)). Table 4-7 show the nuclides that have daughters that are in secular equilibrium, i.e. the dose coefficients of the daughter nuclides (half-life >1 day) are added to the studied parent nuclide. Note that shorter-lived progany have small ingestion dose coefficients and their in-growth following ingestion of their parents is explicitly addressed in the ICRP biokenetic and dosimetric models.

Figure 4-53 shows the results for the central corrosion case. The releases from the geosphere, 0.011 Sv/year, are around four orders of magnitude lower than the SPIN reference value.

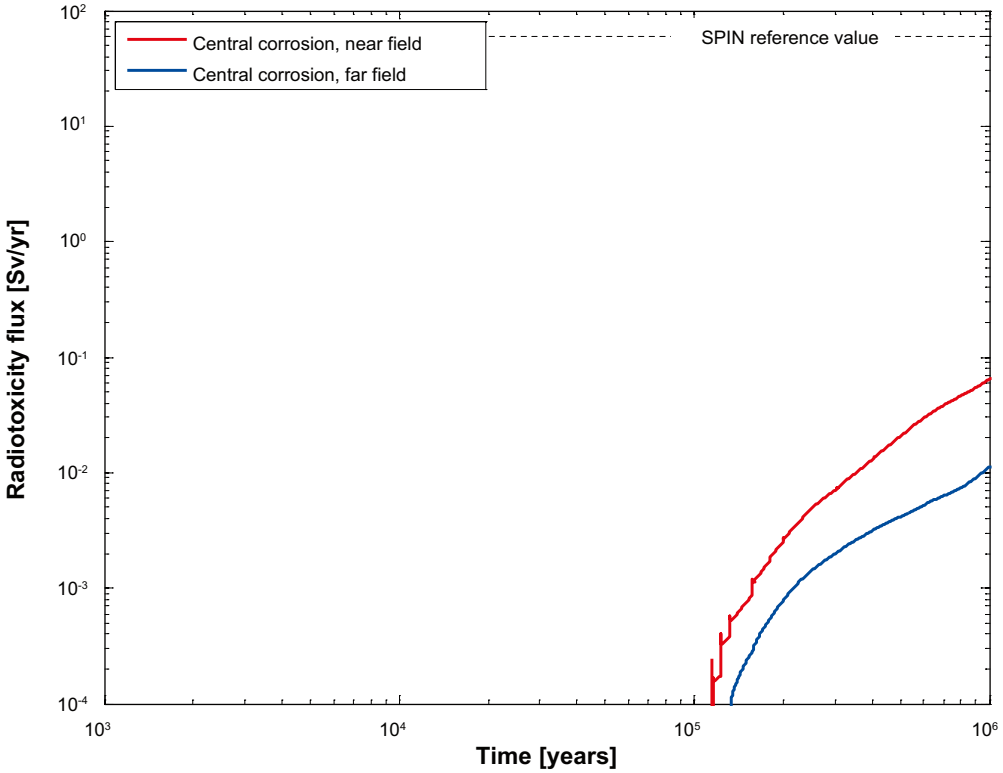

Figure 4-53. *Radiotoxicity flux in the central corrosion case compared to the SPIN reference value.*

Table 4-6. Parent nuclides and nuclides assumed to be in secular equilibrium.

Parent nuclide	Daughter in secular equilibrium (half-life >1 day)
Th-232	+ Ra-228 + Th-228 + Ra-224
Cm-245	+ Pu-241
Np-237	+ Pa-233
Th-229	+ Ra-225 + Ac-225
U-238	+ Th-234
Pb-210	+ Bi-210 + Po-210
Am-242m	+ Cm-242
Am-243	+ Np-239
Ac-227	+ Th-227 + Ra-223

4.9.3 Naturally occurring fluxes of radionuclides at the site

The last alternative indicator to risk used is naturally occurring fluxes of radionuclides at the site. The naturally occurring fluxes of U-238, U-234 and Ra-226, are estimated based on measured activities during the site investigations, see Section 2.2.3. Figure 4-54 shows the far-field release rates of U-238, U-234 and Ra-226 in the central corrosion case compared to the naturally occurring fluxes at Forsmark. The naturally occurring fluxes of U-238, U-234 and Ra-226 have also been converted to effective dose by using the basic LDF values, the obtained dose is shown in Figure 4-55 together with the far-field annual effective dose in the central corrosion case and the case with K_d for U(VI) in the rock. It is noted that the releases from the repository could be concentrated to one or a few of the landscape objects in the release area. There are about ten objects in the area used in the derivation of the naturally occurring fluxes, suggesting that the natural fluxes would exceed those from the repository even if all the release from the repository were to occur to a single landscape object.

The repository-derived flux of Ra-226 is about two orders of magnitude below the naturally occurring flux of Ra-226. For the U isotopes, the fluxes from the repository are about six orders of magnitude below the natural fluxes, irrespective of whether rock K_d-distributions for U(IV) or U(VI) are used.

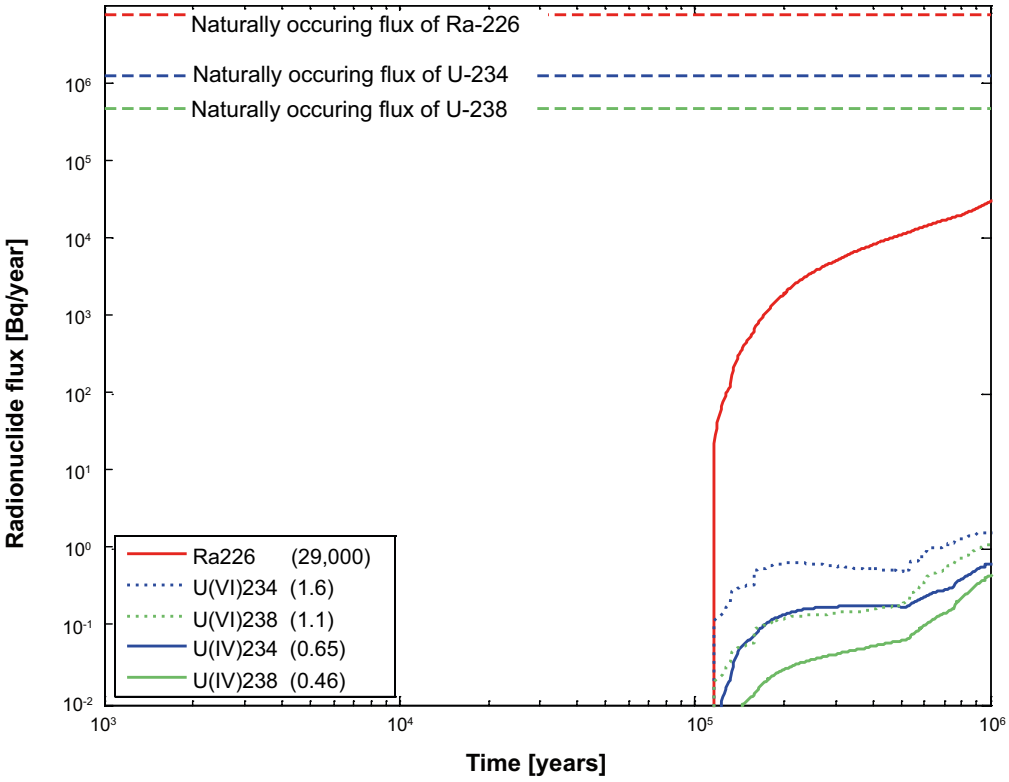

Figure 4-54. *Far-field release rates (Bq/year) of U-238, U-234 and Ra-226 in the central corrosion case compared to the naturally occurring fluxes at Forsmark.*

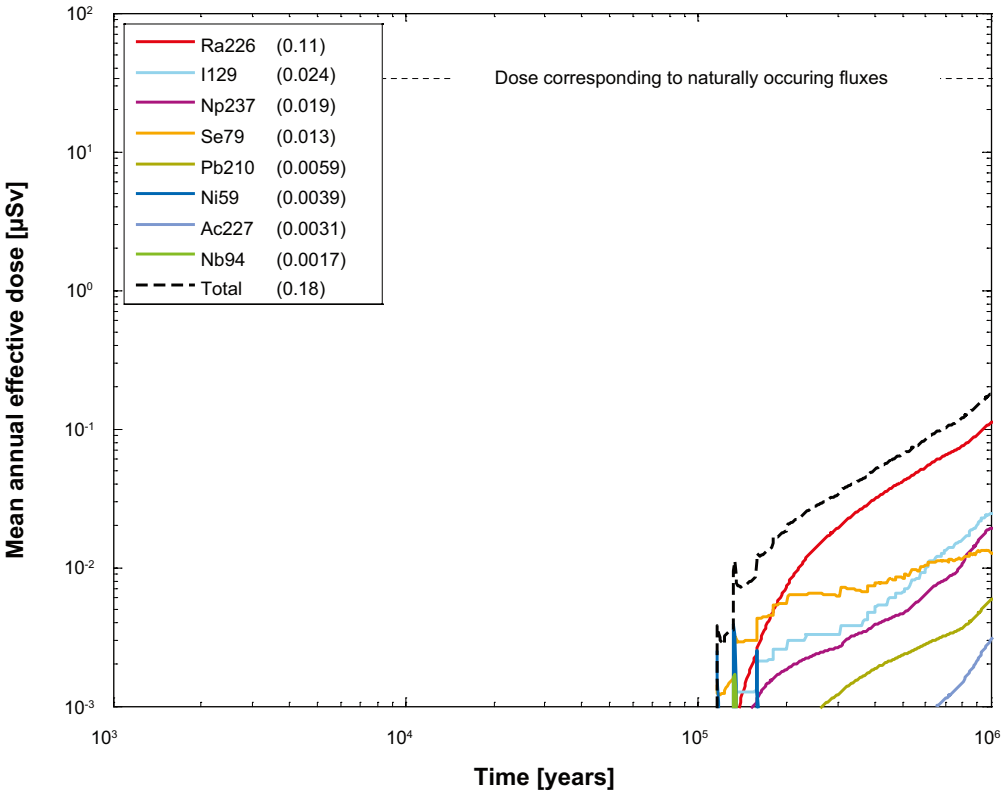

Figure 4-55. *Far-field annual effective dose in the central corrosion case compared to the naturally occurring fluxes of U-238, U-234 and Ra-226 at Forsmark converted to dose using the basic LDF values. The legend is sorted by peak (in the one-million year period) of the mean annual effective dose. The values in brackets are peak dose in units of µSv.*

4.10 Calculation with analytical models

As mentioned in Section 3.6.5, simplified, analytical models are available for the modelling of radionuclide transport in the near field and the far field. The models are documented in Hedin (2002b). The analytical models are applied to the six corrosion variants of the corrosion scenario.

Regarding the application of the models to the corrosion scenario, the following, further simplifying conditions are noted. The near-field release is determined by the rate of radionuclide release to water in the void space because the flow rate in the Q1 fracture is not a limitation (canister failures due to corrosion only occur in the deposition holes with the highest flow rates). Therefore, the release rate from the near field is simply modelled as the dissolution rate of the fuel, alternatively the corrosion rate of the metal parts, in both cases multiplied by the inventory. As in the numerical models, the IRF is not included but handled separately.

The release rate from the far field is in most cases calculated as the release rate from the near field times a geosphere transmission factor (Hedin 2002b). This yields a good approximation in cases of a continuous release over long times.

However, in some cases of relatively short-duration releases caused by corrosion of the metal parts of the fuel, the treatment is overly pessimistic. In such cases the release of the entire inventory in the metal parts, M_0, as a pulse to the geosphere is also considered. This yields a peak release rate from the geosphere of M_0/τ where τ is obtained from SKB (2006a, Appendix B).

Hydrodynamic and molecular dispersion in the flowing fracture are pessimistically neglected when this expression is used. Also, radioactive decay is neglected in the expression since no appreciable decay will take place during the short transients of concern here.

Since both the above approaches overestimate the release rate from the far field, the smaller of the two is chosen in each realisation.

It is also noted that chain decay in the geosphere is not accounted for when applying the transmission factors for geosphere retention. The theory for a full, analytical treatment of chain decay in transmission factors has been developed, but is not yet implemented in the analytical model. Using the numerical models, it has been demonstrated that chain decay of parent nuclides of Ra-226 in the far field has a negligible impact on the releases of Ra-226 in the corrosion scenario.

The result of the analytical modelling of the probabilistic central corrosion case is shown in Figure 4-56. As seen by comparing the results in Figure 4-56 with those of the corresponding numerical case in Figure 4-5, the agreement of the peak doses is very good for nuclides emerging from the fuel matrix, whereas doses from nuclides embedded in metal parts (Ni-59 and Nb-94) are somewhat overestimated with the analytical model. This is due to the pessimistic modelling of nuclides released from corrosion of metal parts discussed above.

The modelling results of the six corrosion variants are shown in Figure 4-57. Each case was modelled with 20 000 realisations using Latin Hypercube Sampling. As seen by comparing the results in Figure 4-57 with those in Figure 4-59, which shows far-field annual effective dose for all corrosion cases calculated with FARF31, the agreement between results obtained with the two sets of models is good. All peak doses over one million years are the same to within less than a factor of 1.5.

That the numerical calculations are in good agreement with the analytical calculations significantly enhances confidence in the dose equivalent releases provided here and in the **Post-closure safety report** for two reasons. First, the comparison provides an important quality assurance check on the numerical modelling of dose equivalent releases. This check applies not only to the numerical calculations but also to the data/parameter transfers, as the data for the analytical calculations were taken directly from the SR-Site data report (SKB 2010b) independently of the numerical calculations. Second, it demonstrates that dose equivalent releases for the corrosion cases are controlled by relatively simple processes that are straightforward to understand.

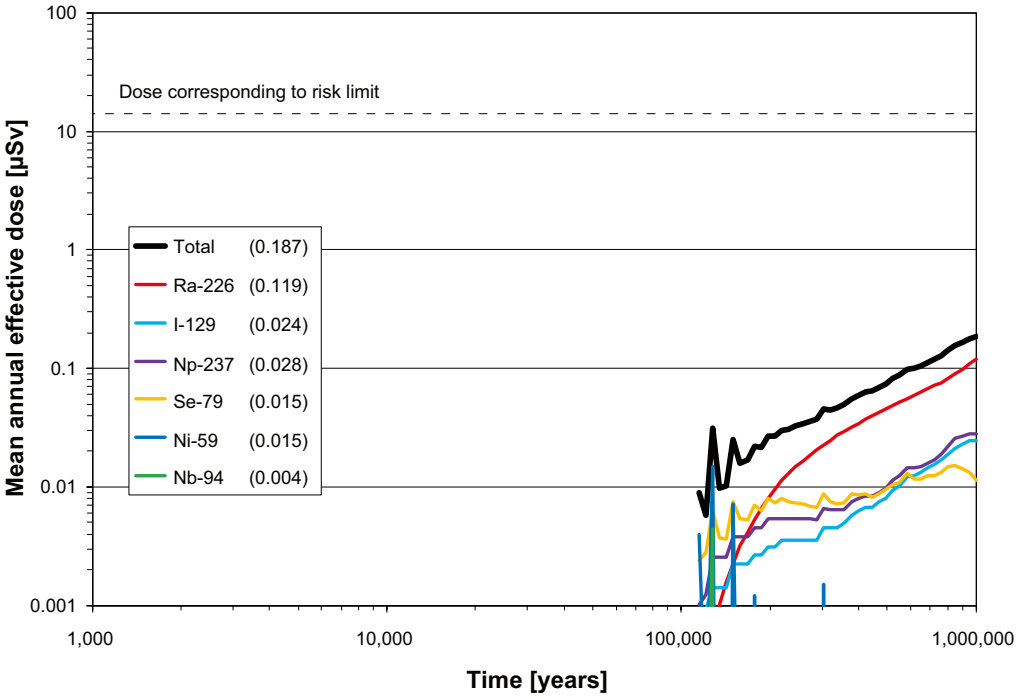

Figure 4-56. *Far-field mean annual effective dose for the central corrosion case, obtained with analytical models. The legend is sorted by peak (in the one-million year period) of the mean annual effective dose. The values in brackets are peak dose in units of µSv.*

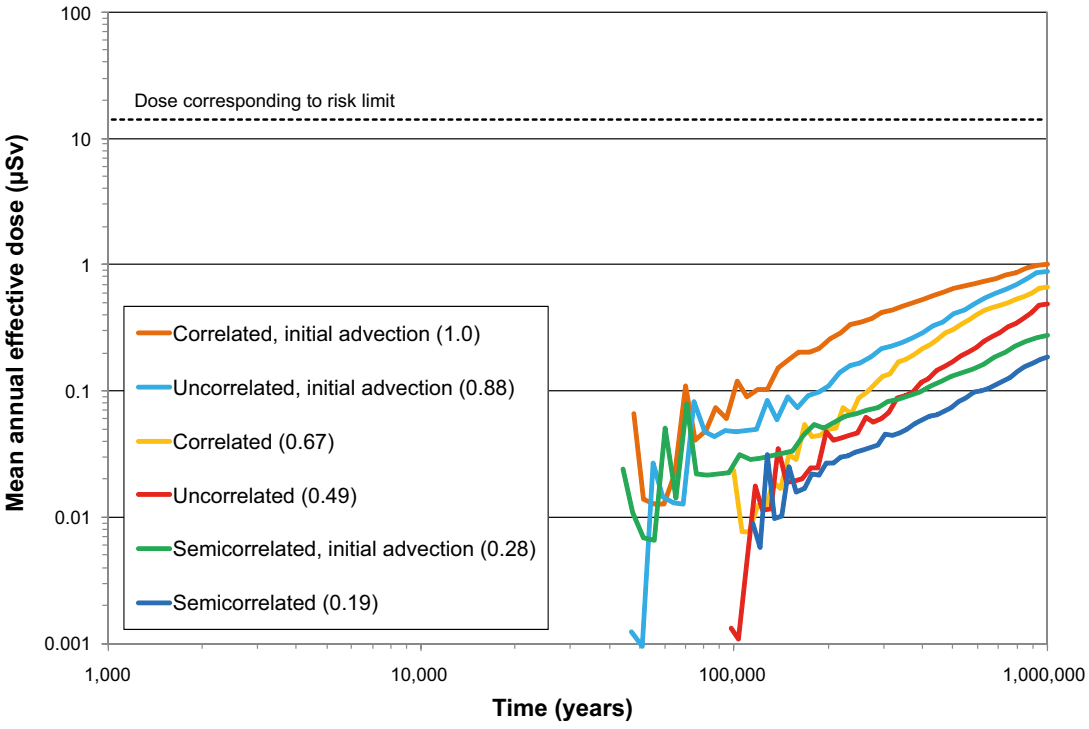

Figure 4-57. *Summary of far-field mean annual effective dose for analytical, probabilistic calculations of the six corrosion variants of the corrosion scenario. These results can be compared to the corresponding results obtained with numerical models in Figure 4-59.*

4.11 Summary and conclusions for the corrosion scenario

Figure 4-58 shows the total dose equivalent releases for cases calculated probabilistically with COMP23 in Chapter 4. All other things being equal, the correlated and the uncorrelated cases produce larger dose equivalent releases from the near field as compared with the semi-correlated cases. Cases with initial advection produce earlier and larger releases than the cases without. Disregarding thorium sorption in the near field in the semi-correlated case results in significantly lower dose equivalent releases. Thus the assumption of thorium sorption in the near field made in all other corrosion cases should be pessimistic.

Figure 4-59 shows the far-field total effective dose calculated with FARF31 for the same cases as in Figure 4-58. The modelling cases that have larger near-field dose equivalent releases experience more attenuation in the far field, thereby reducing the variation among the cases. Significantly, the far-field total effective doses are all at least an order of magnitude smaller than the dose corresponding to the risk limit. Moreover, peaks of the far-field total effective doses span a range of less than one order of magnitude. This relatively tight clustering of results suggests relative insensitivity to the modelling assumptions.

Peak total effective dose for the corrosion cases that relied on COMP23 and MARFA are summarised in Table 4-7. All of these cases used the semi-correlated DFN model. For comparison the peak of the mean annual dose equivalent near-field release is 0.59 µSv (see Figure 4-4).

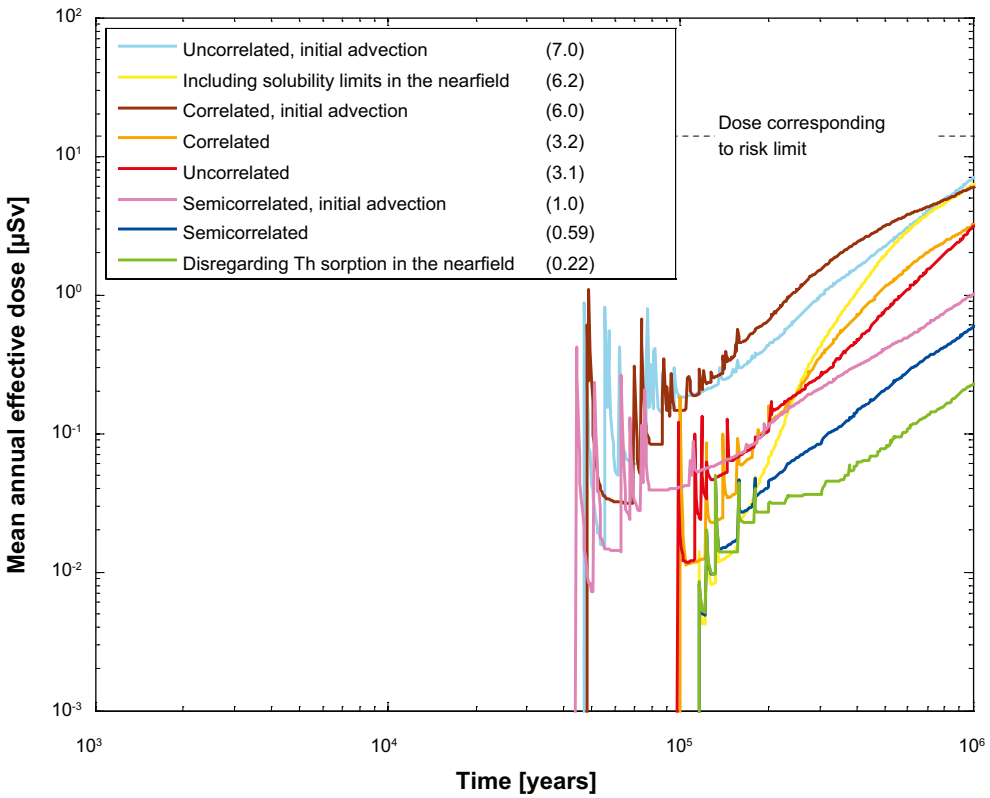

Figure 4-58. *Near-field dose equivalent release for probabilistic corrosion cases. The legend is sorted by peak (in the one-million year period) of the mean annual effective dose. The values in brackets are peak dose in units of µSv.*

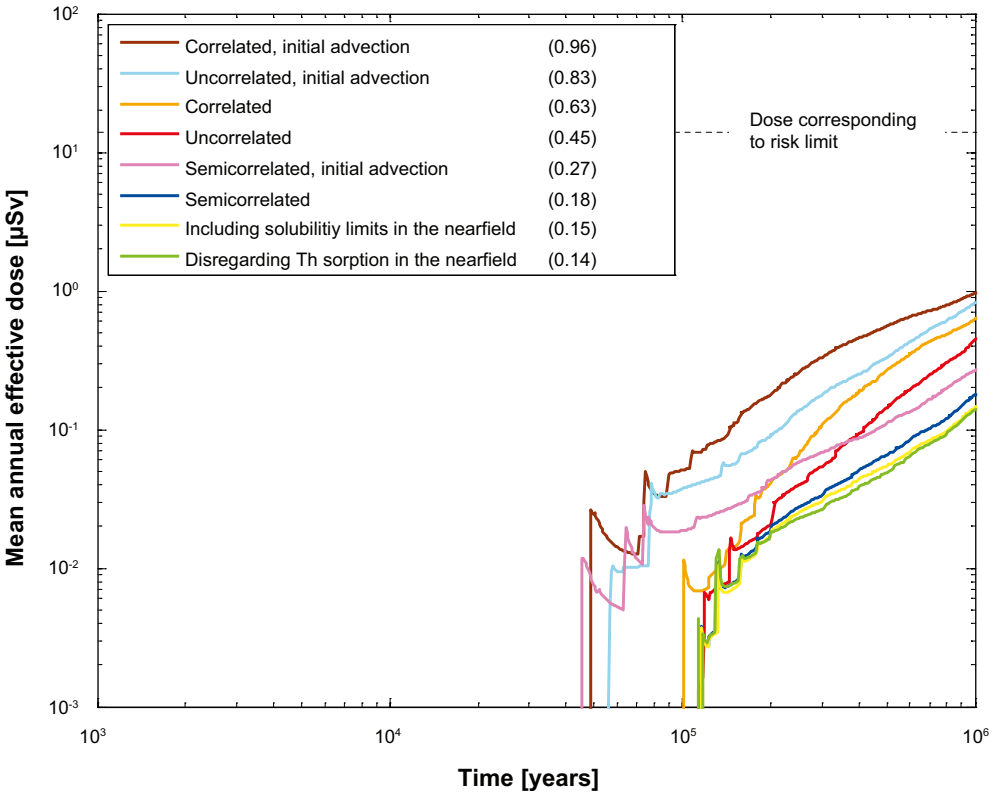

Figure 4-59. *Far-field annual effective dose for probabilistic corrosion cases calculated with FARF31. The legend is sorted by peak (in the one-million year period) of the mean annual effective dose. The values in brackets are peak dose in units of µSv.*

Table 4-7. Far-field peak of the mean annual effective dose for corrosion cases modelled with COMP23 and MARFA.

Calculation case	Far-field peak annual effective dose (µSv)
Steady conditions, no colloids	0.15
Steady conditions, 10 mg/l colloids	0.19
Steady conditions, 10 g/l colloids	0.33
Varying climate, no colloids	0.19
Varying climate, steady colloid concentration of 10 g/l	0.41
Varying climate, unsteady colloid concentrations	0.35

5 Canister failure due to shear load

5.1 Introduction

The results shown in this chapter have not been updated since the SR-Site assessment (SKB 2010d). Instead, in Appendix M, results of recalculation of all cases in the SR-Site shear load scenario are compared to the corresponding calculations using updated input data for the PSAR. The aim is to demonstrate that the differences in results are sufficiently limited that the conclusions drawn from the results of the SR-Site radionuclide transport calculations are still valid with updated input data for the PSAR. The updated input data for the PSAR are given in Appendix L.

In a few places, references in the SR-Site version were made to the main references of the SR-Site assessment, the references written in bold. It has been verified that the PSAR versions of the corresponding reports are equally valid as references in these cases. The references in bold, therefore, refer to the PSAR versions.

In the 'canister failure due to shear load' scenario (called briefly the shear load scenario below), a canister fails as a result of secondary rock movements induced by a large earthquake. It was demonstrated in the **Post-closure safety report** to have a low probability in the reference evolution. Pessimistic estimates of the extent of this failure mode indicate that the probability that one out of the 6 000 canisters has failed at the end of the one million year assessment period is 0.079 (**Post-closure safety report**, Section 10.4.5). A failure frequency as a function of time is also provided in the **Post-closure safety report**, Section 10.4.5 and this is used in the probabilistic assessment of the shear load scenario. For this failure mode, the canister is bypassed, the thickness of the buffer is reduced and the rock retention is insignificant, since a shearing fracture must have a considerable size with properties difficult to assess.

5.2 Calculation of doses for the shear load scenario

An earthquake can cause canister failure at any time after closure of the repository. The likelihood is varying during different time periods. Three different cases of failure times have been considered in the calculations: a postulated failure of one canister at 100 000 years, failure during the period 1 000 years to one million years and early failure. The following data and assumptions are used in the calculation cases:

- In the affected deposition holes the faulting is supposed to be so large that it causes massive failure of the canister, i.e. there will be no delay between failure and the onset of radionuclide transport and no credit from limited transport resistance in the canister.
- The shear movement will not affect the buffer to the extent that its protection against advective flow will be impaired, but effective amount of buffer between the canister and the shearing fracture is assumed to be reduced from 35 cm to 25 cm.
- The canister failure location is assumed to fully coincide with the location of the shearing fracture. Furthermore, the shear is assumed to increase the fracture transmissivity significantly. The Q_{eq} value for the intersecting fracture is, therefore, assumed to be sufficiently high (1 m^3/yr) that it does not contribute to the transport resistance in the near field.
- The shearing fracture is likely to be among the larger in the modelled fracture network and its properties after shearing are difficult to assess. Therefore, no credit for radionuclide retention in the geosphere is taken.
- Solubility limits are included in the calculations, since, contrary to cases in the corrosion scenario, the buffer is in place in the shear load scenario.

- The contributions from the instantly released fraction of nuclides, IRF, are included in the case with early release but not in the other cases. The contribution from the IRF is judged to be negligible based on the low probability for this scenario and the low contribution shown in the central corrosion case in Section 4.4.2.

A detailed description of the discretisation, diffusion resistances and boundary conditions used in COMP23 is given in Appendix G, section Canister failure due to shear load.

5.2.1 Postulated failure of one canister at 100 000 years

Deterministic calculations

Failure time:	100 000 years
Number of failed canisters:	1
Solubility limits:	Yes
Number of realisations:	1
Number of nuclides:	45

A deterministic calculation of the shear load case is performed for a postulated failure of one canister at 100 000 years. No retention in the geosphere occurs and hence the release calculated for the near field is also valid for the far field. The contributions from the instantly released fraction of nuclides, IRF, are not included in the calculations. Table 4-4 shows the peak annual doses from pulse releases of the instantly released fraction, IRF.

Figure 5-1 show the deterministic far-field dose equivalent releases, for the shear load case with a postulated failure of one canister at 100 000 years. Shortly after the canister failure the dose is dominated by releases of Ni-59 and in the longer term the dose is dominated by Ra-226.

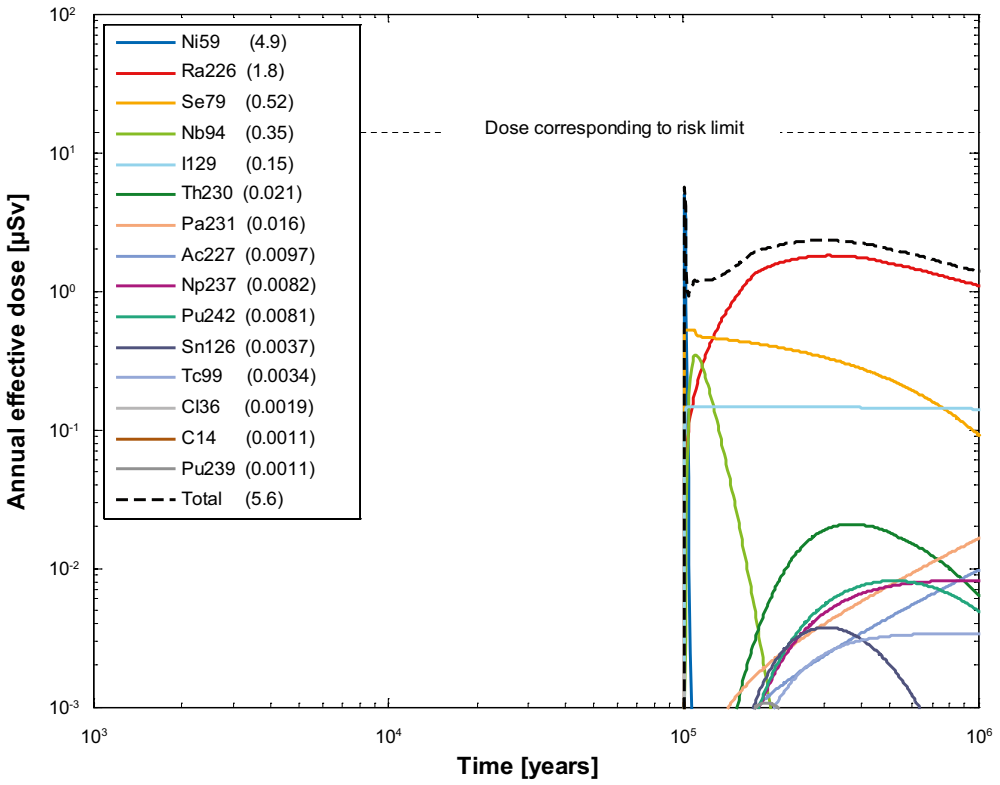

Figure 5-1. *Far-field annual effective dose for a deterministic calculation of the shear load scenario, with a postulated failure of one canister at 100 000 years. The legend is sorted by peak (in the one-million year period) of the annual effective dose. The values in brackets are peak dose in units of µSv.*

Probabilistic calculations

Failure time:	100 000 years
Number of failed canisters:	1 (postulated)
Solubility limits:	Yes
Number of realisations:	1 000
Number of nuclides:	37

A probabilistic calculation of the shear load case is performed for a postulated failure time at 100 000 years. The postulated number of failed canisters is 1. The contributions from the instantly released fraction of nuclides, IRF, are not included in the calculations. Table 4-4 shows the peak annual doses from the pulse releases from the instantly released fraction, IRF. No retention in the geosphere occurs and hence the release calculated for the near field is also valid for the far field.

Figure 5-2 show the far-field dose equivalent releases for the shear load case with a postulated failure of one canister at 100 000 years. Shortly after the canister failure the dose is dominated by releases of Ni-59 and in the longer term the dose is dominated by releases of Ra-226.

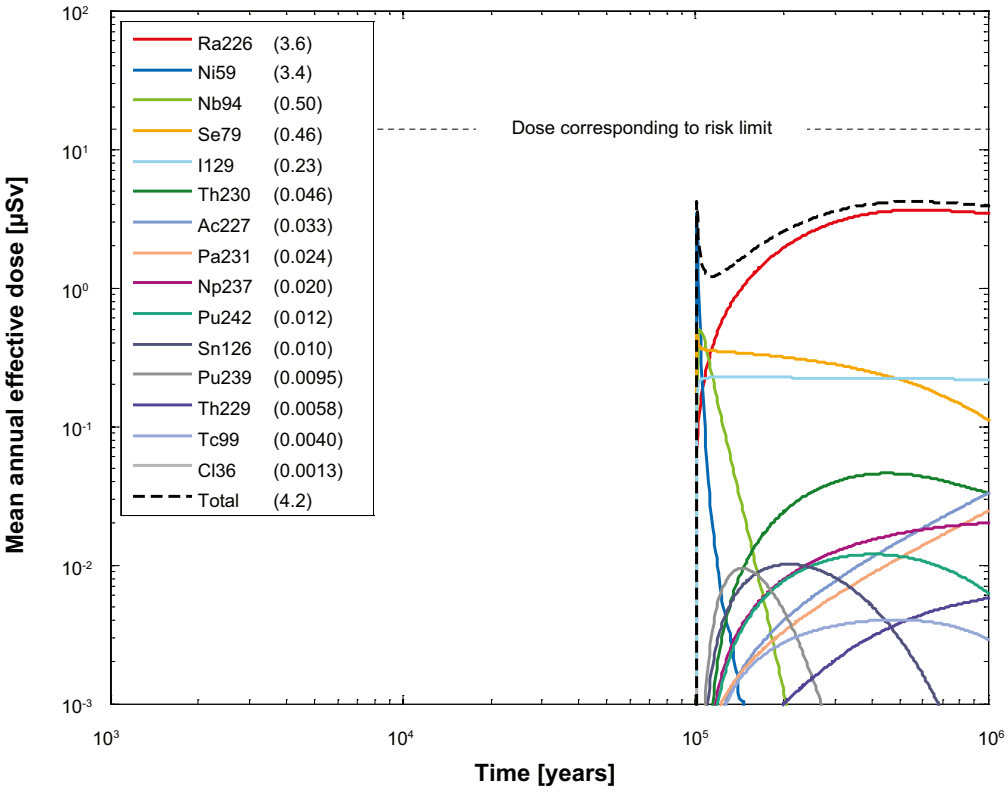

Figure 5-2. *Far-field mean annual effective dose for the probabilistic calculation of the shear load scenario, with a postulated failure of one canister at 100 000 years. The legend is sorted by peak (in the one-million year period) of the mean annual effective dose. The values in brackets are peak dose in units of µSv.*

5.2.2 Failure during the period 1 000 years to one million years

Probabilistic calculations

Failure time:	1 000 to one million years
Mean number of failed canisters:	0.079
Solubility limits:	Yes
Number of realisations:	6 916
Number of nuclides:	37

A probabilistic calculation of the shear load case is performed with failure during the period 1 000 years to one million years. The mean number of failed canisters is 0.079. The contributions from the instantly released fraction of nuclides, IRF, are not included in the calculations, except for Tc-99, which is included. The contribution from the IRF is judged to be negligible based on the low probability for this scenario and the low contribution shown in the central corrosion case in Section 4.4.2. The influence is also shown to be small at early failure times, see 5.2.3. No retention in the geosphere occurs and hence the release calculated for the near field is also valid for the far field.

Figure 5-3 show the near-field and far-field dose equivalent releases for the shear load case with failure during the period 1 000 years to one million years. For an early failure time, the dose is dominated by release of C-14, thereafter by Nb-94 and in the longer term the dose is dominated by Ra-226. The dose at one million years in the present case is about 28 times lower than in the case where one canister fails at 100 000 years, but in the former case the mean number of failed canisters is 0.079 compared to one in the latter.

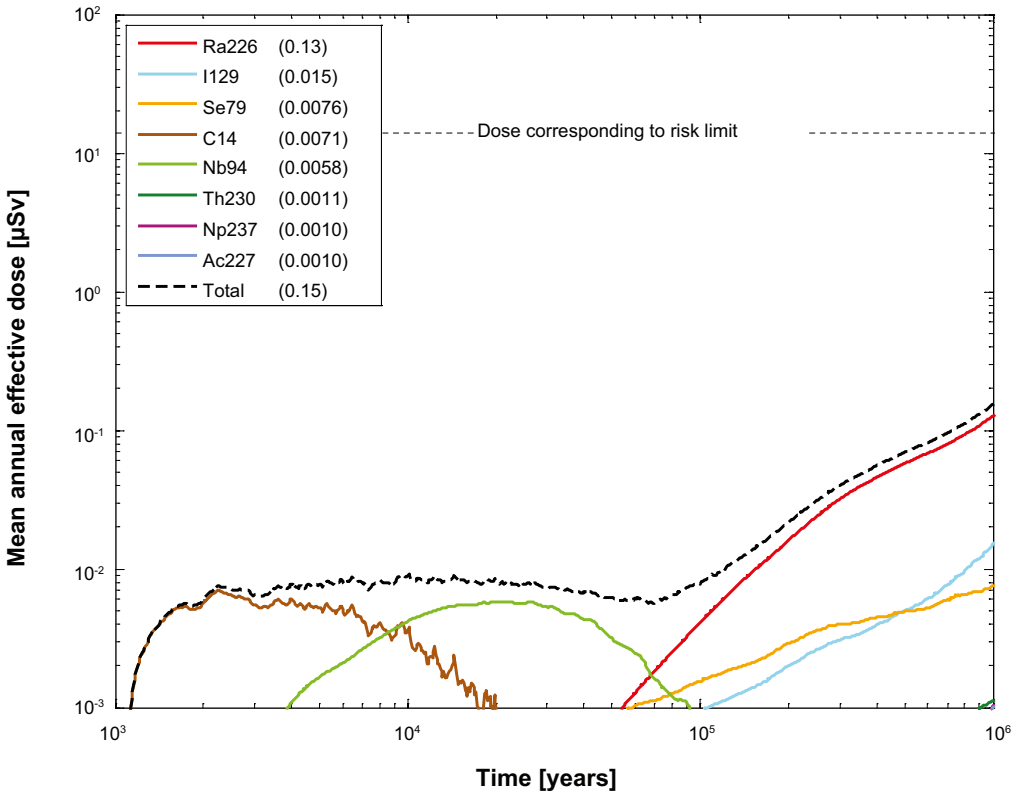

Figure 5-3. *Near-field and far-field mean annual effective dose for the probabilistic calculation of the shear load scenario, with failure during the period 1 000 years to one million years. The legend is sorted by peak (in the one-million year period) of the mean annual effective dose. The values in brackets are peak dose in units of μSv.*

Global sensitivity analysis

A global sensitivity analysis on the results of the probabilistic shear load case using the SRRC method as for the central corrosion case yields results according to Figure 5-4.

Regressing the total dose at 10^6 years on the input variables yields, in descending order, the fuel dissolution rate D_{Fuel}, the solubilities of radium and thorium, and the failure time $t_{Failure}$ as the input parameters most affecting dose results. Regressing on Ra-226 dose at 10^6 years yields a similar result due to the dominance of Ra-226. The significance of the solubility of thorium is due to decay of Th-230 to Ra-226 in the buffer, where the release of Th-230 to the buffer is controlled by the solubility of thorium. A further scrutiny of individual realisations reveals that the significance of the limited solubility overall is due to a relatively limited number of realisations with low solubilities, whereas the total dose is dominated by the larger number of realisations that have solubilities that are sufficiently high so as to not limit the release. Solubilities of neither Th nor Ra (taking into account co-precipitation with Ba) significantly limit the mean release rate of Ra-226. This conclusion is corroborated by the fact that the case with the omitted buffer (Section 5.2.4), where neither sorption in the buffer nor solubility limits are included, increases Ra-226 mean dose by only a factor of 2.

Regressing instead on the maximum of total dose over time yields the failure time and the corrosion release rate, *CRR*, as significant variables. This is consistent with the fact that for early failures, the highest doses occur due to release of e.g. C-14 and Nb-94 congruently with the corrosion of structural parts of the fuel elements.

Risk dilution

Risk dilution for the shear load scenario needs to be considered, because canisters fail at probabilistically determined times.

An illustration is obtained by comparing the results in Figure 5-2 (postulated, deterministic failure time) with those in Figure 5-3 (distribution of failure times). If the result in Figure 5-2 is multiplied by the overall probability of the event occurring during the assessment period, i.e. 0.079, then the dose at one million years (0.28 μSv) is relatively close to that obtained at one million years in Figure 5-3 (0.15 μSv). This small difference is because the consequences are determined i) by in-growth of Ra-226 and ii) by the build-up of Th-230 released from the fuel and precipitated in the canister interior or sorbed in the buffer, which in general occur long after the failure time. The in-growth of Ra-226 is essentially controlled by the build-up of its parent nuclide Th-230, which occurs on a time scale comparable to the half-life of Th-230 (approximately 75 000 years). The build-up of Th-230 occurs on time scales determined by the fuel dissolution rate, which are of the order of one million years.

Risk dilution, including a treatment of the pulse releases, is further discussed in Section 13.9 in the **Post-closure safety report**.

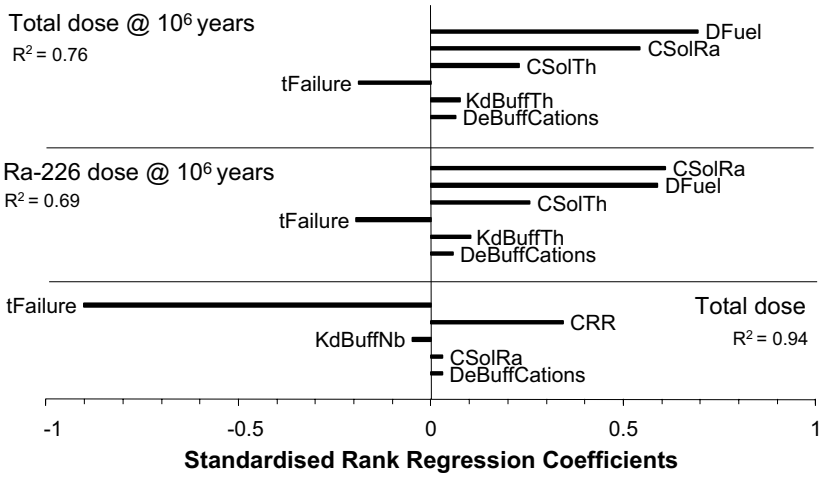

Figure 5-4. *Results of standardised rank regression for the probabilistic calculation of the shear load scenario, with failure during the period 1 000 to one million years. Regressing on total dose at 10^6 years and on Ra-226 dose at 10^6 years yields similar results due to the dominance of Ra-226. Regression on the maximum of total dose over time identifies CRR as an additional sensitive input.*

Probabilistic calculations, disregarding co-precipitation of radium and barium

Failure time:	1 000 to one million years
Mean number of failed canisters:	0.079
Solubility limits:	Yes, disregarding co-precipitation of radium and barium
Number of realisations:	6 916
Number of nuclides:	37

Due to the assumed high equivalent flow rate in the Q1 buffer/rock interface, the release rate of radionuclides from the near field is in general sufficiently high in comparison to the fuel dissolution rate to render solubility limits inside the canister ineffective. As an illustration, a probabilistic case where no credit was taken for co-precipitation of Ra/Ba was calculated, i.e. where the solubility of Ra was increased by a factor of 1 000. Figure 5-5 show the far-field dose equivalent releases for the shear load case with failure during the period 1 000 years to one million years and disregarding co-precipitation of Ra/Ba. This assumption led to an increase of the release rate of Ra by only a factor of about 1.5.

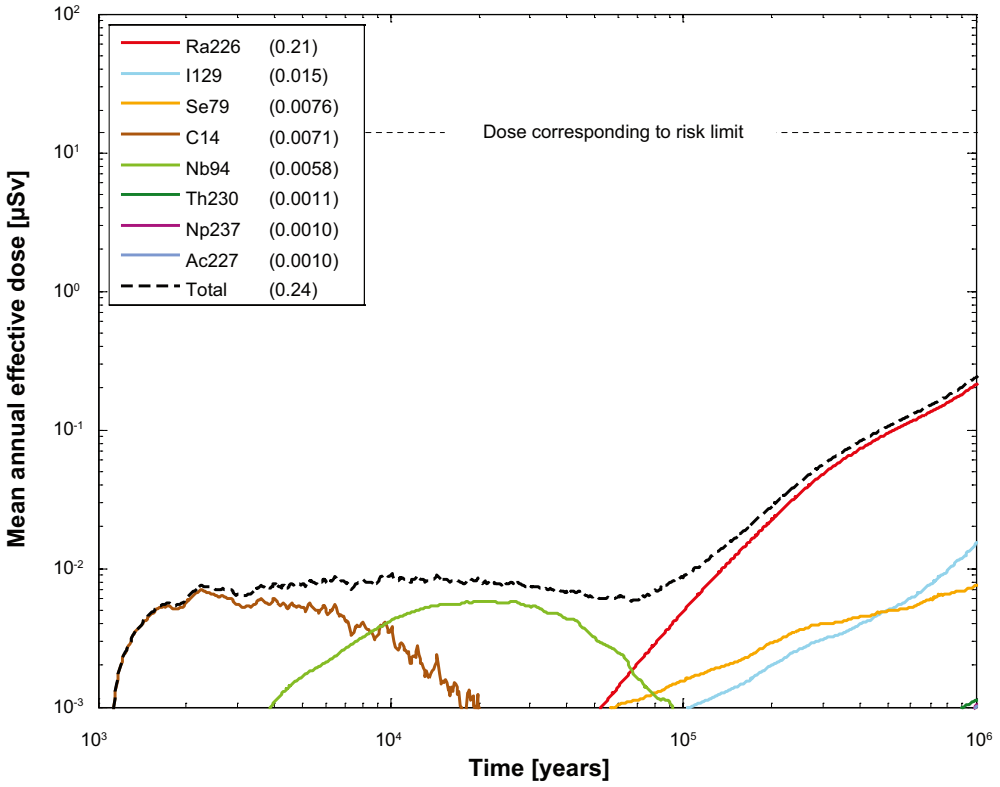

Figure 5-5. *Far-field mean annual effective dose for the probabilistic calculation of the shear load scenario, with failure during the period 1 000 years to one million years, disregarding co-precipitation of radium and barium. The legend is sorted by peak (in the one-million year period) of the mean annual effective dose. The values in brackets are peak dose in units of µSv.*

5.2.3 Early failure

Probabilistic calculations

Failure time:	0–10 000 years
Mean number of failed canisters:	2.4×10^{-8}/year
Solubility limits:	Yes
Number of realisations:	6 916
Number of nuclides:	45

For times up to 1 000 years after closure, the frequency of earthquakes is assessed to be lower, with a probability of failure of one of the 6 000 canisters by the end of the initial 1 000 year period being 2.4×10^{-5} or 2.4×10^{-8}/year (**Post-closure safety report**, Section 10.4.5). Also, the use of basic LDF-values overestimates the doses in this time interval for two reasons. First, the basic LDF is a pessimistic upper bound for releases occurring continuously over an entire interglacial period taking into account accumulation because a large part of the interglacial period has elapsed without any releases when the repository is sealed. Second, it is not meaningful to use the LDF concept for a radionuclide that decays to insignificance over an interglacial period because the concept is based on a continuous uniform release over the period.

A more detailed calculation of the shear load scenario for the initial 10 000 years was done to facilitate comparison with the results for the one million year time frame presented above. In this calculation, releases from the near field were determined as for all other cases; the IRF:s were also included. Because no credit is taken for geosphere retention in the shear scenario, the near-field releases are used as direct input to the biosphere modelling. In addition, because it is not possible to determine a location of the releases among the identified potential landscape objects, the release is fed to each object and the time dependent development of radionuclide transport and dose in the landscape is calculated for each object. The object giving the highest dose is then determined for each point in time and for each radionuclide. This entity is pessimistically defined as the calculated dose consequence for the case of a shear failure during the initial 10 000 years. A well is included in each landscape object in the same way as for the LDF calculations.

The result of this calculation is that the peak dose is almost four orders of magnitude lower than that corresponding to the regulatory risk limit, see Figure 5-6. (Note the extended dose scale compared to most other figures). Releases of Cs-137 and Sr-90 dominate in the beginning and thereafter C-14, I-129, Ag-108m and Nb-94 dominate.

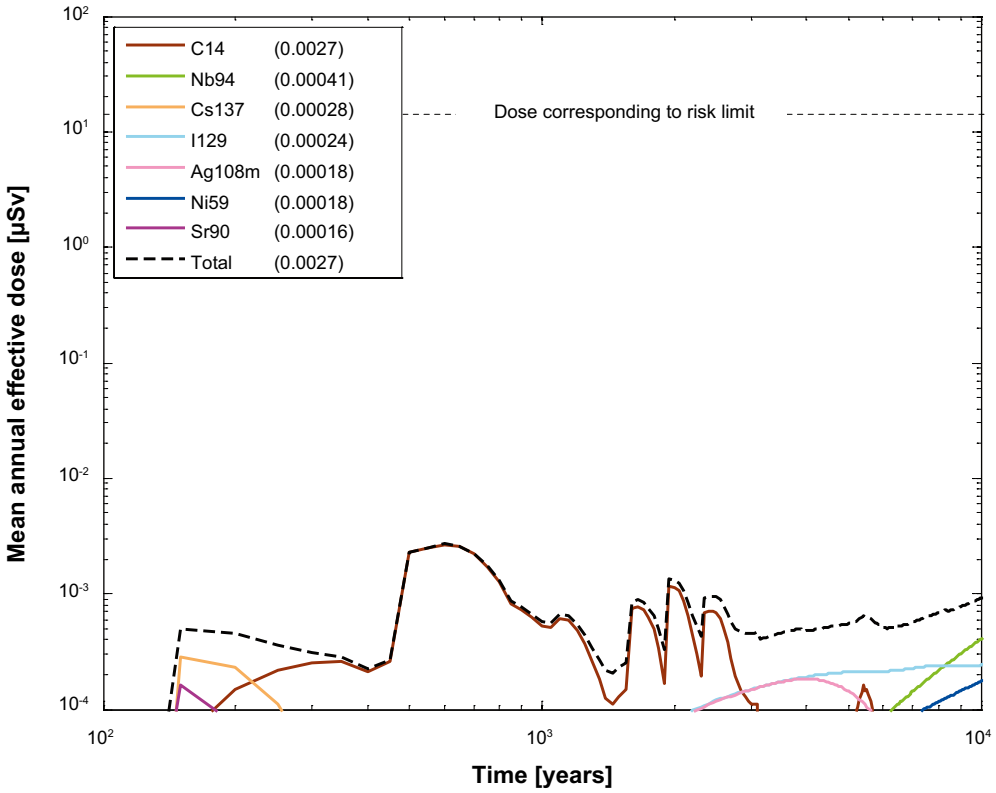

Figure 5-6. *Far-field mean annual effective dose for the probabilistic calculation of the shear load scenario, with failure during the period up to 10 000 years. The legend is sorted by peak (in the one-million year period) of the mean annual effective dose. The values in brackets are peak dose in units of µSv.*

5.2.4 Combination of shear load and buffer advection

Probabilistic calculations

Failure time:	1 000 to one million years
Mean number of failed canisters:	0.079
Solubility limits:	No
Thorium sorption in near field:	Yes (modelled as low solubility limit)
Number of realisations:	6 916
Number of nuclides:	37

In this case the combination of the shear load and the buffer advection scenarios (**Post-closure safety report**, Section 12.9.3) is addressed and the consequences of a shear failure followed by buffer erosion is considered, since it is reasonable to assume that the groundwater flow in a fracture that has undergone a major secondary shear movement could be high. Buffer erosion could then ultimately lead to loss of the buffer and its retardation function in the deposition hole with the canister failed due to shearing. A similar situation could arise if the buffer material is transformed through interaction with iron ions from the failed canister, as discussed in the **Post-closure safety report** in the buffer transformation scenario (**Post-closure safety report**, Section 12.4).

The case with shear failures distributed between 1 000 and one million years was therefore calculated also for near-field conditions with a missing buffer. The conceptualisation of the near field is thus the same as in the corrosion scenario, but near-field flow data are stylised (Q = 1 m^3/yr) and geosphere retention is disregarded as in other consequence calculations for the shear load scenario. The results are shown in Figure 5-7.

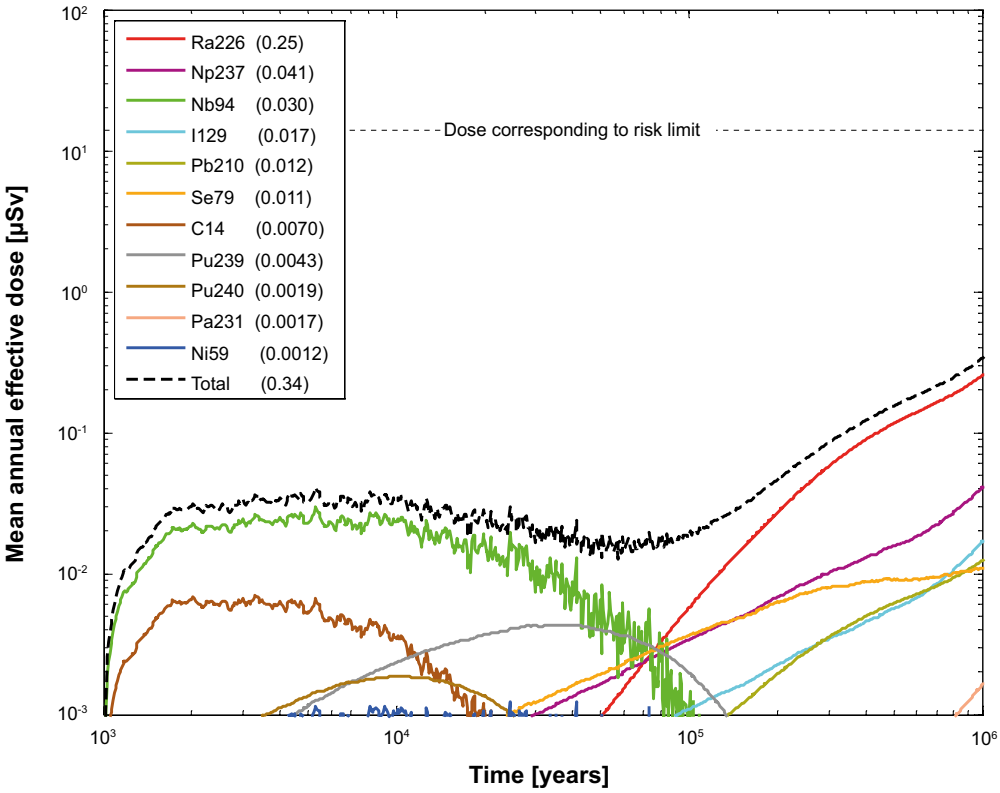

Figure 5-7. *Far-field mean annual effective dose for a probabilistic calculation of the shear load scenario, with advective conditions in the deposition hole, failure during the period between 1 000 years and one million years. The legend is sorted by peak (in the one-million year period) of the mean annual effective dose. The values in brackets are peak dose in units of µSv.*

The result is similar to the situation where the buffer is present in Figure 5-3 especially beyond 100 000 years. The peak annual effective dose from Ra-226 increases by about a factor of 2 from 0.13 µSv/yr to 0.25 µSv/yr. The retardation in the buffer and the limited solubility of the dose driving Ra-226, both of which contribute to retardation only when the buffer is present, are thus of minor importance in the shear load scenario.

The main difference for the radionuclides contributing most to dose is for Nb-94, as this radionuclide is significantly retained in the buffer when it is present. However, Nb-94 contributes to dose mainly before 100 000 years. The above case is only relevant after the buffer has been eroded. Since the near-field hydrogeological conditions are stylised with respect to radionuclide transport in the above case, they are not necessarily relevant for estimating the time taken for buffer erosion to cause advective conditions in the deposition hole. The first advective positions occur after several tens of thousands of years in the buffer advection scenario. However, considering the unknown nature of the hydraulic conditions in the deposition hole after a shear failure, the results in Figure 5-7 are seen as cautiously representative of a combined scenario for times beyond 10 000 years.

5.3 Alternative safety indicators for shear load case 1 000 years to one million years

Four alternative indicators to risk are used: release of activity from the geosphere, radiotoxicity flux from the geosphere, concentrations of radionuclides in ecosystems and natural geosphere fluxes of radionuclides. The following reference values are used when evaluating these indicators.

- The Finnish activity release constraints. These constraints are strictly applicable only in the Finnish regulatory context, but are nevertheless deemed useful as reference values.
- The reference value for radiotoxicity flux from the geosphere suggested by the EU SPIN project.

- Measured concentrations of naturally occurring radionuclides in ecosystems at the Forsmark site or other, comparable sites. Not further described here, see the **Post-closure safety report**, Section 13.5.8.
- Naturally occurring fluxes of radionuclides at the site.

For further descriptions of the indicators, see Alternative safety indicators for the central corrosion case in Section 4.9.

5.3.1 Finnish activity release constraints

The activity release constraints issued by STUK, see Section 4.9.1, have been applied to releases calculated for the shear load scenario, with failure during the period 1 000 years to one million years. The releases are around three orders of magnitude lower than the STUK constraint, see Figure 5-8.

5.3.2 Radiotoxicity flux from the geosphere – EU SPIN Project

The EU SPIN project, see Section 4.9.2, approach was used on the releases calculated for the shear load scenario, with failure during the period 1 000 years to one million years. The releases, 0.0096 Sv/year, are around four orders of magnitude lower than the SPIN reference value, 60 Sv/year, see Figure 5-9.

5.3.3 Naturally occurring fluxes of radionuclides at the site

The last alternative indicator to risk used is naturally occurring fluxes of radionuclides at the site. The naturally occurring fluxes of U-238, U-234 and Ra-226, are estimated based on measured activities during the site investigations, see Section 2.2.3. Figure 5-10 shows the release rates of U-238, U-234 and Ra-226 for the shear load scenario, with failure during the period 1 000 years to one million years, compared to the naturally occurring fluxes at Forsmark. The naturally occurring fluxes of U-238, U-234 and Ra-226 have been converted to effective dose by using the basic LDF values, the obtained dose is shown together with the far-field annual effective dose in the shear load case 1 000 years to one million years in Figure 5-11.

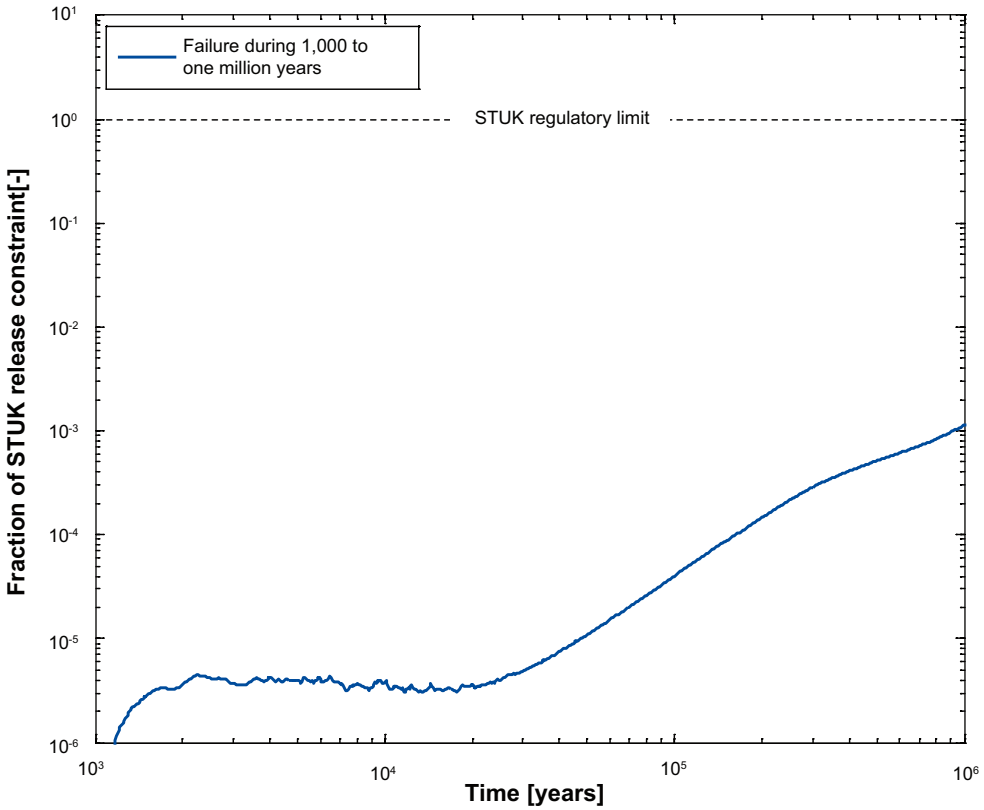

Figure 5-8. *Releases as a fraction of the activity release constraint index adopted by the Finnish regulator for the shear load case with failure during the period 1 000 years to one million years.*

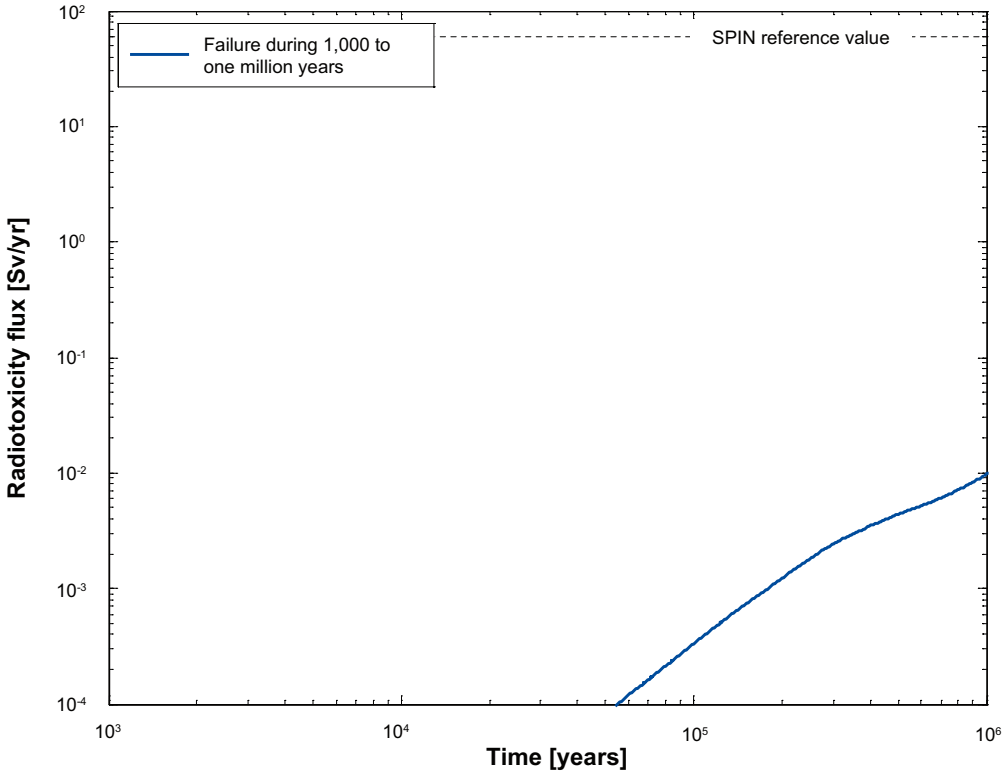

Figure 5-9. *Radiotoxicity flux in the shear load case with failure during the period 1 000 years to one million years compared to the SPIN reference value.*

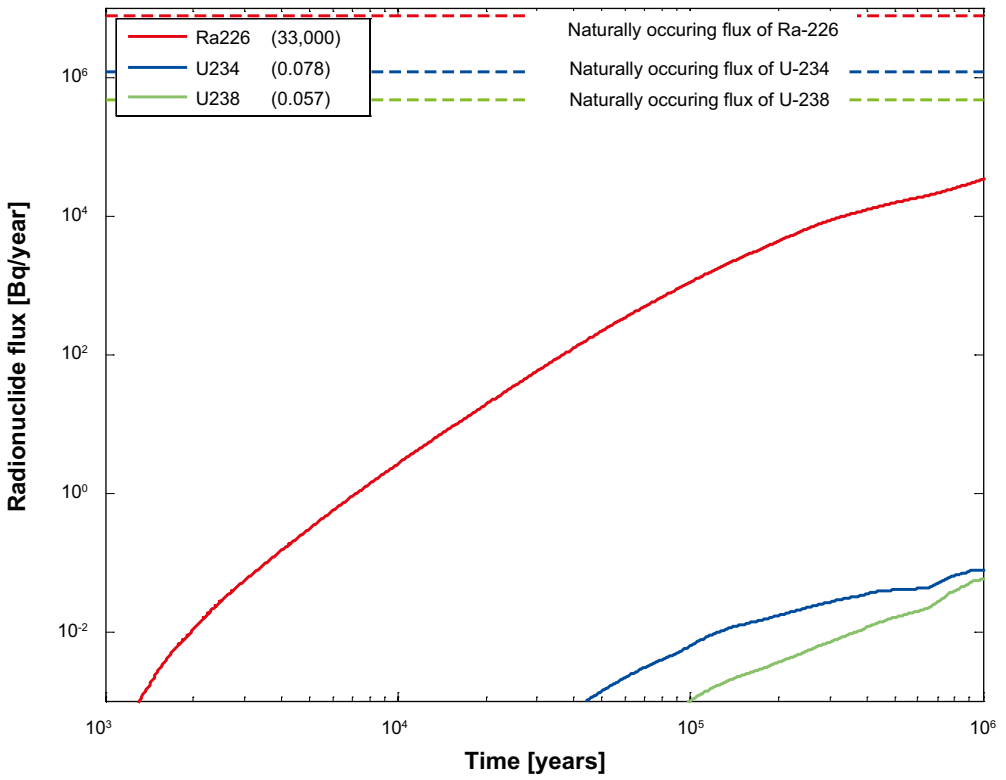

Figure 5-10. *Far-field release rates (Bq/year) of U-238, U-234 and Ra-226 in the shear load case 1 000 years to one million years compared to the naturally occurring fluxes at Forsmark. The legend is sorted by peak (in the one-million year period) of the mean annual radionuclide flux. The values in brackets are peak radionuclide fluxes in units of Bq/yr.*

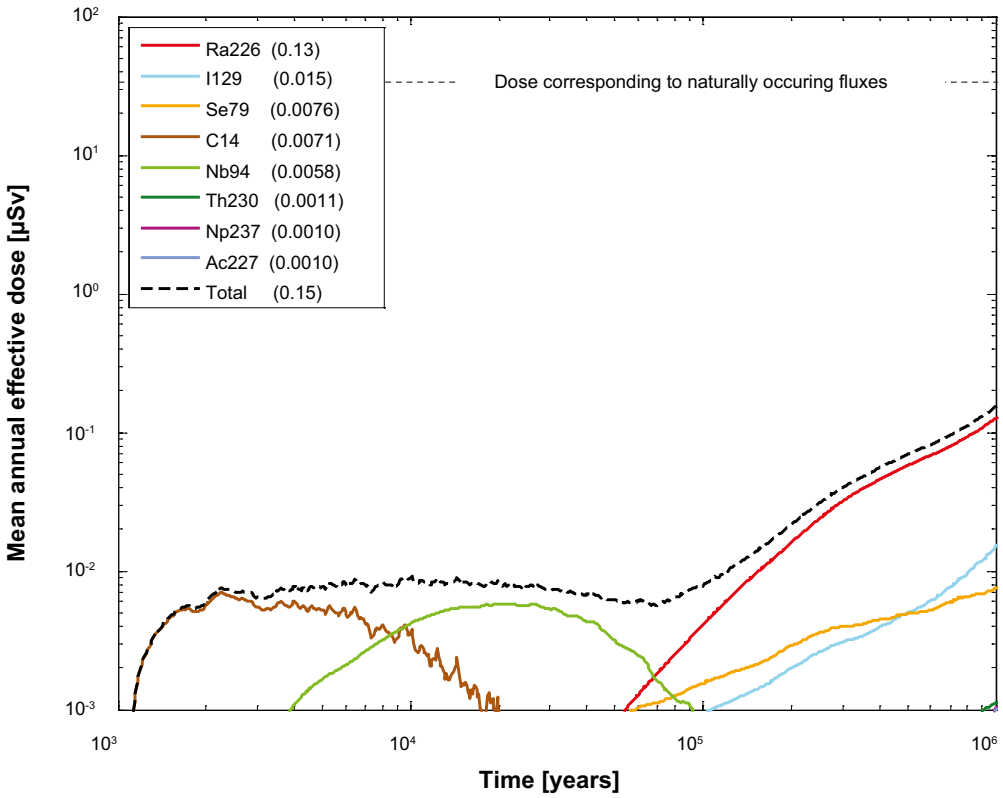

Figure 5-11. *Far-field annual effective dose in the shear load case 1 000 years to one million years compared to the naturally occurring fluxes of U-238, U-234 and Ra-226 at Forsmark converted to dose using the basic LDF values. The legend is sorted by peak (in the one-million year period) of the mean annual effective dose. The values in brackets are peak dose in units of µSv.*

5.4 Calculation with analytical models

For the shear load scenario, analytical models were applied to the variant with the combination of shear load and buffer advection with failure during the period 1 000 years to one million years.

The result of the analytical modelling of the probabilistic shear load and buffer advection case is shown in Figure 5-12. As seen by comparing the results in Figure 5-12 with those of the corresponding numerical case in Figure 5-7, the maximum total doses are almost identical. Together with the good agreement obtained also for the corrosion scenario, Section 4.10, the analytical calculations significantly enhances confidence in the dose equivalent releases provided here and in the **Post-closure safety report.**

5.5 Summary and conclusions for the shear load scenario

Figure 5-13 shows the total effective dose for early failure and for failure during the time period 1 000 years to one million years. No retention in the geosphere occurs and hence the release calculated for the near field is also valid for the far field. Note that the two cases have different probability of failure and that a more detailed calculation was performed for early failure (red curve) where the COMP23 results were used as input to the biosphere modelling while for later failure (blue curve) the COMP23 results were treated as in all other cases with basic LDF values.

It is seen that the early failure peak dose has it maximum of 0.0027 µSv after about 600 years. For later failure the peak dose of 0.15 µSv occurs at one million years and is about two orders of magnitude below the dose corresponding to the regulatory risk limit, 14 µSv.

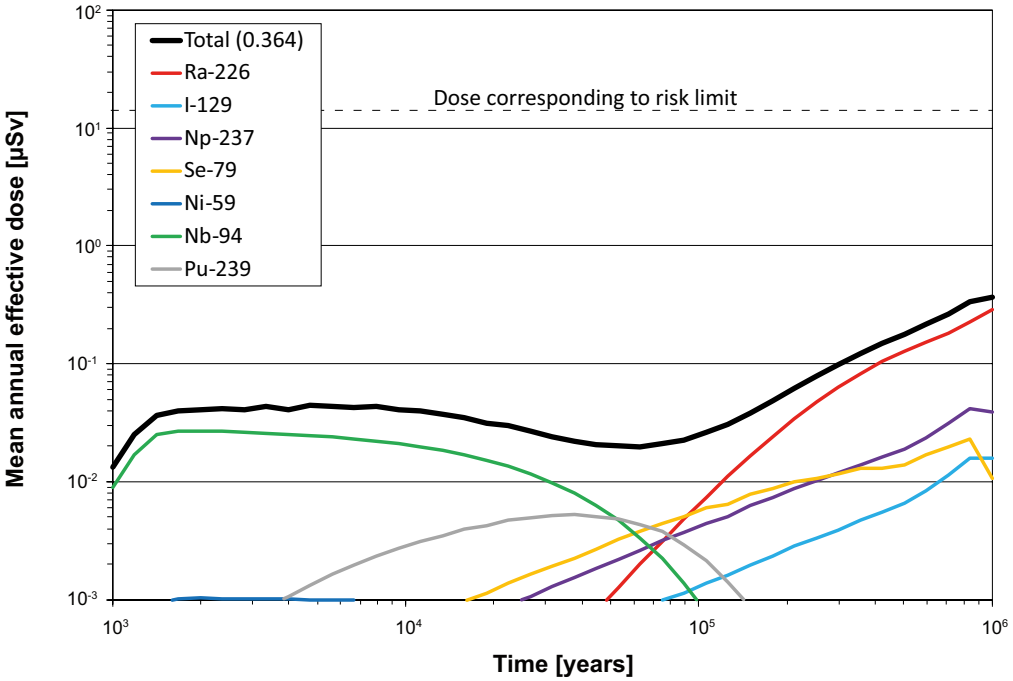

Figure 5-12. *Near-field and far-field mean annual effective dose for the probabilistic calculation of the combined shear load and buffer advection scenario, obtained with analytical models, with failure during 1 000 years to one million years.*

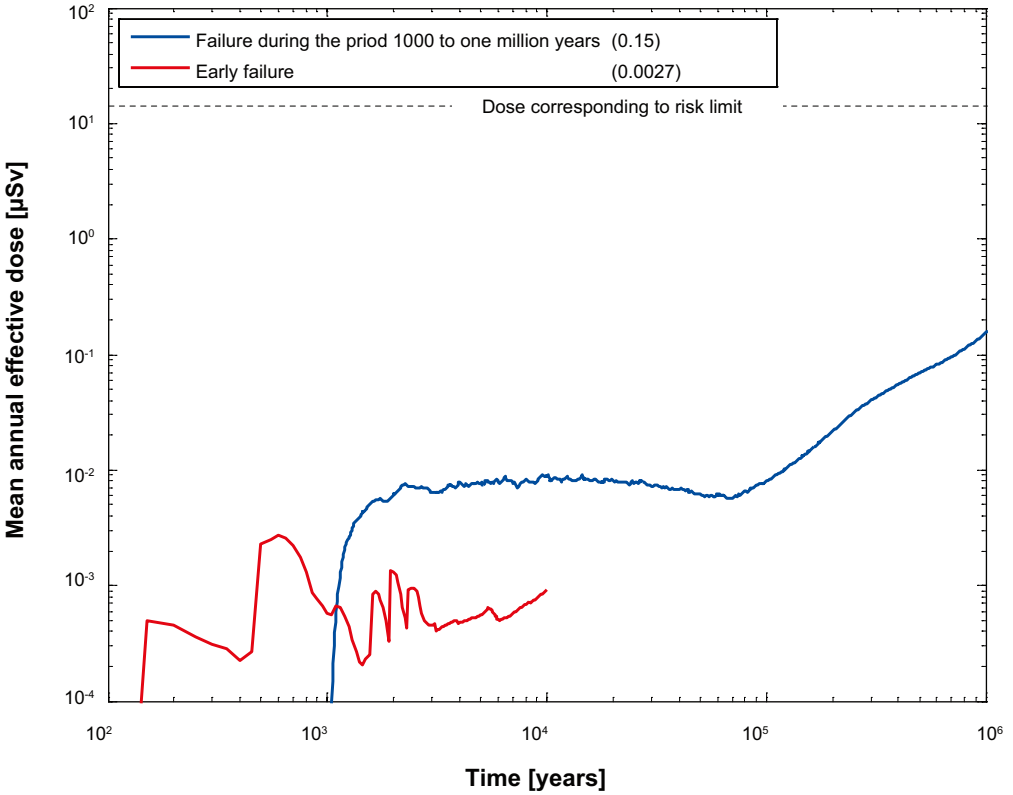

Figure 5-13. *Far-field annual effective dose for the shear load scenario. Note that the case for 1 000 to one million years are calculated with basic LDF values, while the curve for early failure is calculated with time a dependent biosphere model. The legend is sorted by peak (in the one-million year period) of the mean annual effective dose. The values in brackets are peak dose in units of µSv.*

6 Hypothetical residual scenarios to illustrate barrier functions

6.1 Introduction

The results shown in this chapter have not been updated since the SR-Site assessment (SKB 2010d). Instead, in Appendix M, results of recalculation of selected pinhole cases from the SR-Site are compared to the corresponding calculations using updated input data for the PSAR. The aim is to demonstrate that the differences in results are sufficiently limited that the conclusions drawn from the results of the SR-Site radionuclide transport calculations are still valid with updated input data for the PSAR. The updated input data for the PSAR are given in Appendix L. Also, complemenatry cases of hypothetical, early canister failures are analysed in the PSAR to further illustrate barrier functions. This is described in Sections 7.2.

In a few places, references in the SR-Site version were made to the main references of the SR-Site assessment, the references written in bold. It has been verified that the PSAR versions of the corresponding reports are equally valid as references in these cases. The references in bold, therefore, refer to the PSAR versions.

In this section, hypothetical, residual scenarios to illustrate barrier functions are analysed. They encompass *a*) the scenario 'canister failure due to isostatic load', considered as residual according to the analysis in the **Post-closure safety report**, Section 12.7, *b*) a failure mode where a hypothetical initial defect in the form of a penetrating pinhole in the copper shell grows into a larger defect and *c*) a number of additional cases where different barriers are assumed to be completely lost. The canister failure due to isostatic load scenario is analysed in Section 6.2. The pinhole case is analysed in Section 6.3, using the model tools COMP23 and FARF31 and in Section 6.4 using the MARFA code for the far-field transport. Hypothetical cases illustrating consequences of assumed barrier losses in addition to the pinhole case are analysed in Section 6.5.

6.2 Canister failure due to isostatic load

In the 'canister failure to due to isostatic load' scenario (briefly called the isostatic load scenario below) a canister fails due to isostatic collapse. It could occur as a consequence of the increased isostatic pressure due to a glacial overburden. The likelihood for this failure mode is negligible.

For this failure mode the canister is bypassed, whereas the buffer and the geosphere are assumed to have intact retention properties. It thus resembles the final state of the pinhole case, i.e. its state after occurrence of a large failure (Section 6.3).

Three transport paths are modelled:

- Q1, a fracture intersecting the deposition hole at a vertical position of the canister lid. This fracture is placed on the opposite side of the buffer to the canister defect, hence minimising the transport distance and the diffusional transport resistance. Thermally induced spalling is assumed to have occurred in the wall of the deposition hole meaning that the transport resistance at the interface Q1 is decreased.
- Q2, an excavation damage zone, EDZ, in the floor of the deposition tunnel. In the hydrogeological model, EDZ is treated as a thin conductive layer.
- Q3, a fracture intersecting the deposition tunnel. The distance to Q3 is obtained in the hydrogeological model by tracing advectively transported particles released in the deposition tunnel just above the deposition hole. As the distance from the deposition hole to Q3 differs, the longitudinal dimensions of the modelled deposition tunnel are different for different deposition holes.

A detailed description of the discretisation, diffusion resistances and boundary conditions used in COMP23 is given in Appendix G (section Growing pinhole – spalling, large hole).

6.2.1 Postulated failure of one canister at 10 000 years

Deterministic calculations

Hydrogeological case:	Semi-correlated, base realisation
Failure time:	10 000 years
Number of failed canisters:	1
Solubility limits:	Yes
Number of realisations:	1
Number of nuclides:	45

A deterministic calculation of the isostatic load failure was performed with a postulated failure of one canister at 10 000 years.

Figure 6-1 and Figure 6-2 show the deterministic near-field and far-field dose equivalent releases, respectively, for the isostatic load case with a postulated failure of one canister at 10 000 years. The doses from the near field are dominated by releases of I-129 and shortly after canister failure also with contribution of releases of C-14. The doses from the far field are dominated by releases of I-129.

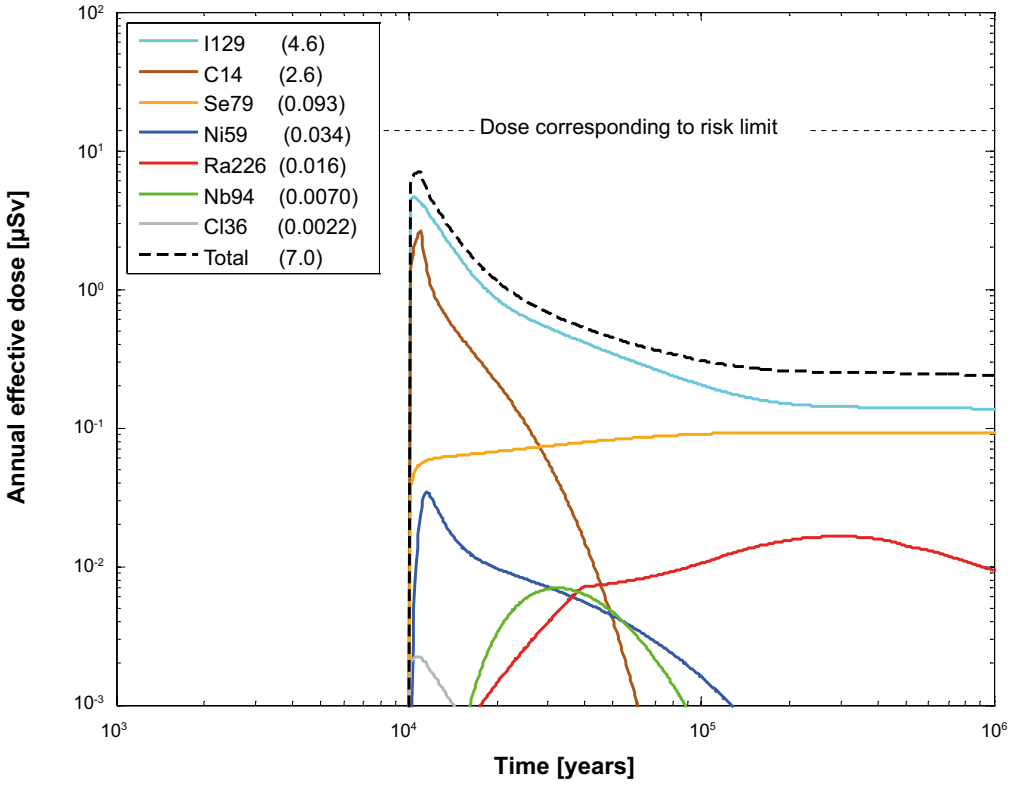

Figure 6-1. *Near-field dose equivalent release for a deterministic calculation of the isostatic load scenario, with a postulated failure of one canister at 10 000 years. The legend is sorted by peak (in the one-million year period) of the annual effective dose. The values in brackets are peak dose in units of µSv.*

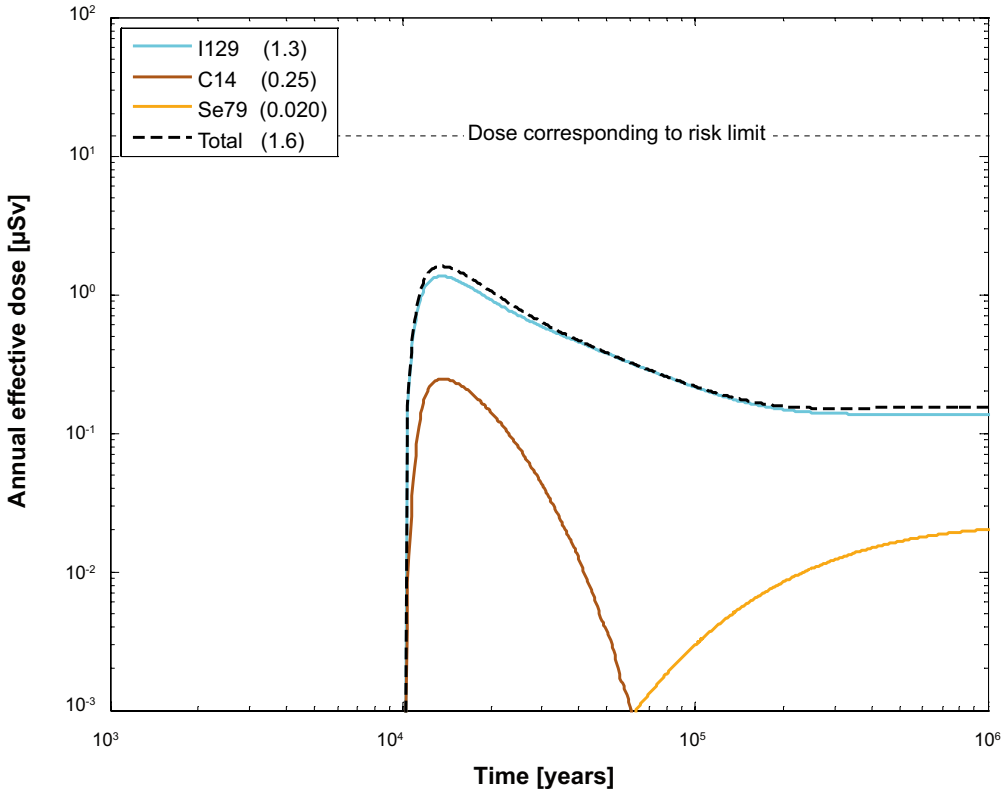

Figure 6-2. *Far-field annual effective dose for a deterministic calculation of the isostatic load scenario, with a postulated failure of one canister at 10 000 years. The legend is sorted by peak (in the one-million year period) of the annual effective dose. The values in brackets are peak dose in units of µSv.*

Probabilistic calculations

Hydrogeological case:	Semi-correlated, base realisation
Failure time:	10 000 years
Number of failed canisters:	1 (postulated)
Solubility limits:	Yes
Number of realisations:	6 916
Number of nuclides:	37

A probabilistic calculation of the isostatic load failure was performed with a postulated failure of one canister at 10 000 years and geosphere transport data from the base realisation of the semi-correlated DFN model.

Figure 6-3 and Figure 6-4 show the near-field and far-field dose equivalent releases, respectively, for the isostatic load failure with a postulated failure of one canister at 10 000 years. Both near-field and far-field doses are dominated by releases of I-129 and shortly after canister failure also with a contribution due to releases of C-14.

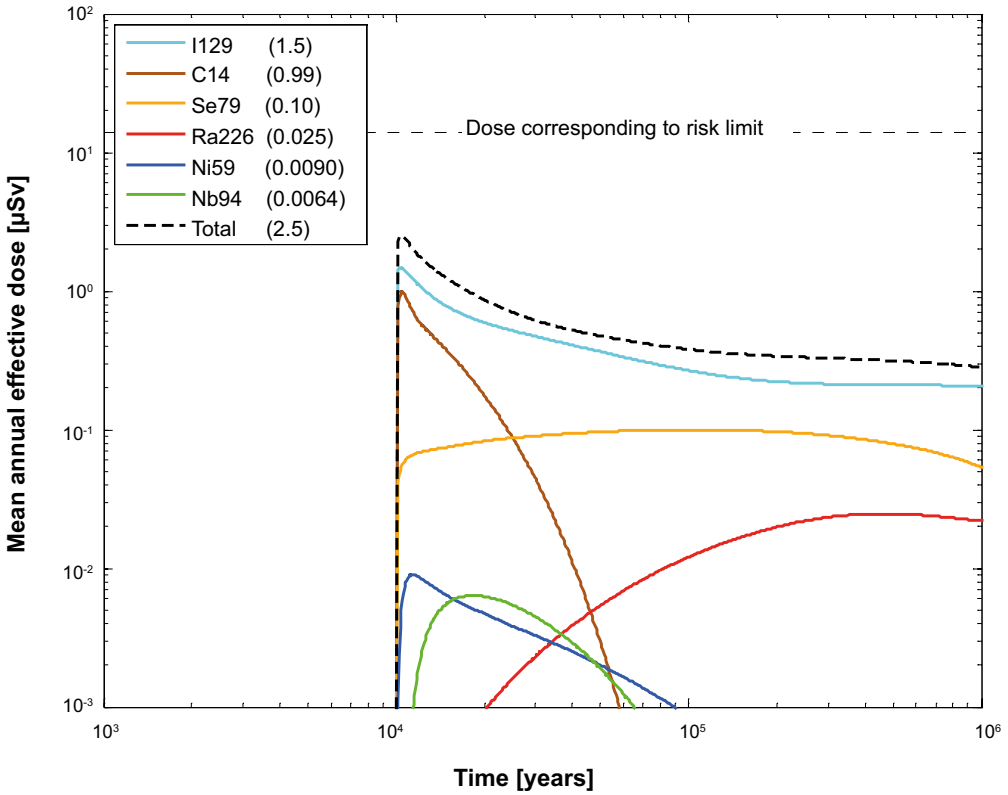

Figure 6-3. *Near-field dose equivalent release for a probabilistic calculation of the isostatic load scenario, with a postulated failure of one canister at 10 000 years. The legend is sorted by peak (in the one-million year period) of the mean annual effective dose. The values in brackets are peak dose in units of µSv.*

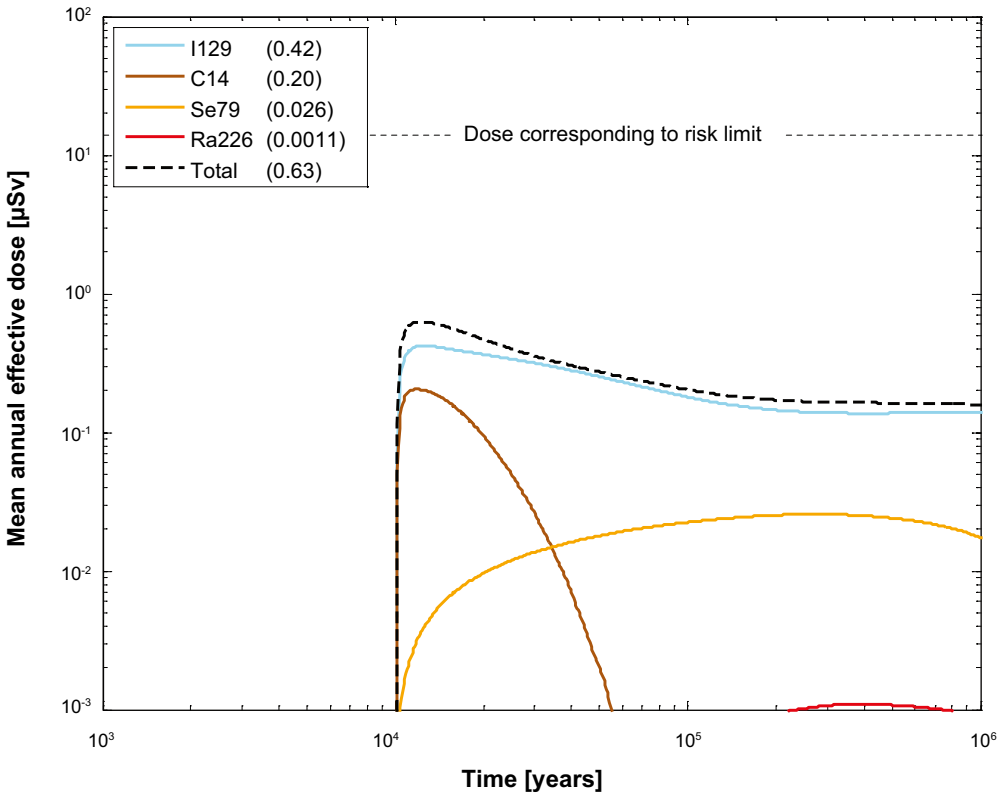

Figure 6-4. *Far-field mean annual effective dose for a probabilistic calculation of the isostatic load scenario, with a postulated failure of one canister at 10 000 years. The legend is sorted by peak (in the one-million year period) of the mean annual effective dose. The values in brackets are peak dose in units of µSv.*

6.2.2 Postulated failure of one canister at 100 000 years

Deterministic calculations

Hydrogeological case:	Semi-correlated, base realisation
Failure time:	100 000 years
Number of failed canisters:	1
Solubility limits:	Yes
Number of realisations:	1
Number of nuclides:	45

A deterministic calculation of the isostatic load failure was performed with a postulated failure of one canister at 100 000 years.

Figure 6-5 and Figure 6-6 show the deterministic near-field and far-field dose equivalent releases, respectively, for the isostatic load case with a postulated failure of one canister at 100 000 years. Both near- and far-field doses are dominated by I-129. Compared to the failure at 10 000 years no peak of C-14 appears shortly after canister failure.

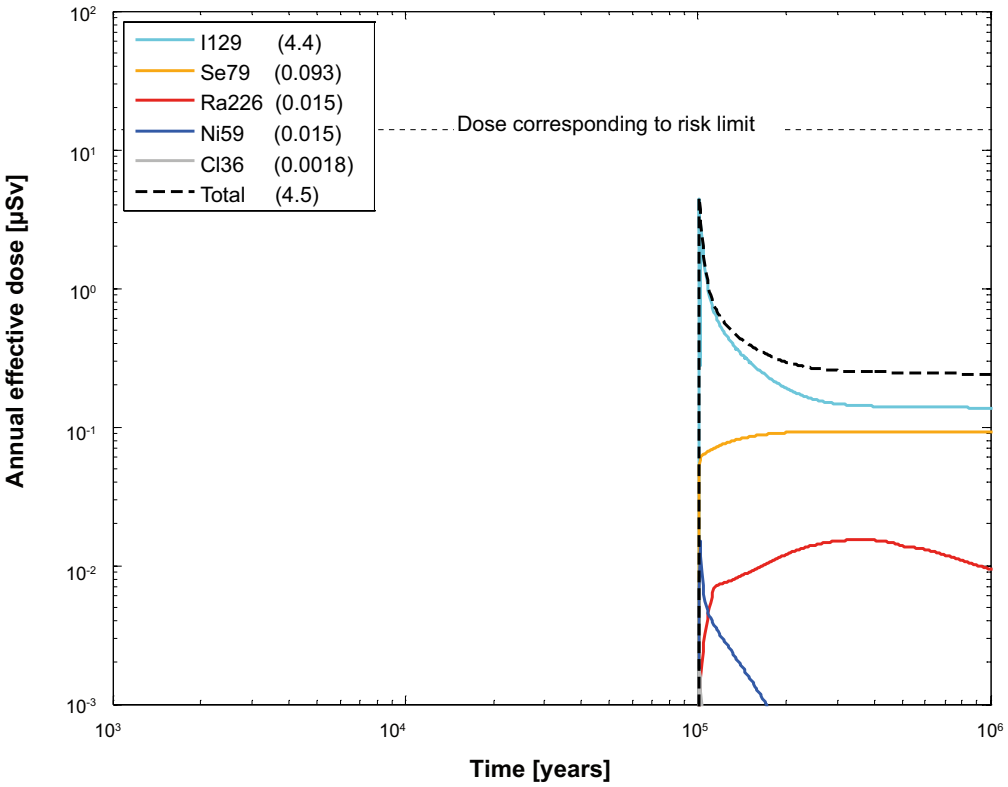

Figure 6-5. *Near-field dose equivalent release for a deterministic calculation of the isostatic load scenario, with a postulated failure of one canister at 100 000 years. The legend is sorted by peak (in the one-million year period) of the annual effective dose. The values in brackets are peak dose in units of µSv.*

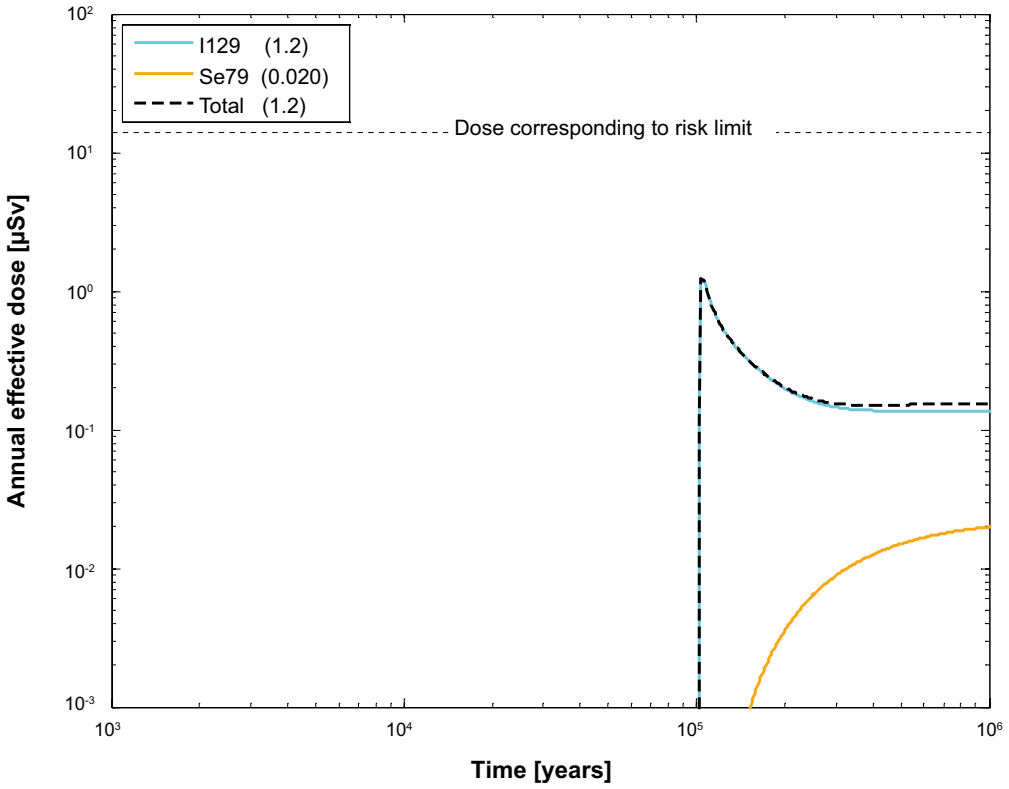

Figure 6-6. *Far-field annual effective dose for a deterministic calculation of the isostatic load scenario, with a postulated failure of one canister at 100 000 years. The legend is sorted by peak (in the one-million year period) of the annual effective dose. The values in brackets are peak dose in units of µSv.*

Probabilistic calculations

Hydrogeological case:	Semi-correlated, base realisation
Failure time:	100 000 years
Number of failed canisters:	1 (postulated)
Solubility limits:	Yes
Number of realisations:	6 916
Number of nuclides:	37

A probabilistic calculation of the isostatic load failure was performed with a postulated failure of one canister at 100 000 years and geosphere transport data from the base realisation of the semi correlated DFN model. The postulated number of failed canisters is 1.

Figure 6-7 and Figure 6-8 show the near-field and far-field dose equivalent releases, respectively, for the isostatic load failure with a postulated failure of one canister at 100 000 years. Both near-field and far-field doses are dominated by releases of I-129. Compared to the case with failure at 10 000 years, the total doses are lower and the contributions to the dose of releases of C-14 are negligible.

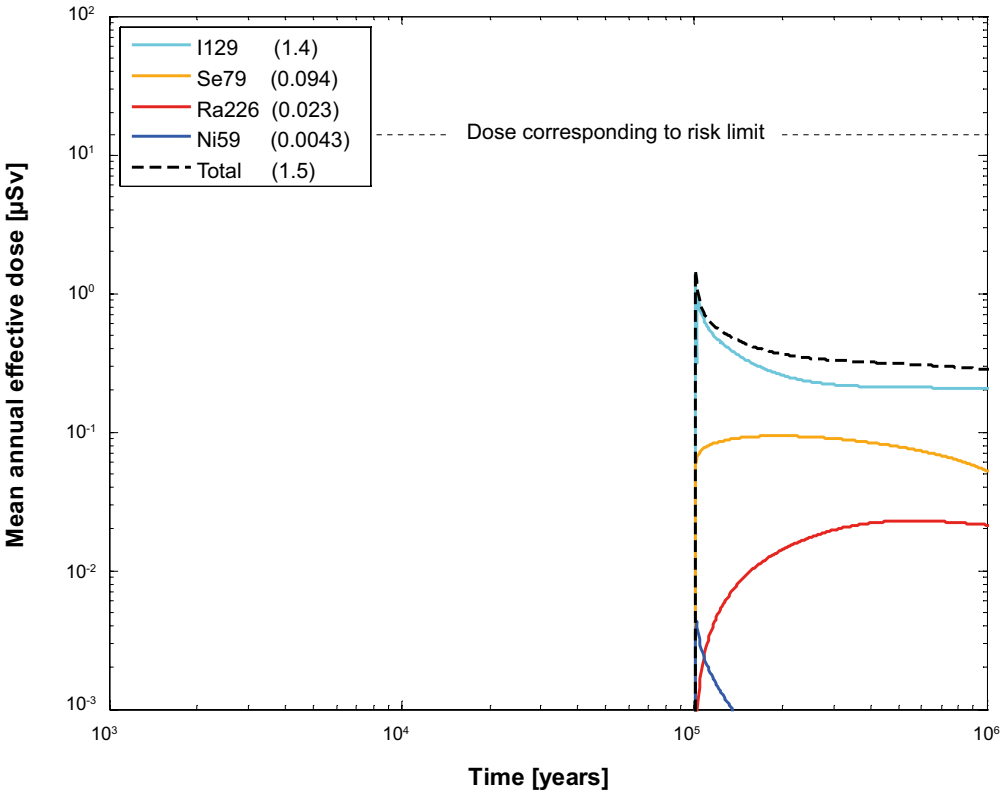

Figure 6-7. *Near-field dose equivalent release for a probabilistic calculation of the isostatic load scenario, with a postulated failure of one canister at 100 000 years. The legend is sorted by peak (in the one-million year period) of the mean annual effective dose. The values in brackets are peak dose in units of µSv.*

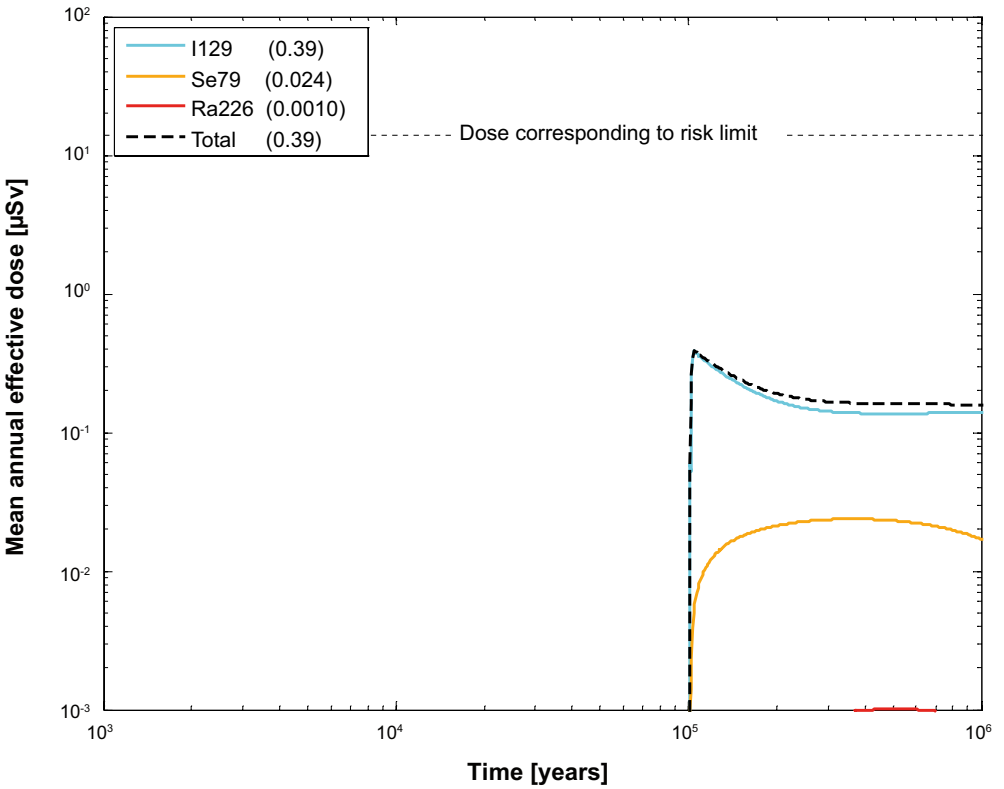

Figure 6-8. *Far-field mean annual effective dose for a probabilistic calculation of the isostatic load scenario, with a postulated failure of one canister at 100 000 years. The legend is sorted by peak (in the one-million year period) of the mean annual effective dose. The values in brackets are peak dose in units of µSv.*

6.2.3 Summary and conclusions for the isostatic load scenario

The consequences of postulated failures of one canister due to isostatic collapse 10 000 years and 100 000 years after repository closure are shown in Figure 6-9 and Figure 6-10 for the near field and far field, respectively. Since both hypothetical global causes (glacial load) and local causes (deficient material properties, higher than intended buffer density) for this scenario can be envisaged, simultaneous failure of more than one canister needs to be considered and would yield consequences in proportion to the number of failed canisters, provided that all releases occur to the same biosphere object. If a large number of canisters fail, it is more appropriate to use the LDF values for a distributed release when converting release to dose (see Table 3-7), since the release can be expected to be distributed over several landscape objects. Illustrations of consequences of extreme cases where all canisters fail at 10 000 and 100 000 years are also shown in Figure 6-9 and Figure 6-10 for the near field and far field, respectively. It is noted that the cases where one canister fails yield lower doses at one million years compared to single failures due both to corrosion where the buffer is eroded away (central corrosion case deterministic calculation, Figure 4-3) and to shear load where geosphere retention is neglected (deterministic calculation with postulated failure at 100 000 years, Figure 5-1).

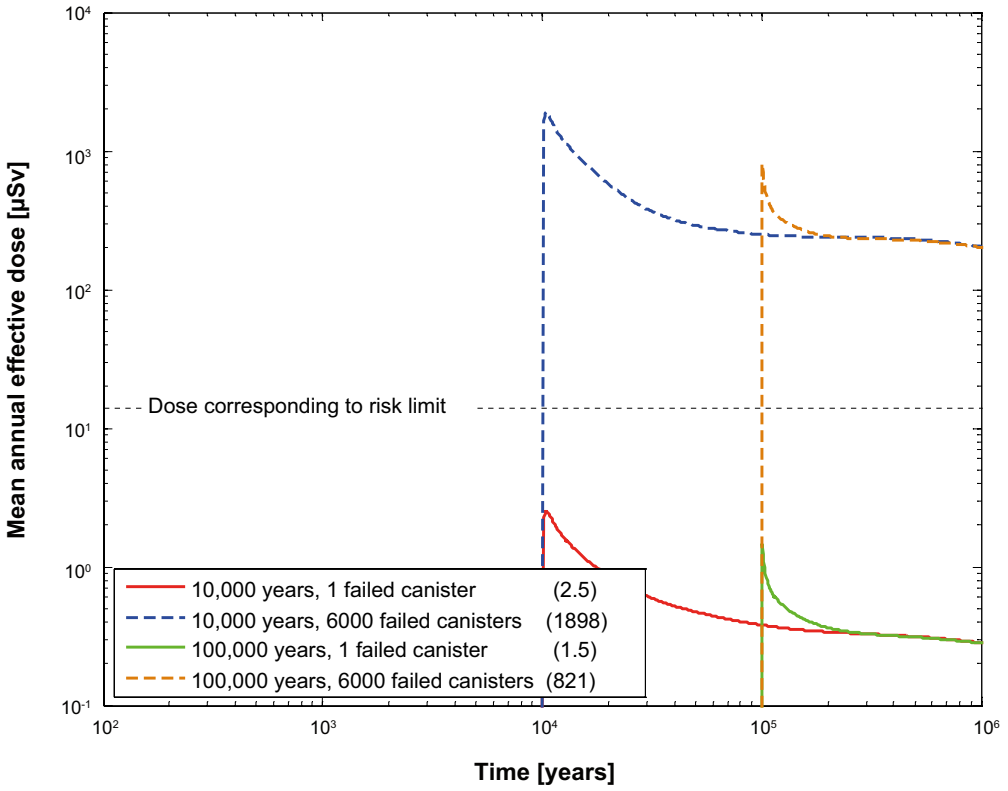

Figure 6-9. *Near-field dose equivalent release, for the isostatic load scenario. One failed canister (basic LDF) and 6 000 failed canisters (distributed LDF) at 10 000 years and 100 000 years. The values in brackets in the legend are peak dose in units of μSv.*

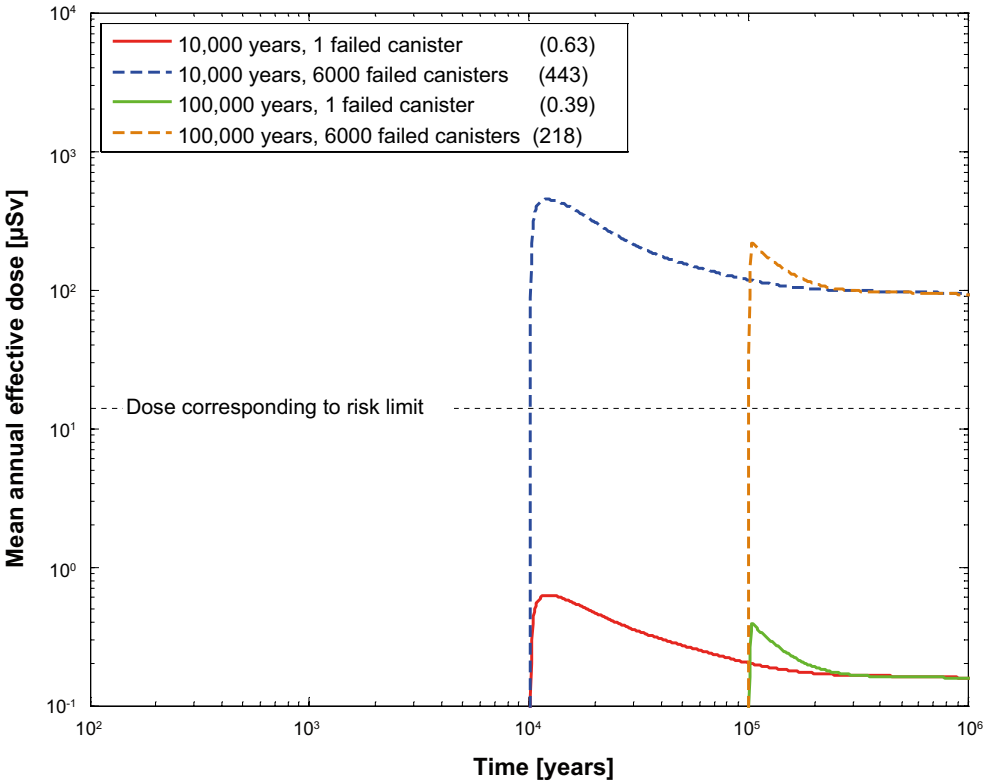

Figure 6-10. *Far-field mean annual effective dose, for the isostatic load scenario. One failed canister (basic LDF) and 6 000 failed canisters (distributed LDF) at 10 000 years and 100 000 years. The values in brackets in the legend are peak dose in units of µSv.*

6.3 The growing pinhole failure

A hypothetical, postulated failure mode where an initial defect in the form of a penetrating pinhole in the copper shell grows over time into a larger defect is analysed. In the pinhole failure mode, a pinhole in the canister wall initially offers considerable transport resistance that is subsequently lost as the defect expands with time, whereas the buffer and the geosphere have intact retention properties. It is, therefore, a convenient case for demonstrating the retarding capacity of the buffer and the geosphere and for exploring uncertainties and sensitivities related to these repository subsystems.

Details of the pinhole scenario are as follows: One canister at an unknown location is assumed to have a small defect. Transport is assumed to start 1 000 years after emplacement. Initially, transport is through a hole with 2-mm radius. At 10 000 years after emplacement, complete loss of transport resistance is assumed for the copper canister. This loss of transport resistance is modelled by allowing the water filled, nuclide containing canister void to directly contact bentonite in a 0.5-m-high region next to the defect. The time-dependent release of radionuclides into the geosphere occurs through the Q1, Q2 and Q3 release path. A more detailed description of the discretisation, diffusion resistances and boundary conditions used in COMP23 is given in Appendix G.

As a base case for the analysis of the pinhole failure mode, the base case of the hydrogeological semi-correlated DFN model was adopted. The EFPC criterion has been applied for the base case, i.e. canister positions intersected by fractures that also intersect the entire tunnel perimeter have been discarded. This means that 612 deposition holes out of 6 916 have been filtered from the results of the hydrogeological calculations. Furthermore, it was assumed that the equivalent flow rates for the path Q1 are affected by spalling.

The following is a brief description of the development of the system, driven by the processes that are quantified in the transport models, as an introduction to the presentation of the results of the calculations.

1. No releases occur from the canister before a continuous water pathway has been formed between the fuel and the exterior of the failed canister, which could take thousands of years. In these calculations the delay time is assigned to be 1 000 years. Radioactive decay reduces the radionuclide content and total radiotoxicity of the fuel.
2. As soon as a continuous water pathway has formed, the instant release fraction of the inventory dissolves in the water in the canister void. If the solubility limit is reached, the concentration of the dissolved nuclide in the water does not increase further. The nuclides dissolved in the water begin to diffuse out of the canister. The release of nuclides embedded in the fuel is determined by the fuel dissolution rate and the release of nuclides in metal parts is determined by the corrosion release rate. Also in this case, the solubilities of the nuclides limit the concentrations that can occur in the water.
3. The nuclides are sorbed with varying efficiency in the buffer and the diffusion and sorption properties determine the time for diffusion through the buffer. If this time is shorter than a few half-lives of the nuclide, it passes out into the rock.
4. In the rock, the nuclide's sorption properties, together with the rock's transport properties, determine the time for transport through the rock to the biosphere. As in the buffer, the half-life of the nuclide determines whether it passes through the geosphere before decaying to a substantial degree.
5. In the biosphere, the nuclide gives rise to a dose that is dependent on its inherent radiotoxicity and its turnover in the biosphere type to which it is released. Both of these factors are included in the LDF value used.

In general, nuclides with a relatively high instant release fraction also tend to be readily soluble and relatively mobile in both buffer and rock. Several percent of the inventory of I-129, for example, is instantly released; iodine has a very high solubility and is not sorbed in either buffer or rock. Plutonium isotopes, on the other hand, lie completely embedded in the fuel matrix, have low solubility and are sorbed strongly in both buffer and rock. Isotopes of uranium, thorium and americium have similar properties to plutonium.

6.3.1 Base case, including the effect of spalling

Deterministic calculations

Hydrogeological case:	Semi-correlated, base case
Failure time:	0 and 10 000 years
Number of failed canisters:	1
Solubility limits:	Yes
Spalling:	Yes
Number of realisations:	1
Number of nuclides:	37

A deterministic calculation of the hypothetical pinhole failure mode including the effect of spalling was performed for a canister with an initial penetrating pinhole that grows to a large hole after 10 000 years. Transport out of the canister is assumed to be established 1 000 years after deposition. Median values of geosphere transport data from the base case of the semi-correlated DFN model are used. The number of failed canisters is 1.

Figure 6-11 shows the deterministic near-field dose equivalent releases for the pinhole case including the effect of spalling. Figure 6-12 shows the same near-field dose equivalent releases decomposed into Q1, Q2 and Q3. Doses from the near field are dominated by C-14 and I-129 and Q1 is the dominating release path. Figure 6-13 shows the far-field dose equivalent releases for the pinhole case including the effect of spalling and Figure 6-14 shows the same releases decomposed into Q1, Q2 and Q3. Also the dose from the far field is dominated by I-129 and Q1 is again the dominating release path.

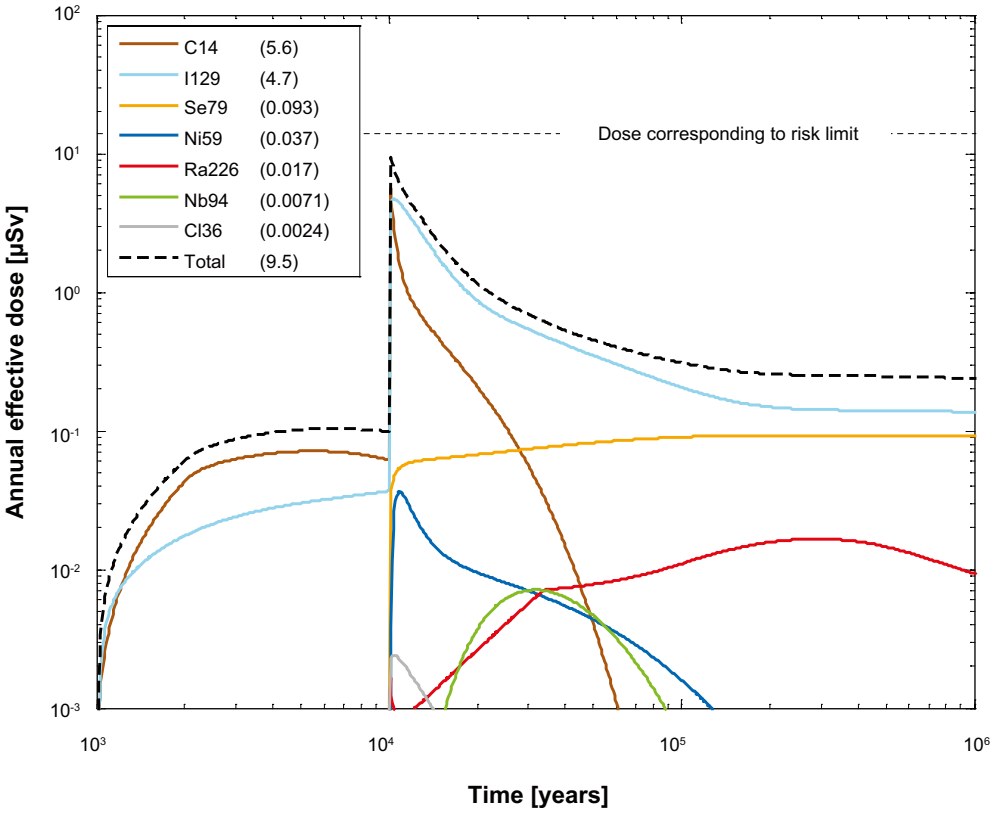

Figure 6-11. *Near-field dose equivalent release for a deterministic calculation of the pinhole case, including the effect of spalling. Summed doses for all release paths (Q1+Q2+Q3). The legend is sorted by peak (in the one-million year period) of the annual effective dose. The values in brackets are peak dose in units of µSv.*

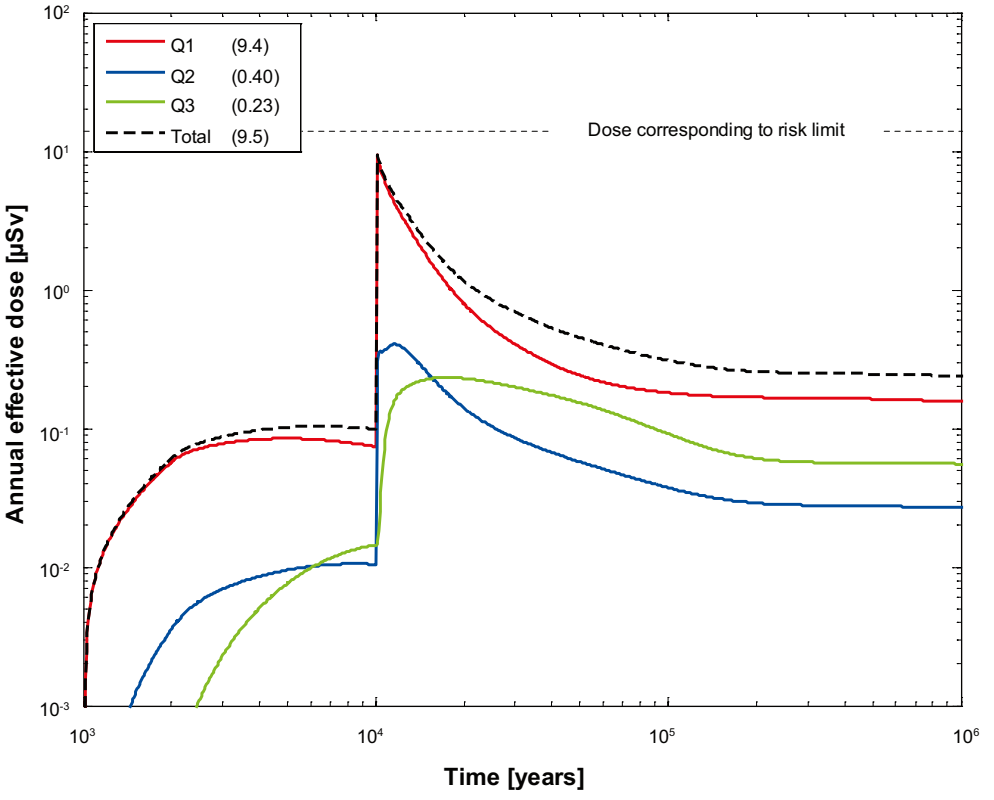

Figure 6-12. *Near-field dose equivalent release for a deterministic calculation of the pinhole case, including the effect of spalling. Doses decomposed into Q1, Q2 and Q3. The legend is sorted by peak (in the one-million year period) of the annual effective dose. The values in brackets are peak dose in units of µSv.*

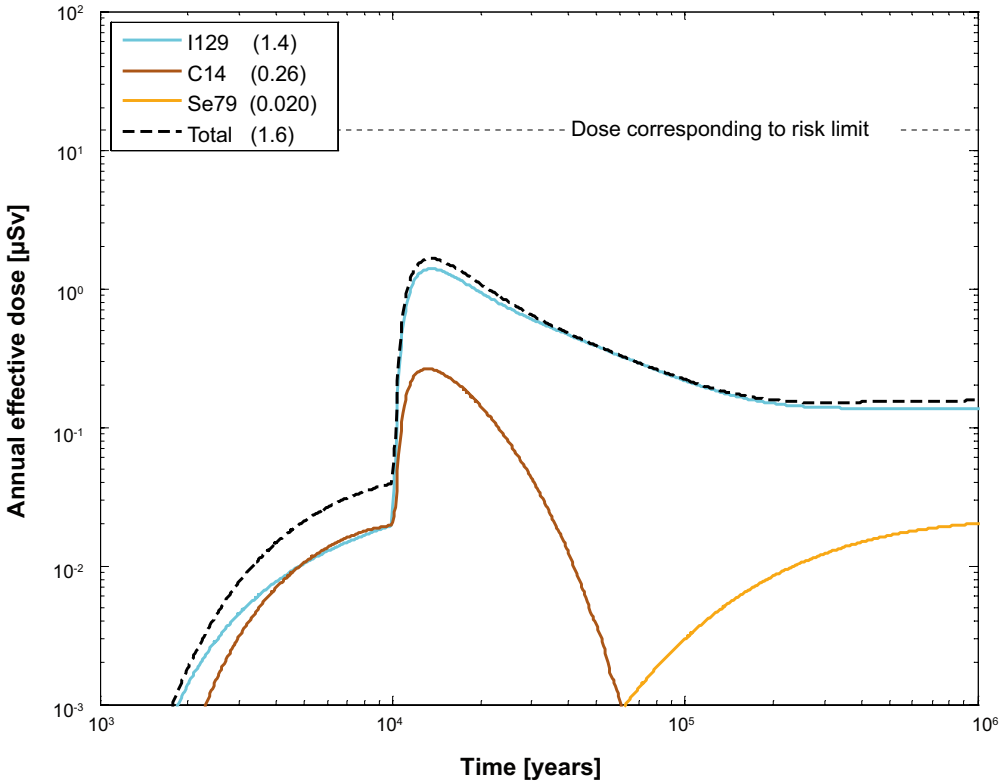

Figure 6-13. *Far-field annual effective dose for a deterministic calculation of the pinhole case, including the effect of spalling. Summed doses for all release paths (Q1+Q2+Q3). The legend is sorted by peak (in the one-million year period) of the annual effective dose. The values in brackets are peak dose in units of µSv.*

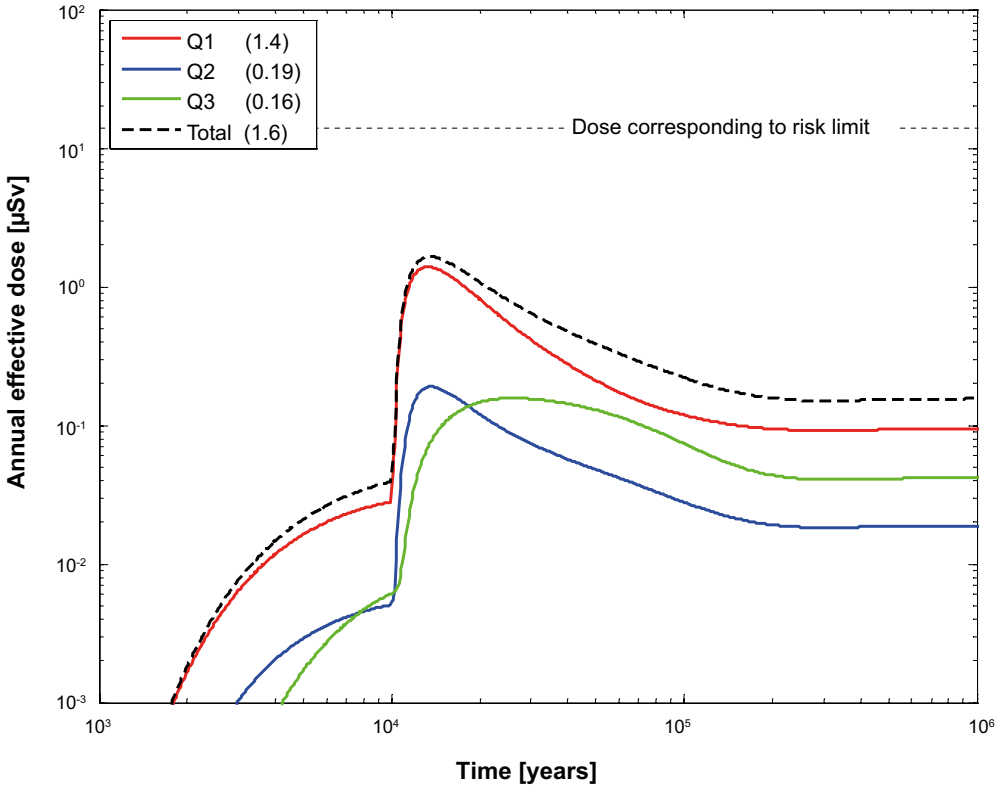

Figure 6-14. *Far-field annual effective dose for a deterministic calculation of the pinhole case, including the effect of spalling. Doses decomposed into Q1, Q2 and Q3. The legend is sorted by peak (in the one-million year period) of the annual effective dose. The values in brackets are peak dose in units of µSv.*

Probabilistic calculations

Hydrogeological case:	Semi-correlated, base case
Failure time:	0 and 10 000 years
Number of failed canisters:	1
Solubility limits:	Yes
Spalling:	Yes
Number of realisations:	6 916
Number of nuclides:	37

A probabilistic calculation of the hypothetical pinhole failure mode including the effect of spalling was performed for one canister with an initial penetrating pinhole that grows to a large hole after 10 000 years. Transport out of the canister is assumed to be established 1 000 years after deposition. Geosphere transport parameters from the base realisation of the semi correlated DFN model are used. The number of failed canisters is 1. The calculation was run for each of the 6 916 positions and a mean result was calculated over all positions.

Figure 6-15 shows the near-field dose equivalent releases for the pinhole case including the effect of spalling and Figure 6-16 shows the same releases decomposed into Q1, Q2 and Q3. Figure 6-17 shows the corresponding far-field dose equivalent releases and Figure 6-18 shows the same releases decomposed into Q1, Q2 and Q3. Doses from both the near field and the far field are dominated by C-14 and I-129. Q1 is the dominating release path till shortly after the large hole in the canister has developed. In the longer term Q3 becomes the dominating release path.

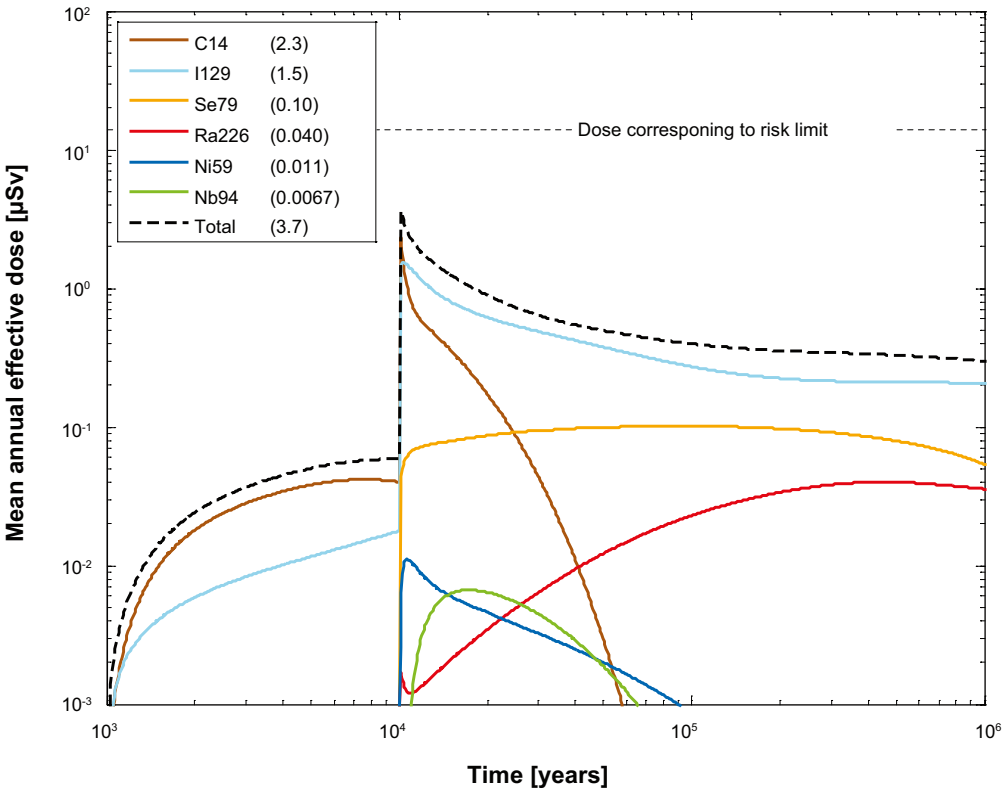

Figure 6-15. *Near-field dose equivalent release for the probabilistic calculation of the pinhole case, including the effect of spalling. Summed doses for all release paths (Q1+Q2+Q3). The legend is sorted by peak (in the one-million year period) of the mean annual effective dose. The values in brackets are peak dose in units of µSv.*

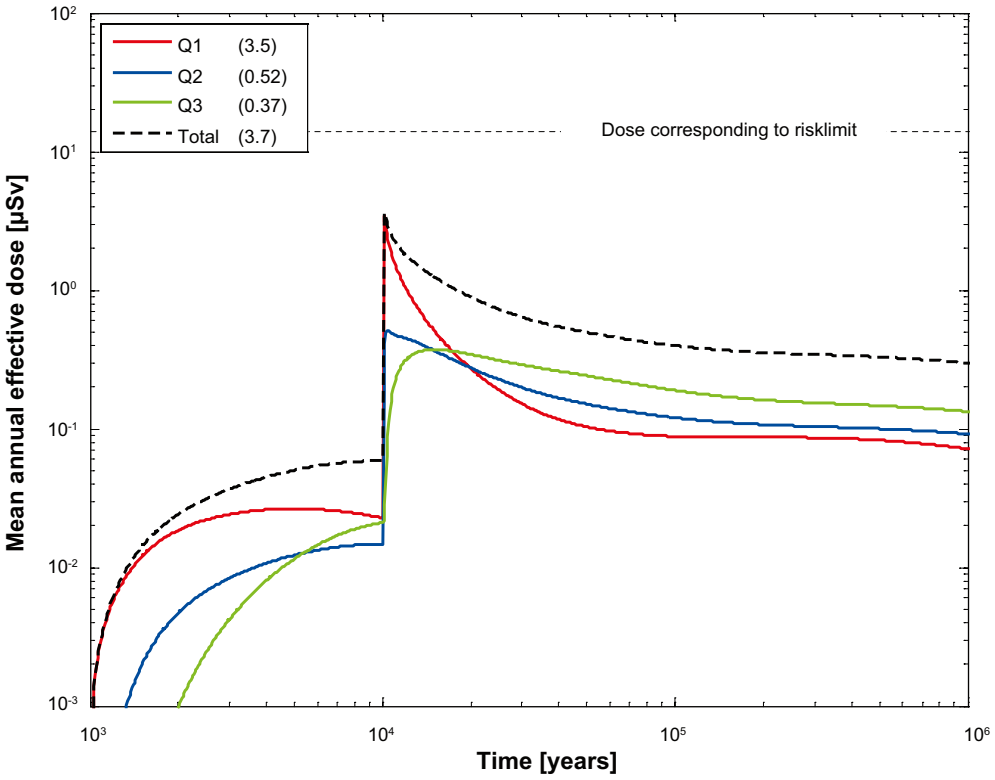

Figure 6-16. *Near-field dose equivalent release for the probabilistic calculation of the pinhole case, including the effect of spalling. Doses decomposed into Q1, Q2 and Q3. The legend is sorted by peak (in the one-million year period) of the mean annual effective dose. The values in brackets are peak dose in units of µSv.*

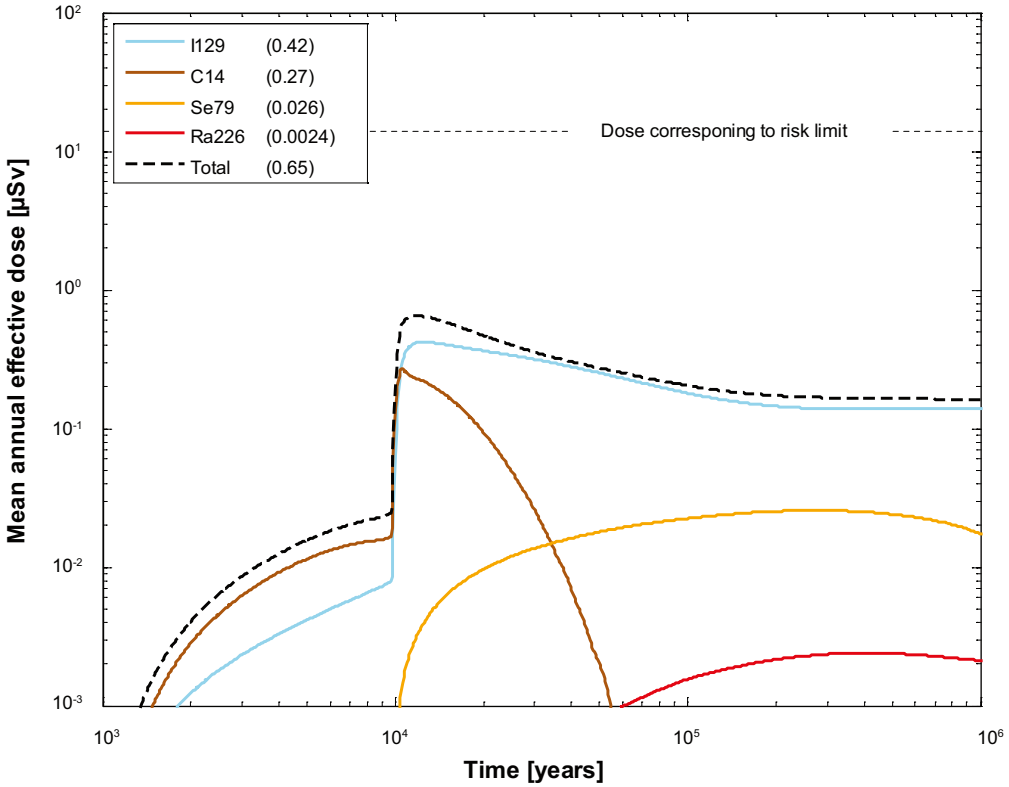

Figure 6-17. *Far-field mean annual mean effective dose for the probabilistic calculation of the pinhole case, including the effect of spalling. Summed doses for all release paths (Q1+Q2+Q3). The legend is sorted by peak (in the one-million year period) of the mean annual effective dose. The values in brackets are peak dose in units of µSv.*

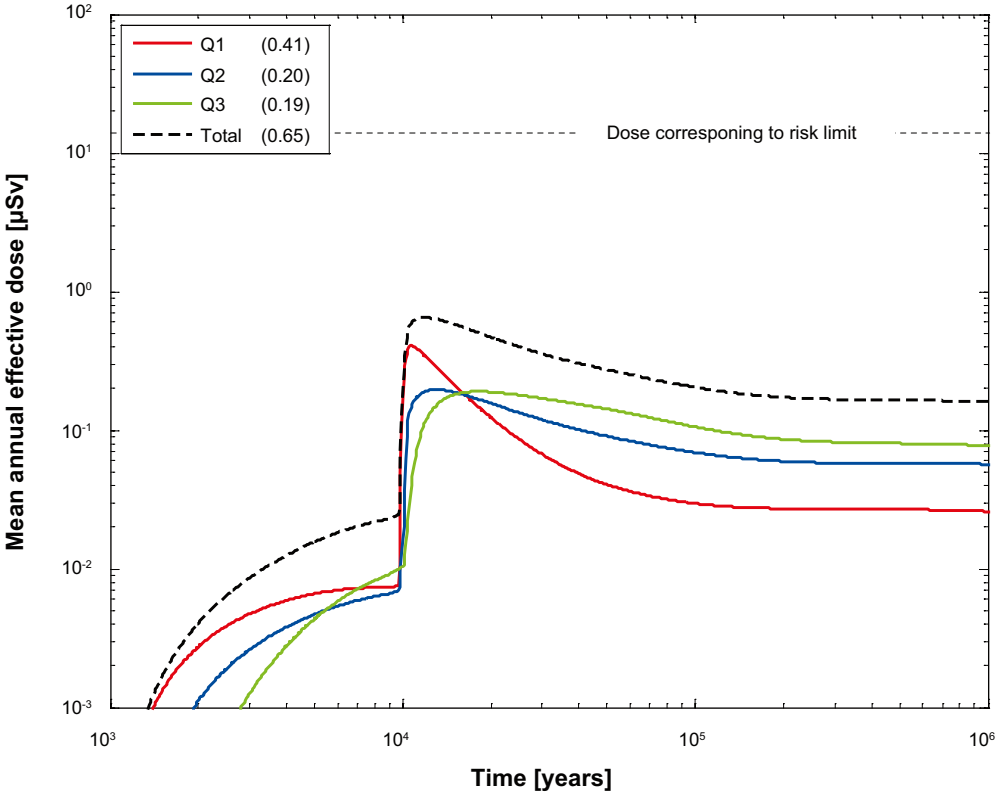

Figure 6-18. *Far-field mean annual effective dose for the probabilistic calculation of the pinhole case, including the effect of spalling. Doses decomposed into Q1, Q2 and Q3. The legend is sorted by peak (in the one-million year period) of the mean annual effective dose. The values in brackets are peak dose in units of µSv.*

6.3.2 Disregarding the effect of spalling

Deterministic calculations

Hydrogeological case:	Semi-correlated, base case
Failure time:	0 and 10 000 years
Number of failed canisters:	1
Solubility limits:	Yes
Spalling:	No
Number of realisations:	1
Number of nuclides:	37

A deterministic calculation of the hypothetical pinhole failure mode disregarding the effect of spalling was performed for a canister with an initial penetrating pinhole that grows to a large hole after 10 000 years. Transport out of the canister is assumed to be established 1 000 years after deposition. Median values of geosphere transport data from the base case of the semi correlated DFN model are used. The number of failed canisters is 1.

Figure 6-19 shows the deterministic near-field dose equivalent releases for the pinhole case disregarding the effect of spalling and Figure 6-20 shows the same near-field dose equivalent releases decomposed into Q1, Q2 and Q3. Disregarding spalling in the near-field results in doses about 13 times lower and release through Q3 are more dominating, compared to the pinhole case including spalling. Figure 6-21 shows the far-field dose equivalent releases for the pinhole case disregarding the effect of spalling and Figure 6-22 shows the same releases decomposed into Q1, Q2 and Q3. Doses from the far field are about 4 times lower and releases through Q3 are dominating.

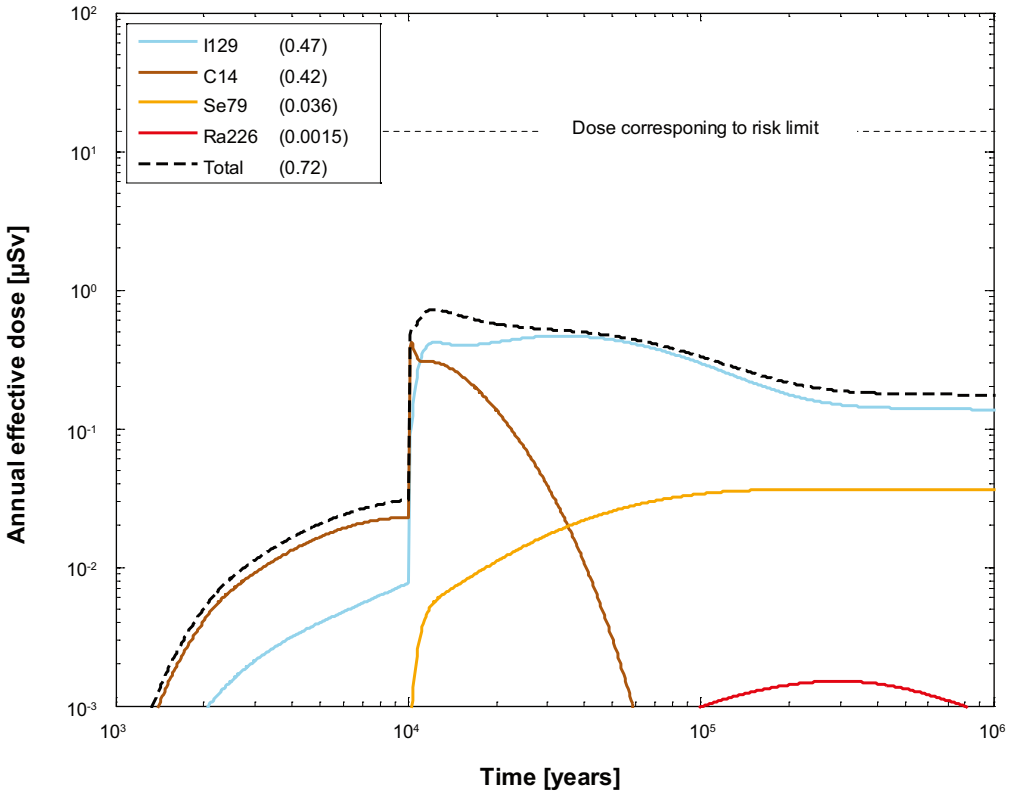

Figure 6-19. *Near-field dose equivalent release for a deterministic calculation of the pinhole case, disregarding the effect of spalling. Summed doses for all release paths (Q1+Q2+Q3). The legend is sorted by peak (in the one-million year period) of the annual effective dose. The values in brackets are peak dose in units of µSv.*

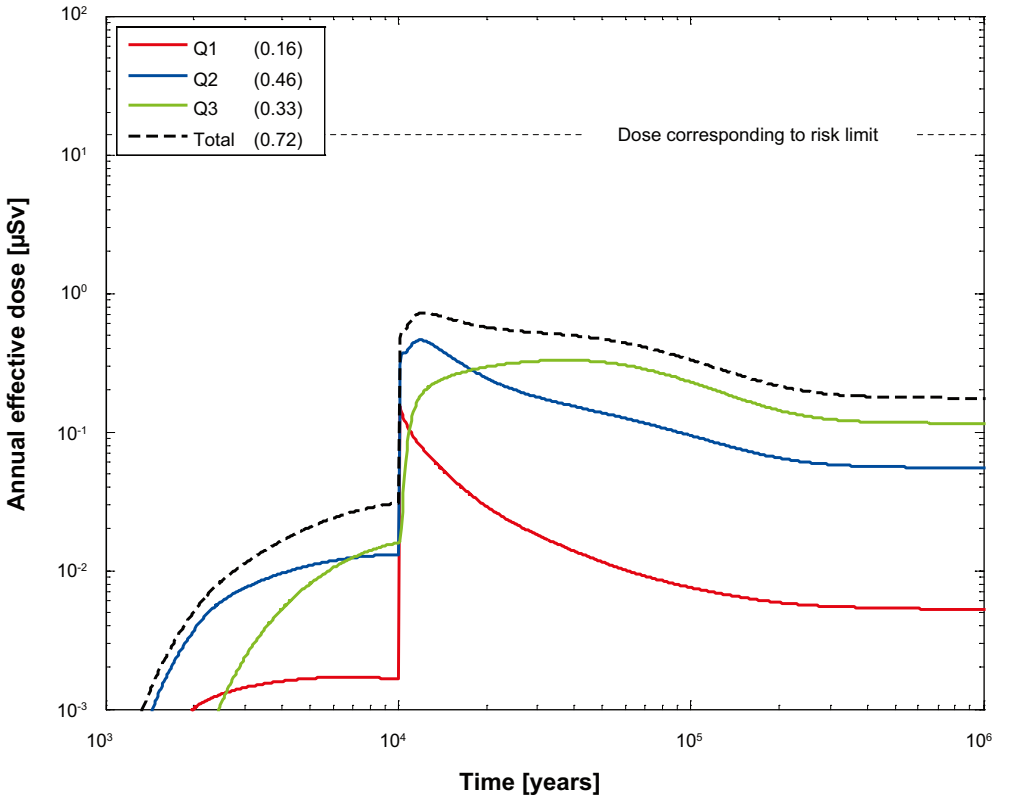

Figure 6-20. *Near-field dose equivalent release for a deterministic calculation of the pinhole case, disregarding the effect of spalling. Doses decomposed into Q1, Q2 and Q3. The legend is sorted by peak (in the one-million year period) of the annual effective dose. The values in brackets are peak dose in units of µSv.*

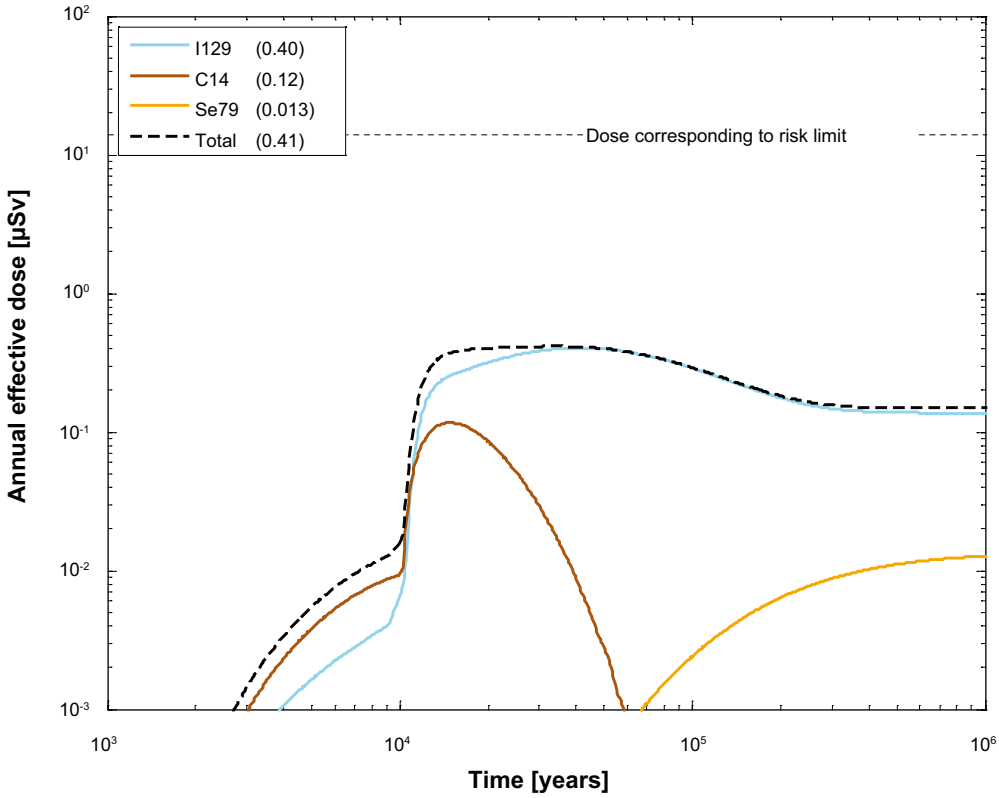

Figure 6-21. *Far-field annual effective dose for a deterministic calculation of the pinhole case, disregarding the effect of spalling. Summed doses for all release paths (Q1+Q2+Q3). The legend is sorted by peak (in the one-million year period) of the annual effective dose. The values in brackets are peak dose in units of µSv.*

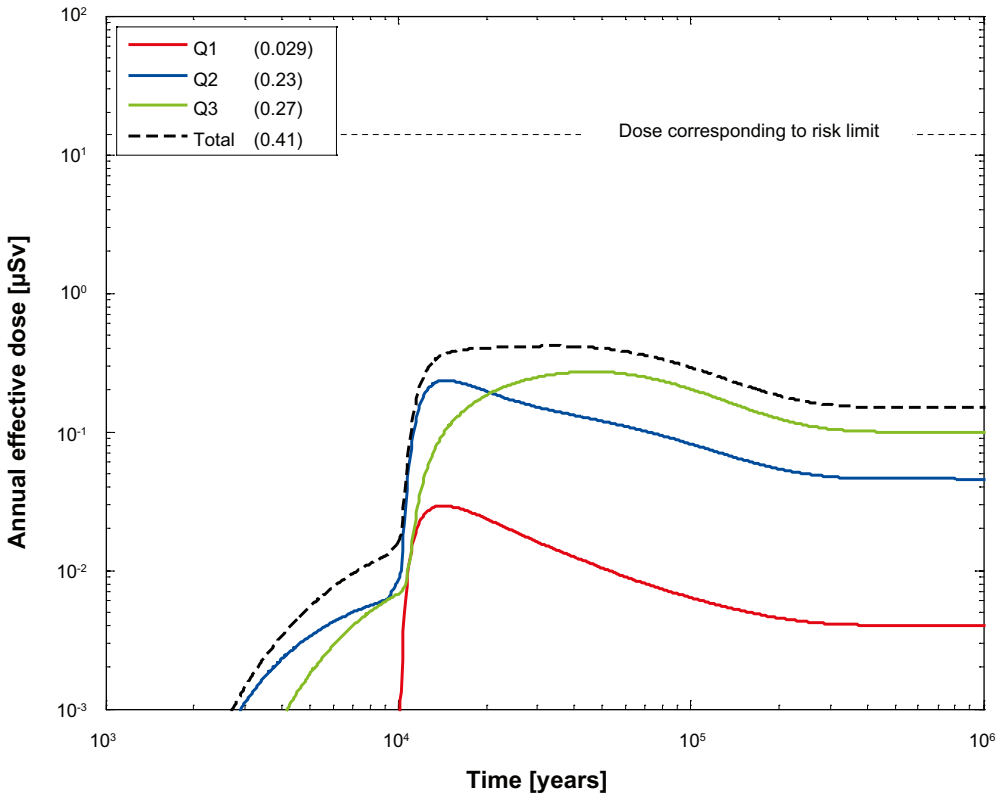

Figure 6-22. *Far-field annual effective dose for a deterministic calculation of the pinhole case, disregarding the effect of spalling. Doses decomposed into Q1, Q2 and Q3. The legend is sorted by peak (in the one-million year period) of the annual effective dose. The values in brackets are peak dose in units of µSv.*

Probabilistic calculations

Hydrogeological case:	Semi-correlated, base case
Failure time:	0 and 10 000 years
Number of failed canisters:	1
Solubility limits:	Yes
Spalling:	No
Number of realisations:	6 916
Number of nuclides:	37

A probabilistic calculation of the hypothetical pinhole failure mode disregarding the effect of spalling was performed for one canister with an initial penetrating pinhole that grows to a large hole after 10 000 years. Transport out of the canister is assumed to be established 1 000 years after deposition. Geosphere transport parameters from the base case of the semi correlated DFN model are used. The number of failed canisters is 1. The calculation was run for each of the 6 916 positions and a mean result was calculated over all positions.

Figure 6-23 shows the near-field dose equivalent releases for the pinhole case disregarding the effect of spalling and Figure 6-24 shows the same releases decomposed into Q1, Q2 and Q3. Disregarding spalling in the near-field results in doses about 4 times lower and release through Q2 and Q3 are completely dominating, compared to the pinhole case including spalling. Figure 6-25 shows the far-field dose equivalent releases for the pinhole case disregarding the effect of spalling and Figure 6-26 shows the same releases decomposed into Q1, Q2 and Q3. Doses from the far field are similar to the doses when the effect of spalling is included, but releases through Q2 and Q3 are completely dominating over Q1.

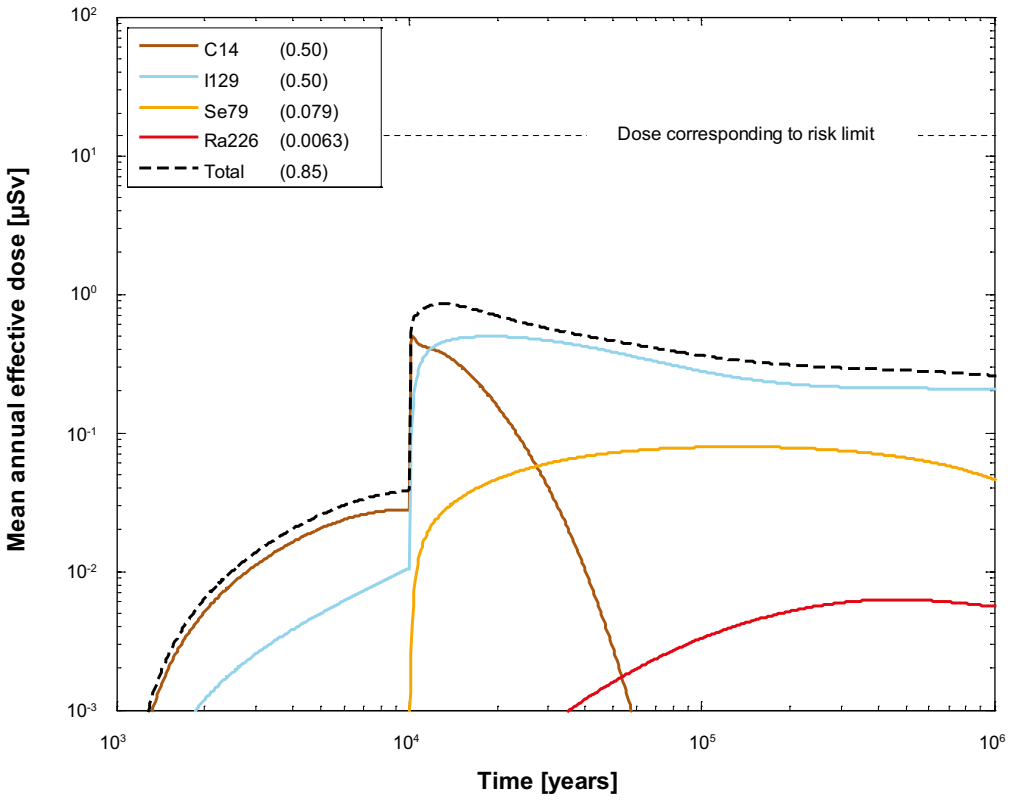

Figure 6-23. *Near-field dose equivalent release for the probabilistic calculation of the pinhole case, disregarding the effect of spalling. Summed doses for all release paths (Q1+Q2+Q3). The legend is sorted by peak (in the one-million year period) of the mean annual effective dose. The values in brackets are peak dose in units of µSv.*

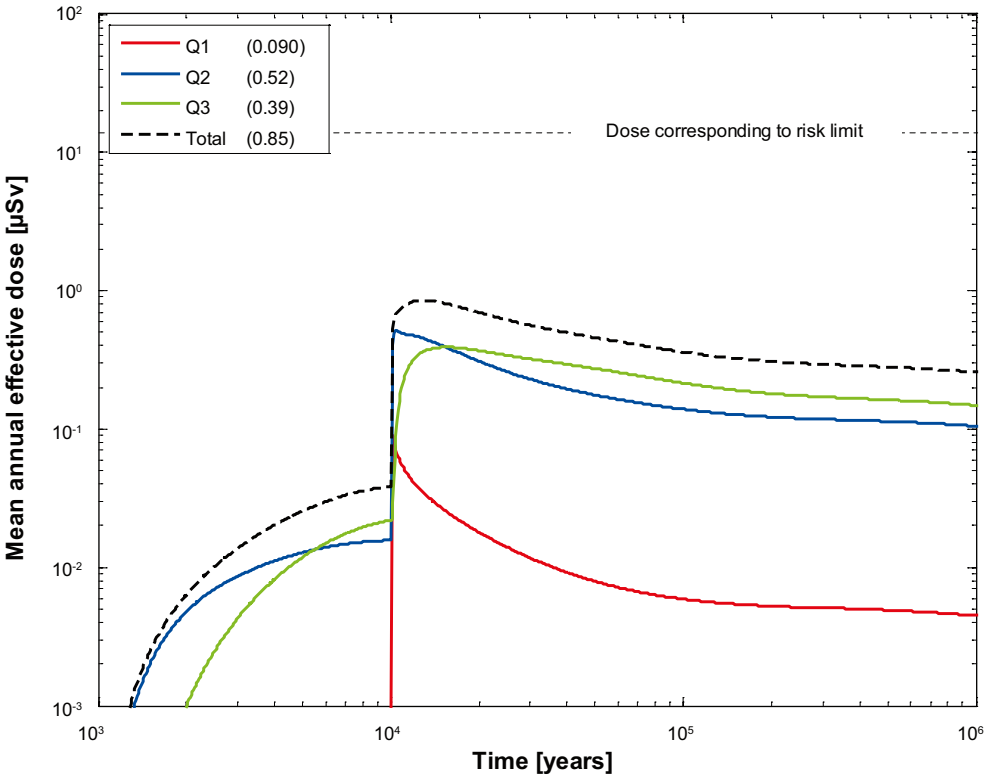

Figure 6-24. *Near-field dose equivalent release for the probabilistic calculation of the pinhole case, disregarding the effect of spalling. Doses decomposed into Q1, Q2 and Q3. The legend is sorted by peak (in the one-million year period) of the mean annual effective dose. The values in brackets are peak dose in units of µSv.*

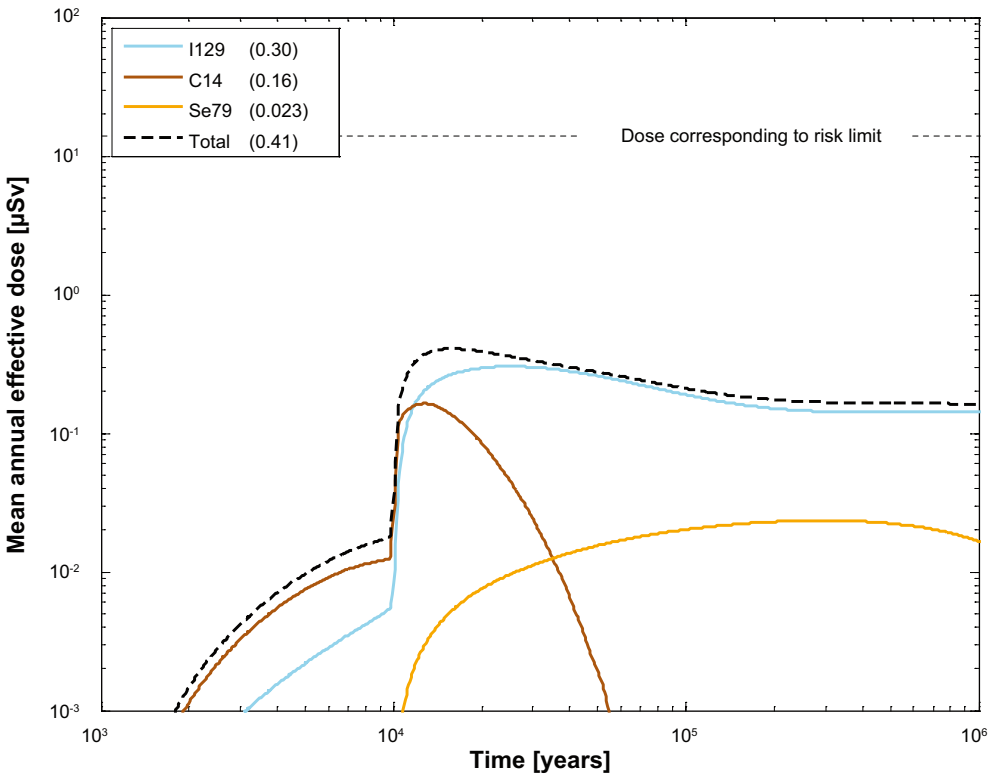

Figure 6-25. *Far-field mean annual mean effective dose for the probabilistic calculation of the pinhole case, disregarding the effect of spalling. Summed doses for all release paths (Q1+Q2+Q3). The legend is sorted by peak (in the one-million year period) of the mean annual effective dose. The values in brackets are peak dose in units of µSv.*

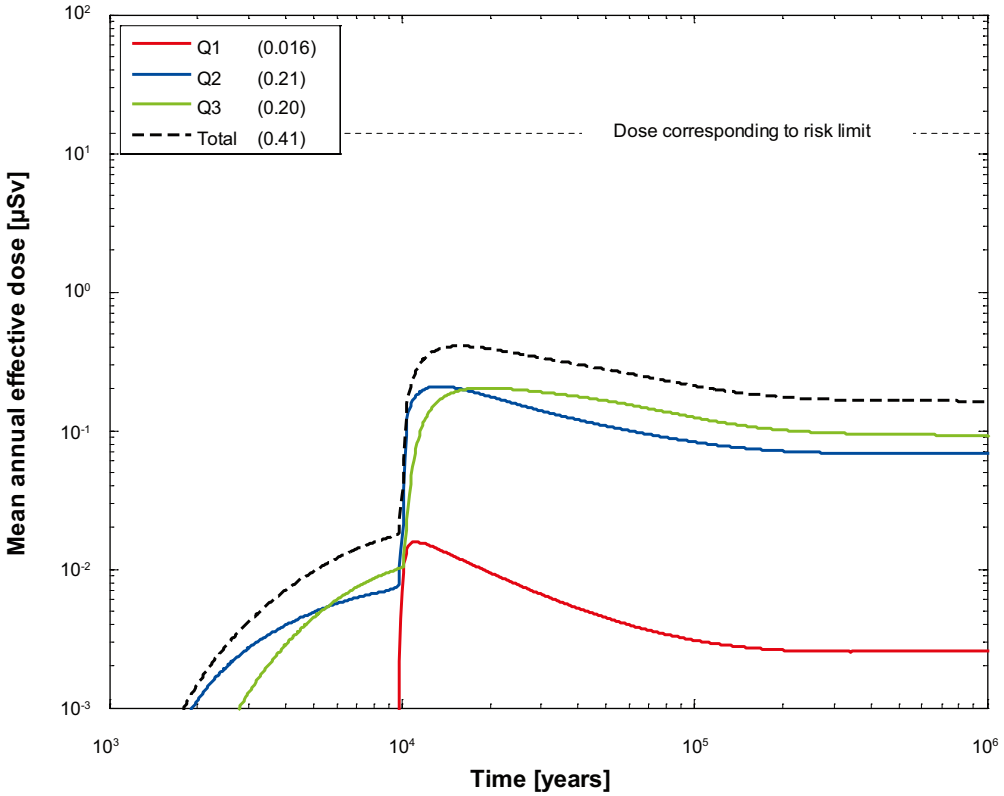

Figure 6-26. *Far-field mean annual effective dose for the probabilistic calculation of the pinhole case, disregarding the effect of spalling. Doses decomposed into Q1, Q2 and Q3. The legend is sorted by peak (in the one-million year period) of the mean annual effective dose. The values in brackets are peak dose in units of μSv.*

6.3.3 Lost swelling pressure in tunnel backfill, "Crown-space"

Deterministic calculations

Hydrogeological case:	Semi-correlated, variant with crown space
Failure time:	0 and 10 000 years
Number of failed canisters:	1
Solubility limits:	Yes
Spalling:	Yes
Number of realisations:	1
Number of nuclides:	37

A deterministic calculation of the hypothetical pinhole failure mode with lost swelling pressure in the tunnel backfill (crown-space) was performed for a canister with an initial penetrating pinhole that grows to a large hole after 10 000 years. Transport out of the canister is assumed to be established 1 000 years after deposition. Median values of geosphere transport data from the variant with crown space of the semi correlated DFN model are used. The number of failed canisters is 1.

Figure 6-27 shows the deterministic near-field dose equivalent releases for the pinhole case with lost swelling pressure in the tunnel backfill and Figure 6-28 shows the same near-field dose equivalent releases decomposed into Q1, Q2 and Q3. The early doses are 1–2 times higher and Q3 is more dominating, as a release path, compared to the pinhole case with an intact tunnel backfill. The doses are at about the same levels after one million years as the pinhole case with intact tunnel backfill (earlier called the pinhole case including the effect of spalling, see Section 6.2.1). Figure 6-29 shows the far-field dose equivalent releases for the pinhole case with lost swelling pressure in the tunnel backfill and Figure 6-30 shows the same releases decomposed into Q1, Q2 and Q3. Early releases of C-14 are considerably higher and contribute more to the total peak dose than in the pinhole case with an intact tunnel backfill.

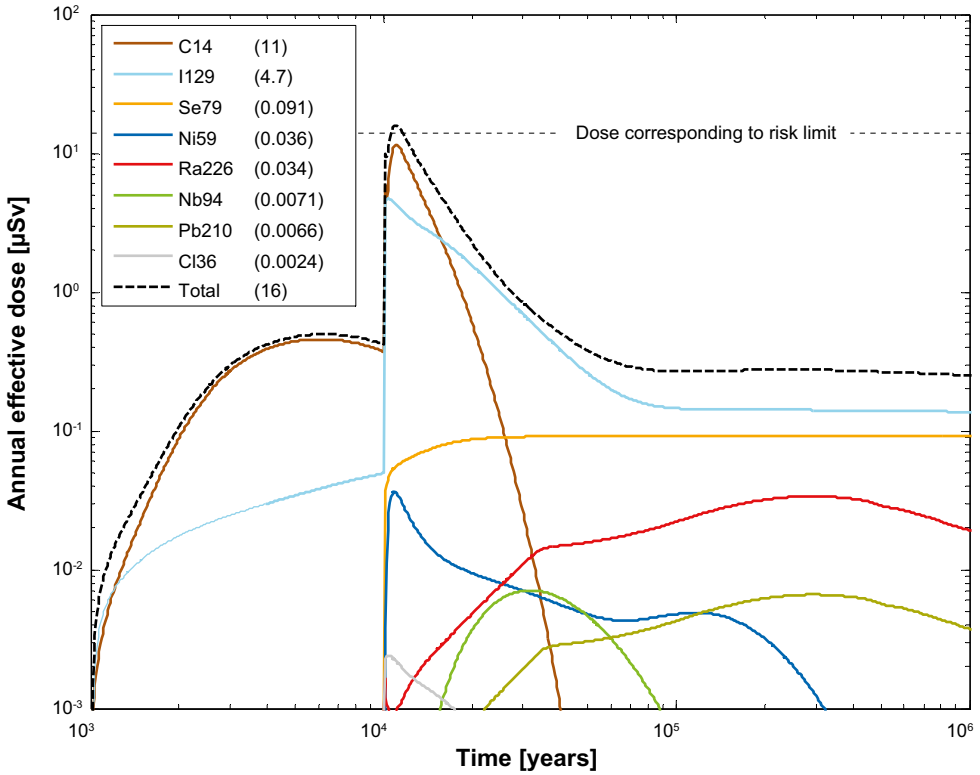

Figure 6-27. *Near-field dose equivalent release for a deterministic calculation of the pinhole case, with lost swelling pressure in tunnel backfill. Summed doses for all release paths (Q1+Q2+Q3). The legend is sorted by peak (in the one-million year period) of the annual effective dose. The values in brackets are peak dose in units of µSv.*

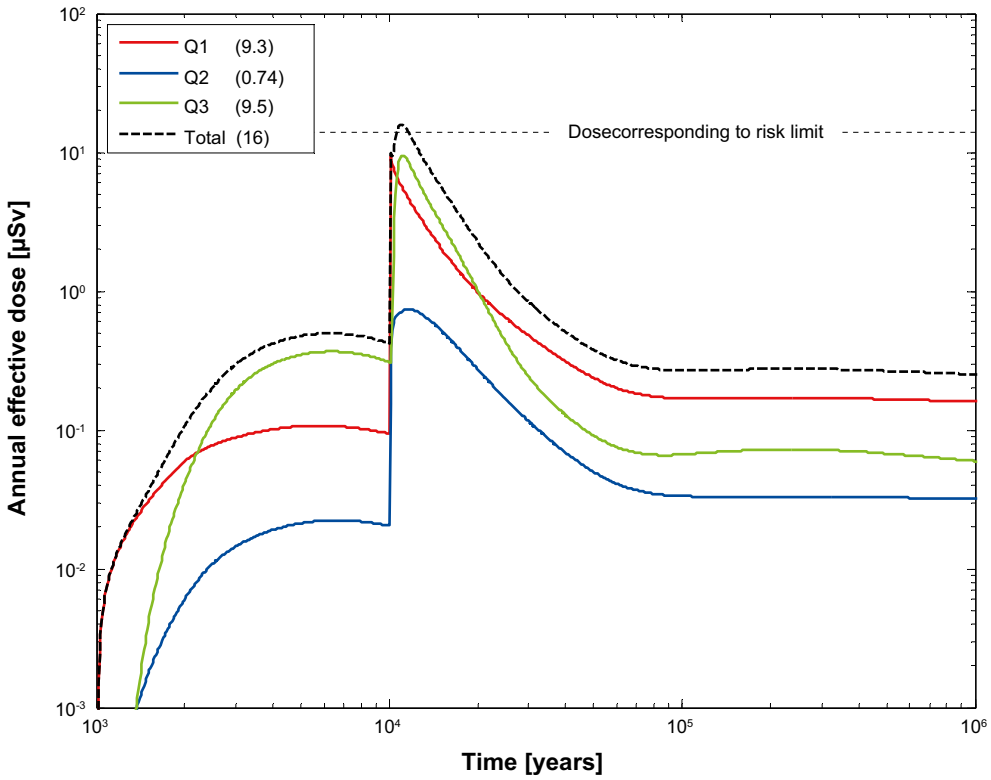

Figure 6-28. *Near-field dose equivalent release for a deterministic calculation of the pinhole case, with lost swelling pressure in tunnel backfill. Doses decomposed into Q1, Q2 and Q3. The legend is sorted by peak (in the one-million year period) of the annual effective dose. The values in brackets are peak dose in units of µSv.*

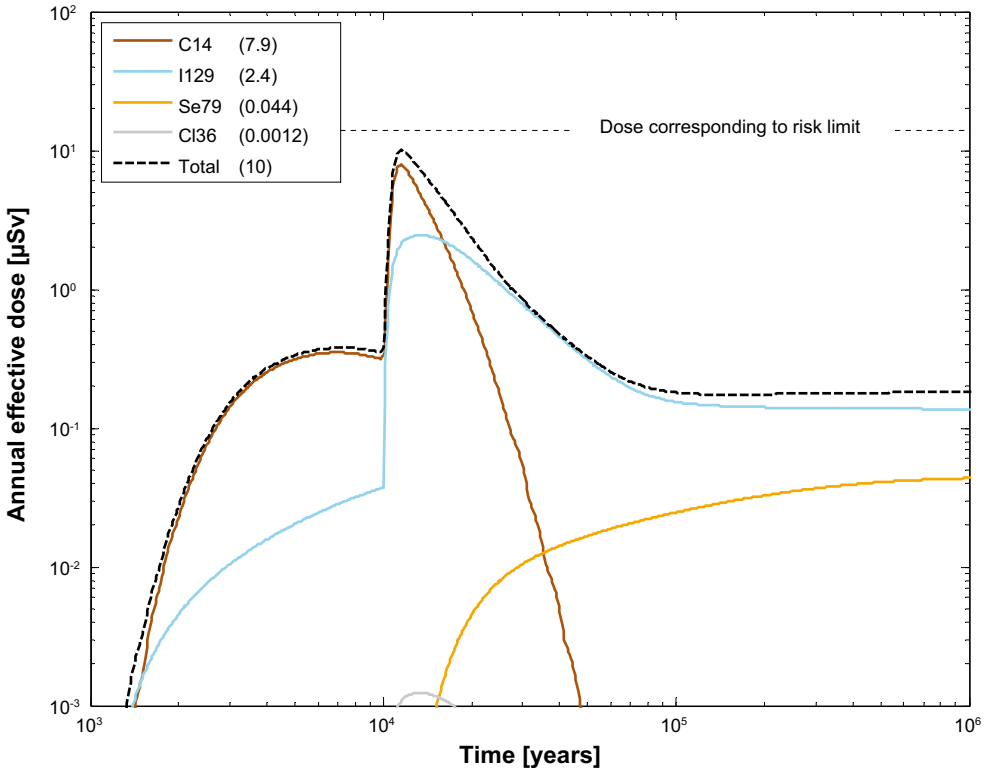

Figure 6-29. *Far-field annual effective dose for a deterministic calculation of the pinhole case, with lost swelling pressure in tunnel backfill. Summed doses for all release paths (Q1+Q2+Q3). The legend is sorted by peak (in the one-million year period) of the annual effective dose. The values in brackets are peak dose in units of µSv.*

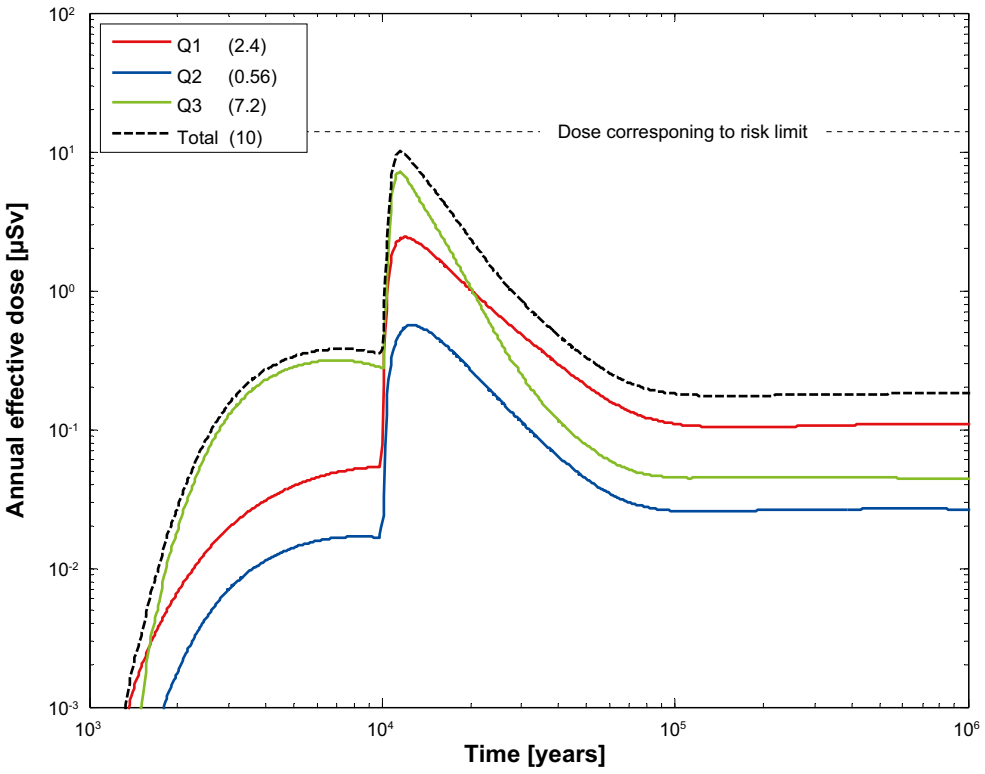

Figure 6-30. *Far-field annual effective dose for a deterministic calculation of the pinhole case, with lost swelling pressure in tunnel backfill. Doses decomposed into Q1, Q2 and Q3. The legend is sorted by peak (in the one-million year period) of the annual effective dose. The values in brackets are peak dose in units of µSv.*

Probabilistic calculations

Hydrogeological case:	Semi-correlated, variant with crown space
Failure time:	0 and 10 000 years
Number of failed canisters:	1
Solubility limits:	Yes
Spalling:	Yes
Number of realisations:	6 916
Number of nuclides:	37

A probabilistic calculation of the hypothetical pinhole failure mode with lost swelling pressure in the tunnel backfill was performed for one canister with an initial penetrating pinhole that grows to a large hole after 10 000 years. Transport out of the canister is assumed to be established 1 000 years after deposition. Geosphere transport parameters from the variant with crown space of the semi correlated DFN model are used. The number of failed canisters is 1. The calculation was run for 6 916 positions and a mean result was calculated over all positions.

Figure 6-31 shows the near-field dose equivalent releases for the pinhole case with lost swelling pressure in the tunnel backfill and Figure 6-32 shows the same near-field dose equivalent releases decomposed into Q1, Q2 and Q3. Peak releases of C-14 are about 3 times higher compared to the pinhole case with an intact tunnel backfill, and Q3 is the dominating release path. In the longer term I-129 and Ra-226 contributes considerably to the total dose. Figure 6-33 shows the far-field dose equivalent releases for the pinhole case with lost swelling pressure in the tunnel backfill and Figure 6-34 shows the same releases decomposed into Q1, Q2 and Q3. Peak releases of C-14 are about 8 times higher compared to the pinhole case with an intact tunnel backfill, and Q3 is the dominating release path. In the longer term, the total dose from the far field is at the same level as in the pinhole case with an intact tunnel backfill.

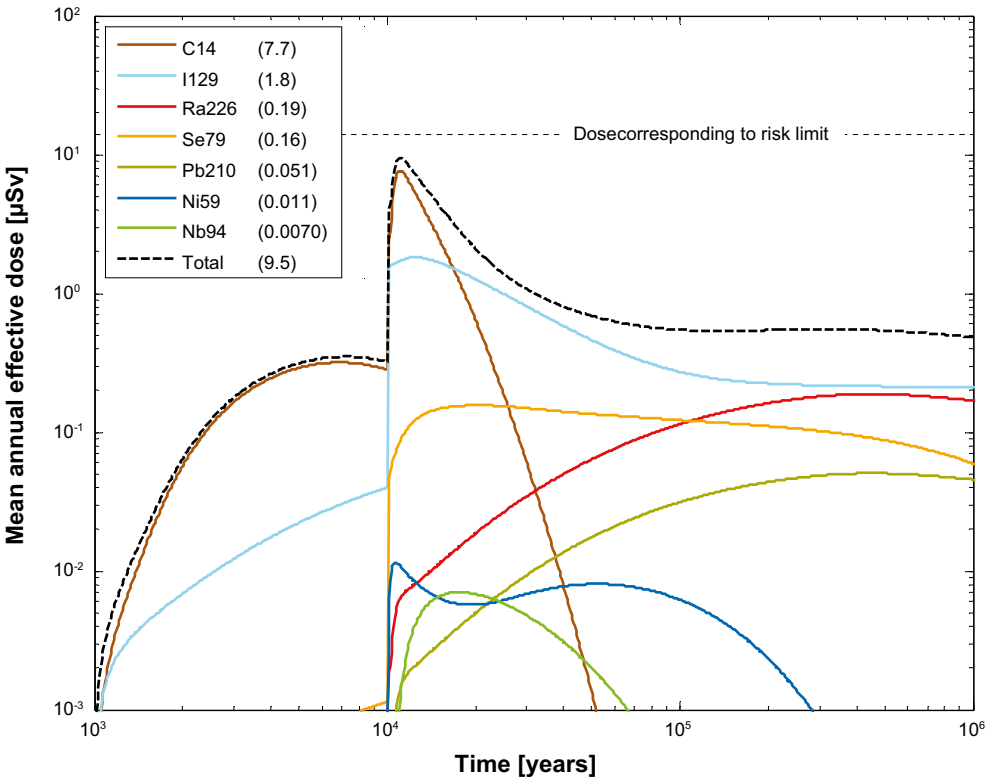

Figure 6-31. *Near-field dose equivalent release for the probabilistic calculation of the pinhole case, with lost swelling pressure in tunnel backfill. Summed doses for all release paths (Q1+Q2+Q3). The legend is sorted by peak (in the one-million year period) of the mean annual effective dose. The values in brackets are peak dose in units of µSv.*

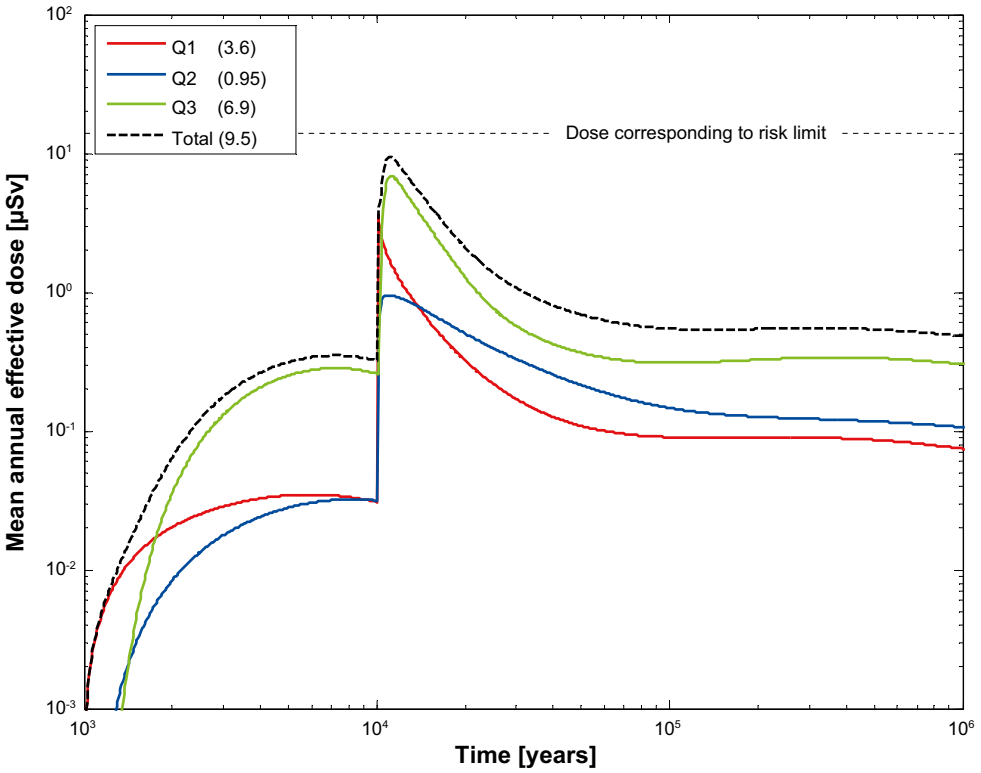

Figure 6-32. *Near-field dose equivalent release for the probabilistic calculation of the pinhole case, with lost swelling pressure in tunnel backfill. Doses decomposed into Q1, Q2 and Q3. The legend is sorted by peak (in the one-million year period) of the mean annual effective dose. The values in brackets are peak dose in units of µSv.*

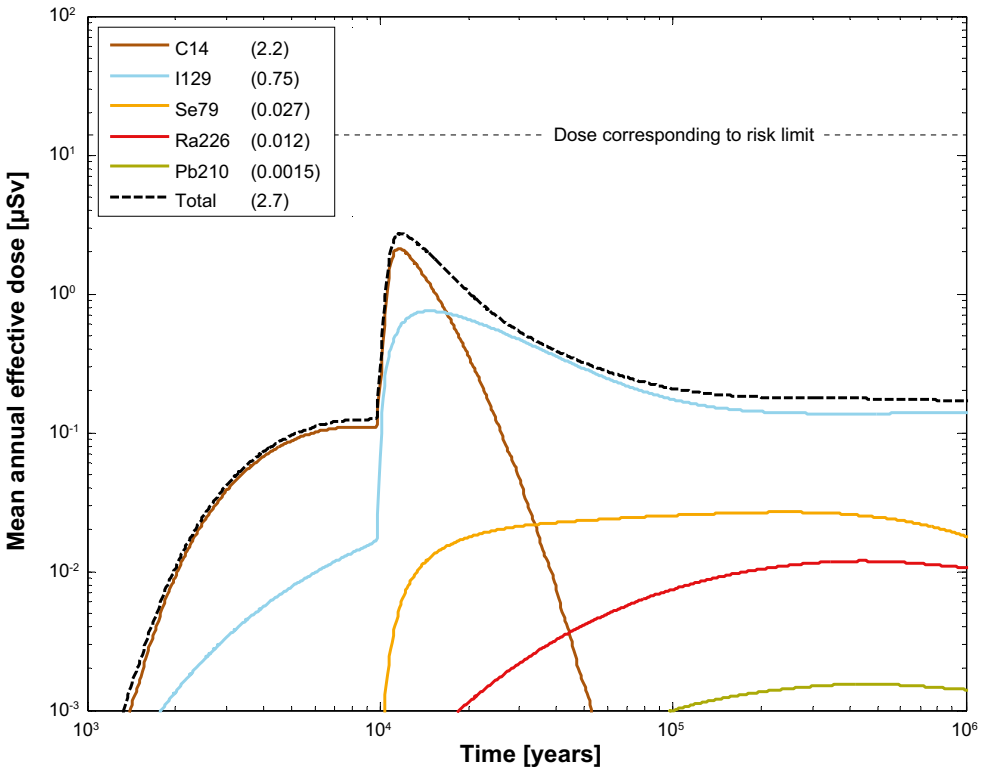

Figure 6-33. *Far-field mean annual mean effective dose for the probabilistic calculation of the pinhole case, with lost swelling pressure in tunnel backfill. Summed doses for all release paths (Q1+Q2+Q3). The legend is sorted by peak (in the one-million year period) of the mean annual effective dose. The values in brackets are peak dose in units of µSv.*

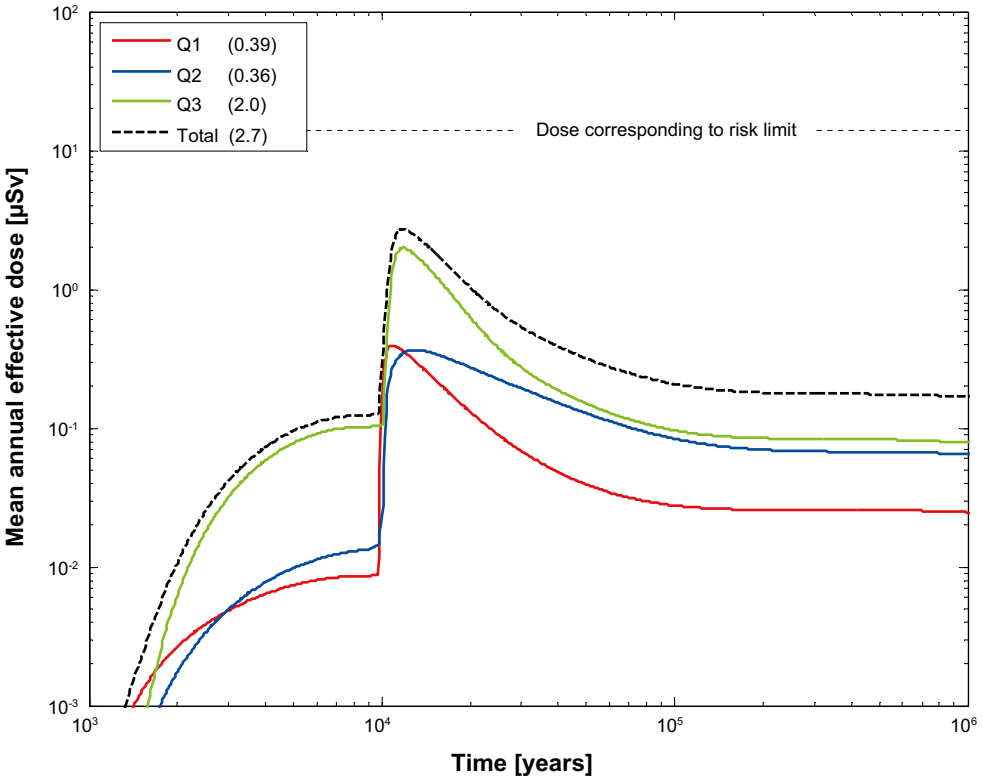

Figure 6-34. *Far-field mean annual effective dose for the probabilistic calculation of the pinhole case, with lost swelling pressure in tunnel backfill. Doses decomposed into Q1, Q2 and Q3. The legend is sorted by peak (in the one-million year period) of the mean annual effective dose. The values in brackets are peak dose in units of µSv.*

6.3.4 Different assumptions regarding EDZ

Hydrogeological case:	Semi-correlated, different variants of EDZ transmissivity
Failure time:	0 and 10 000 years
Number of failed canisters:	1
Solubility limits:	Yes
Spalling:	Yes
Number of realisations:	6 916
Number of nuclides:	37

The excavation damage zone, EDZ, implies a possible release path located in the floor of the deposition tunnel, see Figure 3-1. In the base case (earlier called the pinhole case including the effect of spalling, see Section 6.3.1) is the EDZ transmissivity value 10^{-8} m^2/s. The total near-field dose equivalent releases for the pinhole cases with no EDZ, and EDZ transmissivities of 10^{-6} m^2/s (EDZ 6), 10^{-7} m^2/s (EDZ 7) and 10^{-8} m^2/s (based case) are compared in Figure 6-35 and Figure 6-36 shows the same dose equivalent releases decomposed into Q1, Q2 and Q3. Figure 6-37 and Figure 6-38 show the corresponding far-field dose equivalent releases. Eliminating the EDZ decreases the total doses both from near field and far field. The Q2 and Q3 release paths follows the same pattern and the changes are modest. An increase of the EDZ transmissivity above the base case value of 10^{-8} m^2/s does not increase the doses from Q1.

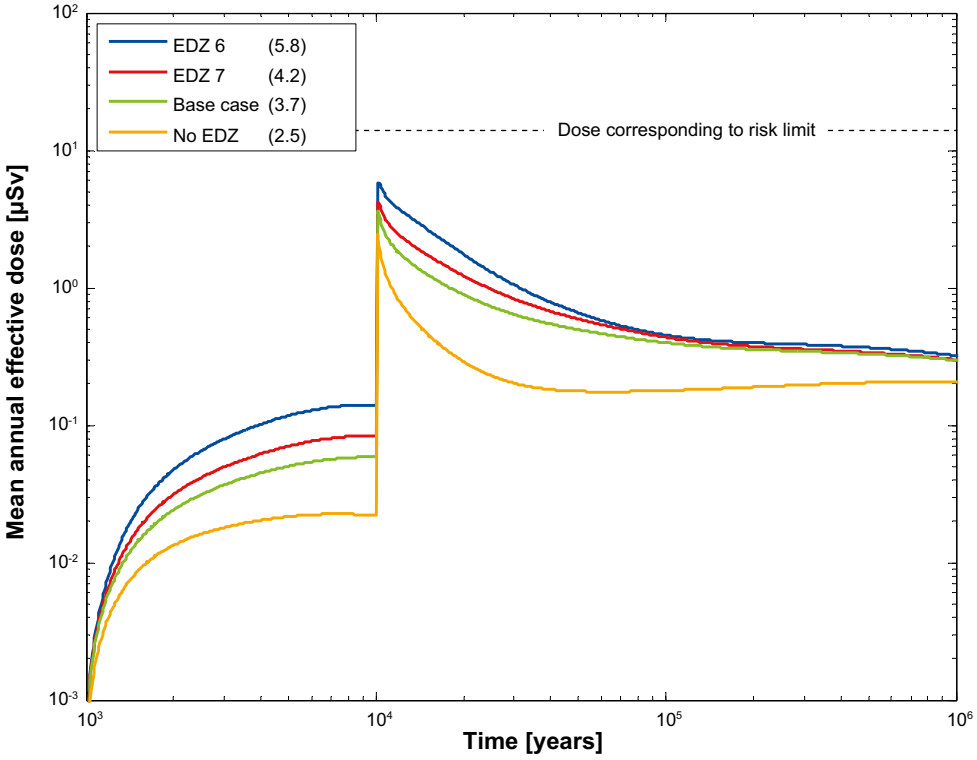

Figure 6-35. *Near-field dose equivalent release for the probabilistic calculation of the pinhole case, comparison between different assumptions regarding EDZ transmissivity (EDZ 6, EDZ 7 and base case correspond to 10^{-6} m^2/s, 10^{-7} m^2/s and 10^{-8} m^2/s, respectively). The legend is sorted by peak (in the one-million year period) of the mean annual effective dose. The values in brackets are peak dose in units of µSv.*

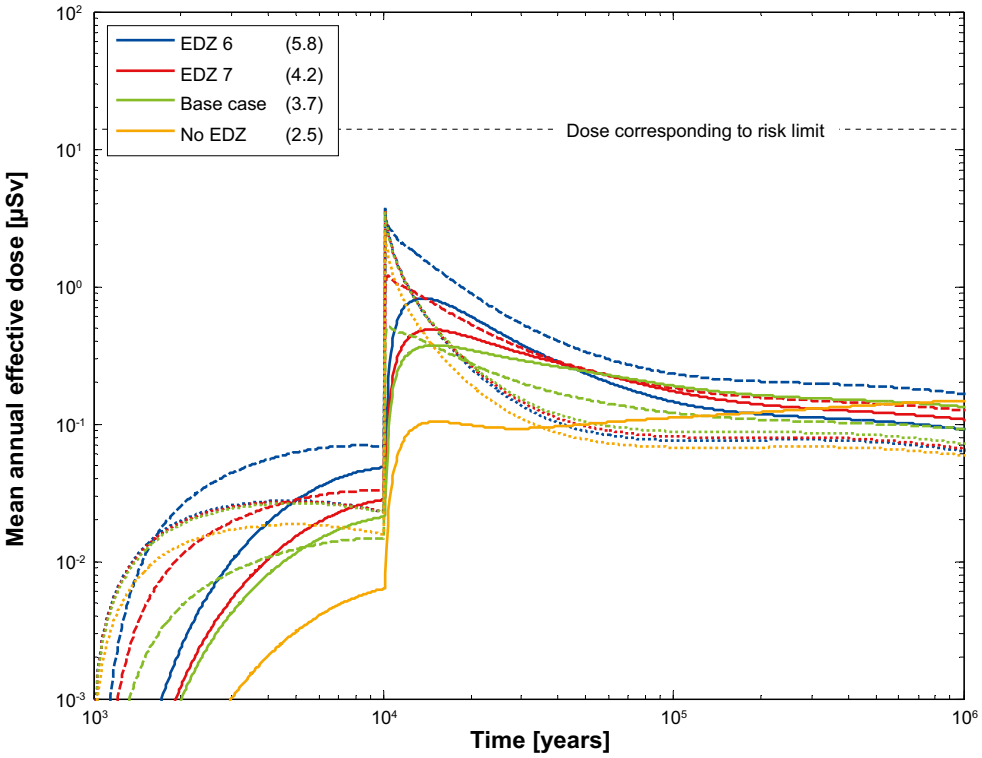

Figure 6-36. *Near-field dose equivalent release for the probabilistic calculation of the pinhole case, comparison between different assumptions regarding EDZ transmissivity (EDZ 6, EDZ 7 and base case correspond to 10^{-6} m^2/s, 10^{-7} m^2/s and 10^{-8} m^2/s, respectively). Doses decomposed into Q1 (dotted lines), Q2 (dashed lines) and Q3 (solid lines). The legend is sorted by peak (in the one-million year period) of the mean annual effective dose. The values in brackets are peak dose in units of µSv.*

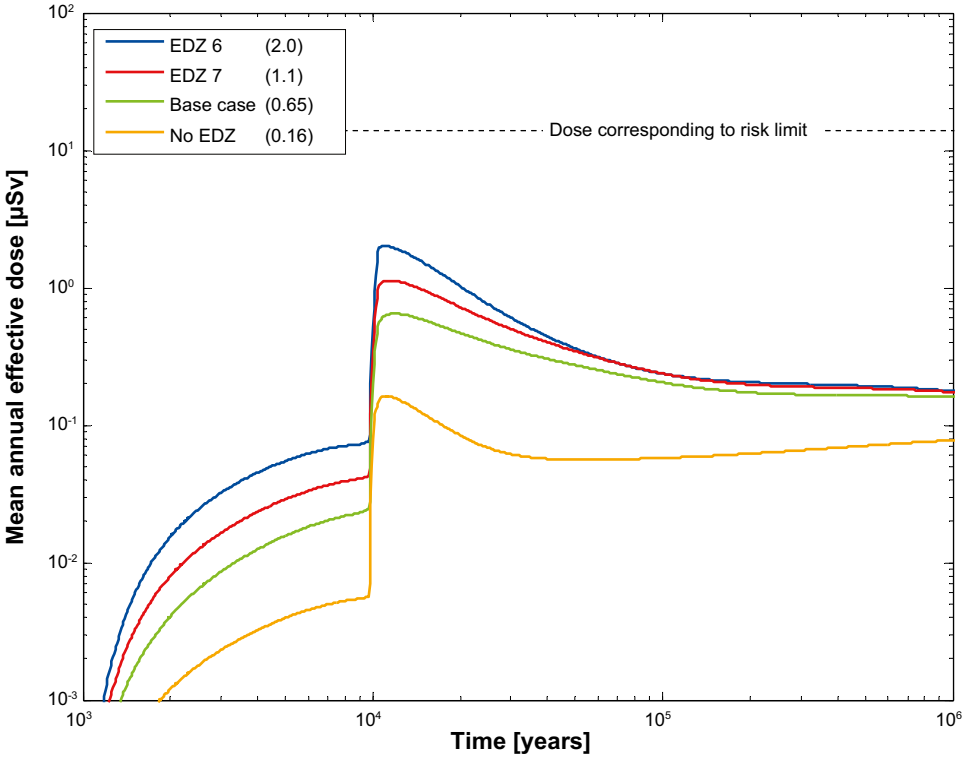

Figure 6-37. *Far-field mean annual effective dose for the probabilistic calculation of the pinhole case, comparison between different assumptions regarding EDZ transmissivity (EDZ 6, EDZ 7 and base case correspond to 10^{-6} m^2/s, 10^{-7} m^2/s and 10^{-8} m^2/s, respectively). The legend is sorted by peak (in the one-million year period) of the mean annual effective dose. The values in brackets are peak dose in units of µSv.*

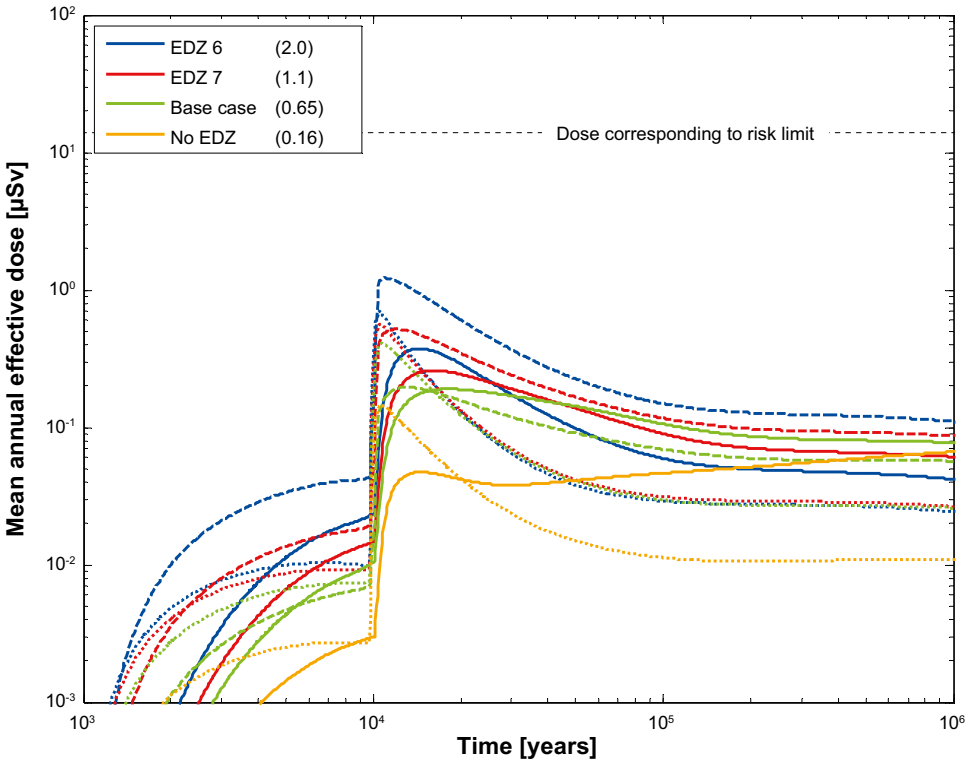

Figure 6-38. *Far-field mean annual effective dose for the probabilistic calculation of the pinhole case, comparison between different assumptions regarding EDZ transmissivity (EDZ 6, EDZ 7 and base case correspond to 10^{-6} m^2/s, 10^{-7} m^2/s and 10^{-8} m^2/s, respectively). Doses decomposed into Q1 (dotted lines), Q2 (dashed lines) and Q3 (solid lines). The legend is sorted by peak (in the one-million year period) of the mean annual effective dose. The values in brackets are peak dose in units of µSv.*

6.3.5 Summary and conclusions for the growing pinhole scenario

Several variants of the growing pinhole scenario have been calculated to examine sensitivities to various transport conditions. The results are summarised in Figure 6-39 and Figure 6-40. The crown space case, in which tunnel backfill has compacted with a resulting gap at the tunnel crown, dominates the releases. Comparing variants with different excavation damage zone (EDZ) transmissivity, shows that the releases decrease with decreasing EDZ transmissivity. Thermally induced spalling is assumed to occur in the walls of the deposition holes and decrease the transport resistance in the interface between the buffer and the rock. The effect of of spalling is assessed by a case that does not include spalling. The maximum dose is about 4 times lower in the case that does not include spalling.

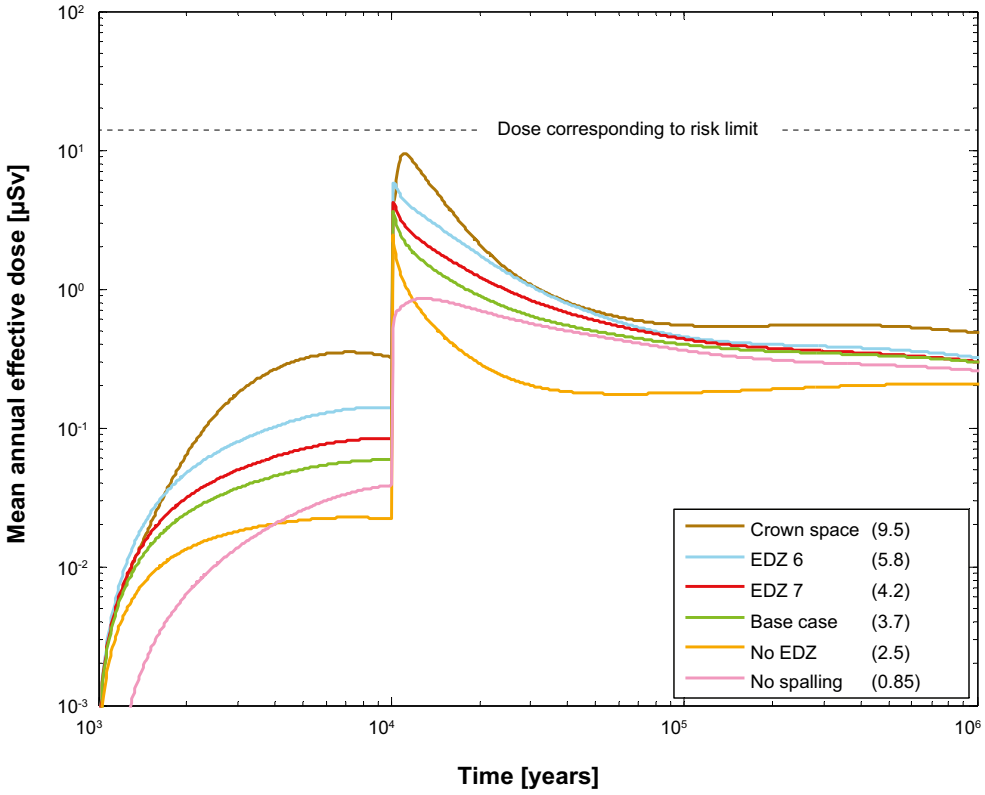

Figure 6-39. *Near-field mean annual effective dose equivalent for the probabilistic calculations of the pinhole base case and cases with no spalling, with different assumptions regarding EDZ and with a crown space in the deposition tunnel. The legend is sorted by peak (in the one-million year period) of the mean annual effective dose. The values in brackets are peak dose in units of μSv. (EDZ 6, EDZ 7 and base case correspond to a transmissivity of 10^{-6} m^2/s, 10^{-7} m^2/s and 10^{-8} m^2/s, respectively).*

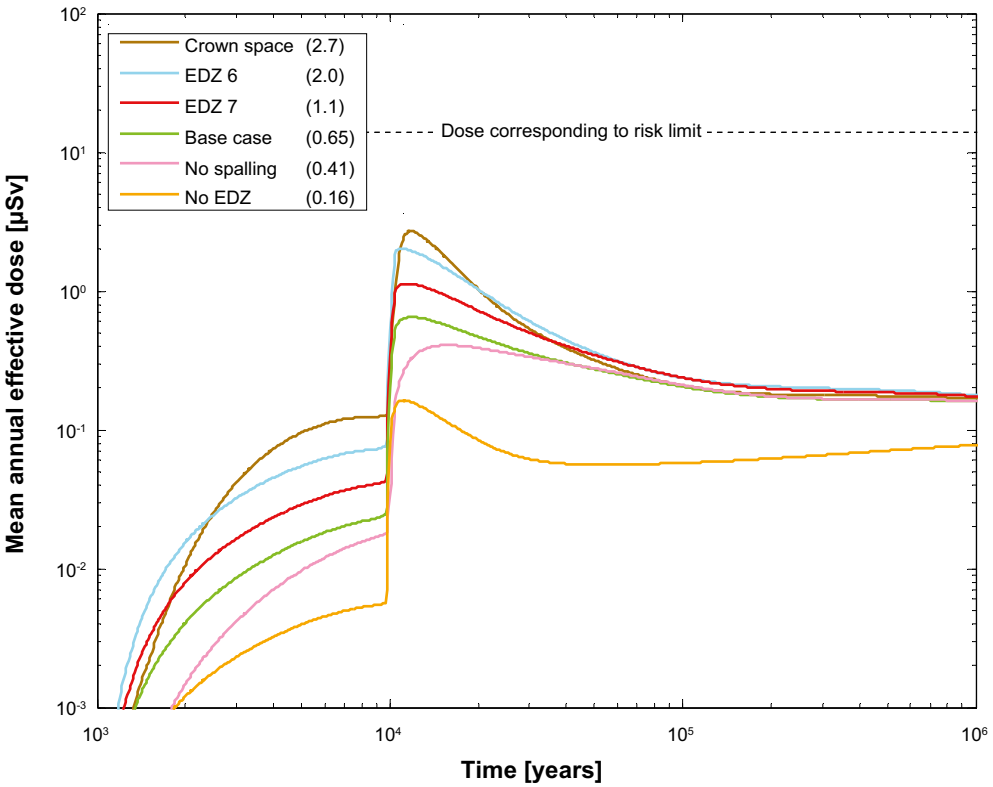

Figure 6-40. *Far-field mean annual effective dose for the probabilistic calculations of the pinhole base case and cases with no spalling, with different assumptions regarding EDZ and with a crown space in the deposition tunnel. The legend is sorted by peak (in the one-million year period) of the mean annual effective dose. The values in brackets are peak dose in units of µSv. (EDZ 6, EDZ 7 and base case correspond to a transmissivity of 10^{-6} m^2/s, 10^{-7} m^2/s and 10^{-8} m^2/s, respectively).*

6.4 Exploration of geosphere barrier performance using the growing pinhole case

The growing pinhole failure case provides a convenient hypothetical scenario to illustrate various sensitivities related to the geosphere barrier. To that end, deterministic values are used for initial radionuclide inventories and for all near-field and far-field parameters not related to flow. However, because the location of the defective canister is not known in this scenario, effective dose results are calculated as mean values over all potential locations of the defective canister. That is, full spatial variability in flow-related parameters is included.

COMP23 and MARFA are used here for the near-field and far-field transport. Recall that MARFA supports spatial variability both along and among transport pathways, thus making it possible to address aspects of geosphere barrier performance that cannot be addressed with FARF31.

Specific sensitivities studied include:

- The role of advective transport in tunnels and soils.
- The role of sorption in tunnels and soils.
- The effect of a crown space formed by compaction of backfill in repository tunnels.
- Sensitivity to assumed fracture transmissivity in excavation damage zones.
- Implications of assuming one or multiple transport pathways per deposition hole.

6.4.1 Input parameters

The sensitivity study described in this section assumes steady groundwater flow corresponding to the temperate period. ConnectFlow ptb- and ptv-files for the reference case flow model and key variants provide the relevant information for use in COMP23 and MARFA, as shown in Table 6-1. The semi-correlated DFN model is used.

Table 6-1. Temperate period flow fields used. Unless otherwise noted, the ptv-/ptb-files include all deposition holes with one pathway per hole.

ptv/ptb file	Description
fs_Q*m*_2000_pline_merged (with *m* = 1,2,3)	Base cases
fs_crown_Q1_2000_pline_merged	Crown space variant, Q1 release
fs_crown_start_Q3_2000_pline_merged	Crown space variant, Q3 release*
fs_maxedz_7_Q*m*_2000_pline_merged (*m* = 1,2,3)	EDZ transmissivity of 10^{-7} m^2/s
fs_maxedz_6_Q*m*_2000_pline_merged (*m* = 1,2,3)	EDZ transmissivity of 10^{-6} m^2/s
fs_noedz_Q*m*_2000_pline_merged (*m* = 1,3)	No EDZ
fs_newtop25_Q1_2000_pline10_merged	Q1 base case for top† 25 % of deposition holes with 10 pathways per hole

* Q3 pathways for the crown space variant were defined by releasing particles into the crown space, to be consistent with COMP23 definition of near-field release for that variant. For all other variants, Q3 pathways were defined by releasing particles in the tunnel 1 m above the deposition hole.

† Based on initial velocity.

The ptv-files provide by ConnectFlow were modified for two combinations of flow variants and transport assumptions. The ConnectFlow ptv-files include pathline segments that pass through tunnels and soils represented as Continuum Porous Medium (CPM) in addition to fractured rock segments. The CPM segments contribute nothing to the flow-related transport resistance (F), but do contribute to the advective travel time t_w. Thus, for variant modelling cases designed to quantify the contribution of tunnels and soils by neglecting travel distances in those regions, CPM segments were removed to prepare new ptv-files. In addition, for Q3 cases that include the CPM segments, the tunnel segments between the release point and the first fracture encountered were removed to enforce consistency between the ptv-file and the near-field release calculation, which defines Q3 release as flux into the fracture intersecting the tunnel nearest to the deposition hole.

The sensitivity studies described in this section were undertaken before SR-Site transport parameters were finalised. Consequently, SR-Can or preliminary SR-Site values are used for radionuclide inventories, near-field transport parameters, and far-field retention parameters. Details are provided in Appendix H.

6.4.2 Reference case

The reference case for this section assumes no sorption in the tunnels and no sorption in the soils. The CPM parts of the pathway, however, are included in the travel time. It is important to note that the inclusion of the CPM parts of the pathway in the advective travel time is in contrast to calculations presented elsewhere in this report. The flow-channelling factor is set to unity to represent no channelling within individual fractures. Colloids are not included.

The pinhole release scenario considers failure of one canister at an unknown deposition hole. To calculate the expected value of release, all canisters are forced to fail and an aggregate release is calculated. The expectation value for release is then calculated by dividing the aggregate release by the number of emplaced canisters. Note that deposition holes that do not have a connected pathway to the geosphere have zero release by definition. In addition, deposition holes for which a ConnectFlow pathway could not be defined because of numerical failure in the ConnectFlow particle tracking calculation (stuck particles, represented by OKFLAG > 0) are also assumed to result in no release. This assumption is based on the observation that stuck particles in the ConnectFlow particle tracking algorithm are caused by nearly stagnant pathways, and these pathways would not contribute significantly

to the expected release. Deposition holes with the full perimeter criterion or effective full perimeter criterion flags set (FPC = 1) or (EFPC > 5) were assumed to not have emplaced canisters. That is, these contribute nothing to the aggregate release and were also not counted in the number of canisters emplaced.

Comparison of release path

Far-field releases expressed as equivalent doses are shown in Figure 6-41 for the three release paths. The Q1 release path results in the largest peak release, followed by Q2 and Q3. Peak release is almost an order of magnitude larger for the Q1 path compared with the Q3 path. The Q2 and Q3 paths result in flatter release histories compared with the Q1 path. At late times, differences between the release paths are much smaller, with the Q2 paths resulting in the largest releases.

Details for the Q1 release path

Total far-field and near-field releases expressed as effective doses for the Q1 release path are shown in Figure 6-42. The far-field geosphere reduces peak dose by a factor of approximately 20. The dose at 1 million years is reduced by a factor of approximately 4 by the geosphere. Observable in Figure 6-42 is an increasing trend in the near-field release, which does not occur in the far field. This behaviour is attributable to ingrowth of Ra-226 at near-field release, which is then retarded in the far field.

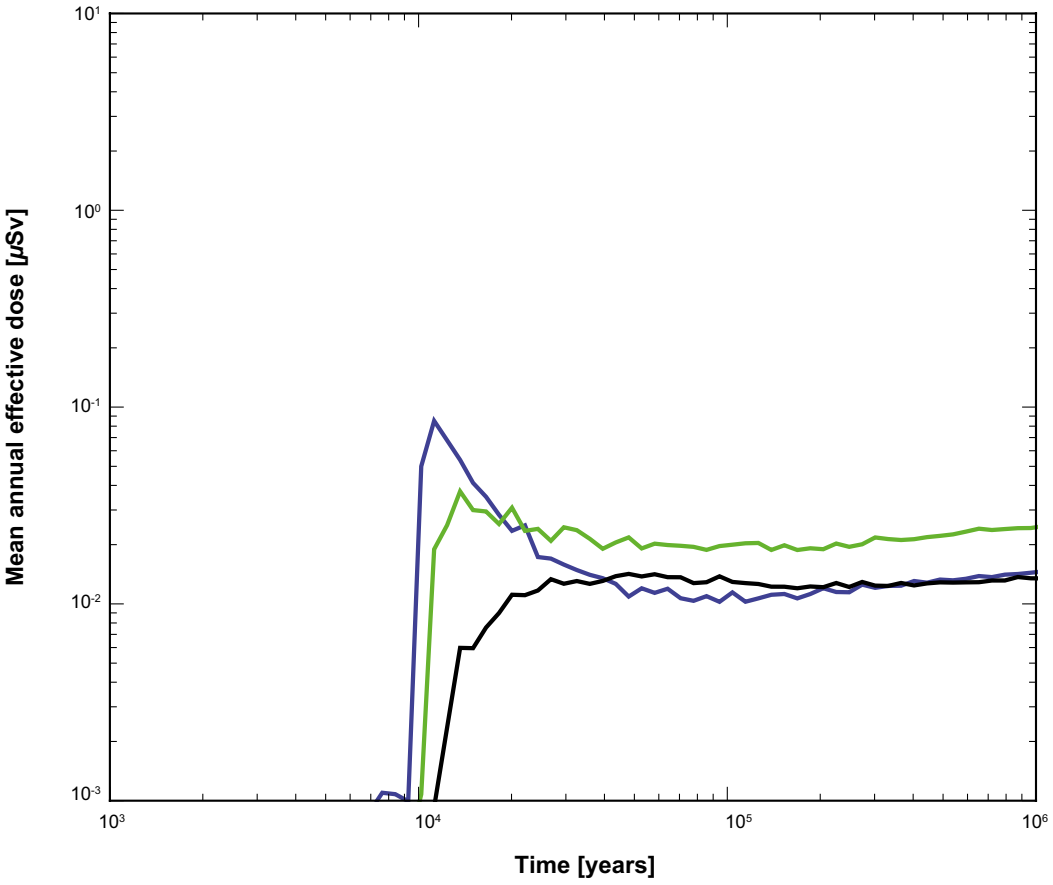

Figure 6-41. *All-nuclides far-field releases expressed as effective dose for the pinhole scenario and different release paths. Expected values are shown for all deposition holes versus time for Q1 (blue), Q2 (green), and Q3 (black) release paths.*

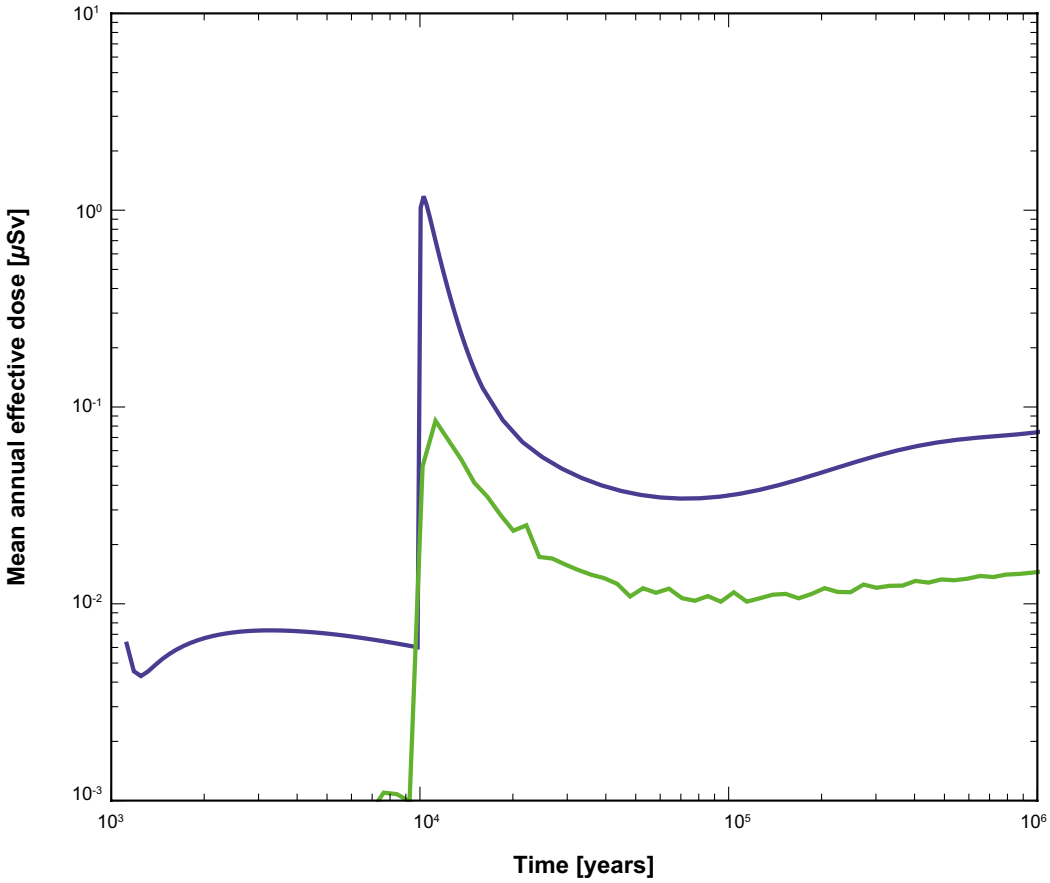

Figure 6-42. *All-nuclides near-field and far-field releases expressed as effective dose for the pinhole scenario, Q1 release path. Expected values are shown for all deposition holes versus time: near-field dose equivalent release (blue) and far-field mean annual effective dose (green).*

Trajectories for the 2 % of pathways contributing the most by total instantaneous far-field release are shown in Figure 6-43. Each trajectory is colour-coded by maximum all-nuclides instantaneous dose as shown in the figure legend. Canister locations are shown as red or green dots. Red signifies that the deposition hole is not connected to the biosphere by a Q1 pathway. Green dots represent holes that contribute to transport through the Q1 pathway. It is noted that the majority of canisters have no connected Q1 pathway. Among those with connected pathways, the majority of radionuclide dose comes from a relatively small fraction of pathways.

Near-field and far-field releases for the 12 radionuclides contributing most to far-field release are shown in Figure 6-44. It is clear that I-129, C-14, and Ra-226 account for almost all the far-field and near-field releases. Far-field attenuation factors range from about two orders of magnitude for Th-230 and Pa-231 to less than an order of magnitude for Se-79.

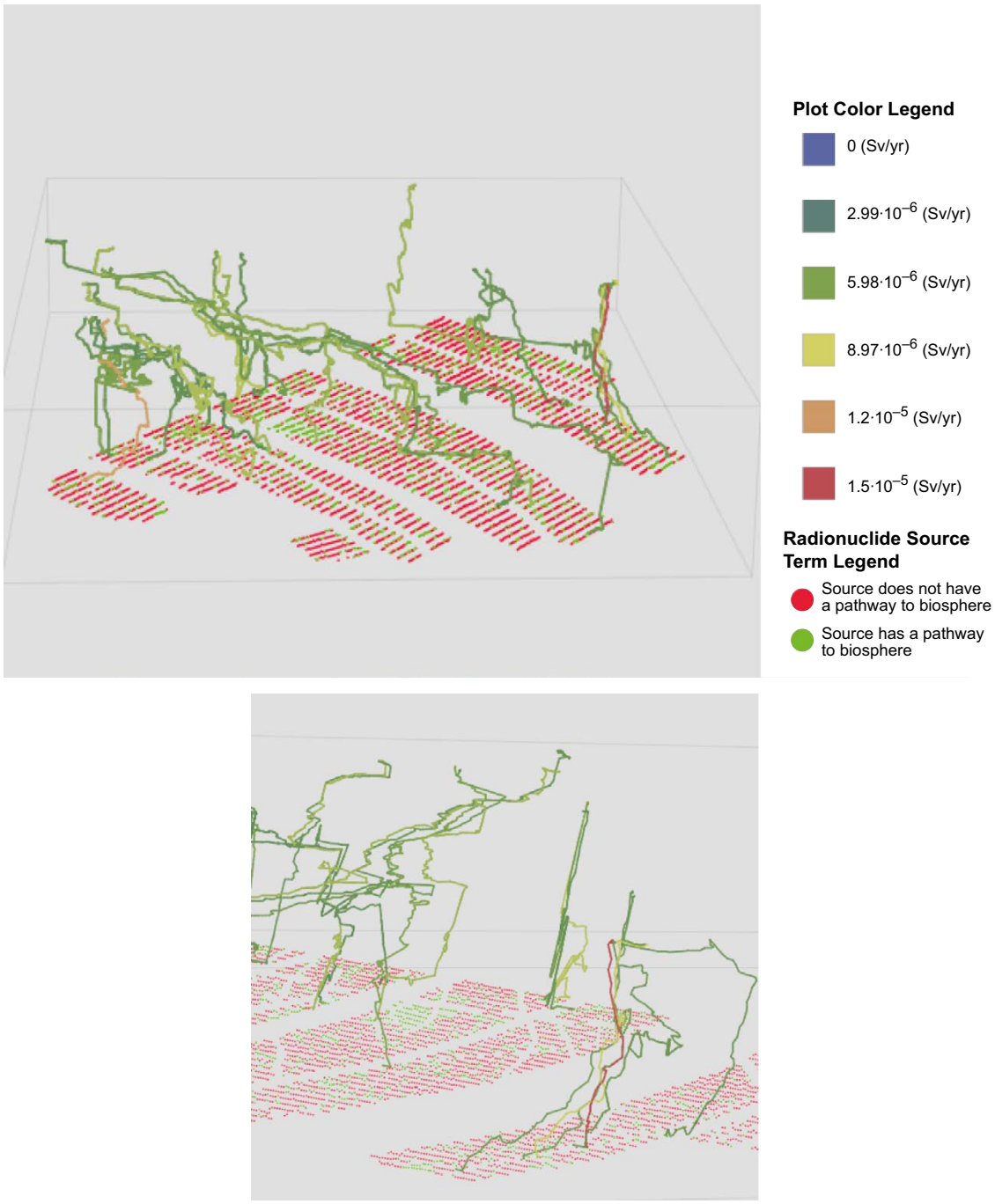

Figure 6-43. *Pathway trajectories for pinhole scenario, Q1 release path for the 2 % of pathways contributing the most to the ensemble release. The top image shows the entire repository. The bottom image is a detail from the larger image (rotated). Trajectories and starting locations are colour-coded as shown in the legend.*

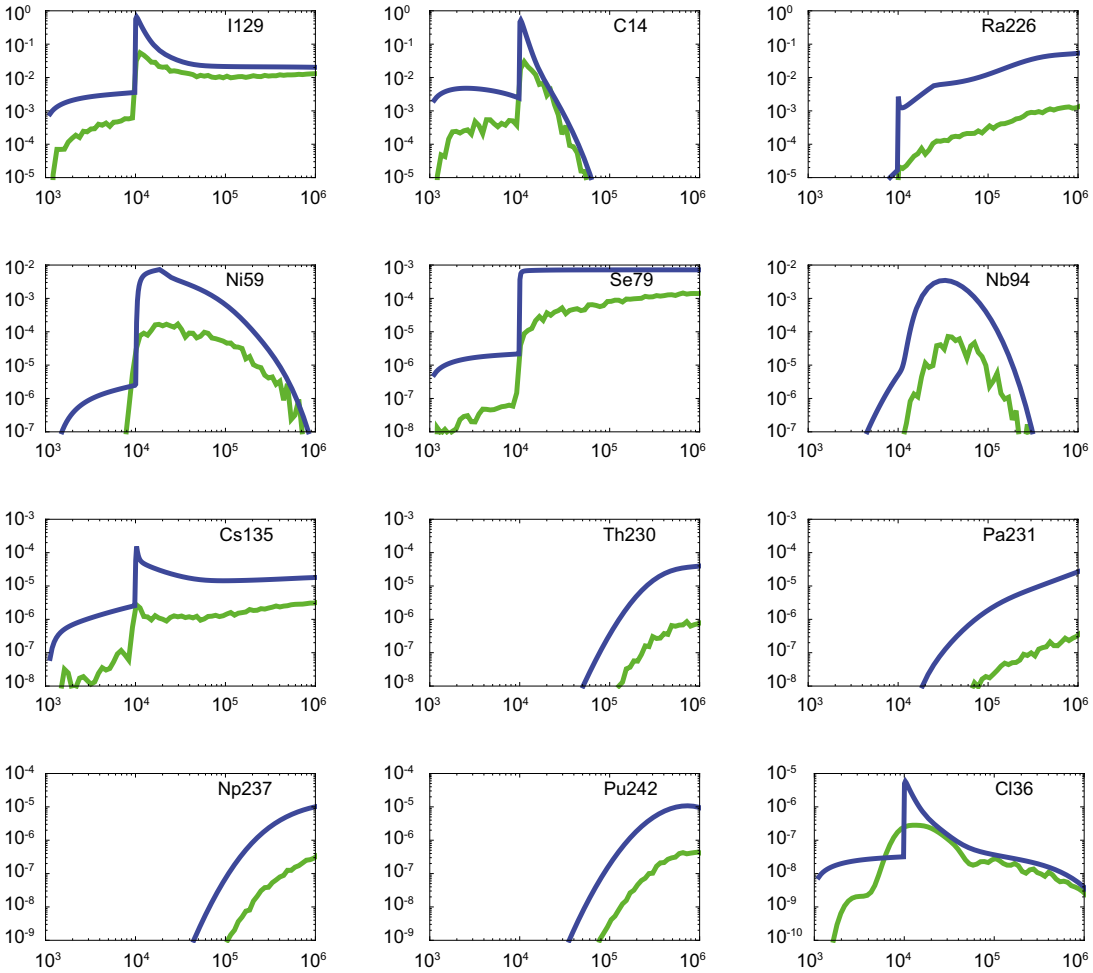

Figure 6-44. *Near-field (blue) and far-field (green) releases for the 12 radionuclides contributing most to the far-field release for the Q1 release path. Units are μSv/yr on the y-axis and year on the x-axis for each plot. Note the scale on the y-axis is different for different radionuclides.*

Details for the Q2 release path

Total far-field and near-field releases expressed as effective dose in Sv/yr for the Q2 release path are shown in Figure 6-45. The far-field geosphere reduces peak dose by a factor of approximately 5. The dose at 1 million years is reduced by a smaller factor. Near-field and far-field releases for the top six contributors (by far-field release) are shown in Figure 6-46. As is the case for the Q1 path, I-129, C-14, and Ra-226 are the largest contributors. The geosphere attenuates the release by factors of approximately 5 for I-129, 4.7 for C-14, and 40 for Ra-226.

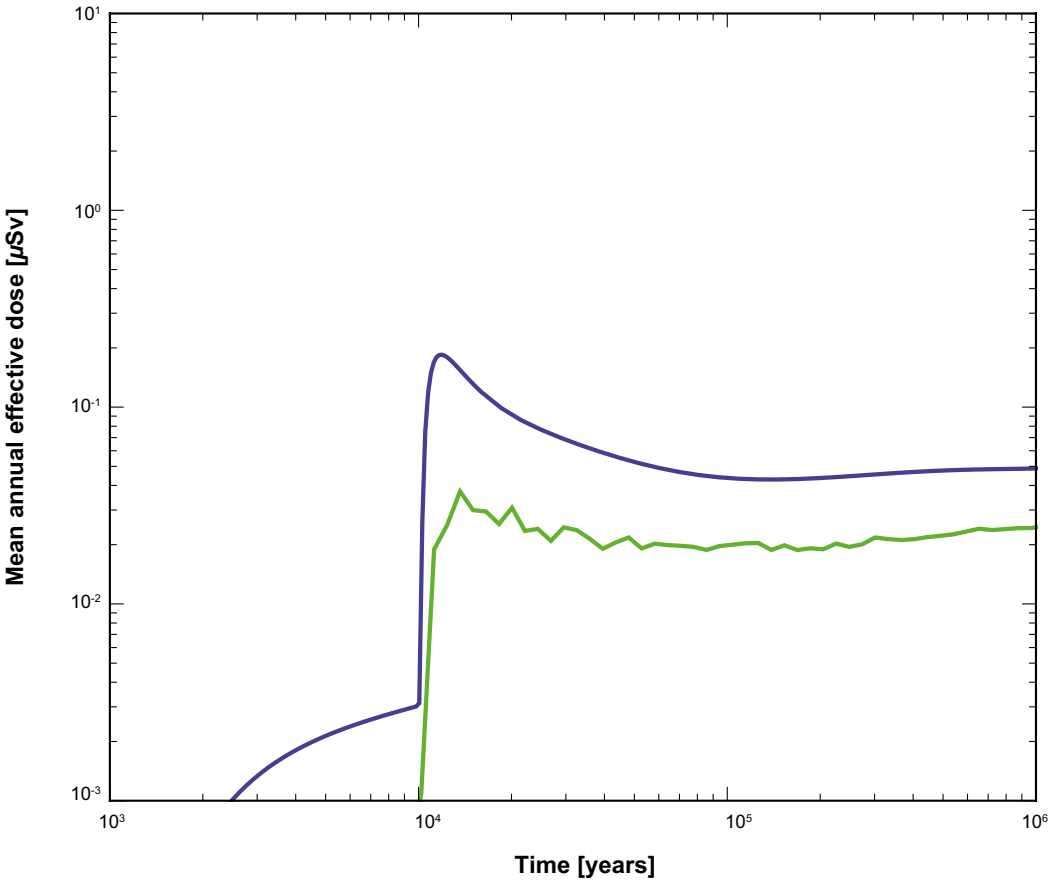

Figure 6-45. *All-nuclides near-field and far-field releases expressed as effective dose for the pinhole scenario, Q2 release path. Expected values are shown for all deposition holes versus time: near-field dose equivalent release (blue) and far-field mean annual effective dose (green).*

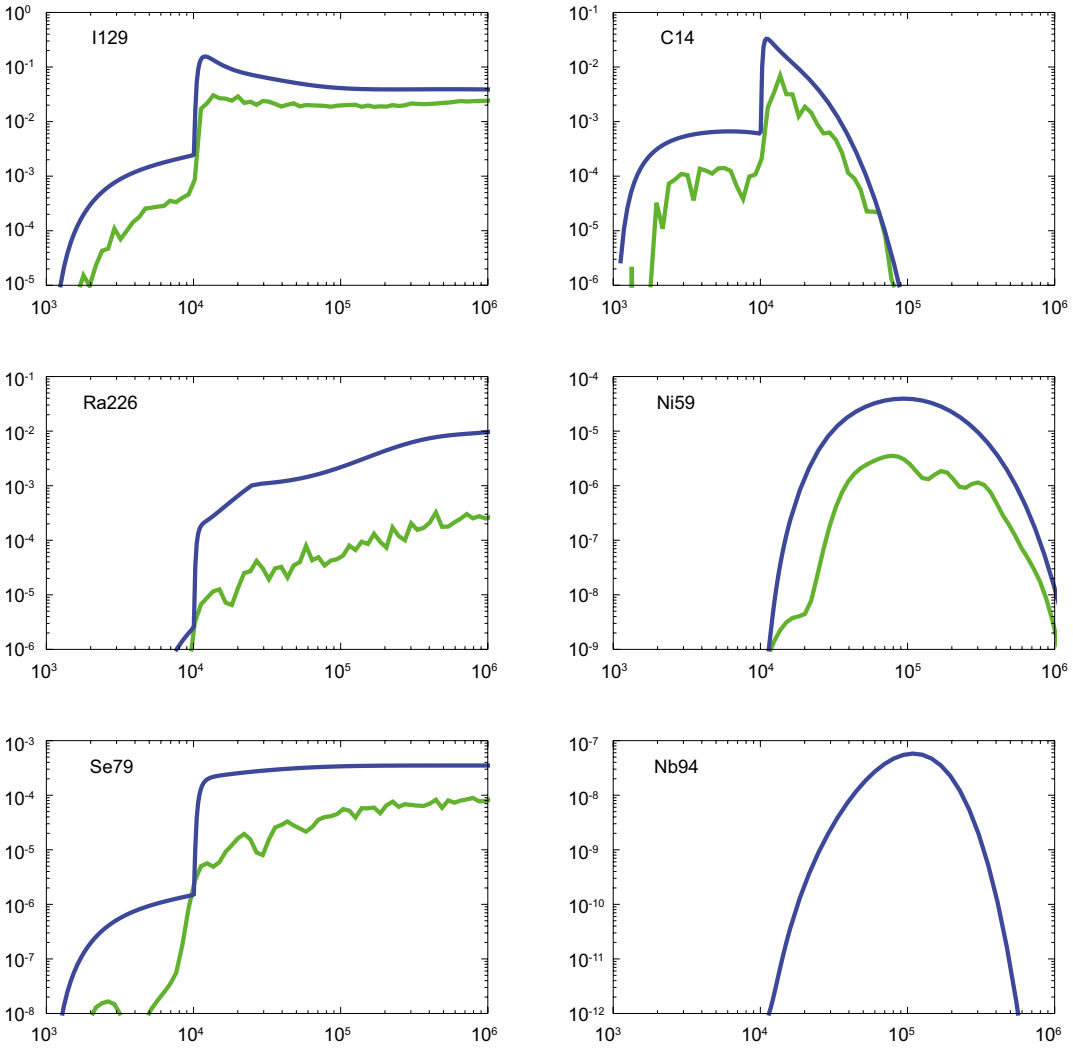

Figure 6-46. *Near-field (blue) and far-field (green) releases for the top six contributors (by far-field release) for the Q2 release path. Units are µSv/yr on the y-axis and year on the x-axis for each plot. Note the scale on the y-axis is different for different radionuclides.*

Details for the Q3 release path

Total far-field and near-field releases expressed as effective dose for the Q3 release path are shown in Figure 6-47. The far-field geosphere does not represent a significant barrier for this release path. However, the near-field Q3 release is smaller than that of the Q1 and Q2 paths.

Trajectories for the 2 % of pathways contributing the most by total instantaneous far-field release are shown in Figure 6-48. Each trajectory is colour-coded by the maximum all-nuclides instantaneous dose as shown in the figure legend. Canister locations are shown as red or green dots. Red signifies that the deposition hole is not connected to the biosphere by a Q3 pathway or that the contribution from that pathway is negligible. Green dots represent holes that contribute to transport through the Q3 pathway. It is noted that in contrast to the Q1 path, many pathways contribute to dose for the Q3 path, primarily because the repository tunnels provide pathways to the fracture network backbone (see detail in lower left of Figure 6-48).

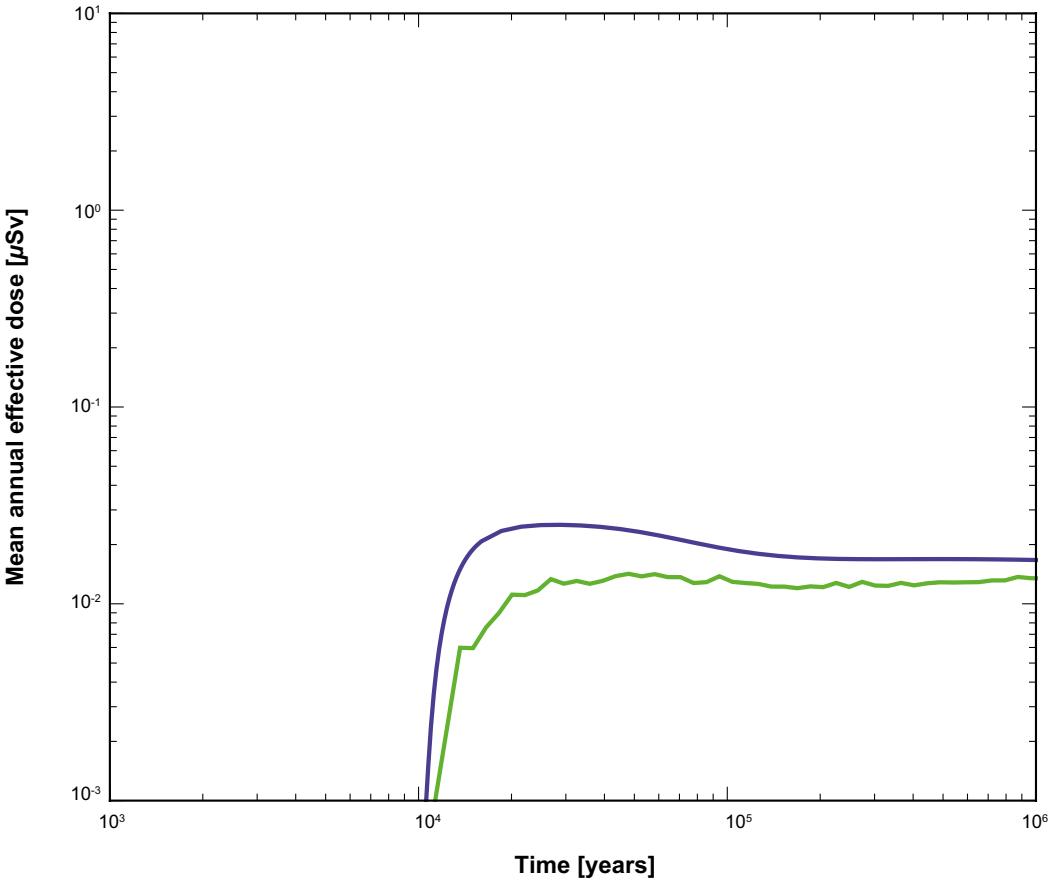

Figure 6-47. *All-nuclides near-field and far-field releases expressed as effective dose for the pinhole scenario, Q3 release path. Expected values are shown for all deposition holes versus time near-field dose equivalent release (blue) and far-field mean annual effective dose (green).*

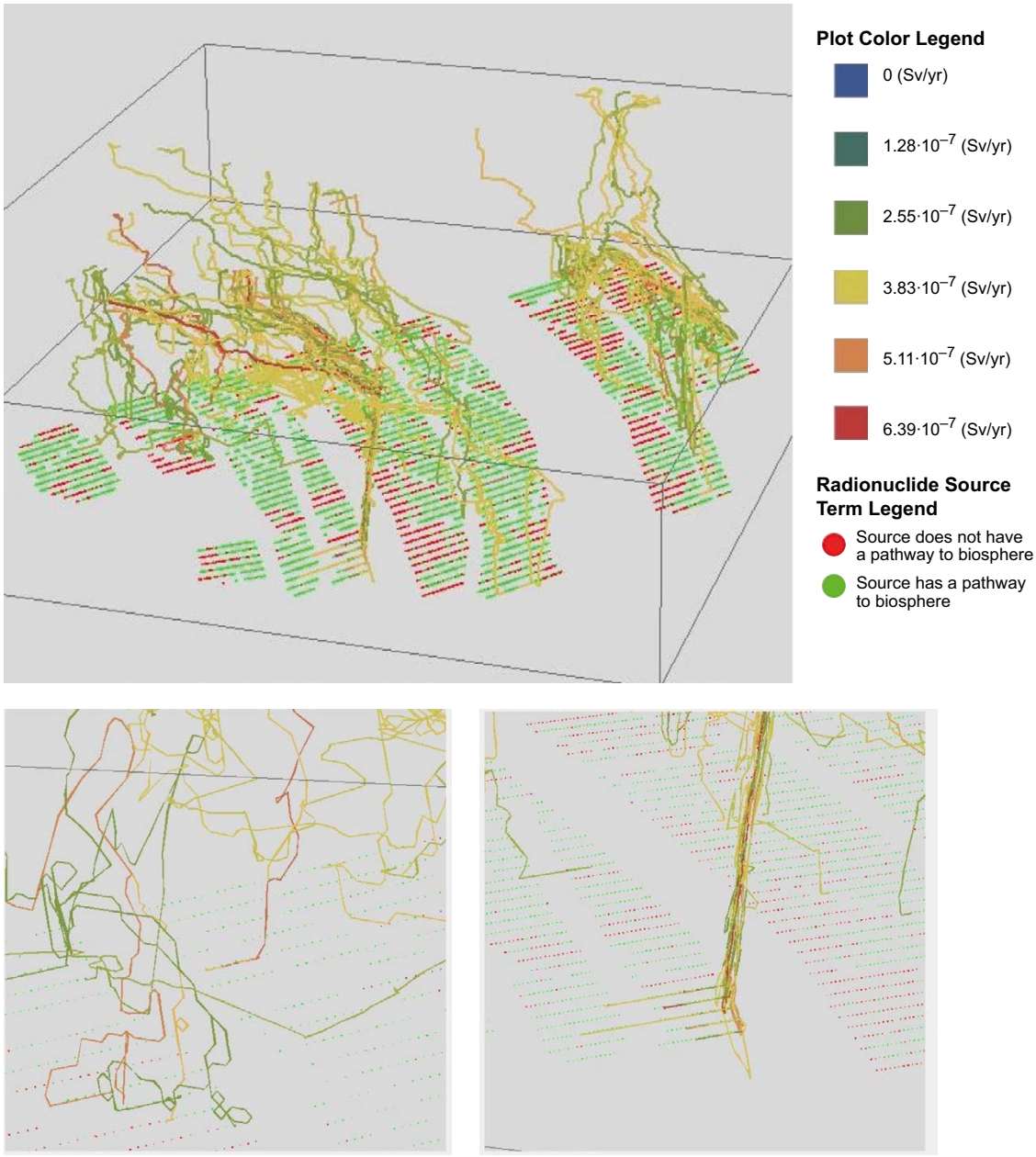

Figure 6-48. *Pathway trajectories for pinhole scenario, Q3 release path for top 2 % of pathways by contribution to the all-nuclides release. The top image shows the entire repository. The bottom images are details from the larger image. Trajectories and starting locations are colour-coded as shown in the legend. Note the MARFA calculations used to calculate the dose rates shown in this figure used COMP23 outputs that were later found to be based on a ConnectFlow ptb-file that contained erroneous values for one parameter. These results should be considered qualitative only.*

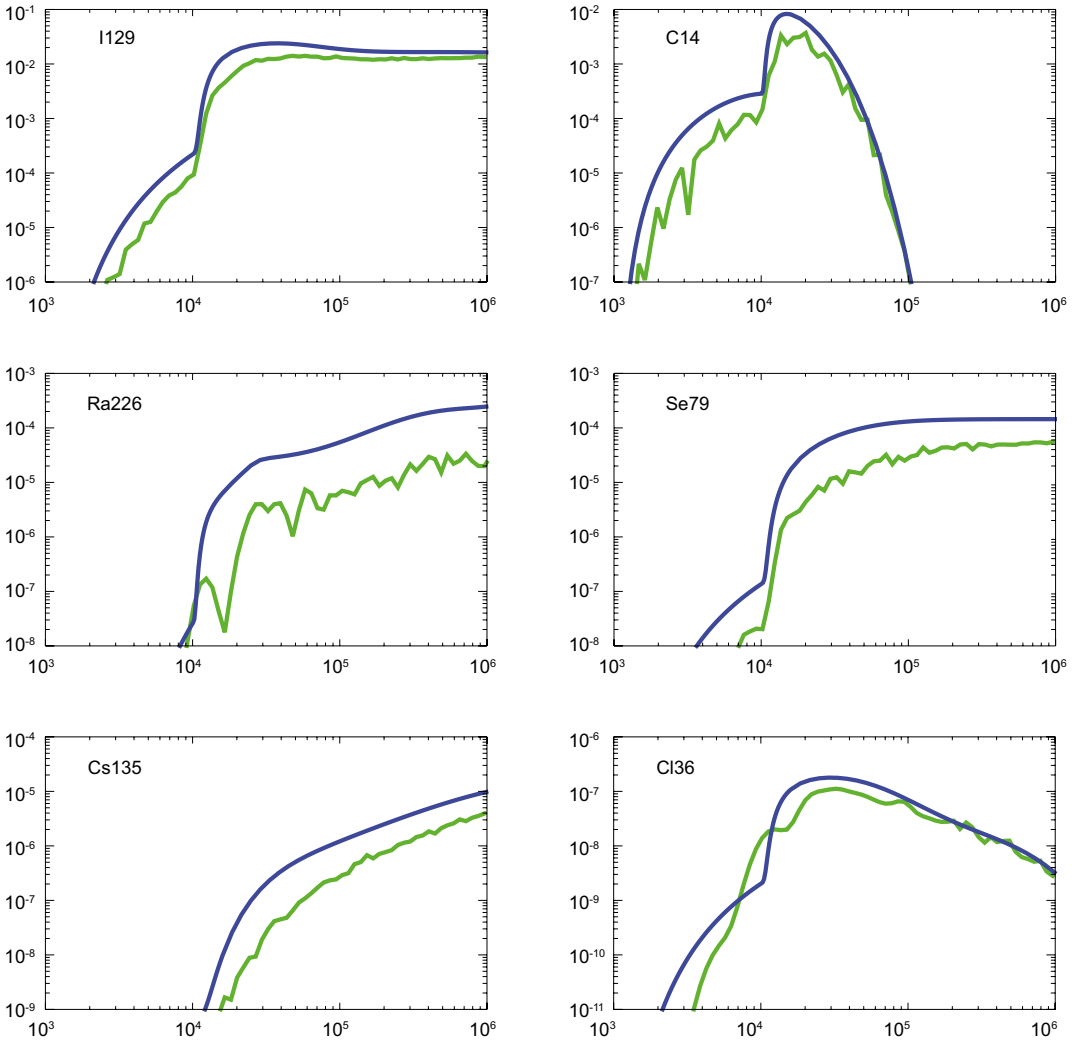

Figure 6-49. *Near-field (blue) and far-field (green) releases for the top six contributors (by far-field release) for the Q3 release path. Units are µSv/yr on the y-axis and year on the x-axis for each plot. Note the scale on the y-axis is different for different radionuclides.*

6.4.3 Issues related to the probabilistic nature of the calculations

Variability about the mean

The pinhole failure scenario presumes one failed canister at an unknown location. Results presented thus far and elsewhere in this report have been for the expected value of discharge averaged over all starting locations. Some locations will contribute much to the expected value and some will contribute little or nothing. For example, approximately 81 % of deposition holes have no connected pathway to the biosphere and thus contribute nothing to the mean value for the Q1 path. To understand the variability about the mean, selected percentiles in the discharge were calculated at each time. Results for the Q1 release path are shown in Figure 6-50 (99th, 95th, 90th, and 85th percentiles in green and mean curve in blue).

More than half of the trajectories have zero release because of no release path. Thus, the median release is zero and is not shown. The peak of the 90th percentile is close to the peak of the mean, although the two peaks occur at different times. Thus, there is a less than 10 % chance that the pinhole release scenario from one package will have a value greater than the peak of the mean. As already noted, there is a greater than 80 % chance that the release will be exactly zero.

The shapes of the curves in Figure 6-50 are markedly different for the different percentiles. It is apparent that most of the deposition holes (90th and smaller percentiles) are either not connected to pathway or are connected to a pathway that provides sufficient retardation to allow key radionuclides to decay. Thus the peak of the mean is strongly influenced by the contributions from the few pathways that exhibit little retardation.

Another way to analyse the range of possible doses delivered to the biosphere is to plot the exceedance probability versus dose (Figure 6-51). This plot is based on a 1-million year interval. There is approximately a 2.7 % probability that the maximum dose rate delivered to the biosphere will exceed 10^{-6} Sv/yr at some time in the 1-million year interval. For 10^{-5} Sv/yr dose, the exceedance probability is 4×10^{4}.

Multiple pathways for each deposition hole

The base case has one pathway per release point. The effect of this assumption was assessed by considering a variant case with 10 Q1 pathways per release point. This calculation was limited to the 25 release points contributing most to the total dose in the base case. Results are shown in Figure 6-52. The blue curve is near-field release. The solid green curve is the base case far-field release. The dashed green curve is the far-field release for the case with 10 pathways per release point. Although transport from any single release point may be different depending on whether 1 or 10 pathways are represented, these differences are averaged out in the ensemble.

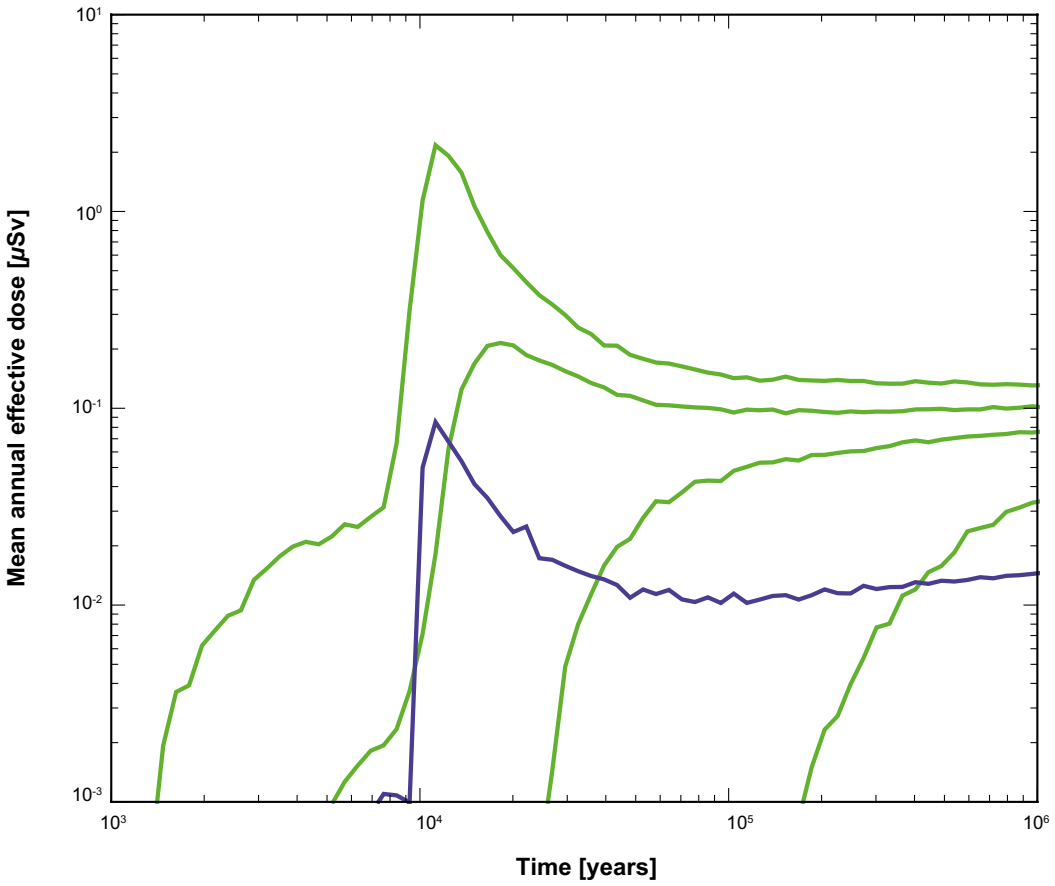

Figure 6-50. *Mean (blue curve) and selected percentiles (green curves) for pinhole Q1 release. Shown are the 99th, 95th, 90th, and 85th percentiles.*

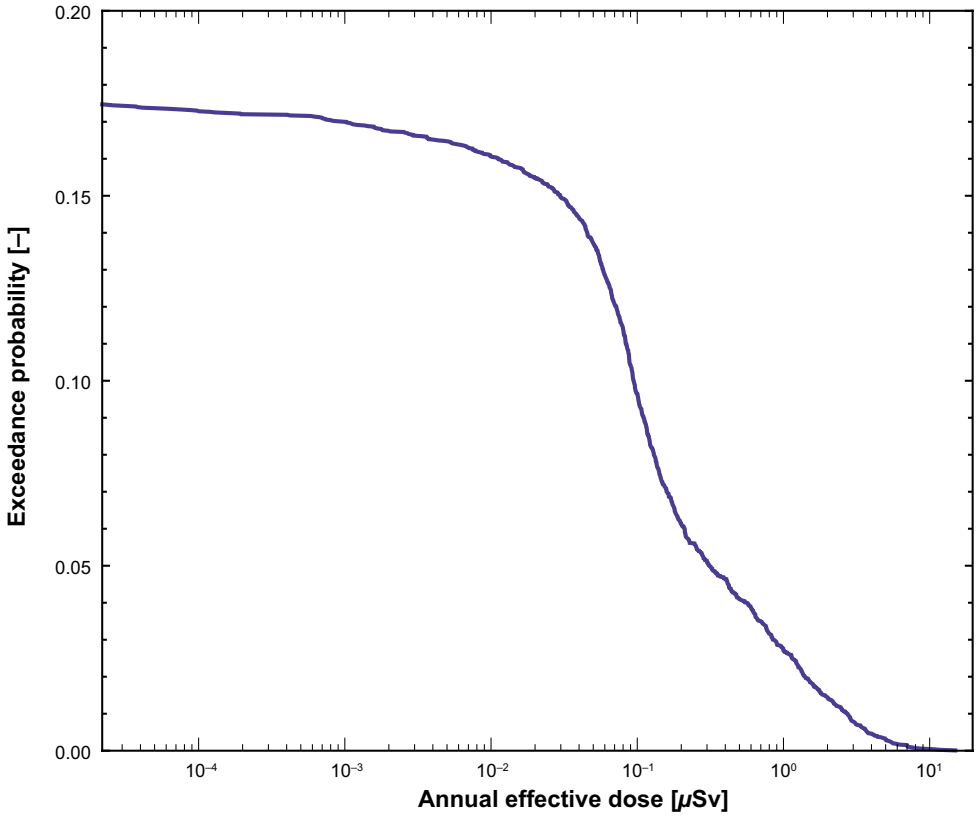

Figure 6-51. *Exceedance probability for a given dose rate (μSv/yr) for the pinhole Q1 release. A 1-million year time window was used to calculate the exceedance probability. Thus, for a given dose rate, the exceedance probability is the probability that the dose rate exceeds that value at some time during the 1-million year period.*

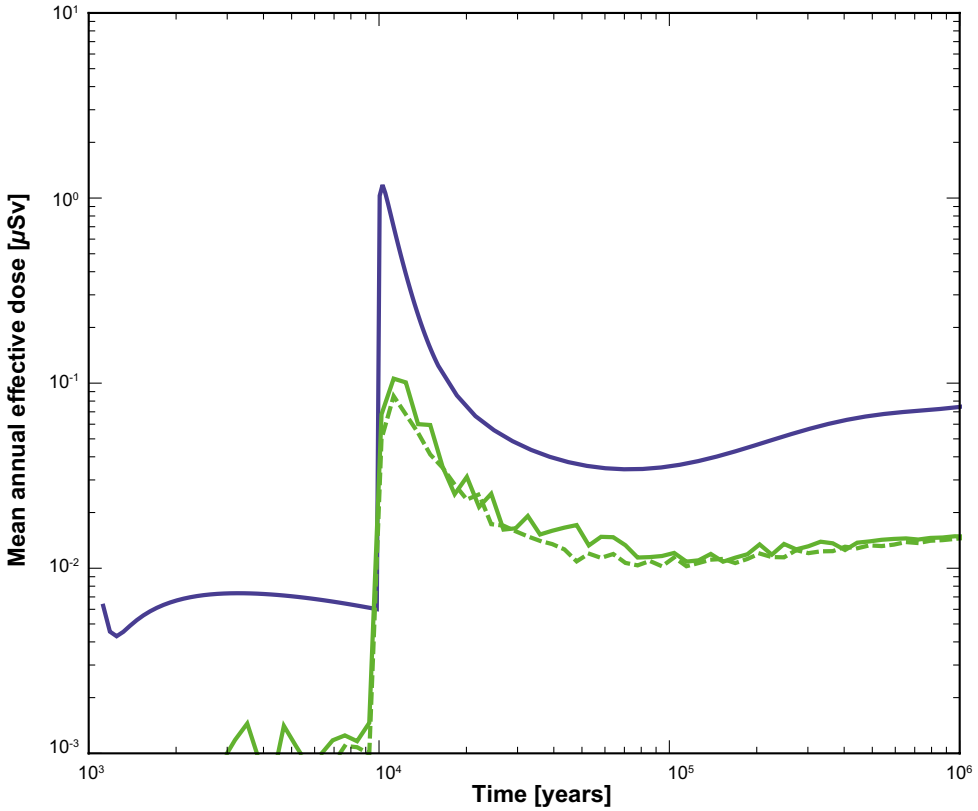

Figure 6-52. *Effect of having multiple Q1 pathways per release point. The blue curve is near-field release. The solid green curve is the base case far-field release. The dashed green curve is the far-field release for the case with 10 pathways per release point.*

6.4.4 Exploration of barrier function of geosphere components

Transport and retention in soils and tunnels

The reference case includes soils and tunnel segments in the transport pathway, but assigns these segments zero equilibrium partitioning coefficients for all elements. Thus, the delay introduced by a non-zero advective travel time through soils and tunnels is accounted for, but retardation of sorbing elements is ignored. Effects of the soils and tunnels are summarised in Figure 6-53 for the Q1 path. The blue curve is near-field release and the green curve is the base case. The pink curve neglects the effect of the CPM parts of the pathways (i.e., tunnels and soils). In calculating the pink curve, CPM segments were removed from the base case ptv-file and a new ptv-file was generated. The black curve uses the base case ptv-file, but with sorption turned on in tunnels and soil layers. There are two main conclusions to be drawn from Figure 6-53. First, the travel time in the CPM part of the pathways decreases the peak dose by a factor of approximately 5 (compare pink to green curves). This decrease is mostly due to the effect on the nonsorbing radionuclides I-129 and C-14. Second, sorption in tunnels and soils has no significant effect on total dose. This lack of sensitivity is a consequence of the dominant role that I-129 and C-14 play in determining the total dose. Indeed, examination of the far-field releases for individual nuclides (Figure 6-54) reveals that releases of sorbing radionuclides such as Ra-226 and Th-230 are significantly reduced by sorption in tunnels and soils.

Effects of the soils and tunnels are summarised in Figure 6-55 for the Q2 path. Without the delay provided by soils and tunnels, the geosphere is not a major barrier to radionuclide transport for a Q2 release. Other sensitivities are similar to the Q1 path.

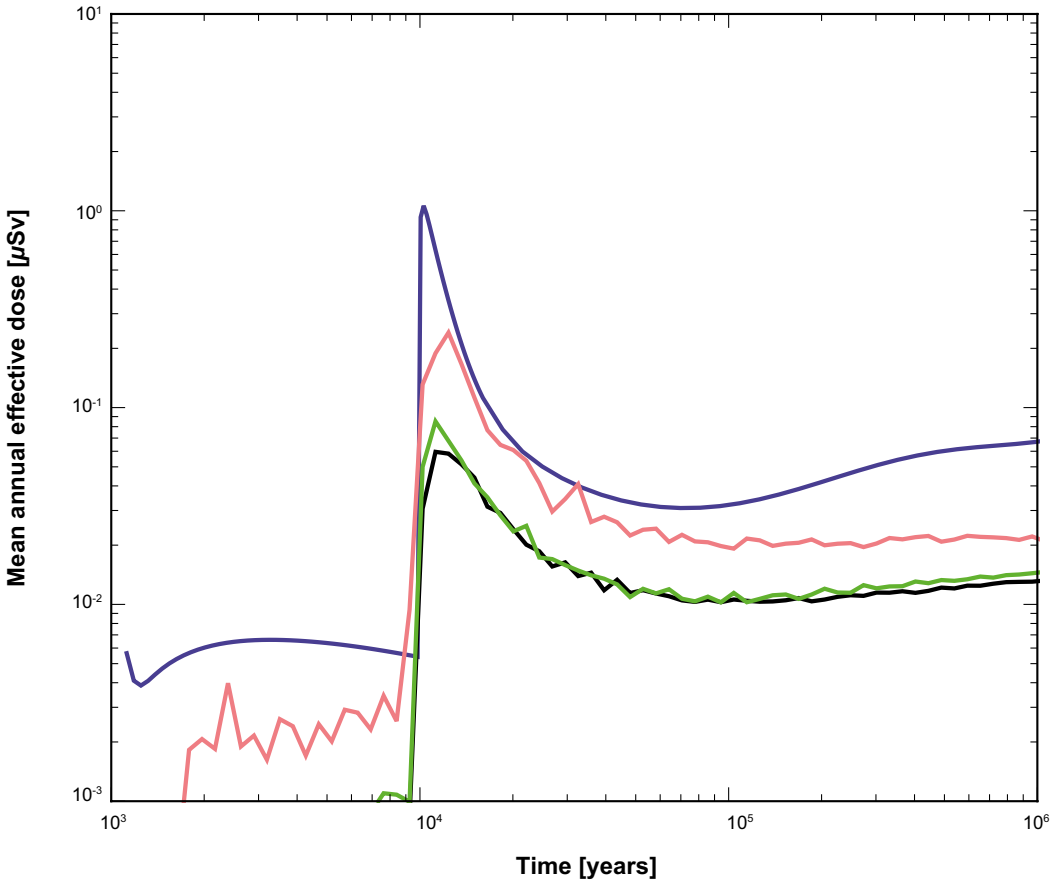

Figure 6-53. *Expected values for all-nuclides releases for the Q1 pinhole release, expressed as equivalent doses. The blue curve is near-field release and the other curves are far-field releases as follows: pink has no CPM segments in the pathway, green curve is the base case (CPM included but with no sorption), black has sorption in tunnels and soils.*

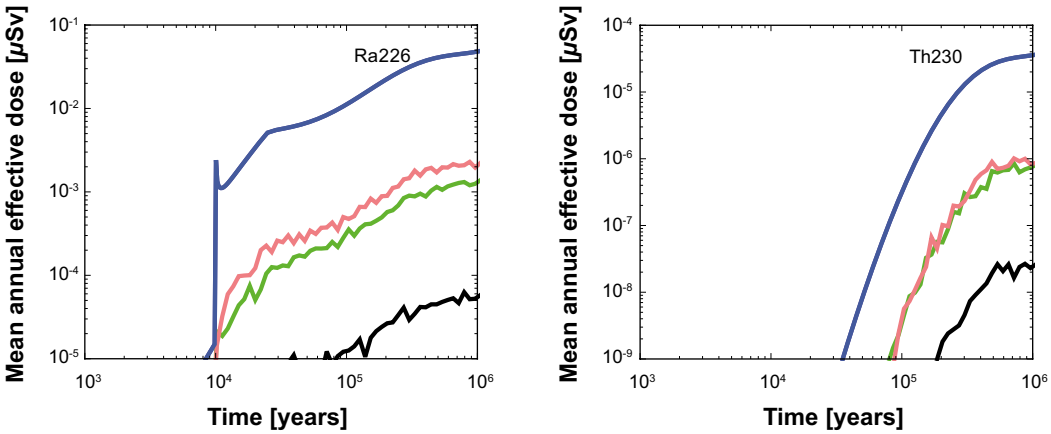

Figure 6-54. *Expected Ra-226 and Th-230 releases for pinhole Q1 release path and different assumptions about the role of tunnels and soils. The blue curve is near-field release and the other curves are far-field releases as follows: pink has no CPM segments in the pathway, green curve is the base case (CPM included but with no sorption), black has sorption in tunnels and soils.*

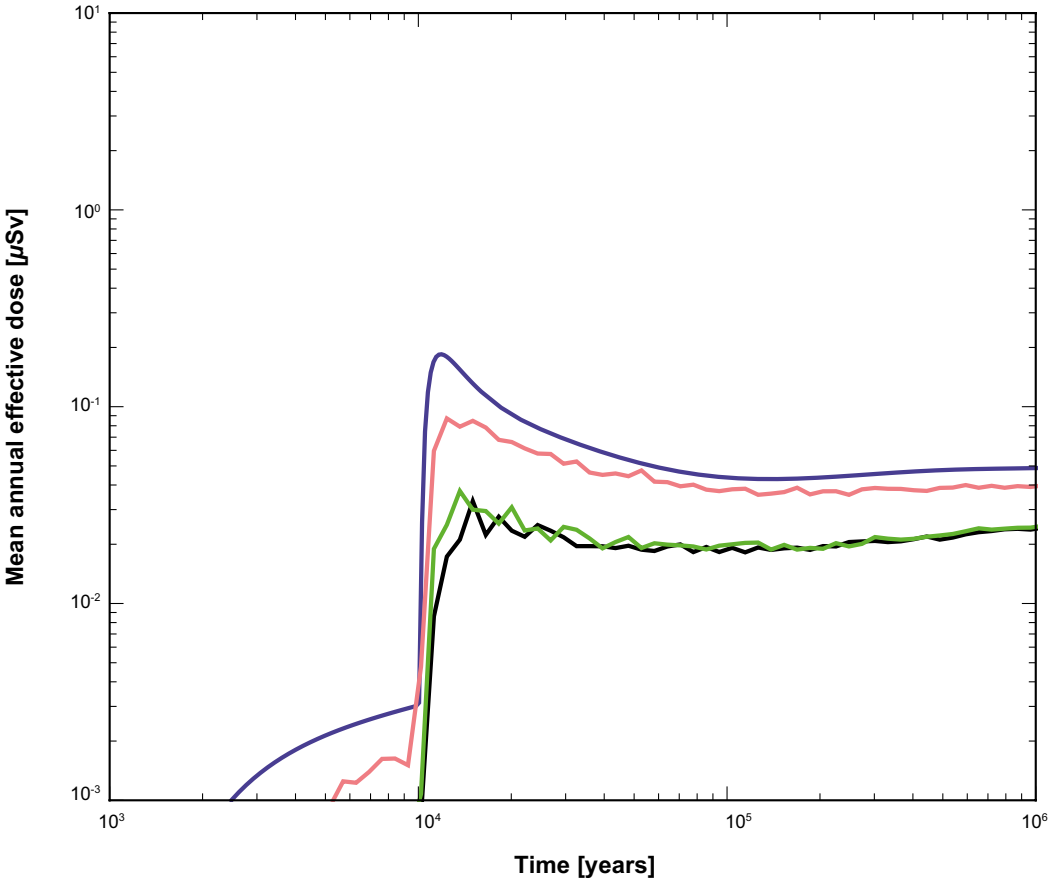

Figure 6-55. *Expected values for all-nuclides releases for the Q2 pinhole release, expressed as equivalent doses. The blue curve is near-field release and the other curves are far-field releases as follows: pink has no CPM segments in the pathway, green curve is the base case (CPM included but with no sorption), black has sorption in tunnels and soils.*

Crown space in tunnels

A variant flow model is considered in which tunnel backfill has compacted thus allowing a gap to form at the tunnel crown. Note that the tunnel crown case has different near-field releases as well as far-field releases, but the differences in near-field releases are small.

Results for the Q1 and Q3 release paths are shown in Figure 6-56 and Figure 6-57. In each figure, the green curve is the base case (i.e. no crown space). The black and pink curves have crown space. For the black curve, matrix diffusion into the neighbouring backfill is allowed. For the pink curve, this mitigating process is not active. Note that the differences between the crown space and no-crown space are not due to differences in the near-field releases; the base case has slightly higher near-field releases, but the differences are not large.

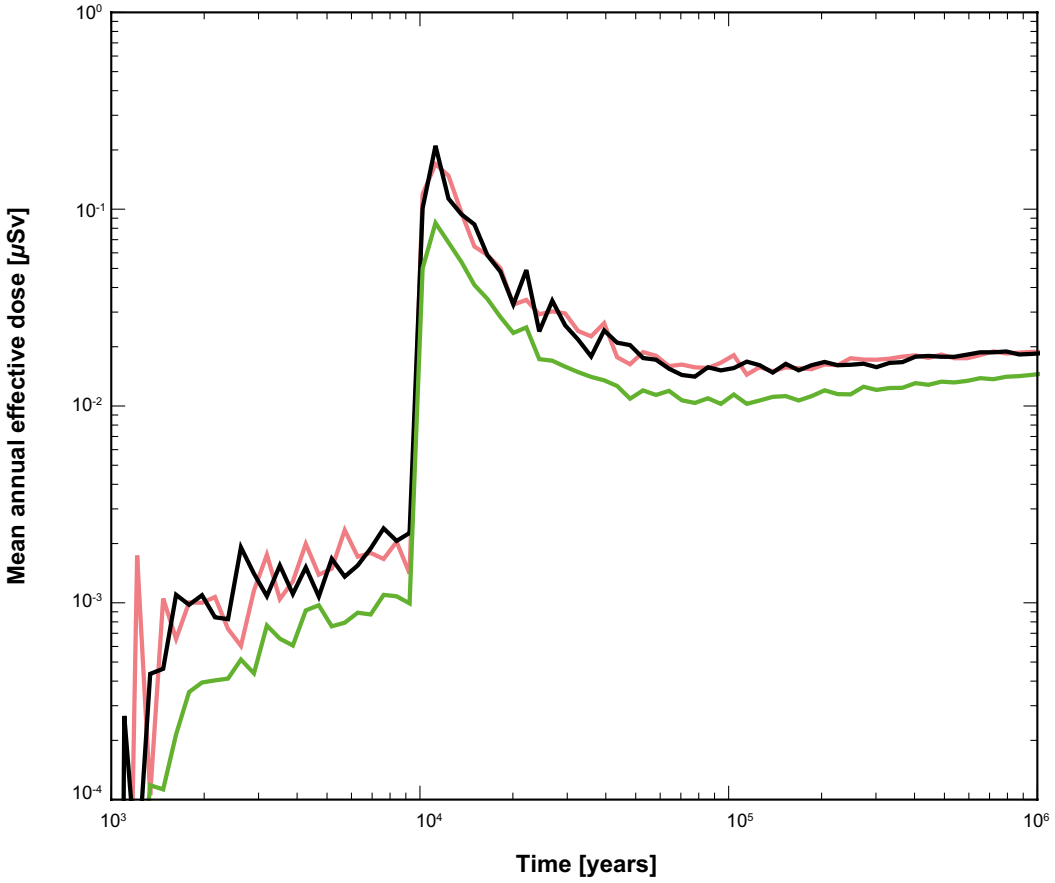

Figure 6-56. *Expected far-field release as equivalent dose for pinhole Q1 release path and different assumptions about the tunnel crown space. The green curve is the Q1 base case, which has no crown space represented. The black and pink curves are for cases with crown space with and without retention in the crown space.*

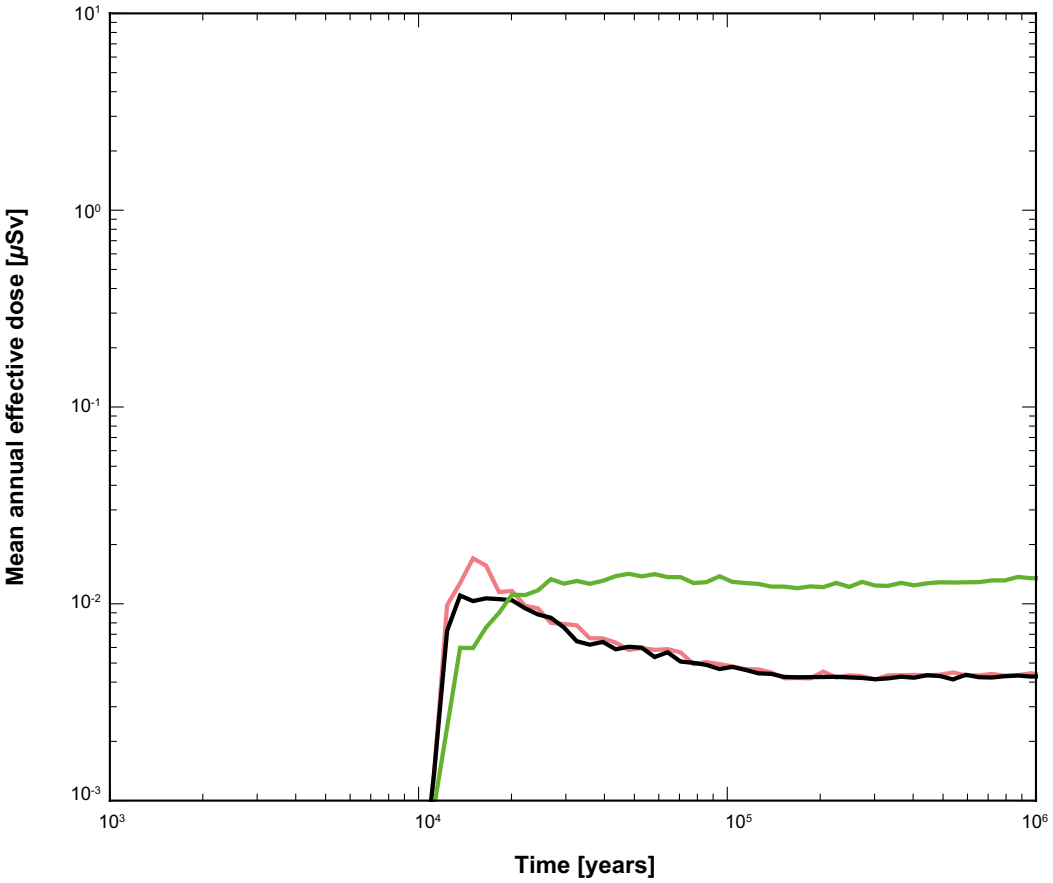

Figure 6-57. *Expected far-field release as equivalent dose for pinhole Q3 release path and different assumptions about the tunnel crown space. The green curve is the Q3 base case, which has no crown space represented. The black and pink curves are for cases with crown space with and without retention in the crown space.*

EDZ transmissivity

The base case has an excavation damage zone (EDZ) transmissivity of 10^{-8} m^2/s. The effects of different EDZ transmissivity for the Q1 release path are shown in Figure 6-58. The blue curve is the base case. The black curve is the case with no EDZ. The green and pink curves are results for EDZ transmissivity of 10^{-6} m^2/s and 10^{-7} m^2/s. The no-EDZ case is lower than the others. The presence of an EDZ increases the dose. Making the EDZ transmissivity larger than 10^{-8} m^2/s, however, does not further increase the dose. Instead, the dose drops slightly when going from an EDZ transmissivity of 10^{-7} m^2/s to 10^{-6} m^2/s, most likely because of subtle changes in flow paths. It is noted that the base case assumption for the uncertain EDZ transmissivity (10^{-8} m^2/s) results in the largest dose.

Effects of EDZ transmissivity on the Q2 releases are shown in Figure 6-59. Curves are coloured as in Figure 6-58. Note that the no-EDZ variant is not meaningful for the Q2 release path. Increasing the EDZ transmissivity above the base case value of 10^{-8} m^2/s does increase the dose somewhat, as expected. However, the effect is not large and quickly saturates; the doses for 10^{-7} m^2/s and of 10^{-6} m^2/s are not significantly different.

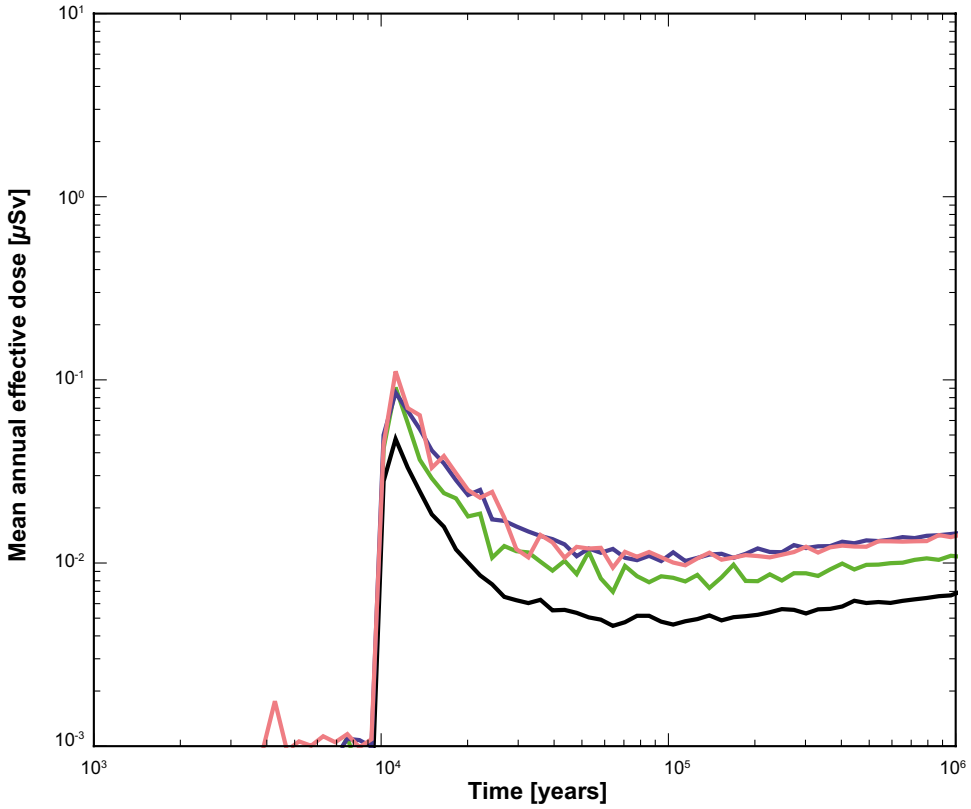

Figure 6-58. *Expected far-field release as equivalent dose for pinhole Q1 release path and different assumptions about the EDZ. The blue curve is the Q1 base case, which has EDZ transmissivity of 10^{-8} m^2/s. The black is the case for no EDZ. The green and pink curves are results for EDZ transmissivity of 10^{-6} m^2/s and 10^{-7} m^2/s, respectively.*

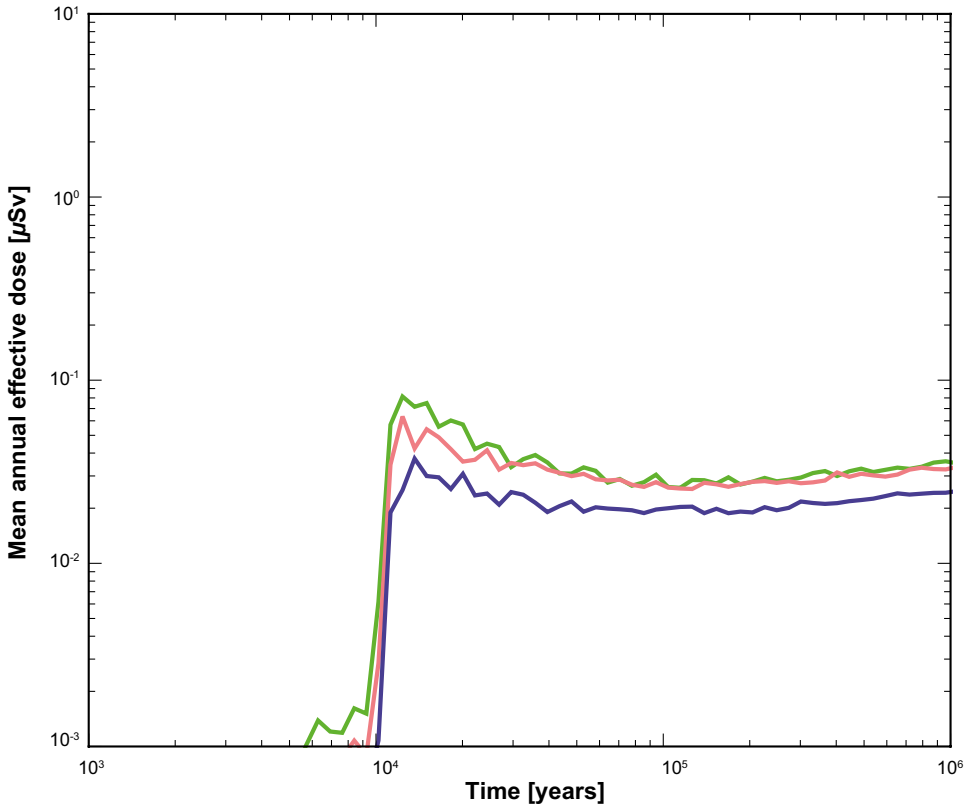

Figure 6-59. *Expected far-field release as equivalent dose for pinhole Q2 release path and different assumptions about the EDZ. The blue curve is the Q2 base case, which has EDZ transmissivity of 10^{-8} m^2/s. The green and pink curves are results for EDZ transmissivity of 10^{-6} m^2/s and 10^{-7} m^2/s.*

6.4.5 Colloid-facilitated transport assuming irreversible sorption

As discussed in Section 4.5.6, sorption onto mobile bentonite colloids has the potential to increase the mobility of some radionuclides. Two limiting cases can be identified depending on the kinetics of desorption: (i) radionuclide desorption from colloids is rapid relative to the advective travel time, and (ii) radionuclide desorption from colloids is slow compared to the advective travel time and may thus be represented as irreversible. Sorption of radionuclides onto bentonite is understood to be reversible and rapid relative to the advective travel times of interest (**Buffer, backfill and closure process report**); thus, irreversible sorption is not considered plausible. Nevertheless, consideration of irreversible sorption to bentonite colloids can help understand how the engineered and natural barriers function.

Several processes help mitigate the potential effects of irreversible sorption to colloids. These mitigating processes include permanent filtration of the colloids, colloid retardation, the fact that permanent sorption onto bentonite would dramatically reduce near-field release, and limited availability of sorption sites on bentonite colloids. The last process is considered and other mitigating processes neglected. The competitive Langmuir-type sorption model described in Appendix I.2 is used. In this model, radionuclides releases from the COMP23 code are partitioned between colloids and solution, taking into account competition for the limited number of available sites on colloids. Once partitioned, MARFA is used to transport colloid-associated radionuclides without retention processes. Radionuclides in solution are transported as in the reference case described in Section 6.4.2.

Dose-equivalent near-field releases based on the colloid-partitioning model are shown in Figure 6-60 for the pinhole reference case, Q1 release path. In this calculation, actinide species and transition metals were assumed to sorb irreversibly onto colloids that are present at a concentration of 10 mg/l. The blue curve is dose equivalent near-field release for all radionuclides. The solid green curve is release for all actinides and transition metals including both the dissolved and colloid-associated mass. The green dashed curve is the colloid-associated component. The actinide and transition metal portions of the total release are an order of magnitude smaller than the total release in the time period 20 000 to 50 000 years, and is even smaller before and after that time period. Moreover, when the actinide/transition metal release is largest, the availability of sites limits the colloid-associated release to even smaller fractions of the total release, mostly because Ni-59 and Nb-94 releases are large enough to saturate sorption sites. At late times, site limitations are less important, but the total actinide/transition metal release is small and not a significant contribution to the total.

Far-field effective doses for the same cases with and without colloids are shown in Figure 6-61. At its largest, the colloid-associated far-field release is approximately 1 % of the total release.

Results in Figure 6-60 and Figure 6-61 are based on a colloid concentration of 10 mg/l. Although this number is representative of clay colloid concentrations in waters that are not highly dilute, it is an uncertain parameter. As discussed in Section 4.5.8, colloid concentrations may be higher during brief periods if dilute water reaches the repository horizon. An upper bound on colloid-facilitated transport for this situation can be established by allowing all actinides and transition metals to be transported unretarded through the geosphere. This modelling case assumes that colloids are transported unretarded through the geosphere, an unlimited supply of sorption sites on colloids, and no desorption from colloids. Even with this extreme bounding approximation, colloids have no significant effect on the all-nuclides dose (Figure 6-62). This lack of sensitivity is a consequence of the dominant role that the three nuclides I-129, C-14, and Ra-226 play in controlling the overall dose. I-129 and C-14 are already transported without sorbing in the MARFA far-field calculation, and their transport thus cannot be enhanced by colloids. Ra-226 sorbs by ion exchange, and is not expected to irreversibly sorb.

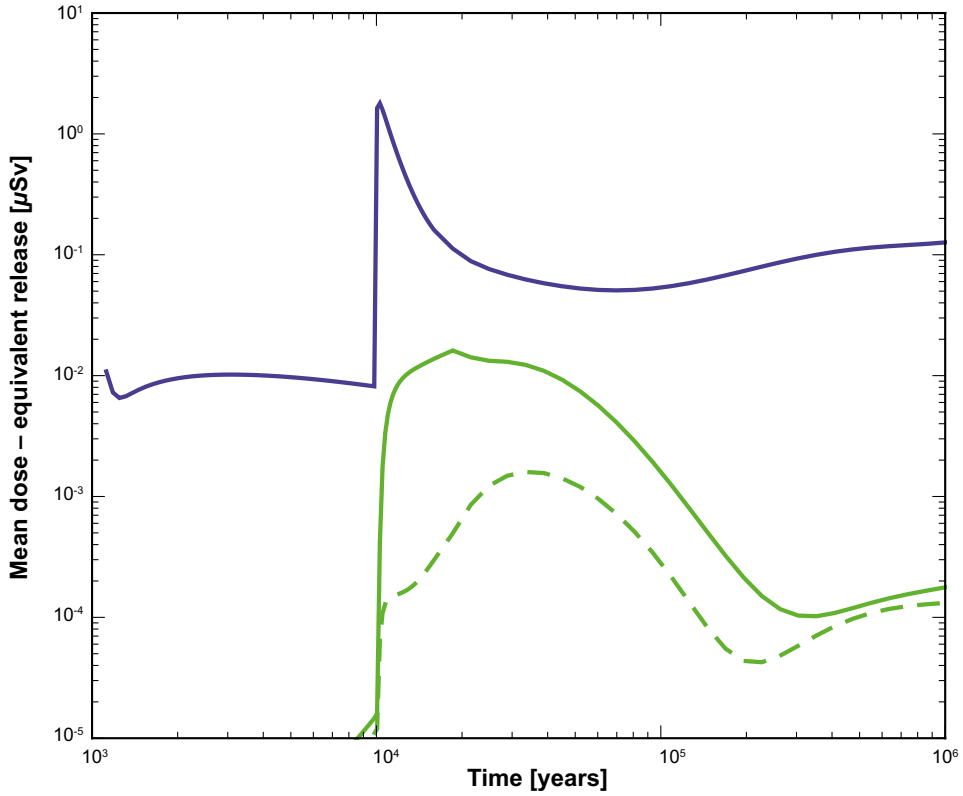

Figure 6-60. *Mean dose-equivalent near-field release for pinhole Q1 release path with irreversible sorption to colloids. The blue curve is total release, the solid green curve is the actinide and transition metal portion including the colloidal-associated and dissolved component, and the dashed green curve is the colloid-associated release of actinides and transition metals.*

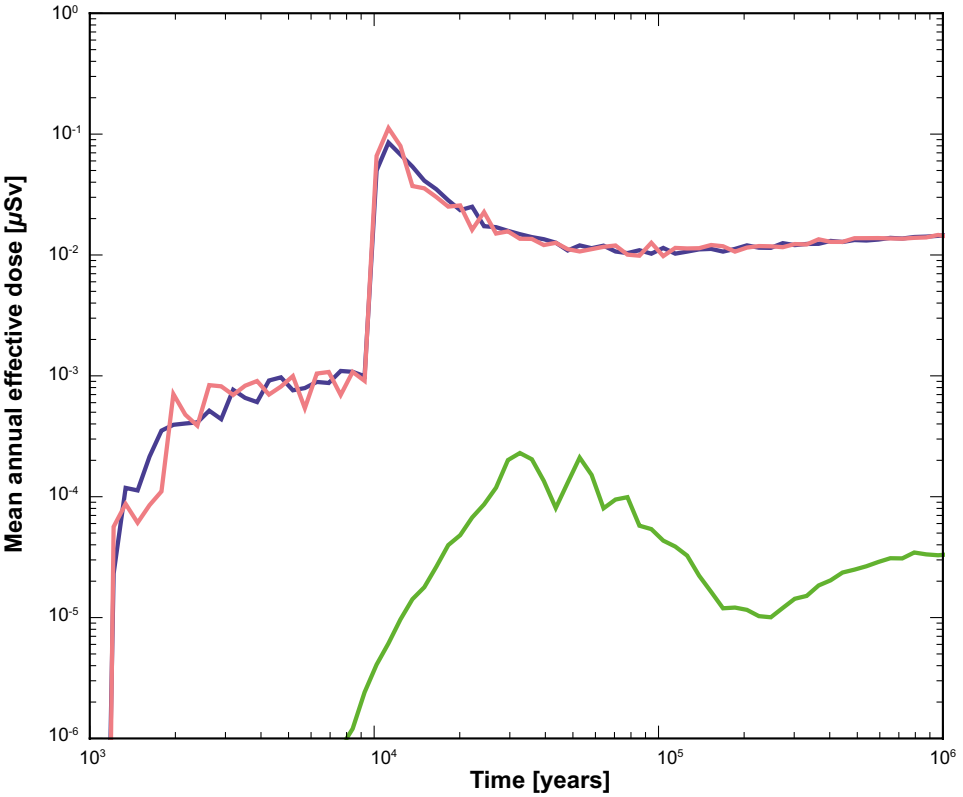

Figure 6-61. *Mean far-field effective dose for pinhole Q1 release path with and without irreversible sorption to colloids. The blue curve is total (all-nuclides) dose without colloids, while the pink curve is total dose with irreversible sorption to colloids at a concentration of 10 mg/l. The green curve is the dose due to the colloid-associated component.*

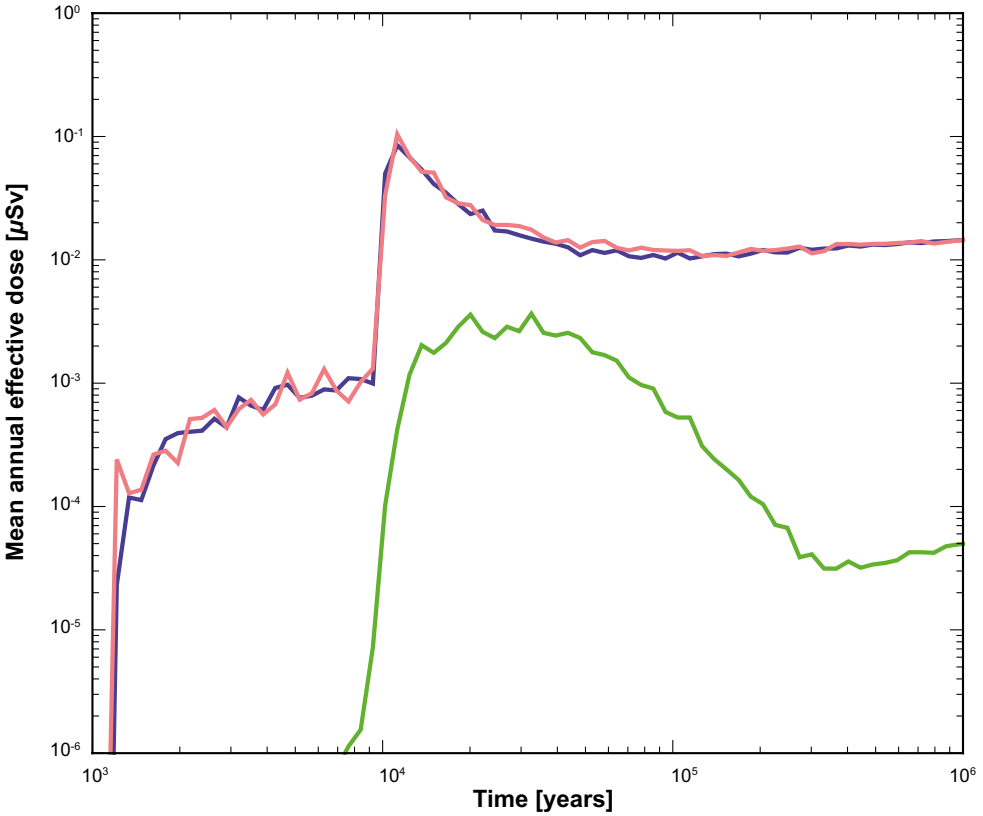

Figure 6-62. *Mean far-field effective dose for pinhole Q1 release path with irreversible sorption to colloids assuming unlimited sorption sites on colloids. The blue curve is total (all-nuclides) dose without colloids, while the pink curve is total dose with irreversible sorption to colloids. The green curve is the dose due to the colloid-associated component.*

6.5 Additional cases to illustrate barrier function

Some conclusions regarding loss of barrier functions can be drawn from the analyses already presented. In order to provide a fuller treatment, the following cases of barrier deficiencies are postulated:

A. An initial absence of enough buffer to cause advective conditions in the deposition hole for all deposition holes.

B. An initial pinhole in the copper shell for all canisters.

C. An initial, large opening in the copper shell and in the cast iron insert for all canisters.

D. A combination of cases A and C, i.e. an initial large opening in all canisters and advective conditions due to loss of buffer for all deposition holes.

E. A combination of case C with an assumption of fast fuel dissolution and fast corrosion of metal parts. An initial, large opening in every canister is combined with the assumption of complete fuel dissolution and metal corrosion in only 100 years.

A loss of the radionuclide retention capability of the rock is combined with each of the five cases, yielding a total of ten release situations. The cases without geosphere retention are denoted A* through E*.

In all cases it is assumed that the backfill and closure are installed and perform as expected. Also, all aspects of the rock other than those related to retention, e.g. the near-field groundwater flow, which is generally low and with only about one sixth of the deposition holes connected to water conducting fractures, as well as the stable and favourable groundwater composition in the near field, are assumed to be present. Elemental solubilities are imposed on concentrations of radionuclides in the canister void volume only if the buffer is in place. This is the same approach as used in the analyses of the corrosion and shear load scenarios, Chapters 4 and 5. The analyses in this Section have not been updated since the SR-Site assessment, with the exception of the treatment of Ag-108m in cases D

and D*. The releases of Ag-108m dominated the early doses in these cases in SR-Site, where they were calculated very pessimistically due to lack of corrosion data for the alloy in the control rods that contains Ag. New data has allowed a more realistic treatment as reflected in the updated Figure 6-65 and Figure 6-66 (and the follow-on figures where all cases are summarised).

Table 6-2 gives an overview of the status of the retardation related safety functions.

The transport and dose calculations are probabilistic, since it is desirable to take into account both uncertainties due to lack-of-knowledge in general and the spatial variability of the properties of the deposition holes and their associated transport paths in the geosphere. The semi-correlated hydrogeological DFN model is used for these stylised calculations. Except for the case specific assumptions regarding failed barrier functions, all transport data are taken from the SR-Site data report (SKB 2010b). This applies to e.g. corrosion rates, fuel dissolution rate, sorption and diffusion data and LDF values.

The biosphere is here represented by the constant LDF values obtained when the release is distributed in the landscape according to the time dependent distribution of release locations from the repository during an interglacial. Furthermore, since the LDF values are suited primarily to handle releases that are constant over periods of time that are comparable to the duration of an interglacial, i.e. typically 10 000 years, the releases for these cases are, as a variant, also evaluated with fully time dependent modelling of the biosphere. Here, the releases are distributed in the landscape and the time dependent doses are presented, rather than a time dependent release converted to dose by a constant LDF value.

In the following, each case is discussed briefly using distributed, constant LDFs. The section is concluded with summarising accounts of all cases both with LDFs and with time dependent modelling of the biosphere.

Table 6-2. Status of safety functions for the ten release situations. In cases denoted with an asterisk also geosphere retention is absent.

Green: Safety function intact
Yellow: Safety function deteriorates over time
Red: Safety function absent initially

	A. Buffer missing	A*	B. Pinhole damage	B*	C. Large canister defect	C*	D. Large canister defect and buffer missing	D*	E. Large canister defect, rapid fuel and metal conversion	E*
Limited fuel dissolution rate										
Limited corrosion rate of metal parts										
Limited solubilities										
High transport resistance in canister/buffer interface										
Retardation in buffer										
High transport resistance in buffer/rock interface[1)]										
Geosphere retention										

[1)] When this safety function is present, spalling is still pessimistically assumed in all deposition holes. When this safety function is not present, i.e. when the buffer is missing, the groundwater turnover in the deposition hole is still limited by the hydraulic properties of the rock.

Cases A and A, initial absence of buffer*

A 0.5 m high section of the bentonite buffer is assumed to be missing, leaving a void in the form of a hollow cylinder between the canister and the wall of the deposition hole. The Q1 fracture, if it exists, intersects the deposition hole at the location of the void. The deposition hole is otherwise filled with buffer and the deposition tunnel backfill is assumed to be intact. For most of the deposition holes, the groundwater flow and sulphide concentrations are not sufficient to cause canister failure during the one million year assessment period. The corrosion calculation takes both the natural variability of flow rates for the ensemble of 6 000 deposition holes and the distribution of sulphide concentrations in the groundwater into account. This yields a calculated mean number of failed canisters of 0.17 at one million years, used also here. Only the deposition holes with the highest flow rates in the Q1 fracture contribute. This also means that releases to Q2 and Q3 release paths are negligible for these positions.

Radionuclide transport in the near field and far field is modelled as the semi-correlated case with initial advection, see Section 4.5.9. The consequences are similar to those shown in Figure 4-30 and Figure 4-31. The only differences is that the distributed LDF values are applied and the results are shown in Figure 6-69. Many of the radionuclides have decayed to insignificance when the first failures occur after close to 50 000 years. Near-field release equivalent doses are dominated by Nb-94 from metal parts of the fuel and Ra-226, Pb-210 and Np-237 from the fuel matrix. Far-field doses are dominated by Nb-94, Ra-226, Se-79 and I-129.

Cases B and B, initial, penetrating pinhole defect in all canisters*

The canister defects are assumed to be the same as the growing pinhole failure. Near-field and far-field radionuclide transport is modelled as the probabilistic calculation of the hypothetical pinhole failure mode including the effect of spalling, see Section 6.3.1, but with growing holes in all canisters. The deposition hole buffer and the deposition tunnel backfill are assumed to be intact. The dose consequences in the biosphere are calculated with the distributed LDF values since this is a more realistic approach when releases occur from all over the repository.

The consequences are similar to those in the pinhole scenario, see Figure 6-15 and Figure 6-17 for the near field and the far field, respectively. The only difference is that all canisters are now assumed to have defects, meaning that the probabilistic single-canister results should be multiplied by 6 000 and that the distributed LDF values are applied, leading to a reduction of the consequences by typically one order of magnitude. The far-field results with all 6 000 canisters are shown in the summary Figure 6-69 later in this section.

Cases C and C, initial, large opening in all canisters*

The canister defects are assumed to be in the form of a large opening in the copper shell and the cast iron insert. The deposition hole buffer and the deposition tunnel backfill are assumed to be intact.

In the reference evolution, some of the deposition holes are affected by buffer erosion to the extent that advective conditions occur in the hole. For the stylised case considered here, no such erosion is, however, assumed, in order to more clearly demonstrate the role of the canister if all other barriers are intact. Combinations of canister and buffer defects are analysed in one of the cases described below.

The calculation case is similar to the failure due to isostatic load, see Section 6.2. Near-field and far-field radionuclide transport is modelled as a probabilistic calculation case where the failure is postulated at 100 years for all canisters.

The dose equivalent release from the near field is shown in Figure 6-63. The dose is dominated the initial 10 000 years by C-14, Cs-137, Sr-90, Ag-108m, I-129 and Se-79. After about 10 000 years Se-79, C-14, Ra-226 and I-129 contribute most to the total dose. Releases of nuclides that sorb strongly in the buffer, e.g. Pu-238 and Pu-239, are strongly reduced compared to case D* below where the buffer is also assumed to be missing. There is a considerable reduction also of the release of Cs-137, Sr-90 and Ag-108m compared to the case in which the buffer is missing.

The dose from the far-field release is shown in Figure 6-64. The peak total dose is reduced by less than an order of magnitude compared to the near-field release, whereas doses from many of the short-lived or sorbing nuclides are considerably reduced.

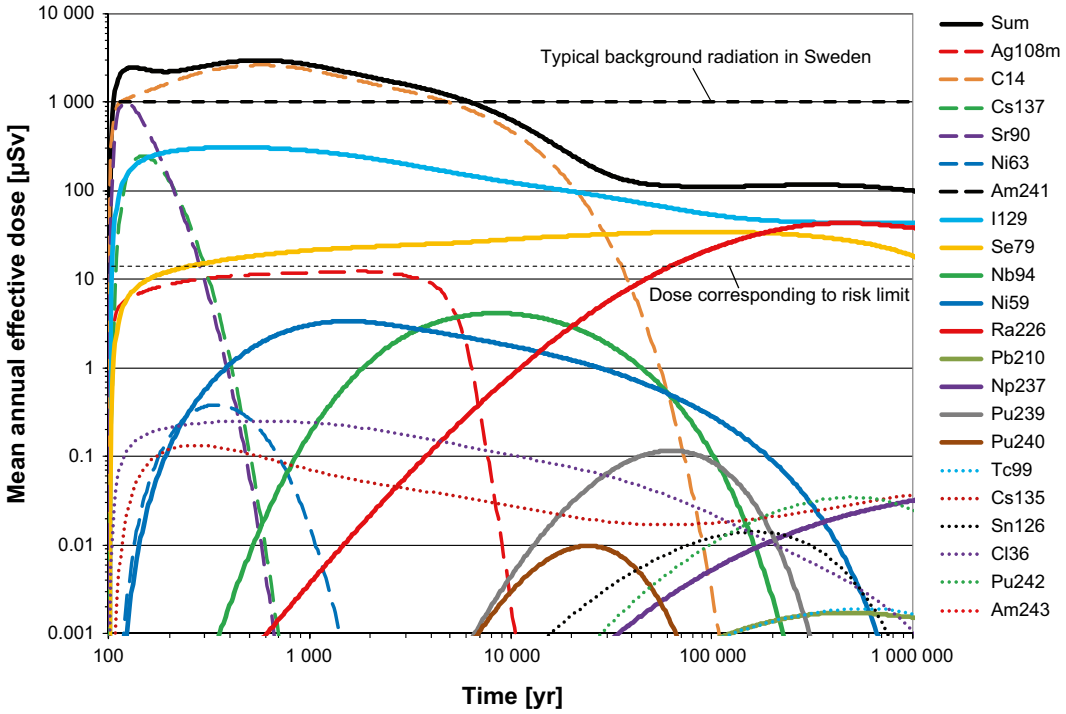

Figure 6-63. *Near-field dose equivalent release for case C*, i.e. all canisters have an initial large defect and the buffer is intact.*

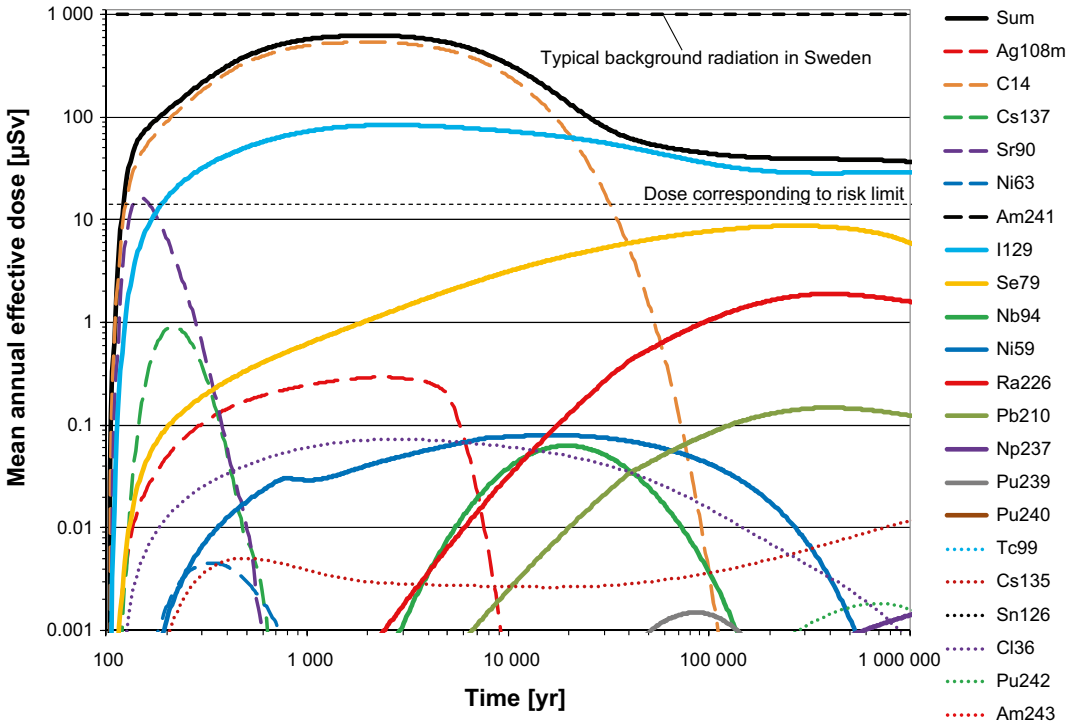

Figure 6-64. *Far-field dose for case C, i.e. all canisters have an initial large defect and the buffer is intact.*

It is noteworthy that this completely unrealistic case of initial loss of containment function for all canisters in the repository yields far-field releases, converted to doses, which never exceed the background radiation. However, the containment function is required for a majority of the canisters in order to fulfil the regulatory requirement on risk at Forsmark.

The long-term release rate of I-129 equals, to a good approximation, the release rate of this nuclide from the fuel matrix. This is caused by the assumed absence of sorption and long half-life of I-129. Regarding the calculated dose from I-129 for this and other hypothetical cases in this section, it is noted that the mitigating effect of mixing of I-129 with naturally occurring stable iodine is disregarded in the biosphere models.

Cases D and D, initial large opening in all canisters and advective conditions due to loss of buffer for all deposition holes*

The defects are assumed to be the same as those modelled in the corrosion scenario, i.e. a large opening in the copper shell and the cast iron insert and a section of the bentonite buffer is missing where the canister is damaged, leaving a void between the canister and the wall of the deposition hole in the form of a hollow cylinder. The deposition hole is otherwise filled with buffer and the deposition tunnel backfill is assumed to be intact. This means that releases occur predominantly to the Q1 fracture, if it exists. Near-field and far-field radionuclide transport is modelled as a corrosion case where all canisters fail after 100 years.

Only the Q1 release path is evaluated in detail, since releases from Q1 will dominate in this situation. In the base case realisation of the semi-correlated hydrogeological DFN model used, 1 169 out of the 6 000 deposition holes have a Q1 fracture. This means that virtually all radionuclides will leave through Q1 from these deposition holes. The analysis is, for technical reasons, limited to the 1 000 deposition holes with the lowest F values and hence lowest geosphere retention. For the remaining 5 000 deposition holes, Q2 and Q3 releases need to be considered. The analysis of the isostatic load scenario shows i) that the Q1 release path dominates the initial approximately 10 000 years even with the buffer in place, ii) that I-129 dominates the total release after approximately 10 000 years and iii) that the retention of I-129 is close to zero. Therefore, the calculated release of I-129 from the 1 000 deposition holes with a Q1 path is multiplied by 6 to approximately account for releases through Q2 and Q3 from the remaining deposition holes.

The dose equivalent release from the near field is shown in Figure 6-65. The dose is dominated the initial 10 000 years by the IRF and/or CRF of Cs-137, Sr-90, C-14 and Nb-94. Note that only the generally low flow rates at Forsmark limits the releases for the IRF/CRF. After about 10 000 years Nb-94, Pu-239, Pu-240, Np-237, Ra-226, Pb-210 and I-129 contribute most to the total dose. The figure has been altered compared to the SR-Site version in that the Ag-108m curve has been multiplied by a factor of 3×10^{-4}, reflecting the reduction in IRF from 1 to 0.0003. This reduction is facilitated by the improved understanding of corrosion of the PWR control rods. The CRF yields a dose contribution comparable to that of the reduced IRF, but the CRF-contribution has not been quantified in detail in this simplified approach to demonstrating the insignificance of Ag-108m for the total dose. Ag-108m now gives a negligible contribution to the total dose at all times, whereas it was dose dominating during the initial several hundred years in SR-Site. Corrosion data for the control rods are discussed in the **Data report**, Section 3.2.7.

The dose from the far-field release is shown in Figure 6-66. The total dose is reduced by about a factor of 10 compared to the near-field release. For the earliest releases this is an effect of the advective travel time in the geosphere. In the long term, strongly sorbing nuclides like Pu-239 and Pu-240 are retained in the geosphere. It is noteworthy that this completely unrealistic case of initial absence of all transport limitations in the engineered parts of the repository yields far-field releases, converted to doses, that are comparable to the background radiation during the initial 10 000 years and that in the long term are less than a factor of ten above the risk limit. This figure has been altered in the same way as the near field Figure 6-65 for Ag-108m.

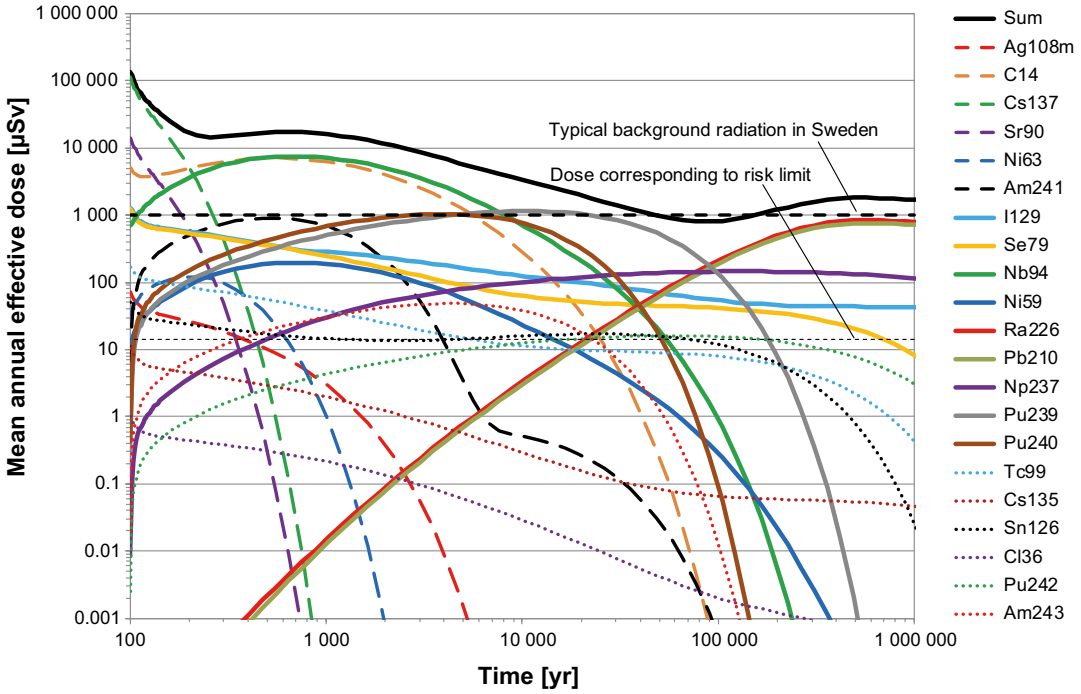

Figure 6-65. *Near-field dose equivalent release for case D*, i.e. all canisters have an initial large defect and the buffer is missing between the defect in the canister and the wall of the deposition hole.*

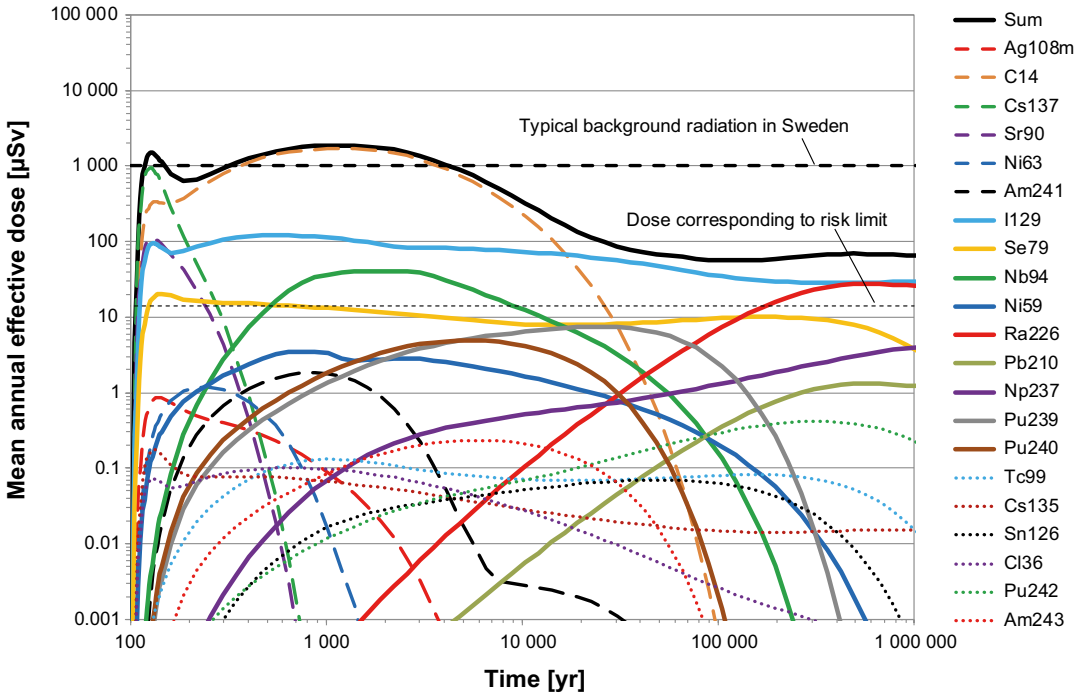

Figure 6-66. *Far-field dose for case D, i.e. all canisters have an initial large defect and the buffer is missing between the defect in the canister and the wall of the deposition hole.*

Cases E and E, initial, large opening in all canisters and rapid fuel dissolution and metal corrosion*

These cases are identical to cases C and C*, (all canisters have a large opening in the copper shell and the cast iron insert), except that for cases E and E* complete fuel dissolution and metal corrosion is assumed to occur in 100 years after water contacts the fuel. The containment function of not only the canister but also of the fuel matrix and the structural parts of the fuel is thus assumed to be absent. The deposition hole buffer and the deposition tunnel backfill are assumed to be intact.

The near-field and far-field developments for these cases are identical to those for cases C and C* with the exception of the fast conversion of the fuel and metal corrosion.

The dose equivalent release from the near field is shown in Figure 6-67. The dose is dominated by C-14, Cs-137, Sr-90 and I-129 for more than 10 000 years. In the longer term, Ra-226 and Se-79 together with I-129 contribute most to the total dose. Note that the release of Ag-108m is identical to that in case C* since this release is controlled by the solubility of Ag and not by corrosion in the model. The early releases of Sr-90, Cs-137 and I-129 have increased in inverse relation to the IRF values for these nuclides; cases E and E* are similar to assuming 100 % IRF for all nuclides. The decrease of I-129 at very long times is caused by depletion of I-129 from the repository and the host rock through outward transport and not through decay.

The dose from the far field release is shown in Figure 6-68. The peak total dose is reduced by more than an order of magnitude compared to the near field release, whereas doses from many of the short-lived or sorbing nuclides are considerably reduced.

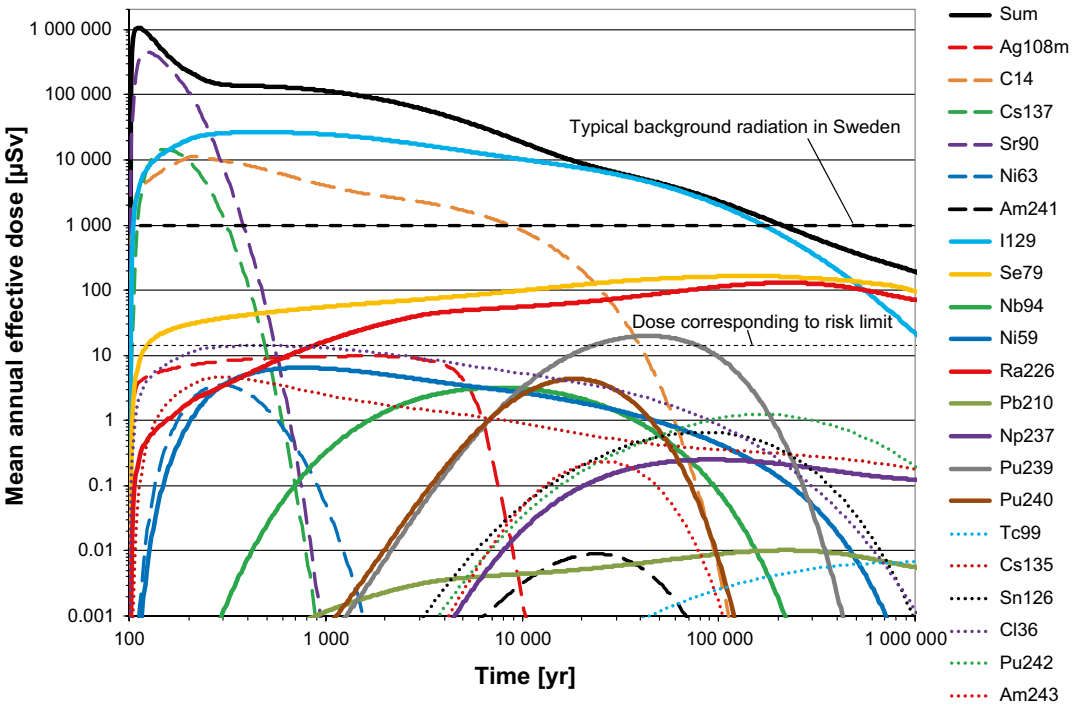

Figure 6-67. *Near-field dose equivalent release for case E*, i.e. all canisters have an initial large defect in combination with a rapid fuel and metal conversion and the buffer is intact.*

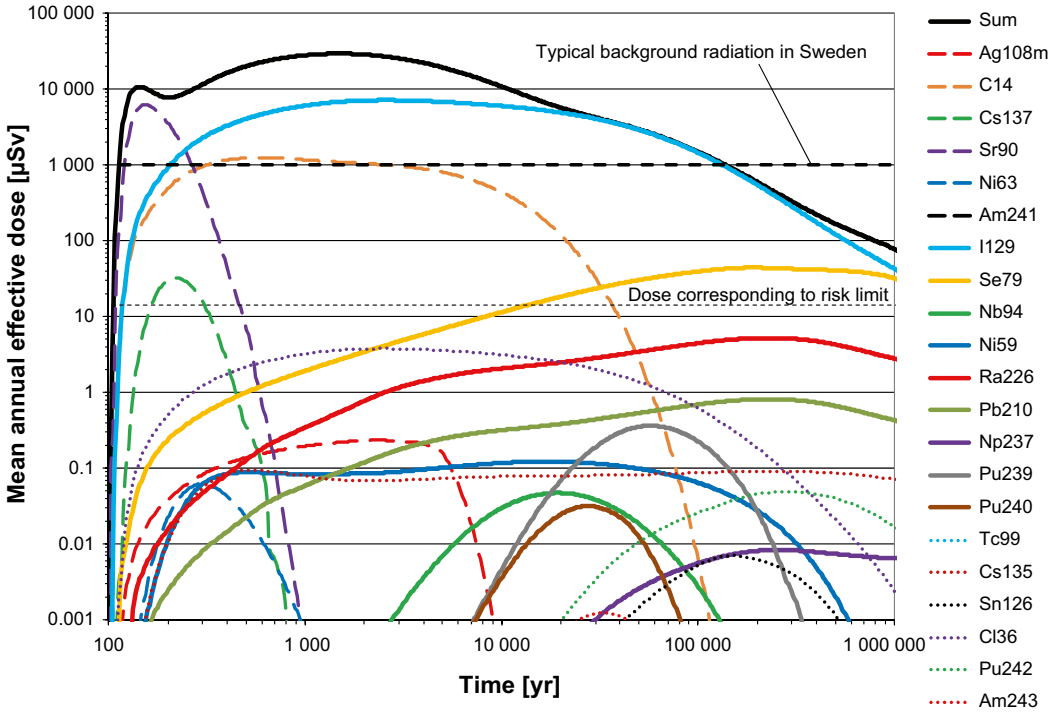

Figure 6-68. *Far-field dose for case E, i.e. all canisters have an initial large defect in combination with a rapid fuel and metal conversion and the buffer is intact.*

Summary of results with distributed LDF values

The summed dose for each case discussed above is given in Figure 6-69.

The following are noted.

After about 10 000 years, the doses for all cases are below the dose caused by typical background radiation in Sweden, except for the case in which retention properties of canisters, buffer and rock are all disregarded (case D*) and those with rapid fuel dissolution in combination with failed canisters (cases E and E*). The low flow and favourable groundwater chemistry of the rock and the presence of backfill and closure of the repository tunnel thus provide substantial protection from a fuel with unaltered dissolution rate.

If all canisters have large defects initially, but the barrier system is otherwise intact, case C, the peak annual dose to the most exposed individuals in the landscape does not exceed that caused by typical background radiation in Sweden, i.e. 1 mSv. Beyond 10 000 years this annual dose is less than an order of magnitude above the risk limit of 0.014 mSv.

If all canisters have large defects initially, and if also the buffer is assumed to be missing between the canister damage and the wall of the deposition hole, case D, the dose is comparable to the background radiation the first 10 000 years, and is thereafter quite similar to the case where the buffer is in place, case C. This suggests that the buffer is, from the point of view of total dose, not important as a retention barrier in this time perspective. However, a comparison between Figure 6-64 and Figure 6-63 shows that the buffer has a considerable impact on near-field releases of many sorbing nuclides that do not dominate the dose.

With a large degree of damage to the canisters, the buffer missing and retention in the rock disregarded, case D*, the calculation results suggest annual doses in the 0.1 Sievert range in the initial 1 000 years. This is a demonstration of the necessity of properly protecting man and the environment from the spent nuclear fuel, in particular in the 1 000 year time frame.

Beyond 10 000 years, the total dose is comparable to that caused by the background radiation even when neglecting the retention properties of all three barriers, case D*.

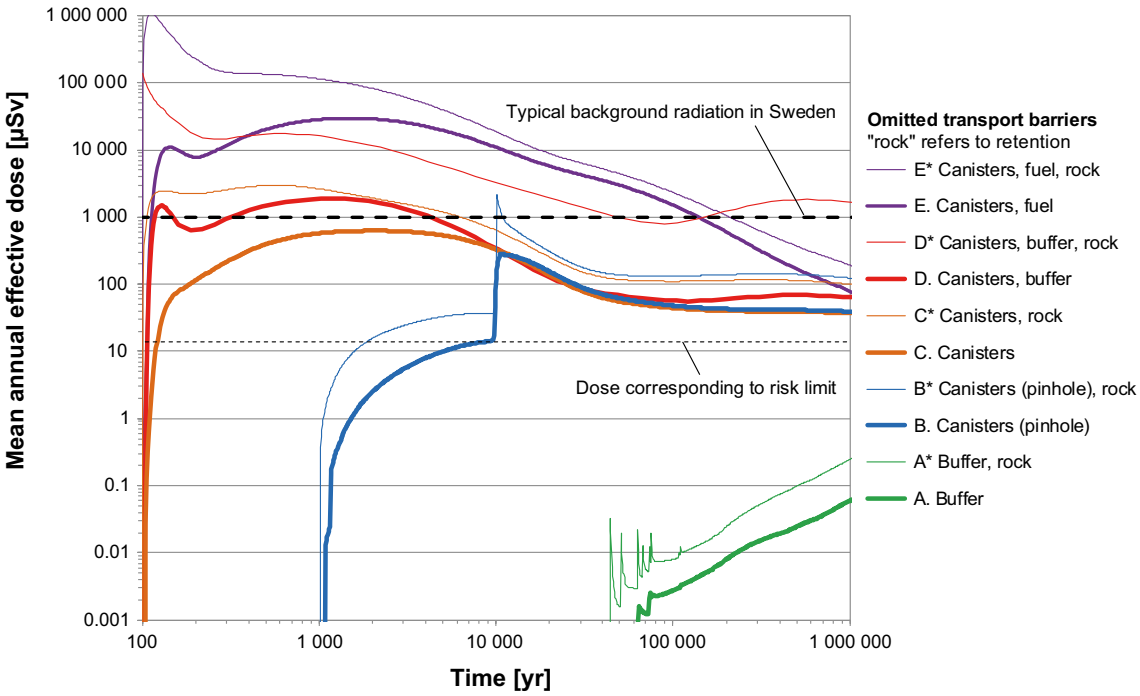

Figure 6-69. *Results of stylised cases to illustrate loss of barrier functions. Note that an omission of the "rock" barrier in these cases refers to omission of retention of radionuclides in the rock fractures only, whereas the favourable, low flow rate at repository depth and the favourable geochemical conditions are still taken into account.*

As expected, the case with initial pinhole defects, case B, and those with large initial defects, case C, are quite similar beyond 10 000 years, when the pinhole defects are assumed to have grown into large defects. It is also noted that neglect of rock retention does not affect the total dose much for these cases after about 1 000 years. However, a comparison between Figure 6-66 and Figure 6-64 shows that the rock has a considerable impact on far-field releases of many sorbing nuclides that do not dominate the dose.

A comparison of cases C and E shows the considerable containment function of the waste form for more than 100 000 years.

Summary of results with time dependent modelling of the biosphere

As mentioned in the introduction, the LDF values are suited primarily to handle releases that are constant over periods of time that are comparable to the duration of an interglacial, i.e. typically 10 000 years. Therefore, the releases for most of the above cases were also evaluated with a fully time dependent modelling of the biosphere. Here, the releases are distributed in the landscape according to the time dependent spatial distribution of release points from the repository and the time dependent doses are presented, rather than a time dependent release converted to dose by a constant LDF value. This modelling was for assumed temperate conditions over a period of 60 000 years. The results are given in Figure 6-70. The solid curves are doses obtained with distributed LDF values (i.e. the same curves as in Figure 6-69) and the dashed curves are the corresponding doses obtained with time dependent modelling of the biosphere.

The time dependent, dashed curves are generally within an order of magnitude of, but below, the curves obtained with LDF values. The one exception is the case where the retention properties of the canister, the buffer and the rock are all disregarded, case D*. Here, the time dependent dose from C-14 around 20 000 years slightly exceeds that obtained using the LDF. This is caused by accumulation and delay effects in the biosphere.

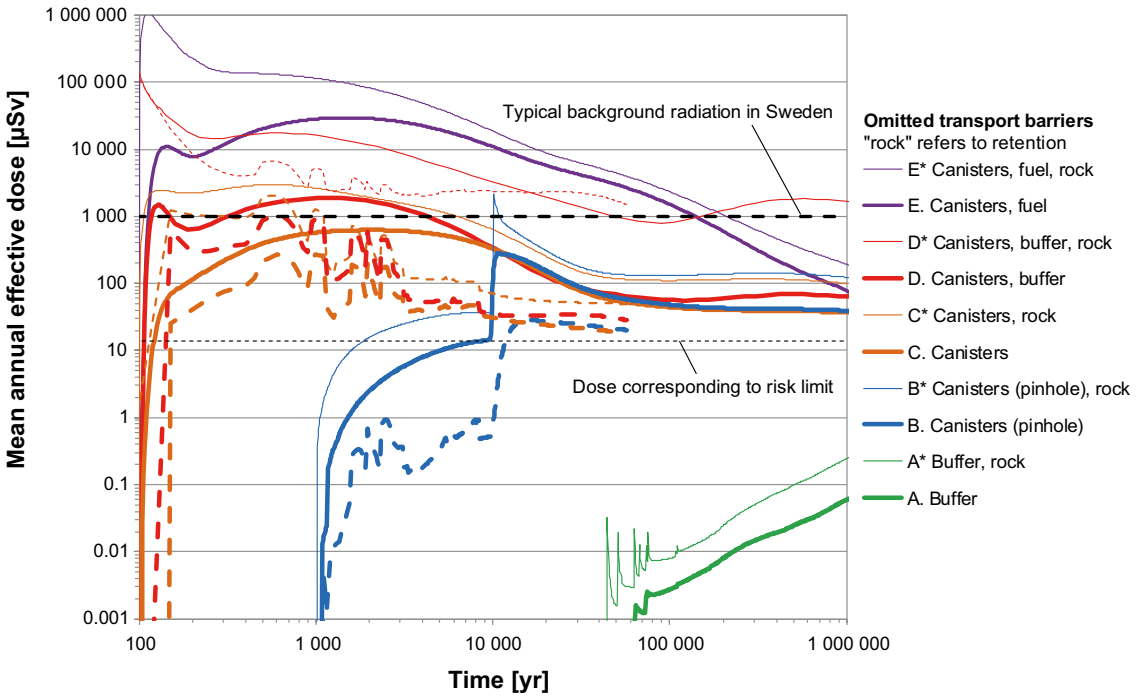

Figure 6-70. *Results of stylised cases to illustrate loss of barrier functions. Solid lines: Same as in Figure 6-69 (dose conversion through distributed LDF). Dashed lines: Corresponding cases with time dependent modelling of the biospehere.*

7 Complementary calculations for the safety assessment PSAR

In this chapter, complementary calculations performed for the safety assessment PSAR are analysed. They encompass:

- Two corrosion cases with a fuel inventory containing irregular fuels.
- Hypothetical cases to illustrate barrier function where early failures in all canisters are postulated. Two base cases, (A) with an intact buffer, and (B) with buffer loss due to erosion and sedimentation are analysed and, in addition, four sensitivity cases are studied.

7.1 Fuel inventory containing irregular fuels

There is a small fraction of fuel types in the fuel inventory that contain irregular fuels. To account for these, calculations of risk contributions have been performed for:

- containers with fuel with failed cladding (Evins and Hedin 2020) and,
- containers with fuel residues from Studsvik (Evins and Hedin 2013).

These cases are both calculated as variants of the fully correlated corrosion case with initial advection, i.e. the case yielding the highest doses of the corrosion cases. The calculated doses for these two cases should be added as contributions to the dose calculated for the fully correlated corrosion case with initial advection, see Appendix M, Section M.9.

7.1.1 Corrosion, failed fuel case

In the special containers containing failed fuel, it is estimated that there is a certain fraction of oxidised fuel matrix. It is pessimistically assumed that this oxidised fuel fraction has not lost any radionuclides during the oxidation. A variant of the fully correlated corrosion case with initial advection is used to estimate the contribution to the dose from the oxidised fraction of fuel. In this case, the fraction of oxidised fuel of the full repository inventory is estimated to be 6.8×10^{-5}, and the dissolution rate of this fraction is estimated to be 2.9×10^{-4}/yr (Evins and Hedin 2020). The limited fraction of the inventory of concern is taken into account in the probabilistic calculation by multiplying the mean number of failed canisters for the fully correlated corrosion case (0.70) by 6.8×10^{-5}, yielding a mean number of failed canisters of 4.78×10^{-5} for this calculation case. This is under the assumption that the occurrence of failed fuel in a canister and the likelihood of canister failure are uncorrelated. This is seen as justified as there is no basis to assume such a correlation.

Probabilistic calculations

Hydrogeological case:	Fully correlated, five realisations
Erosion/corrosion model:	Initial advection
Failure time:	163 times according to the erosion/corrosion calculations
Mean number of failed canisters:	4.78×10^{-5}
Fuel dissolution rate	2.9×10^{-4}/yr
Solubility limits:	No
Thorium sorption in near field:	Yes (modelled as low solubility limit)
Number of realisations:	50 per canister failure time
Number of nuclides:	38

A probabilistic calculation of the failed fuel case based on the fully correlated corrosion case with initial advection is performed with failure times and geosphere transport data from the five realisations of the fully correlated hydrogeological model and the updated erosion/corrosion model (**Post-closure safety report**, Section 10.3.13).

The contributions from the instantly released fraction of nuclides, IRF, are not included in the calculations except for Tc-99 that is modelled and included in the figure showing results for the far field. The IRF was not included since this fraction of the inventory is not affected by an oxidised fuel matrix and hence the IRF results in Section 4.4.2 are representative also for the present case.

The dose equivalent releases from the near field and far field are shown in Figure 7-1 and Figure 7-2, respectively. The total mean annual effective dose from the fully correlated corrosion case with initial advection for regular fuel (described in Section M.9) is added to the figures for comparison.

The results show that the maximum total dose contribution from the failed fuel is almost three orders of magnitude lower than the corresponding corrosion case for regular fuel for both the near field and the far field, sustained over the entire one-million year period. The contribution from the failed fuel to the total dose is hence negligible. For the failed fuel, the radionuclides released from the near field are dominated by Pb-210, Ra-226, Se-79 and Np-237, while the dominating radionuclides released from the far field are Se-79, I-129 and Ra-226.

It is, finally, noted that the case discussed above aims at calculating the overall risk contribution from the failed fuel. A mean dose is calculated without consideration of how the failed fuel is distributed over the 6 000 canisters in the repository, which is justified for an overall risk assessment. As a complement, it is also of interest to compare the consequences of a failure of a canister with a postulated content of failed fuel to that of a regular BWR canister. For a BWR canister containing one special container with failed fuel and 11 regular BWR elements, the inventory of failed fuel is estimated at 0.7 % of that of a regular BWR canister, based on data in Evins and Hedin (2020). This fraction is pessimistically assessed to have a dissolution rate of 2.9×10^{-4}/yr according to the above, whereas the regular fuel has a mean dissolution rate of 10^{-7}/yr. If such a canister fails, the dose can be crudely estimated to be increased by a factor of $2.9 \times 10^{-4}/10^{-7} \times 0.007 \approx 20$ compared to a regular BWR canister for the approximately 3 000 years after failure during which the oxidised fraction of the failed fuel is assumed to be dissolved. If a BWR canister would be fully filled with 12 special containers, this factor would increase by approximately an order of magnitude.

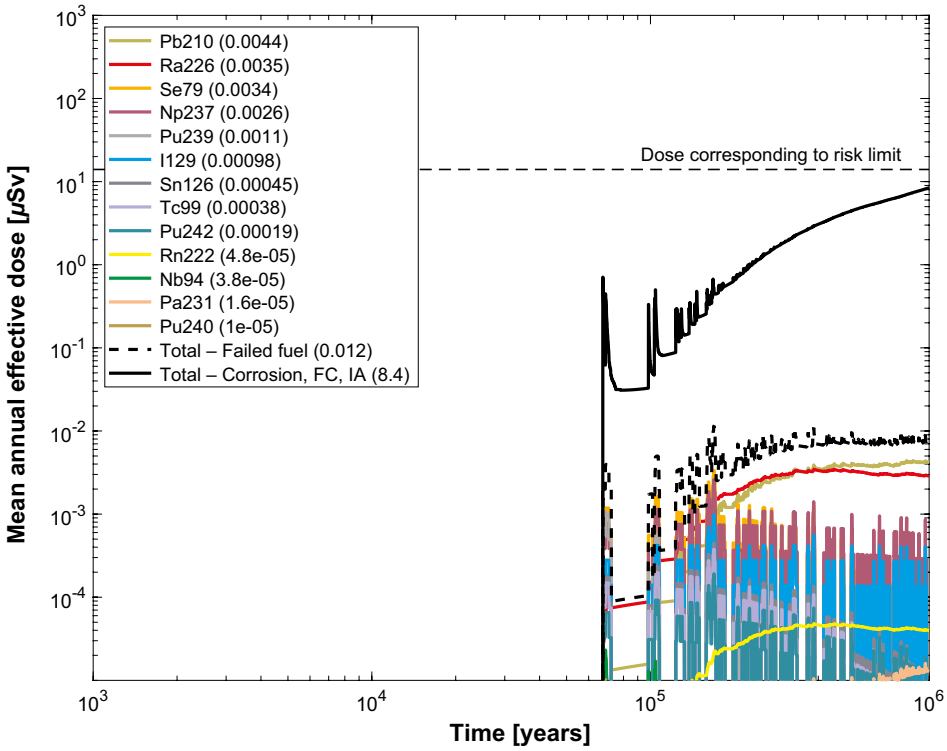

Figure 7-1. *Near-field dose equivalent release for the probabilistic calculation of the failed fuel case, which is based on the corrosion scenario, with hydrogeological data from the fully correlated model and initial advection in the erosion/corrosion model. The total mean annual effective dose from the corresponding corrosion case for regular fuel is shown as a black solid line for comparison. The legend is sorted by peak (in the one-million year period) of the mean annual effective dose. The values in brackets are peak dose in units of μSv.*

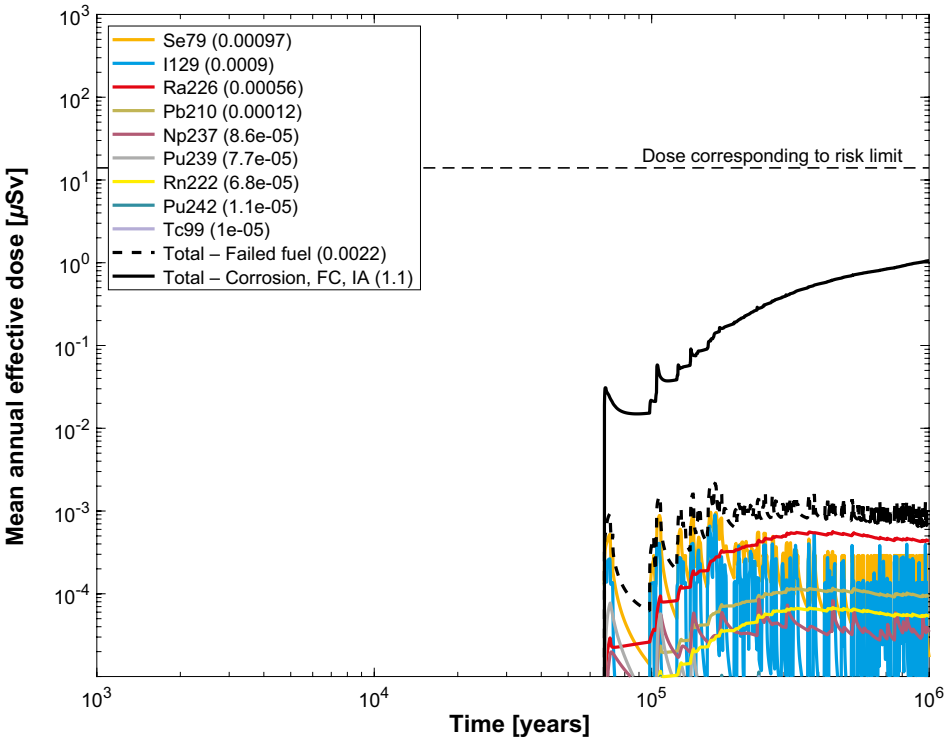

Figure 7-2. *Far-field dose mean annual effective dose for the probabilistic calculation of the failed fuel case, which is based on the corrosion scenario, with hydrogeological data from the fully correlated model and initial advection in the erosion/corrosion model. The total mean annual effective dose from the corresponding corrosion case for regular fuel is shown as a black solid line for comparison. The legend is sorted by peak (in the one-million year period) of the mean annual effective dose. The values in brackets are peak dose in units of μSv.*

7.1.2 Corrosion, fuel residues case

The content of the special containers containing fuel residues is described by Evins and Hedin (2013). In this calculation case, it is assumed that the rapidly dissolved fraction in these containers is released over a period of 1 000 years. A variant of the fully correlated corrosion case with initial advection is used to estimate the contribution to the dose from the fuel residues. In this case, the rapidly dissolved fraction is estimated to be 5.67×10^{-6}, and the dissolution rate of this fraction is estimated to be 1.0×10^{-3}/yr (Evins and Hedin 2013). The limited fraction of the inventory of concern is taken into account in the probabilistic calculation by multiplying the mean number of failed canisters for the fully correlated corrosion case (0.70) by 5.67×10^{-6}, yielding a mean number of failed canisters of 3.97×10^{-6} for this calculation case. This is under the assumption that the occurrence of fuel residues in a canister and the likelihood of canister failure are uncorrelated. This is seen as justified as there is no basis to assume such a correlation.

Probabilistic calculations

Hydrogeological case:	Fully correlated, five realisations
Erosion/corrosion model:	Initial advection
Failure time:	163 times according to the erosion/corosion calculations
Mean number of failed canisters:	3.97×10^{-6}
Fuel dissolution rate	1.0×10^{-3}/yr
Solubility limits:	No
Thorium sorption in near field:	Yes (modelled as low solubility limit)
Number of realisations:	50 per canister failure time
Number of nuclides:	38

A probabilistic calculation of the fuel residues case based on the fully correlated corrosion case with initial advection is performed with failure times and geosphere transport data from the five realisations of the fully correlated hydrogeological model and the updated ersosion/corrosion model (**Post-closure safety report**, Section 10.3.13).

The contributions from the instantly released fraction of nuclides, IRF, are not included in the calculations except for Tc-99 that is modelled and included in the figure showing results for the far field. The IRF was not included since this fraction of the inventory is not affected by an oxidised fuel matrix and hence the IRF results in Section 4.4.2 are representative also for the present case.

The dose equivalent releases from the near field and far field are shown in Figure 7-3 and Figure 7-4, respectively. The total mean annual effective dose from the fully correlated corrosion case with initial advection for regular fuel (described in Section M.9) is added to the figures for comparison.

The results show that the maximum total dose contribution from the fuel residues is almost four orders of magnitude lower than the corresponding corrosion case for regular fuel for both the near field and the far field, sustained over the entire one-million year period. The contribution from the fuel residues to the total dose is hence negligible. For the fuel residues, the radionuclides released from the near field are dominated by Pb-210, Ra-226, Se-79 and Np-237, while the dominating radionuclides released from the far field are Se-79, I-129 and Ra-226.

As for the case of failed fuel analysed in Section 7.1.1, it is also of interest to compare the consequences of a failure of a canister with a postulated content of fuel residues to that of a regular canister. Of the canisters with residual fuel considered in Evins and Hedin (2013), the one containing all the epoxy residues (canister #5) has the highest inventory of fuel with a high dissolution rate. This content corresponds to about 3.4 % of the inventory of a regular PWR canister according to data in Evins and Hedin (2013). If that canister fails, the dose can be crudely estimated to be increased by a factor of $10^{-3}/10^{-7} \times 0.034 \approx 340$ compared to a regular PWR canister for the approximately 1 000 years after failure during which the oxidised fraction of the fuel residues is assumed to be dissolved.

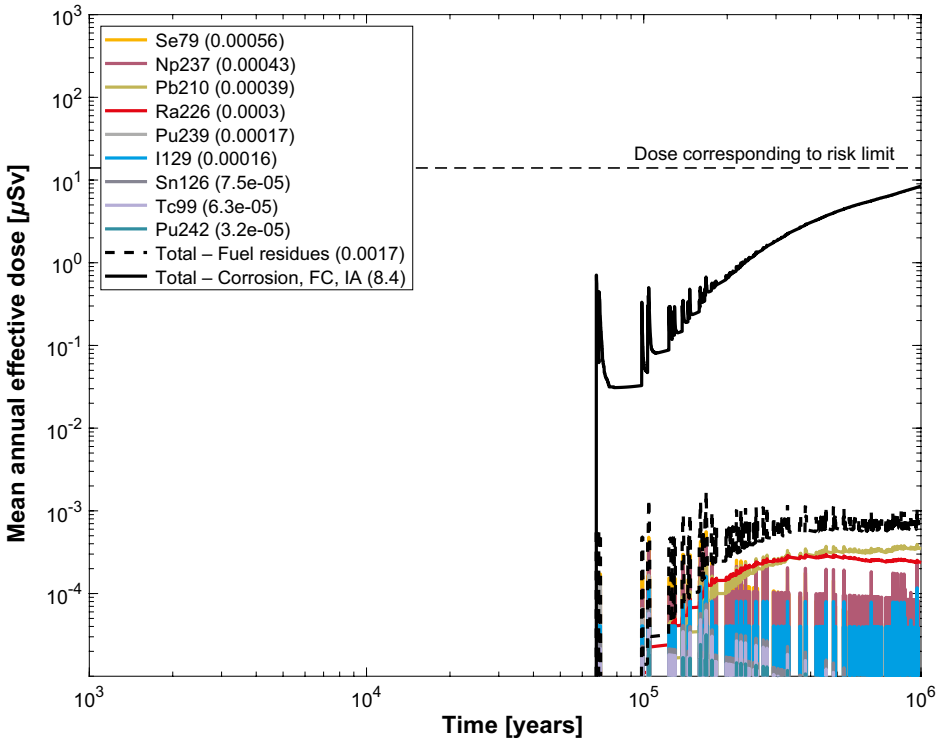

Figure 7-3. *Near-field dose equivalent release for the probabilistic calculation of the fuel residues case, which is based on the corrosion scenario, with hydrogeological data from the fully correlated model and initial advection in the erosion/corrosion model. The total mean annual effective dose from the corresponding corrosion case is shown as a black solid line for comparison. The legend is sorted by peak (in the one-million year period) of the mean annual effective dose. The values in brackets are peak dose in units of μSv.*

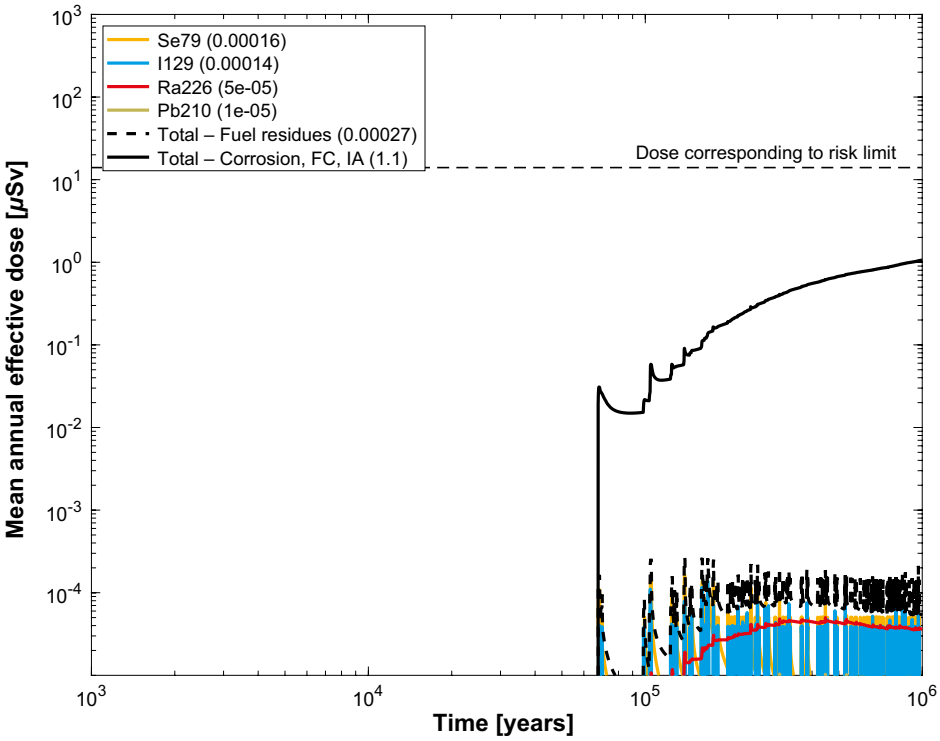

Figure 7-4. *Far-field mean annual effective dose for the probabilistic calculation of the fuel residues case, which is based on the corrosion scenario, with hydrogeological data from the fully correlated model and initial advection in the erosion/corrosion model. The total mean annual effective dose from the corresponding corrosion case is shown as a black solid line for comparison. The legend is sorted by peak (in the one-million year period) of the mean annual effective dose. The values in brackets are peak dose in units of μSv.*

7.2 Cases to illustrate hypothetical, early canister failures

This section describes additional cases to the ones performed to illustrate barrier functions, see Section 6.5. The basis for these additional cases with hypothetical early canister failures are described in detail in the **Post-closure safety report**, Section 13.7.3. In these cases, initial failures in **all** canisters are **postulated**. Two base cases with associated sensitivities are studied. Reasonably cautious assumptions are made for the performance of other parts of the repository system as base cases, and more pessimistic assumptions, for both the performance of the failed canisters and of other parts, are made in sensitivity cases.

A delay time between failure and the time when a water pathway is established (i.e the onset of transport) of 1 000 years is assumed, in the same way as in the corrosion scenario and the pinhole failure mode.

Further, it is assumed that 10 % of the canisters have lost their transport resistance already when the water pathway is established and the remaining 90 % do so after 10 000 years. The assumption is based on pessimistic evaluations of the time-scale for processes leading to a widening of an initially small failure and of the extent of initial cladding failures, see further Section 13.7.3 of the **Post-closure safety report**. A sensitivity case where the transport resistance is completely lost in all canisters already when the water pathway is established is also analysed.

The fuel, including the fuel matrix, the IRF and the fraction of the inventory embedded in metal parts of the fuel is assumed to perform as in all cases previously analysed.

The buffer is generally expected to remain intact and this is the assumption in case A in Table 7-1. In case B the buffer is assumed to be gradually lost due to erosion and sedimentation (**Post-closure safety report**, Section 13.7.3). A sensitivity case where the buffer is completely lost in all deposition holes after 20 000 years is also considered.

The semi-correlated hydrogeological model is used as a basis for these calculations and to cover variability and uncertainty as regards the hydrogeological conditions at the deposition holes and for the transport paths between the deposition positions and the biosphere, sensitivity calculations for case A are made also for the uncorrelated and fully correlated hydrogeological models.

For case A, the near field and far field models and other input data are the same as for the base case of the growing pinhole failure, see Section 6.3. For case B, the model and input data for times before the buffer is lost are the same as for case A. After the buffer is lost, the corrosion model and other input data are used for the radionuclide transport calculations.

The dynamic biosphere model, where the temporal development of the biosphere due to e.g. land-uplift is explicitly modelled, is used in these calculations. The release from the repository is distributed to the landscape objects according to the temporally developing release points of the transport paths in the geosphere. At each time step and for each nuclide the maximum total dose over all biosphere objects is used.

The analysed cases are summarised in Table 7-1.

Table 7-1. Summary of cases of hypothetical early canister failure.

Case	A	B
Failure time	0 yr	
Delay between failure and onset of transport	1 000 yr	
Delay between failure and loss of transport resistance	Base case: 0 yr for 10 % of the canisters and 10 000 yr for 90 % of the canisters. Sensitivity case: 0 yr for all canisters.	0 yr for 10 % of the canisters and 10 000 yr for 90 % of the canisters.
Buffer	Intact.	Base case: Gradually lost due to erosion and sedimentation. Sensitivity case: Buffer lost in all deposition holes after 20 000 years.
Hydrogeology	Base case: Semi-correlated. Sensitivity cases: Uncorrelated and fully correlated.	Semi-correlated.
Biosphere	Dynamic landscape model.	

7.2.1 Results for base case A, intact buffer

Figure 7-5 shows the mean annual effective dose for base case A where all canisters have failed initially and the buffer is intact. The peak annual dose is 32.8 μSv, i.e. slightly more than twice the dose corresponding to SSM's risk limit. The peak dose is completely dominated by I-129 and it occurs after around 15 000 years, reflecting the increased release from the canisters at 10 000 years, the point in time when the transport resistance in all canisters is assumed to have been completely lost. At earlier times, the sum dose is dominated by relatively rapid variations in C-14 dose. The C-14 dose is dominated by exposure through consumption of fish and the variations are caused by changes in the landscape due to changes in relative sea-level affecting the occurrence of lakes in the vicinity of the site. Beyond a few thousand years, the landscape is relatively unaffected by further changes in relative sea-level.

7.2.2 Results for base case B, gradually lost buffer

Figure 7-6 shows the mean annual effective dose for base case B where all canisters have failed initially and the buffer is gradually lost due to erosion and sedimentation. The peak annual dose is 32.8 μSv, the same as in base case A. The limited difference compared to base case A occurs beyond 100 000 years when the gradually lost buffer leads to somewhat higher doses in base case B.

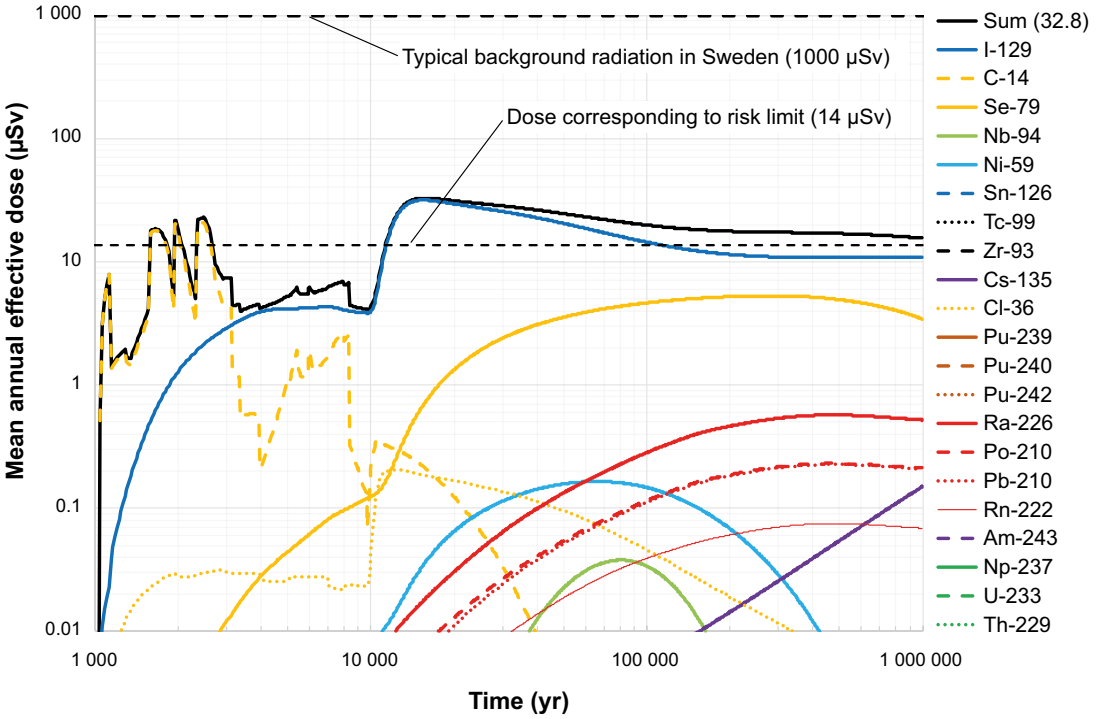

Figure 7-5. *Results for the hypothetical early canister failure scenario, base case A, with an initial failure in all canisters and intact buffer.*

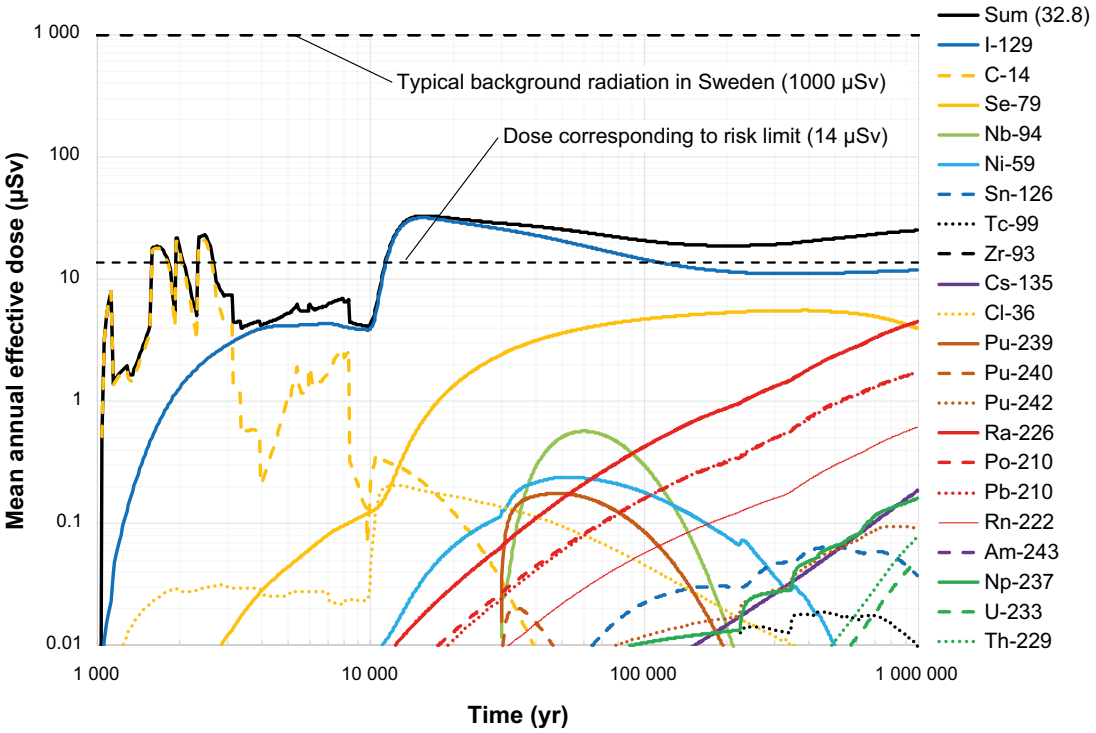

Figure 7-6. *Results for the hypothetical early canister failure scenario, base case B, with an initial failure in all canisters and where the buffer is gradually lost.*

7.2.3 Results for sensitivity cases

Sensitivity case A1, initial loss of transport resistance in all canisters

In sensitivity case A1 all canisters, rather than 10 % in the base case, are assumed to have no transport resistance as soon as a continuous water path is established. This case results in a peak dose of 216 µSv after around 2 500 years, again completely dominated by C-14, with the peak lasting for a few hundred years (the same curve structure before 10 000 years as in base case A, but elevated a factor of 10), see Figure 7-7.

Sensitivity cases A2 and A3, uncorrelated and fully correlated hydrogeological models

Two cases, A2 and A3, to address the sensitivity to the choice of hydrogeological model are calculated, using the uncorrelated and the fully correlated models instead of the semi-correlated model in base case A, see Figure 7-8 and Figure 7-9, respectively. This yields peak annual effective doses of 43 µSv and 53 µSv for the uncorrelated and fully correlated cases, respectively, i.e. less than a factor of 2 higher than in base case A. The peak doses occur after about 15 000 years, as for the base case. The doses are slightly higher than the base case beyond 100 000 years.

Sensitivity case B1, buffer lost in all deposition holes after 20 000 years

The pessimistic sensitivity case B1with completely lost buffer in all deposition holes after 20 000 years yields slightly higher doses than base case B beyond 20 000 years, reaching at most 66 µSv at around 55 000 years after repository closure. The total dose in this case is dominated by I-129 and Nb-94 and, at times beyond 200 000 years, by Ra-226, see Figure 7-10.

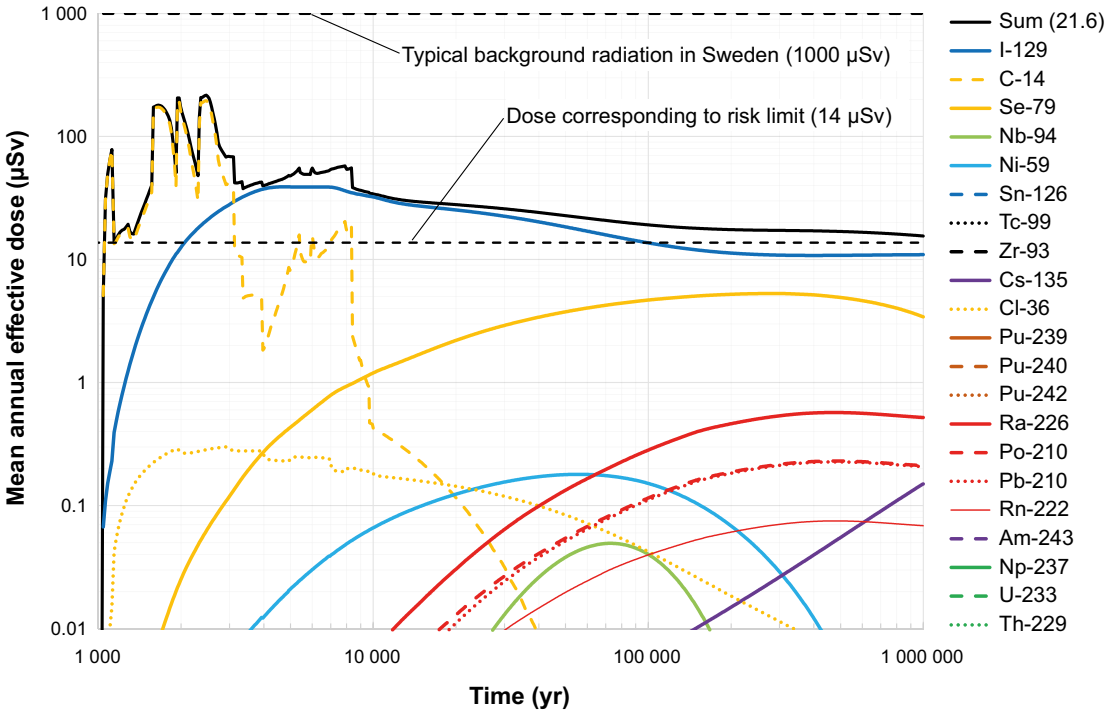

Figure 7-7. *Results for the hypothetical early canister failure scenario, with an initial failure in all canisters and intact buffer. Sensitivity case A1 with initial complete loss of transport resistance in all canisters (semi-correlated hydrogeological model).*

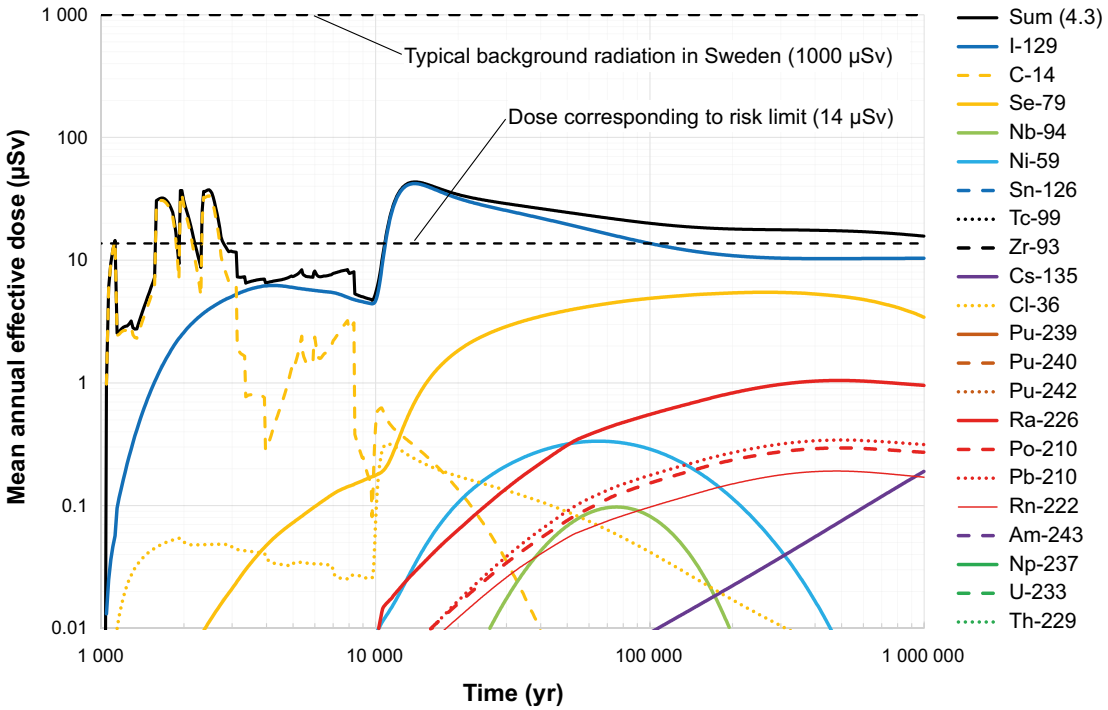

Figure 7-8. *Results for the hypothetical early canister failure scenario, with an initial failure in all canisters and intact buffer. Sensitivity case A2 with uncorrelated hydrogeological model.*

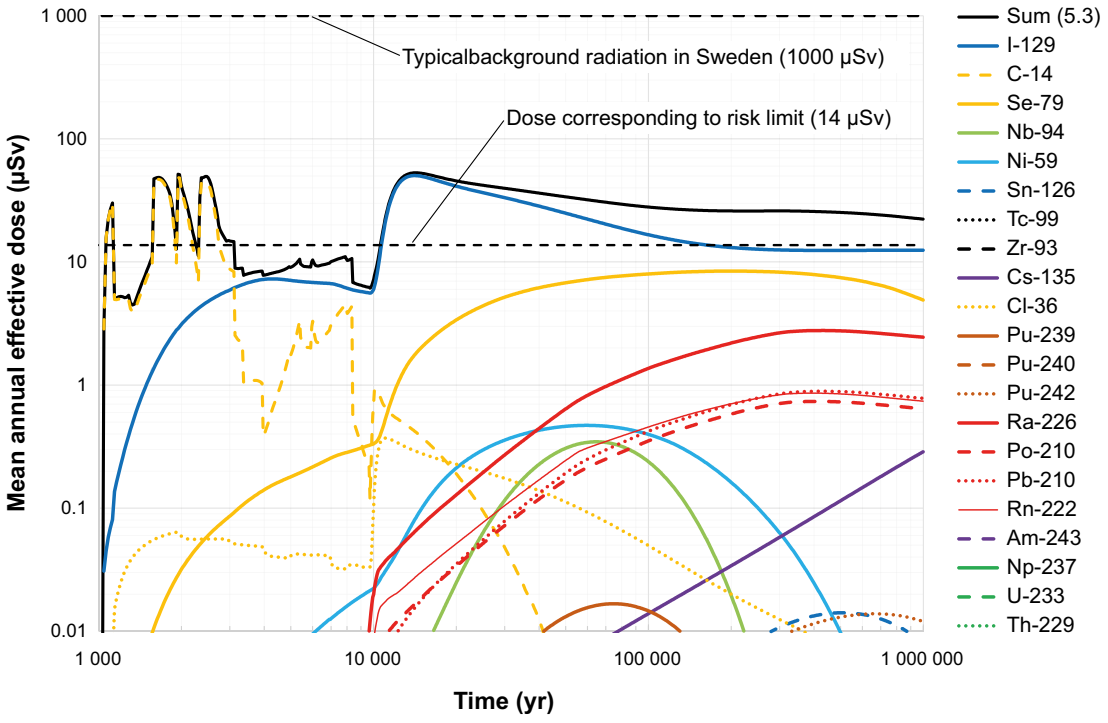

Figure 7-9. *Results for the hypothetical early canister failure scenario, with an initial failure in all canisters and intact buffer. Sensitivity case A3 with fully correlated hydrogeological model.*

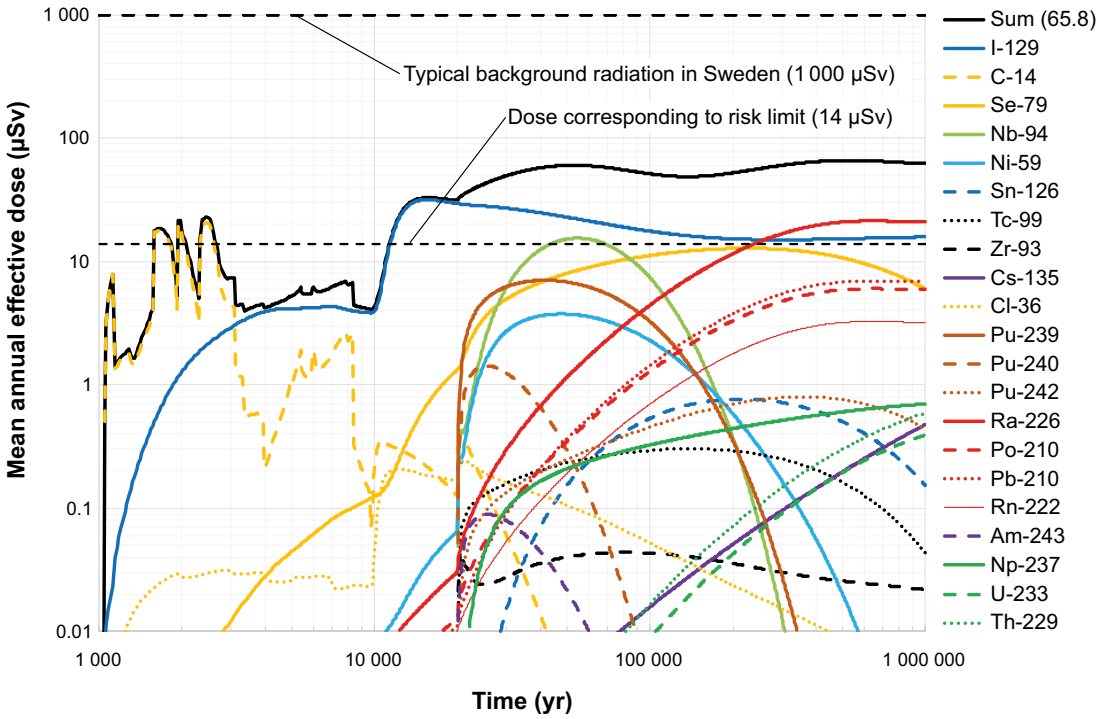

Figure 7-10. *Results for the hypothetical early canister failure scenario, with an initial failure in all canisters. Sensitivity case B1 with buffer lost in all deposition holes at 20 000 years (semi-correlated hydrogeological model).*

7.2.4 Summary and conclusions for the hypothetical early canister failure

This section discusses analyses of hypothetical, early canister failures, with reasonably cautious assumptions as to other parts of the repository system in two base cases. The results of the base cases show that even when all canisters are assumed to be failed at deposition, the resulting doses are about twice as high as that corresponding to the regulatory risk limit and occur around 15 000 years after deposition.

Disregarding also the transport resistance in an initially failed canister leads to doses around 15 times the risk limit. Sensitivity cases with more pessimistic assumptions concerning buffer loss and the hydrogeological model yields doses of at most five times the risk limit dose.

These analyses demonstrate that the protective capacity of other parts of the system is considerable. The canisters are required to strictly demonstrate compliance with the regulatory risk criterion. The analyses presented in this section imply, however, that even with completely hypothetical early failures in about half of the 6 000 canisters, the risk criterion can be met for the base cases. The most pessimistic sensitivity case yields peak doses that are about 20 % of that caused by the natural background radiation in Sweden and that last for about 1 000 years.

8 Summary and conclusions

The transport models for the near and far field are identical in the SR-Site assessment and the PSAR. Also, most of the calculated cases are the same and the input data to most cases are nearly identical. Therefore, the approach to accounting for radionuclide transport in the PSAR has been to calculate all cases related to compliance with all appropriate updates, whereas most of the cases used for illustrative and completeness purposes have not been recalculated. The recalculated cases are compared to the corresponding SR-Site cases and the minor differences in results is seen to justify the chosen approach.

Table 8-1 shows a summary of near-field and far-field maximum dose-equivalent releases for probabilistic numerical calculation cases discussed in this report. Results are given for both safety assessments, SR-Site and the PSAR, in separate columns. Note that not all SR-Site cases have been recalculated for the PSAR, which is why these results are missing for the PSAR. Similarly, there are complementary PSAR cases calculated where there are no corresponding SR-Site results. These comprise cases for irregular fuels in the corrosion scenario and cases to illustrate barrier function for hypothetical early canister failures. Contributions from the IRF are not included in the table. The maximum doses do not appear at the same time in all cases. In the corrosion cases and shear load cases the maximum normally appears at one million years while isostatic load cases and pinhole cases in general have their maximum shortly after the large failure in the canister is postulated.

For all probabilistic cases considered, the maximum over the one million year assessment time of the mean total far-field effective dose is smaller than the dose corresponding to the risk limit (except for hypothetical cases to illustrate barrier function). Excluding hypothetical cases (e.g. growing pinhole and postulated failure at 100 000 years due to shear load) and the cases supporting the discussion of best available technique, the far-field effective dose is at least one order of magnitude smaller than the dose corresponding to the risk limit. The two scenarios contributing to the calculated risk, i.e. failure of the copper canister by corrosion and earthquake-induced shear failure of the copper canister, the peak of the mean annual effective dose is estimated to be 0.17 μSv/yr and 0.18 μSv/yr, respectively. These doses, which assume reference conditions, can be compared with the dose corresponding to the risk limit of 14 μSv/yr and the dose corresponding to typical natural background radiation of approximately 1 000 μSv/yr. Further discussion of dose estimates associated with these and other scenarios and results of risk summation can be found in the **Post-closure safety report**.

In the scenario of failure of the copper canister due to corrosion, the geosphere provides only a modest (factor of 4) attenuation of the dose-equivalent release for the central case. The annual dose-equivalent release is relatively small because the geosphere provides benign geochemical and hydrological environments, thus limiting release from the waste form and engineered barriers. In variant corrosion cases that result in higher near-field releases, the far-field attenuation is somewhat stronger. This tendency to attenuate more strongly the larger near-field releases means that the geosphere also tends to reduce uncertainty in the far-field dose-equivalent releases.

The numerical radionuclide transport calculations are in good agreement with an analytical calculation using simplified modelling assumptions. This agreement significantly enhances confidence in the calculated dose-equivalent releases for two reasons. First, the comparison provides an important quality assurance check on the numerical modelling of dose-equivalent releases. This check applies not only to the numerical calculations but also to the data/parameter transfers, as the data for the analytical calculations were taken directly from the **Data report** independently of the numerical calculations. Second, it demonstrates that the effective dose for the corrosion cases and shear load case are controlled by relatively simple processes that are straightforward to understand. Additional confidence in the calculated results is provided by extensive sensitivity analyses and detailed calculations used to screen out effects of channelised flow, penetration of dilute waters and fracture mineral retention.

Table 8-1. Summary of results for numerical probabilistic calculation cases in the SR-Site and the PSAR. All cases are included except the multitude of cases to illustrate hypothetical barrier functions reported in Section 6.5 (calculated in SR-Site only) and the cases of hypothetical, early canister failures reported in Section 7.2 (calculated in the PSAR only).

Calculation case	SR-Site		PSAR	
	Maximum total near-field dose equivalent release (μSv/yr)	Maximum total far-field mean effective dose (μSv/yr)	Maximum total near-field dose equivalent release (μSv/yr)	Maximum total far-field mean effective dose (μSv/yr)
Dose corresponding to background radiation	1 000			
Dose corresponding to risk limit	14			
Canister failure due to corrosion				
Semi-correlated, central corrosion case	0.59	0.18	0.69	0.17
Semi-correlated, disregarding thorium in the near field	0.22	0.14	0.34	0.13
Semi-correlated including solubility limits	6.2	0.15	16	0.14
Semi-correlated, Kd for U(VI) instead of U(IV) in the geospehre	0.59	0.18	Not calculated	
Semi-correlated, 10 mg/l colloids	0.59	0.19	Not calculated	
Semi-correlated, 10 g/l colloids	0.59	0.33	Not calculated	
Semi-correlated, varying climate, no colloids	0.59	0.19	Not calculated	
Semi-correlated, varying climate, 10 g/l colloids	0.59	0.41	Not calculated	
Semi-correlated, varying climate and colloid concentration	0.59	0.35	Not calculated	
Semi-correlated with initial advection	1.0	0.27	1.1	0.24
Uncorrelated	3.1	0.45	5.2	0.6
Uncorrelated with initial advection	7.0	0.83	8.7	0.85
Fully correlated	3.2	0.63	5.5	0.82
Fully correlated with initial advection	6.0	0.96	8.4	1.1
Failed fuel	Not calculated		0.012	0.0022
Fuel residues	Not calculated		0.0017	0.00027
Canister failure due to shear load				
Postulated failure of one canister at 100 000 years	4.2	4.2	5.7	5.7
Failure during the period 1 000 years to one million years	0.15	0.15	0.18	0.18
Failure during the period 1 000 years to one million years, disregarding co-precipitation of radium and barium	0.24	0.24	0.28	0.28
Early failure	0.0027	0.0027	0.0028	0.0028
Combination of shear load and buffer advection	0.34	0.34	0.39	0.39
Canister failure due to isostatic load				
Postulated failure of one canister at 10 000 years	2.5	0.63	Not calculated	
Postulated failure of one canister at 100 000 years	1.5	0.39	Not calculated	
The growing pinhole failure				
Including the effect of spalling	3.7	0.65	5.1	0.85
Disregarding the effect of spalling	0.85	0.41	1.1	0.53
Lost swelling pressure in tunnel backfill, “Crown space”	9.5	2.7	Not calculated	
EDZ with a transmissivity of 10^{-6} m^2/s	5.8	2.0	Not calculated	
EDZ with a transmissivity of 10^{-7} m^2/s	4.2	1.1	Not calculated	
No EDZ	2.5	0.16	Not calculated	
Cases addressing best available technique (BAT)				
Copper shell thickness 25 mm	1.2	0.36	Not calculated	
Copper shell thickness 100 mm	0.25	0.078	Not calculated	
No T/L-filtering	1.3	0.71	Not calculated	
Neither T/L- nor EFPC-filtering	20	12	Not calculated	

9 References

SKB's (Svensk Kärnbränslehantering AB) publications can be found at www.skb.com/publications. SKBdoc documents will be submitted upon request to document@skb.se, with the exception of internal documents.

References with abbreviated names

Buffer, backfill and closure process report, 2022. Post-closure safety for the final repository for spent nuclear fuel at Forsmark – Buffer, backfill and closure process report, PSAR version. SKB TR-21-03, Svensk Kärnbränslehantering AB.

Canister production report, 2022. Produktionsrapport Kapsel. SKBdoc 1407944 ver 2.0, Svensk Kärnbränslehantering AB. (In Swedish.) (Internal document.)

Climate report, 2020. Post-closure safety for the final repository for spent nuclear fuel at Forsmark – Climate and climate related issues, PSAR version. SKB TR-20-12, Svensk Kärnbränslehantering AB.

Data report, 2022. Post-closure safety for the final repository for spent nuclear fuel at Forsmark – Data report, PSAR version. SKB TR-21-06, Svensk Kärnbränslehantering AB.

Fuel and canister process report, 2022. Post-closure safety for the final repository for spent nuclear fuel at Forsmark – Fuel and canister process report, PSAR version. SKB TR-21-02, Svensk Kärnbränslehantering AB.

Geosphere process report, 2022. Post-closure safety for the final repository for spent nuclear fuel at Forsmark – Geosphere process report, PSAR version. SKB TR-21-04, Svensk Kärnbränslehantering AB.

Model summary report, 2022. Post-closure safety for the final repository for spent nuclear fuel at Forsmark – Model summary report, PSAR version. SKB TR-21-05, Svensk Kärnbränslehantering AB.

Post-closure safety report, 2022. Post-closure safety for the final repository for spent nuclear fuel at Forsmark – Main report, PSAR version, SKB TR-21-01, Svensk Kärnbränslehantering AB.

Spent fuel report, 2021. Använt kärnbränsle att hantera i KBS-3-systemet. SKBdoc 1380282 ver 3.0, Svensk Kärnbränslehantering AB. (In Swedish.) (Internal document.)

Regular references

Abelin H, Birgersson L, Gidlund J, Neretnieks I, 1991a. A large-scale flow and tracer experiment in granite: 1. Experimental design and flow distribution. Water Resources Research 27, 3107–3117.

Abelin H, Birgersson L, Moreno L, Widén H, Ågren T, Neretnieks I, 1991b. A large-scale flow and tracer experiment in granite: 2. Results and interpretation. Water Resources Research 27, 3119–3135.

Abelin H, Birgersson L, Widen H, Ågren T, Moreno L, Neretnieks I, 1994. Channeling experiments in crystalline fractured rocks. Journal of Contaminant Hydrology 15, 129–158.

Amundson R G, Davidson E A, 1990. Carbon dioxide and nitrogenous gases in the soil atmosphere. Journal of Geochemical Exploration 38, 13–41.

André M, Neretnieks I, Malmström M, 2008. Measuring sorption coefficients and BET surface areas on intact drillcore and crushed granite samples. Radiochimica Acta 96, 673–677.

Arnorsson S, Stefansson A, 1999. Assessment of feldspar solubility constants in water in the range of 0 degrees to 350 °C at vapor saturation pressures. American Journal of Science 299, 173–209.

Avila R, Ekström P-A, Åstrand P-G, 2010. Landscape dose conversion factors used in the safety assessment SR-Site. SKB TR-10-06, Svensk Kärnbränslehantering AB.

Bath A, 2012. Groundwater chemistry in SKB's safety assessment SR-Site: initial review. Technical Note 2013:32, Swedish Radiation Safety Authority.

Bosbach D, Böttle M, Metz V, 2010. Experimental study on Ra^{2+} uptake by barite ($BaSO_4$). Kinetics of solid solution formation via $BaSO_4$ dissolution and $Ra_xBa_{1-x}SO_4$ (re) precipitation. SKB TR-10-43, Svensk Kärnbränslehantering AB.

Brantley S L, Olsen A A, 2014. Reaction kinetics of primary rock-forming minerals under ambient conditions. In Holland H D, Turekian K K (eds). Treatise on geochemistry. 2nd ed. Amsterdam: Elsevier, 69–113.

Bruno J, Bosbach D, Kulik D, Navrotsky A, 2007. Chemical thermodynamics of solid solutions of interest in nuclear waste management: a state-of-the-art report. Paris: OECD/NEA. (Chemical Thermodynamics 10)

Byegård J, Selnert E, Tullborg E-L, 2008. Bedrock transport properties. Data evaluation and retardation model. Site descriptive modelling, SDM-Site Forsmark. SKB R-08-98, Svensk Kärnbränslehantering AB.

Cherniak D J, 1997. An experimental study of strontium and lead diffusion in calcite, and implications for carbonate diagenesis and metamorphism. Geochimica et Cosmochimica Acta 61, 4173–4179.

Cherniak D J, 1998. REE diffusion in calcite. Earth and Planetary Science Letters 160, 273–287.

Cherniak D J, 2010. Diffusion in carbonates, fluorite, sulfide minerals, and diamond. Reviews in Mineralogy and Geochemistry 72, 871–897.

Chu S Y F, Ekström L P, Firestone R B, 1999. WWW table of radioactive isotopes, version 2.0. Available at: http://nucleardata.nuclear.lu.se/toi/

Cliffe K A, Kelly M, 2006. COMP23 version 1.2.2 user's manual. SKB R-04-64, Svensk Kärnbränslehantering AB.

Crank J, 1975. The mathematics of diffusion. 2nd ed. Oxford: Oxford University Press.

Crawford J, 2006. Modelling in support of bedrock transport property assessment. Preliminary site description. Laxemar subarea – version 1.2. SKB R-06-28, Svensk Kärnbränslehantering AB.

Crawford J, 2008. Bedrock transport properties Forsmark. Site descriptive modelling, SDM-Site Forsmark. SKB R-08-48, Svensk Kärnbränslehantering AB.

Crawford J, 2010. Bedrock K_d data and uncertainty assessment for application in SR-Site geosphere transport calculations. SKB R-10-48, Svensk Kärnbränslehantering AB.

Crawford J, 2014. Memorandum: Retardation of radionuclide transport in cement affected groundwater – response to the request by SSM for supplementary information on retention of radionuclides (SSM2011-2426-110), item 1. SKBdoc 1421672 ver 1.0, Svensk Kärnbränslehantering AB.

Crawford, J, Löfgren, M, 2019. Modelling of radionuclide retention by matrix diffusion in a layered rock model. SKB R-17-22, Svensk Kärnbränslehantering AB.

Curti E, 1999. Coprecipitation of radionuclides with calcite: estimation of partition coefficients based on a review of laboratory investigations and geochemical data. Applied Geochemistry 14, 433–445.

Curti E, Kulik D A, Tits J, 2005. Solid solutions of trace Eu(III) in calcite: thermodynamic evaluation of experimental data over a wide range of pH and pCO_2. Geochimica et Cosmochimica Acta 69, 1721–1737.

Cvetkovic V, Selroos J-O, Cheng H, 1999. Transport of reactive tracers in rock fractures. Journal of Fluid Mechanics 378, 335–356.

de Hoog F R, Knight J H, Stokes A N, 1982. An improved method for numerical inversion of Laplace transforms. SIAM Journal of Scientific and Statistical Computing 3, 357–366.

Dodson M H, 1973. Closure temperature in cooling geochronological and petrological systems. Contributions to Mineralogy and Petrology 40, 259–274.

Doerner H A, Hoskins W M, 1925. Co-precipitation of radium and barium sulphates. Journal of the American Chemical Society 47, 662–675.

Duro L, Grivé M, Cera E, Domènech C, Bruno J, 2006. Update of a thermodynamic database for radionuclides to assist solubility limits calculation for performance assessment. SKB TR-06-17, Svensk Kärnbränslehantering AB.

Ekberg C, Englund S, Liljenzin J-O, 2011. Uncertainty analysis of correlated stability constants. Accreditation and Quality Assurance 16, 185–189.

Eklund S, Mattsson K-J, 2008. Oskarshamn site investigation. Quantitative mapping of fracture minerals in Laxemar. SKB P-08-38, Svensk Kärnbränslehantering AB.

Eklund S, Mattsson K-J, 2009. Quantitative mapping of fracture minerals in Forsmark. Forsmark site investigation. SKB P-08-47, Svensk Kärnbränslehantering AB.

Elert M, Gylling B, Lindgren M, 2004. Assessment model validity document FARF31. SKB R-04-51, Svensk Kärnbränslehantering AB.

EU, 1996. Council Directive 96/92/EURATOM of 13 May 1996 laying down basic safety standards for the protection of the health of workers and the general public against the dangers arising from ionizing radiation. Luxembourg: European Commission.

EU, 2002. Testing of safety and performance indicators (SPIN). EUR 19965, European Commission.

Evins L Z, Hedin A, 2013. Uppskattning av riskbidrag från bränslerester. SKBdoc 1395834 ver 1.0, Svensk Kärnbränslehantering AB. (In Swedish.)

Evins L Z, Hedin A, 2020. Failed fuel in special containers: potential contribution to risk calculated in the post-closure safety for the spent nuclear fuel repository. SKBdoc 1872793 ver 1.0, Svensk Kärnbränslehantering AB.

Fenter P, Geissbühler P, DiMasi E, Srajer G, Sorensen L B, Sturchio N C, 2000. Surface speciation of calcite observed in situ by high-resolution X-ray reflectivity. Geochimica et Cosmochimica Acta 64, 1221–1228.

Fisler D K, Cygan R T, 1999. Diffusion of Ca and Mg in calcite. American Mineralogist 84, 1392–1399.

Follin S, 2008. Bedrock hydrogeology Forsmark. Site descriptive modeling, SDM-Site Forsmark. SKB R-08-95, Svensk Kärnbränslehantering AB.

Follin S, Johansson P-O, Hartley L, Jackson P, Roberts D, Marsic N, 2007. Hydrogeological conceptual model development and numerical modelling using CONNECTFLOW. Forsmark modelling stage 2.2. SKB R-07-49, Svensk Kärnbränslehantering AB.

Fransson Å, 2009. Literature survey: relations between stress change, deformation and transmissivity for fractures and deformation zones based on in situ investigatons. SKB R-09-13, Svensk Kärnbränslehantering AB.

Ganguly J, Tirone M, 1999. Diffusion closure temperature and age of a mineral with arbitrary extent of diffusion: theoretical formulation and applications. Earth and Planetary Science Letters 170, 131–140.

Giffaut E, Grivé M, Blanc P, Vieillard Ph, Colàs E, Gailhanou H, Gaboreau S, Marty N, Madé B, Duro L, 2014. Andra thermodynamic database for performance assessment: ThermoChimie. Applied Geochemistry 49, 225–236.

Gimeno M J, Auqué L F, Gómez J B, Acero P, 2008. Water-rock interaction modelling and uncertainties of mixing modelling. SDM-Site Forsmark. SKB R-08-86, Svensk Kärnbränslehantering AB.

Graly J A, Humphrey N F, Landowski C M, Harper J T, 2014. Chemical weathering under the Greenland Ice Sheet. Geology 42, 551–554.

Grivé M, Domènech C, Montoya V, Garcia D, Duro L, 2010. Simple Functions Spreadsheet tool presentation. SKB TR-10-61, Svensk Kärnbränslehantering AB.

Hamby D M, 1994. A review of techniques for parameter sensitivity analysis of environmental models. Environmental Monitoring and Assessment 32, 135–154.

Harker J H, Richardson J F, Backhurst J R, 2002. Chemical engineering. Vol 2. Particle technology and separation processes. 5th ed. Oxford: Butterworth-Heinemann.

Hedin A, 2002a. Safety assessment of a spent nuclear fuel repository: sensitivity analyses for prioritisation of research. In Bonano E J, Camp A L, Majors M J, Thompson R A (eds). Probabilistic Safety Assessment and Management, PSAM6: proceedings of the 6th International Conference on Probabilistic Safety Assessment and Management, 23–28 June 2002, San Juan, Puerto Rico. Amsterdam: Elsevier Science.

Hedin A, 2002b. Integrated analytic radionuclide transport model for a spent nuclear fuel repository in saturated fractured rock. Nuclear Technology 138, 179–205.

Hedin A, 2003. Probabilistic dose calculations and sensitivity analyses using analytic models. Reliability Engineering & System Safety 79, 195–204.

Hedin A, 2013. Documentation of the code for erosion and corrosion calculations in SR-Site. SKBdoc 1396663 ver 1.0, Svensk Kärnbränslehantering AB.

Hedin A, 2021a. Erosion, sedimentation and corrosion input and output data. SKBdoc 1939004 ver 2.0, Svensk Kärnbränslehantering AB.

Hedin A, 2021b. Models, input data and results for analytical erosion, sedimentation and corrosion calculations. SKBdoc 1927770 ver 1.0, Svensk Kärnbränslehantering AB.

Helton J C, 1993. Uncertainty and sensitivity analysis techniques for use in performance assessment for radioactive waste disposal. Reliability Engineering & System Safety 42, 327–367.

Henderson L M, Kraček F C, 1927. The fractional precipitation of barium and radium chromates. Journal of the American Chemical Society 49, 739–749.

Hodgkinson D P, Maul P R, 1988. 1-D modelling of radionuclide migration through permeable and fractured rock for arbitrary length decay chain using numerical inversion of Laplace transforms. Annals of Nuclear Energy 15, 175–189.

Hollenbeck K, 1998. INVLAP.M: A matlab function for numerical inversion of Laplace transforms by the de Hoog algorithm. Available at: https://www.mathworks.com/matlabcentral/answers/uploaded_files/1034/invlap.m

Håkansson R, 2000. Beräkning av nuklidinnehåll, resteffekt, aktivitet samt doshastighet för utbränt kärnbränsle. SKB R-99-74, Svensk Kärnbränslehantering AB. (In Swedish.)

IAEA, 1996. International basic safety standards for protection against ionizing radiation and for the safety of radiation sources. Vienna: International Atomic Energy Agency. (Safety Series 115)

ICRP, 1996. Age-dependent doses to members of the public from intake of radionuclides: Part 5. Compilation of ingestion and inhalation dose coefficients. Oxford: Pergamon for International Commission on Radiological Protection. (ICRP Publication 72)

Iman R L, Conover W J, 1979. The use of the rank transform in regression. Technometrics 21, 499–509.

IUPAC, 1997. Compendium of chemical terminology: IUPAC recommendations. 2nd ed. (the “Gold Book”). Compiled by A. D. McNaught and A.Wilkinson. Oxford: Blackwell Scientific Publications.

Joyce S, Simpson T, Hartley L, Applegate D, Hoek J, Jackson P, Swan D, Marsic N, Follin S, 2010. Groundwater flow modelling of periods with temperate climate conditions – Forsmark. SKB R-09-20, Svensk Kärnbränslehantering AB.

Kautsky U, 2012. Svar till SSM på begäran om förtydligande information angående ”Distributed LDF”. SKBdoc 1339994 ver 1.0, Svensk Kärnbränslehantering AB. (In Swedish.)

Kelly M, Cliffe K A, 2006. Validity document for COMP23. SKB R-06-76, Svensk Kärnbränslehantering AB.

Kesten H, 1982. Percolation theory for mathematicians. Boston: Birkhäuser.

Koyama T, 2005. Numerical modelling of fluid flow and particle transport in rock fractures during shear. Lic. thesis. Land and Water Resources Engineering, Royal Institute of Technology (KTH), Sweden.

Kulik D, Berner U, Curti E, 2004. Modelling chemical equilibrium partitioning with the GEMS-PSI code. PSI Scientific Report 2003, Volume IV, Nuclear energy and safety. Paul Scherrer Institute, Switzerland, 109–122.

Laaksoharju M, Smellie J, Tullborg E-L, Gimeno M, Hallbeck L, Molinero J, Waber N, 2008. Bedrock hydrogeochemistry Forsmark. Site descriptive modelling, SDM-Site Forsmark. SKB R-08-47, Svensk Kärnbränslehantering AB.

Laaksoharju M, Smellie J, Tullborg E-L, Wallin B, Drake H, Gascoyne M, Gimeno M, Gurban I, Hallbeck L, Molinero J, Nilsson A-C, Waber N, 2009. Bedrock hydrogeochemistry Laxemar. Site descriptive modelling, SDM-Site Laxemar. SKB R-08-93, Svensk Kärnbränslehantering AB.

Lahav N, Bolt G H, 1964. Self-diffusion of Ca45 into certain carbonates. Soil Science 97, 293–299.

Lichtner P C, 1988. The quasi-stationary state approximation to coupled mass transport and fluid-rock interaction in a porous medium. Geochimica et Cosmochimica Acta 52, 143–165.

Lindgren M, Lindström F, 1999. SR 97. Radionuclide transport calculations. SKB TR-99-23, Svensk Kärnbränslehantering AB.

Lindgren M, Widén H, 1998. Discretization in COMP23 for SR97. SKB R-98-03, Svensk Kärnbränslehantering AB.

Lindgren M, Pettersson M, Karlsson S, Moreno L, 2001. Project SAFE. Radionuclide release and dose from the SFR repository. SKB R-01-18, Svensk Kärnbränslehantering AB.

Lindgren M, Gylling B, Elert M, 2002. FARF31 Version 1-2 – User's guide. SKB TS-02-03, Svensk Kärnbränslehantering AB.

Löfgren M, 2014. Artefacts associated with electrical measurements of the rock matrix formation factor – response to the request by SSM for supplementary information on retention of radionuclides (SSM2011-2426-110). SKBdoc 1417017 ver 1.0, Svensk Kärnbränslehantering AB.

Löfgren M, 2015. Artefacts associated with electrical measurements of the rock matrix formation factor. With comments on handling in, and potential consequences for, the safety assessment SR-Site. SKB R-14-20, Svensk Kärnbränslehantering AB.

Löfgren M, Crawford J, 2014. Modelling of radionuclide retention by matrix diffusion in a layered rock model – Response to the request by SSM for supplementary information on retention of radionuclides (SSM2011-2426-110), items 4 and 6. SKBdoc 1421960 ver 1.0, Svensk Kärnbränslehantering AB.

Löfgren M, Sidborn M, 2010a. Statistical analysis of results from the quantitative mapping of fracture minerals in Forsmark. Site descriptive modelling – complementary studies. SKB R-09-30, Svensk Kärnbränslehantering AB.

Löfgren M, Sidborn M, 2010b. Statistical analysis of results from the quantitative mapping of fracture minerals in Laxemar. Site descriptive modelling – complementary studies. SKB R-09-31, Svensk Kärnbränlsehantering AB.

Mahmoudzadeh B, Liu L, Moreno L, Neretnieks I, 2013. Solute transport in fractured rocks with stagnant water zone and rock matrix composed of different geological layers – Model development and simulations. Water Resources Research 49, 1709–1727.

Molinero J, Trinchero P, de Vries L M, Ebrahimi H, Svensson U, 2016. The BRIDGE Project. Development, testing and application of a high performeance computing framework for reactive transport modelling in crystalline rocks (iDP). SKB R-15-17, Svensk Kärnbränslehantering AB.

Moreno L, Crawford J, 2009. Can we use tracer tests to obtain data for performance assessment of repositories for nuclear waste? Hydrogeology Journal 17, 1067–1080.

Neretnieks I, 1986. Stationary transport of dissolved species in the backfill surrounding a waste canister in fissured rock: some simple analytical solutions. Nuclear Technology 72, 194–200.

Neretnieks I, 2004. Predicting solute transport in fractured rocks-processes, models and some concerns. In Stephanson O (ed). Coupled thermo-hydro-mechanical-chemical processes in geo-systems – fundamentals, modelling, experiments and applications. Amsterdam: Elsevier. (Geo-engineering book series 2), 19–30.

Neretnieks I, 2006. Flow and transport through a damaged buffer – exploration of the impact of a cemented and an eroded buffer. SKB TR-06-33, Svensk Kärnbränslehantering AB.

Neretnieks I, Liu L, Moreno L, 2010. Mass transfer between waste canister and water seeping in rock fractures. Revisiting the Q-equivalent model. SKB TR-10-42, Svensk Kärnbränslehantering AB.

Nordén S, Avila R, de la Cruz I, Stenberg K, Grolander S, 2010. Element-specific and constant parameters used for dose calculations in SR-Site. SKB TR-10-07, Svensk Kärnbränslehantering AB.

Norman S, Kjellbert N, 1990. FARF31 – A far field radionuclide migration code for use with the PROPER package. SKB TR 90-01, Svensk Kärnbränslehantering AB.

Oelkers E H, 2001. General kinetic description of multioxide silicate mineral and glass dissolution. Geochimica et Cosmochimica Acta 65, 3703–3719.

Painter S, 2006. Effect of single-fracture aperture variability on field-scale transport. SKB R-06-25, Svensk Kärnbränslehantering AB.

Painter S, 2013. Responses to SSM on radionuclide transport. SKBdoc 1396392 ver 1.0, Svensk Kärnbränslehantering AB.

Painter S, Mancillas J, 2009. MARFA version 3.2.2 user's manual: migration analysis of radionuclides in the far field. SKB R-09-56, Svensk Kärnbränslehantering AB.

Painter S, Trinchero P, Sanglas J, 2020. MARFA User's manual: Migration analysis of radionuclides in the Far Field version 5.0. Available at: https://bitbucket.org/marfa_account/marfa-docs_git/downloads/marfa_user_manual_v5.0_rn1.pdf

Plummer L, Parkhurst, D, Wigley T, 1979. Critical review of the kinetics of calcite dissolution and precipitation. In Jenne E A (ed). Chemical modeling in aqueous systems: speciation, sorption, solubility, and kinetics. American chemical society. (ACS symposium series 93), 537–573.

Posiva SKB, 2017. Safety functions, performance targets and technical design requirements for a KBS-3V repository. Conclusions and recommendations from a joint SKB and Posiva working group. Posiva SKB Report 01, Posiva Oy, Svensk Kärnbränslehantering AB.

Rasilainen K, Nordman H, Suksi J, Marcos N, 2006. Direct alpha-recoil as aprocess to generate U-234/U-238 disequilibrium in groundwater. In Van Iseghem P (ed). Scientific basis for nuclear waste management XXIX. Warrendale, PA: Materials Research Society. (Materials Research Society Symposium Proceedings 932), 159.

Romero L, 1995. The near-field transport in a repository for high-level nuclear waste. PhD thesis. Department of Chemical Engineering and Technology, Royal Institute of Technology, Sweden.

Romero L, Moreno L, Neretnieks I, 1995. Fast multiple-path model to calculate radionuclide release from the near field of a repository. Nuclear Technology 112, 89–98.

Salas J, Gimeno M J, Molinero J, Auqué L F, Gómez J, Juárez I, 2010. SR-Site. Hydrogeochemical evolution of the Forsmark site. SKB TR-10-58, Svensk Kärnbränslehantering AB.

Saltelli A, Andres T H, Homma T, 1993. Sensitivity analysis of model output: an investigation of new techniques. Computational Statistics & Data Analysis 15, 211–238.

Saltelli A, Chan K, Scott E M (eds), 2000. Sensitivity analysis. Chichester: Wiley.

Sandström B, Stephens M, 2009. Mineralogy, geochemistry, porosity and redox properties of rocks from Forsmark. Compilation of data from the regional model volume for SR-Site. SKB R-09-51, Svensk Kärnbränslehantering AB.

Sandström B, Tullborg E-L, Smellie J, MacKenzie A B, Suksi J, 2008. Fracture mineralogy of the Forsmark site. SDM-Site Forsmark. SKB R-08-102, Svensk Kärnbränslehantering AB.

Selroos J-O, Cheng H, Painter S, Vidstrand P, 2013. Radionuclide transport during glacial cycles: comparison of two approaches for representing flow transients. Physics and Chemistry of the Earth, Parts A/B/C 64, 32–45.

Serco, 2008. CONNECTFLOW, release 9.6. Technical summary document. Serco Report SA/ENV/CONNECTFLOW/15, Serco Assurance, UK.

Shao H, Dmytrieva S V, Kolditz O, Kulik D A, Pfingsten W, Kosakowski G, 2009a. Modeling reactive transport in non-ideal aqueous-solid solution system. Applied Geochemistry 24, 1287–1300.

Shao H, Kulik D A, Berner U, Kosakowski G, Kolditz O, 2009b. Modeling the competition between solid solution formation and cation exchange on the retardation of aqueous radium in an idealized bentonite column. Geochemical Journal 43, e37–e42.

Sidborn M, Marsic N, Crawford J, Joyce S, Hartley L, Idiart A, de Vries L M, Maia F, Molinero J, Urban Svensson U, Vidstrand P, Alexander R, 2014. Potential alkaline conditions for deposition holes of a repository in Forsmark as a consequence of OPC grouting. Revised final report after review. SKB R-12-17, Svensk Kärnbränslehantering AB.

SKB, 1995. SR 95. Template for safety reports with descriptive example. SKB TR 96-05, Svensk Kärnbränslehantering AB.

SKB, 1999. Deep repository for spent nuclear fuel. SR 97 – Post-closure safety. Main report – Volume I, Volume II and Summary. SKB TR-99-06, Svensk Kärnbränslehantering AB.

SKB, 2004. Interim main report of the safety assessment SR-Can. SKB TR-04-11, Svensk Kärnbränslehantering AB.

SKB, 2006a. Long-term safety for KBS-3 repositories at Forsmark and Laxemar – a first evaluation. Main report of the SR-Can project. SKB TR-06-09, Svensk Kärnbränslehantering AB.

SKB, 2006b. Data report for the safety assessment SR-Can. SKB TR-06-25, Svensk Kärnbränslehantering AB.

SKB, 2008. Site description of Forsmark at completion of the site investigation phase. SDM-Site Forsmark. SKB TR-08-05, Svensk Kärnbränslehantering AB.

SKB, 2010a. Corrosion calculations report for the safety assessment SR-Site. SKB TR-10-66, Svensk Kärnbränslehantering AB.

SKB, 2010b. Data report for the safety assessment SR-Site. SKB TR-10-52, Svensk Kärnbränslehantering AB.

SKB, 2010c. Handling of future human actions in the safety assessment SR-Site. SKB TR-10-53, Svensk Kärnbränslehantering AB.

SKB, 2010d. Radionuclide transport report for the safety assessment SR-Site. SKB TR-10-50, Svensk Kärnbränslehantering AB.

SKB, 2010e. Underground openings construction report. SKB TR-10-18, Svensk Kärnbränslehantering AB.

SKB, 2011. Long-term safety for the final repository for spent nuclear fuel at Forsmark. Main report of the SR-Site project. SKB TR-11-01, Svensk Kärnbränslehantering AB.

SKB, 2013a. Svar till SSM på begäran om förtydligande angående radionuklidtransport. SKBdoc 1396389 ver 1.0, Svensk Kärnbränslehantering AB. (In Swedish.)

SKB, 2013b. Svar till SSM på begäran om komplettering rörande dokumentation och kvalitetssäkring av koder. SKBdoc 1396660 ver 1.0, Svensk Kärnbränslehantering AB. (In Swedish.)

Steefel C, MacQuarrie K, 1996. Approaches to modeling reactive transport in porous media. In Lichtner P C, Steefel C I, Oelkers E H (eds). Reactive transport in porous media. Washington, DC: Mineralogical Society of America. (Reviews in mineralogy 34), 83–125.

Stefansson A, 2001. Dissolution of primary minerals of basalt in natural waters: I. Calculation of mineral solubilities from 0 °C to 350 °C. Chemical Geology 172, 225–250.

Stipp S L, Hochella M F, Parks G A, Leckie J O, 1992. Cd^{2+} uptake by calcite, solid-state diffusion, and the formation of solid-solution: interface processes observed with near-surface sensitive techniques (XPS, LEED, and AES). Geochimica et Cosmochimica Acta 56, 1941–1954.

Stipp S L S, Konnerup-Madsen J, Franzreb K, Kulik A, Mathieu H J, 1998. Spontaneous movement of ions through calcite at standard temperature and pressure. Nature 396, 356–359.

Stoessell R K, 1991. Effects of sulfate reduction on $CaCO_3$ dissolution and precipitation in mixing-zone fluids. Journal of Sedimentary Petrology 62, 873–880.

STUK, 2001. Long-term safety of disposal of spent nuclear fuel. Guide YVL 8.4, Radiation and Nuclear Safety Authority, Finland.

Tang J, Dietzel M, Böhm F, Köhler S J, Eisenhauer A, 2008a. Sr^{2+}/Ca^{2+} and $^{44}Ca/^{40}Ca$ fractionation during inorganic calcite formation: II. Ca isotopes. Geochimica et Cosmochimica Acta 72, 3733–3745.

Tang J, Köhler S J, Dietzel M, 2008b. Sr^{2+}/Ca^{2+} and $^{44}Ca/^{40}Ca$ fractionation during inorganic calcite formation: I. Sr incorporation. Geochimica et Cosmochimica Acta 72, 3718–3732.

Thiel K, Vorwerk R, Saager R, Stupp H D, 1983. ^{235}U fission tracks and ^{238}U-series disequilibria as a means to study recent mobilization of uranium in Archaean pyritic conglomerates. Earth and Planetary Science Letters 65, 249–262.

Trinchero P, Painter S L, Poteri A, Sanglas J, Cvetkovic V, Selroos J-O, 2020. A particle-based conditional sampling scheme for the simulation of transport in fractured rock with diffusion into stagnant water and rock matrix. Water Resources Research 56. doi:10.1029/2019WR026958|

Vahlund F, Hermansson H, 2006. Compulink. Implementing the COMP23 model in Simulink. SKB R-06-86, Svensk Kärnbränslehantering AB.

van Calsteren P, Thomas L, 2006. Uranium-series dating applications in natural environmental science. Earth-Science Reviews 75, 155–175.

Vidstrand P, Follin S, Zugec N, 2010. Groundwater flow modelling of periods with periglacial and glacial conditions – Forsmark. SKB R-09-21, Svensk Kärnbränslehantering AB.

Watson E J, 1981. Laplace transforms and applications. New York. (Van Nostrand Reinhold new mathematics library 10)

Watson E B, 1996. Surface enrichment and trace-element uptake during crystal growth. Geochimica et Cosmochimica Acta 60, 5013–5020.

Watson E B, 2004. A conceptual model for near-surface kinetic controls on the trace-element and stable isotope composition of abiogenic calcite crystals. Geochimica et Cosmochimica Acta 68, 1473–1488.

Watson E B, Baxter E F, 2007. Diffusion in solid-Earth systems. Earth and Planetary Science Letters 253, 307–327.

Wold S, 2010. Sorption of prioritized elements on montmorillonite colloids and their potential to transport radionuclides. SKB TR-10-20, Svensk Kärnbränslehantering AB.

Yang J, 2012. Reactive silica transport in fractured porous media: Analytical solution for a single fracture. Computers & Geosciences 38, 80–86.

Zhu C, 2004. Coprecipitation in the barite isostructural family: 2. Numerical simulations of reactions and mass transport. Geochimica et Cosmochimica Acta 68, 3339–3349.

Appendix A

On the impact of channelised flow

This appendix has not been changed since the SR-Site assessment.

A.1 Overview of channelling phenomena

Dynamically channelised flow within the plane of individual fractures is a frequently encountered channelling phenomenon. This appendix deals primarily with screening calculations involving this type of flow channelling to demonstrate that the effects on the flow-related transport resistance (F) used in radionuclide transport calculations can be ignored. Network-scale flow channelling arising due to the heterogeneity and hydraulic connectivity of sparse fracture networks is included implicitly in hydrogeological discrete fracture network models used to assess groundwater flow and is not discussed here. Physical flow channels in the form of erosion pipes and other geologically predicated features are thought to be less important partly owing to their limited extent and fixed localisation in the fracture network thereby implying that they are not expected to form contiguous, unbroken pathways through the geosphere (Crawford 2008).

The results obtained by Painter (2006) show that internal transmissivity variability of a fracture has only a minor effect on the distribution of F and advective travel times provided network scale transmissivity variability governs the overall rate of flow in a fracture system. This is not an unreasonable assumption since transmissivities of individual fractures as assessed by borehole measurements typically range over some orders of magnitude and are customarily represented as log-normally distributed in hydrogeological modelling. It is also becoming increasingly apparent that connectivity effects related to restriction of flow in *hydraulic chokes* or *bottlenecks* can also have an overwhelmingly dominant effect on the flow of water in a fracture system regardless of how transmissivities are assigned on the level of individual fractures (Follin et al. 2007). These aspects are, however, neglected in the treatment given here and the focus is upon assessment of the flow-wetted surface in an individual fracture hosting channelised flow.

Studies of excavated single fractures suggest that the composite surface topography of the pore space and, by extension, the local hydraulic transmissivity can be reasonably well approximated as a lognormal distribution with spatially correlated variations. These are frequently described as being self-affine in character where opposing surfaces are closely matched at long wavelengths although mismatched at shorter wavelengths usually due to shear displacement of the opposing surfaces. This results in a decaying power law spectrum for the aperture field where wavelengths beyond a certain cut-off limit can be neglected. Although there are small differences between different spectral representations of the aperture variation, the general principle is consistent with a conventional geostatistical model with specified correlation lengths as noted by Painter (2006).

Although not all fractures are under compression, contacting fracture surfaces are expected to occur owing to the need for fracture surfaces to be in physical contact in order to transmit stress under in situ conditions. As demonstrated in Crawford (2008), increasing compression of the fracture pore spaces results in increasing surface contact, decreasing transmissivity and more intense flow channelling. This is expected behaviour regardless of whether fracture asperities are destroyed by compressive forces or whether they deform elastically. Provided the distance over which a hydraulic gradient is applied is significantly greater than the characteristic length of aperture variation, whether defined in terms of a correlation length or some equivalent fractal measure, a theoretical percolation limit is reached at a surface contact fraction of approximately 50 % (Kesten 1982). Although the relation between in situ fracture normal stress and surface asperity contact fraction is complex, increasing contact fractions appears to result in a rapidly (hyperbolic) decaying transmissivity (e.g. (Koyama 2005, Fransson 2009).

This should not be taken to mean that at least 50 % of the fracture surface is always accessible in a flow-bearing fracture since one also must take into consideration the locations and extent of source and sink terms for the externally applied flow regime and the distribution of flow velocities in the

available advective pore space. A typical example of the dynamic nature of flow channelling in a self-affine, variable aperture fracture is shown in Figure A-1 based on a finite difference simulation described in Crawford (2008).

As can be readily appreciated from the simple demonstration in Figure A-1, local flowrates can vary over many orders of magnitude and the area of fracture surface in contact with the bulk of the flow may only be a very small fraction of the total surface area. It is interesting to note, however, that even at very large relative surface contact fractions (< 50 %) most of the mechanically open parts of the fracture are hydraulically accessible at least in principle. Large portions of the fracture surface while not hosting significant amounts of flow will experience flow of some kind owing to the presence of hydraulic gradients. Although this means that it is not possible to strictly speak in terms of truly stagnant zones, large parts of the fracture will experience sufficiently low flows that they can be regarded as being effectively stagnant for all practical purposes.

The analysis of dynamic flow channelling with increasing surface contact fraction indicates that the most compressed fractures exhibit the lowest transmissivities and greatest flow channelling effects. Fractures that are subject to very little compression will exhibit far less flow channelling. It therefore can be argued that the most transmissive flowpaths through the fractured rock will exhibit relatively little flow channelling on the level of individual fractures even if network scale flow channelling is significant.

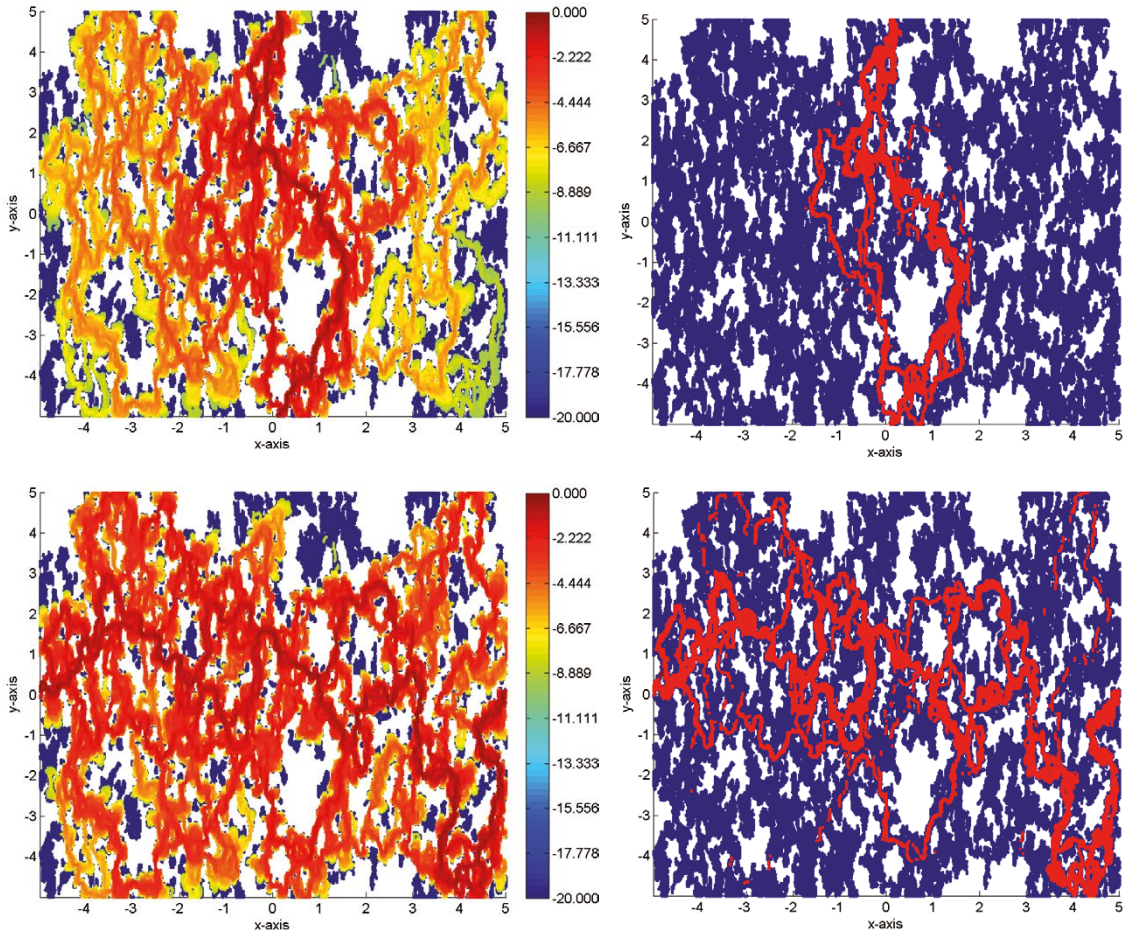

Figure A-1. *Example of typical dynamic flow channels arising in a self-affine, variable aperture fracture with a surface asperity contact fraction of 40 % and hydraulic gradient applied vertically (top) and horizontally (bottom) for a simple line source/sink dipole boundary condition of limited extent. Hydraulically inaccessible regions of the fracture are non-coloured. The left-hand images indicate the flow magnitude normalised with respect to the maximum flowrate (log_{10} units). The right-hand images show flow channels featuring flow > 1 % (arithmetic units) of the maximum flowrate highlighted in red.*

A.2 Scoping calculations of channelised flow

In order to ascertain the likely impact of flow channelling in fractures where it does occur, it is instructive to consider some very simplified examples. Figure A-2 shows an idealised representation of a flowpath of length L hosting a hypothetical flow channel of width W_c where the channelled flow-wetted surface is about 10 % of the total fracture surface area. If the F for the case (1) where flow contacts the entire surface area of the fracture is denoted F_0, the F value for the case with flow channelling (2) can be shown to be 10 % of this, or $0.1 \cdot F_0$.

It is not known with certainty how wide the dynamic flow channels in fractured rock should be although it has been speculated by e.g. Abelin et al. (1994) and Neretnieks (2004) that they are most likely in the range of a few cm to a few tens of cm at most. For the calculations in this Appendix, a flow channel width, W_c of 10 cm and an average stagnant zone aperture, δ_s of 0.1 mm are assumed as a basis for scoping calculations. For comparison, the assumed aperture may be taken to be roughly the thickness of a standard sheet of A4 paper. The half-width, W_s of the stagnant zone is 4.5 times greater than the width of the flow channel.

If one accounts for the normal matrix diffusion process (direct uptake) plus the additional effect of diffusion within the stagnant zone and subsequent diffusive uptake to the rock matrix (indirect uptake), the following Laplace space equation describes the residence time distribution of a non-decaying solute in the fracture (Crawford 2006, 2008):

$$\tilde{c}_f = \frac{1}{s}\exp\left(-t_w\sqrt{s}\right)\cdot\exp\left(-F\left(\psi_m + R_s\psi_s\right)\right) \tag{A-1}$$

Since we are mostly interested in ascertaining the impact of flow channelling on the early breakthrough of the residence time distribution, the rock matrix can be assumed to be effectively infinite for the scoping calculation. The direct matrix flux term, ψ_m and the additional indirect matrix flux term, ψ_s can then be given as:

$$\psi_m = \sqrt{D_e\left(\theta_m + K_d\rho_r\right)s} \tag{A-2}$$

$$\psi_s = \sqrt{D_w\left(s + \frac{2}{\delta_s}\sqrt{D_e\left(\theta_m + K_d\rho_r\right)s}\right)}\tanh\left(W_s\sqrt{\frac{1}{D_w}\left(s + \frac{2}{\delta_s}\sqrt{D_e\left(\theta_m + K_d\rho_r\right)s}\right)}\right) \tag{A-3}$$

The variables and parameters in equation A-1 to A-3 represent the following physical quantities:

- D_e (m^2/y) is the effective diffusivity of the rock matrix.
- D_w (m^2/y) is the free component diffusivity in fracture water.
- K_d (m^3/kg) is the sorption partitioning coefficient for the rock matrix.
- s is the operator variable in the Laplace domain (or simply, Laplace space variable).
- W_s (m) is the average width of the stagnant zone.
- δ_s (m) is the average transport aperture of the effectively stagnant zone.
- ρ_r (kg/m^3) is the bulk density of the rock matrix.
- θ_m (m^3/m^3) is the transport porosity of the rock matrix.

The parameter R_s is simply the aspect ratio of mass transfer surface area (i.e. for mass transfer to the stagnant zone relative to the surface area of fracture in contact with the advective flow). For a flow channel with symmetric flanking stagnant zones, R_s is given by:

$$R_s = \frac{\delta_s}{W_c} \tag{A-4}$$

Since a closed form analytical solution in the time plane is not available for this problem, the Laplace space solution in Equation A-1 can be inverted numerically using a suitable algorithm. In the present analysis, the algorithm described by de Hoog et al. (1982) and implemented in the Matlab function developed by Hollenbeck (1998) has been used. For illustrative purposes, a relatively low range F of $F_0 = 5 \times 10^5$ yr/m is assumed for the flowpath under consideration. It is implicitly assumed that the flanking stagnant zone persists along the whole flowpath, although the R_s parameter can simply be re-scaled to accommodate other possible scenarios. For the channelling scenario (Case 2) and assuming

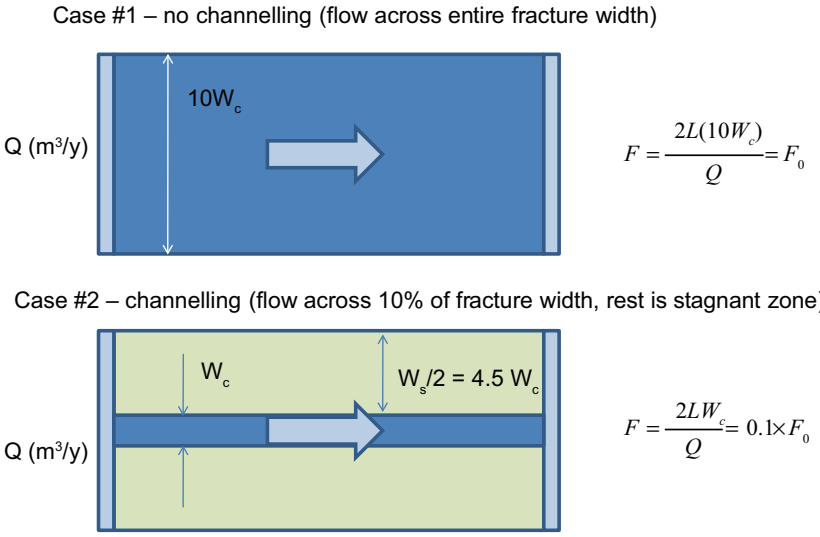

Figure A-2. *Idealised example of a simple flow channel of width W_c equal to 10 % of the fracture width hosted in a fracture of length L (Case 2 – bottom) as compared with the null case of a fracture where flow contacts the entire surface (Case 1 – top). Case 2 approximately corresponds to the F scaling assumption used in SR-Can (SKB 2006a).*

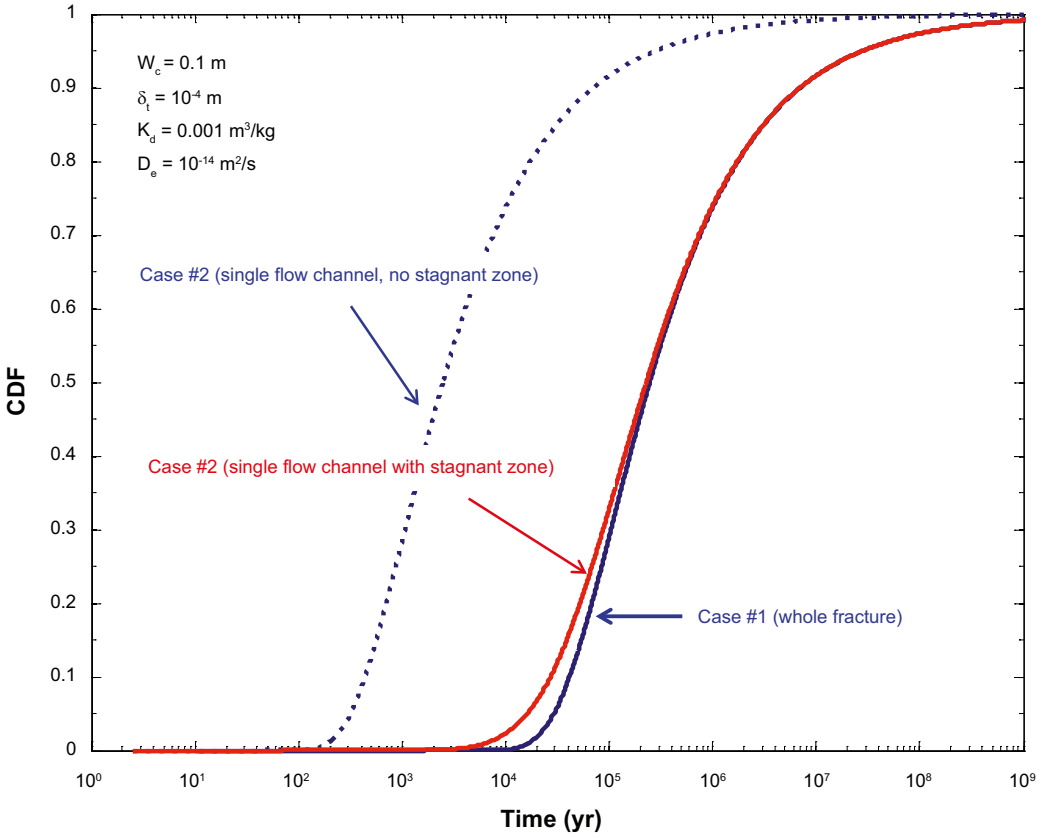

Figure A-3. *Residence time distribution for a weakly sorbing solute (K_d = 0.001 m^3/kg) assuming no channelling (Case 1, solid blue curve), flow channelling without stagnant zone diffusion (Case 2, broken blue curve), and flow channelling with stagnant zone diffusion (Case 2, red curve). The reference F value for Case #1 is 5×10^5 yr/m. Results are shown as a cumulative probability density function (CDF).*

the scaling rule adopted in SR-Can, the whole fracture F value is reduced by a factor of ten, thereby giving an effective F of $F = 5 \times 10^4$ yr/m. Figure A-3 shows the residence time distribution calculated of a moderately sorbing solute ($K_d = 0.001$ m^3/kg) for the reference scenario (Case 1) and the flow channelling scenario (Case 2) both with and without consideration of stagnant zone diffusion and neglecting advective travel time.

As can be readily appreciated from the results shown in Figure A-3, diffusion of solute within the stagnant zone allows the solute to contact much of the surface area of the fracture not directly contacted by the advective flow. There is, however, some deviation at very early breakthrough times, which indicates that the stagnant zone does not fully equilibrate diffusively at short times. This is more apparent if the result is plotted on a log-log scale as in Figure A-4. At very short times, the red curve depicting channelling with stagnant zone diffusion approaches the case depicted by the blue curve where the stagnant zone is neglected.

At first glance this would appear to indicate that although much of the surface area in the stagnant zone may be accessible for matrix diffusion, the early breakthrough of solute still occurs at much earlier time than for the reference scenario (Case 1). Having said this, however, it is important to realise that the scenario depicted in Figure A-2 is somewhat unrealistic given that flow channels are predicted to bifurcate and rejoin repeatedly, fanning out in a similar fashion to that shown in Figure A-1. If we consider the case where there are more numerous although smaller flow channels, a simplified representation might look like that shown in Figure A-5. In this case, there are 10 smaller flow channels of width 1 cm, although still occupying roughly 10 % of the fracture surface area.

There are two key differences between the two different channelling scenarios illustrated by Case 2 and Case 3. The first is that the aspect ratio parameter R_s is ten times greater in Case 3. The second key difference is that the width of the stagnant zone is ten times smaller in Case 3. These differences fundamentally alter the timescale of diffusive mass transfer between the advective and stagnant zones. Results for channelling scenario where there are 10 smaller flow channels (Case 3) is shown in Figure A-6 together with the other flow channelling scenarios for reference purposes. The same results are plotted in Figure A-7 although on log-log axes to illustrate the early time breakthrough behaviour of Case 3.

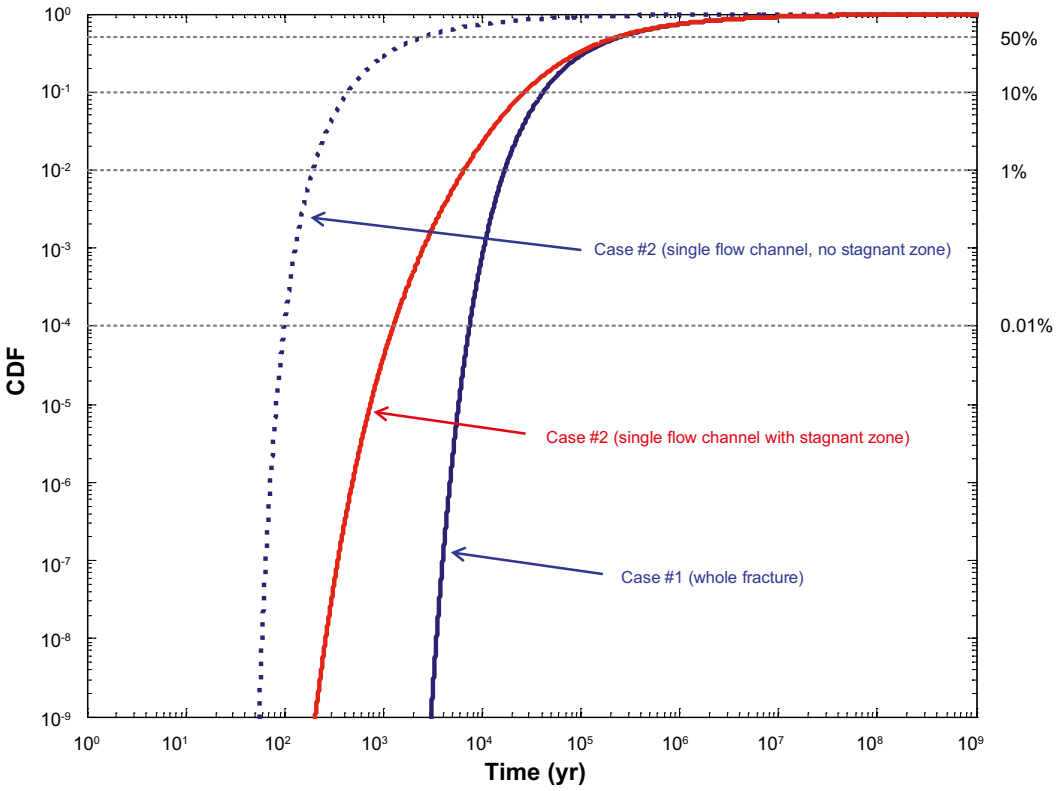

Figure A-4. *Same results as in the previous Figure although plotted on a log-log axis. Different recovery fractions corresponding to 0.01 % - 50 % of released solute are also indicated by the horizontal broken lines for reference purposes.*

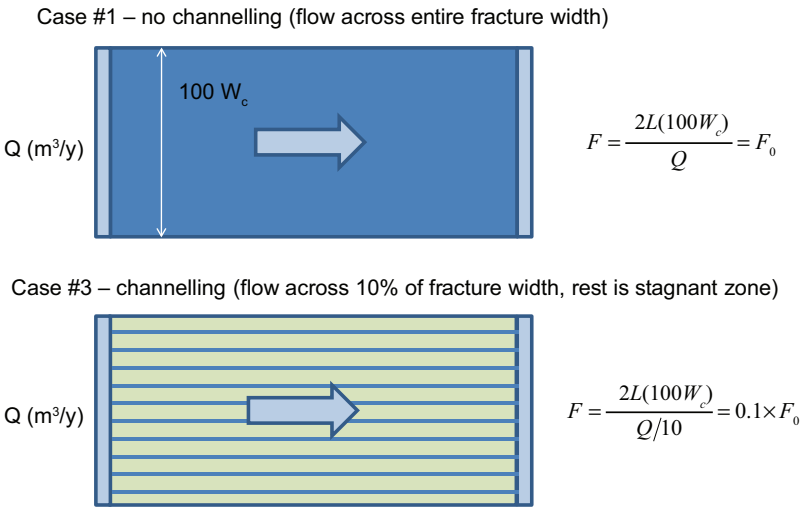

Figure A-5. *Idealised example of 10 flow channels of width W_c equal to 1 % of the fracture width hosted in a fracture of length L (Case 3 – bottom) as compared with the null case of a fracture where flow contacts the entire surface (Case 1 – top). Case 3 approximately corresponds to the F scaling assumption used in SR-Can (SKB 2006a).*

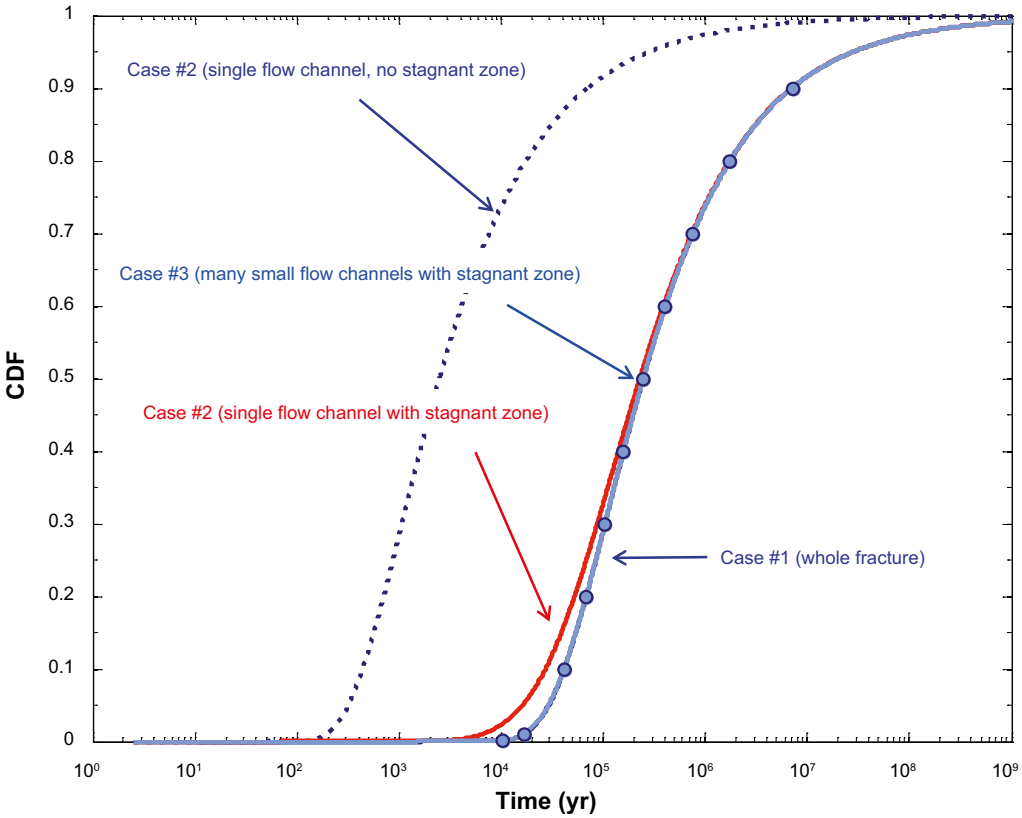

Figure A-6. *Residence time distribution for a weakly sorbing solute (K_d = 0.001 m^3/kg) for the channelling scenario involving 10 smaller flow channels although for the same total flow-wetted surface (10 % of fracture surface area). The same channelling scenarios as in the previous Figures are also shown for comparison. The reference F value for Case #1 is 5×10^5 yr/m. Results are shown as a cumulative probability density function (CDF).*

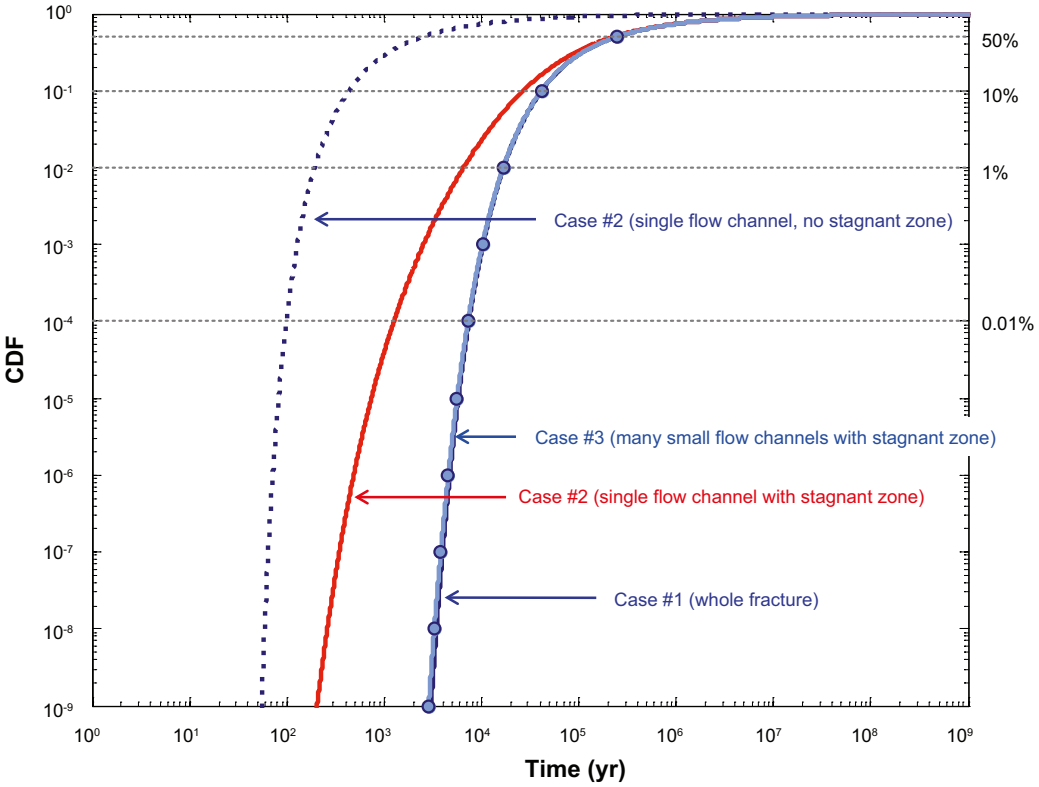

Figure A-7. *Same results as in the previous Figure although plotted on a log-log axis. Different recovery fractions corresponding to 0.01 % - 50 % of released solute are also indicated by the horizontal broken lines for reference purposes.*

As can be seen from Figure A-6, the 10 times larger R_s and 10 times smaller W_s in Case 3 results in a much faster diffusive equilibration of the stagnant zone. It is difficult to see any difference between the reference scenario without channelling (Case 1) and the scenario with 10 small flow channels (Case 3) down to at least 1 ppb of the solute residence time distribution function. For this channelling case it is therefore entirely reasonable to not scale down the original F value by an order of magnitude. The mass transfer occurs sufficiently quickly that the main flow channel can be assumed to be in diffusive equilibrium with the stagnant zone.

In general, the characteristic of the transient at early times before diffusive equilibrium is achieved depends on the R_s parameter, the width of the stagnant zone, and the F for the flow channel. The width of the stagnant zone also sets an upper limit on the maximum diffusion accessible surface area in the fracture. It is also interesting to note that the magnitude of the mechanical aperture of the fracture in the stagnant region has very little effect on the result since the storage capacity of the stagnant zone pore space is miniscule in comparison to the storage capacity of the rock matrix with which it is in contact. The only way that the aperture, δ_s impacts on the result is by way of its influence on the mass transfer area aspect ratio parameter, R_s as it is defined in Equation A-4. Figure A-8 shows the effect that varying the reference F (i.e. F_0 in Case 1) has upon the result where channelling and stagnant zone diffusion is considered (Case 2). The same results are presented in Figure A-9 although plotted on log-log axes.

As can be seen from Figure A-8 and Figure A-9, increasing the F value by a factor of 10 increases the recovery time by a factor of 100. This is expected behaviour based on the quadratic scaling of matrix retention time with the F as described elsewhere (Crawford 2008). Extremely low F values ($\sim 5 \times 10^4$ yr/m and less) result in very little transport retardation and there is generally insufficient time for diffusive equilibrium to be established throughout the stagnant zone. For larger F values, however, the stagnant zone reaches diffusive equilibrium sufficiently quickly that the early break-through promoted by channelling is much reduced.

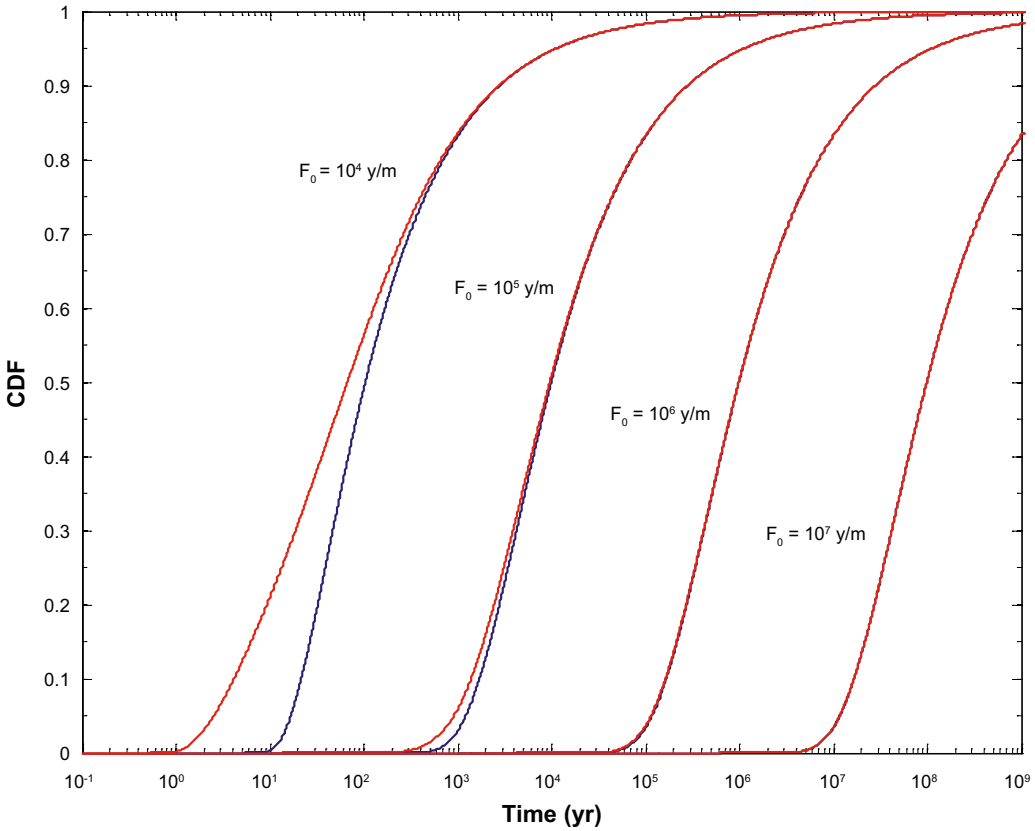

Figure A-8. *Residence time distribution for a weakly sorbing solute (K_d = 0.001 m^3/kg) for the simplified channelling scenario (red curves, Case 2) as compared to the reference scenario (blue curves, Case 1). Results are shown as a cumulative probability density function (CDF) for different reference case F as indicated.*

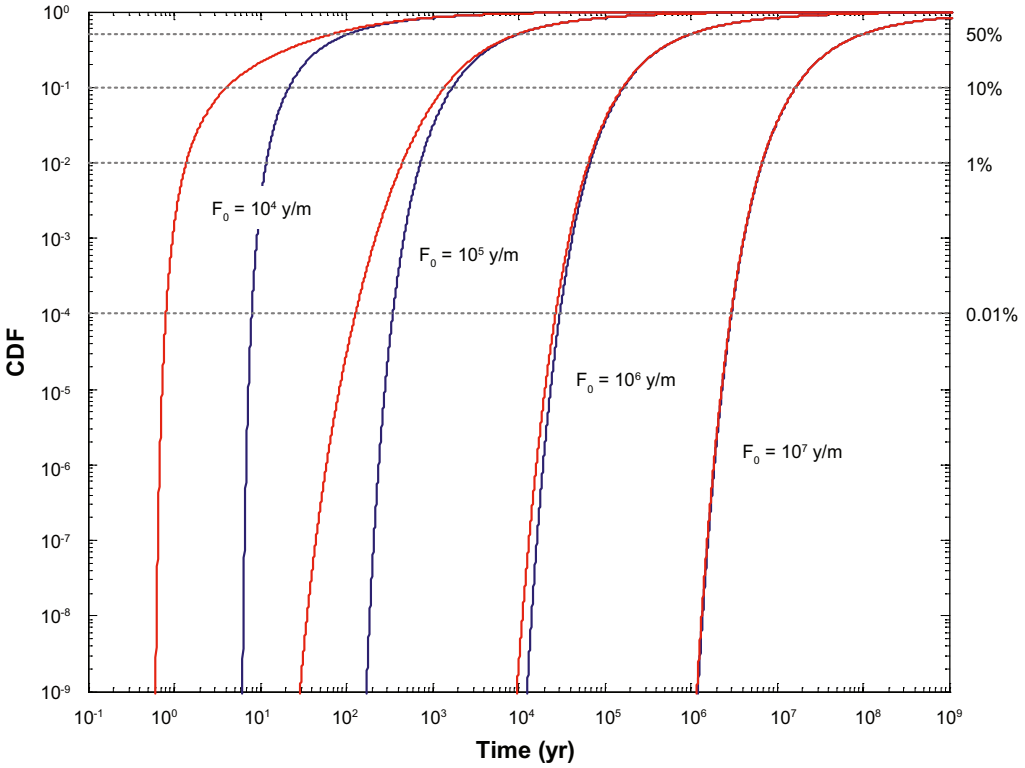

Figure A-9. *Same results as in the previous Figure although plotted on a log-log axis. Different recovery fractions corresponding to 0.01 % - 50 % of released solute are also indicated by the horizontal broken lines for reference purposes.*

It is also noted that the general conclusion regarding diffusive equilibration of the stagnant zone is not appreciably influenced by sorptivity. Figure A-10 shows the results obtained if the analysis is made for a more strongly sorbing solute (K_d = 0.1 m^3/kg). This, however, is expected behaviour since the sorptive properties of the rock matrix adjacent to the flow channel and in the stagnant zone are identical and the matrix uptake characteristic therefore scales proportionally for both zones.

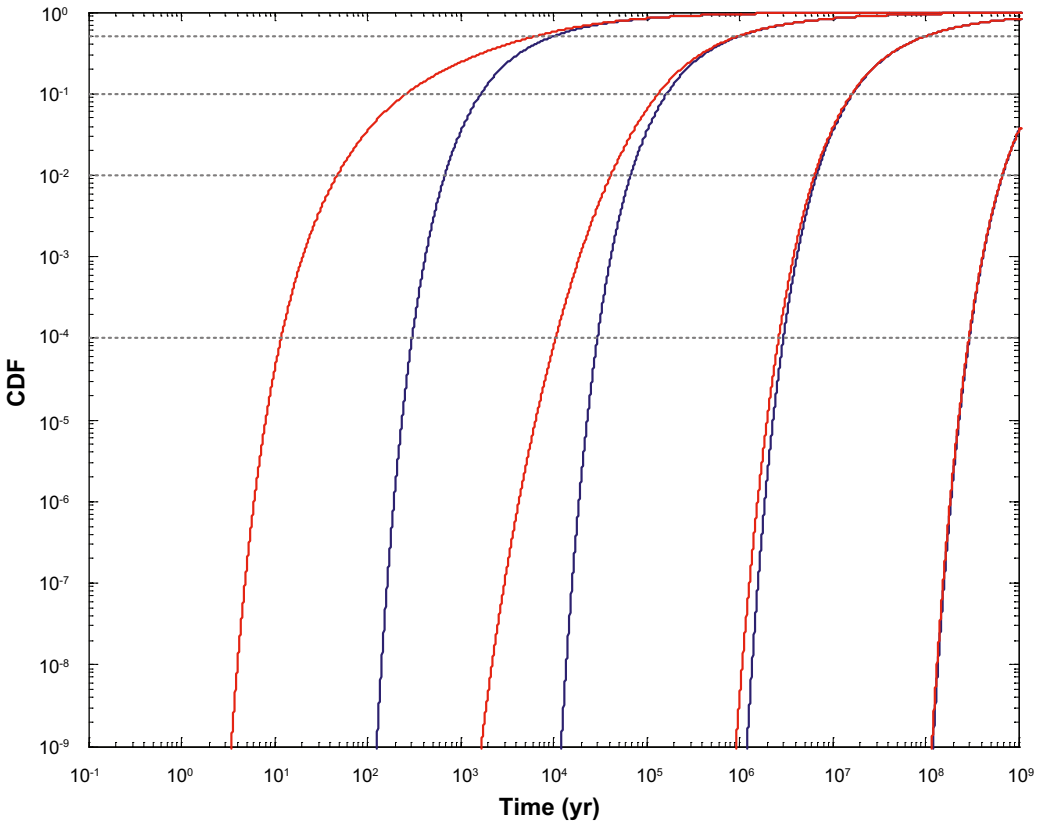

Figure A-10. *Residence time distribution for a strongly sorbing solute (K_d = 0.1 m^3/kg) for the simplified channelling scenario (red curves, Case 2) as compared to the reference scenario (blue curves, Case 1). Results are shown as a cumulative probability density function (CDF) for different reference case F values as indicated.*

Appendix B

Scoping calculations involving fracture mineral retention processes

This appendix has not been changed since the SR-Site assessment. In a few places, references in the SR-Site version were made to the main references of the SR-Site assessment, the references written in bold. It has been verified that the PSAR versions of the corresponding reports are equally valid as references in these cases. The references in bold, therefore, refer to the PSAR versions.

B.1 Overview of modelling simplifications in SR-Site

Matrix diffusion coupled with linear sorption on rock matrix microsurfaces is considered to be the primary retardation mechanism that limits the transport of radionuclides in the geosphere. These are modelling simplifications of what is, in reality, a complex coupled reactive transport process. Generally, such simplifications are justified on the basis that the transported radionuclides are considered to be extremely dilute, trace components within the groundwater and will not exert a large influence on the groundwater chemistry itself in the far-field environment.

Other immobilisation mechanisms known to be active in natural systems are sometimes not readily quantifiable for site specific conditions and are therefore neglected in safety assessment calculations. This is motivated by the fact that it is difficult to convincingly show that these processes are valid over the spatial and temporal scales of interest for safety assessment using data derived primarily from surface based site investigations. Such additional simplification is considered reasonable given that the aim of the exercise is to assess radiological risks associated with different scenarios of repository evolution, rather than attempting to simulate solute retention processes *exactly* as they would occur in nature. The guiding philosophy when performing safety assessment calculations is thus to avoid the possibility of overestimating retention so that radiological consequences are pessimistically predicted even if this might lead to a loss of fidelity with regard to the dynamics of the actual migration process.

As noted in Crawford (2010) great care must be exercised nevertheless since a pessimistic estimate of the retention strength and capacity for a given migration scenario will possibly underestimate the load of radionuclides available upon remobilisation resulting from changes in chemical or physico-chemical conditions. If an excessively low K_d value (although cautiously estimated for retention in steady conditions) is used, for example, the actual amount of radionuclide that is remobilised may be subsequently underestimated owing to that it may have diffused to a greater depth in the rock matrix than if a larger K_d value were to have been selected. In such situations, the peak load and the timing of the release of radionuclides may be erroneously predicted with possibly negative consequences for safety assessment risk metrics. This argumentation can also be extended to additional retention processes either included or neglected in safety assessment transport calculations. Chief among the additional retention processes that are neglected is the sorptive interaction of radionuclides with secondary minerals lining the pore space of flow-bearing fractures.

For the purpose of modelling retention in the rock matrix, the most important sorption mechanisms are considered to be ion-exchange and surface complexation and the term sorption has been used strictly to refer only to these processes in the various reports comprising SR-Site (**Geosphere process report**). Ion exchange involves a purely electrostatic adsorption process whereas (inner sphere) surface complexation typically involves covalent bonding to chemically reactive surface groups on mineral surfaces. The term sorption, however, is a very broad concept that describes a number of processes by which dissolved solutes are adsorbed on, or absorbed in another substance (e.g. IUPAC 1997). There is also a recognised continuum of mechanistic processes whereby ion-exchange and surface complexation are of greatest importance at very low concentration with a transition to surface precipitation and pure phase precipitation at much higher levels of concentration.

For radionuclide immobilisation processes in the fracture pore space, the definition of sorption is expanded here to include the formation of solid solutions with naturally occurring minerals such as calcite, ferric oxyhydroxides, and barite in addition to the standard definition of sorption used to describe purely adsorptive interactions. This is because the additional retardation effect arising due

to this process may, in some cases, be comparable to or greater than that arising due to ion exchange and surface complexation. Unlike a pure phase precipitation process, however, solid solution formation begins to exert an influence on radionuclide sorption already at very low concentrations, usually far below solubility limits of a pure phase and thus is an particularly relevant process for safety assessment.

In this appendix chapter, scoping calculations are made to assess the magnitude of retention potentially available if such additional processes were to be quantitatively accounted for in the safety assessment. The available data are examined and estimates made of the additional effect and uncertainties concerning their magnitude are discussed. These scoping calculations are then used as a basis to inform discussions concerning potential risks associated with neglecting the additional retention mechanisms, principally with regard to remobilisation scenarios.

B.2 Sorptive transport retardation on fracture minerals

Under the assumption of approximately linear sorptivity, the retardation factor, R_{fA} for equilibrium sorption in a porous mineral layer lining the advective pore space of a fracture is given by the formula:

$$R_{fA} = 1 + \frac{\delta_s}{\delta_t}\left(\theta_s + \left(1-\theta_s\right) K_{ds}\rho_s\right) \qquad \text{B-1}$$

Here, δ_s (m) is the total thickness of the fracture coatings, δ_t (m) represents the transport aperture of the fracture, θ_s (m^3/m^3) is the porosity of the fracture coating, ρ_s (kg/m^3) is the solid (crystallographic) density of the fracture minerals, and K_{ds} (m^3/kg) is the sorption partitioning coefficient. Since the advective travel time, t_w (y) is equal to the product of the flow-related transport resistance, F (yr/m) and average half-aperture of the fracture, the retarded travel time in the fracture due to equilibrium sorption can then be written as:

$$R_{fA}t_w = t_w + t_a = t_w + \frac{F}{2}\left(\delta_s\theta_s + K_{ds}m_s\right) \qquad \text{B-2}$$

Here, t_a (y) is the residence time attributable to equilibrium sorption in the fracture mineral and m_s (kg/m^2) is the specific mass of sorbing mineral per unit area of the fracture (i.e. half of the flow-wetted surface). The product of K_{ds} and m_s is also equal to the fracture surface area normalised equilibrium sorption coefficient, customarily denoted K_a (m):

$$K_a = K_{ds}m_s \qquad \text{B-3}$$

It should be noted that this definition of K_a differs from the BET-surface area normalised sorption coefficient, K_a with which it is frequently confused and has a different physical interpretation. Assuming that armouring effects can be neglected, it is not unreasonable to assume that the net retardation effect for a mixed layer of n distinct mineral types will be approximately linearly additive and given by:

$$R_{fA}t_w = F\frac{\delta_t}{2} + F\frac{\delta_s}{2}\theta_s + \frac{F}{2}\sum_{k=1}^{n} K_{ds(k)}m_{s(k)} \qquad \text{B-4}$$

B.3 Quantities of fracture filling minerals at the Forsmark site

In two complementary studies carried out subsequently to the Forsmark and Laxemar site investigations, the abundance of fracture minerals associated with thousands of drill core fracture surfaces has been quantitatively mapped (Eklund and Mattsson 2008, 2009). These data have been examined and statistical models developed for the distribution of different minerals in typical flow-bearing fractures at Forsmark (Löfgren and Sidborn 2010a) and Laxemar (Löfgren and Sidborn 2010b).

On account of their relative abundance, the most important minerals for the scoping calculations made here are assumed to be calcite, chlorite, and other phyllosilicates referred to collectively as clay minerals (which includes illite, smectite, and mixed layer clays). It is interesting to note that barite ($BaSO_4$) has only been positively identified in a small number of samples, typically as small inclusions in galena (PbS) (e.g. Sandström et al. 2008) and is not included in the quantitative assessment of fracture minerals for the Forsmark or Laxemar sites. Although the existence of non-trivial amounts of barite was not quantifiable by the microscopic visual inspection methods used in the abovementioned studies, its presence can be reasonably inferred from the only slight oversaturation with regard to barite solubility in Forsmark and Laxemar groundwater which indicates close-to-equilibrium conditions (Crawford 2010). The consequences of this for radionuclide migration will be discussed later with regard to Ra retention processes.

Hematite in quantifiable amounts has been identified in 0.4 % of the fractures at the Forsmark site although there is a somewhat larger proportion (~14 %) of fractures in which hematite stained minerals have been identified qualitatively. Although hematite and ferric oxyhydroxides are known to sorb surface complexing solutes relatively strongly, hematite has been neglected from the present analysis owing to uncertainties concerning both its abundance as well as the strength of sorption for the range of groundwater compositions considered likely.

In the compilations by Löfgren and Sidborn (2010a, b), apparent surface coverage, C_k (m^2/m^2) and layer thickness, d_k (m) was estimated for the different fracture mineral classes. The lower limit of resolution for fracture coverage was estimated by the authors at 1 % averaged over two surfaces of the fracture (effectively, 0.5 %) while the upper limit was 100 % for full surface coverage. The authors modelled the surface coverage using a truncated normal distribution, whereas the mineral layer thickness was modelled as a lognormally distributed variable.

Although the lognormal distribution has an automatic lower bound at zero, when mineral layer thicknesses are assigned stochastically there is a high likelihood that values will be generated that are lower than the effective resolution of the method and would therefore be categorised as being absent if considered in the quantitative mapping of fracture minerals. If a given percentage of fractures are known to contain quantifiable amounts of a specific mineral, then this might lead to under-assignment of mineral abundances in those fractures. Another particular problem with the lognormal distribution is that it has an unbounded upper limit, which could potentially lead to overestimates of mineral abundance if not capped at some appropriate level. From inspection of the data histograms and the authors' comments in Löfgren and Sidborn (2010a, b) it was judged that the operational resolution of the layer thickness estimate was bounded by a lower limit of about 1 mm and an upper limit of approximately 1 mm (or just over). Although this assessment is probably inaccurate, it is considered sufficient for the purpose of making scoping calculations.

For the computation of fracture mineral abundances, a very simple procedure was adopted whereby the mass of each mineral per unit area was estimated independently for each mineral. In this procedure, the visual coverage and layer thickness were stochastically generated assuming a truncated normal distribution for the coverage and truncated lognormal distribution for the layer thickness. This was done by simple rejection sampling of the non-truncated multivariate normal distribution assuming various amounts of correlation between surface coverage and layer thickness.

Although correlations between paired measurements of surface coverage and layer thicknesses were not investigated by Löfgren and Sidborn (2010a, b), it is reasonable to expect that such a positive correlation should exist. Although it may not be an accurate assessment for all minerals, those mapped with a large surface coverage are also more likely to have greater thickness since a relatively large quantity of the mineral must be present for it to be mapped quantitatively. Minerals with simultaneously small coverage and layer thickness, on the other hand, are very likely to be missed or at least noted as being present in only qualitative amounts. In order to address this possibility, calculations were made assuming different amounts of correlation. Based on the outcome of these calculations, a cautiously chosen estimate of the mineral mass was made so as to avoid possible overestimation of the fracture mineral retention capacity. Given the known proportion, f_k of fractures mapped as not containing fracture mineral k, the specific mass per unit area of fracture surface is then approximately given by:

$$m_{s(k)} = (1 - f_k) V_k (1 - \theta_k) \rho_k \qquad \text{B-5}$$

Where, the specific volume of fracture mineral, V_k (m^3/m^2) is given by the product of surface coverage and layer thickness:

$$V_k = C_k d_k \qquad \text{B-6}$$

It is acknowledged that the distribution of fracture mineral proportions might be more accurately represented as a Dirichlet stochastic process (i.e. a multivariate beta distribution). For the present purposes, however, the method described above is considered sufficiently accurate. There are a number of other known biases in the quantification procedure that might be relevant for this discussion if one intended to make very accurate estimates of fracture mineral abundance. These additional features are neglected and are considered to be of only second order importance although they are discussed in some detail in the compilation by Löfgren and Sidborn (2010a, b).

Table B-1. Volumetric abundance, V_k (m^3/m^2) of fracture minerals estimated as the product of stochastically generated visual coverage and layer thickness assuming different amounts of correlation as specified by the correlation coefficient ranging from no correlation (ρ = 0) to fully correlated (ρ = 1). Estimates are based on the arithmetic average of 10^6 stochastically generated, paired deviates of C_k and d_k.

	V_k (ρ = 0)	V_k (ρ = 0.25)	V_k (ρ = 0.5)	V_k (ρ = 0.75)	V_k (ρ = 1)
Calcite	1.3×10^{-5}	1.6×10^{-5}	1.9×10^{-5}	2.3×10^{-5}	2.9×10^{-5}
Chlorite	4.9×10^{-5}	5.2×10^{-5}	5.6×10^{-5}	5.9×10^{-5}	5.9×10^{-5}
Clay	4.1×10^{-5}	4.4×10^{-5}	4.7×10^{-5}	4.8×10^{-5}	4.7×10^{-5}

The porosities of the agglomerations of individual mineral components in the surface layers have not been measured, so some type of average must be assumed. The crystallographic density of calcite is roughly 2 710 kg/m^3. The true density of chlorite and other clay minerals taken as a group is difficult to define owing to their finely divided state and different swelling properties. Given the various uncertainties, however, it is probably not unreasonable to assume a crystallographic density in the range of about 2 600 – 3 000 kg/m^3. For the purpose of making scoping calculations, an average of about 2 700 kg/m^3 is therefore assumed for all fracture filling minerals. Since the porosities of the fracture coatings have not been measured, a range of 0.3–0.7 has been assumed by analogy with typical theoretical ranges reported for various types of spherical packing (e.g. Harker et al. 2002). The expected broad particle size distribution of fracture minerals and sometimes cementitious nature (particularly for calcite) would suggest that higher packing densities may be obtained than are achievable with homogeneous particle sizes. The assumed porosity range is therefore likely to be overestimated and therefore will underestimate the specific mass of fracture minerals contributing towards the enhanced retention.

Since the assumption of uncorrelated C_k and d_k (i.e. ρ = 0) seems to give the lowest average volumetric abundance (see Table B-1), this is assumed in subsequent calculations as it will tend to underestimate the specific mass of fracture minerals. Based on this and other abovementioned assumptions, the most likely ranges of fracture mineral specific mass have been estimated and are given in Table B-2. Although there are number of uncertain input parameters to this calculation, the average porosity is assumed to dominate the overall uncertainty and the calculated range of specific mass therefore only reflects this assumed range. Provided the sampled fractures are representative of potential migration paths at the Forsmark site, the values are likely to underestimate the actual specific masses of available minerals.

Table B-2. Estimated specific mass, m_s (kg/m^2) of fracture minerals calculated using Equation B-5. The mean estimate is calculated assuming a bulk porosity of 50 %, while the minimum and maximum values correspond to 70 % and 30 % porosity, respectively. The second column gives the proportion, f_k of fractures where the indicated mineral is quantifiably absent.

	f_k	m_s (mean)	m_s (min)	m_s (max)
Calcite	0.43	9.7×10^{-3}	5.8×10^{-3}	1.4×10^{-2}
Chlorite	0.48	3.4×10^{-2}	2.0×10^{-2}	4.8×10^{-2}
Clay	0.72	1.6×10^{-2}	9.4×10^{-3}	2.2×10^{-2}

B.4 Retention of radionuclides by ion-exchange and surface complexation

To quantify the potential for sorption of radionuclides by ion-exchange and surface complexation on chlorite and the clay mineral group, data derived for the bentonite buffer have been used although rescaled to match the approximate range of cation exchange capacities (CEC) estimated for the fracture minerals. These data are defined in the **Data report** for a reference bentonite porewater (RPW) deemed appropriate for both non-saline and mildly saline conditions, as well as a reference saline porewater of a much higher salinity (HSPW). Although derivation of K_d values "from scratch" for illite and smectite clay mixtures and specific groundwater compositions using thermodynamic modelling might give a more accurate assessment, the simplified approach outlined above is deemed appropriate for

the current purpose. As also pointed out in the **Data report**, the uncertainty and variability of groundwater composition implies that a more sophisticated modelling approach may not necessarily reduce data uncertainty to any great extent over that already implicit in the recommended data ranges.

From the groundwater hydrochemical simulations (Salas et al. 2010) used as a basis for rock matrix K_d data selection, it is possible to conclude that most saline conditions (on average) occur during the temperate period at roughly 2 000–3 000 y after which there is a temporal trend featuring declining salinity and increasing carbonate concentration and only a very slightly decreasing pH based on averages for the repository volume as a whole. The HSPW groundwater does not appear to be representative of groundwater salinities dominating the temperate phase of repository evolution although could potentially reflect the transient saline conditions achieved during short bursts of brine upconing associated with ice front advance and retreat. The RPW groundwater, however, appears to be approximately representative of the groundwater salinity variability existing during the more saline period of groundwater evolution during the temperate phase. Both the RPW and HSPW represent pH and carbonate concentration ranges not unlike the compositions predicted by Salas et al. (2010). The data corresponding to the RPW water composition are therefore used in the present scoping calculations as a reference case.

Since the purpose of this appendix is to facilitate the discussion of relative merits of different modelling assumptions with regard to risk assessment, only a small subset of radionuclides have been selected for the analysis. These are chosen partly on the basis of their importance in safety assessment but mainly owing to their differing geochemical behaviour. This serves mainly to highlight relevant differences between different groups of analogue elements in the scoping calculations. The rescaled fracture mineral K_d values used as a basis for the transport calculations are given in Table B-3.

Table B-3. Estimated K_d data for chlorite (CEC ≈ 5 meq/100 g) and clay minerals taken as a group (CEC ≈ 20 meq/100 g, assuming illite as an approximate analogue). The data are based on the corresponding values for MX-80 bentonite (CEC ≈ 85 meq/100 g) described in the Data report although rescaled relative to the CEC of the indicated fracture minerals. The best estimate K_d value is assumed to be the median.

Element (Redox state)	*Best estimate K_{ds}* (m^3/kg)	*Lower limit K_{ds}* (m^3/kg)	*Upper limit K_{ds}* (m^3/kg)
Chlorite			
Am(III)	3.6	0.59	22
Cs(I)	5.3×10^{-3}	1.2×10^{-3}	3.3×10^{-2}
Ni(II)	1.8×10^{-2}	1.8×10^{-3}	1.9×10^{-1}
Ra(II)	2.6×10^{-4}	4.7×10^{-5}	1.6×10^{-3}
U(IV)	3.7	0.21	65
U(VI)	0.18	2.9×10^{-2}	1.1
Clay mineral group (assuming Na-illite as an analogue)			
Am(III)	14	2.4	89
Cs(I)	2.1×10^{-2}	4.7×10^{-3}	0.13
Ni(II)	7.1×10^{-2}	7.1×10^{-3}	0.78
Ra(II)	1.1×10^{-3}	1.9×10^{-4}	6.4×10^{-3}
U(IV)	15	0.85	262
U(VI)	0.71	0.12	4.2

B.5 Retention of radionuclides by solid solution equilibrium

One feature that does connect ion-exchange and surface complexation sorption processes with solid solution formation is that there is always a direct correspondence between the aqueous phase concentration and the sorbed concentration at equilibrium (all other things being equal). This feature is absent from pure phase precipitation where the aqueous phase concentration is determined by solubility equilibrium and is independent of the amount of mineral present. When immobilisation is predicated on pure phase solubility considerations, detailed mass balance accounting must then be used to model mobilisation of a precipitated pure phase component undergoing reactive transport.

This similarity means that solid solution formation can, at least in a limited sense, be treated in a conditionally constant K_d framework in a similar fashion to ion-exchange and surface complexation. In general, the conditional K_d is highly sensitive to groundwater composition; if the concentration of major components of the groundwater change in such a way that the extent of solid solution formation is influenced in a fundamentally non-linear fashion then the use of the constant K_d modelling approach is invalid. The same caveats, however, also exist for the use of conditionally constant K_d values in the modelling of ion-exchange and surface complexation phenomena so this should not be considered to be a special concern regarding solid solutions.

A couple of recent studies highlight situations in which a constant K_d approach is not appropriate. Simulations made by Zhu (2004) involve the transport of Ra along a flowpath where radiobarite is dissolved and mobilised at the beginning of the path. The mobilisation of Ra results in a self-enrichment front of radiobarite that is slowly displaced downstream over time under the influence of an infiltrating simple saline solution. The self-enrichment front of radiobarite results in a porewater composition that changes with distance along the flowpath until a steady state condition is reached relative to the downstream radiobarite concentration. The dissolution of radiobarite at the start of the flowpath also results in a spatially variable Ba^{2+} and SO_4^{2-} concentration which implies a strong multicomponent effect on the reactive transport of Ra.

Another study by Shao et al. (2009a) examines the impact of simultaneous counter-diffusion of Ra^{2+} and SO_4^{2-} from opposite boundaries of a domain initially containing small amounts of solid $BaCO_3$ as an initial contaminant of a clay buffer material. This work was followed up by a further study (Shao et al. 2009b) where the competition between solid solution formation and cation exchange on the major clay component of the buffer was modelled along the same lines.

The results obtained for Ra migration in these systems clearly indicate the inadequacy of the constant K_d approach for the particular boundary conditions considered in these studies. For the purposes of the safety assessment, however, the transport of radionuclides is considered to occur against a background of relatively static groundwater compositions evolving slowly over time and featuring only mild geochemical gradients moderated by matrix diffusion processes. Provided the source nuclide concentration is sufficiently low, Henry law behaviour for the solid solution equilibrium is not an unreasonable assumption in many cases if the background concentrations of solutes comprising the primary end member of the solid solution are also relatively static in the repository environment.

A situation in which changes in barite abundance and solubility might occur against the background of relatively static groundwater chemistry is in the case of microbial (dissimilatory) sulphate reduction. Such behaviour could have consequences for Ra re-mobilisation scenarios if shown to be active in the geosphere environment. This process, however, requires an organic carbon source to function as an electron donor even if sulphate reducing bacteria are present in the geosphere as they are known to be (Laaksoharju et al. 2008). The main source of organic carbon in the deep geosphere is expected to be methane. As noted in the **Post-closure safety report**, methane concentrations are low (less than 0.2 ml/l) and might be reasonably expected to be depleted even further in the presence of significant quantities of sulphate containing fracture minerals.

Sulphate reduction can potentially lead to the precipitation of calcite owing to the generation of carbonate when methane is oxidised and thus the process can even have an impact on solid solutions involving calcite. The effect can be even stronger if the sulphate reduction is accompanied by precipitation of iron sulphides (either amorphous FeS or pyrite) since this also results in an increase in pH (Stoessell 1991). The process is limited, however, by the availability of methane and any effect on the abundance and distribution of calcite at repository depth is likely to be very slow during the repository evolution. Possible evidence for this process having occurred in the distant geological past (Palaeozoic era) can be found in the extremely low $\delta^{13}C$ values for some fracture filling calcites at Forsmark (Laaksoharju et al. 2008) which is generally taken to be indicative of a biogenic process (i.e. isotope depletion with respect to ^{13}C in the carbonate content of calcite).

The strong multicomponent effects apparent in Zhu (2004) and Shao et al. (2009a, b) are not expected to occur to the same extent in the geosphere transport although they may have some relevance for near-field transport. Moreover, unlike the well defined boundary and initial conditions in the above-mentioned modelling studies, the uncertainty range of the spatially variable groundwater compositions

in most cases dwarfs the predicted temporal changes at any given location in the repository environment. It was not considered feasible to track detailed spatial and temporal changes in groundwater chemistry along radionuclide migration pathlines associated with specific source locations (i.e. individual canister deposition positions). For this reason it is only strictly possible to consider relative variations between different time periods for the full groundwater composition distribution in the repository volume when making judgements on the influence of spatial and temporal variability or uncertainty in groundwater chemistry. Detailed consideration of multicomponent reactive transport therefore may not necessarily result in a reduced span of uncertainty for radiological risk unless this can be resolved on the level of individual migration paths. In the scoping calculations documented in this Appendix chapter, the uncertainties introduced by the evolving groundwater composition are therefore discussed qualitatively.

Since the current generation of safety assessment codes cannot model temporally variable sorption, K_d values are typically recommended for the most unfavourable conditions expected during the repository groundwater evolution. For the recommended K_d values describing sorption in the rock matrix this corresponds to the saline conditions attained at about 3 000 y in the temperate phase of repository groundwater evolution.

In these scoping calculations, however, we are interested in examining the consequences of this assumption. Although this is the stated aim, reference K_d values are still estimated for groundwater compositions at 3 000 y to maintain consistency with the recommended rock matrix sorptivities. This comprises the reference state, which is then used as a basis for comparison. The impact of evolving groundwater composition is then assessed qualitatively by consideration of how the groundwater compositions might change over time in such a way as to influence the mobility of radionuclides sorbed on fracture minerals lining the advective pore space.

Estimation of partitioning coefficients for solid solutions

The reaction equation for an isovalent binary solid solution between a trace substance A and a mineral end-member MX can be described by the reaction equation:

$$MX_{(s)} + A^{z+} \Leftrightarrow AX_{(s)} + M^{z+} \qquad \text{B-7}$$

In this case, the equilibrium partitioning coefficient, ${\omega_A}^0$ for the binary solid solution MX-AX is conventionally defined in terms of the mole fraction, X_A of incorporated solute as:

$$\omega_A^0 = \frac{X_A}{1-X_A} \Big/ \frac{c_A}{c_M} \qquad \text{B-8}$$

Where c_A and c_M are the free aqueous concentrations of dissolved components A and M. It is additionally noted that, although partitioning coefficients in the literature are often denoted using the symbol λ, we use the notation ω_A and ω_A here to avoid confusion with radioactive decay constants, which are also customarily represented using the symbol λ.

The thermodynamic equilibrium constant for the reaction would be defined in a law of mass action (LMA) framework as:

$$K = \omega_A^0 \left(\frac{\gamma_{AX}}{\gamma_{MX}} \cdot \frac{\gamma_{M^{n+}}}{\gamma_{A^{n+}}} \right) \qquad \text{B-9}$$

Where, γ_{AX} and γ_{MX} are the activity coefficients for the solid phase end-members, while $\gamma_{A^{n+}}$ and $\gamma_{M^{+}}$ are the activity coefficients of the free aqueous ions A and M. Although ω_A is not a true constant since its value is also dependent on the activity coefficients defined in Equation B-9, it may nevertheless be regarded as a *thermodynamic* partitioning coefficient. In the literature, however, partitioning coefficients are frequently defined in terms of total concentrations in conformity with the convention adopted by Henderson and Kraček (1927):

$$\omega_A = \frac{X_A}{1-X_A} \Big/ \frac{c_{AT}}{c_{MT}} \qquad \text{B-10}$$

These may be referred to as phenomenological partitioning constants (Curti 1999) since, being de-fined in terms of total concentration, they do not strictly follow the thermodynamic definition of the reaction equilibrium for Equation B-7. As such, ω_A defined according to Equation B-10 must be regarded as only conditionally constant as it is additionally dependent on groundwater speciation effects as well as the solid phase and aqueous ion activity coefficients.

In many cases the free concentration of a solute, c_A is only a small fraction of the total concentration, c_{AT} owing to the distribution of the solute amongst various aqueous complexed forms. In order to make a reasonably accurate estimate of radionuclide transport retardation and how this responds to changes in groundwater composition, strictly one would also need to consider the impact of aqueous speciation in solution. In order to account for this additional effect, a speciation correction factor can be defined for both the major (M) and minor (A) components:

$$\varphi_M = \frac{c_M}{c_{MT}} \qquad \text{B-11}$$

$$\varphi_A = \frac{c_A}{c_{AT}} \qquad \text{B-12}$$

In principle, one could therefore convert between the thermodynamic and phenomenological forms of the partitioning coefficient using the relation:

$$\omega_A^0 = \omega_A \left(\frac{\varphi_M}{\varphi_A} \right) \qquad \text{B-13}$$

This would also allow extrapolation of a phenomenological partitioning constant from a given reference state (1) to another (2) using the relation:

$$\omega_{A(2)} \cdot \left(\frac{\varphi_{M(2)}}{\varphi_{A(2)}} \right) \cdot \left(\frac{\gamma_{AX(2)}}{\gamma_{MX(2)}} \cdot \frac{\gamma_{M(2)}}{\gamma_{A(2)}} \right) = \omega_{A(1)} \cdot \left(\frac{\varphi_{M(1)}}{\varphi_{A(1)}} \right) \cdot \left(\frac{\gamma_{AX(1)}}{\gamma_{MX(1)}} \cdot \frac{\gamma_{M(1)}}{\gamma_{A(1)}} \right) \qquad \text{B-14}$$

If differences in the activity coefficients between state (1) and (2) are small, Equation B-14 simplifies to:

$$\omega_{A(2)} \approx \omega_{A(1)} \cdot \left(\frac{\varphi_{M(1)}}{\varphi_{M(2)}} \right) \cdot \left(\frac{\varphi_{A(2)}}{\varphi_{A(1)}} \right) \qquad \text{B-15}$$

This, however, is only useful if relatively detailed information is known concerning the water composition used in the experiments used to estimate ω_A. This is particularly problematic in the case of calcite, since the partial pressure of CO_2 can vary greatly depending on whether the experiment is carried out under open or closed batch conditions. Moreover, for many solutes of interest it is not always possible to describe the solid solution equilibrium using a simple reaction template such as Equation B-7. This is particularly the case for non-isovalent processes where additional aqueous components may be required to balance the overall reaction stoichiometry and to compensate charge imbalance in the solid solution. In many cases, it also may not be possible to accurately describe the solid solution equilibrium as a simple binary reaction and one may need to consider multiple processes simultaneously in a correct thermodynamic description. There is considerable evidence to suggest, for example, that the non-ideal solid solution of Eu(III) with calcite is best described using a ternary solid solution description involving the end-members $EuH(CO_3)_2$, Eu(O)OH, and $CaCO_3$ (Curti et al. 2005). As noted by Kulik et al. (2004), such systems cannot be readily modelled using LMA approaches and more generalised, Gibbs free energy minimisation calculation methods are typically required.

While a reaction equilibrium equation can theoretically always be formulated in terms of free component concentrations, the conversion between thermodynamic and phenomenological forms of the partitioning coefficient is strongly influenced by the underlying assumptions of reaction stoichiometry and how this relates to the calculation of speciation correction factors. The choice of an inappropriate basis specie for the minor component speciation correction factor might then give rise to considerable errors. This may be of particular significance in cases where the free component concentration is many orders of magnitude less than the aqueous complexed form that is actually substituted into the crystal structure. Conversion between a phenomenological and thermodynamic form of the partitioning

coefficient is therefore subject to considerable uncertainty if the underlying assumptions implicit in the reaction equation used to describe the formation of the solid solution are not correct.

Assuming for the moment, however, that a simple equilibrium relation of the kind described by Equation B-8 is reasonable, it is still possible to speculate on relative magnitudes of radionuclide retention at different times during repository groundwater evolution. Provided the trace substance A is of sufficiently low concentration, asymptotically ideal behaviour can be reasonably assumed and the aqueous concentration of the major component, M is determined by Raoult's law:

$$c_M = \left(1 - X_A\right) c_M^0 \qquad \text{B-16}$$

Where, $c_M{}^0$ is the theoretical free concentration of component M which would be in equilibrium with the pure phase of the corresponding end-member at the prevailing groundwater composition. In reality there are many different groundwater constituents which are likely to form solid solutions with readily soluble fracture minerals, so Equation B-16 can only be regarded as a rough approximation of the true situation. If the other end-members comprising the multicomponent system are sufficiently dilute, however, the approximation is likely to be reasonable.

If Equation B-16 is combined with Equation B-8, we obtain:

$$\omega_A^0 = \frac{X_A}{1 - X_A} \Bigg/ \frac{c_A}{\left(1 - X_A\right) c_M^0} \qquad \text{B-17}$$

Assuming $\omega_A{}^0$ to be approximately constant over the groundwater and solid solution composition region of interest (i.e. neglecting activity coefficients and other non-idealities), allows us to solve explicitly for X_A:

$$X_A \approx \frac{c_A \omega_A^0}{c_M^0} \qquad \text{B-18}$$

For an approximately constant molar mass of the solid solution, $M^{ss}{}_w$ (justifiable if one end-member dominates), the concentration of tracer substance, c_s (mol/kg) in the solid solution can then be given as:

$$c_s = \frac{X_A}{M_w^{ss}} \approx \left(\frac{\omega_A^0 \varphi_A}{c_M^0 M_w^{ss}} \right) c_{AT} \qquad \text{B-19}$$

can also be given in the form:

$$c_s = K_{ds}\, c_{AT} \qquad \text{B-20}$$

Where,

$$K_{ds} \approx \left(\frac{\omega_A^0 \varphi_A}{c_M^0 M_w^{ss}} \right) \qquad \text{B-21}$$

This is essentially a restatement of the Henry law equilibrium assumption for a dilute component where K_{ds} is the liquid-solid phase partitioning coefficient defined in an analogous fashion to the standard definition of K_d. In situations where only a phenomenological partitioning coefficient is known at some reference state (i.e. $\omega_{A(1)}$), however, K_{ds} must be defined as:

$$K_{ds} \approx \left(\frac{\omega_{A(1)}}{c_{MT} M_w^{ss}} \right) \cdot \left(\frac{\varphi_{M(1)}}{\varphi_M} \right) \cdot \left(\frac{\varphi_A}{\varphi_{A(1)}} \right) \qquad \text{B-22}$$

In general, phenomenological partitioning constants reported in the literature are not sufficiently well documented to allow the estimation of K_{ds} according to Equation B-22and one is therefore compelled to neglect the speciation correction terms when making scoping calculations. Although this implies that it is not always feasible to calculate an accurate K_{ds} value, it is still possible to speculate on the magnitude of change in K_{ds} in response to evolving groundwater chemistry relative to a given reference case. By analogy with the definition in Crawford (2010), a chemistry correction factor, f_{chem} which accounts for spatial and temporal changes in the K_{ds} value could then be defined as:

$$f_{chem} = \frac{K_{ds}}{K_{ds}^{ref}} = \left(\frac{c_{MT(ref)}}{c_{MT}} \right) \cdot \left(\frac{\varphi_A}{\varphi_{A(ref)}} \right) \cdot \left(\frac{\varphi_{M(ref)}}{\varphi_M} \right) \qquad \text{B-23}$$

Although Equation B-23 can be extended to additionally include the effect of aqueous phase activity coefficients, this implies a level of accuracy in the calculation that may not be supported giving the uncertainty concerning actual reaction mechanisms. In cases where such uncertainty exists, it would be reasonably justified to neglect the correction for the minor component speciation and simply assume:

$$f_{chem} \approx \left(\frac{c_{MT(ref)}}{c_{MT}} \right) \cdot \left(\frac{\varphi_{M(ref)}}{\varphi_M} \right) = \frac{c^0_{M(ref)}}{c^0_M} \qquad \text{B-24}$$

For radionuclides that are strongly complexed in the aqueous phase, an incorrect assumption of the minor component basis specie in Equation B-23 can result in extrapolation errors that are likely to be orders of magnitude larger than those resulting from neglecting the changes in minor component speciation altogether. This is particularly the case for solutes that are strongly complexed by carbonate such as the trivalent actinides and lanthanides as well as for U. The issue is further complicated in these cases by the fact that the reaction is non-isovalent with regard to the major component (Ca^{2+} in the case of calcite). For this reason, Equation B-24 is assumed in subsequent scoping calculations for calcite solid solutions involving Am(III), U(IV), and U(VI). On the other hand, since the reaction mechanisms for Ra(II) and Ni(II) solid solutions with calcite and barite are expected to conform relatively well to the simplified isovalent binary reaction template, Equation B-23 is used in these particular cases.

Although only a very approximate treatment, the relative measure implied by the f_{chem} value defined by Equation B-24 is convenient to work with since it is independent of the identity of the radionuclide under consideration. This is a useful property since it allows us to speculate on the relative impact of changing groundwater compositions for radionuclides where distribution coefficients have not actually been measured or estimated at this time. It is acknowledged, however, that even under the relatively ideal conditions assumed in this analysis (i.e. dilute Henry law behaviour), there is considerable uncertainty concerning the magnitude of the sorption owing to the handling of aqueous speciation effects and the assumption of a simple equilibrium reaction for the solid solution. Since we generally do not know the exact conditions under which phenomenological partitioning coefficients are obtained, we are also compelled to simplify Equation B-22 to:

$$K_{ds} \approx \left(\frac{\omega_A}{c_{MT} M^{ss}_w} \right) \qquad \text{B-25}$$

Where c_{MT} is the total concentration of the cation forming the solid solution major end-member at the prevailing groundwater composition (i.e. Ca^{2+} for calcite, Ba^{2+} for barite). Since the total concentration of the major component is always larger than the free concentration, this will tend to underestimate the correct value of the K_{ds} value, all other things being equal.

In order to facilitate discussion concerning potential changes in sorptivity throughout the glacial cycle, the glacial IIa and IVa scenarios have been chosen as being representative of periods where groundwater compositions and flows deviate most strongly from the conditions established during the temperate phase. The glacial IIa scenario corresponds to where the advancing ice front is approximately above the repository and is characterised by a strong upconing of deep saline groundwater. The glacial IVa scenario corresponds to the case where the ice margin is just past the repository and large hydraulic gradients force dilute meltwater into the fracture system. In both cases, the non-permafrost scenarios are chosen since these appear to be associated with the strongest flow and hydrochemical deviations. Subsequent calculations and qualitative discussions are therefore based on the base case simulations of the temperate period 2 000 y, 3 000 y, 5 000 y, and 9 000 y together with glacial case IIa and IVa. For the temperate cases, the groundwater compositions corresponding to the $Fe^{2+}/Fe(OH)_{3\ (s)}$ redox pair are assumed. It is noted, however, that the assumption of the data set corresponding to this redox couple may have some significance for barite equilibrium on account of differences in sulphate concentrations between this case and the $Fe^{2+}/FeS_{\ (am)}$ redox system.

The exact details of the examples chosen, however, are not important for this discussion since the focus is more on how groundwater compositional trends are likely to affect migration processes in a broad qualitative sense rather than precise calculation of nuclide fluxes. The glacial IIa and IVa groundwater profiles shown in Figure B-1 reflect the most saline and most dilute groundwater compositions (respectively) expected during the glacial cycle within a control volume surrounding the repository (Salas et al. 2010). The groundwater profiles existing at 3 000 y and 9 000 y are shown in Figure B-2 for comparative purposes.

Figure B-3 shows the distribution of total Ca^{2+} and Ba^{2+} concentrations at different times during the predicted groundwater evolution. These data are based on the groundwater compositions initially calculated by Salas et al. (2010) although re-estimated imposing simultaneous calcite and barite equilibrium. Since the groundwater compositions were already calculated assuming calcite equilibrium, the addition of barite makes very little difference to the overall groundwater compositional balance on account of its low solubility. The calculations were made using PHREEQC and the SKB thermodynamic database (Duro et al. 2006).

Although the groundwater temperature is not specified in the data from Salas et al. (2010), calculations indicate a relatively small, but non-negligible influence of temperature on the estimated total concentrations of Ca^{2+} and Ba^{2+}. A temperature of 12 °C has been assumed in the calculations for the temperate groundwaters and 4 °C for glacial IIa and IVa groundwaters. Since the dissolution of calcite is exothermic ($\Delta H_r^0 = -24.51$ kJ/mol), decreased temperatures are expected to result in a slightly elevated equilibrium concentration of Ca^{2+} and consequently lower K_d values than those predicted for higher temperatures. The dissolution of barite, on the other hand, is an endothermic reaction ($\Delta H_r^0 = +26.57$ kJ/mol) which implies the opposite behaviour. The net effect, however, also depends on the reaction enthalpy of other aqueous phase complexation reactions.Figure B-4 shows the effect of temperature on the equilibrium of calcite and barite calculated with the aid of PHREEQC and for the groundwater compositional profile existing during the glacial IIa period.

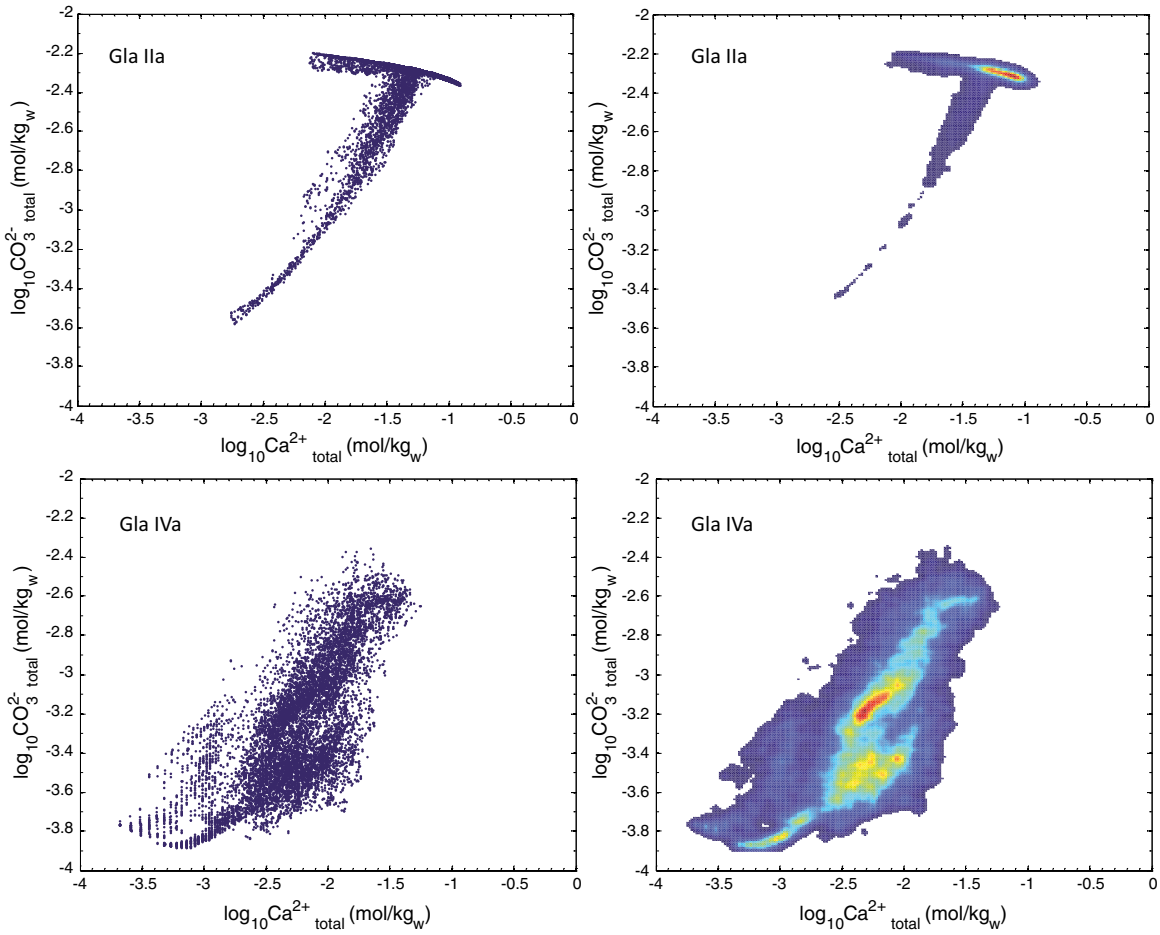

Figure B-1. *Groundwater compositional data (total carbonate vs. total calcium) visualised in scatterplot form (left) and in the form of a smoothed 2D histogram (right) for the glacial IIa and IVa epochs. Warmer colours in the histograms correspond to a greater frequency of the indicated composition. Aliasing in the lower left hand figure is due to round-off errors owing to the number of significant figures in the data sets calculated by Salas et al. (2010).*

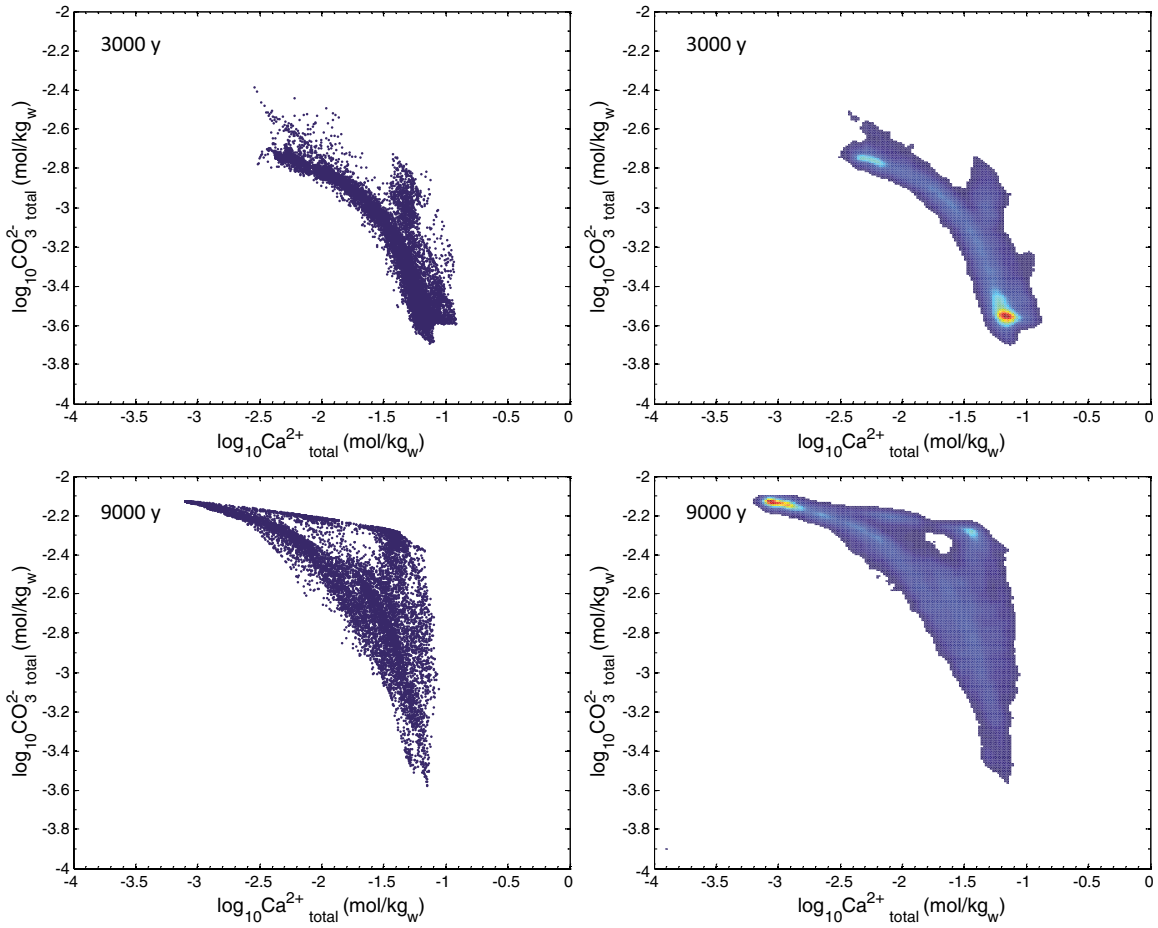

Figure B-2. *Groundwater compositional data (total carbonate vs. total calcium) visualised in scatterplot form (left) and in the form of a smoothed 2D histogram (right) for the temperate 3 000 y and 9 000 y epochs. Warmer colours in the histogram plots correspond to a greater frequency of the indicated composition.*

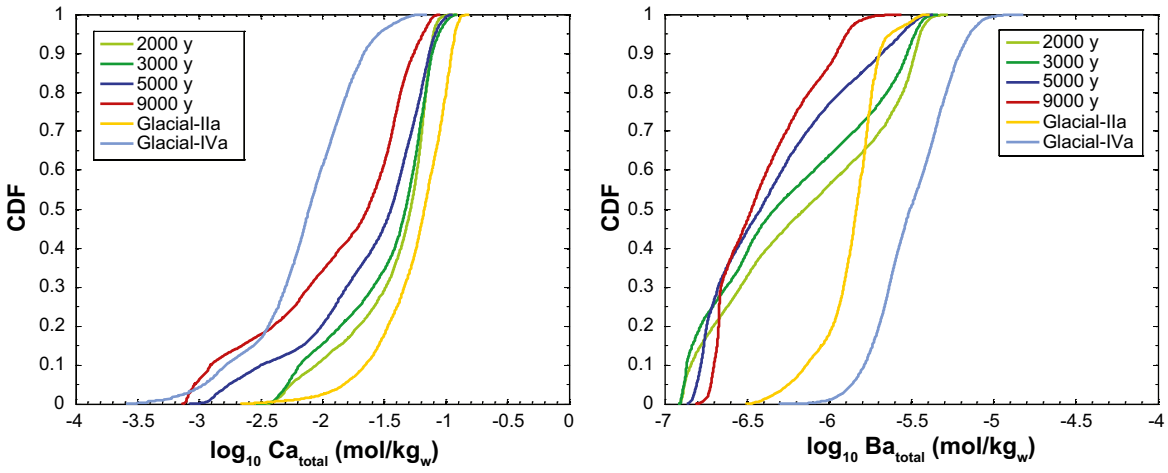

Figure B-3. *Total concentration of Ca^{2+} and Ba^{2+} plotted as a cumulative distribution function (CDF) for groundwater compositions at different times during repository evolution. Calculations assume simultaneous barite/calcite equilibrium re-estimated for the groundwater compositional ranges initially calculated by Salas et al. (2010). An average temperature of 12 °C is assumed for the temperate groundwaters and 4 °C for the glacial IIa and IVa groundwaters.*

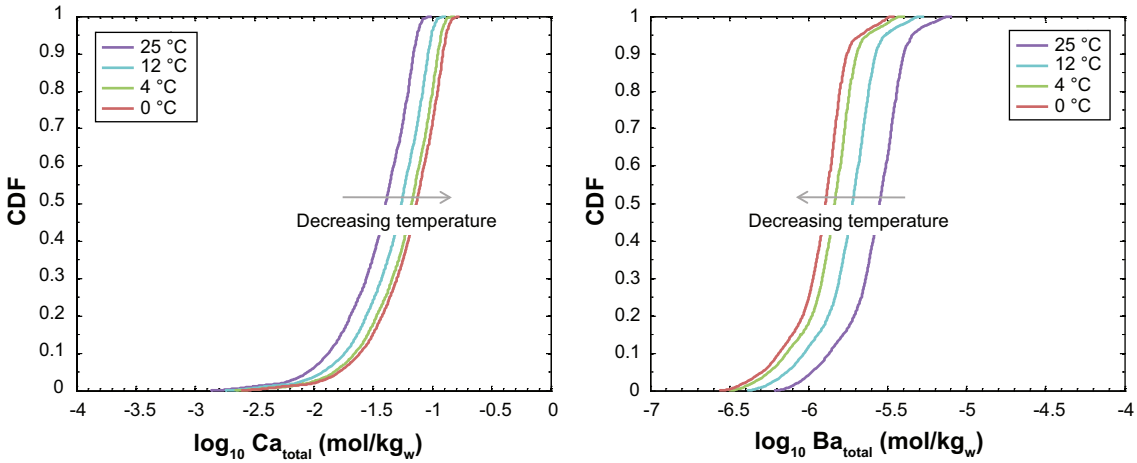

Figure B-4. *Effect of temperature on calcite (Ca^{2+}) and barite (Ba^{2+}) equilibrium for the glacial IIa case plotted as a cumulative distribution function (CDF) for different temperatures in the range 0 °C to 25 °C. Calculations assume simultaneous barite/calcite equilibrium re-estimated for the groundwater compositional ranges initially calculated by Salas et al. (2010). The data show an increase in solubility of calcite and decrease in solubility of barite with decreasing temperature as expected.*

Curti (1999) gives a summary of estimated or measured values of phenomenological partitioning coefficients (ω_A) for solid solutions with calcite, based on an analysis of literature data. These values are used in the scoping calculations to provide an estimated range of K_{ds} values for solid solutions with calcite using Equation B-25. For radiobarite, the ω_A value given by Doerner and Hoskins (1925) is used. Table B-4 gives the estimated K_{ds} ranges estimated for various nuclides. The best estimate K_{ds} value is based on the median ω_A and total Ca^{2+} and Ba^{2+} concentrations estimated for the temperate period at 3 000 y to be consistent with the K_d values derived for rock matrix sorptivity. A lower limit for the apparent K_{ds} value is also calculated based on the lower limit of the reported ω_A value and the 97.5 % percentile of the estimated total concentrations of Ca^{2+} and Ba^{2+}. An upper limit is calculated using the upper limit of ω_A with the 2.5 % percentile for Ca^{2+} and Ba^{2+}. The estimated range of K_{ds} values therefore implicitly includes the full uncertainty range of spatially variable groundwater composition for a random location in the repository volume as far as this is possible to quantify.

Table B-4. Estimated K_{ds} for the formation of solid solutions with calcite and barite. The median K_{ds} value assumes the median of the given range for ω_A together with the estimated median value of total Ca^{2+} and Ba^{2+} concentration at 3 000 y (temperate groundwater). The lower and upper limits of the K_{ds} range are given by the lower and upper bounds for ω_A together with the 97.5 % and 2.5 % percentiles of the calculated range of total Ca^{2+} and Ba^{2+} concentration, respectively.

Element (Redox state)	ω_A (-)	Best estimate K_{ds} (m^3/kg)	Lower limit K_{ds} (m^3/kg)	Upper limit K_{ds} (m^3/kg)
Solid solution with barite:				
Ra(II)	~1.8	1.6×10^{4}	2.2×10^{3}	6.1×10^{4}
Solid solution with calcite:				
Am(III)	200–1 000	9.5×10^{1}	2.1×10^{1}	2.2×10^{3}
Ni(II)	0.8–6	4.6×10^{-1}	8.2×10^{-2}	1.3×10^{1}
Ra(II)	0.003–0.053	2.7×10^{-3}	3.1×10^{-4}	1.2×10^{-1}
U(IV)	20–200	1.3×10^{1}	2.1	4.4×10^{2}
U(VI)	< 0.02	4.2×10^{-3}	2.1×10^{-3}	4.4×10^{-2}

B.6 Estimation of equilibrium retardation of radionuclide transport in fracture coatings

The total retarded travel time for a transported radionuclide can be shown to be equal to the sum of advective and equilibrium sorption residence times plus the matrix retention time (e.g. Moreno and Crawford 2009):

$$t = t_w + t_a + t_m = t_w + \frac{F}{2}\left(\delta_s\theta_s + K_{ds}m_s\right) + \frac{D_e\left(\theta_m + K_{dm}\rho_b\right)}{4\left(erf^{-1}\left(X\right)\right)^2}F^2 \qquad \text{B-26}$$

Where the variable X is the recovery fraction of released solute. Since we are interested in characterising situations where equilibrium sorption in the fracture minerals is relatively strong, the advective travel time and free storage porosity of the fracture coatings can be neglected. The residence time accumulated due to equilibrium sorption can therefore be given as:

$$t_a \approx \frac{F}{2}\sum_{k=1}^{n} K_{ds(k)}m_{s(k)} = \frac{F}{2}\sum_{k=1}^{n} K_{a(k)} \qquad \text{B-27}$$

If there is concern that some fracture minerals might exhibit kinetically hindered uptake, one could define an additional factor, f_{eq} accounting for the fraction of the mineral mass that is actually equilibrated on the timescale of radionuclide transport. This would give a modified form of Equation B-27:

$$t_a \approx \frac{F}{2}\sum_{k=1}^{n} K_{ds(k)}f_{eq(k)}m_{s(k)} = \frac{F}{2}\sum_{k=1}^{n} f_{eq(k)}K_{a(k)} \qquad \text{B-28}$$

For sorption processes such as ion-exchange and surface complexation, one could reasonably assume f_{eq} approximately equal to unity. For uptake of radionuclides to solid solutions, on the other hand, it is possible that f_{eq} is much less than unity thereby giving a reduced retardation effect. The impact of kinetically limited uptake to solid solutions is discussed further in Section B.9 where scoping calculations are also made to assess its possible impact on transport retardation.

It is noted that the equilibrium transport time given by Equation B-27 is proportional to half of the F on account of the fact that we consider the total amount of fracture mineral per area of fracture (i.e. not flow-wetted surface) within the advective pore space in this formulation. In Moreno and Crawford (2009) the problem was formulated in terms of the individual fracture coating thicknesses on opposing surfaces of the fracture. The only difference between the different model formulations is in the definition of K_a although the calculated value of t_a is the same in both cases. The median retention time, $t_{m50\,\%}$ (i.e. for 50 % recovery of an instantaneous pulse release) due to matrix diffusion and sorption is given by:

$$t_{m50\%} = \frac{D_e\left(\theta_m + K_{dm}\rho_b\right)}{4\left(0.477\right)^2} \times F^2 \qquad \text{B-29}$$

Using Equation B-27 and B-29 it is possible to estimate the relative change (increase) in retardation effect for different F values and estimated K_a values for the fracture minerals lining the advective pore space:

$$\chi = \frac{t_a + t_{m\ddot{u}}}{t_{m\ddot{u}}} \qquad \text{B-30}$$

The relative enhancement of transport retardation is shown in Figure B-5 for Am(III), Cs(I), Ni(II), and Ra(II) for the estimated specific mineral masses given in Table B-2 together with the K_{ds} values estimated for chlorite, other clay minerals as a group (Table B-3) and equilibrium solid solution with calcite (Table B-4). The calculations assume a mix of chlorite, assorted clay minerals, and calcite where sorptivity is assumed to be linearly additive as indicated in Equation B-4. The data are plotted as a function of the F in the form of shaded uncertainty intervals spanning the upper and lower limits of the estimated retardation effect. It should be also noted that the calculations assume an equilibrium retardation effect for the solid solution retention (i.e. f_{eq} = 1). The relative enhancement of radionuclide retardation is likely to be less that suggested by the equilibrium assumption if uptake to the solid solution is kinetically hindered. Figure B-6 shows the corresponding result for U(IV) and U(VI).

The association of Am(III) and Ni(II) with the fracture minerals has a considerable impact on the transport of these two solutes, whereas the impact on Cs(I) and Ra(II) transport is predicted to be significantly less. It is important to note that the results presented in Figure B-5 and Figure B-6 are relative to the median matrix retention time which varies considerably amongst the various nuclides. This is particularly important to note for the U(IV) and U(VI) cases where the matrix retardation time for U(IV) sorption is roughly 500 times greater than for U(VI) and the same F value. In general, the matrix retention time is approximately proportional to the K_d value assigned to the rock matrix (as can be ascertained by inspection of Equation B-29 noting that the free storage porosity, θ_m is in most cases very small).

Although barite has not been visually observed in sufficient amounts to be quantifiable at the Forsmark site, it is possible to use the K_{ds} values estimated for the selected groundwater compositions to speculate on the possible magnitude of the equilibrium retardation effect if it were present. The results of this analysis are plotted in Figure B-7 and show the relative enhancement of transport retardation as a function of F. As can be seen from the Figure, even very small amounts of barite on the order of only a couple of mg/m^2 of fracture surface might add considerably to the overall transport retardation of Ra(II), particularly for flowpaths featuring low F values.

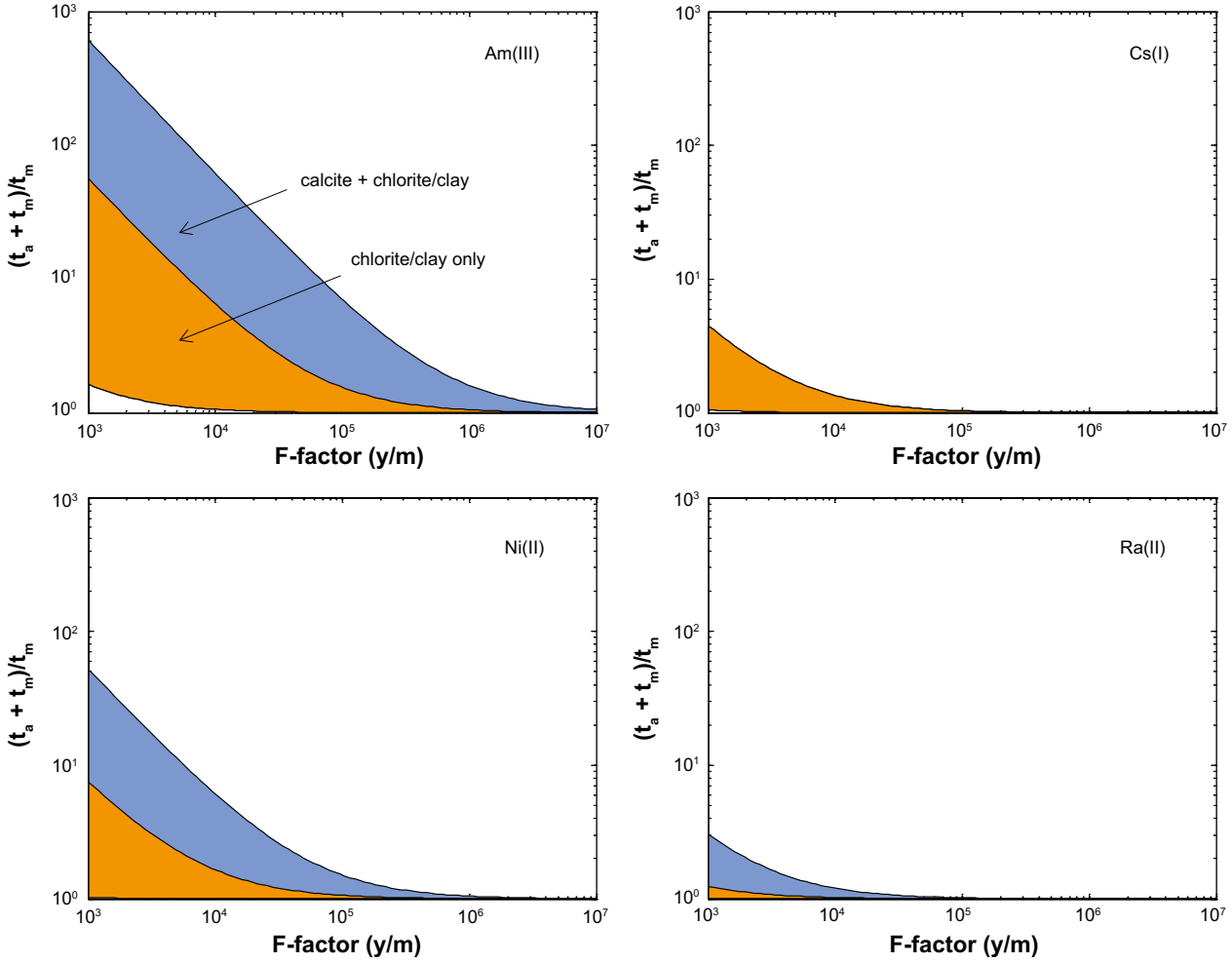

Figure B-5. *Estimated relative enhancement (χ as defined by Equation B-30 plotted versus F) of retardation effect for Am(III), Cs(I), Ni(II), and Ra(II) owing to equilibrium sorption on fracture minerals. Calculations assume a mix of chlorite, assorted clay minerals, and calcite where sorptivity is assumed to be linearly additive. Sorption on chlorite and clay minerals is assumed to occur by way of ion-exchange and surface complexation. Sorption in association with calcite is modelled assuming solid solution formation and a Henry law partitioning mechanism. Orange shaded regions indicate the retardation effect of chlorite and clay minerals only where the coloured region represents the approximate range of uncertainty. Blue shaded regions indicate the additional retardation effect potentially achievable if calcite forms a solid solution.*

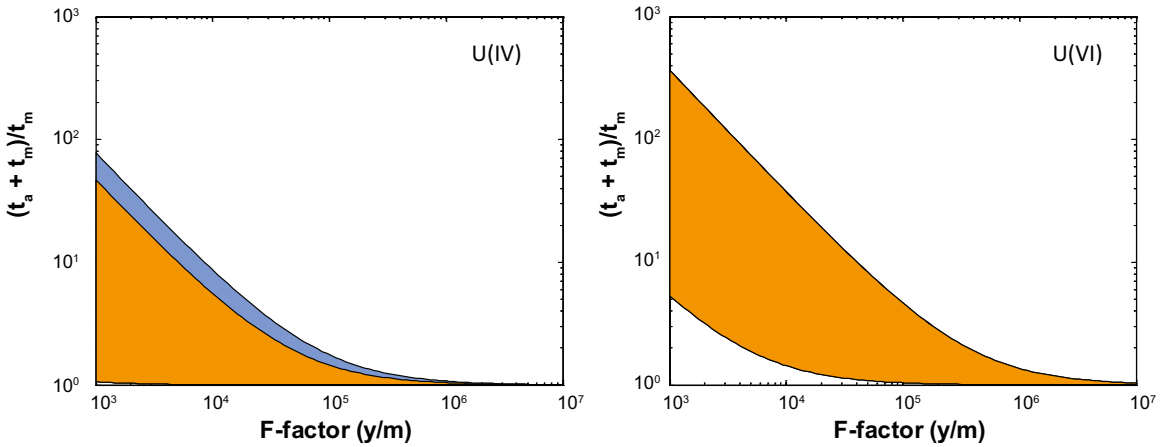

Figure B-6. *Estimated relative enhancement (χ as defined by Equation B-30 plotted versus F) of retardation effect for U(IV) and U(VI) owing to equilibrium sorption on fracture minerals. Calculations assume a mix of chlorite, assorted clay minerals, and calcite where sorptivity is assumed to be linearly additive. Sorption on chlorite and clay minerals is assumed to occur by way of ion-exchange and surface complexation. Sorption in association with calcite is modelled assuming solid solution formation and a Henry law partitioning mechanism. Orange shaded regions indicate the retardation effect of chlorite and clay minerals only where the coloured region represents the approximate range of uncertainty. Blue shaded regions indicate the additional retardation effect potentially achievable if calcite forms a solid solution.*

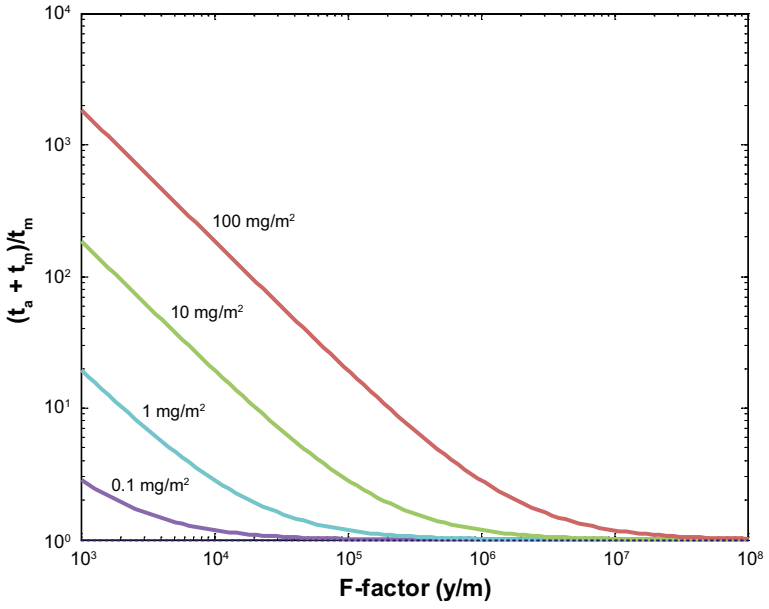

Figure B-7. *Estimated relative enhancement (χ as defined by Equation B-30 plotted versus F) of retardation effect for Ra(II) owing to solid solution equilibrium with barite. The impact of barite solid solution formation is shown for varying amounts of barite in the fracture coatings from 0.1 mg/m² to 100 mg/m². Curves are calculated for the best estimate K_{ds} value for barite solid solution estimated using Equation B-25 and assume fast uptake kinetics (i.e. f_{eq} = 1).*

B.7 Implications for remobilisation scenarios with evolving groundwater chemistry

Although the scoping calculations presented in the previous section indicate a relatively strong enhanced transport retardation effect, it is important to also consider how this might change with evolving groundwater compositions over time. In order to facilitate this discussion, a chemistry correction factor, f_{chem} can be defined which relates the K_{ds} at any given time and spatial location with some suitably chosen reference value. Since the scoping calculations are based on the assumption of the median total Ca^{2+} and Ba^{2+} concentration existing at 3 000 y during the temperate phase, the K_{ds} calculated for this condition is the most relevant reference value. Figure B-8 shows the estimated f_{chem} for calcite based solid solutions while Figure B-9 shows the corresponding data for Ra(II) in both calcite and barite based solid solutions. According to the definitions developed in Section B.5, an f_{chem} value greater than unity (i.e. $\log_{10} f_{chem} > 0$) implies enhanced sorptivity relative to the reference groundwater composition, while an f_{chem} value less than unity (i.e. $\log_{10} f_{chem} < 0$) implies reduced sorptivity. The uncertainty distribution for f_{chem} presented in Figure B-8 and Figure B-9 represents f_{chem} calculated for the full distribution of groundwater compositions projected for the repository environment at different times.

Interestingly, the results indicate that K_{ds} values for calcite based solid solutions are generally greater than the reference value for most of the different climate regimes considered in the calculations with an only slightly increased probability of reduced retention by solid solution during the glacial IIa period and at 2 000 y during the temperate phase. Although this could be considered a generally positive result with regard to the choice of the reference condition (i.e. being cautious with regard to the magnitude of enhanced retention), the result must also be considered in the context of implications for remobilisation scenarios. This deliberation therefore also requires careful consideration of the magnitude of groundwater flows and likely F distributions existing at different times during the repository evolution. It is also important to note that the modelled changes are relative to the median groundwater composition (total Ca^{2+} concentration) in the reference case and the spatial variability at any given time can be seen in Figure B-8 to be sufficiently large that the overall span of possible K_{ds} values that can exist in a random location in the repository volume does not change significantly for calcite.

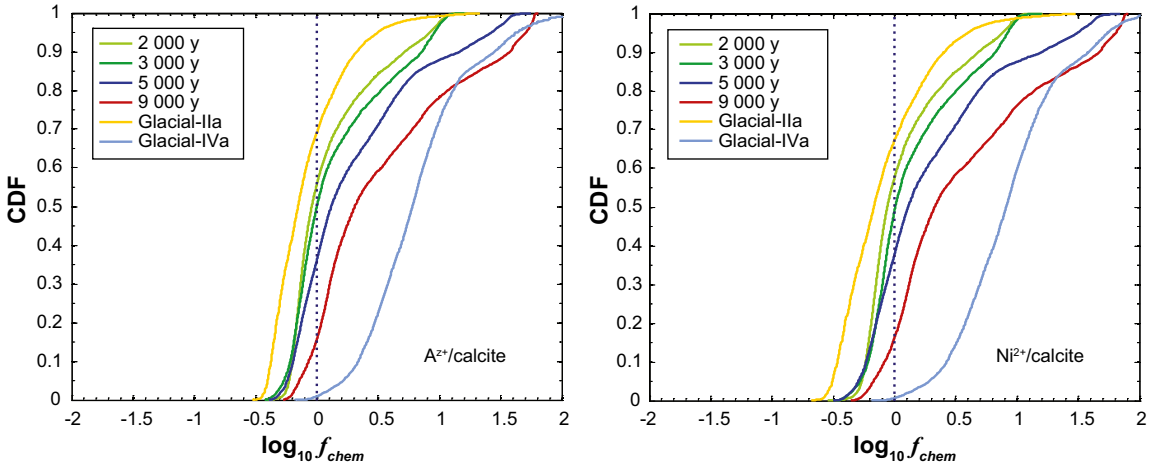

Figure B-8. *Estimated groundwater chemistry correction factors (fchem) for calcite solid solutions relative to the reference groundwater used in the scoping calculations. Data are plotted as a cumulative distribution function (CDF) for groundwater compositions at different times during repository evolution. The left-hand figure shows the approximate generic correction factor calculated using Equation B-24; the right-hand figure shows the nuclide specific correction factor for Ni^{2+} calculated using Equation B-23.The vertical broken line indicates the relative location of the reference groundwater composition (i.e. median Ca^{2+} concentration at 3 000 y).*

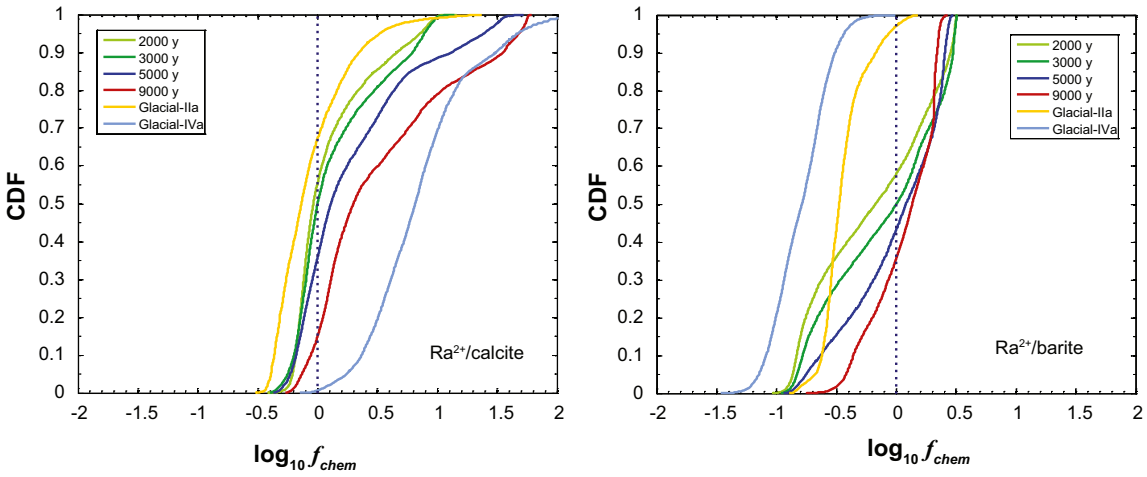

Figure B-9. *Estimated groundwater chemistry correction factors (fchem) for calcite (left) and barite (right) solid solutions relative to the reference groundwater used in the scoping calculations. Data are plotted as a plotted as a cumulative distribution function (CDF) for groundwater compositions at different times during repository evolution. The correction factor for Ra^{2+} in both figures is calculated using Equation B-23. The vertical broken line indicates the relative location of the reference groundwater composition (i.e. median Ca^{2+} or Ba^{2+} concentration at 3 000 y).*

In the description of the hydrogeological evolution during a glacial cycle in the **Post-closure safety report**, the Darcy fluxes typical of the glacial ice front location II and IV models are about two orders of magnitude higher than the Darcy flux at 2 000 y during the temperate phase (approximately the same as the flow conditions at 3 000 y). Typical F values during the glacial IIa and IVa epochs are also reduced by roughly two orders of magnitude. Since radionuclide retention in the fracture minerals is more important at lower F values, the increased average sorptivity predicted for calcite solid solution suggests a mitigating effect relative to predicted radionuclide transport in the absence of fracture retention. This, however, is also dependent on calcite not being significantly depleted from the fracture system during periods of high flow. Whether, or not this is likely to occur is discussed in the next section.

As can be seen in Figure B-9, solid solutions involving Ra^{2+} association with barite appear to behave in a somewhat different fashion to those involving calcite. In this case, K_{ds} values for barite based solid solutions are generally lower than the reference value for most of the different climate regimes considered in the calculations. This means that solid solutions of barite are more likely to be remobilised thereby resulting in a pulse like release of Ra(II) during the glacial IIa and IVa epochs. It should be noted that the changes in calcite and barite solubility are mutually correlated to the groundwater compositions by the assumption of simultaneous equilibrium of barite and calcite as described in Section B.5.

Comparison of the left- and right-hand images in Figure B-9 suggests that changes in calcite and barite solid solution partitioning in response to the changing groundwater chemistry seem to partially counteract each other depending on the relative amounts of each mineral present (and assuming that neither is fully depleted by dissolution). If the currently unknown, average specific mass of barite in the fracture system was to be on the order of about 0.1 mg/m^2, the results indicate that the changes in sorptivity of calcite and barite with respect to Ra^{2+} should approximately cancel each other out giving rise to a net zero change in overall fracture mineral sorptivity due to solid solution equilibrium (all other things being equal). Larger quantities of barite would generally indicate decreased fracture mineral retention relative to the reference groundwater condition, whereas smaller quantities of barite would suggest the opposite behaviour.

Another feature of significant relevance for the safety assessment is the relative mobility of U both observed and inferred during the site investigation (Laaksoharju et al. 2008) and also considered possible for the groundwater system at Forsmark during the repository evolution scenarios (Crawford 2010). This is not unexpected since U is found to be considerably more sensitive to changes in redox potential

than most of the other redox sensitive radionuclides considered. This sensitivity is the main reason why both U(IV) and U(VI) redox speciation cases are propagated forward in the radionuclide transport calculations. The calculations detailed in Crawford (2010) suggest that the predominance of the hexavalent state cannot be excluded as a possibility in the repository environment at times when carbonate concentrations are elevated (particularly noted at 9 000 y during the temperate phase).

The reduced U(IV) redox speciation is considered to be the more pessimistic assumption with regard to far-field dose rates since the stronger sorptivity of the tetravalent state limits the migration of ^{238}U. The relatively immobile U(IV) then constitutes a more concentrated source of the weakly sorbing ^{226}Ra daughter radionuclide; a feature of great importance for the assessment of the overall radiological risk. The solid solution calculations indicate that U is sorbed relatively strongly by calcite under reducing conditions as U(IV), although much less strongly if redox conditions are such that the hexavalent state, U(VI) is predominant. In both cases sorption on chlorite and clay minerals appears to be greater than sorption in association with calcite. Since the retardation of U(IV) transport is very strong anyway (by way of retention in the rock matrix), the neglection of U(IV) retention in fracture minerals does not appear to have great significance for the overall assessment of risk.

B.8 Rate of calcite depletion by infiltrating dilute groundwater

The rate of calcite depletion in the fracture system can be estimated by a mass balance approach where calcite lining an advective flowpath dissolves under the influence of infiltrating dilute, glacial groundwater. Figure B-10 illustrates the calcite dissolution process whereby dilute groundwater dissolves calcite before reaching equilibrium at some distance downstream after which no further dissolution occurs.

After a brief transient period, a quasi-stationary state is achieved (Lichtner 1988) after which, the shape of the reaction front and its rate of propagation in space may be regarded as being approximately constant. At this time, the velocity of the reaction front, *dx/dt* is proportional to the rate of depletion of calcite as given by the mass balance:

$$q\left(C_{eq}-C_0\right)=\left(\frac{W_c m_s}{M_w^{calcite}}\right)\frac{dx}{dt} \qquad \text{B-31}$$

Where W_c is the width of the flowpath, m_s is the mineral mass, $M_w^{calcite}$ is the molecular weight of calcite, C_0 is the total concentration of Ca^{2+} in the infiltrating glacial water and C_{eq} is the downstream equilibrium concentration. This variables separable equation can be integrated to give the time required, t_d to deplete an entire flowpath of its calcite inventory in terms of the flow-related transport resistance, F:

$$t_d=\left(\frac{m_s/M_w^{calcite}}{C_{eq}-C_0}\right)\cdot\frac{F}{2} \qquad \text{B-32}$$

It should be noted that the depletion time given by Equation B-32 assumes only calcite residing in the main flow channel hosting advective flow and doesn't consider additional calcite inventory residing in stagnant zones or in flanking regions of partially annealed fractures. Figure B-11shows the estimated calcite depletion time plotted as a function of F. The calculations are based on the difference in calcium concentration of the dilute glacial end-member as given by Gimeno et al. (2008) and the concentration for the same initial groundwater in equilibrium with calcite calculated using PHREEQC for an assumed temperature of 0 °C of the infiltrating groundwater (i.e. giving the highest calcite solubility).

As can be readily appreciated from Figure B-11, many thousands of years of constant leaching are required to deplete the calcite even for recharge flowpaths featuring extremely low F values. Since high flow conditions involving infiltration of dilute glacial water is only expected to occur sporadically under brief time intervals, it is thought that the depletion of calcite can be largely neglected. This is supported by the near ubiquitous presence of very old calcite mineralisations (dating from the Paleozoic era, 542–251 Ma as inferred from isotopic composition) in the Forsmark fracture system (Sandström et al. 2008). Although there are some indications of newly formed calcites (Cenozoic era, ≤ 65.5 Ma) in the near surface fractures and in conductive zones, this indicates that the overall calcite inventory should be relatively stable over time.

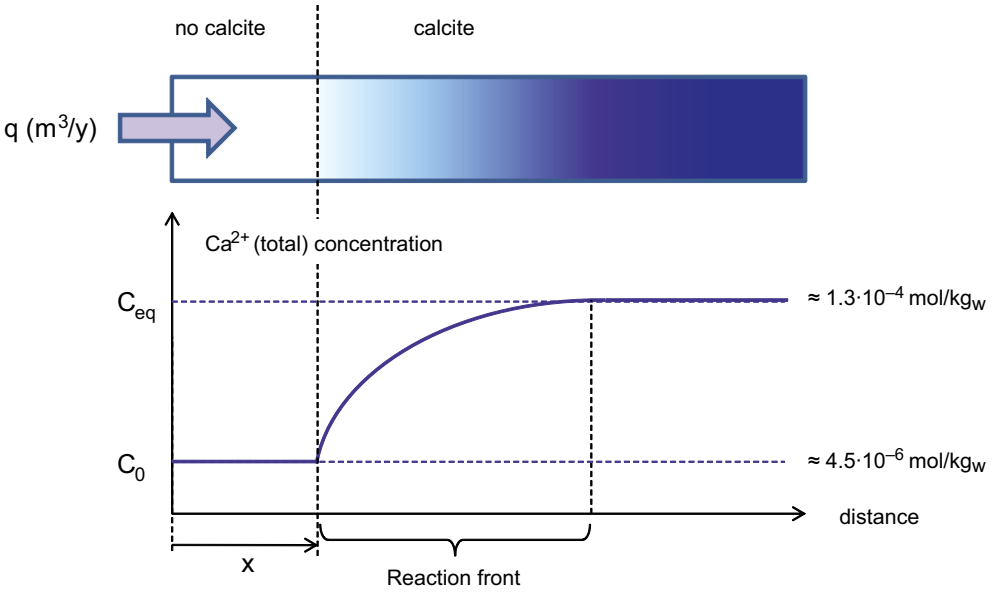

Figure B-10. *Illustration of calcite mobilisation process for a flowpath where infiltrating dilute, glacial groundwater (with concentration, C_0) dissolves calcite. The dissolution products eventually reach their equilibrium concentration (C_{eq}) over a distance determined by the particular chemical kinetics of the dissolution reaction (and diffusion kinetics), the reactive surface area, and advective travel time. The transient concentration region separating the initial and equilibrium states is referred to as the reaction front.*

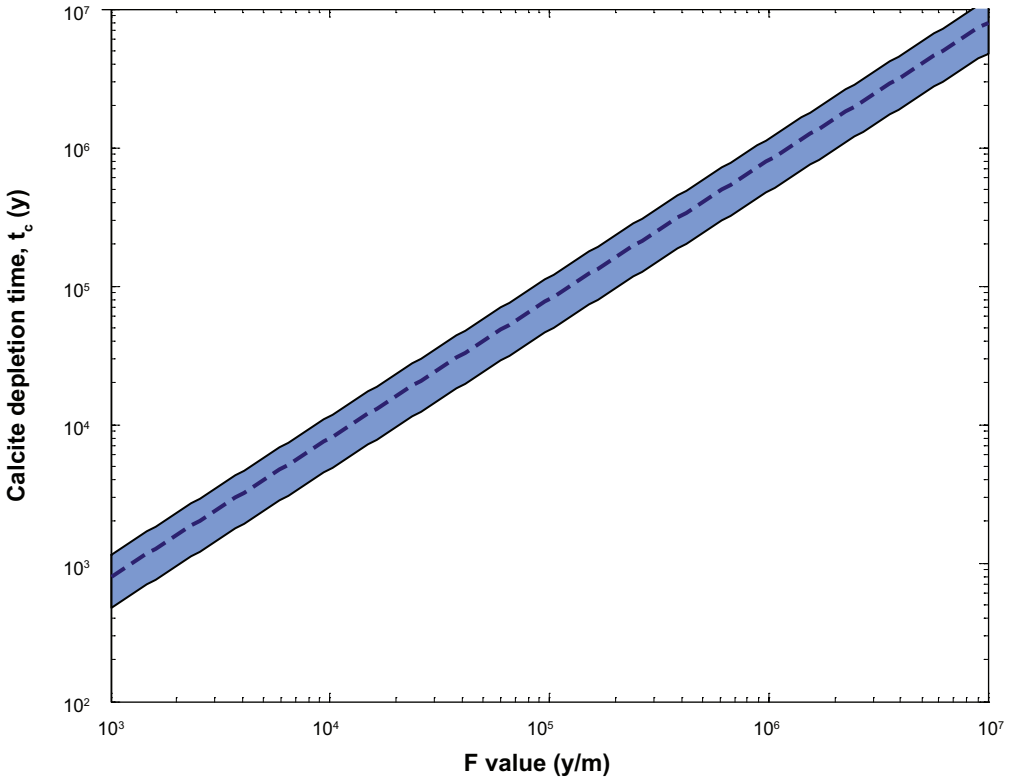

Figure B-11. *Time to deplete calcite from an advective flowpath as a function of F. Calculations assume estimated specific mass of calcite given in Table B-2 and only calcite residing along the main flowpath. The shaded region represents the minimum-maximum range and the broken line is the best estimate. Additional calcite buffering capacity may reside in stagnant zones of the fracture or in partially annealed sections flanking the flowpath.*

B.9 Kinetics of radionuclide uptake during solid solution formation

In the analyses presented in the preceding sections, only equilibrium partitioning processes have been considered. For ion-exchange and surface complexation, the assumption of equilibrium on the timescale of the migration process is generally considered to be a reasonable assumption. For solid solutions, on the other hand, the assumption of equilibrium is not so certain. One of the main objections to the assumption of solid solution equilibrium is that uptake to the solid phase is expected to be an essentially diffusion mediated process in the absence of strong geochemical gradients causing mineral crystal reformation by dissolution and re-precipitation. Since solid-state diffusion is a much slower process than chemical kinetics, the assumption of equilibrium could result in the significant over-estimation of transport retardation potential.

In many of the experimental studies described in the literature, solid solution formation is studied under conditions giving rise to end-member re-crystallisation or precipitation (see e.g. Bruno et al. (2007) and references therein). Although there are a large number of studies that probe kinetic effects related to solid solution formation, the vast majority of these involve far from equilibrium conditions and may not be strictly applicable to natural systems.

At this time there are few studies that specifically attempt to elucidate kinetics of solid solution partitioning under conditions approximating those found in nature. Even in tracer studies where approximately static solution compositions are used, it is difficult to completely exclude transient effects of surface reformation due to re-crystallisation (dynamic equilibrium) and Ostwald ripening effects (i.e. thermodynamically favoured growth of large crystals at the expense of smaller dissolving crystals) over the limited duration of laboratory experiments (see e.g. Curti et al. 2005). The carefully performed experiments described by Bosbach et al. (2010), however, are a welcome addition to the body of knowledge concerning solid solution formation since they hint at the possibility that full equilibration of solid solutions might be achievable over a relatively short period of time. In these experiments barite samples pre-equilibrated for 4 weeks were exposed to a spiked $^{133}Ba^{2+}$ solution specifically to study the uptake kinetics against an approximately constant background of non active Ba^{2+}. The authors conclude that since the tracer being incorporated into the barite crystals is, for all practical purposes, chemically identical to the non-active solute the process must be purely entropy driven (Bosbach et al. 2010).

The question remains, however, whether the process observed is related to re-crystallisation or an example of fast solid state diffusion. If the former, then it is necessary to outline a mechanism by which the process can be expected to occur under in situ conditions in the repository environment where fracture minerals are in dynamic equilibrium with the groundwater. To the best knowledge of the authors, a cogent mechanistic description that explains how this might occur does not currently exist. It also raises the question whether 4 weeks of pre-equilibration is sufficient time to guarantee cessation of re-crystallisation transients in an initially perturbed experimental system. It is also unclear whether the results can be automatically extrapolated to situations where the incorporated solute is chemically dissimilar to the end-member. This is of particular relevance for solid-state diffusion since the mechanism driving the process may not be the same for different solutes being incorporated (e.g. whether the diffusion mechanism is based on vacancy, interstitial, or an exchange random walk process (Watson and Baxter 2007)).

In natural systems such as a deep repository environment, groundwater conditions are expected to change only very slowly (with the possible exception of periodic glacial water penetration events, etc.). Under such conditions, the crystalline morphology of readily soluble fracture minerals such as calcite and less soluble barite would be expected to reach a steady state condition where significant changes due to surface re-formation (dynamic equilibrium) or Ostwald ripening effects should diminish to a low level. Even if such effects do not disappear entirely, it is not clear whether they should influence mineral compositions over more than a few molecular layers in calcite or barite mineral crystals. In the absence of an alternative mechanistic description of uptake kinetics involving surface renewal/re-crystallisation under relevant conditions, it seems that solid state diffusion is the only other feasible process by which solute uptake can occur. In the following sections, scoping calculations are therefore made concerning the possible role of diffusion kinetics limiting the uptake of radionuclides in solid solutions.

A simplified diffusion kinetic formulation of solid solution partitioning

To the extent that the uptake of radionuclides in solid solution can be approximately described as a Fickian process, diffusive disequilibrium is relatively straight-forward to model since it is analogous to the corresponding problem involving depth-limited matrix diffusion. Here, we assume a porous fracture coating comprised of a mineral that forms solid-solutions. The surface coating is furthermore assumed to be sufficiently porous that instantaneous porewater diffusive equilibrium is attained throughout the thickness of the mineral layer over the timescale of solute transport (see Figure B-12).

The transport problem involving simultaneous diffusion into the rock matrix as well as diffusion-limited uptake to the solid solution can be given by analogy to the problem described in Appendix A for diffusion into an effectively stagnant zone. The Laplace space equation describing the residence time distribution of a non-decaying solute in the fracture can then be given as:

$$\tilde{c}_A = \frac{c_{A0}}{s}\exp\left(-R_{fw}t_w s\right)\exp\left(-F\left(\psi_m + \alpha\psi_x\right)\right) \qquad \text{B-33}$$

Where, the parameter α (m^2/m^2) is the ratio of solid solution specific surface area to flow-wetted surface, while ψ_m and ψ_x are the rock matrix and solid solution flux terms. For unlimited matrix diffusion, ψ_m is defined by Equation A-2, whereas the flux term for depth limited solid-state diffusion into the solid solution forming mineral is given by the expression:

$$\psi_x = K_{ds}\rho_s\sqrt{D_c\, s}\,\tanh\left(\delta_x\sqrt{\frac{s}{D_c}}\right) \qquad \text{B-34}$$

Equation B-34 is essentially the same as that given in Crawford (2006, 2008) for a limited rock matrix although with the solid-state diffusion coefficient in place of apparent diffusivity. Another difference is the leading term $K_{ds}\rho_s$ which accounts for the difference in aqueous and solid phase concentration at the phase boundary. Here, it is implicitly assumed that the diffusive uptake to the possibly irregularly shaped particles comprising the solid solution can be described as a simple one-dimensional process. Other formulations are, of course, possible although then the flux term, ψ_x is a more complex function. Given that calcite and barite crystals are frequently euhedral in shape this is not considered to be an unreasonable approximation.

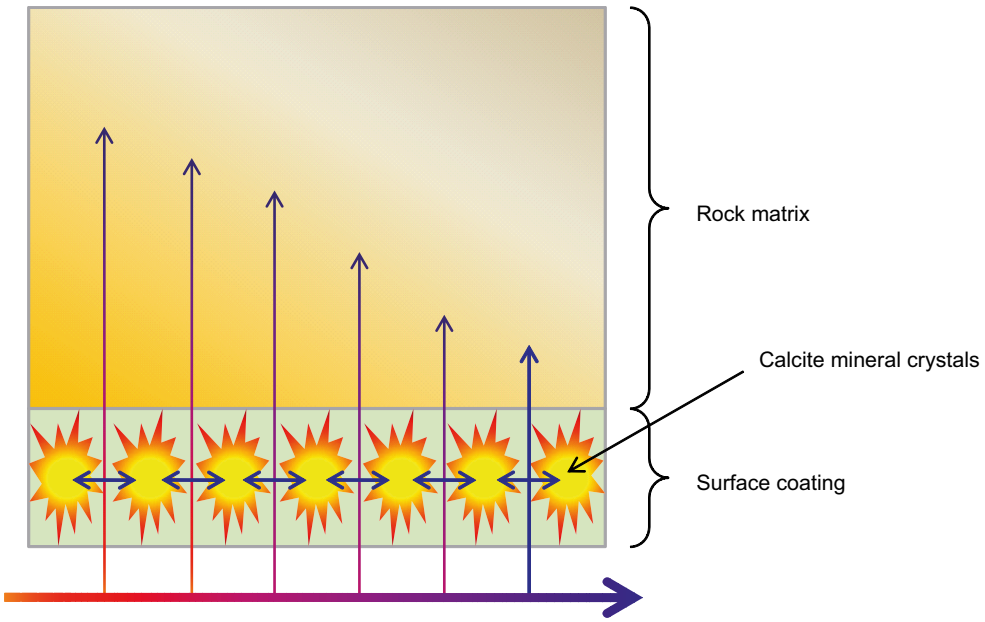

Figure B-12. *Illustration of transport problem where diffusive uptake to solid solution forming surface minerals (principally calcite) is considered as a parallel retardation sink for migrating radionuclides. The arrows indicate the notional direction of solute flux in the system.*

If the BET surface area, A_s (m^2/kg) of the solid solution forming mineral is known, the parameter α can be simply given as:

$$\alpha = \frac{A_s m_s}{2} \qquad \text{B-35}$$

It should be noted that the division by a factor of 2 is required to account for the fact that the specific mass of solid-solution forming mineral, m_s is defined in terms of fracture surface area rather than flow-wetted surface. Based upon conservation of volume, the BET surface area can also be used to estimate the effective maximum depth of penetration, δ_x (m) for the mineral crystal:

$$\delta_x \approx \frac{1}{A_s \rho_s} \qquad \text{B-36}$$

A BET surface area of roughly 2.2 m^2/g is reported by Byegård et al. (2008) for calcite dominated fracture types at the Forsmark site. If it is assumed that this is approximately representative of the calcite mineral grains comprising the fracture coating, this implies a maximum penetration depth on the order of ~0.17 μm.

It is noted that the formulation given by B-33 also can accommodate the possibility of additional equilibrium sorption processes in the fracture coating by suitable definition of the R_{fw} retardation term. In the present analysis, however, the kinetic uptake to the solid solution is considered in isolation and R_{fw} is only used to account for the relatively minor impact of free storage porosity in the fracture coating.

Limits on solid state diffusivities in calcite at ambient temperatures

Isotope and elemental zonation in naturally occurring mineral crystals is well known in the geological literature and diffusion profiles established at elevated temperatures are frequently used to estimate the likely duration and temperature of ancient episodes of hydrothermal activity and to understand processes related to contact metamorphism (e.g. Watson and Baxter 2007). In studies of contact metamorphism described in the literature one frequently refers to the *closure temperature* of a mineral grain which is the critical temperature at which diffusive re-equilibration processes are thought to cease. This facilitates formation age dating of minerals since isotope ratios of effectively trapped tracer substances and their decay products can then be measured and used to establish absolute ages (e.g. using the Sm-Nd, Lu-Hf, Rb-Sr dating systems). The relation between closure temperature and solid-state diffusivity is formalised in the Dodson equation (Dodson 1973) and its various derivative forms (e.g. Ganguly and Tirone 1999).

In such studies, solid state diffusivities are typically assessed independently by laboratory measurements. There are very few measurements of solid state diffusivity reported at ambient temperatures in the literature. Most data are reported for non-aqueous conditions and at temperatures in the range 400 °C–800 °C since this is the relevant range for studies of contact metamorphism (e.g. Watson and Baxter 2007). Some data for diffusion in calcite are reported for some rare earth elements (REE) in Cherniak (1998), and for Sr^{2+} and Pb^{2+} in Cherniak (1997). Solid state diffusivities for Ca^{2+} and Mg^{2+} in calcite are also reported by Fisler and Cygan (1999). A detailed overview of the literature data for solid state diffusion in calcite is given by Cherniak (2010) although for temperatures generally in excess of 400 °C. Extrapolation of the reported diffusivities to ambient temperatures through use of the Arrhenius equation (IUPAC 1997) typically implies solid state diffusivities less than10^{-35} m^2/s and in some cases, 10^{-50} m^2/s or less in the case of the data reported by Fisler and Cygan (1999). This would virtually guarantee very little solute diffusion if shown to be valid at such temperatures.

One of key assumptions concerning the existence of a closure temperature for a particular mineral is that the diffusivity measured at high temperature can be extrapolated to low temperatures using the Arrhenius approach (effectively implying a single rate of diffusion). Although some mineral types obviously preserve their isotopic and elemental signatures over effectively infinite (≥ 1 Ga) timescales this does not automatically hold for all minerals. For minerals such as calcite (and barite) high-temperature studies of solid-state diffusion may indicate diffusion mechanisms that might not extrapolate well to low temperature conditions and it is possible that other diffusion mechanisms may dominate in the ambient temperature range. Under the assumption that solid state diffusion is at least

possible at ambient temperatures, the persistence of isotopic and elemental zonation to modern times can therefore (at least in some cases) be used to rule out solid state diffusivities above certain limits at ambient temperature.

It has been known for some time (Lahav and Bolt 1964) that solid state diffusivities at ambient temperatures in natural systems can be as much as 10^{-24} m^2/s for self diffusion of $^{45}Ca^{2+}$ in calcite. Although not strictly under natural conditions, similar rates of apparent solid-state diffusivity have been qualitatively observed by Stipp et al. (1992, 1998) for diffusion of surface sorbed Cd^{2+} in calcite, although for relatively pristine samples stored in humid air forming an adsorbed surface layer of moisture. For solutes other than Ca^{2+} with unfavourable ionic radii relative to the calcite lattice, one would expect lower diffusivities than this estimate would otherwise suggest.

Independent estimates of apparent solid state diffusivity in calcite can potentially be obtained from uranium series disequilibrium studies involving site-specific fracture minerals themselves. Estimates based on such data are likely to be more relevant for characterisation of solid solution retention processes, since the data should reflect microscale processes occurring at the aqueous/solid phase interface rather than deep within a mineral structure. It is suggested here that even if the uptake of solute to a solid-solution forming mineral is actually a chemical reactive process related to dynamic equilibrium rather than a true solid state diffusion process, the dynamics of the inward migration of the solute in the mineral grain should still be amenable to an approximately Fickian mathematical treatment (being effectively an entropy driven mixing process). At the very least, the existence of a disequilibrium between isotopic profiles of the fracture minerals and the groundwater can be cited as evidence of a relatively slow uptake mechanism.

It is important to remember, however, that a number of different processes involving deposition and leaching of uranium (or various combinations thereof) over geological time can give rise to similar patterns of $^{234}U/^{238}U$ and $^{230}Th/^{234}U$ disequilibrium, so robust interpretation is very difficult. Although it is not strictly possible to directly estimate solid state diffusivities from such data, it is possible to rule out diffusivities above a certain threshold owing to the very existence of isotopic disequilibrium between the groundwater and the fracture minerals.

For fast partitioning processes such as ion-exchange and surface complexation one would expect sorbed isotopic concentrations to be reasonably representative of dissolved concentrations. Even in the case of microscopic surface precipitates, one would still expect reasonable agreement between sorbed and dissolved isotopic concentrations given contact times of a few decades to some hundreds of years. The fact that the average isotopic composition of natural tracer substances in association with fracture minerals appears to differ so much to that of the groundwater therefore suggests that the sorbed solutes are present in a relatively inaccessible form.

This assumes, of course that the measured groundwater composition is actually representative of the water that has been in contact with the fracture minerals which may not always be a correct assumption, particularly for redox sensitive solutes such as U. If it can be assumed that the groundwater compositions are approximately representative, then it is possible to estimate the time elapsed to reach a steady state with regard to the isotopic composition in a calcite mineral grain. The one-dimensional solid-state diffusion equation for the ^{238}U decay series can be given as:

$$\frac{\partial \overline{c}_s}{\partial t} = \overline{\overline{D}}_c \frac{\partial^2 \overline{c}_s}{\partial x} - \begin{pmatrix} -\lambda_{238U} & 0 & 0 & 0 \\ +\lambda_{238U} & -\lambda_{234U} & 0 & 0 \\ 0 & +\lambda_{234U} & -\lambda_{230Th} & 0 \\ 0 & 0 & +\lambda_{230Th} & -\lambda_{226Ra} \end{pmatrix} \overline{c}_s \qquad \text{B-37}$$

Here, $\overline{c}_s$ is the concentration vector of ^{238}U, ^{234}U, ^{230}Th, and ^{226}Ra tracers and $\overline{\overline{D}}_c$ is the diagonal matrix of tracer diffusivities. Customarily, the intermediate daughter nuclides ^{234}Th and ^{234m}Pa can be neglected on account of their extremely short half-lives and are therefore not included in Equation B-37. If one assumes that the calcite initially precipitates with a composition approximately representative of the contacting groundwater composition, then it is relatively straightforward to calculate the evolution of tracer concentration profiles within the mineral grain for a given solid state diffusivity (assuming that all tracers have roughly the same order of magnitude diffusivity). If the concentration profiles are integrated over the diameter of the mineral grain then one can estimate an average concentration and thus an average measure of the isotope activity ratio for the whole mineral crystal can be calculated.

In general, the contemporary groundwater at Forsmark exhibits $^{234}U/^{238}U$ activity ratios mostly ranging between 2–3 (Laaksoharju et al. 2008). $^{234}U/^{238}U$ activity ratios greater than unity are common for groundwater in granitic rock. Possible mechanisms for this include direct α- recoil addition to matrix porewater (e.g. Rasilainen et al. 2006) as well as preferential geochemical leaching of ^{234}U due to radioactive decay-related mineral crystal disruption (e.g. van Calsteren and Thomas 2006). The precise nature of the cause of the initial groundwater disequilibrium is less important for these calculations and it is sufficient to state that an activity ratio greater than unity is generally expected. Owing to the extremely low solubility of Th, on the other hand, the groundwater $^{230}Th/^{234}U$ ratio is typically measured to be on the order of 10^{-3} although can be as much as 0.08 in certain borehole sections at the Forsmark site. Since ^{230}Th has a much shorter half-life than either ^{238}U or ^{234}U, however, it can be neglected from the initial inventory of the calcite mineral without introducing significant errors. Equation B-37 can be readily solved using the partial differential equation tool (*pdepe.m*) in Matlab. Figure B-13 shows the simulated temporal evolution of the activity ratio for $^{234}U/^{238}U$ and $^{230}Th/^{234}U$ averaged over the calcite mineral crystal assuming a maximum penetration depth of 0.17 µm (as estimated using Equation B-36) and a constant $^{234}U/^{238}U$ isotopic ratio in the contacting groundwater.

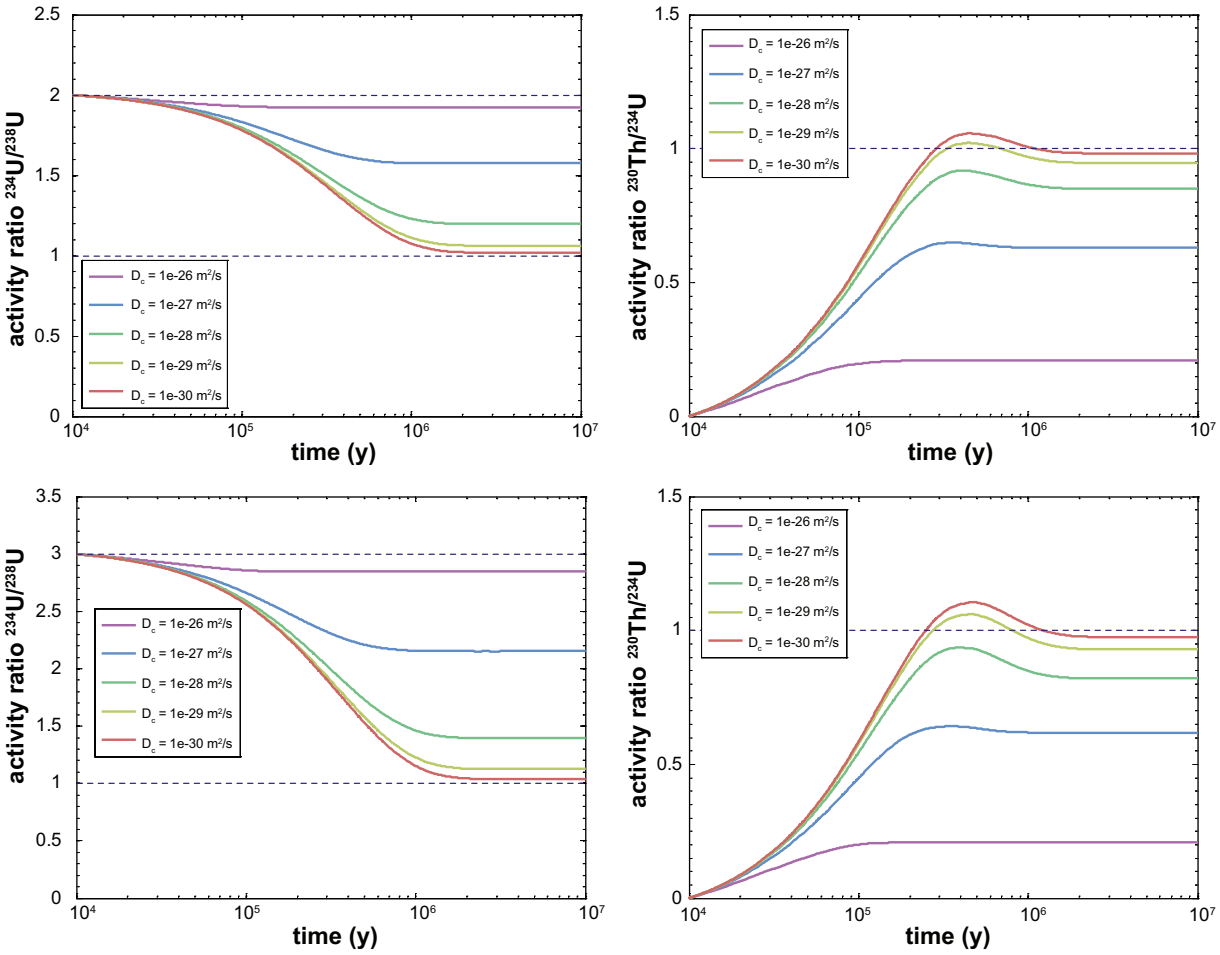

Figure B-13. *Evolution of $^{234}U/^{238}U$ (left) and $^{230}Th/^{234}U$ (right) disequilibrium as a function of time for different solid state diffusivities in the range of 10^{-26} m^2/s to 10^{-30} m^2/s and for a constant groundwater $^{234}U/^{238}U$ activity ratio of 2 (top) and 3 (bottom) indicated by the upper broken line in each of the plots on the left-hand side. Calculations assume a calcite crystal with an accessible diffusion depth of 0.17 µm. A steady-state is typically achieved after roughly 2 Ma although not necessarily corresponding to secular equilibrium (activity ratio = 1 indicated by the lower broken line). Secular equilibrium is only achieved for very low solid-state diffusivities (< 10^{-30} m^2/s).*

It is interesting to note that the existence of solid state diffusion causes a steady state to be reached with regard to $^{234}U/^{238}U$ and $^{230}Th/^{234}U$ activity ratios that does not represent secular equilibrium. Since $^{234}U/^{238}U$ activity ratios are significantly closer to unity in the fracture minerals than the assumed boundary value of 2–3, this suggests relatively slow diffusion. If the estimated average diffusion depth of 0.17 μm is reasonable, this would tend to rule out diffusivities much above 10^{-27} m^2/s for U-series environmental tracers. A corollary is that U-series ages of fracture minerals may be underestimated if solid state diffusion is neglected and the characteristic time of solid state diffusion is sufficiently low relative to the isotopic equilibration time for mineral grains of given size (generally only small crystals).

It is noted that measured $^{230}Th/^{234}U$ activity ratios in fracture minerals sampled from conductive, open fractures (presumed also to be flow-bearing) are typically higher than unity, although the diffusion model predicts ratios lower than unity (apart from brief transients above unity for very low diffusivities). This might suggest that the bulk of ^{230}Th sequestered in fracture minerals is in the form of surface sorbed species or surface precipitates rather than being hosted in calcite crystals. This interpretation, however, assumes a continuous deposition process and it is also possible that outer layers of calcite minerals are selectively leached of their ^{234}U content at different times thereby giving anomalously high $^{230}Th/^{234}U$ ratios. It is relevant to note here that even if this process has occurred at various times in the geological past, the persistence to modern times of the apparent disequilbrium between the groundwater $^{234}U/^{238}U$ ratios relative to the fracture minerals still does not appear to be compatible with a fast uptake mechanism. If uptake to the solid solution is relatively fast one would still expect re-equilibration of the isotope compositions to the prevailing groundwater values given sufficient time.

Since the above analysis considers differences in isotope ratios between the groundwater and the sorbed phases, it is not especially sensitive to variations in the concentration of uranium provided the ratio is relatively constant over time. This can be demonstrated by way of a sensitivity analysis using a periodic concentration boundary condition that preserves the groundwater $^{234}U/^{238}U$ activity ratio. In this case, a sinusoidally varying absolute concentration boundary condition has been assumed with a period of 10 ka and amplitude of variation corresponding to six orders of magnitude in absolute ^{238}U boundary activity (i.e. $\log_{10}$ units). Given the timescale associated with glaciation, this can be taken to be a reasonably relevant periodicity of variation. A solid state diffusivity of 7×10^{-28} m^2/s has been arbitrarily chosen to illustrate the impact of the variable boundary condition since this gives a steady state condition that is neither in diffusive equilibrium with the groundwater activity ratio nor in secular equilibrium. As can be readily seen from Figure B-14, the periodic boundary condition has a minimal impact on the simulation result and the asymptotic steady state condition is approximately the same in both cases. It should be noted that the characteristic time of diffusion in this case is sufficiently large that the diffusion process acts effectively as a low pass filter and it is generally only temporal variations on the longest timescales that have any appreciable impact on the activity ratios at long contact times.

In cases where the groundwater $^{234}U/^{238}U$ activity ratio varies periodically, the steady state activity ratio in the mineral crystal tends to reflect the average boundary condition. This can be demonstrated by simulating a boundary condition where the absolute concentration is constant, although the $^{234}U/^{238}U$ activity ratio is allowed to vary. In this simulation, a constant concentration of ^{238}U is assumed while the ^{234}U concentration is made to vary sinusoidally with a 10 ka period to give a $^{234}U/^{238}U$ activity ratio in the range 2–4 with an average of 3. To illustrate the additional impact of the initial conditions on the trajectory of the average activity ratio, two separate cases have been modelled for the initial conditions. Figure B-15 shows the development of the activity ratio over time for an initial activity ratio of 3 (i.e. for both the groundwater and the calcite). Figure B-16 shows the corresponding result for an initial activity ratio of 1.5.

As can be readily appreciated from Figure B-15 and Figure B-16, the final steady state reflects a balance between diffusive exchange with the groundwater and the rate of production and decay of ^{234}U in the calcite. The initial composition of the calcite has no impact on the final steady state condition although it does influence the trajectory of the transient activity preceding the onset of steady state conditions. The 10 ka periodic, activity ratio boundary condition also has a minimal impact on the final steady state that corresponds to the average boundary condition.

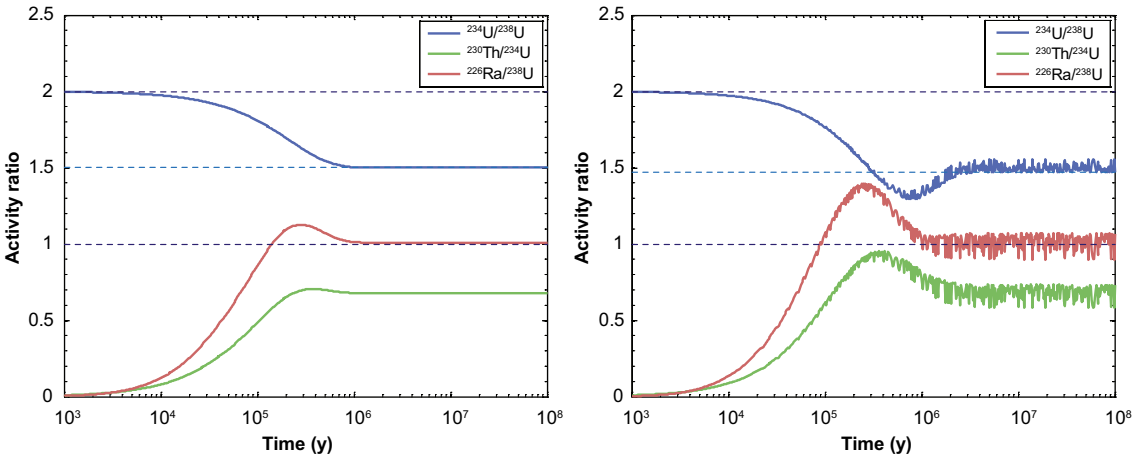

Figure B-14. *Evolution of U-series disequilibrium as a function of time for a solid state diffusivity of 7×10^{-28} m^2/s and for a constant groundwater $^{234}U/^{238}U$ activity ratio of 2. The left-hand figure shows the result for a constant concentration boundary condition, while the right-hand figure shows the impact of a periodic variation in absolute U concentration (6 orders of magnitude variability with a period of 10 ka although constant $^{234}U/^{238}U$ activity ratio). Calculations assume a calcite crystal with an accessible diffusion depth of 0.17 µm as in previous calculations.*

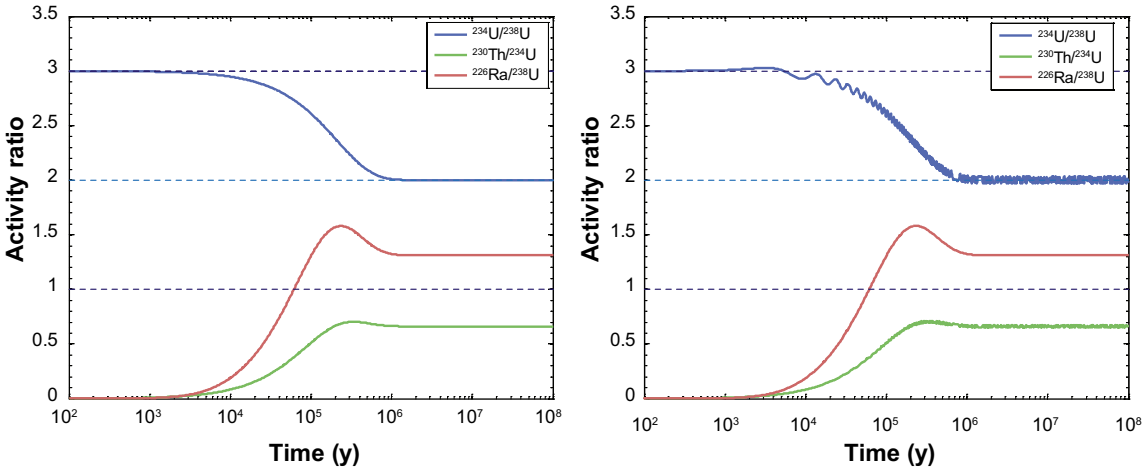

Figure B-15. *Evolution of U-series disequilibrium as a function of time for a solid state diffusivity of 7×10^{-28} m^2/s and for a groundwater $^{234}U/^{238}U$ activity ratio varying in the range 2–4. The left-hand figure shows the result for a constant concentration boundary condition representing the average, while the right-hand figure shows the impact of a periodic variation in the activity ratio in the range 2–4 (although for constant groundwater ^{238}U activity). Calculations assume a calcite crystal with an accessible diffusion depth of 0.17 µm as in previous calculations and an initial $^{234}U/^{238}U$ activity ratio of 3.*

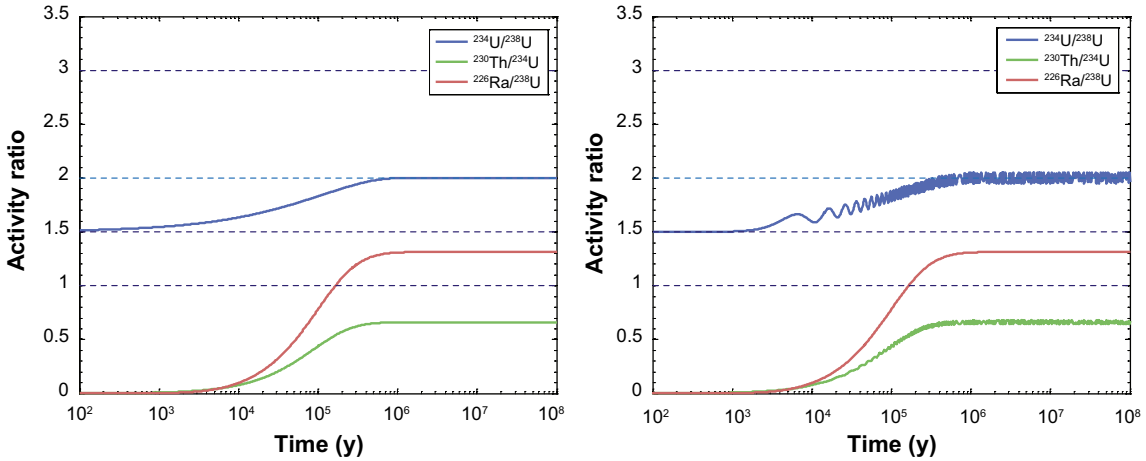

Figure B-16. *Evolution of U-series disequilibrium as a function of time for a solid state diffusivity of 7×10^{-28} m^2/s and for a groundwater $^{234}U/^{238}U$ activity ratio varying in the range 2–4. The left-hand figure shows the result for a constant concentration boundary condition representing the average, while the right-hand figure shows the impact of a periodic variation in the activity ratio in the range 2–4 (although for constant groundwater ^{238}U activity). Calculations assume a calcite crystal with an accessible diffusion depth of 0.17 µm as in previous calculations and an initial $^{234}U/^{238}U$ activity ratio of 1.5.*

When interpreting U-series disequilibrium it is customary to plot the activity ratio of $^{234}U/^{238}U$ against that of $^{230}Th/^{234}U$ in a Thiel diagram (Thiel et al. 1983) as an aid to interpretation. The isotopic disequilibrium represented by the time series in Figure B-13 is plotted in Figure B-17 as a Thiel diagram. As can be seen from the trajectory of the curves for different diffusivities, it is clear that it is generally not possible to reach the measured compositional ranges for fracture mineral $^{234}U/^{238}U$ activity ratios with diffusivities much larger than about 10^{-27} m^2/s to 10^{-28} m^2/s for the assumed crystal size if the disequilibrium is modelled as a continuous deposition process involving calcite solid solution with a constant apparent diffusivity. It is noted that the crystal size as reflected by the diffusion depth parameter, δ_x is a key assumption in the model with regard to this assertion. If the average crystal size is larger than the estimate of 0.17 µm, then the possible upper limit of solid-state diffusivity may be higher. On the other hand, if the average crystal size is smaller, then the upper limit of solid-state diffusivity may be lower. This interpretation is also dependent on the modern $^{234}U/^{238}U$ groundwater activity ratios not being significantly elevated over their paleo-averages.

Since it is not possible to give a definitive estimate of apparent solid state diffusivities for calcite (or, for that matter, barite) a range of likely values must be considered in scoping calculations. Furthermore, even if the process is not strictly a solid state diffusion mechanism in the classical sense, the characteristic equilibration time associated with solute uptake should still be able to be approximately modelled in terms of an apparent solid state diffusivity. If a range of 10^{-22} m^2/s to 10^{-28} m^2/s is considered, the solution given by Crank (1975, 2 ed, Eq 4.18, pp 48) for diffusive uptake to a slab can be used to predict likely equilibration times for a solid solution featuring a maximum diffusion depth on the order of that predicted for the calcite minerals lining the fractures at Forsmark. The results of these calculations are shown in Figure B-18. Although it is not possible to rule out solid-state diffusivities less than 10^{-28} m^2/s, these are sufficiently low that retention by solid solution is not likely to be significant and is therefore not modelled.

Alternative modes of solute uptake

Although in the previous section solid state diffusion has been characterised as a single rate process, there are other possibilities that bear consideration. In an attempt to reconcile the disparity between fast solute uptake from solution under ambient conditions and the very low estimated solid state diffusivities in calcite as extrapolated from measurement data obtained at high temperature, Watson (1996, 2004) has proposed a *surface entrapment model* (SEMO). Essentially this model assumes diffusivity at the mineral surface that is significantly enhanced relative to that deep within the mineral crystal. Normally this would require the mineral interface to have physical properties that differ in some way

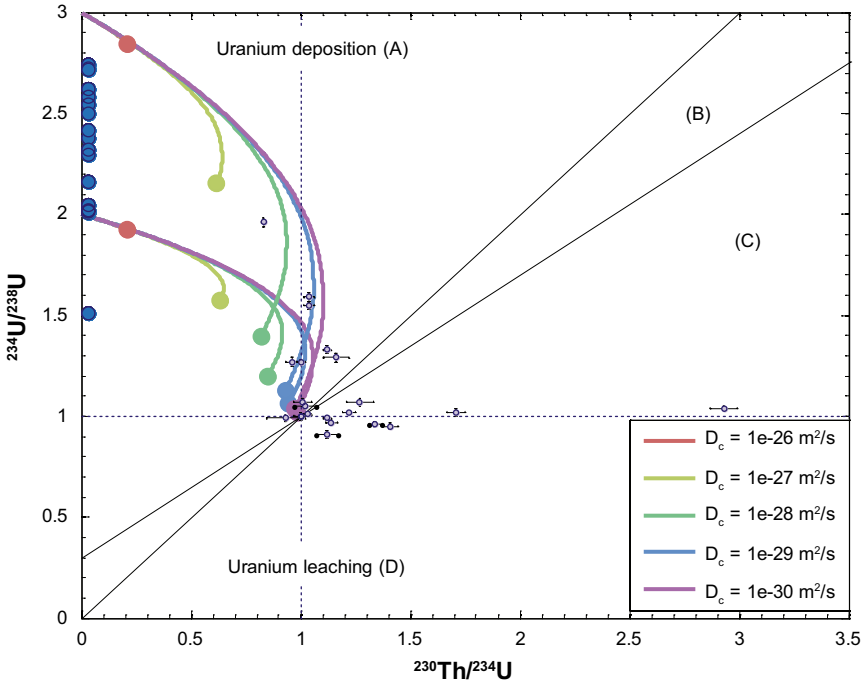

Figure B-17. *Cross plot of $^{234}U/^{238}U$ vs. $^{230}Th/^{234}U$ activity ratio in the manner described by Thiel et al. (1983). Secular equilibrium corresponds to the intersection of the vertical and horizontal broken lines at an activity ratio of unity. The upper (A) and lower (D) sectors correspond to U deposition and leaching, respectively. Sector (B) is the forbidden sector for any single continuous process, while sector (C) is the forbidden sector for any single process. Small markers with error bars indicate measured values for Forsmark fracture minerals (data taken from Sandström et al. (2008)) while blue markers along the vertical axis indicate approximate range of $^{234}U/^{238}U$ activity ratios in contemporary groundwater at Forsmark (Laaksoharju et al. 2008). Endpoint markers of simulated curves indicate the steady state condition for the particular solid state diffusivity modelled.*

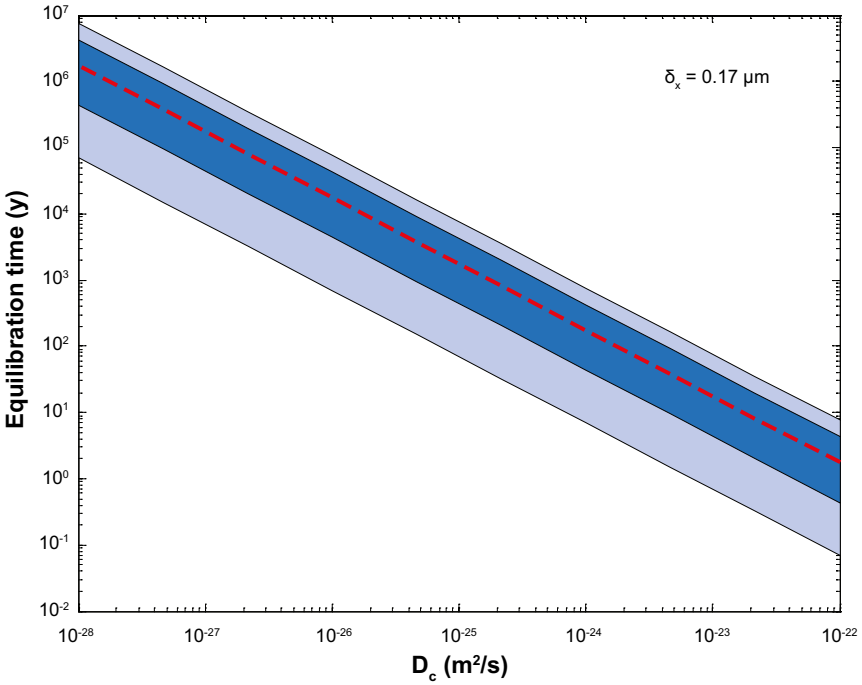

Figure B-18. *Typical equilibration times for diffusive uptake to a solid-solution as a function of solid state diffusivity for a limited penetration depth of 1.7×10^{-7} m estimated for calcite fracture mineralisations at Forsmark. The broken red line shows the time required for 50 % equilibration of the assumed slab geometry while the limits of the dark band represent the time for 25 %–75 % equilibration. The limits of the outer lightly shaded band show the range of times required for 10 %–90 % diffusive equilibration.*

from those within the bulk of the crystal structure. By analogy with alteration layers formed during leaching of glass phases (e.g. Oelkers 2001) one could conceive of an amorphous, hydrated layer existing at the mineral surface and extending some depth into the crystal. As pointed out by Watson (2004), however, very careful spectroscopic measurements made by Fenter et al. (2000) indicate that the termination of the crystal lattice is very abrupt at the mineral surface and an alteration layer, if it exists, does not appear to extend more than a few nm into the crystal. The observations of Stipp et al. (1992, 1998), on the other hand, suggest enhanced regions of diffusivity at the calcite surface of at least some tens of nm. The mechanistic reason for this is not yet fully understood, although semi-empirical models such as Watson (1996, 2004) provide a means by which such processes can be approximately modelled. One of the model formulations explored by Watson (1996, 2004) assumes a variable diffusivity, $D_c(x)$ that decays exponentially as a function of depth, x into the calcite crystal using an equation of the form:

$$D_c(x) = D_L + (D_0 - D_L)\exp(-\alpha x) \qquad \text{B-38}$$

In this relation, D_0 is the diffusivity at the mineral surface, D_L is the solid state diffusivity within the bulk crystal, and α is an empirical parameter associated with the depth dependency. To simplify the treatment of this parameter in the current discussion, we relate it to the apparent distance, d_c over which the log-transformed diffusivity falls to half its initial value at the crystal surface by the relation:

$$\alpha \approx \frac{\ln(2)}{d_c} \qquad \text{B-39}$$

Figure B-19 shows calculated diffusivity profiles calculated using Equation B-38 assuming d_c values ranging between 0.1 nm and 10 nm together with estimated mean diffusivities averaged over the maximum penetration depth of the calcite crystal. The limiting solid-state diffusivity, D_L is assumed to be 10^{-30} m^2/s since this gives negligible mass transfer on the time scale of transport (c.f. Figure B-18). Lower values are possible, although it makes essentially no difference to the results. The diffusivity at the mineral surface, on the other hand, is simply an assumed value based on the estimate of Lahav and Bolt (1964). As also noted by Watson (2004), the true value of the diffusivity at the mineral surface is not particularly consequential since the width of the surface entrapment zone can be scaled to give any required average diffusivity.

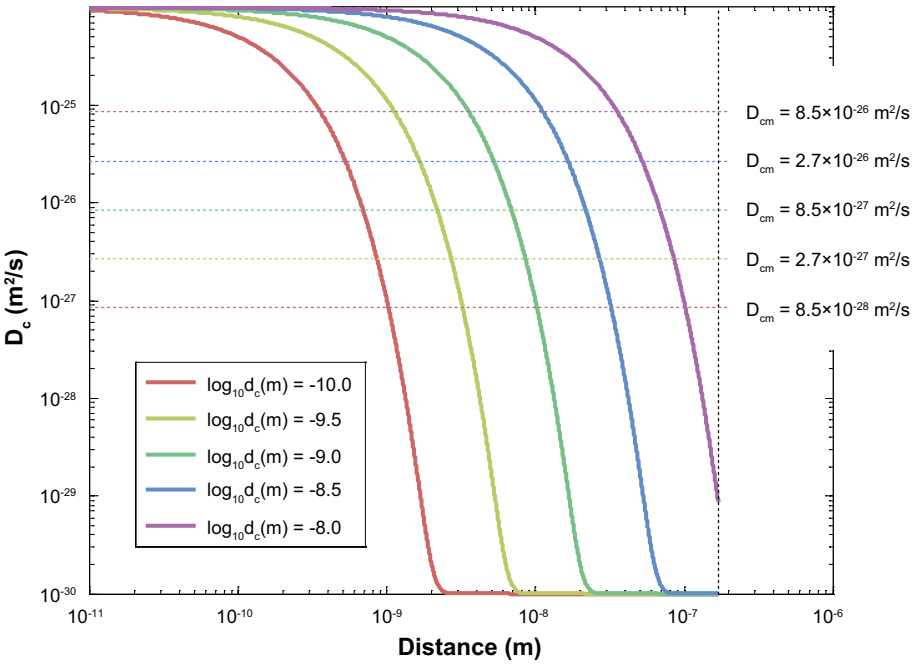

Figure B-19. *Diffusivity profiles calculated using Equation B-38 assuming an exponentially decaying trend of solid state diffusivity bounded between 10^{-24} m^2/s and 10^{-30} m^2/s. Mean diffusivities averaged over the hypothetical maximum penetration depth of the calcite crystal (0.17 µm as indicated by the vertical broken line) are shown as horizontal broken lines and are matched by colour with the corresponding diffusivity profiles (numerical values are shown to the right hand side).*

The numerical model used in the previous section in the context of U-series disequilibrium (i.e. Equation B-37) can be adapted to model the depth dependent solid state diffusivity illustrated in Figure B-19. Figure B-20 shows the average isotopic disequilibrium for $^{234}U/^{238}U$ and $^{230}Th/^{234}U$ simulated under the assumption of a depth dependent solid state diffusivity. As can be seen from the figure, the results are very similar to those obtained using the simplified model of a single apparent solid state diffusivity. Although only very approximate comparisons can be made on the basis of average solid state diffusivities (as indicated in Figure B-19), this is only strictly relevant in the region of the crystal where diffusive equilibration can be assumed on the timescale of transport. The consequences of this for transport retardation of radionuclides released from a hypothetical repository are discussed briefly in the next section.

The practical applications of SEMO have mostly focused upon isotopic and elemental partitioning during growth of calcite crystals on account of its importance for understanding the interaction between kinetics and equilibrium with regard to isotopic enrichment coefficients for modelling of paleoclimate proxies involving corals and speleothems (e.g. Tang et al. 2008a, b). The use of SEMO to describe solid solution retardation processes under approximately static groundwater hydrochemical conditions (i.e. no net dissolution or precipitation) has not been previously addressed in the context of safety assessment and is only discussed here as an annex to the previous scoping calculations. What these calculations do show, however, is that there are different conceptualisations of kinetic solute uptake that can be shown to be approximately consistent with measurement data if modelled using appropriately scaled model parameters.

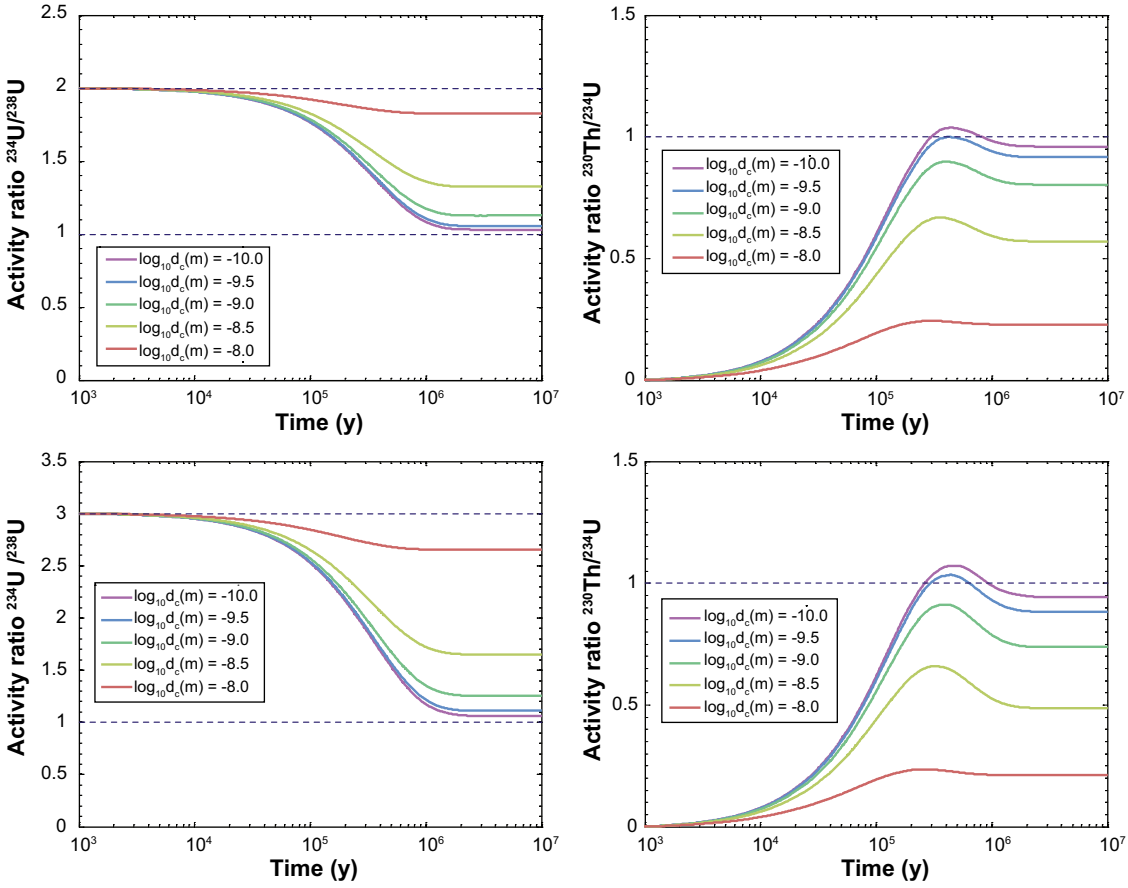

Figure B-20. *Evolution of $^{234}U/^{238}U$ (left) and $^{230}Th/^{234}U$ (right) disequilibrium as a function of time for different surface entrapment zone widths in the range of 0.1 nm to 10 nm and for a constant groundwater $^{234}U/^{238}U$ activity ratio of 2 (top) and 3 (bottom) indicated by the upper broken line in each of the plots on the left-hand side. Calculations assume a calcite crystal with an accessible diffusion depth of 0.17 µm. A steady-state is typically achieved after roughly 2 Ma although not necessarily corresponding to secular equilibrium (activity ratio = 1 indicated by the lower broken line). Secular equilibrium is only achieved for very low surface entrapment zone widths (d_c~0.1 nm).*

Simulation of solid-state diffusion-limited uptake in calcite

The retardation factors estimated for retention by solid solution by calcite are, in most cases, too low to adequately demonstrate the impact of uncertain solid-state diffusivity in an unambiguous manner. For Am(III), however, the equilibrium retention is sufficiently large that this is relatively easy to demonstrate over a large range of apparent solid state diffusivities and F. Here, the Laplace space model given by Equation B-31 is used to simulate the dynamics of radionuclide retention for a range of different solid state diffusivities between 10^{-24} m^2/s and 10^{-28} m^2/s. Although chlorite and other clay minerals are expected to contribute towards the fracture mineral retardation effect, these are neglected in the present simulations since the retention capacity is of comparable magnitude to that potentially attributable to solid solution formation with calcite (and would therefore mask the effects of calcite diffusion kinetics).

Although ^{241}Am has a relatively short half life of 432 y, decay is also neglected in these simulations since the primary objective is to illustrate the impact of diffusive equilibration time. It should be clear to the reader, however, that the transport times calculated for Am(III) are in many cases equivalent to some tens of half-lives of the nuclide and therefore one would not expect significant Am(III) far-field activity dose rates. Am(III) is, however, a good geochemical analogue for other trivalent actinides and lanthanides which do have somewhat longer half-lives.

Figure B-21 shows the impact of assumed solid-state diffusivity on the retardation of Am(III) for a low range F value of 10^4 yr/m. The calculations indicate a relatively important role for diffusion kinetics towards the lower end of the assumed range (e.g. $D_c \leq 10^{-26}$ m^2/s) and the additional retention is all but negligible on the timescale of the nuclide transport. For larger F values, on the order of 10^5 yr/m, diffusion kinetics are still important for early breakthrough of the nuclide although the overall impact on the residence time distribution is much reduced (Figure B-22). For the largest F values, on the order of 10^6 yr/m or higher, the impact of diffusion kinetics is reduced even more, although this is due at least in part to the increasing prominence of matrix retention for higher F values which tends to mask the impact of fracture mineral retention (Figure B-23).

In this analysis it is important to note that the solid state diffusion kinetics have the largest impact on the nuclide residence time distribution for flowpaths featuring low F values, which are also the flowpaths where the greatest enhancement of retardation is predicted to occur if only the equilibrium retardation effect is considered (see Figure B-5).

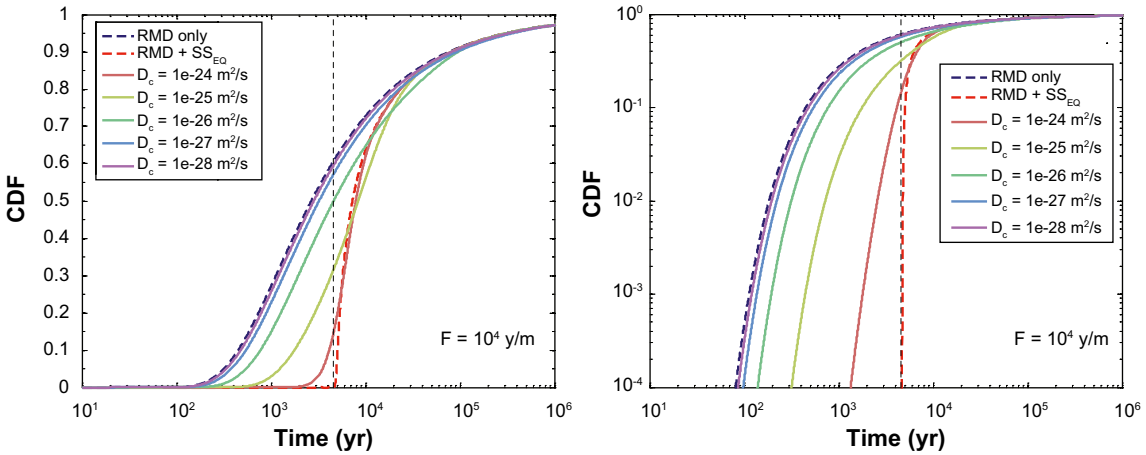

Figure B-21. *Simulated residence time distribution curves for trivalent actinide transport assuming an F value of 10^4 yr/m and calcite solid solution for solid state diffusivities ranging from 10^{-28} m^2/s to 10^{-24} m^2/s. In the left-hand figure, data are plotted on a log-linear axis and on a log-log axis in the right-hand figure. The broken blue curve is the limiting case where only matrix diffusion and equilibrium sorption in the rock matrix is considered. The vertical broken line indicates the equilibrium retardation time for the solid solution, and the accompanying broken red curve shows the theoretical residence time distribution for matrix diffusion coupled with equilibrium retention by the solid solution.*

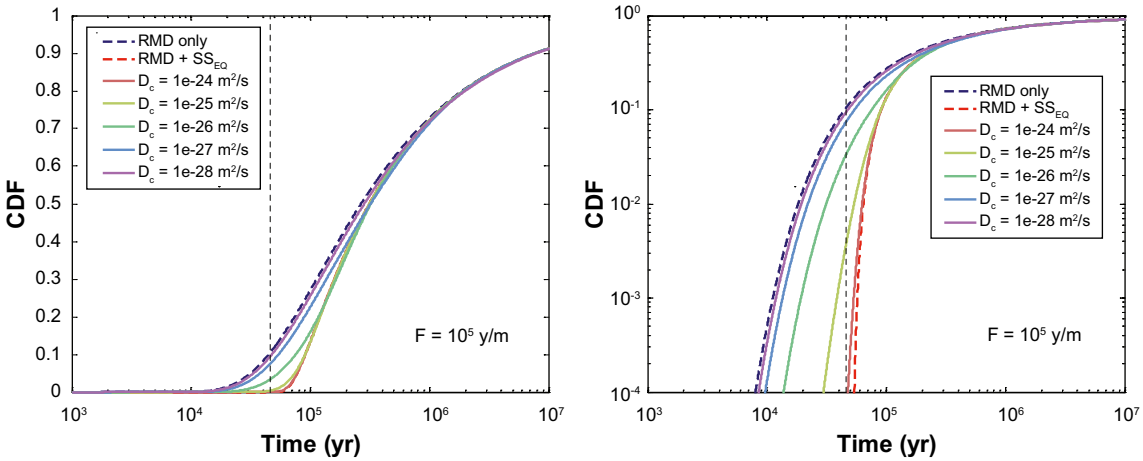

Figure B-22. *Simulated residence time distribution curves for trivalent actinide transport assuming an F value of 10^5 yr/m and calcite solid solution for solid state diffusivities ranging from 10^{-28} m^2/s to 10^{-24} m^2/s. In the left-hand figure, data are plotted on a log-linear axis and on a log-log axis in the right-hand figure. The broken blue curve is the limiting case where only matrix diffusion and equilibrium sorption in the rock matrix is considered. The vertical broken line indicates the equilibrium retardation time for the solid solution, and the accompanying broken red curve shows the theoretical residence time distribution for matrix diffusion coupled with equilibrium retention by the solid solution.*

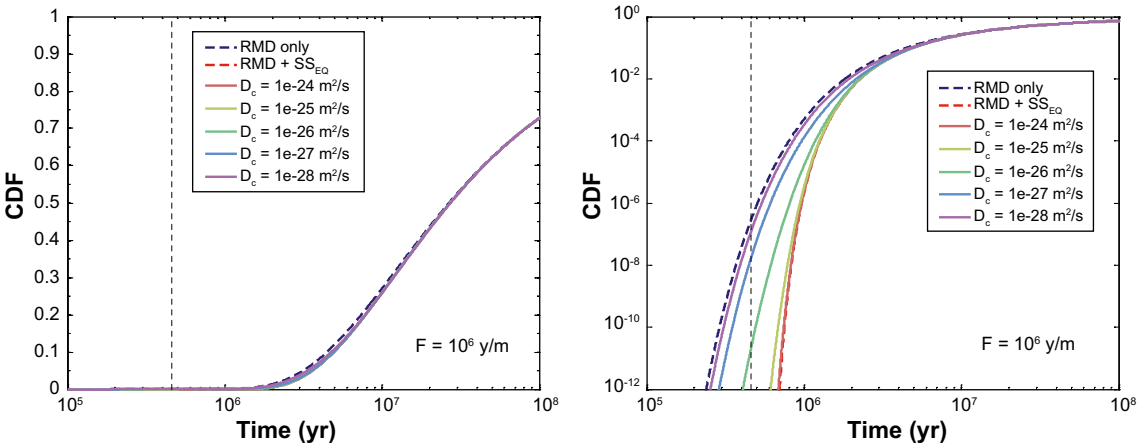

Figure B-23. *Simulated residence time distribution curves for trivalent actinide transport assuming an F value of 10^6 yr/m and calcite solid solution for solid state diffusivities ranging from 10^{-28} m^2/s to 10^{-24} m^2/s. In the left-hand figure, data are plotted on a log-linear axis and on a log-log axis in the right-hand figure. The broken blue curve is the limiting case where only matrix diffusion and equilibrium sorption in the rock matrix is considered. The vertical broken line indicates the equilibrium retardation time for the solid solution, and the accompanying broken red curve shows the theoretical residence time distribution for matrix diffusion coupled with equilibrium retention by the solid solution.*

In general, for smaller F values one would expect smaller matrix retardation effects and larger relative enhancement of retardation by sorption on fracture minerals. Since the total transport time is also less in these situations, the effective contact time available for diffusion into the calcite mineral grains is also much less which results in a substantially reduced retardation effect for solid state diffusivities below a certain threshold (and for a given calcite grain size). The range of solid state diffusivity where disequilibrium cannot be neglected corresponds to the most likely range as assessed by semi-quantitative consideration of the natural analogue data from the Forsmark site as discussed in the previous section. As mentioned previously, if the assumption of the maximum diffusion depth of 0.17 µm for the calcite mineral grains is inaccurate then the diffusivities could potentially be higher than the simulated range of 10^{-24} m^2/s to 10^{-28} m^2/s. If this is indeed the case, however, the simulations shown in Figure B-21 to Figure B-23 would also need to reflect this increased diffusion depth and would therefore still be strongly influenced by diffusive disequilibrium effects.

It should be noted that the modelling results shown in Figure B-21 to Figure B-23 are only meant to be illustrative of the possible impact of diffusive disequilibrium for the very simplest case of a single rate, diffusive uptake mechanism. The simulated diffusivity ranges are scaled with regard to what appears to be feasible upper limits based on consideration of natural analogue data although it is also recognised that these generally have very poor constraining power. One particular danger of modelling transport retardation using a single rate model is that it does not predict an upper limit to the effective penetration depth if there happens to be a systematic transition to very low solid state diffusivities in the interior of mineral grains that might form solid solutions. It is also clear that bulk solid state diffusivities on the order of 10^{-30} m^2/s (or less) imply essentially negligible solute mass transfer on safety assessment timescales. This suggests that it may only be possible to diffusively equilibrate the outermost layers of calcite mineral grains lining the advective pore space. Effective penetration depths would then range from perhaps as little as a few nm to some tens of nm as proposed by Watson (2004).

A continuously variable solid state diffusivity of the kind hypothesised in Equation B-38, however, is difficult to implement in transport calculations since a simple closed form analytical solution does not exist. Nevertheless, it is possible to approximate the problem by assuming multiple discrete surface layers of fixed diffusivity that differ from that of the bulk mineral grain. A modified flux term, ψ_x for use together with the Laplace space solution (Equation B-33) can then be defined by analogy with the recursive formula given in Crawford (2006) for an arbitrary number of rock matrix layers. The simplest case of course would be to use a single surface layer of limited depth, although greater realism would undoubtedly be achieved by abstracting the problem to several layers.

Although actual simulations have not been made for the multilayered approximation outlined above, it is still possible to speculate on the impact that a continuously variable solid-state diffusivity might have on the dynamics of solute retardation along a transport path by consideration of the corresponding results for multilayered matrix diffusion as discussed in Crawford (2006). The main difference is that the assumption of a constant diffusivity tends to underestimate the extent of radionuclide retardation for low F values (and early breakthrough times) while overestimating the retardation effect for higher F values (and later breakthrough times). Since the additional retardation effect provided by solid solution retention appears to be most important at low F values this might not be a large deficiency if one could make a reliable estimate of the effective thickness of the surface entrapment zone width so as to avoid overestimating the retardation effect.

Although there are many uncertainties in this analysis and more accurate estimates of solute uptake at mineral surfaces forming solid solutions are certainly necessary, the present results do suggest that equilibrium solid solution retention is a non-cautious assumption for safety assessment calculations given that the uptake kinetics themselves and the actual mechanism of the kinetic uptake is not well established at present. This means that the retention capacity of solid solutions involving fracture calcites and barite is likely to be significantly less than the estimates of equilibrium retention discussed in Section B.6 would suggest. Consequently the transport retardation effect provided by minerals lining the advective porosity of flow-bearing fractures is likely to be dominated by chlorite and the other clay minerals.

Appendix C

Comparison between MARFA and FARF31

This appendix has not been changed since the SR-Site assessment.

In this appendix, a comparison between MARFA version 3.2.2 and FARF31 is used to verify that the two codes produce the same results when presented with the same input. Recall from Section 3.5 that the MARFA has capabilities not included in FARF31. A modelling case that can be represented in both codes is used for the comparison. Note that this comparison tests not only the numerical solution method but also that the input parameters are defined consistently between the two codes.

The growing pinhole case of Section 6.3.1 and two combinations of release path and deposition hole were selected for the comparison. Specifically, hole 5574 with the Q1 release path and hole 2433 with the Q3 path were used. The Q1 pathway for the 5574 hole has the smallest F of all the Q1 pathways in the temperate period. The Q3 pathway for the 2433 hole has an F value near the median value.

Figure C-1 shows the comparison for 2 radionuclides for each pathway examined. MARFA results are shown in green, FARF31 results in blue. The two codes are in good agreement. Two minor deviations are apparent. With pathway 5574, the I129 release is very spiky and MARFA overly smooths the peak. This oversmoothing is consequence of the MARFA algorithm for reconstructing the breakthrough curve from particle histories and can be eliminated, albeit with increased statistical noise in the result, by increasing the MARFA smoothing parameter. With the same pathway, Ra226 has a small peak at 10 000 years that is represented in the MARFA results but not in the FARF31 results. The peak is in the near-field release and is thus real and not an artefact. It is not in the FARF31 results simply because of limited temporal resolution in those results.

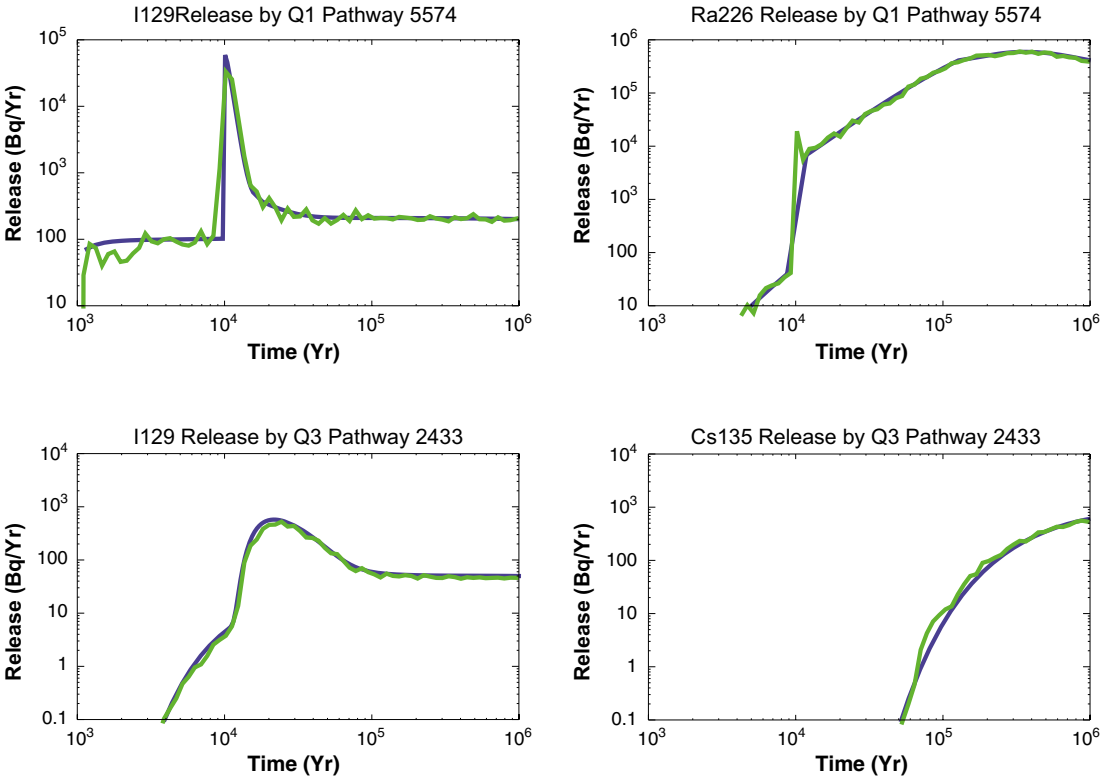

Figure C-1. *Comparison between MARFA and FARF31 for two release points in the growing pinhole case.*

Appendix D

Selection of radionuclides

This appendix has not been changed since the SR-Site assessment.

Spent nuclear fuel contains a large number of different radionuclides. The radionuclide transport calculations are computationally demanding and the compilation of data for the calculations is also time consuming. Fortunately, some radionuclides will not contribute to overall risk and can be eliminated from the dose calculations. The selection of radionuclides based on radiotoxicity, inventory and half-life is summarised in this Appendix. This selection is based on data from the SR-Can data report (SKB 2006b).

One aim of the selection of radionuclides is to identify the radionuclides for which data needs to be compiled. The nuclides are divided into three groups: important, less important and nuclides that only need data on inventory and half-life, see Table D-6. The group of less important nuclides is composed of those nuclides that might be important only in "what if" cases involving an initial defect in the canister.

For most transport calculation cases, probabilistic calculations with thousands of realisations will be performed. It is thus important to minimise the number of nuclides in the probabilistic calculations.

To support the selection a hypothetical case has been set up, see Section D.1. The selection is further described below for fission and activation products in Section D.2 and for decay chain nuclides in Section D.3.

Another aspect that needs to be considered is the influence of the radionuclide on the shared solubility. The solubility may be dominated by different isotopes during different time-periods due to the different half-lives of the isotopes. Section D.4 deals with the shared solubility considerations.

D.1 Hypothetical case to support the selection

A hypothetical case has been set up and radionuclide transport calculations have been performed with COMP23 to support the selection. The setup was the same as for the corrosion case where the buffer and the canister are bypassed. The canister had an initial large defect and the rock retention was neglected. Fuel dissolution rate (10^{-7}/yr) and IRF were taken into account. This hypothetical case results in faster release than in any realistic case in order to show potential dose from short-lived radionuclides that might be of interest in "what if" cases. The inventory is BWR38 from Håkansson (2000).

D.2 Fission and activation products

Starting from all fission and activation products in the inventory appearing in Håkansson (2000), the total radiotoxicity of a nuclide (product of inventory 40 years after operation [Bq] and dose coefficient [Sv/Bq] for oral intake (EU 1996) was plotted against half-life to yield the plot in Figure D-1.

It should be rather straightforward to *i*) exclude any nuclide with a half-life less than 10 years, *ii*) any nuclide with a total hazard index less than 0.01 since e.g. the readily transported I-129 has a hazard index of around 10^2. Already this very simple sorting reduces the list considerably with only 23 nuclides remaining: H-3, C-14, Cl-36, Ni-59, Ni-63, Se-79, Sr-90, Mo-93, Nb-93m, Zr-93, Nb-94, Tc-99, Pd-107, Ag-108m, Cd-113m, Sn-121m, Sn-126, I-129, Cs-135, Cs-137, Sm-151, Eu-152 and Ho-166m.

A further selection might be possible to perform based on the fact that the contribution to the dose for any normal case is lowest in the lower left corner of Figure D-1 and hence a third line is shown in the figure. This line indicates that a further exclusion might be possible, retaining only 13 nuclides: C-14, Cl-36, Ni-59, Se-79, Sr-90, Zr-93, Nb-94, Tc-99, Pd-107, Sn-126, I-129, Cs-135 and Cs-137. The 10 nuclides excluded here might be of importance in "what if" cases with an initial defect in the canister.

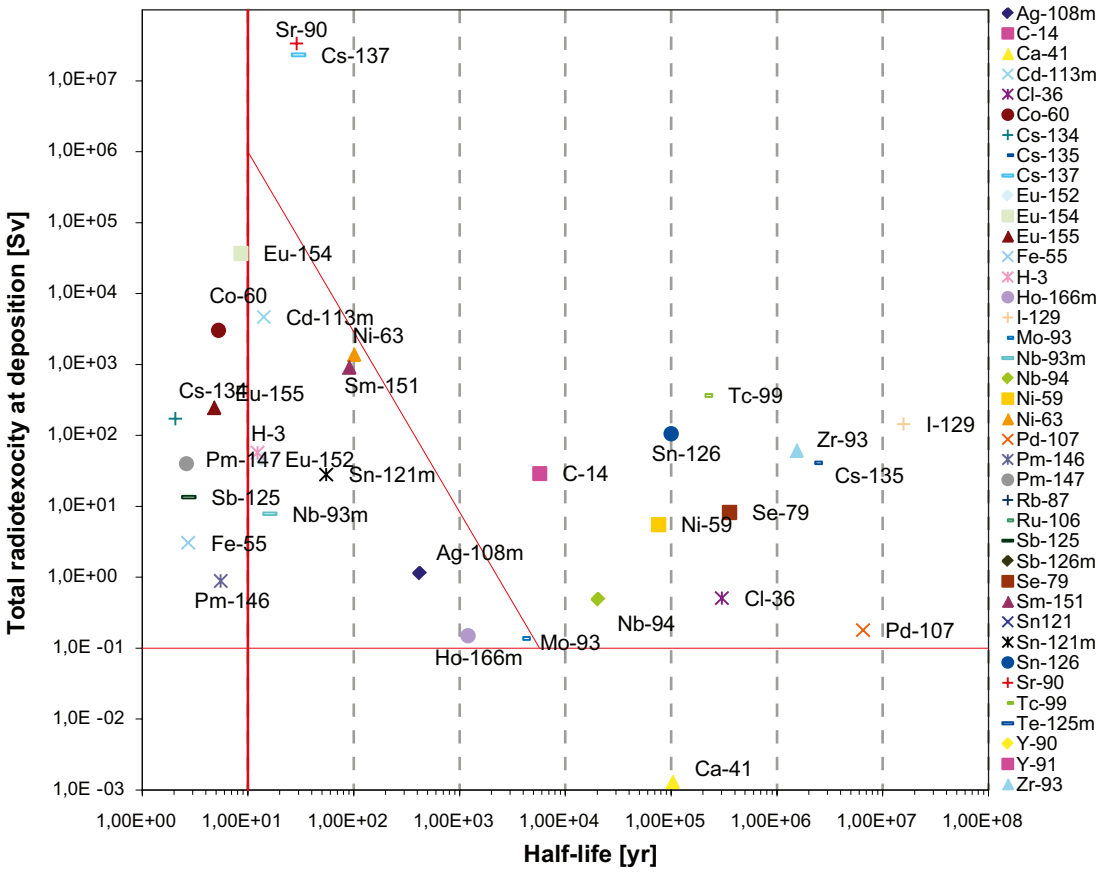

Figure D-1. *Radiotoxicity as a function of half-life for all fission and activation products in the spent fuel. All nuclides considered are shown in the list to the right, whereas only some of them has a sufficiently long half-life and a sufficiently high radiotoxicity to appear in the plot.*

The selection of nuclides is partly performed to determine the need of data for the radionuclide release calculations. The need for data was sorted into two groups: important and less important. The 13 remaining nuclides were sorted as important, whereas the 10 nuclides that it might be possible to exclude were sorted as less important. Hence, data are available in the **Data report** for all 23 nuclides remaining after the first sorting.

Figure D-2 shows calculated annual doses, in the hypothetical case, from the 23 nuclides (COMP23 calculations). The figure confirms the grouping of the nuclides into 13 important and 10 less important nuclides except for Ni-59 and Nb-94. These two nuclides were selected as important from Figure D-1 but in Figure D-2 they do not seem to be of importance in the longer term. This can be explained by their high instant release fraction (100 %) assumed in this hypothetical case. Therefore, these two nuclides will still be of importance for the transport calculations.

D.3 Decay chain nuclides

All actinides and some other nuclides are included in one of four decay chains. There is no link between the chains. The handling of the chains in radionuclide transport calculations may be simplified according to the following.

- In general, daughters with short half-lives can be assumed to be in equilibrium with their parent nuclide, and hence the nuclide is excluded from the radionuclide transport calculations. However, they are included in the LDF for their parent nuclide.
- Some nuclides with short half-lives in the beginning of a chain can also be treated in a simplified manner by adding the initial amount (moles) of the nuclide in question to a daughter nuclide. Thereby the influence is included in the total dose, without including the nuclide in the radionuclide transport calculations.

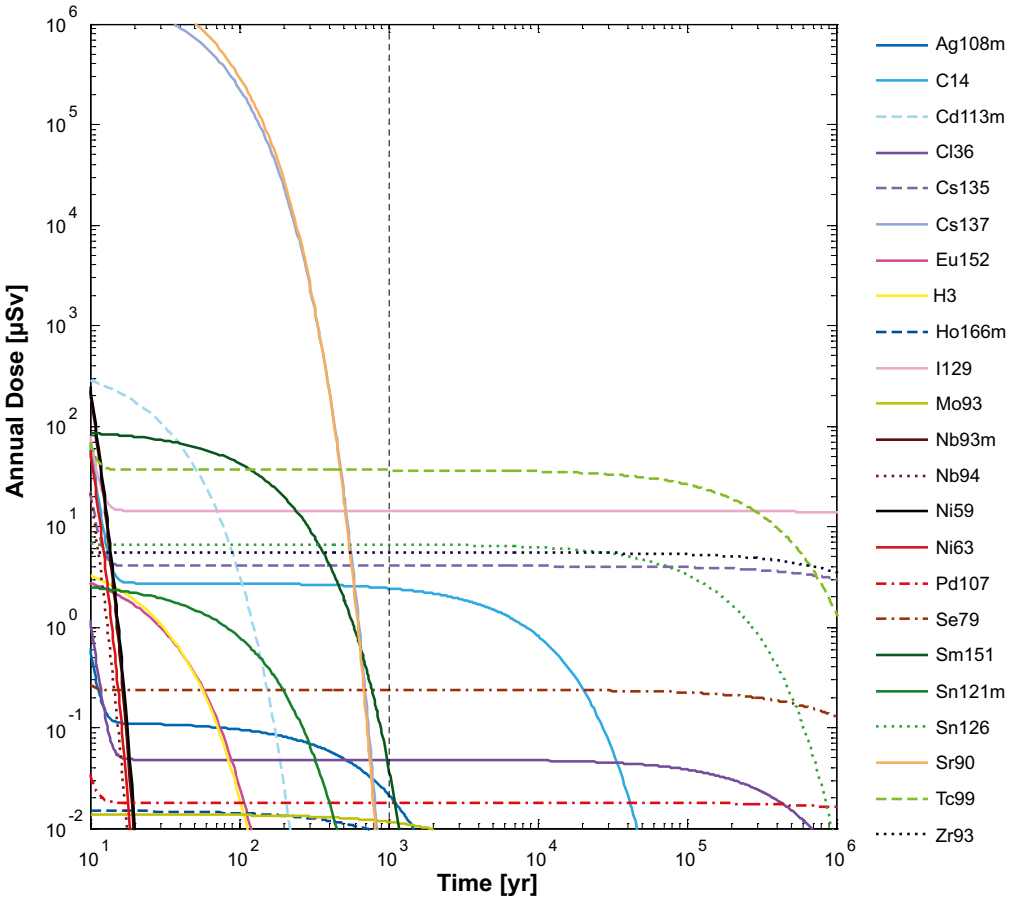

Figure D-2. *Calculated annual dose in the hypothetical case to support the selection of radionuclides for the radionuclide transport calculations of fission and activation products. The vertical black dashed line denotes 1 000 years after closure.*

For each decay chain a first selection of nuclides was made before the calculations with the hypothetical case set up in Section D.1. Parent nuclides not present in the inventory were excluded and nuclides with a half-life shorter than 1 year were treated as described in the previous paragraph.

Below, the four chains are presented with background information and the simplified chains used for the hypothetical calculation case. Based on the results from the hypothetical case it is stated whether or not a nuclide is included in the radionuclide transport calculations. If the nuclide is excluded the reason for this is given.

Decay chains are especially time consuming in the COMP23 and FARF31 transport calculations. Therefore it is desirable to exclude nuclides with negligible contribution. For some nuclides it is difficult to decide prior to the calculations whether they could be excluded or not. To be on the safe side such nuclides are included in all deterministic calculations. If the contribution to the dose from these nuclides is negligible, they have been excluded from the more time consuming probabilistic calculations.

The 4n chain

The 4n chain is shown in Figure D-3 in addition to the simplified chain used in the hypothetical calculation case. Figure D-4 shows the annual dose for the hypothetical calculation case. The dose is totally dominated by Pu-240 during the first 100 000 years and thereafter U-236 dominates the dose, but at a low level. All other nuclides in the 4n chain have small or negligible contributions to the total dose from this chain.

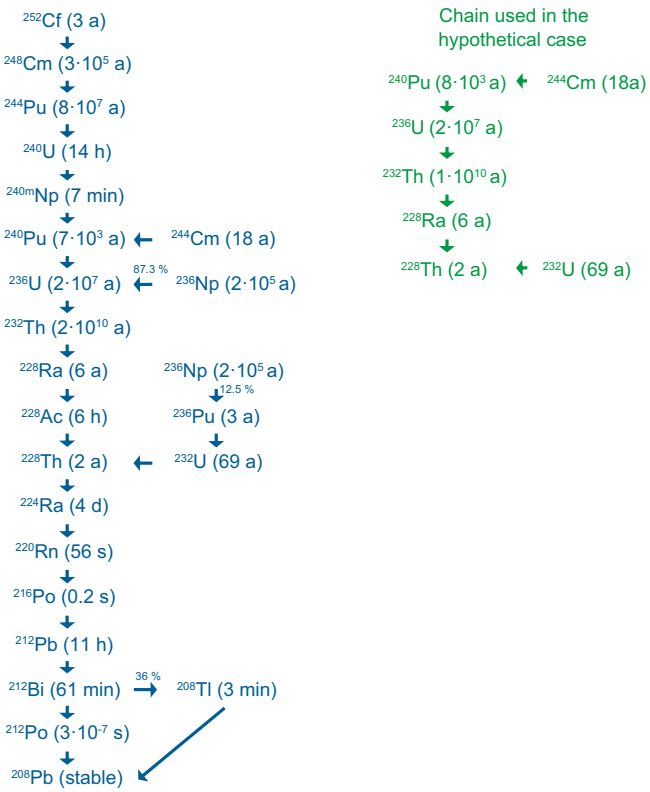

Figure D-3. *The 4n chain. The half-lives are given within brackets. The simplified chain is used in the hypothetical calculation case to support the selection of radionuclides for the radionuclide transport calculations. Nuclides at the beginning of the chain without any inventory have been excluded in the simplified chain as have nuclides with a half-life shorter than 1 year. Approximate half-lives shown are derived from Table D-1.*

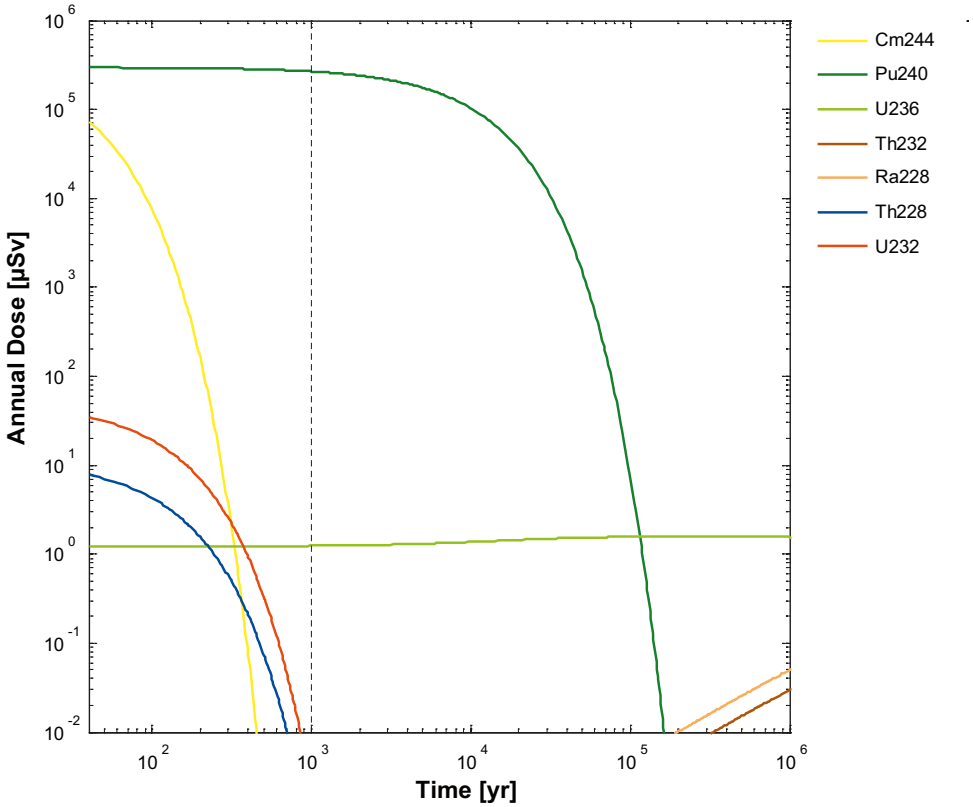

Figure D-4. *Calculated annual dose in the hypothetical case supporting the selection of radionuclides for radionuclide transport calculations of the 4n chain. The vertical black dashed line denotes 1 000 years after closure.*

Table D-1. The 4n chain – Background data and arguments for including or excluding the member radionuclides in the transport calculations.

Nuclide	Half-life [a]	Inventory BWR38[b] (Bq/tU)	Inventory BWR38[b] (mol/tU)	Dose conversion factor[c] (Sv/Bq)	Treatment in radionuclide transport calculations Arguments for including or excluding
Cf-252	2.65 a	–	–	No	Excluded, no inventory
Cm-248	3.40e5 a	–	–	7.7e–7	Excluded, no inventory
Pu-244	8.08e7 a	–	–	2.4e–7	Excluded, no inventory
U-240	14.1 h	–	–	1.1e–9	Excluded, no inventory
Np-240m	7.22 min	–	–	No	Excluded, no inventory
Cm-244	18.1 a	2.84e13	3.88e–2	1.2e–7	Excluded. Short half-life, the results shown in Figure D-4 grant the possibility to simplify the treatment of Cm-244. Include initial inventory (mol) in Pu-240 (however negligible contribution, see Figure D-6) Solubility – Excluding Cm-244 imply somewhat higher initial release from Cm-245.
Pu-240	6.56e3 a	1.18e13	5.85	2.5e–7	**Included** High inventory, high dose conversion factor
U-236	2.34e7 a	1.04e10	18.4	4.7e–8	**Included** Low dose, but if the initial inventory is added to Th-232 the dose from Th-232(+U-236) will be too pessimistic.
Th-232	1.41e10 a	–	–	2.3e–7	**Included** The amount of Th-232 after 40 000 years is more than 50 % of the total thorium and hence Th-232 is included to give a more accurate description of the thorium solubility.
Np-236	1.54e5 a	–	–	1.7e–8	Excluded, no inventory
Pu-236	2.86 a	2.52e6*	5.44e–10*	8.7e–8	Excluded, no inventory.
U-232	68.9 a	1.58e9**	8.21e–6**	3.3e–7	Excluded. Short half-life and the results shown in Figure D-4 grant the possibility to simplify the treatment of U-232.
Ra-228 Ac-228 Th-228 Ra-224 Rn-220 Po-216 Pb-212 Po-212 Tl-208	<5.8 a	–	–		Excluded. No initial inventory, much shorter half-life than Th-232, therefore in equilibrium with Th-232, see Figure D-5

a) Chu et al. (1999).
b) Inventory 40 years after discharge (Håkansson 2000).
c) Oral intake adults (EU 1996).
* Inventory not given for 40 years after discharge in Håkansson (2000), calculated from 10 years.
** Inventory not given for 40 years after discharge in Håkansson (2000), calculated from 45 years.

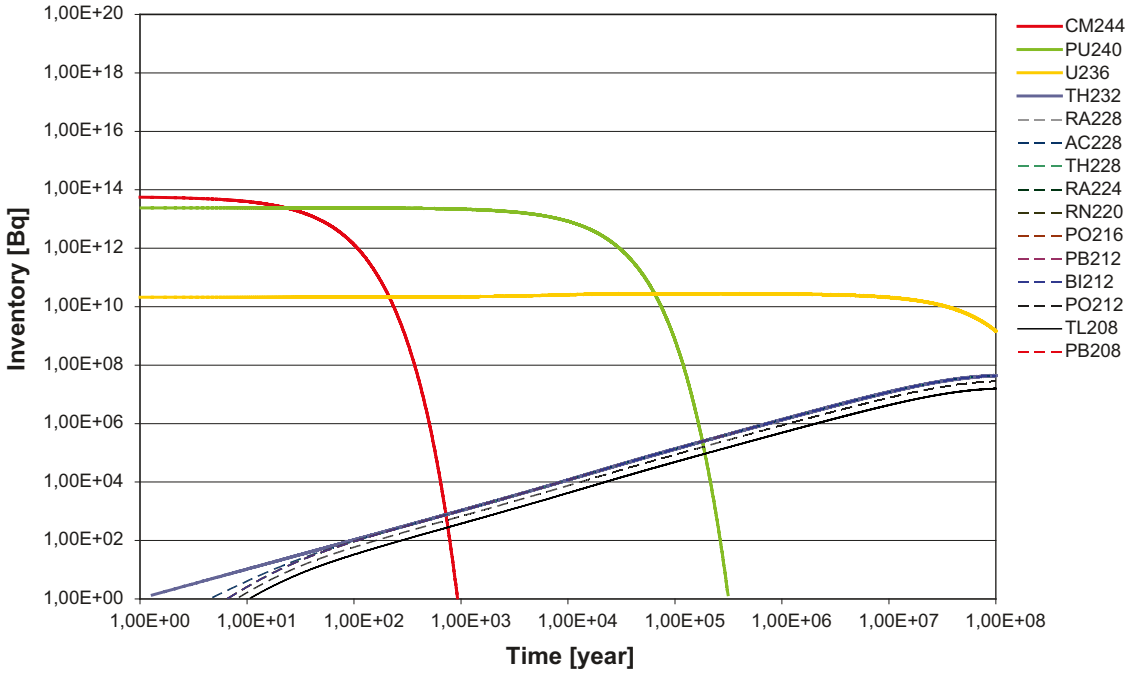

Figure D-5. *Activity (Bq/tU) as a function of time for radionuclides in the 4n chain. Initial inventory from Håkansson (2000).*

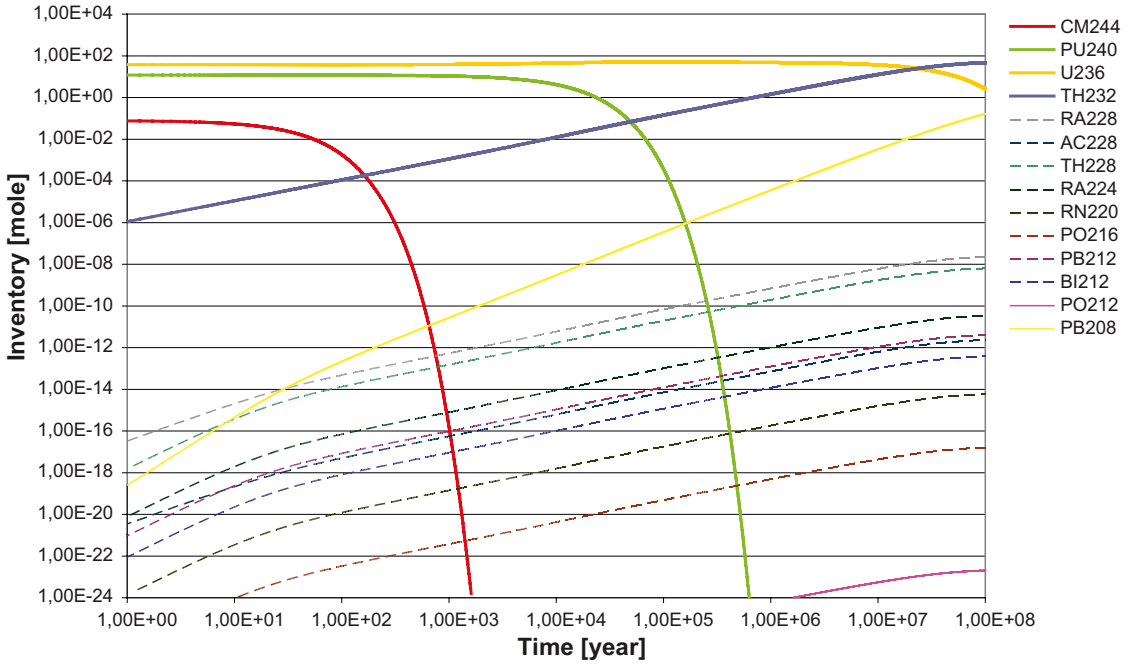

Figure D-6. *Radionuclide content (mol/canister) as a function of time for radionuclides in the 4n chain. Initial inventory from Håkansson (2000).*

The 4n+1 chain

The 4n+1 chain is shown in Figure D-7 along with a simplified chain used in the hypothetical calculation case supporting the selection. Figure D-8 shows the annual dose for the hypothetical calculation case. The dose is dominated by Am-241, Np-237 and Th-229. All other nuclides in the 4n+1 chain have small or negligible contributions to the total dose from this chain. However, U-233 must be included in order to obtain a correct result for its daughter nuclides.

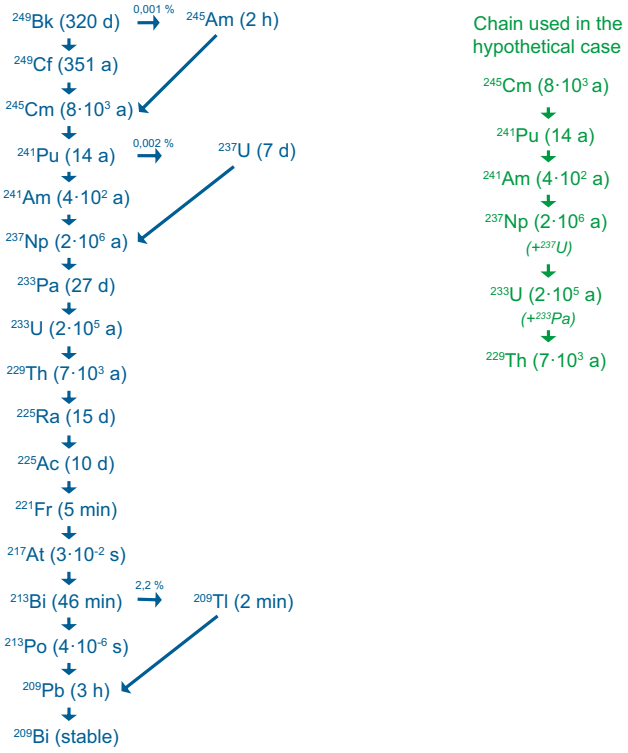

Figure D-7. *The 4n+1 chain. The simplified chain is used in the hypothetical case to support the selection of radionuclides for the radionuclide transport calculations. Nuclides at the beginning of the chain without any inventory have been excluded in the simplified chain as have nuclides with a half-life shorter than 1 year but their inventories have been included in those of their daughters. Approximate half-lives shown are derived from Table D-2.*

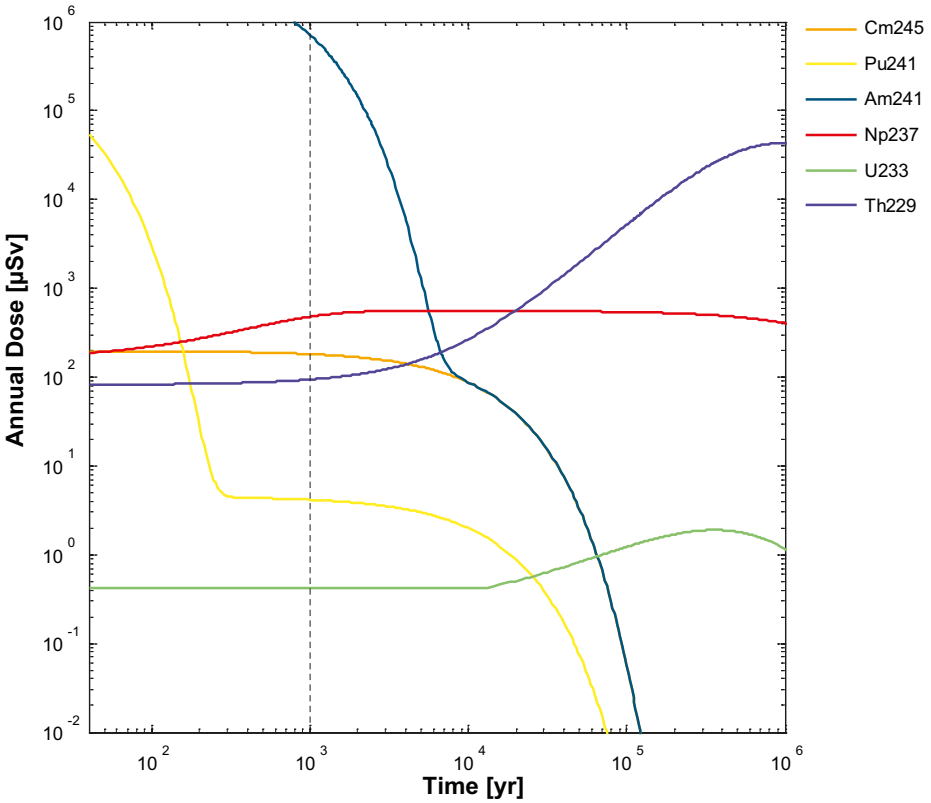

Figure D-8. *Calculated annual dose in the hypothetical case supporting the selection of radionuclides for the radionuclide transport calculations of 4n+1 chain. The vertical black dashed line denotes 1 000 years after closure.*

Table D-2. The 4n+1 chain – Background data and arguments for including or excluding the radionuclides in the transport calculations.

Nuclide	Half-life[a)]	Inventory BWR38[b)] (Bq/tU)	Inventory BWR38[b)] (mol/tU)	Dose conversion factor[c)] (Sv/Bq)	Treatment in radionuclide transport calculations Arguments for including or excluding
Bk-249	230 d	d)	d)	9.7e–10	Excluded. Short half life (<1year)
Cf-249	351 a		–	3.5e–7	Excluded, no inventory.
Am-245	2.05 h		–	6.2e–11	Excluded, no inventory.
Cm-245	8.50e3 a	9.37e9*	6.02e–3*	2.1e–7	**Included** If neglected Am-241 will decline too fast.
Pu-241	14.4 a	7.72e14	83.7	4.8e–9	Excluded. Short half-life and the results shown in Figure D-8 grant the possibility to simplify the treatment of Pu-241. **Include initial inventory (mol) in Am-241** (however negligible contribution, see Figure D-10) Solubility – Pu-241 constitute mostly 3 % (initially) of the total Plutonium content and hence the exclusion of Pu-241 is of minor importance from solubility point of view.
U-237	6.75 d	1.85e10	2.58e–8	7.6e–10	Excluded. Short half-life (<1year), small inventory. Initially small and small yield of Pu-241 decay to U-237 (see Figure D-10). **Include initial inventory (mol) in Np-237** (however negligible contribution, see Figure D-10). All the U-237 formed by decay from Pu-241 is treated by including the initial inventory of Pu-241 in Am-241.
Am-241	4.32e2 a	1.51e14	4.93	2.0e–7	**Included**
Np-237	2.14e6 a	1.5e10	2.43	1.1e–7	**Included**
Pa-233	27.0 d	1.5e10	8.37e–8	8.7e–10	Excluded. Short half-life (<1year). **Include initial inventory (mol) in U-233**, however negligible contribution.
U-233	1.59e5 a	2.15e9**	2.58e–2**	5.1e–8	**Included** Long half-life, necessary to include for the calculation of Th-229
Th-229	7.34e3 a	1.67e9**	9.26e–4**	4.9e–7	**Included** Amount increases with time, high dose conversion factor
Ra-225 Ac-225 Fr-221 At-217 Bi-213 Po-213 Tl-209	<15 d				Excluded. No initial inventory, much shorter half-life (<1year) than Th-229, therefore in equilibrium with Th-229, see Figure D-9

a) Chu et al. (1999).
b) Inventory 40 years after discharge (Håkansson 2000).
c) Oral intake adults (EU 1996).
d) Only included in inventory with high burn-up (BWR55, PWR60).
* Inventory not given for 40 years after discharge in Håkansson (2000), calculated from 45 years.
** Inventory not given for 40 years after discharge in Håkansson (2000), calculated from 10 000 years.

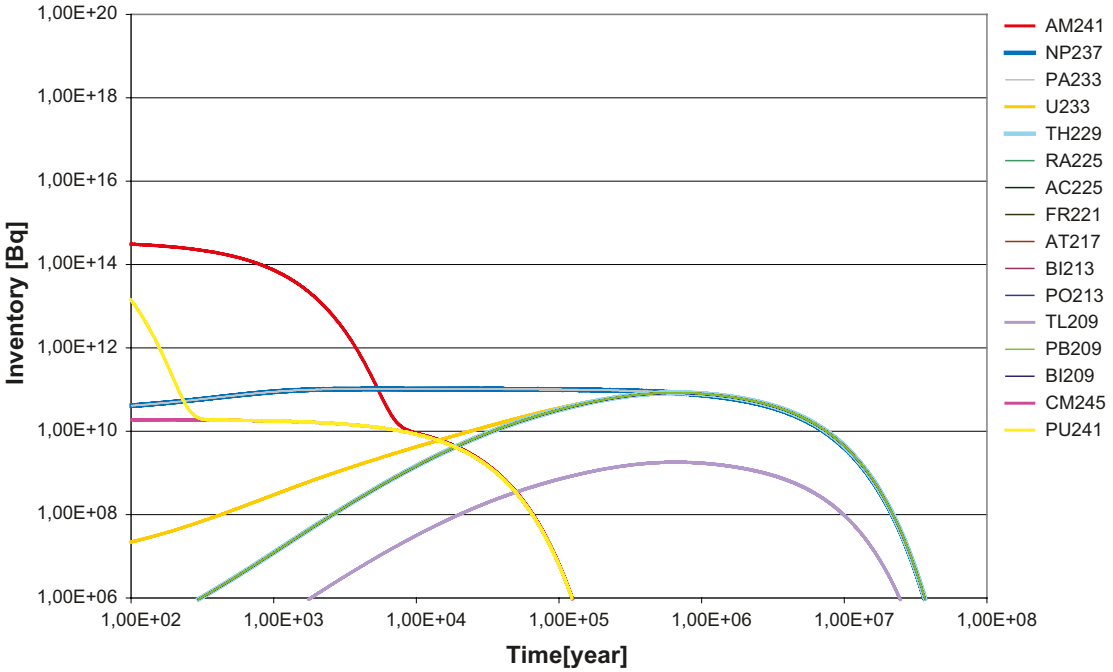

Figure D-9. *Activity (Bq/tU) as a function of time for radionuclides in chain 4N+1. Initial inventory from Håkansson (2000).*

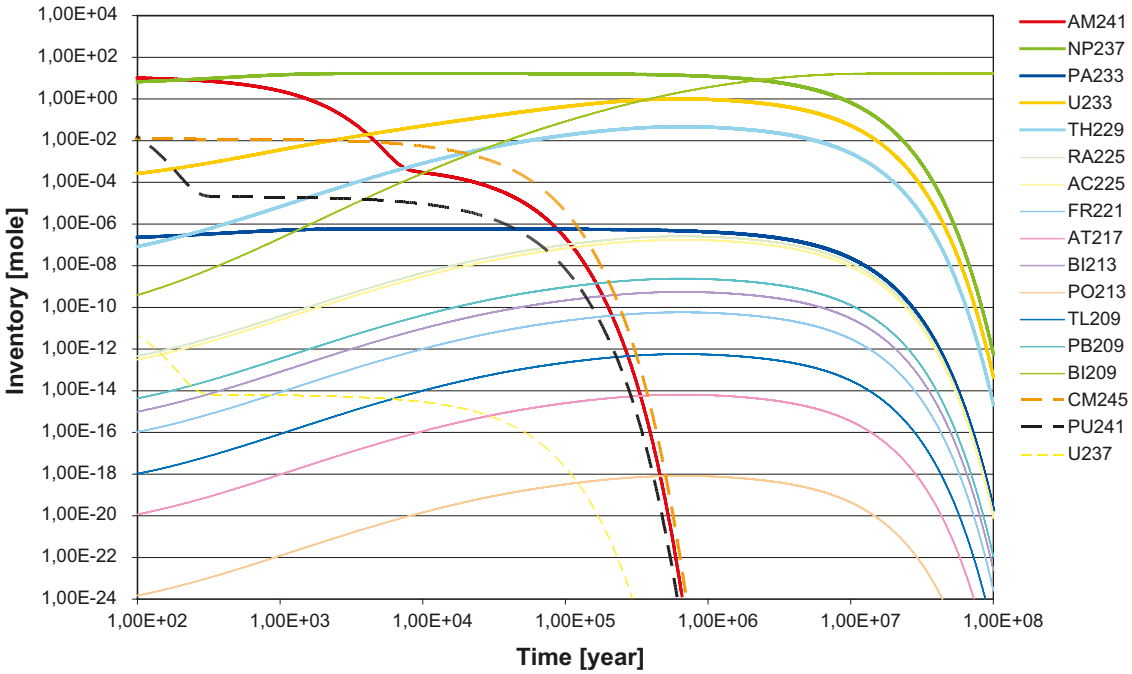

Figure D-10. *Radionuclide content (mol/canister) as a function of time for radionuclides in chain 4N+1. Initial inventory from Håkansson (2000).*

The 4n+2 chain

The 4n+2 chain is shown in Figure D-11 along with the simplified chain used in the hypothetical calculation case supporting the selection. Figure D-12 shows the annual dose for the hypothetical calculation case. The dose is dominated by Pu-238, Pu-242, Pb-210, Th-230 and Ra-226. All other nuclides in the 4n+2 chain have small or negligible contributions to the total dose from this chain. However, U-238 and U-234 must be included in order to obtain correct results for their daughter nuclides.

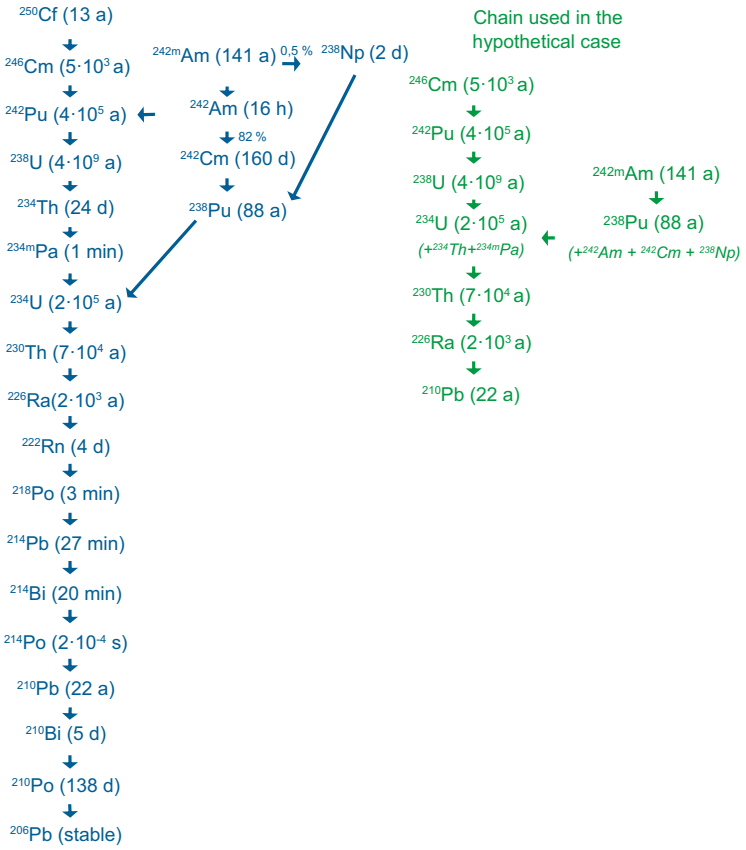

Figure D-11. *The 4n+2 chain. The simplified chain is used in the hypothetical case to support the selection of radionuclides for the radionuclide transport calculations. Nuclides at the beginning of the chain without any inventory have been excluded in the simplified chain as have nuclides with a half-life shorter than 1 year but their inventories have been included in their daughter's inventory. Approximate half-lives shown are derived from Table D-3.*

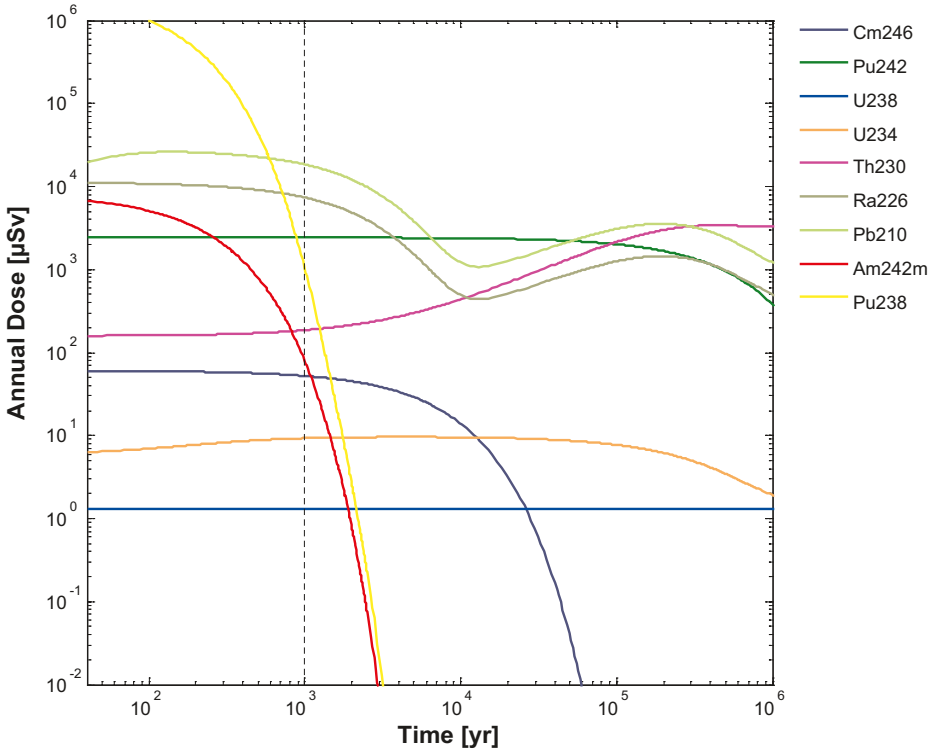

Figure D-12. *Calculated annual dose in the hypothetical case supporting the selection of radionuclides for the radionuclide transport calculations of the 4n+2 chain. The vertical black dashed line denotes 1 000 years after closure.*

Table D-3. The 4n+2 chain – Background data and arguments for including or excluding the radionuclides in the transport calculations.

Nuclide	Half-life[a]	Inventory BWR38[b] (Bq/tU)	Inventory BWR38[b] (mol/tU)	Dose conversion factor[c] (Sv/Bq)	Treatment in radionuclide transport calculations Arguments for including or excluding
Cf-250	13.1 a	–	–	1.6e–7	Excluded, no inventory
Cm-246	4.73e3 a	2.89e9*	1.03e–3*	2.1e–7	**Included**
Am-242m	141 a	4.53e11	4.82e–3	1.9e–7	Excluded. Include initial inventory in Pu-238 or U-234. **Included in calculations with fast release.** Needed to represent Pu-238 correctly. The high dose from Pu-238 is determined from the initial amount of Pu-238, but the duration is strongly influenced by Am-242m.
Np-238	2.12 d	–	–	9.1e–10	Excluded. Short half life (<1 year), only <0.5 % of the Am-242m decay to Np-238.
Am-242	16.0 h	4.51e11	6.23e–8	3.0e–10	Excluded. Short half-life (<1 year), simplify by including inventory in Pu-242 and Pu-238/U-234, however negligible.
Pu-242	3.73e5 a	1.01e11	2.85	2.4e–7	**Included**
U-238	4.47e9 a	1.17e10	3.95e3	4.5e–8	**Included**
Cm-242	163 d	3.37e11	1.14e–5	1.2e–8	Excluded. Short half-life (<1year), **Include initial inventory in Pu-238 or U-234**
Pu-238	87.7 a	9.45e13	6.26e–1	2.3e–7	**Included in calculations with fast release.** **Check with deterministic calculations if the contribution is possible to neglect.** If possible to neglect the initial inventory is added to U-234. Solubility – Pu consist of max 2 % Pu-238 and hence exclusion of Pu-238 is of minor importance from a solubility point of view.
Th-234	24.1 d	1.17e10	5.84e–8	3.4e–9	Excluded. Short half-life (<1 year), simplify, include inventory (mol) in U-234 (however negligible contribution) Solubility – negligible content compared to other isotopes of Th.
Pa-234m	1.17 min	1.17e10	1.97e–12	No	Excluded. Short half-life (<1 year), simplify, include inventory (mol) in U-234 (however negligible contribution)
U-234	2.46e5 a	4.46e10	8.6e–1	4.9e–8	**Included**
Th-230	7.54e4 a	7.57e9**	4.31e–2**	2.1e–7	**Included**
Ra-226	1.60e3 a	4.02e9**	4.86e–4**	**2.8e–7**	**Included**
Rn-222 Po-218 Pb-214 Bi-214 Po-214	<4 d	–	–		Excluded[3], No initial inventory. Much shorter half-life than Ra-226, therefore in equilibrium with Ra-226, see Figure D-13. Short half-lives compared to the time scale for their transport to the biosphere.
Pb-210	22.3 a	3.94e9	6.63e–6	6.9e–7	**Included**
Bi-210 Po-210	<140 d	–	–		Excluded[3], No initial inventory. Much shorter half-life than Pb-210, therefore in equilibrium with Pb-210, see Figure D-13. Short half-lives compared to the time scale for their transport to the biosphere.

a) Chu et al. (1999)
b) Inventory 40 years after discharge (Håkansson 2000).
c) Oral intake adults (EU 1996).
* Inventory not given for 40 years after discharge in Håkansson (2000), calculated from 45 years.
** Inventory not given for 40 years after discharge in Håkansson (2000), calculated from 10 000 years.

[3] Excluded in SR-Site. Included in the PSAR, see Appendix L, Section L.15.

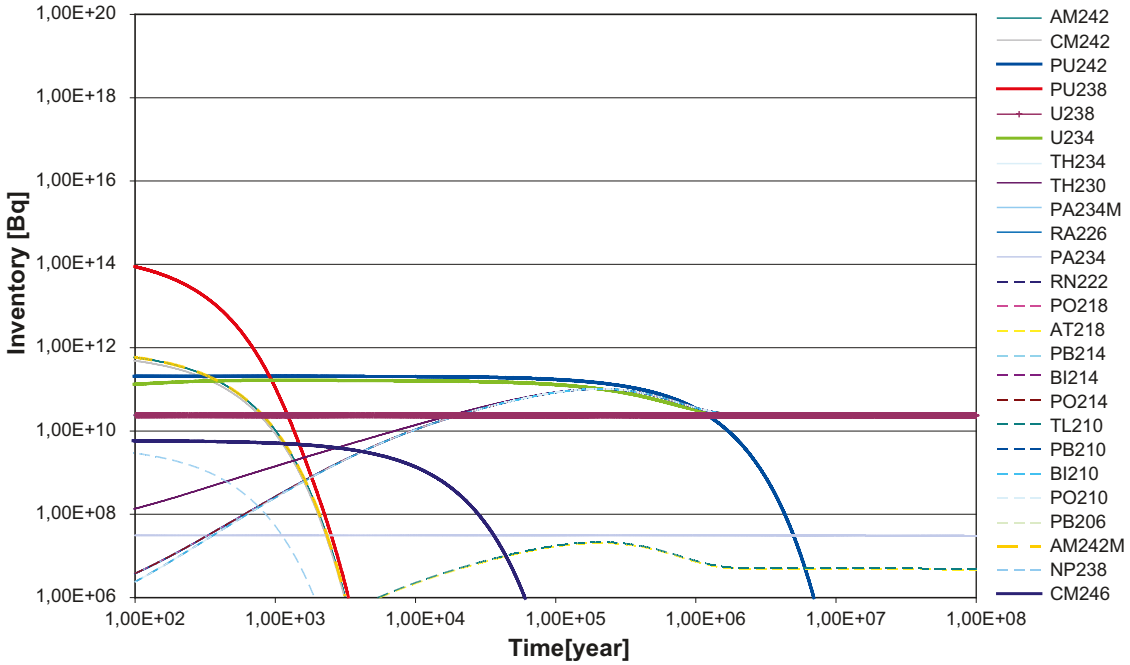

Figure D-13. *Activity (Bq/tU) as a function of time for radionuclides in chain 4N+2. Initial inventory from Håkansson (2000).*

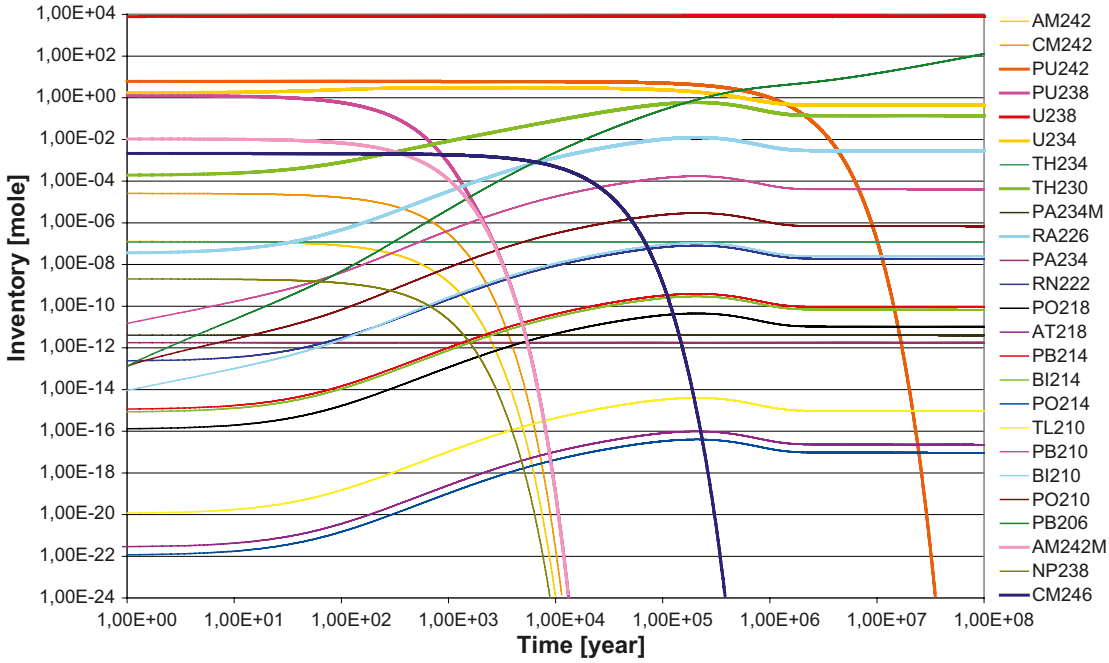

Figure D-14. *Radionuclide content (mol/canister) as a function of time for radionuclides in chain 4N+2. Initial inventory from Håkansson (2000).*

The 4n+3 chain

The 4n+3 chain is shown in Figure D-15 along with the simplified chain used in the hypothetical calculation case supporting the selection. Figure D-16 shows the annual dose for the hypothetical calculation case. The dose is dominated by Pu-239 and Pa-231, but Am-243 and Ac-227 also contribute. All other nuclides in the 4n+3 chain have small or negligible contribution to the total dose from this chain. However, U-235 must be included in order to obtain correct results for its daughter nuclides.

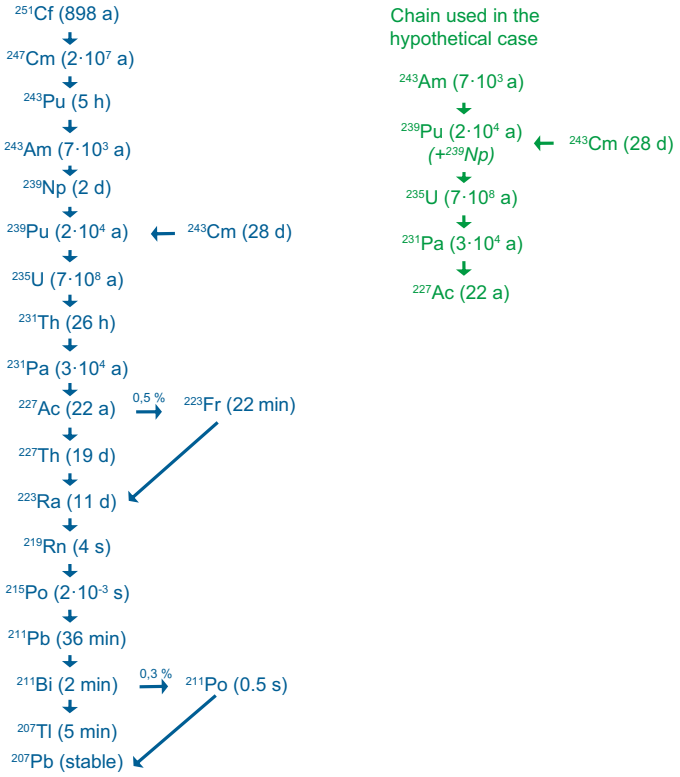

Figure D-15. *Chain 4N+3. The simplified chain is used in the hypothetical case to support the selection of radionuclides for the radionuclide transport calculations. Nuclides in the beginning of the chain without any inventory have been excluded in the simplified chain as have nuclides with a half-life shorter than 1 year, but their inventories have been added to their daughter's inventory. Approximate half-lives shown are derived from Table D-4.*

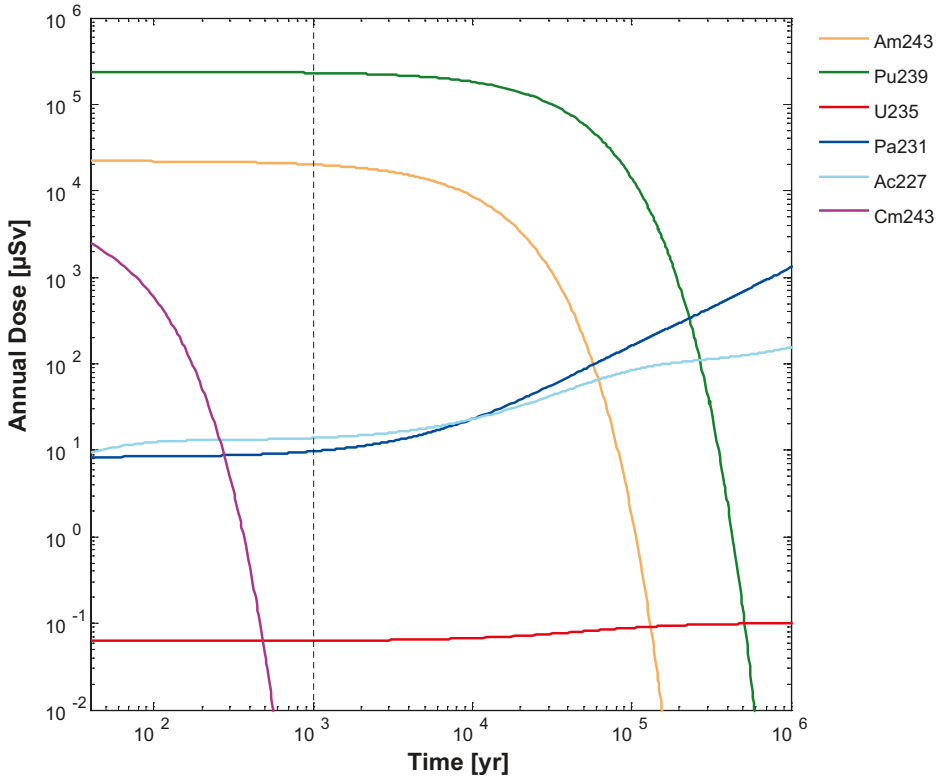

Figure D-16. *Calculated annual dose in the hypothetical case supporting the selection of radionuclides for the radionuclide transport calculations of the 4n+3 chain. The vertical black dashed line denotes 1 000 years after closure.*

Table D-4. Chain 4N+3 – Background data and arguments for including or excluding the radionuclides in the transport calculations.

Nuclide	Half-life[a)]	Inventory BWR38[b)] (Bq/tU)	Inventory BWR38[b)] (mol/tU)	Dose conversion factor[c)] (Sv/Bq)	Treatment in radionuclide transport calculations Arguments for including or excluding
Cf-251	898 a	–	–		Excluded, no inventory
Cm-247	1.56e7 a	–	–	1.9e–7	Excluded, no inventory
Pu-243	4.96 h	–	–		Excluded, short half-life
Am-243	7.37e3 a	1.17e12	6.19e–1	2.0e–7	**Included**
Np-239	2.36 d	1.17e12	5.81e–7	8.0e–10	Excluded. Short half-life (< 1year). Include inventory (mol) in Pu-239 (however negligible contribution)
Cm-243	29.1 a	4.44e11	9.39e–4	1.5e–7	Excluded. Short half-life and the results shown in Figure D-16 grant the possibility to simplify the treatment of Cm-243. Include initial inventory (mol) in Pu-239 (however negligible contribution).
Pu-239	2.41e4 a	9.5e12	1.73e1	2.5e–7	**Included**
U-235	7.04e8 a	5.32e8**	2.83e1**	4.7e–8	**Included**
Th-231	25.5 h	–	–	3.4e–10	Short half-life (<1year) simplify, include inventory (mol) in Pa-231 (however negligible contribution) Solubility – negligible content compared to other isotopes of Th.
Pa-231	3.28e4 a	1.18e8**	9.53e–4**	7.1e–7	**Included**
Ac-227	21.8 a	–	–		**Included**
Th-227 Fr-223 Ra-223 Rn-219 Po-215 Pb-211 Bi-211 Po-211 Tl-207	>19 d				Excluded, No initial inventory. Much shorter half-life than Ac-227, therefore in equilibrium with Ac-227, see Figure D-17. Short half-lives compared to the time scale for their transport to the biosphere.

a) Chu et al. (1999).
b) Inventory 40 years after discharge (Håkansson 2000).
c) Oral intake adults (EU 1996).
* Inventory not given for 40 years after discharge in Håkansson (2000), calculated from 45 years.
** Inventory not given for 40 years after discharge in Håkansson (2000), calculated from 10 000 years.

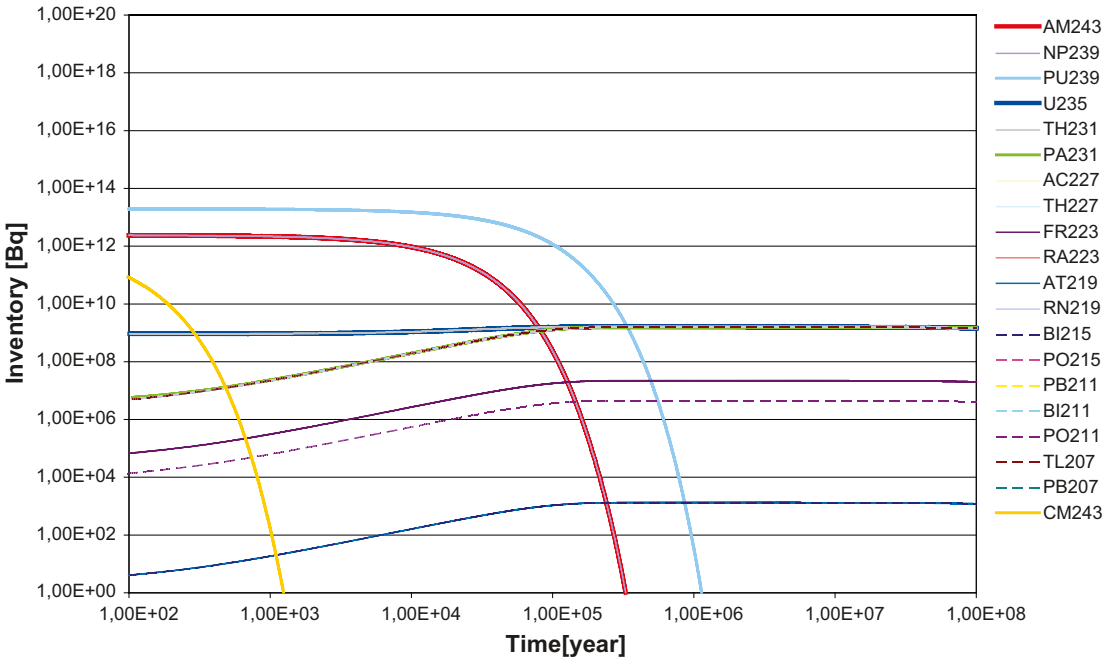

Figure D-17. *Activity (Bq/tU) as a function of time for radionuclides in the 4n+3 chain. Initial inventory from Håkansson (2000).*

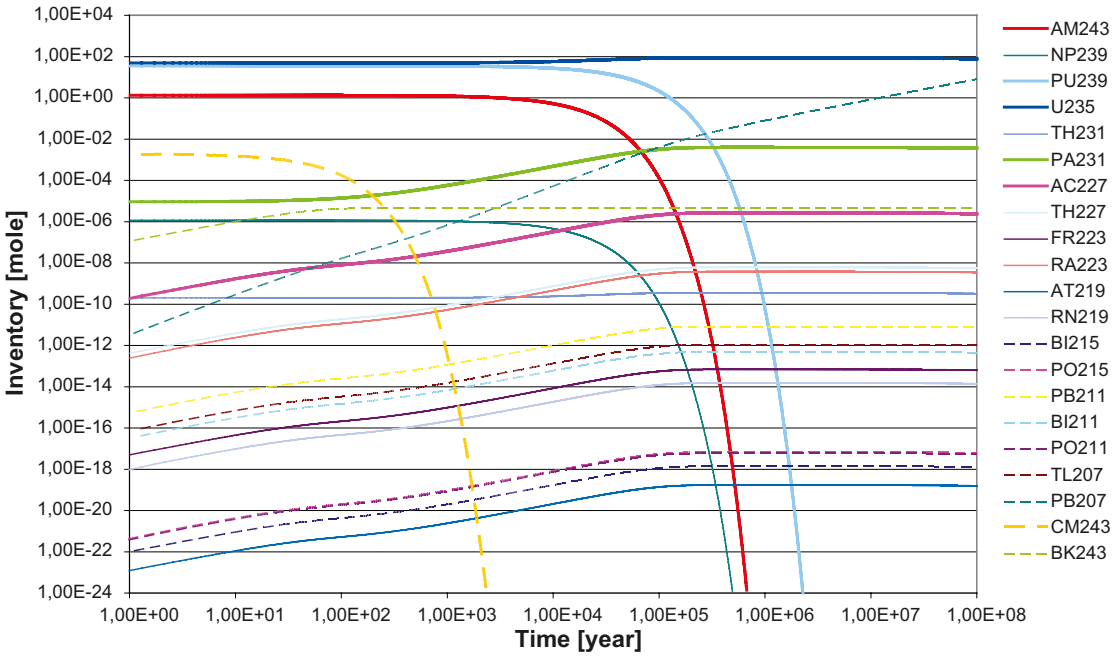

Figure D-18. *Radionuclide content (mol/canister) as a function of time for radionuclides in chain 4n+3. Initial inventory from Håkansson (2000).*

D.4 Shared solubilities

The inventory of uranium, see Figure D-19, is dominated by U-238. U-235, U-236, U-234 and U-233 contribute to the inventory to a less extent, but they are included in the transport calculations for other reasons.

The inventory of plutonium, see Figure D-20, is dominated by Pu-239, Pu-240 and Pu-242. These three isotopes of plutonium are included in the transport calculations. Pu-241 contributes with at most 3 % of the inventory and Pu-238 with 2 %, and hence exclusion of Pu-238 and Pu-241 is of minor importance from the solubility perspective.

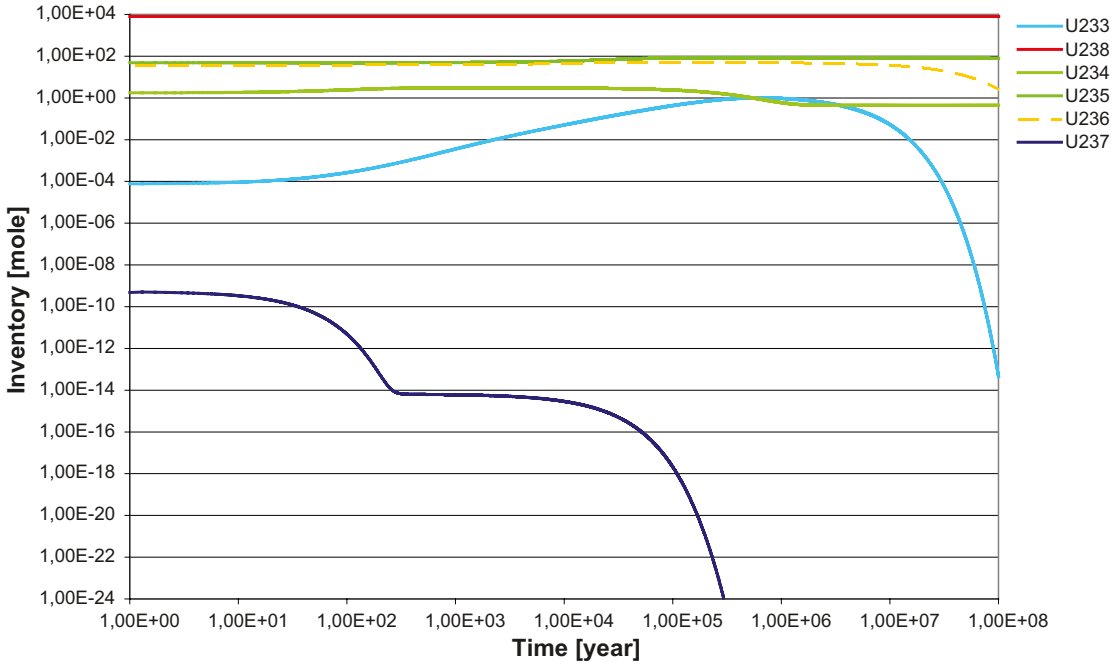

Figure D-19. *Inventory (mole/canister) of uranium isotopes.*

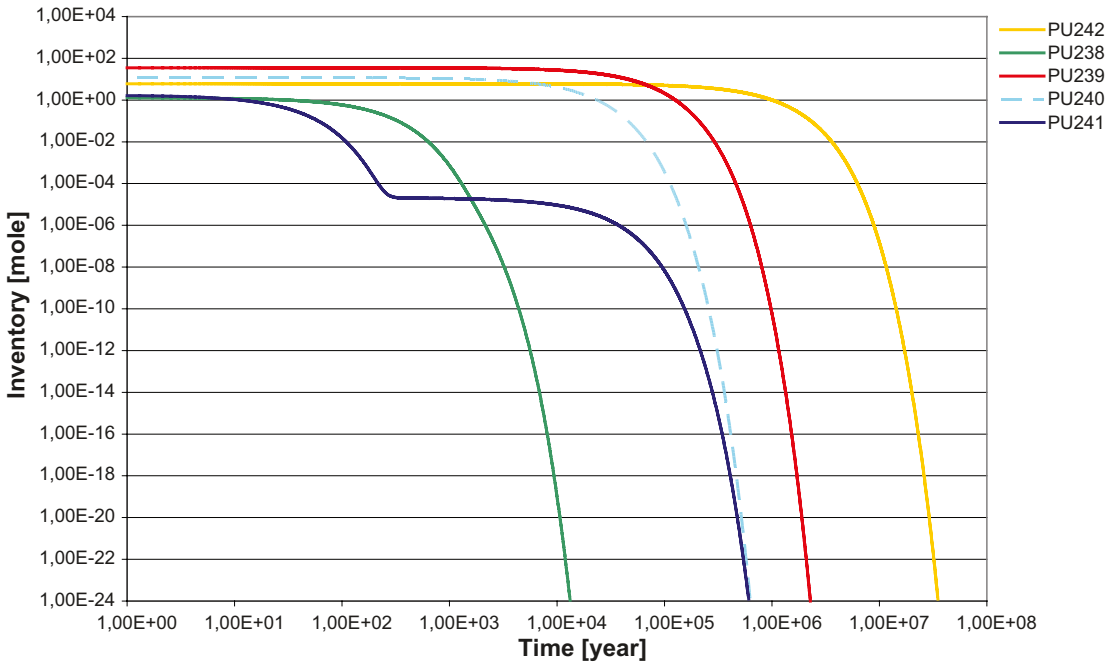

Figure D-20. *Inventory (mole/canister) of plutonium isotopes.*

The inventory of thorium, see Figure D-21, is dominated by Th-230 and Th-232 and also Th-229. These three isotopes of thorium are included in the transport calculations.

The inventory of americium, Figure D-22, is dominated by Am-241 and Am-243. Both these isotopes of americium are included in the transport calculations.

The inventory of curium, Figure D-23, is dominated by Cm-244 and Cm-245. Cm-243 and Cm-246 contribute with about 2 % each, hence exclusion of them is of minor importance from a solubility point of view.

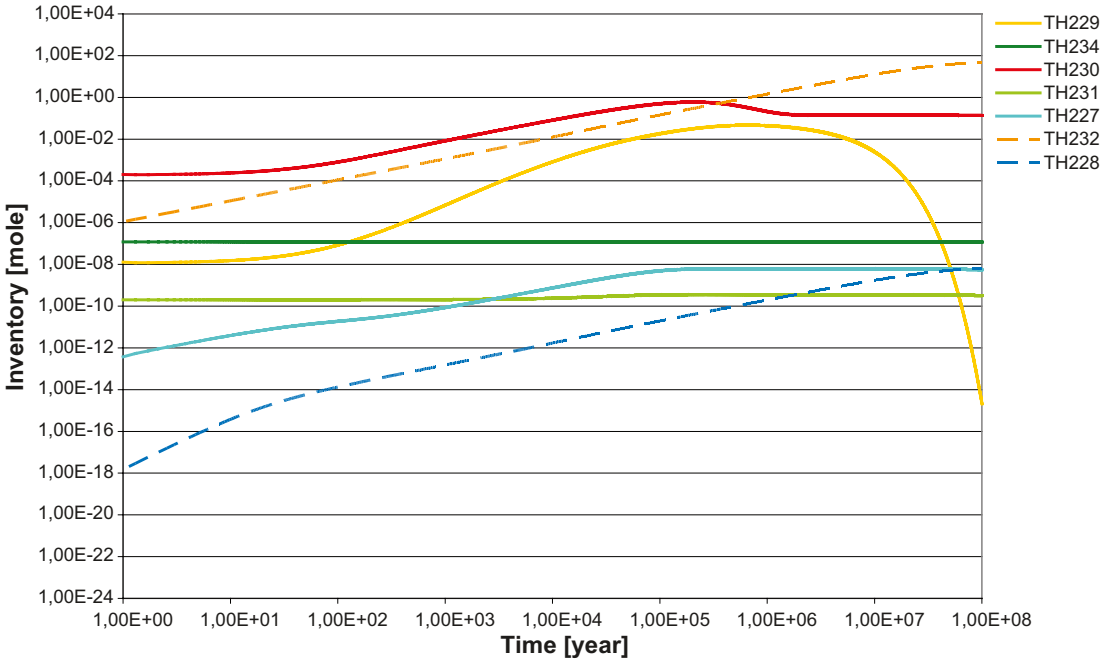

Figure D-21. *Inventory (mole/canister) of thorium isotopes.*

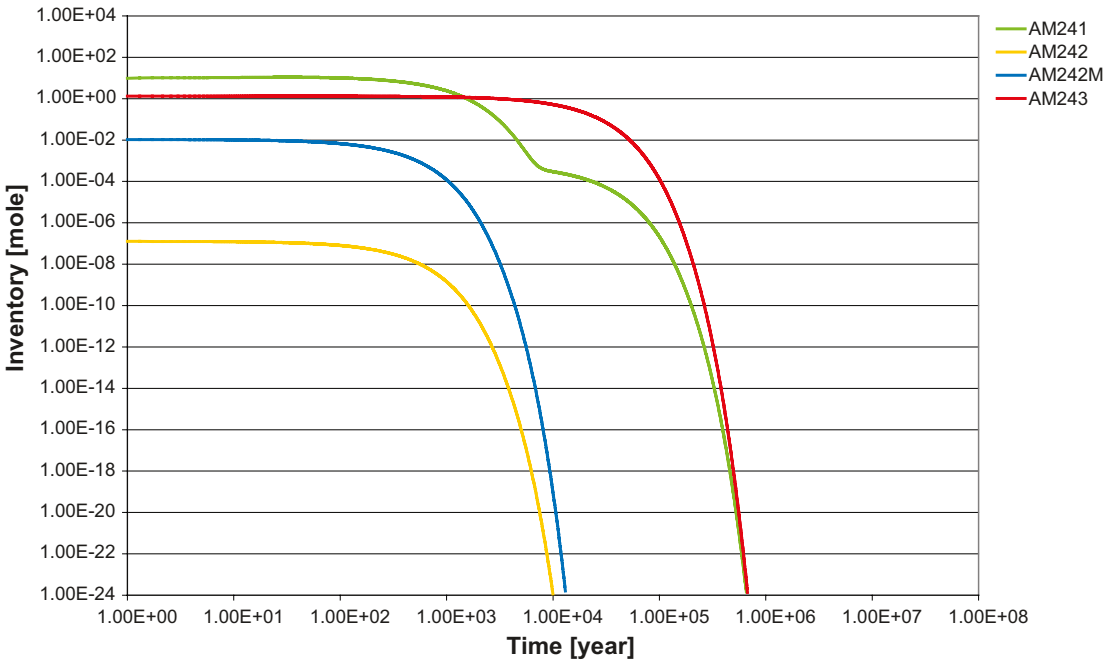

Figure D-22. *Inventory (mole/canister) of americium isotopes.*

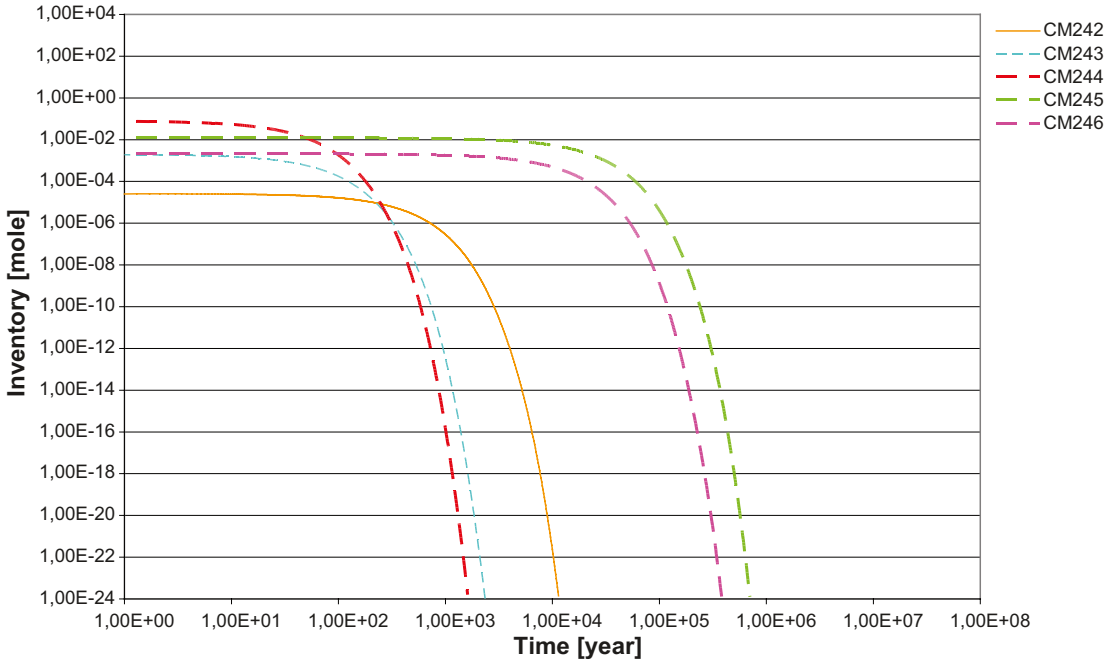

Figure D-23. *Inventory (mole/canister) of curium isotopes.*

D.5 Selected radionuclides

In Table B-2 the radionuclides selected for the radionuclide release calculations are summarised.

Table D-5. Selected radionuclides for the radionuclide release calculations.

Radionuclide	Comment
Fission and activation products	
H-3	Less important, might be important in “what if” cases with initial defect in the canister
C-14	
Cl-36	
Ni-59	
Ni-63	Less important, might be important in “what if” cases with initial defect in the canister
Se-79	
Sr-90	
Mo-93	Less important, might be important in “what if” cases with initial defect in the canister
Nb-93m	Less important, might be important in “what if” cases with initial defect in the canister
Zr-93	
Nb-94	
Tc-99	
Pd-107	
Ag-108m	Less important, might be important in “what if” cases with initial defect in the canister
Cd-113m	Less important, might be important in “what if” cases with initial defect in the canister
Sn-121m	Less important, might be important in “what if” cases with initial defect in the canister
Sn-126	
I-129	
Cs-135	
Cs-137	
Sm-151	Less important, might be important in “what if” cases with initial defect in the canister
Eu-152	Less important, might be important in “what if” cases with initial defect in the canister
Ho-166m	Less important, might be important in “what if” cases with initial defect in the canister

Radionuclide	Comment
4n	
Pu-240	Add initial inventory of Cm-244
U-236	
Th-232	
4n+1	
Cm-245	Only included to give a correct description of the behaviour of Am-241.
Am-241	Add initial inventory of Pu-241
Np-237	Add initial inventory of U-237
U-233	Add initial inventory of Pa-233
Th-229	Daughters will be in equilibrium
4n+2	
Cm-246	
Am-242m	Include in calculations with fast release. Possible to show in deterministic calculations that Am-242m is possible to neglect, if so include initial inventory of Am-242m in Pu-238 or U-234 if also Pu-238 is excluded.
Pu-242	Add 82 % of the initial content of Am-242
U-238	
Pu-238	Include in calculations with fast release. Add initial inventory of Cm-242, Np-238 and 18 % of the initial inventory of Am-242. If shown in deterministic calculations that Am-242m is possible to neglect add the initial inventory of Am-242m. Possible to show in deterministic calculations that it is negligible, if so include initial inventory of Pu-238 and the parent nuclides in U-234.
U-234	Add initial inventory of Th-234 and Pa-234m. If shown in deterministic calculations that Pu-238 is possible to neglect add initial inventory of Pu-238 and parent nuclides.
Th-230	
Ra-226	
Pb-210	Daughters will be in equilibrium
4n+3	
Am-243	
Pu-239	Add initial inventory of Cm-243 and Np-239.
U-235	
Pa-231	
Ac-227	Daughters will be in equilibrium

Table D-6. Selected radionuclides for which data needs to be compiled.

Important	Less important*	Need only inventory and half-lives
Fission and activation products		
C-14	Ag-108m	
Cl-36	Cd-113m	
Cs-135	Eu-152	
Cs-137	H-3	
I-129	Nb-93m	
Nb-94	Ni-63	
Ni-59	Sm-151	
Pd-107	Sn-121m	
Se-79	Ho-166m	
Sn-126	Mo-93	
Sr-90		
Tc-99		
Zr-93		
Decay chains		
4n		
Pu-240	Cm-244	
U-236		
Th-232		
4n+1		
Cm-245	Pu-241	U-237
Am-241		Pa-233
Np-237		
U-233		
Th-229		
4n+2		
Cm-246	Am-242m	Am-242
Pu-242	Pu-238	Cm-242
U-238		Np-238
U-234		Th-234
Th-230		Pa-234m
Ra-226		
Pb-210		
4n+3		
Am-243	Cm-243	Np-239
Pu-239		
U-235		
Pa-231		
Ac-227		

* Nuclides that might be important in hypothetical cases with initial defect in the canister.

Appendix E

Inventory for SR-Site

This appendix has not been changed since the SR-Site assessment.

E.1 Average inventory used in the calculations

COMP23 requires an inventory of radionuclides expressed in moles per canister as input data and then the code can calculate the decay over time. Transport of radionuclides out of the canister is in most calculation cases assumed to occur thousands of years after deposition. Therefore, to reduce the calculation time, the main part of the transport calculations start after 1 000 years. After that time short-lived radionuclides will have decayed to insignificant levels and are not necessary to include in the calculations. In a few cases the canister fails earlier and the calculations have to start at failure time or at repository closure time. In these cases the calculations include some short-lived nuclides. For more information about nuclides considered as important in all calculation cases or just important in cases with early failure time, see Appendix D.

Considering calculations with different starting times, different batches of inventories are required. The SR-Site data report (SKB 2010b) delivers the inventory in mole per average canister at year 2045. This inventory has been used as input to COMP23 to calculate the inventory at different times and the result has then been used as input to COMP23 in the radionuclide transport calculations. Thus COMP23 has been used for two different purposes: to calculate the inventory at a specific time and to calculate the radionuclide transport.

The repository is assumed to close at year 2070 and this year is considered as year 0 in the calculations. Therefore, 25 years of decay is applied to the original inventory from the SR-Site data report (SKB 2010b) to the inventory used in calculations starting at closure time and 1 025 years of decay is applied to the inventory used for calculations starting at 1 000 years. Inventories calculated by COMP23 and used as input to the transport calculations starting at 0 years, 100 years and 1 000 years are shown in Table E-1.

Late in the SR-Site process, after most of the calculations were completed, the inventory was corrected for all nuclides present in the PWR control rod clusters. For all nuclides, the corrected average inventory is lower, see Table E-2. The correction has been performed completely in the SR-Site data report (SKB 2010b). In the radionuclide transport calculations the correction was applied for Ag-108m in the shear load case with early failure and in the additional cases to illustrate barrier function. No more corrections were implemented because the changes are either negligibly small or only affect nuclides with doses lower than visible in the figures. Some details to justify neglecting the corrections:

1. The correction was judged to be negligible for C-14 (0.978), Cl-36 (0.999), Nb-93m (0.999), Nb-94 (0.999), Ni-59 (0.959) and Ni-63 (0.966). It is also pessimistic to not apply the correction. (The numbers given in brackets are the ratios between the corrected inventory and the old inventory.)
2. The changes for Cd-113m (0.252) and Mo-93 (0.855) are not negligible, but since the dose is always lower than shown in the figures the correction would not be visible in the reported results. However, it should be noted that the files archived at SKB[4] include results for these nuclides that are not corrected.
3. Change for Ag-108m (0.250) is only performed in the shear load case with early failure and in the additional cases to illustrate barrier function; for all other cases no change has been performed for the same reason as described for Cd-113m and Mo-93.

[4] SKB, 2010. Radionuclide transport calculations with MARFA. SKBdoc 1266150 ver 1.0, Svensk Kärnbränslehantering AB. (Internal document.)

In summary all results visible in figures and tables represents the corrected inventory, whereas the files archived at SKB[5] do not.

Table E-1. Inventory (mol/canister) calculated by COMP23 and used in the radionuclide transport calculations.

Radionuclide	Inventory in average canister (mol/canister)				
	From SKB (2010b), year 2045	Calculated, year 2070 (0 yr)	Calculated, year 2170 (100 yr)	Calculated, year 2370 (300 yr)	Calculated, year 3070 (1 000 yr)
Pu-240 (+Cm-244)	2.06×10^{1} ($+1.14 \times 10^{-1}$)	2.07×10^{1}	2.04×10^{1}	2.00×10^{1}	1.86×10^{1}
U-236	3.91×10^{1}	3.92×10^{1}	3.94×10^{1}	3.98×10^{1}	4.12×10^{1}
Th-232	4.49×10^{-5}	7.39×10^{-5}	1.90×10^{-4}	4.24×10^{-4}	1.26×10^{-3}
Cm-245	2.30×10^{-2}	2.30×10^{-2}	2.28×10^{-2}	2.24×10^{-2}	2.12×10^{-2}
Am-241 (+Pu-241)	9.21 (+1.86)	1.06×10^{1}	9.06	6.57	2.14
Np-237 (+U-237)	4.71 ($+5.79 \times 10^{-8}$)	5.15	6.72	9.21	1.36×10^{1}
U-233 (+Pa-233)	9.53×10^{-5} ($+1.63 \times 10^{-7}$)	1.35×10^{-4}	3.28×10^{-4}	8.46×10^{-4}	3.52×10^{-3}
Th-229	1.46×10^{-8}	2.71×10^{-8}	1.25×10^{-7}	6.19×10^{-7}	6.82×10^{-6}
Cm-246	2.42×10^{-3}	2.41×10^{-3}	2.38×10^{-3}	2.31×10^{-3}	2.08×10^{-3}
Pu-242 (+Am-242)	5.22 ($+9.79 \times 10^{-8}$)	5.22	5.22	5.22	5.21
U-238	7.20×10^{3}	7.20×10^{3}	7.20×10^{3}	7.20×10^{3}	7.20×10^{3}
U-234 (+Cm-242 + Th-234 + Pa-234m)	1.82 ($+1.98 \times 10^{-5}$ + 1.07×10^{-7}+ 3.67×10^{-12})	2.08	2.73	3.16	3.27
Th-230	1.75×10^{-4}	3.13×10^{-4}	1.00×10^{-3}	2.69×10^{-3}	9.08×10^{-3}
Ra-226	3.03×10^{-8}	8.54×10^{-8}	6.63×10^{-7}	3.85×10^{-6}	3.64×10^{-5}
Pb-210	1.29×10^{-10}	5.02×10^{-10}	6.14×10^{-9}	4.44×10^{-8}	4.78×10^{-7}
Am-242m	7.58×10^{-3}	6.70×10^{-3}	4.10×10^{-3}	1.53×10^{-3}	4.91×10^{-5}
Pu-238	1.45	1.19	5.42×10^{-1}	1.13×10^{-1}	5.16×10^{-4}
Am-243	1.27	1.27	1.26	1.23	1.15
Pu-239 (+Cm-243 + Np-239)	4.21×10^{1} ($+1.72 \times 10^{-3}$+ 1.12×10^{-6})	4.21×10^{1}	4.20×10^{1}	4.17×10^{1}	4.10×10^{1}
U-235	5.76×10^{1}	5.76×10^{1}	5.78×10^{1}	5.80×10^{1}	5.88×10^{1}
Pa-231	5.92×10^{-6}	7.34×10^{-6}	1.30×10^{-5}	2.43×10^{-5}	6.39×10^{-5}
Ac-227	2.34×10^{-9}	3.51×10^{-9}	7.45×10^{-9}	1.50×10^{-8}	4.13×10^{-8}
*Ag-108m**	*4.31×10^{-1}*	*4.14×10^{-1}*	*3.54×10^{-1}*	*2.58×10^{-1}*	*8.51×10^{-2}*
*C-14**	*3.70×10^{-2}*	*3.69×10^{-2}*	*2.66×10^{-2}*	*3.56×10^{-2}*	*3.27×10^{-2}*
*Cd-113m**	*3.16×10^{-3}*	*9.25×10^{-4}*	*6.75×10^{-6}*	*3.55×10^{-10}*	*1.00×10^{-23}*
*Cl-36**	*8.79×10^{-3}*	*8.79×10^{-3}*	*8.79×10^{-3}*	*8.78×10^{-3}*	*8.77×10^{-3}*
Cs-135	6.73	6.73	6.73	6.73	6.73
Cs-137	8.69	4.88	4.87×10^{-1}	4.83×10^{-3}	4.56×10^{-10}
Eu-152	8.32×10^{-5}	2.31×10^{-5}	1.38×10^{-7}	4.79×10^{-12}	1.00×10^{-23}
H-3	5.84×10^{-3}	1.43×10^{-3}	5.15×10^{-6}	6.53×10^{-11}	$1.00E \times 10^{-23}$
Ho-166m	6.79×10^{-4}	6.69×10^{-4}	6.32×10^{-4}	5.63×10^{-4}	3.76×10^{-4}
I-129	2.70	2.70	2.70	2.70	2.70
*Mo-93**	*1.65×10^{-4}*	*1.64×10^{-4}*	*1.61×10^{-4}*	*1.56×10^{-4}*	*1.38×10^{-4}*
*Nb-93m**	*4.98×10^{-2}*	*1.70×10^{-2}*	*2.31×10^{-4}*	*4.21×10^{-8}*	*2.76×10^{-21}*
*Nb-94**	*2.34×10^{-1}*	*2.34×10^{-1}*	*2.33×10^{-1}*	*2.31×10^{-1}*	*2.26×10^{-1}*
*Ni-59**	*1.69*	*1.69*	*1.69*	*1.68*	*1.67*
*Ni-63**	*2.37×10^{-1}*	*1.99×10^{-1}*	*9.97×10^{-2}*	*2.50×10^{-2}*	*1.96×10^{-4}*
Pd-107	4.78	4.78	4.78	4.78	4.78
Se-79	1.36×10^{-1}	1.36×10^{-1}	1.36×10^{-1}	1.36×10^{-1}	1.36×10^{-1}
Sm-151	1.56×10^{-1}	1.29×10^{-1}	5.96×10^{-2}	1.28×10^{-2}	5.81×10^{-5}
Sn-121m	7.07×10^{-3}	5.16×10^{-3}	1.46×10^{-3}	1.18×10^{-4}	1.72×10^{-8}
Sn-126	3.39×10^{-1}	3.39×10^{-1}	3.39×10^{-1}	3.38×10^{-1}	3.37×10^{-1}
Sr-90	5.43	2.97	2.68×10^{-1}	2.16×10^{-3}	9.91×10^{-11}
Tc-99	1.79×10^{1}	1.79×10^{1}	1.79×10^{1}	1.79×10^{1}	1.78×10^{1}
Zr-93	1.97×10^{1}	1.97×10^{1}	1.97×10^{1}	1.97×10^{1}	1.97×10^{1}

* The inventory for nuclides marked with * is old and not the same as given in the SR-Site data report (SKB 2010b). Some results have been updated to reflect the new inventory, see the text above. The corrected inventories for these nuclides are obtained by multiplying with the ratios given in Table E-2.

[5] SKB, 2010. Results from radionuclide transport calculations with COMP23 and FARF31. SKBdoc 1260295 ver 1.0, Svensk Kärnbränslehantering AB. (Internal document.)

Table E-2. Ratio between the corrected inventory and the old inventory.

Radionuclide	Corrected inventory / Old inventory
Ag-108m	0.250
C-14	0.978
Cd-113m	0.252
Cl-36	0.999
Mo-93	0.855
Nb-93m	0.999
Nb-94	0.999
Ni-59	0.959
Ni-63	0.966

E.2 Comments on differences between different type of canisters

The implications of using an average inventory in the calculations are discussed in this section. In Figure E-1 the spread in data of the inventory per type canister normalised with the inventory per average canister is shown. Nuclides that contribute significantly to the total dose are (in alphabetic order): Ag-108m, C-14, Cs-137, I-129, Nb-94, Ni-59, Np-237, Ra-226, Se-79, Sr-90 (and in one of the additional cases illustrating barrier function also Pu-239 and Pb-210). The implications by using an average inventory for these nuclides are:

- Ag-108m is mainly present in the PWR control rods, and as can be seen in Figure E-1 the inventory in BWR canisters is very small. This implies that using the average canister inventory overestimates the dose for a BWR canister by about four orders of magnitude, but underestimates the dose for a PWR canister by a factor of 4.
- C-14, Cs-137 and I-129 have only minor differences between PWR and BWR canisters as can be seen in Figure E-1. Maximum change is a factor of 1.4.
- Nb-94 is mainly present in PWR canisters, and as can be seen in Figure E-1, the inventory in BWR canister is very small. This implies that using the average canister inventory overestimates the dose for a BWR canisters by a factor of more than 10, but underestimates the dose for a PWR canister by about a factor of 4.
- Ni-59, Np-237 have only minor differences between PWR and BWR canisters as can be seen in Figure E-1. Maximum change is a factor of 1.5.
- Ra-226 is dependent of the inventories of some of its decay parents, U-238, Pu-238, U-234 and Th-230. The inventories of these nuclides vary between different type canisters, but not in a systematic way depending on BWR or PWR. The maximum change for U-238 is 1.15, for Pu-238 1.60, for U-234 1.49 and for Th-230 1.95.
- Se-79, Sr-90, only minor differences between PWR and BWR canisters as can be seen in Figure E-1. Maximum change is a factor of 1.3.
- Pu-239 and Pb-210 only contribute to the dose in one of the additional cases illustrating barrier function.

In summary, the inventories for most nuclides that contribute significantly to the dose vary by less than a factor of 1.5. An exception is Ag-108m, which has negligible inventory in a BWR canister and a PWR inventory that is a factor of 4 times greater than the average inventory used. Ag-108m only contributes to the total dose in the shear failure case with early failure and in the additional cases used to illustrate barrier function. Most of the dose-contributing radionuclides are single nuclides and hence the doses are directly scaled to the inventories. The dose from Ra-226 is dependent of the inventories of some of its decay parents, U-238, Pu-238, U-234 and Th-230. None of them differ more than a factor of two between the different canister types.

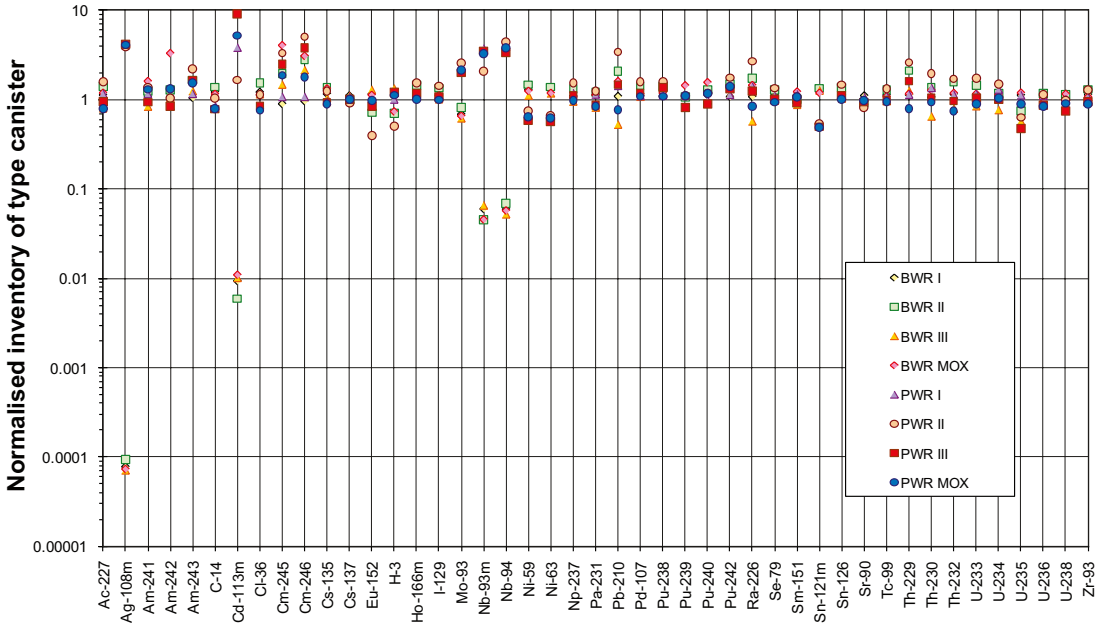

Figure E-1. *Spread in data of inventory per type canister, as normalised with the inventory per average canister. All data taken from the SR-Site data report (SKB 2010b), i.e. data for the corrected inventory.*

Appendix F

Solubility calculations

F.1 Introduction

This appendix has not been changed since the SR-Site assessment. In a few places, references in the SR-Site version were made to the main references of the SR-Site assessment, the references written in bold. It has been verified that the PSAR versions of the corresponding reports are equally valid as references in these cases. The references in bold, therefore, refer to the PSAR versions.

If groundwater enters the canister and comes in contact with the spent fuel, radionuclides may be released into the water in the void inside the canister. If the aqueous concentration of an element reaches saturation with respect to the solid phase, then its solubility limit is attained and the element will precipitate, provided that this is kinetically favoured. As a result, only the aqueous fraction of the element may migrate with the water flowing from the canister while the fraction that has precipitated remains in the canister. Only the dissolved fraction of the element may follow any outgoing water from the canister while the precipitated solid phase remains in the canister void.

The Simple Functions spreadsheet, which is a tool developed in an Excel spreadsheet (Grivé et al. 2010), was used in the safety assessment to determine the solubility limits of radionuclides. The median values of the solubility limits calculated in this appendix are given in Table 3-4 and are used for deterministic radionuclide transport calculations. Simple Function is further described in the **Model summary report**. Solubility data are based on chemical equilibrium calculations for given groundwater compositions: pH, Eh (mV), IS (mol/kg), $[HCO_3^-]$ (m), $[SO_4^{-2}]_{tot}$ (m), $[Cl]_{tot}$ (m), $[Ca]_{tot}$ (m), $[Na]_{tot}$ (m), $[Fe]_{tot}$ (m) and $[Si]_{tot}$. The Simple Functions calculates solubility limits at 25 °C and the total ionic strength should be lower than 0.2 M to ensure correct calculations. If the calculated solubility limit exceeds 0.01 M the element should be considered as not solubility limited.

Version B of the Simple Functions was used for the solubility calculations. This version calculates the solubility limits in a groundwater that has interacted with Fe-corrosion products.

The solubility limiting phases, reactions and equilibrium constants used in the Simple Functions spreadsheet are given in the **Data report** (Section 3.4). The redox conditions used are those determined by magnetite – goethite, due to the corrosion of iron inside the canister as recommended in the **Data report**. The ground water compositions used are provided to Simple Functions as input data-files, see Section F.2.

The elements Simple Function calculates solubility limits for and for which data are required are: Ag, Am, Cm, Ho, Nb, Ni, Np, Pa, Pb, Pd, Pu, Ra, Se, Sm, Sn, Sr, Tc, Th, U and Zr. Elements included in the assessment but not included in the Simple Functions: Ac, C, Cd, Cl, Cs, Eu, H, I and Mo, were treated as not solubility limited in the calculations as recommended in the **Data report**. The treatment of the solubility limits for Ra-226 and Ag-108m is further described in Section F.5.

F.2 Input to Simple Functions

In Figure F-1 the data files used as input to Simple Functions are listed. How the files were used to model solubility limits are discussed in Section F.4.[6]

[6] SKB, 2010. Hydrogeochemistry: SR-Site and comparative analysis. SKBdoc 1262945 ver 1.0, Svensk Kärnbränslehantering AB. (Internal document.)

Table F-1. Groundwater composition files used for solubility calculations (archived at SKB[4]).

Climate period	Input data file
Temperate	F_2000y_470m_FeOH3+FeS_coup.xlsx*
	F_3000y_470m_FeOH3+FeS_coup.xlsx*
	F_5000y_470m_FeOH3+FeS_coup.xlsx
	F_9000y_470m_FeOH3+FeS_coup.xlsx
Permafrost	F470_perm0_BaseCase.xlsx
Glacial	F470_GlaVa_BaseCase.xlsx
Submerged	F470_Gla0r_Basecase.xlsx

* Used in future human action cases (SKB 2010c).

F.3 The impact of groundwater composition compared to variations in thermodynamic data

In this section, the impact of varying groundwater compositions on the radionuclide solubilities is shown. Groundwaters are chosen to represent four climate periods: temperate, permafrost, glacial and submerged, see Table F-1. For each climate period, a set of 6916 groundwater compositions were randomly chosen from the files listed in Table F-1 as input data to the Simple Functions. By using @risk in combination with Simple Functions a normal distribution could be applied to the equilibrium constants ($\mu = \log_{10} K°$ and $\sigma = ½\Delta\log_{10}K°$).In Figure F-1 to Figure F-8 solubilities for the four different climate conditions are compared for the elements: Np, Pb, Pu, Ra, Se Th, U and Zr.

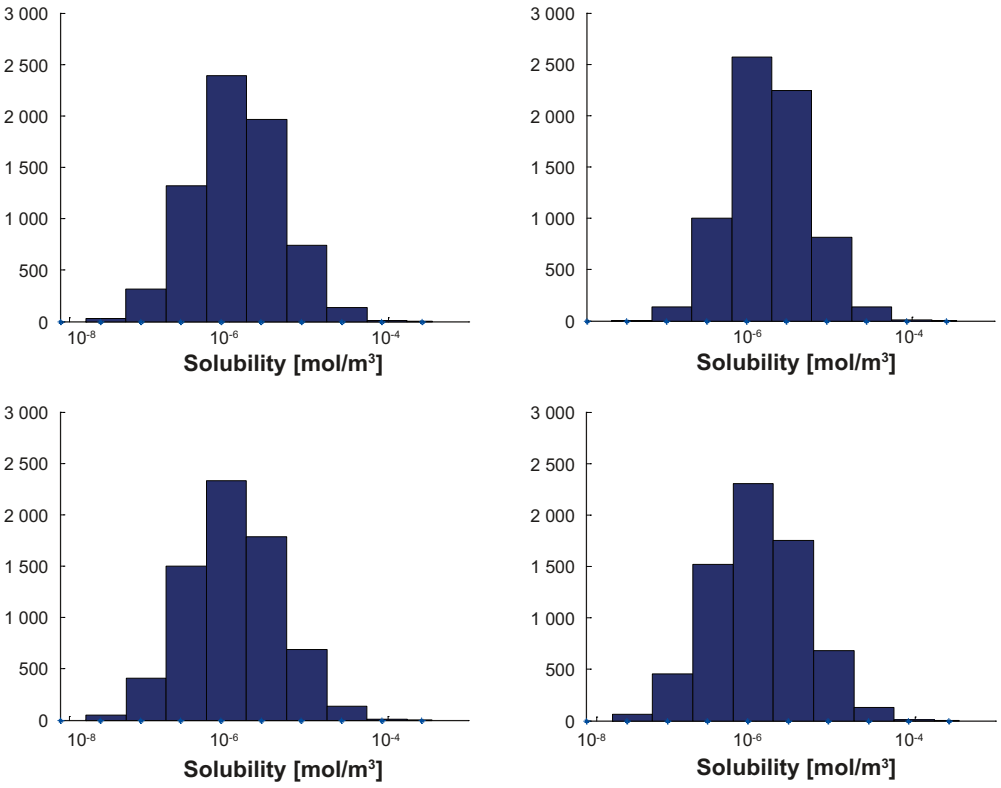

Figure F-1. *Solubility limits for Np using groundwater data from temperate conditions (upper left), permafrost conditions (upper right), glacial conditions (lower left) and submerged conditions (lower right). The y-axis shows the number of realisations in each bin.*

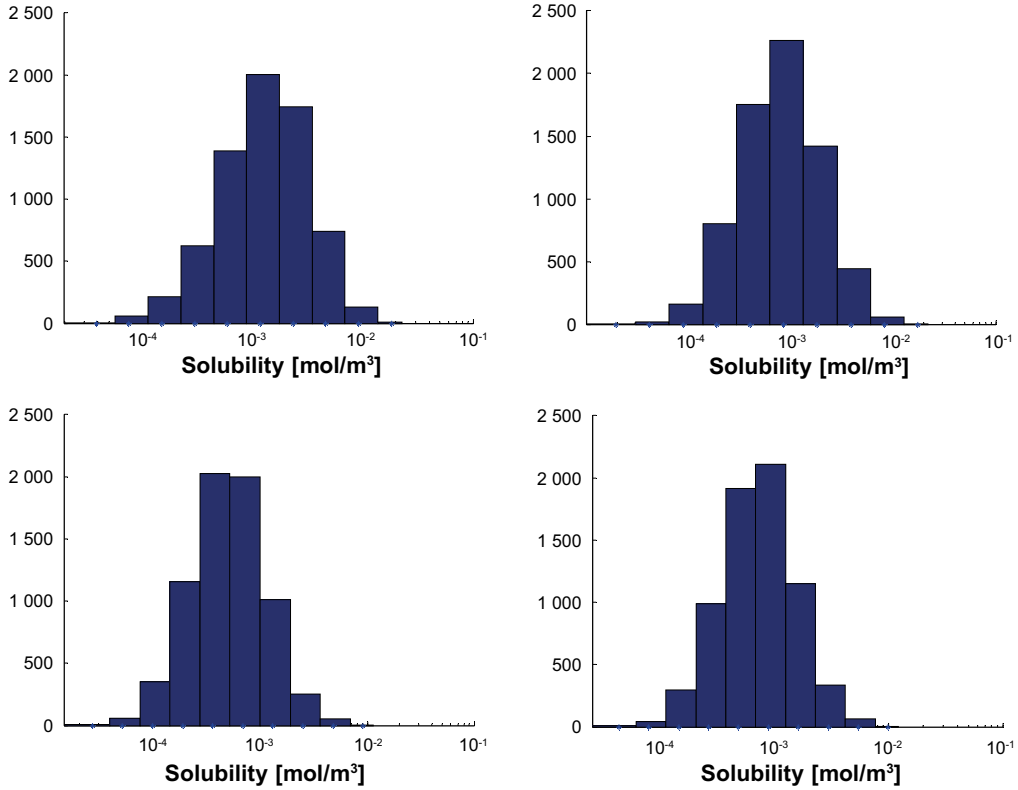

Figure F-2. *Solubility limits for Pb using groundwater data from temperate conditions (upper left), permafrost conditions (upper right), glacial conditions (lower left) and submerged conditions (lower right). The y-axis shows the number of realisations in each bin.*

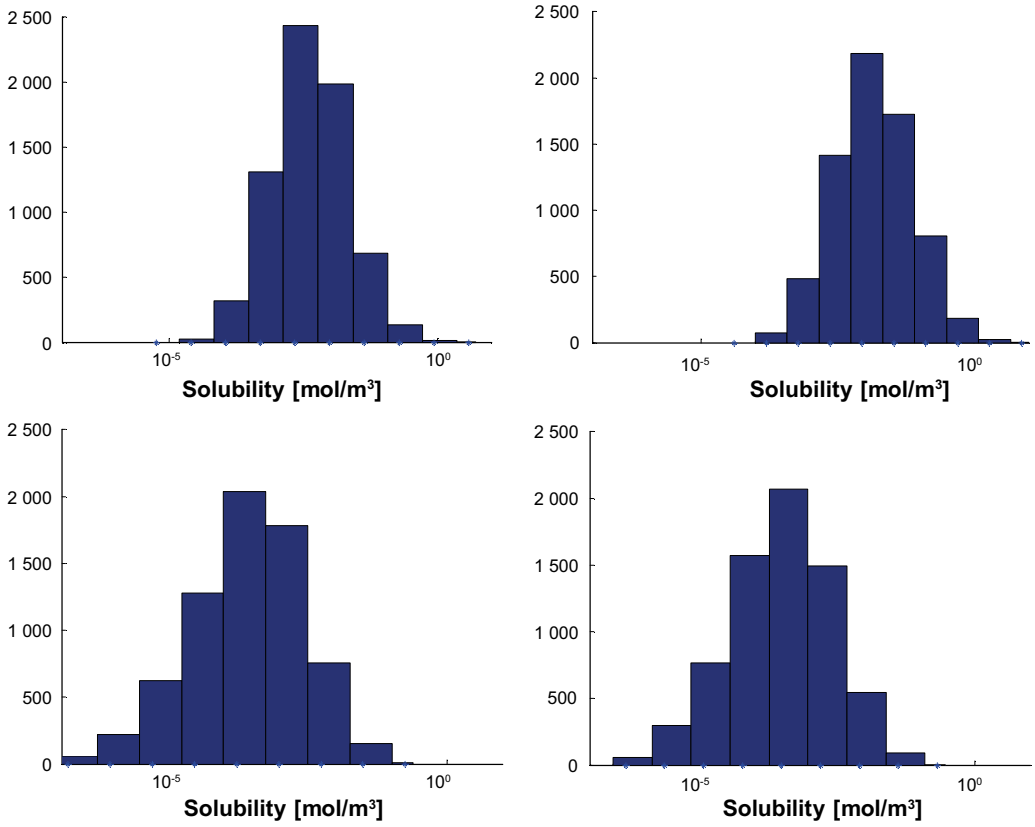

Figure F-3. *Solubility limits for Pu using groundwater data from temperate conditions (upper left), permafrost conditions (upper right), glacial conditions (lower left) and submerged conditions (lower right). The y-axis shows the number of realisations in each bin.*

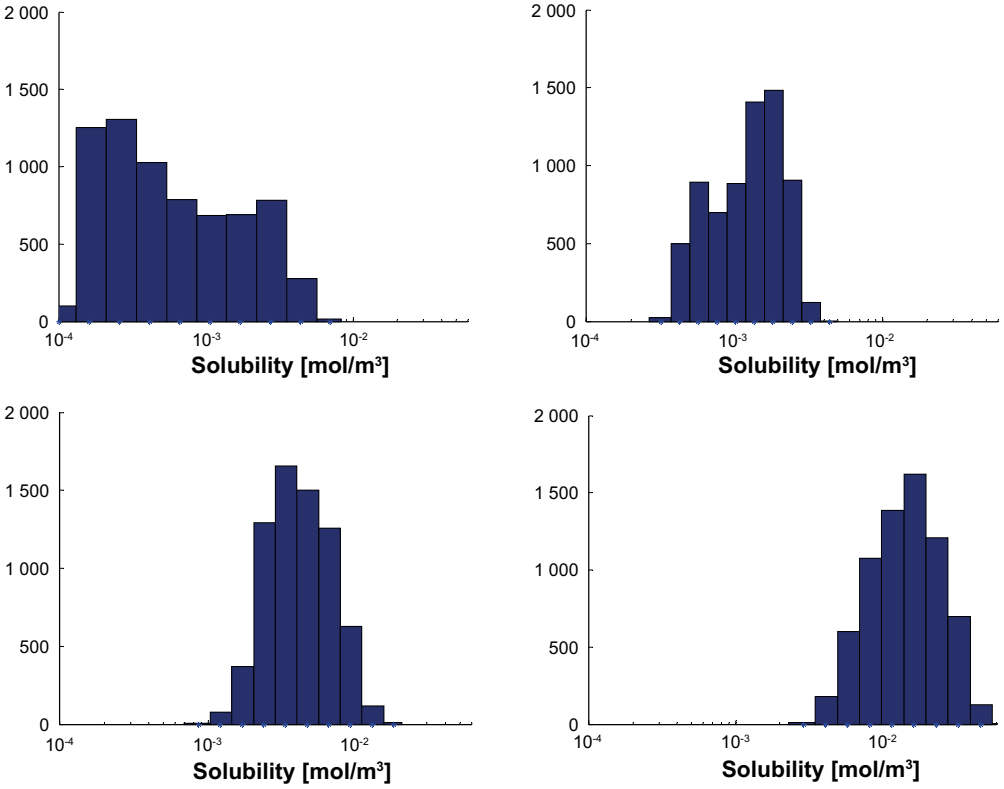

Figure F-4. *Solubility limits for Ra using groundwater data from temperate conditions (upper left), permafrost conditions (upper right), glacial conditions (lower left) and submerged conditions (lower right). The y-axis shows the number of realisations in each bin.*

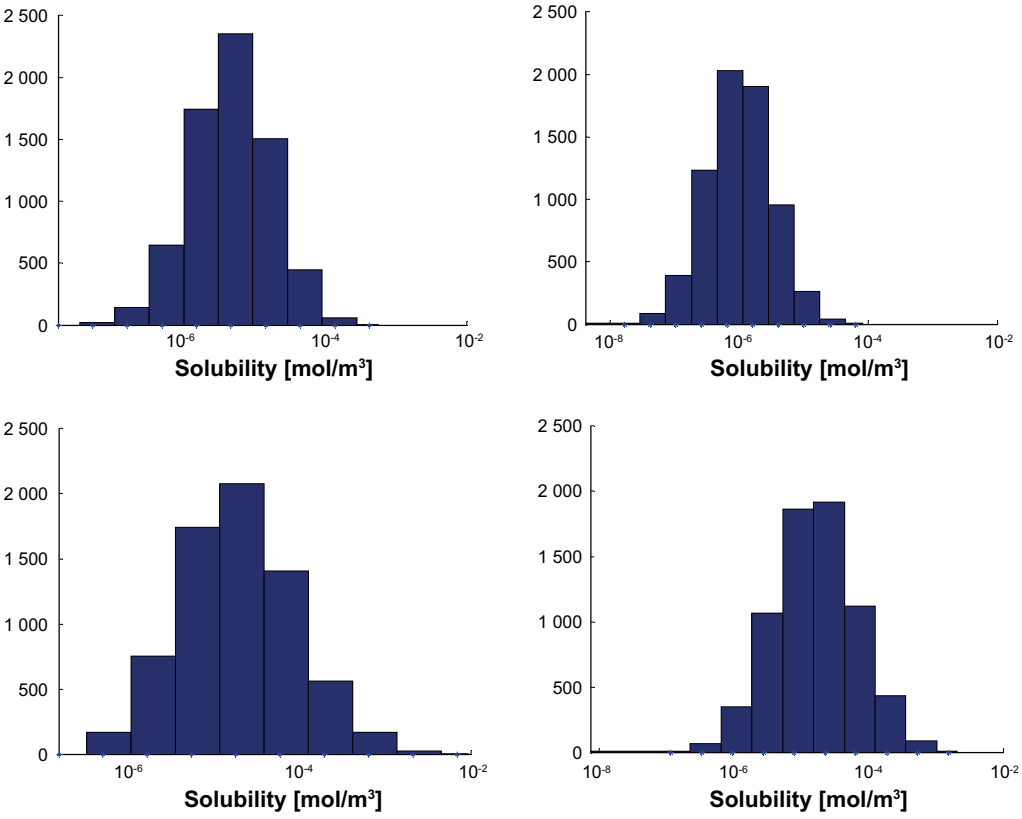

Figure F-5. *Solubility limits for Se using groundwater data from temperate conditions (upper left), permafrost conditions (upper right), glacial conditions (lower left) and submerged conditions (lower right). The y-axis shows the number of realisations in each bin.*

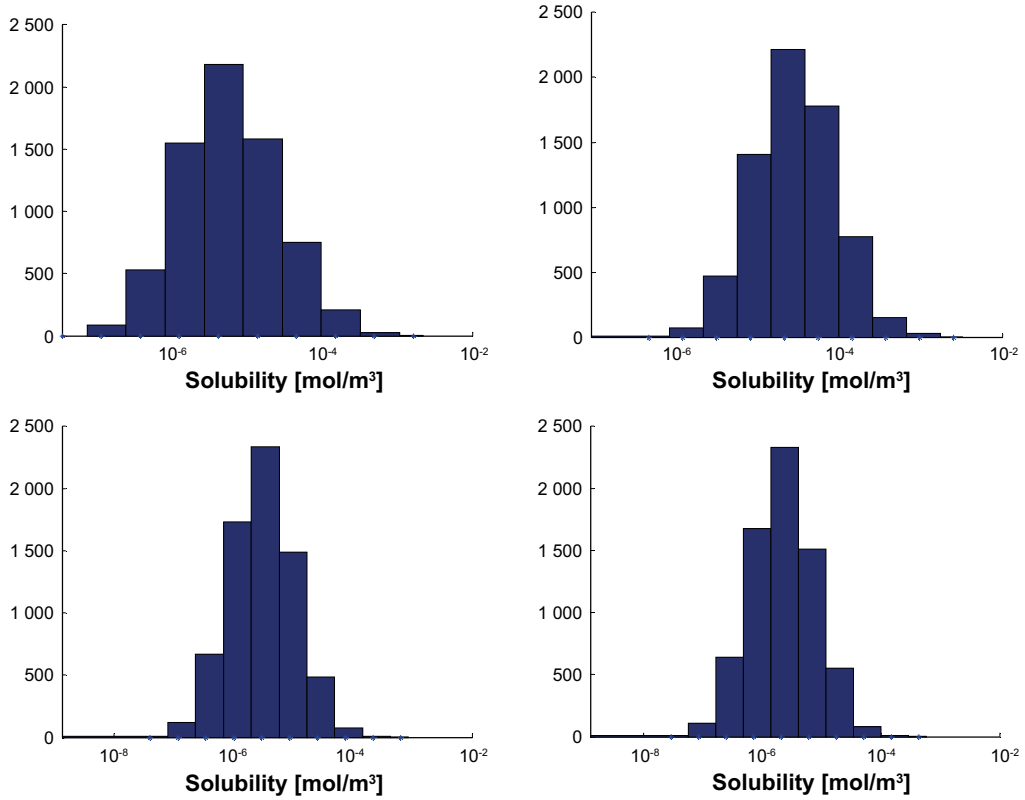

Figure F-6. *Solubility limits for Th using groundwater data from temperate conditions (upper left), permafrost conditions (upper right), glacial conditions (lower left) and submerged conditions (lower right). The y-axis shows the number of realisations in each bin.*

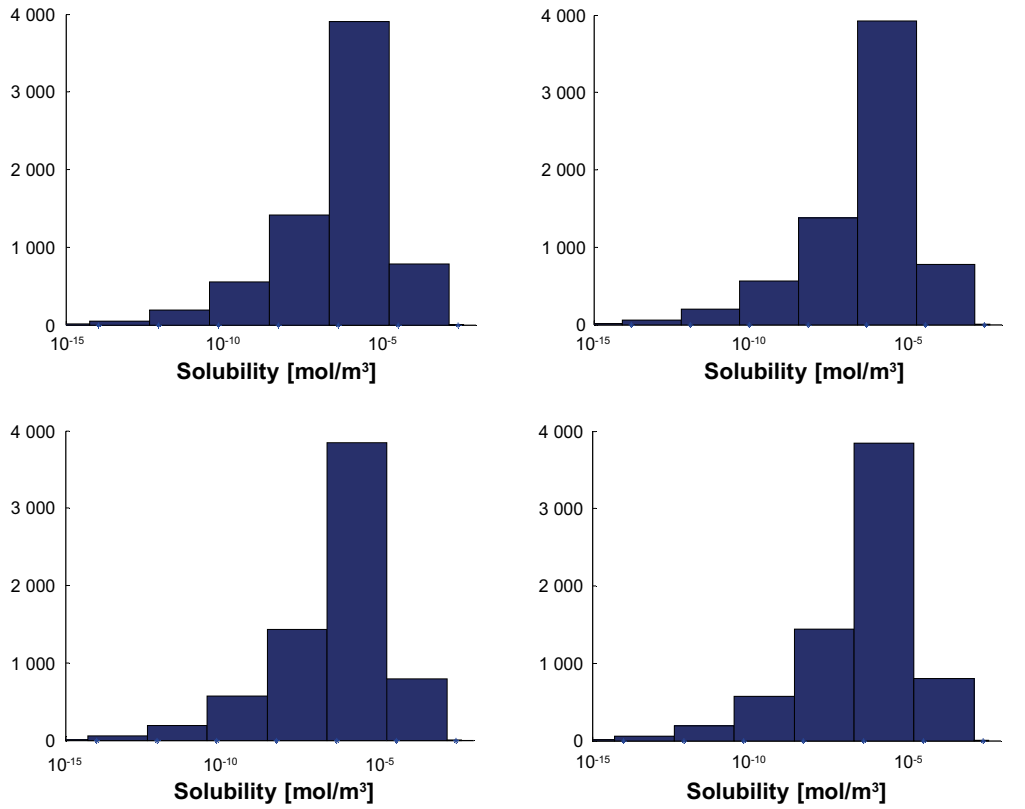

Figure F-7. *Solubility limits for U using groundwater data from temperate conditions (upper left), permafrost conditions (upper right), glacial conditions (lower left) and submerged conditions (lower right). The y-axis shows the number of realisations in each bin.*

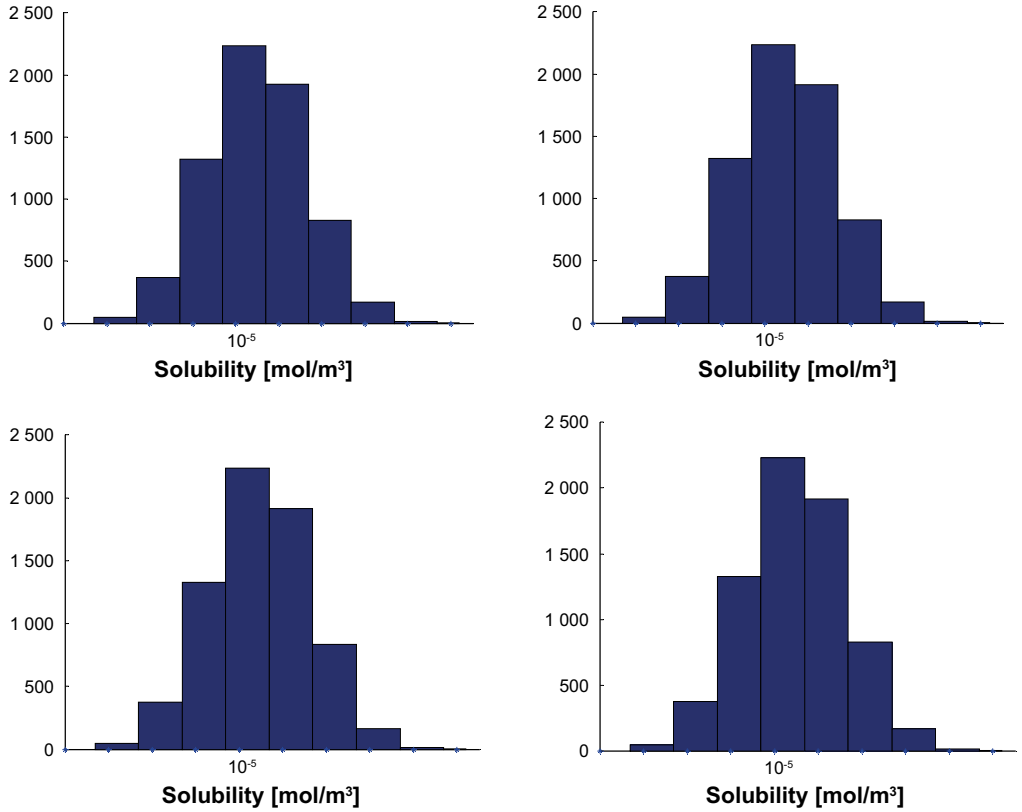

Figure F-8. *Solubility limits for Zr using groundwater data from temperate conditions (upper left), permafrost conditions (upper right), glacial conditions (lower left) and submerged conditions (lower right). The y-axis shows the number of realisations in each bin.*

To investigate the impact of the equilibrium constants, a representative groundwater composition from the temperate period was used as input, see Table F-2. This composition was kept the same for 6 916 iterations whereas a normal distribution was applied to the equilibrium constants. The resulting solubility limits were compared to the solubility limits calculated using 6 916 groundwater compositions sampled from the files in Table F-1 for the temperate climate conditions, but with the equilibrium constants unvarying (without any distribution). The solubilities for the two alternatives are compared in Figure F-9 to Figure F-16 for the elements: Np, Pb, Pu, Ra, Se Th, U and Zr.

It should be noted that the use of independent normal distributions for the uncertainties in the equilibrium constants will in general overestimate the uncertainties in the resulting solubility limits, because as discussed for example in Ekberg et al. (2011), equilibrium constants are correlated. However, because correlation data are in general not published, it is not possible to apply correlated uncertainties in the equilibrium constants. The striking difference in the distributions presented in Figures F-9 to F-16 indicates that a slight overestimation of uncertainty in equilibrium constants (by neglecting their unknown correlations), would not change the overall picture of the influence of uncertainties. The conclusion is nevertheless that the variability in groundwater compositions has less influence on the solubility limits than the reported uncertainties in the equilibrium constants.

Table F-2. Temperate groundwater composition used in Figure F-9 to Figure F-16.

Input parameters	
pH	7.43
Eh (mV)	–437
IS (mol/kg)	2.25×10^{-1}
$[HCO^{3-}]$ (m)	3.20×10^{-4}
$[SO_4^{-2}]$tot (m)	1.58×10^{-3}
$[Cl]_{tot}$ (m)	1.66×10^{-1}
$[Ca]_{tot}$ (m)	5.12×10^{-2}
$[Na]_{tot}$ (m)	6.47×10^{-2}
$[Si]_{tot}$ (m)	1.28×10^{-4}

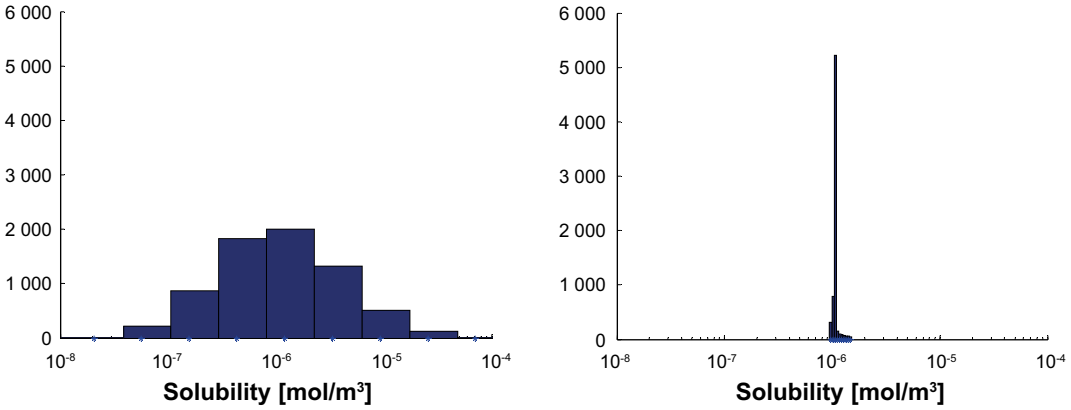

Figure F-9. *Solubility limits for Np using groundwater data from temperate conditions. Fixed groundwater composition and varying thermodynamic data (left). Varying groundwater composition and fixed thermodynamic data (right). The y-axis shows the number of realisations in each bin.*

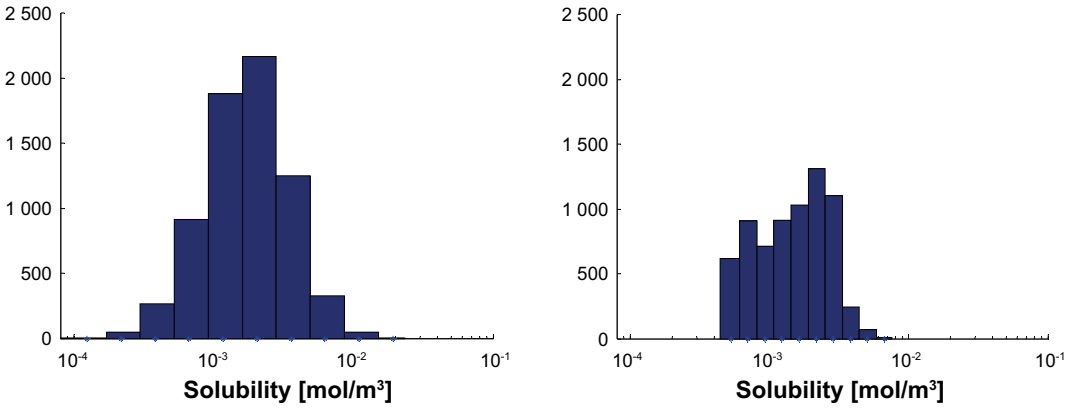

Figure F-10. *Solubility limits for Pb using groundwater data from temperate conditions. Fixed groundwater composition and varying thermodynamic data (left). Varying groundwater composition and fixed thermodynamic data (right). The y-axis shows the number of realisations in each bin.*

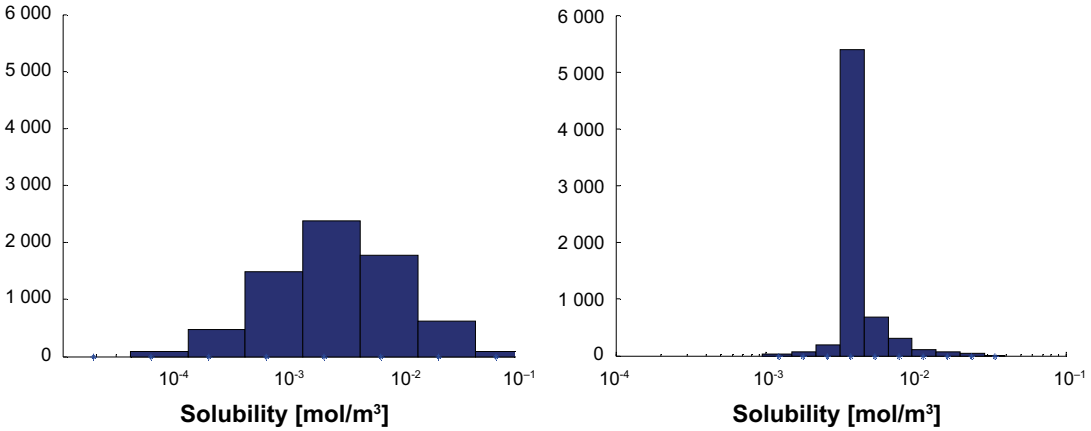

Figure F-11. *Solubility limits for Pu using groundwater data from temperate conditions. Fixed groundwater composition and varying thermodynamic data (left). Varying groundwater composition and fixed thermodynamic data (right). The y-axis shows the number of realisations in each bin.*

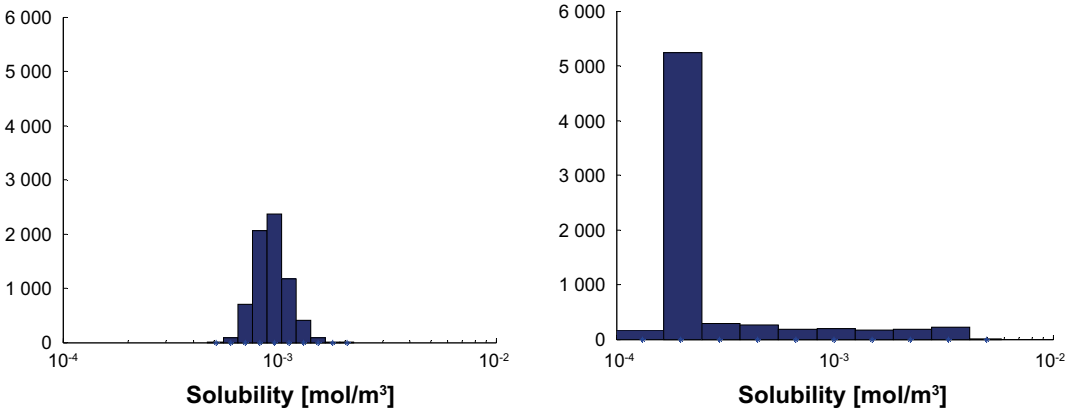

Figure F-12. *Solubility limits for Ra using groundwater data from temperate conditions. Fixed groundwater composition and varying thermodynamic data (left). Varying groundwater composition and fixed thermodynamic data (right). The y-axis shows the number of realisations in each bin.*

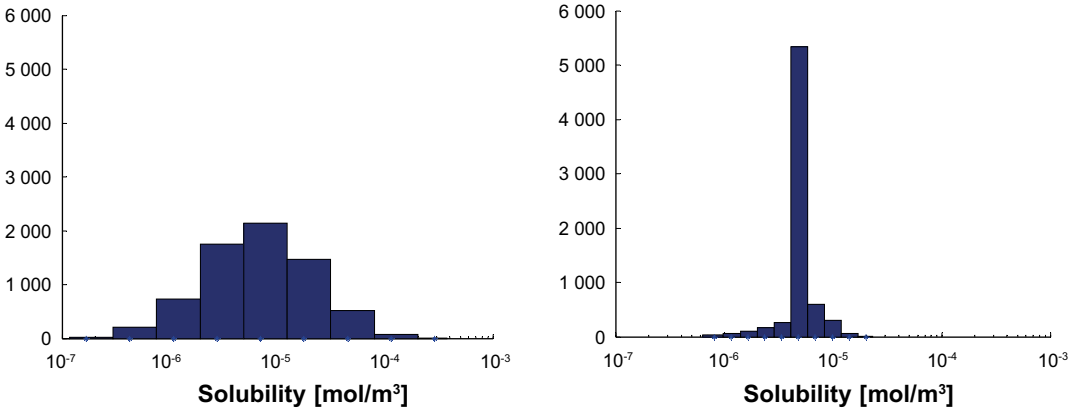

Figure F-13. *Solubility limits for Se using groundwater data from temperate conditions. Fixed groundwater composition and varying thermodynamic data (left). Varying groundwater composition and fixed thermodynamic data (right). The y-axis shows the number of realisations in each bin.*

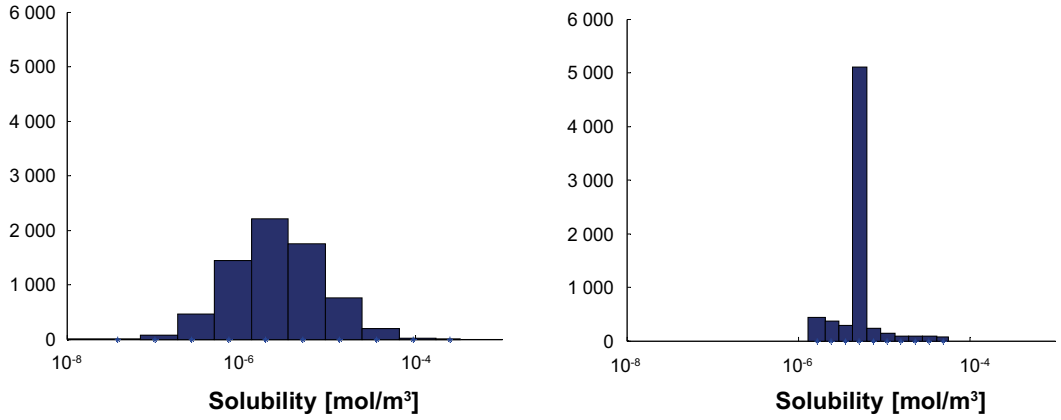

Figure F-14. *Solubility limits for Th using groundwater data from temperate conditions. Fixed groundwater composition and varying thermodynamic data (left). Varying groundwater composition and fixed thermodynamic data (right). The y-axis shows the number of realisations in each bin.*

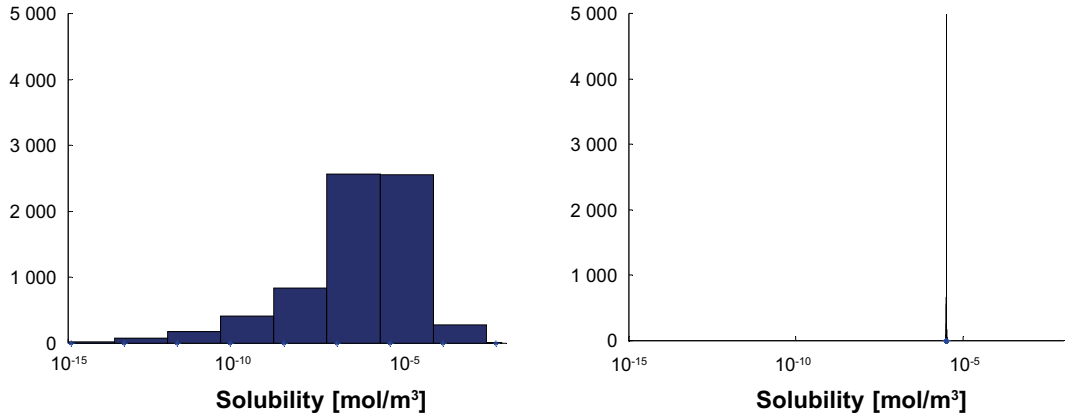

Figure F-15. *Solubility limits for U using groundwater data from temperate conditions. Fixed groundwater composition and varying thermodynamic data (left). Varying groundwater composition and fixed thermodynamic data (right). The y-axis shows the number of realisations in each bin.*

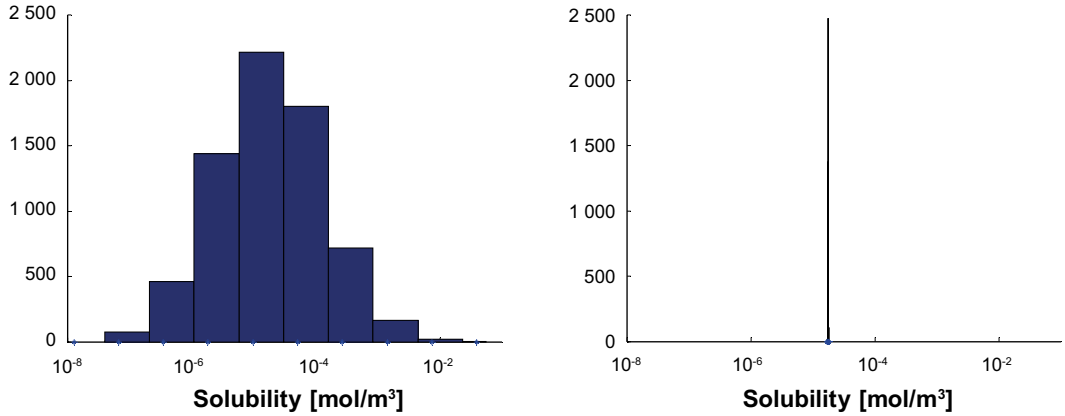

Figure F-16. *Solubility limits for Zr using groundwater data from temperate conditions. Fixed groundwater composition and varying thermodynamic data (left). Varying groundwater composition and fixed thermodynamic data (right). The y-axis shows the number of realisations in each bin.*

F.4 Modelling of solubility limits

COMP23 does not allow changes in solubility limits with time. Therefore, groundwater compositions representative all climate periods (temperate, permafrost, glacial and submerged) must be chosen when performing the solubility limit calculations for the safety assessment. As shown in Figures F-9 to F-16 for the temperate period, the uncertainty in the solubility limits is in general more affected by variation in thermodynamic data than by the variations in groundwater composition. Thus, the choice of groundwater compositions for the solubility limits should be of lesser importance. The solubility limits for the safety assessment were thus calculated by sampling groundwater compositions representing 25 % of temperate climate, 25 % of permafrost climate, 25 % of glacial climate and 25 % of submerged climate, see also Table F-1. The calculated solubility limits used in the radionuclide transport calculations in the safety assessment are shown in Figure F-17 to Figure F-26.

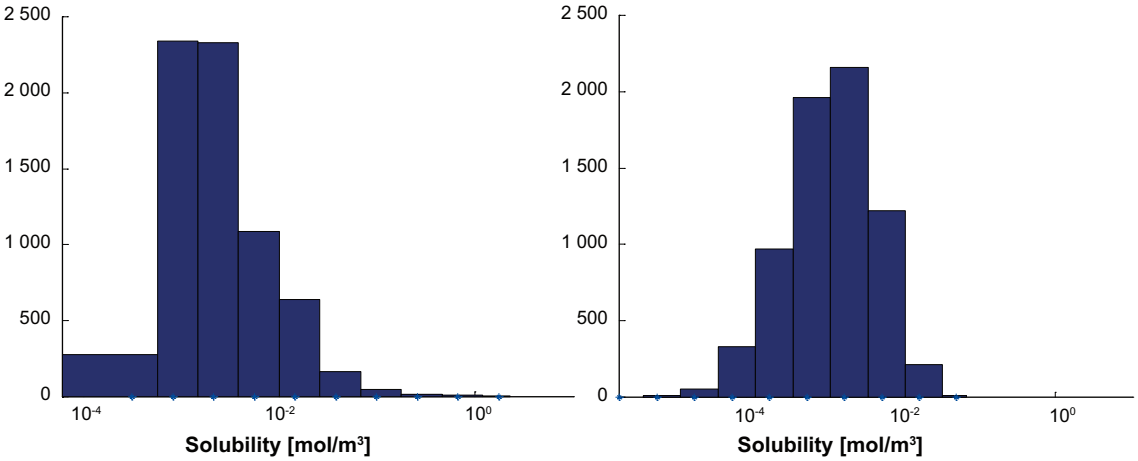

Figure F-17. *Solubility limits for Ag (left) and Am (right) used as input data for COMP23. The y-axis shows the number of realisations in each bin.*

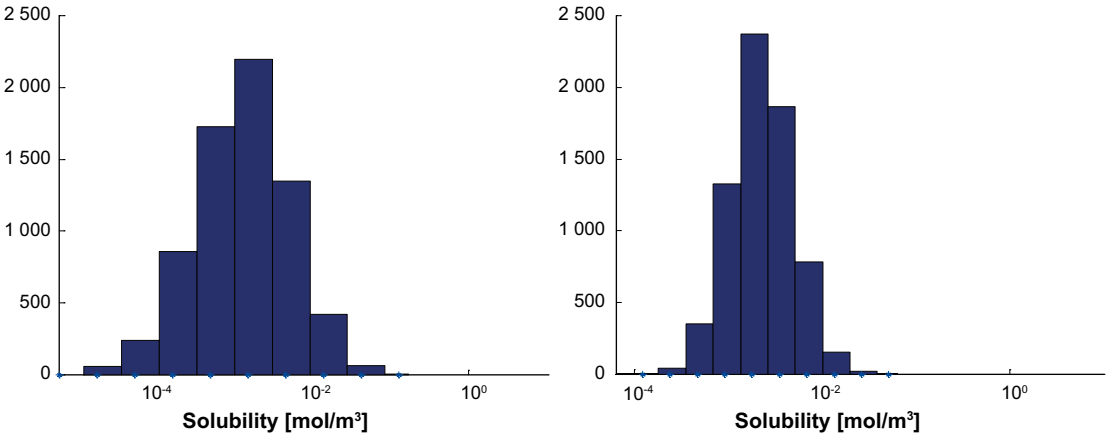

Figure F-18. *Solubility limits for Cm (left) and Ho (right) used as input data for COMP23. The y-axis shows the number of realisations in each bin.*

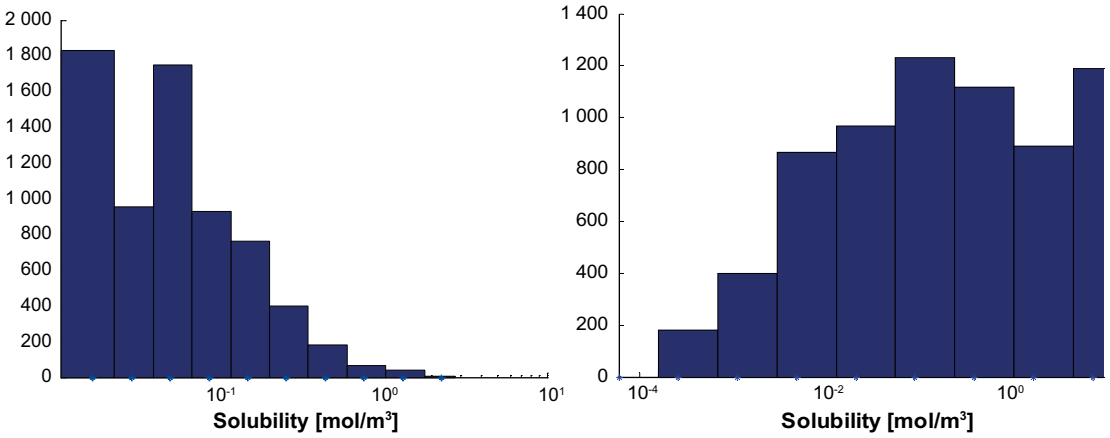

Figure F-19. *Solubility limits for Nb (left) and Ni (right) used as input data for COMP23. The y-axis shows the number of realisations in each bin.*

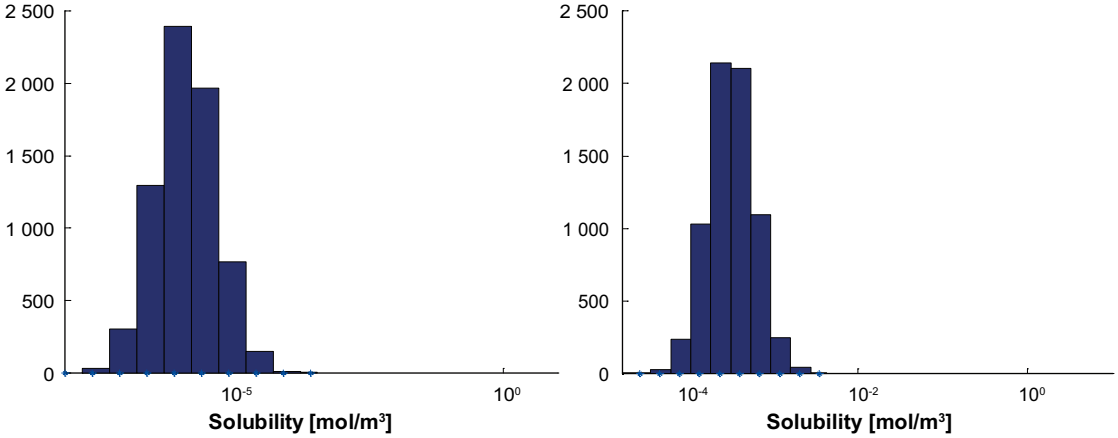

Figure F-20. *Solubility limits for Np (left) and Pa (right) used as input data for COMP23. The y-axis shows the number of realisations in each bin.*

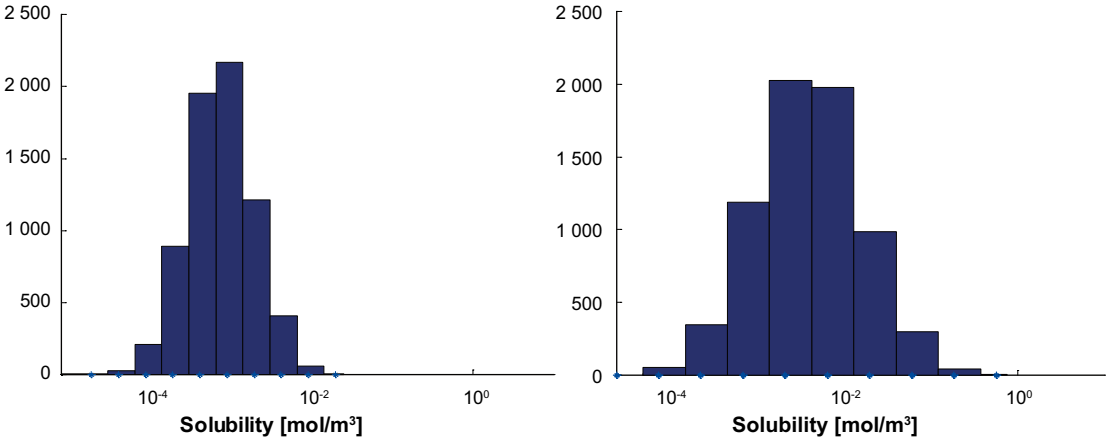

Figure F-21. *Solubility limits for Pb (left) and Pd (right)used as input data for COMP23. The y-axis shows the number of realisations in each bin.*

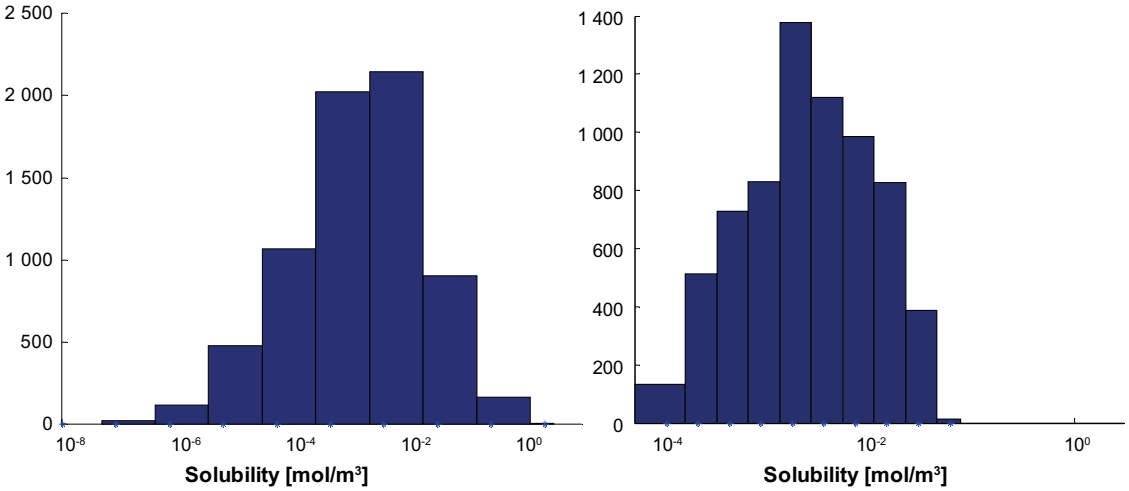

Figure F-22. *Solubility limits for Pu (left) and Ra (right) used as input data for COMP23. The y-axis shows the number of realisations in each bin.*

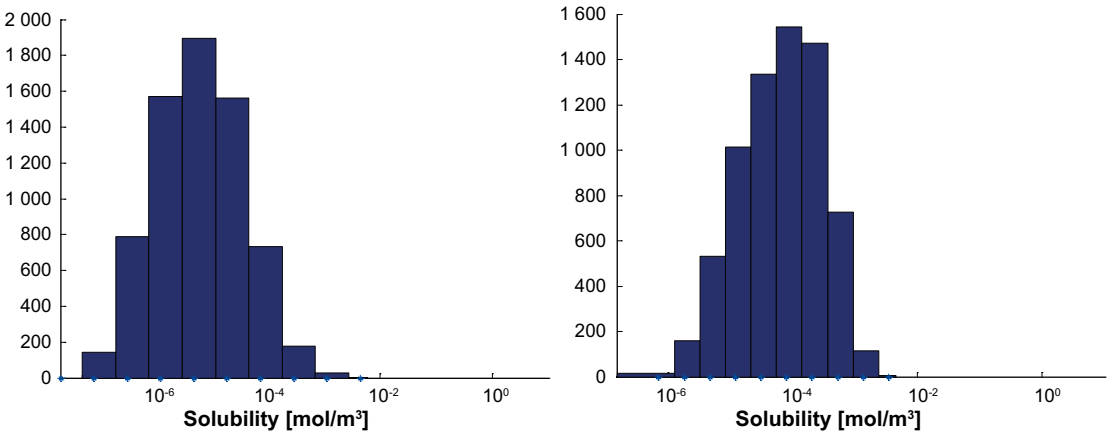

Figure F-23. *Solubility limits for Se (left) and Sm (right) used as input data for COMP23. The y-axis shows the number of realisations in each bin.*

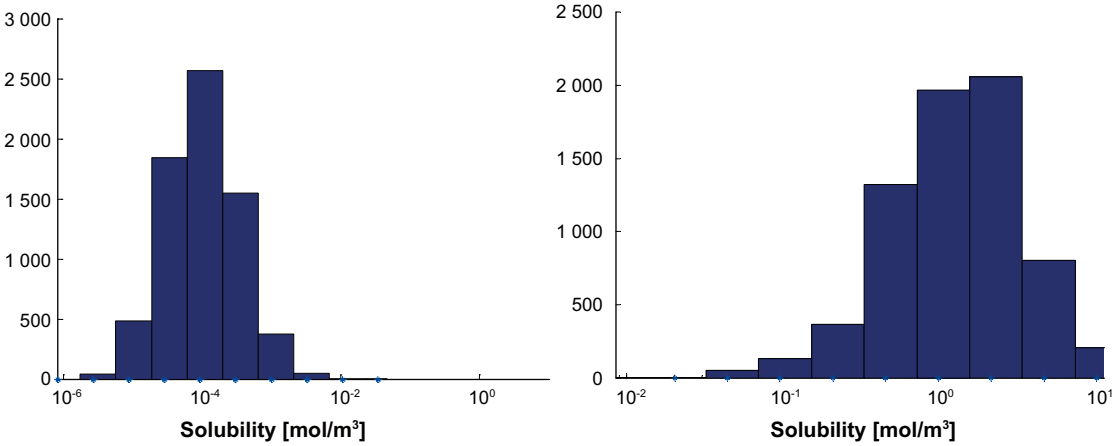

Figure F-24. *Solubility limits for Sn (left) and Sr (right) used as input data for COMP23. The y-axis shows the number of realisations in each bin.*

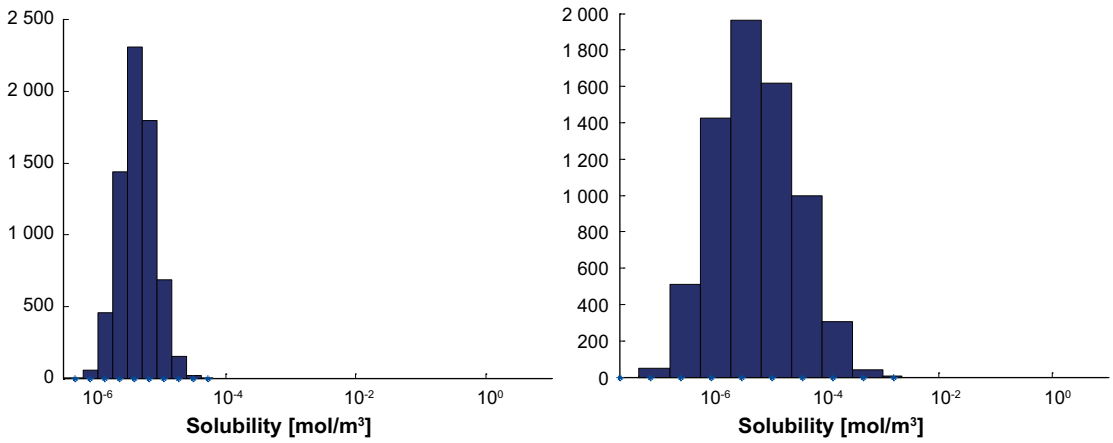

Figure F-25. *Solubility limits for Tc (left) and Th (right) used as input data for COMP23. The y-axis shows the number of realisations in each bin.*

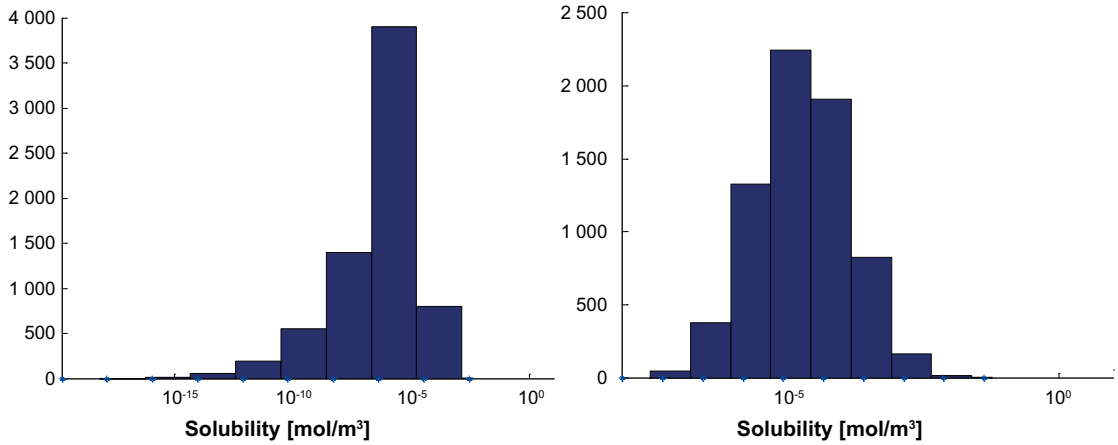

Figure F-26. *Solubility limits for U (left) and Zr (right) used as input data for COMP23. The y-axis shows the number of realisations in each bin.*

F.5 Applied solubility limits

As radionuclides of the same element have identical chemical properties, the solubility limits are calculated for elements instead of nuclides. If more than one nuclide of the same element appears in the calculations, the solubility limit is shared proportionally between the nuclides. Hence, the solubility limit for a single nuclide is changing with time and is handled by COMP23.

In calculation cases without any solubility limits all limits were set to 1×10^{20} mol/m^3. In calculations with low solubility limits the limit was set to 1×10^{-27} mol/m^3.

F.5.1 Uranium

The solubility limit of uranium governs the stability of the UO_2 fuel matrix. Therefore the solubility limit for U calculated above was applied unmodified in all calculation cases.

F.5.2 Radium

Co-precipitation between radium and barium

To take into account for the Ba-Ra co-precipitation described in the **Fuel and canister process report** in the process "Speciation of radionuclides, colloid formation" the recommendation from the **Data report** was applied in the calculations. The recommendation in the **Data report** is to use the Simple Functions spread-sheet with $RaSO_4$ (s) as the solubility-limiting phase, and to multiply the outcome by a factor of 0.001.

F.5.3 Silver

The decrease of solubility of silver described below is only used in SR-Site.

Decrease of solubility for Ag-108m due to high content of stable Ag

The solubility limit calculated for silver is valid for the total amount of silver. Since most of the silver is stable and only part of the silver is in the form of Ag-108m, it is possible to decrease the solubility for Ag-108m in proportion to the amount of total silver. Below is an estimate of the ratio between Ag-108m and total silver.

Amount of total Ag

Most of the silver, both stable and radioactive, is present in absorber pins in the PWR rod clusters. The absorber pins are made of an alloy with 80 % Ag 15 % In and 5 % Cd (**Spent fuel report**, Table B-5). The total weight of this alloy is 51.4 kg/PWR canister (**Spent fuel report**, Table B-5) and hence the weight of Ag is 41.1 kg/PWR canister.

The average canister used in the calculations is calculated from the assumption of a total 6 103 canisters, whereof 1 652 are PWR, i.e. 27 % of the canisters are PWR canisters (**Spent fuel report**, Table B-5).

The mol weight of Ag is 108 g/mol

Together this means that the amount of silver in an average canister is $41.1 \times 10^3/108 \times 0.27 = 103$ mol/canister.

Amount of Ag-108m

The initial inventory of Ag-108m is 0.431 mol/canister (average canister).

Decrease of solubility for Ag-108m

The decrease of the solubility is calculated from the ratio between the amounts of Ag-108m and total silver, which is about 1/250.

Comment

Looking at only BWR canisters, the content of silver is very low, less than 10^{-5} mol/canister, and hence the concentration will probably not reach the solubility limit.

Looking at only PWR canisters, the ratio between Ag-108m and total silver is equal to the average canister, since both the amount of Ag-108m and total silver are about 4 times higher.

Appendix G

Discretisation, diffusion resistances and boundary conditions used in COMP23

This appendix has not been changed since the SR-Site assessment. In a few places, references in the SR-Site version were made to the main references of the SR-Site assessment, the references written in bold. It has been verified that the PSAR versions of the corresponding reports are equally valid as references in these cases. The references in bold, therefore, refer to the PSAR versions.

G.1 Geometry

The geometry data of importance for the near-field radionuclide transport calculations is summarised in Table G-1.

Table G-1. Dimensions used to describe the geometry of the near field.

Parameter	Value	Reference
Height of the canister	4.835 m	Reference design from the **Canister production report**
Outer diameter of the canister	1.05 m	Reference design from the **Canister production report**
Thickness of canister wall	0.05 m	Reference design from the **Canister production report**
Void inside canister	1.0 m^3	**Data report**, Section 4.1
Diameter of the deposition hole	1.75 m	SKB 2010e, Figure 2-1
Thickness of buffer outside canister	0.35 m	Reference design from the **Buffer production report**, Figure 3-3
Height of buffer below canister in deposition hole	0.5 m	Reference design from the **Buffer production report**, Figure 3-3
Height of buffer above the canister in the deposition hole	1.5 m	Reference design from the **Buffer production report**, Figure 3-3
Height of backfill above the canister and buffer in the deposition hole	1.25 m	SKB 2010e, Figure 5-2
Height of the deposition tunnel	4.8 m	SKB 2010e, Figure 2-2
Width of the deposition tunnel	4.2 m	SKB 2010e, Figure 2-2

G.2 Growing pinhole – no spalling

COMP23 is a multiple-path model that calculates transient radionuclide transport in the near field of a repository system by use of a network of coupled resistances and capacitances in analogy with an electrical circuit network. Analytical solutions, instead of fine discretisation, at sensitive zones, i.e. at the exit point of the canister hole and at the entrance to fractures, are embedded to enhance calculation speed. A schematic picture of the transport path straight out from the canister, i.e. from a defect canister through the buffer and into flowing water in fracture rock is given in Figure G-1.

Discretisation

A schematic picture of the modelled system in the case with growing pinhole failure without including the effect of spalling is given in Figure G-2. Each block consists of one compartment or several sub-compartments, see Figure G-3.

COMP23 has the possibility to calculate the radionuclide transport in up to three dimensions. Since the geometry of the modelled system consists of compartments with a cylindrical shape, the geometry can be described in two dimensions, axial and radial.

z-direction has been assigned as the axial direction
x-direction has been assigned as the radial direction

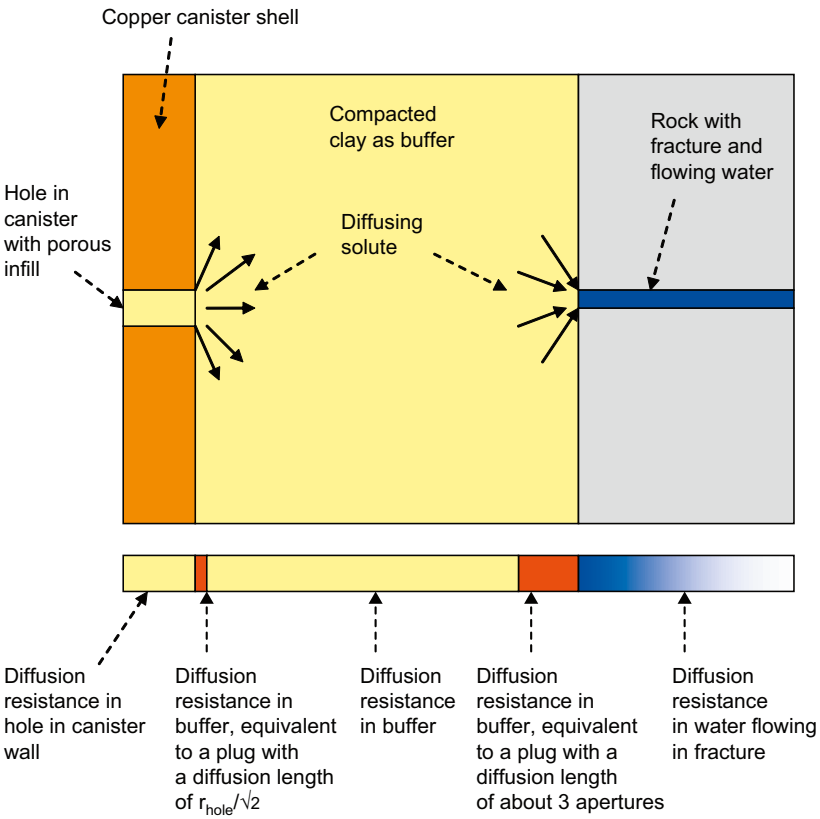

Figure G-1. *Transport from a defect canister through the buffer and into a flowing water in fracture rock (modified from Neretnieks (2006) and Neretnieks et al. (2010)).*

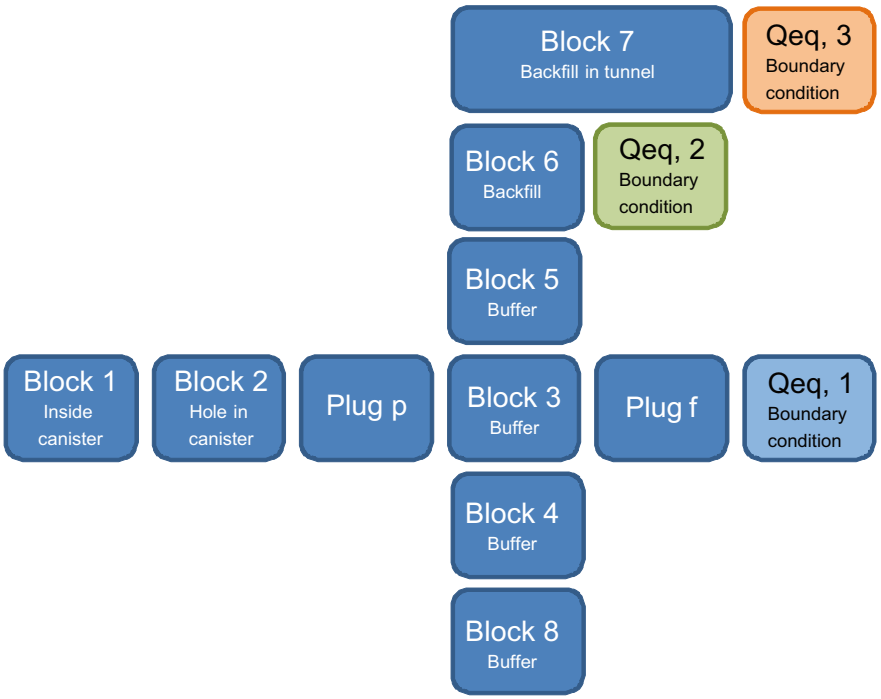

Figure G-2. *Schematic picture of the blocks, plugs and boundary conditions in the case with growing pinhole failure without including the effect of spalling.*

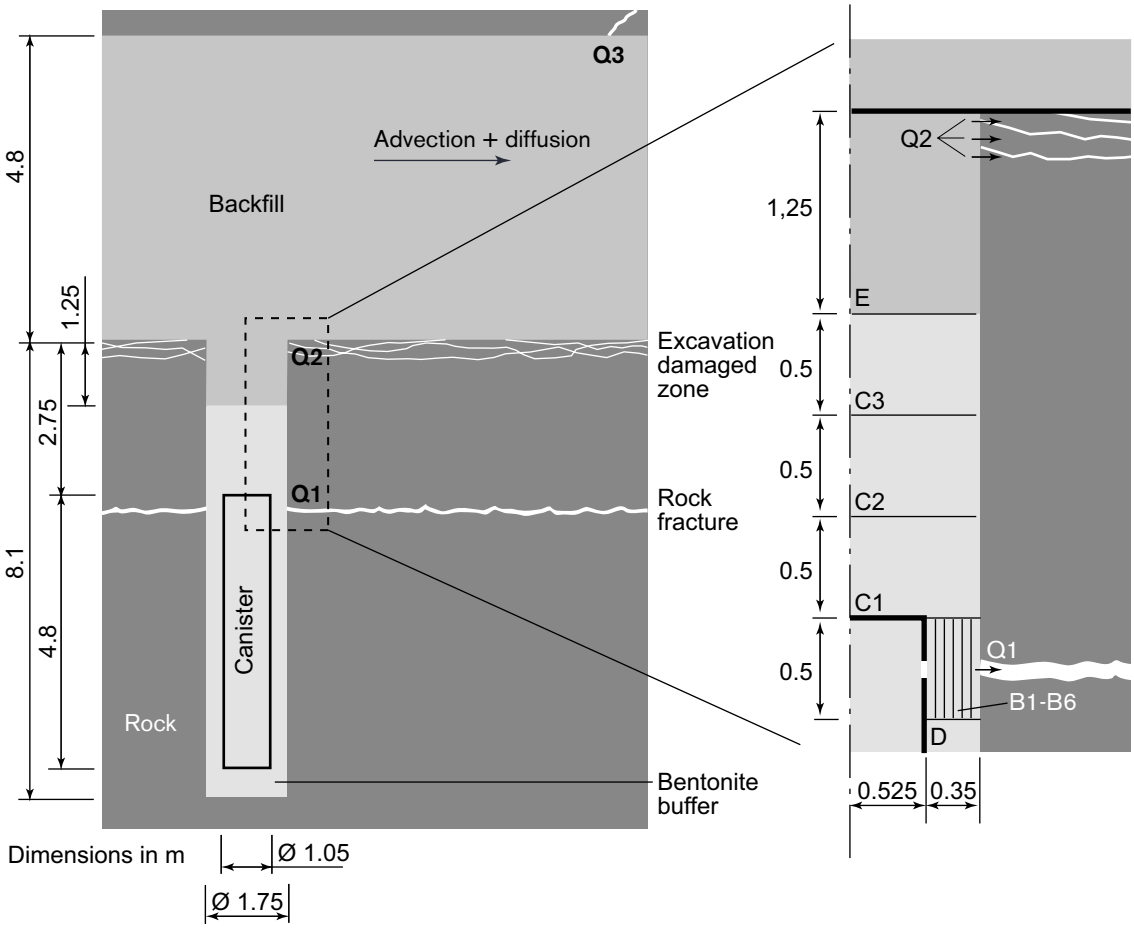

Figure G-3. *Schematic picture of the compartments (including sub-compartments) B1-B6, C1-C3, D and E in the case with growing pinhole failure. The transport paths Q1, Q2 and Q3 to a fracture intersecting the deposition hole, to the excavation damaged zone, and to a fracture intersecting the deposition tunnel, respectively, are also shown.*

The transport resistance in the y-direction is neglected by assigning Y_LENGTH to zero and Y_AREA to 1 for all compartments.

Block 1 is the internal of the canister, no transport resistance is assumed and hence Z_LENGTH and X_LENGTH are set to zero and Z_AREA and X_AREA are 1. A void volume of 1 m^3 was used.

Block 2 is the hole in the canister wall. It is assumed to be a horizontal cylinder. Thus, the Z-direction is horizontal. No transport resistance is assumed in radial direction and hence X_LENGTH is set to zero and X_AREA is 1. Z_LENGTH is the length of the hole, i.e. corresponding to the thickness of the canister wall, 0.05 m. Z_AREA is the diffusion area in the z-direction, i.e. the size of the hole. The initial size of the hole is 10^{-5} m^2 and at 10 000 years, TLARGE, the hole momentarily grows to unlimited size (set to 100 m^2), i.e. the diffusion resistance in the hole according to Cliffe and Kelley (2006, Equation 35) is 0.02 yr/m^3,which is considered as negligible. The hole is assumed to be filled with water.

Block 3 is the buffer outside the hole. It has a shape of a standing cylindrical shell. Z-direction is vertical. The sub-compartments are defined with equal thicknesses of the cylindrical shells. The diffusion lengths in the radial direction X_LENGTH, i.e. from the hole to the fracture, Q1, are equal for all sub-compartments, 0.35/6 = 0.058 m. The diffusion area for transport in the radial direction X_AREA is calculated as the average envelope surface of the cylindrical shells, i.e. $2 \cdot \pi \cdot (r_o + r_i)/2 \cdot h$, where r_o is the outer radii, r_i is the inner radii and h is the height of the sub-compartments i.e. equal to Z_LENGTH. The transport in the z-direction is described by the diffusion length Z_LENGTH that is set to be 0.5 m and by the diffusion area Z_AREA, i.e. the end surface of the cylindrical shells, $\pi \cdot (r_o^2 - r_i^2)$. The parameters for block 3 together with the outer and inner radius are given in Table G-2.

Table G-2. Dimensions used for Block 3.

Sub-compartment number	Z_LENGTH	Z_AREA	X_LENGTH	X_AREA	Inner radii, r_i	Outer radii, r_o
1	0.500	0.203	0.058	1.741	0.525	0.583
2	0.500	0.224	0.058	1.924	0.583	0.642
3	0.500	0.246	0.058	2.107	0.642	0.700
4	0.500	0.267	0.058	2.291	0.700	0.758
5	0.500	0.289	0.058	2.474	0.758	0.817
6	0.500	0.310	0.058	2.657	0.817	0.875

Block 4 is the buffer outside the canister below the hole in the canister. It has the shape of a standing cylindrical shell. Z-direction is vertical. No transport resistance is assumed in the radial direction and hence X_LENGTH is set to zero and X_AREA is 1. The diffusion length in the z-direction, Z_LENGTH, is the height of the cylindrical shell. Two sub-compartments were made, the upper 1 m and the lower 3.33 m. The diffusion area, Z_AREA, corresponds to the end surface of the cylindrical shell, $\pi \cdot (r_o^2 – r_i^2) = \pi \cdot (0.875^2 – 0.525^2) = 1.539$ m^2.

Block 5 is the buffer above the canister. It has the shape of a standing cylinder. Z-direction is vertical. It has been divided into three sub-compartments, with equal height. No transport resistance is assumed in the radial direction and hence X_LENGTH is set to zero and X_AREA is 1. The diffusion length in the z-direction, Z_LENGTH, is equal to the height, i.e. 0.5 m for each sub-compartment. The diffusion area Z_AREA is the end surface of the cylinder, $\pi \cdot r^2 = \pi \cdot 0.875^2 = 2.405$ m^2.

Block 6 is the backfill above the buffer above the canister. It has the shape of a standing cylinder. Z-direction is vertical. Transport is assumed in both directions. In the radial direction the transport is described by the diffusion length X_LENGTH, that corresponds to the diameter of the cylinder, 1.75 m, and by the diffusion area X_AREA, that corresponds to the envelope surface of the cylinder $2 \cdot \pi \cdot r \cdot h = 2 \cdot \pi \cdot 0.875 \cdot 1.25 = 6.872$ m^2. The transport in the z-direction is described by the diffusion length Z_LENGTH that corresponds to the height of the cylinder, 1.25 m, and by the diffusion area Z_AREA corresponding to the end surface of the cylinder, $\pi \cdot r^2 = \pi \cdot 0.875^2 = 2.405$ m^2.

Block 7 is the backfill in the tunnel. This part of the modelled near-field system has a large volume in comparison with the other blocks. To avoid a detailed discretisation without underestimation of the release, due to large dilution volume and large transport resistance, the upper part of the tunnel has been neglected. Block 7 has been assigned the shape of a horizontal cylinder, with a diameter of 2 m. The Z-direction is horizontal. Transport is assumed in both directions. Block 7 starts with a sub-compartment upstream the deposition hole followed by a sub-compartment above the deposition hole and thereafter a number of compartments depending on the distance between the deposition hole and the first fracture in the tunnel. The diffusion length of the sub-compartments in the z-direction, Z_LENGTH, are 2.125 m for the upstream sub-compartment, 1.75 m for the sub-compartment above the deposition hole and the downstream sub-compartments are dependent on the distance between the deposition holes and the first fracture in tunnel, see Section G.7. The diffusion area, Z_AREA, is the end surface area of the cylinder, i.e. $\pi \cdot r^2 = \pi \cdot 2^2 = 12.6$ m^2. The diffusion length in the radial direction, X_LENGTH, has been assigned the value 2 m. The diffusion area, X_AREA, has been calculated as the envelope surface for the outer diameter $2 \cdot \pi \cdot r \cdot h$, i.e. $2 \cdot \pi \cdot 2 \cdot 2.125 = 26.7$ m^2 for the upstream sub-compartment, $2 \cdot \pi \cdot 2 \cdot 1.75 = 22.0$ m^2 for the sub-compartment above the deposition hole and $2 \cdot \pi \cdot 2 \cdot l_i$ m^2 for the downstream sub-compartments, where l_i is the length of sub-compartment i.

Advective transport is assumed in Block 7.

Block 8 is the buffer below the canister. It has the shape of a standing cylinder. The Z-direction is vertical. The transport in the radial direction is neglected. The transport in the z-direction is described by the diffusion length Z_LENGTH, i.e. the height of the cylinder 0.5 m, and the diffusion area Z_AREA that is the end surface of the cylinder, $\pi \cdot r^2 = \pi \cdot 0.875^2 = 2.405$ m^2.

Transport from the hole into the buffer

The transport of species through the canister hole would require a fine discretisation in a pure compartment model. To make the model more computationally effective, the transport out through the canister hole is instead treated analytically.

Species diffusing out from a circular hole are spread out spherically. Near the hole, the cross sectional area is still of the order of the size of the hole. Further away, the cross section increases as the ”sphere” grows. Thus, most of the resistance to diffusion is concentrated near the mouth of the hole. In the model this is handled by using a plug with a resistance, R_p, between the compartments representing the water in the hole and the buffer outside the canister (Romero et al. 1995).

$$R_p = \frac{d}{AD_e} = \left\{ A = A_{hole} = \pi r_{hole}^2 \text{ and } d = \frac{r_{hole}}{\sqrt{2}} \right\} = \frac{1}{\pi r_{hole} D_e \sqrt{2}} \qquad \text{G-1}$$

where

d is the diffusion length of the plug (m) (set equal to $r_{hole}/\sqrt{2}$)

A is the diffusion area (m^2) (set equal to the area of the hole, A_{hole})

D_e is the effective diffusivity in the buffer (m^2/s)

r_{hole} is the radius of the hole (m).

The diffusion area, which has been set fictitiously at a high value to obtain negligible resistance, is 100 m^2, which gives the hole a radius of 5.6 m. With effective diffusivity for bentonite as 4.2×10^{-3} m^2/yr for Ra-226 in the deterministic case, Equation G-1 gives R_p as 9.5 yr/m^3, which is considered as negligible.

Transport into a narrow fracture

For the diffusive transport into a narrow fracture, most of the resistance to transport will be located nearest to the fracture. Again, a fine discretisation is avoided by adding a plug. An analytical model (Neretnieks 1986), solving the steady-state two-dimensional diffusion equations for a sector of the buffer representing half the fracture spacing, was used to derive a simplified expression for the plug resistance. The resulting expression for the plug resistance is:

$$R_f = \frac{\left(F_{x,0}/b\right)b}{D_e A_f} \qquad \text{G-2}$$

where

b is the half-width of the fracture aperture (m)

D_e is the effective diffusivity (m^2/yr)

A_f is the diffusion area (m^2) (set equal to the area of the fracture opening)

$F_{x,0}$ is the effective diffusion length function (m).

Neretnieks (1986) evaluated the value of the $F_{x,0}/b$ for this system with variations in the input parameters. According to Neretnieks the following relationship gives a good approximation to the exact solution (Neretnieks 1986, Equation 24):

$$F_{x,0}/b = 1 - 1.35 \log b/a + 1.6 \log d/a \qquad \text{G-3}$$

in the regime $10^{-6} < b/a < 10^{-1}$ and $0.03 < d/a < 1$.

a is the height of the compartment in connection with the fracture (m)

b is the half-width of the fracture aperture (m)

d is the thickness of the buffer/backfill (m).

Input to COMP23 is a plug length, corresponding to $F_{x,0}$ and a plug area corresponding to the diffusion area set equal to the area of the fracture opening in contact with the buffer.

Plug in connection with Q1

Since the resistance of the plug is dependent of the fracture aperture the dependence is evaluated by comparison between resistances calculated for two different fracture apertures. One of the fracture apertures chosen is 1×10^{-4} m. This is the same value as was used in SR-Can. In the hydrogeological base case calculations with the semi-correlated model (090827_fs_Q123_2000_pline_merged_ptb) more than 99 % of the fractures are less than 1×10^{-4} m. The resistance for the plug is calculated as follows:

$\delta = 2b = 1 \times 10^{-4}$ m

$a = 0.5$ m

$d = 0.35$ m

δ is the fracture aperture (m).

The plug area is $A_f = \pi \times$ deposition hole diameter $\times\ \delta = \pi \times 1.75 \times 1 \times 10^{-4}$ m^2 $= 5.5 \times 10^{-4}$ m^2.

The plug length is $F_{x,0} = (F_{x,0}/b)\ b$. Since, $b/a = \delta/2/a = 1 \times 10^{-4}/2/0.5 = 1 \times 10^{-4}$ and $d/a = 0.35/0.5 = 0.7$, Equation G-3 is valid for calculation of $(F_{x,0}/b)$. The plug length is hence $(F_{x,0}/b)\ b = (1–1.35 \log (1 \times 10^{-4}/2/0.5) + 1.6 \log (0.35/0.5))1 \times 10^{-4}/2 = 3.1 \times 10^{-4}$ m.

The resistance is $R_f = \dfrac{3.1 \times 10^{-4}}{D_e 5.5 \times 10^{-4}} = \dfrac{0.56}{D_e}$.

The other fracture aperture is chosen to be 10^{-6} m. The resistance for the plug is calculated as follows:

$\delta = 2b = 1 \times 10^{-6}$ m

$a = 0.5$ m

$d = 0.35$ m

The plug area is $A_f = \pi \times$ deposition hole diameter $\times \delta = \pi \times 1.75\ \times\ 1 \times 10^{-6}$ m^2 $= 5.5 \times 10^{-6}$ m^2.

The plug length is $F_{x,0} = (F_{x,0}/b)\ b$. Since, $b/a = \delta/2/a = 1 \times 10^{-6}/2/0.5 = 1 \times 10^{-6}$ and $d/a = 0.35/0.5 = 0.7$, Equation G-3 is valid for calculation of $(F_{x,0}/b)$. The plug length is hence $(F_{x,0}/b)\ b = (1–1.35 \log (1 \times 10^{-6}/2/0.5) +1.6 \log (0.35/0.5))1 \times 10^{-6}/2 = 4.4 \times 10^{-6}$ m.

The resistance is $R_f = \dfrac{4.4 \times 10^{-6}}{D_e 5.5 \times 10^{-6}} = \dfrac{0.81}{D_e}$.

The two studied fracture apertures varying with two orders of magnitude show that the resistance only varies slightly with the fracture aperture. Hence, the resistance can be approximated to be independent of the fracture aperture. In the COMP23 calculations the plug in connection with Q1 is assigned the plug length and plug area for a fracture aperture of 1×10^{-4} m, i.e.

PLUG_LENGTH = 3.1×10^{-4} m

PLUG_AREA = 5.5×10^{-4} m^2.

Connection with Q2

No extra resistance is used in connection with Q2, since Q2 represents transport through the excavation damage zone, EDZ.

Connection with Q3

No extra resistance is used in connection with Q3 although an extra resistance was used in previous assessments (SKB 2006a, Lindgren and Lindström 1999).

Advective flow

The advective flow (m^3/yr) in the tunnel is calculated as:

$$q = \frac{L_{LR\_TUN}}{t_{TR\_TUN}} \varepsilon_{backfill} A_{tunnel} \qquad \text{G-4}$$

where

L_{LR_TUN}, t_{TR_TUN}, $\varepsilon_{backfill}$ and A_{tunnel} are the length and advective travel time in the tunnel from the top of the deposition hole to the first fracture intersecting the tunnel, the physical porosity of the back-filled tunnel, and the cross-sectional area of the tunnel, respectively. L_{LR_TUN} and t_{TR_TUN} are calculated within the hydrogeological modelling and given in the ptb-files as LR_TUN and TR_TUN. The porosity of the back-filled tunnel is also read from the ptb-file in the column named TRAPP. The area of the tunnel is the area between the first and second advective compartment. (All compartments in the tunnel have the same area).

Boundary conditions

For the near-field compartments that are in contact with fractures in the near-field rock, the rate of diffusive transport is modelled by the use of sinks, Q_{eq} (Neretnieks et al. 2010, Romero 1995). Q_{eq} is a fictitious flow rate that can be visualised as the flow rate of water that carries away dissolved species with the concentration at the compartment interface resulting in the release of radionuclides. It has been derived by solving the equations for diffusive transport to the passing water by boundary layer theory. The value of Q_{eq} depends on the geometry of the contact area, the water flux, the flow porosity and the diffusivity. The resistance at the boundary is calculated as the inverse of the Q_{eq}-value. The Q_{eq}-values are calculated within the hydrogeological modelling and given in the ptb-files and directly used as input data to COMP23. (QEQ for connection with Q1 and Q2, QEQR for the connection at Q3).

Equivalent groundwater flow-rate, Q_{eq1}

The following equation is used to calculate Q_{eq1} in the hydrogeological model (Joyce et al. 2010, Section 3.2.6):

$$Q_{eq1} = \sum_f \left(\frac{Q_f}{\sqrt{a_f}} \sqrt{\frac{4 D_w t_{wf}}{\pi}} \right) \qquad \text{G-5}$$

where

$$t_{wf} = \frac{L_f \cdot e_{tf}}{Q_f / \sqrt{a_f}} \qquad \text{G-6}$$

If there are several fractures intersecting a single deposition hole, then a conservative approach to calculate the equivalent groundwater flow rate requires the flow to be summed across all the fractures, with t_{wf} calculated separately for each fracture. Hence, the average equivalent flux, U_{r1}, for all fractures intersecting the deposition hole is:

$$U_{r1} = \frac{1}{w_c} \sum_f \frac{Q_f}{\sqrt{a_f}} \qquad \text{G-7}$$

where:

D_w is the diffusivity in water [m^2/yr]

t_{wf} is the time the water is in contact with the deposition hole within each fracture [yr]

L_f is the length of the fracture intersection with the wall of the deposition hole [m]

U_{r1} is the equivalent initial flux in the fracture system averaged over the rock volume adjacent to the deposition hole [m/yr]

Q_f is the volumetric flow rate in the fracture intersecting the deposition hole [m^3/yr]

e_{tf} is the transport aperture of the fracture intersecting the deposition hole [m]

a_f is the area of the fracture plane intersecting the deposition hole [m^2]

w_c is the deposition hole height [m].

D_w was set to 0.0316 m^2/yr and w_c was set to 5 m, although this is strictly the canister height. All other values were determined in the flow simulations.

Equivalent groundwater flow-rate, Q_{eq2}

The following equation is used to calculate Q_{eq2} in the hydrogeological model (Joyce et al. 2010, Section 3.2.6):

$$Q_{eq2} = \sum_E \left(\frac{Q_E}{\sqrt{a_E}} \sqrt{\frac{4 D_w t_{wE}}{\pi}} \right) \quad \text{G-8}$$

where

$$t_{wE} = \frac{L_E \, e_{tE}}{Q_E / \sqrt{a_E}} \quad \text{G-9}$$

The equivalent initial flux, U_{r2}, for flow in the EDZ is:

$$U_{r2} = \frac{1}{w_E} \sum_E \frac{Q_E}{\sqrt{a_E}} \quad \text{G-10}$$

where

D_w is the diffusivity in water [m^2/yr]

t_{wE} is the time the water is in contact with the deposition hole within each EDZ fracture [yr]

L_E is the length of the EDZ fracture intersection with the wall of the deposition hole [m]

U_{r2} is the equivalent initial flux in the EDZ fracture system averaged over the EDZ fracture cross-sectional area [m/yr]

Q_E is the volumetric flow rate in the EDZ fracture intersecting the deposition hole [m^3/yr]

e_{tE} is the transport aperture of the EDZ fracture intersecting the deposition hole [m]

a_E is the area of the EDZ fracture plane intersecting the deposition hole [m^2]

w_E is the EDZ thickness [m].

D_w was set to 0.0316 m^2/yr and w_E was set to 0.3 m. All other values were determined in the flow simulations.

Equivalent groundwater flow-rate, Q_{eq3}

The equivalent groundwater flow-rate, Q_{eq3}, in the first fracture intersecting the tunnel can be written as (Joyce et al. 2010, Section 3.2.6):

$$Q_{eq3} = 2 \sqrt{\frac{4 D_w L e_{tf} \left(Q_f / \sqrt{a_f} \right)}{\pi}} \quad \text{G-11}$$

The initial flux, U_{r3}, for flow in the first fracture intersecting the tunnel is:

$$U_{r3} = \frac{Q_f}{w_T \sqrt{a_f}} \quad \text{G-12}$$

where:

D_w is the diffusivity in water [m^2/yr]

L is the half circumference of the tunnel [m]

Q_f is the volumetric flow rate in the fracture intersecting the tunnel [m^3/yr]

w_T is the fracture width intersecting the tunnel [m]

a_f is the area of the fracture plane intersecting the tunnel [m^2]

e_{tf} is the transport aperture of the fracture intersecting the tunnel [m].

D_w was set to 0.0316 m^2/yr, L was set to 7 m and w_T was set to 2.5 m. All other values were determined in the flow simulations.

The boundary conditions for the advective transport are automatically handled within COMP23. At the upstream boundary the concentration is zero and no diffusion is allowed. At the downstream boundary the radionuclides are transported out of the model through an automatically generated advective sink, also here no diffusion is allowed. The additional advective component is given by:

$$Q_{eq3,adv} = \frac{L_{LR\_TUN}}{t_{TR\_TUN}} \varepsilon_{backfill} A_{tunnel} \qquad \text{G-13}$$

where

L_{LR_TUN}, t_{TR_TUN}, $\varepsilon_{backfill}$ and A_{tunnel} are the length and advective travel time in the tunnel from the top of the deposition hole to the first fracture intersecting the tunnel, the physical porosity of the back-filled tunnel, and the cross-sectional area of the tunnel, respectively.

Summary of resistance for diffusion in the near field

The resistances for the compartments are calculated as:

$$R = \frac{d}{AD_e} \qquad \text{G-14}$$

d is the diffusion length (m)

A is the diffusion area (m^2)

D_e is the effective diffusivity (m^2/yr).

The total resistance for diffusion from the canister through the boundary at Q1 is:

$$R_{TOT\ Q1} = R_{Block1} + R_{Block2} + R_{Plug\ p} + R_{Block3\ horis} + R_{Plug\ f} + R_{Qeq,1} \qquad \text{G-15}$$

where

$$R_{Block3\ horis} = \sum_{i=i\ to\ 5} R_{Block3,compartment\ i,horis} + \frac{R_{Block3,compartment\ 6,horis}}{2} \qquad \text{G-16}$$

$$R_{Qeq,1} = \frac{1}{Q_{eq,1}} \qquad \text{G-17}$$

The total resistance for diffusion from the canister through the boundary at Q2 is:

$$R_{TOT\ Q} = R_{Block} + R_{Block} + R_{Plug\ p} + R_{Block\ vert} + R_{Block} + R_{Block\ verthoris} + R_{Qeq} \qquad \text{G-18}$$

where:

$$\frac{1}{R_{Block3\ vert}} = \sum_{i=1\ to\ 6} \frac{1}{R_{Block3\ ,compartment\ i,vert}} \qquad \text{G-19}$$

$$R_{Block6\ verthoris} = \frac{R_{Block6,vert}}{2} + \frac{R_{Block6,horis}}{2} \qquad \text{G-20}$$

$$R_{Qeq,2} = \frac{1}{Q_{eq,2}} \qquad \text{G-21}$$

The total resistance for diffusion from the canister through the boundary at Q3 is:

$$R_{TOT\ Qeq} = R_{Block} + R_{Block} + R_{Plug\ p} + R_{Block\ vert} + R_{Block} + R_{Block\ vert} + R_{Block} + R_{Qeq} \qquad \text{G-22}$$

$$R_{Block7} = \frac{R_{Block7,compartmet2,vert}}{2} + \frac{R_{Block7,compartmet2,horis}}{2} + \sum_{i=3to(NDSE+2-1)} R_{Block7,compartment\ i,horis} + \qquad \text{G-23}$$

$$+ \frac{R_{Block7,compartmetNDSE+2,horis}}{2} + \frac{R_{Block7,compartmetNDSE+2,vert}}{2}$$

where NDSE is the number of downstream compartments in Block 7, see Section G.7.

$$R_{Qeq,3} = \frac{1}{Q_{eq,3} + Q_{eq3,adv}} \qquad \text{G-24}$$

The effective diffusivities are material and nuclide specific and are assigned probability density functions and hence the transport resistances will vary. In Table G-3 the size of the resistances for Ra-226 in the deterministic case is given. The effective diffusivities are assigned median values in the deterministic case. The calculations performed in Excel are archived at SKB.[7,8]

Table G-3. Example of diffusion resistances in the near-field model in the case with growing pinhole failure (without including the effect of spalling). Deterministic case for Ra-226 ($D_{e,buffer} = 1.33 \times 10^{-10}$ m^2/s, $D_{e,\ backfill} = 1.6 \times 10^{-10}$ m^2/s). The transport resistance between two compartments is the sum of half the resistance of the respective compartments according to Cliffe and Kelley (2006, Equation 34). The resistance for the boundary conditions are calculated from the median Q_{eq}-values, LR_TUN and TR_TUN from the hydrogeological base case with the semi-correlated model[6].

	Diffusion resistance (yr/m^3)	
	Small hole (r_{hole}=2 × 10^{-3} m)	Large hole (unlimited)
Canister to Q1		
Block 1	0	0
Block 2	126 313	negligible
Rp	26 813	negligible
Block 3 horis	36	36
Rf,1	135	135
Qeq,1	238 095	238 095
Total	391 392	238 266
Canister to Q2		
Block 1	0	0
Block 2	126 313	negligible
Rp	26 813	negligible
Block 3 vert	78	78
Block 5	149	149
Block 6 verthoris	77	77
Qeq,2	10 753	10 753
Total	164 183	11 056
Canister to Q3		
Block 1	0	0
Block 2	126 313	negligible
Rp	26 813	negligible
Block 3 vert	78	78
Block 5	149	149
Block 6 vert	103	103
Block 7	80	80
Qeq,3	3 780	3 780
Total	157 315	4 189

[7] SKBdoc 1260107 ver 1.0. Supporting calculations related to radionuclide transport. SKB 2010. (Internal document.)

[8] SKBdoc 1256019 ver 1.0. Hydrogeological model data and results – Forsmark. SKB 2010. (Internal document.)

G.3 Growing pinhole – spalling

The model for the growing pinhole failure including the effect of spalling, i.e. a damaged zone in the rock walls of the deposition hole, is almost the same as the model without including the effect of spalling.

There are three differences:

1. The plug at the inlet to the fracture is not present.
2. The resistance in the half of the last buffer compartment next to the rock is included.
3. An additional term, accounting for the effect of the damaged zone, is included in the calculation of $Q_{eq,1}$.

A schematic picture of the transport path straight out from the canister, i.e. from a defect canister through the buffer and into rock, is given in Figure G-4.

Discretisation

A schematic picture of the modelled system in the case with growing pinhole including the effect of spalling is given in Figure G-5.

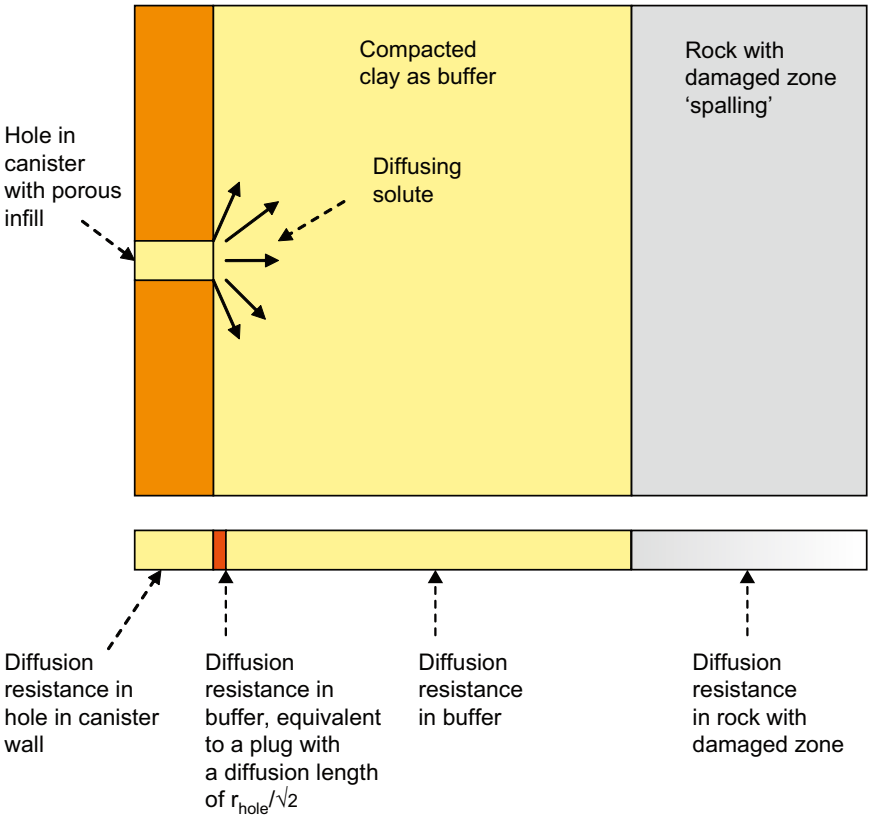

Figure G-4. *Transport from a defect canister through the buffer and into the damaged zone in the case with growing pinhole failure including the effect of spalling (modified from Neretnieks (2006)).*

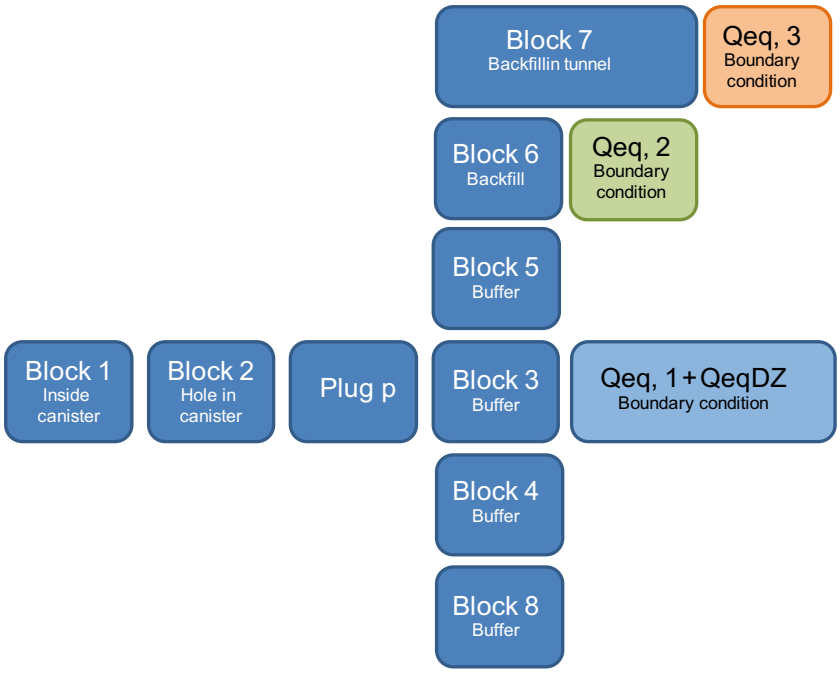

Figure G-5. *Schematic picture of the blocks, plugs and boundary conditions in the case with growing pinhole failure including the effect of spalling.*

Summary of resistance for diffusion in the near field

Most of the resistances are the same as in the case with the case with growing pinhole failure without including the effect of spalling, see Section G.2. The differences are described here.

The resistance in Block 3 is calculated as:

$$R_{Block3\ horis} = \sum_{i=1 to 6} R_{Block3,compartment\ i,horis} \qquad \text{G-25}$$

An additional term, accounting for the effect of the damaged zone Q_{eqDZ}, is included in the calculation of $Q_{eq,1}$ (Neretnieks et al. 2010). Neretnieks et al. (2010) also gives a more cautious suggestion for the boundary at Q1, that $Q_{eq} = q$. This more cautious suggestion has not been used in this hypothetical residual scenario.

$$Q_{eqDZ} = 1.13\sqrt{\frac{D_p q W_{zone} L_{zone} \varepsilon_{zone}}{d_{zone}}} \qquad \text{G-26}$$

where:

D_p is the pore diffusivity in the damaged zone, set to 10^{-11} m^2/s

q is the water flow rate (m^3/s)

W_{zone} is the width of the damaged zone, set to 0.5 m

L_{zone} is the length of the damaged zone, set to 8 m

ε_{zone} is the porosity of the damaged zone, set to 0.02

d_{zone} is the thickness of the damaged zone, set to 0.1 m

The water flow rate, q (m^3/s), is estimated as:

$$q = U_0 w_c \min 2L_{zone}, L_{fracture}] \qquad \text{G-27}$$

where:

U_0 is water flux (m^3/m^2, s), obtained from the ptb-file (U0)

w_c is the canister height, set to 5 m

$L_{fracture}$ is the length of the fracture intersecting the damaged zone, obtained from the ptb-file (FLEN).

In Table G-4 the size of the resistances for Ra-226 in the deterministic case is given.

Table G-4. Example of diffusion resistances in the near-field model in the case with growing pinhole failure including the effect of spalling. Deterministic case for Ra-226 ($D_{e,buffer}$= 1.33 × 10^{-10} m^2/s, $D_{e,\ backfill}$ =1.6 × 10^{-10} m^2/s). The transport resistance between two compartments is the sum of half the resistance of the respective compartments according to Cliffe and Kelley (2006, Equation 34). The resistance for the boundary conditions are calculated from the median Q_{eq}-values, LR_TUN and TR_TUN from the hydrogeological base case with the semi-correlated model.

	Diffusion resistance (yr/m^3)	
	Small hole (r_{hole} = 2 × 10^{-3} m)	Large hole (unlimited)
Canister to Q1		
Block 1	0	0
Block 2	126 313	negligible
Rp	26 813	negligible
Block 3 horis	39	39
Rf,1	0	0
Qeq1	6 649	6 649
Total	159 814	6 687
Canister to Q2		
Block 1	0	0
Block 2	126 313	negligible
Rp	26 813	negligible
Block 3 vert	78	78
Block 5	149	149
Block 6 verthoris	77	77
Qeq2	10 753	10 753
Total	164 183	11 056
Canister to Q3		
Block 1	0	0
Block 2	126 313	negligible
Rp	26 813	negligible
Block 3 vert	78	78
Block 5	149	149
Block 6 vert	103	103
Block 7	80	80
Qeq3	3 780	3 780
Total	157 315	4 189

G.4 Lost swelling pressure in tunnel backfill “Crown space”

If the swelling pressure of the deposition tunnel backfill is lost, a conductive channel could develop at the tunnel ceiling. In this case the discretisation of the tunnel has been simplified. The backfill is represented with only the backfill straight above the deposition hole. All blocks except Block 7 are unchanged compared to the growing pinhole with spalling. One additional block is used, Block 8, representing the water at the tunnel ceiling. (Block 9 is the same as the growing pinhole Block 8.)

Block 7 is modified to be only the backfill in the tunnel above the deposition hole. It has the shape of a standing cylinder. The Z-direction is vertical. It has been divided into ten subcompartments, with equal height. No transport resistance is assumed in the radial direction and hence X_LENGTH is set to zero and X_AREA is 1. The diffusion length in the z-direction, Z_LENGTH, is equal to the height, i.e. 0.470 m for each sub-compartment. The diffusion area Z_AREA is the end surface of the cylinder, $\pi \cdot r^2 = \pi \cdot 0.875^2 = 2.405$ m^2. No advective transport is assumed in Block 7.

Block 8 is the water at the tunnel ceiling. The shape of this block is rectangular. Diffusive transport is assumed in all directions. In the vertical direction the transport is described by the diffusion length, Z_LENGTH, that corresponds to the height of the conductive channel, 0.1 m and by the diffusion area that is the contact area to Block 7 below, i.e. 2.405 m^2. In the horizontal direction the transport is described by the diffusion lengths X_LENGTH and Y_LENGTH, that are chosen to be equal to the diameter of the cylinder shaped Block 7 below, i.e. 1.75 m and by the diffusion areas X_AREA and Y_AREA that are calculated as the height times the lengths, i.e. $0.1 \times 1.75 = 0.175$ m^2.

Advective transport is assumed in Block 8.

A schematic picture of the modelled system in the case where the swelling pressure of the deposition tunnel backfill is lost and a conductive channel is developed at the tunnel ceiling is given in Figure G-6.

Summary of resistance for diffusion in the near field

In Table G-5 the size of the resistances for Ra-226 in the deterministic case is given.

Table G-5. Example of diffusion resistances in the near-field model in the case "Lost swelling pressure in backfill". Deterministic case for Ra-226 ($D_{e,buffer}$=1.33 × 10^{-10} m^2/s, $D_{e,\ backfill}$ = 1.6 × 10^{-10} m^2/s). The resistance for the boundary conditions are calculated from the median Q_{eq}-values from the hydrogeological case including the effect of lost swelling pressure in backfill.

	Diffusion resistance (yr/m^3)	
	Small hole (r_{hole}=2 × 10^{-3} m)	Large hole (unlimited)
Canister to Q1		
Block 1	0	0
Block 2	126 313	negligible
Rp	26 813	negligible
Block 3 horis	39	39
Rf,1	0	0
Qeq1	6 840	6 840
Total	160 005	6 879
Canister to Q2		
Block 1	0	0
Block 2	126 313	negligible
Rp	26 813	negligible
Block 3 vert	78	78
Block 5	149	149
Block 6 verthoris	77	77
Qeq2	10 526	10 526
Total	163 956	10 830
Canister to Q3		
Block 1	0	0
Block 2	126 313	negligible
Rp	26 813	negligible
Block 3 vert	78	78
Block 5	149	149
Block 6 vert	103	103
Block 7	388	388
Qeq3	43	43
Total	153 887	760

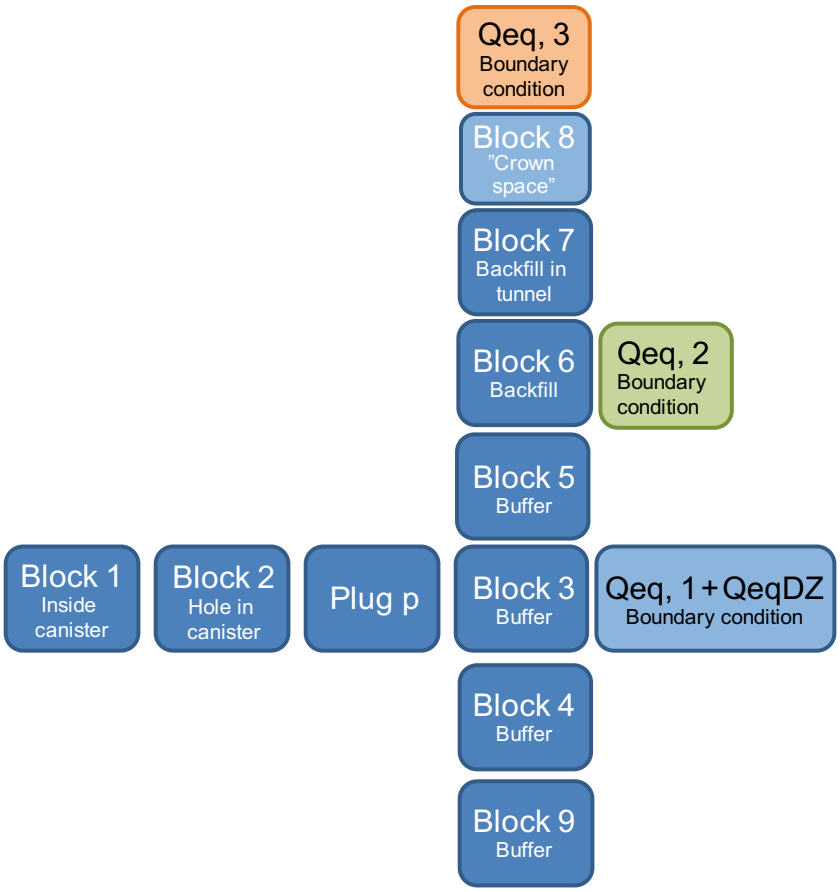

Figure G-6. *Schematic picture of the blocks, plugs and boundary conditions in the case with lost swelling pressure in the backfill in the tunnel.*

G.5 Canister failure due to shear load

One of the identified failure modes of the canister is failure due to rock shear load caused by a large earthquake in the vicinity of the repository. A very simplified model has been used to calculate the radionuclide release in this case. Neretnieks (2006) shows the possibility to include the resistance for the diffusion from the "slit" in the sheared canister into the buffer. It is also possible to include a resistance at the entrance to the fracture described by Equation G-2 as well as a limited $Q_{eq,1}$-value. However, the size of the shear aperture in the canister as well as the fracture aperture is difficult to assign, wherefore a simplified pessimistic model has been used. The bentonite thickness is assumed to be reduced from 35 cm to 25 cm.

Discretisation

A schematic picture of the modelled system in the case with failure due to shear load is given in Figure G-7.

Block 1 is the internal of the canister, no transport resistance is assumed and hence Z_LENGTH and X_LENGTH are set to zero and Z_AREA and X_AREA are 1. A void volume of 1 m^3 was used.

Block 3 is the buffer outside the hole. It has a shape of a standing cylindrical shell. The Z-direction is vertical. The sub-compartments are made with equal thickness of the cylindrical shells. The diffusion lengths in the radial direction X_LENGTH, i.e. from the hole to the fracture, Q1, are equal for all sub-compartments, 0.25/6 = 0.042 m. The diffusion area for the transport in the radial direction X_AREA are calculated as the average envelope surface of the cylindrical shells, i.e. $2 \cdot \pi \cdot (r_o+r_i)/2 \cdot h$, where r_o is the outer radii, r_i is the inner radii and h is the height of the sub-compartments i.e. equal to Z_LENGTH. The transport in the z-direction is described by the diffusion length Z_LENGTH that is set to be 0.5 m and by the diffusion area Z_AREA, i.e. the end surface of the cylindrical shells, $\pi \cdot (r_o^2-r_i^2)$. The parameters for block 3 together with the outer and inner radius are given in Table G-6.

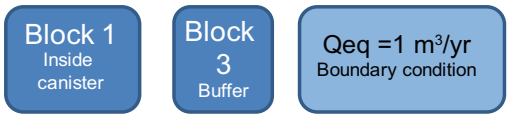

Figure G-7. *Schematic picture of the blocks and boundary condition in the case with shear load failure.*

Table G-6. Dimensions used for Block 3 in the shear load cases.

Sub-compartment number	Z_LENGTH	Z_AREA	X_LENGTH	X_AREA	Inner radii, r_i	Outer radii, r_o
1	0.5	0.182	0.042	2.186	0.675	0.717
2	0.5	0.193	0.042	2.317	0.717	0.758
3	0.5	0.204	0.042	2.448	0.758	0.800
4	0.5	0.215	0.042	2.579	0.800	0.842
5	0.5	0.226	0.042	2.710	0.842	0.883
6	0.5	0.237	0.042	2.841	0.883	0.925

Boundary conditions

The canister failure location is assumed to fully coincide with the location of the shearing fracture. The shear is assumed to increase the fracture significantly. The $Q_{eq,1}$ value for the intersecting fracture is assumed to be sufficiently high, $1 m^3/yr$, that it does not contribute to transport resistance.

Summary of resistance for diffusion in the near field

In Table G-7 the size of the resistances for Ra-226 in the deterministic case is given.

Table G-7. Example of diffusion resistances in the near-field model in the case with shear load failure. Deterministic case for Ra-226 ($D_{e,buffer} = 1.33 \times 10^{-10}$ m^2/s).

	Diffusion resistance (yr/m^3)
Canister to Q1	
Block 1	0
Block 3 horis	24
Qeq1	1
Total	25

G.6 Canister failure due to corrosion

Discretisation

A schematic picture of the modelled system in the case with failure due to corrosion is given in Figure G-8.

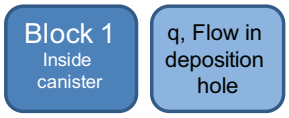

Figure G-8. *Schematic picture of the blocks and boundary condition in the case with failure due to corrosion.*

Flow in deposition hole

The water flow in the deposition hole, when the buffer is eroded, is calculated from the Darcy flux (U_0) given in the ptb-files according to the following equation (SKB 2010a):

$$q = f_{conc} U_0 2 r_h h_{can} \qquad \text{G-28}$$

where f_{conc} is the flow concentration factor (2), r_h is the radius of the deposition hole (0.875 m) and h_{can} is the height of the canister (5 m).

The calculations of the water flow in the deposition holes are performed together with the corrosion calculations (SKB 2010a) and are archived at SKB.[9]

Summary of resistance for diffusion in the near field

There is no diffusion resistance in the near field in the case with failure due to corrosion.

G.7 Test of discretisation

The discretisation, is almost the same as in SR97 and SR-Can and, is based on the optimised discretisation performed for SR97 (Lindgren and Widén 1998). However, since the length of the tunnel in the present calculations is dependent on the length to the first fracture in the tunnel a study has been performed to achieve a suitable discretisation for the tunnel.

The tunnel in the SR-Can assessment was geometric as a block starting in the tunnel above the deposition hole and ending at the first fracture in the tunnel. The tunnel block was divided into sub-compartments. The first sub-compartment had the length 2.125 metres, the second 1.75 metres and the rest had lengths of 2.125 metres. To get an integer of sub-compartments, the path length from the deposition hole to the first fracture in the tunnel was divided by 2.125 and rounded to nearest higher integer. MATLAB might run out of memory for large numbers of compartments. It was not a problem in SR-Can but in SR-Site some pathways are long enough, typical above 200 metres. Although, 85 % of the pathways are shorter than 10 metres and over 99 % are shorter than 100 metres, see Table G-8, a new geometrical discretisation of the tunnel has been implemented in the SR-Site assessment.

Table G-8. Sub-compartment lengths in the new tunnel discretisation.

L_{LR_TUN} (m)	L (m)	NDSE	Sub-compartment length (m)	Amount of shorter pathways
2.4950	1.6200	1	1.6200	10 %
6.8240	5.9490	3	1.7883, 1.9764, 2.1843	72 %
10.2600	9.3850	4	2.0069, 2.2179, 2.4512, 2.7090	88 %
44.8200	43.9450	12	1.9920, 2.2015, 2.4331, 2.6890, 2.9718, 3.2843, 3.6297, 4.0115, 4.4333, 4.8996, 5.4149, 5.9844	99 %
103.8000	102.9250	18	2.1437, 2.3691, 2.6183, 2.8936, 3.1980, 3.5343, 3.9060, 4.3168, 4.7708, 5.2725, 5.8271, 6.4399, 7.1172, 7.8657, 8.6930, 9.6072, 10.6176, 11.7343	99.8 %

[9] SKBdoc 1265612 ver 1.0. Scripts and data used for Analytical erosion corrosion calculations. SKB 2010. (Internal document.)

The present section describes the new discretisation of the tunnel and compares it to the old discretisation used in SR-Can. The tunnel block starts with a sub-compartment upstream the deposition hole followed by a sub-compartment above the deposition hole. These two sub-compartments are independent of the path length to the first fracture in the tunnel and are always 2.125 m and 1.75 m, respectively. To avoid the problem with too many sub-compartments downstream the deposition hole but still assure the accuracy, the lengths of the sub-compartments are increasing along the tunnel block in the new discretisation. The geometry is shown in Figure G-9. The path length to the first fracture in the tunnel is measured from a point centred in the tunnel above the deposition hole. In the hydrogeological ptb-files this parameter is named LR_TUN and hence named L_{LR_TUN} in this text. The total length of the tunnel block, Block 7, is therefore 2.125 m plus 1.75/2 m plus the path length to the first fracture (L_{LR_TUN}). The number of downstream sub-compartments, NDSE, is calculated from:

$$NDSE = \frac{ln\left[1+\frac{L}{l_1}(k-1)\right]}{ln(k)} \qquad \text{G-29}$$

where:

$$L = L_{LR\_TUN} - 1.75/2\ (m) \qquad \text{G-30}$$

l_1 is the length of the first downstream sub-compartment, initially set to 2.125 m
k is $e^{0.1}$

NDSE is rounded to the closest integer and to secure that the sub-compartments exactly covers the path length to the first fracture the length of the first downstream sub-compartment, l_1, is recalculated from:

$$l_1 = L\,\frac{k-1}{k^{NDSE}-1} \qquad \text{G-31}$$

Since the sub-compartments are increasing in length along the pathway, ≥ 1 for n=2, 3,...NDSE, the lengths of the sub-compartments (not the first) can be calculated from:

$$l_n = k\,l_{n-1} \qquad \text{G-32}$$

Some examples of NDSE and sub-compartment lengths when the routine described above is used are shown in Table G-8. The share of pathways shorter than the specific pathway length used in the calculation in the example is also stated.

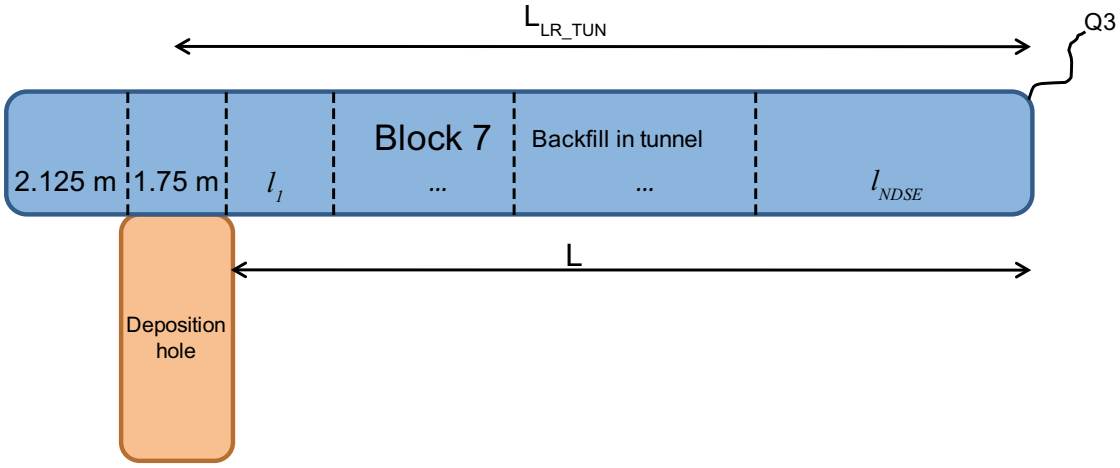

Figure G-9. *Discretisation for the tunnel block, Block 7. The sink Q3 is located at the first fracture in the tunnel.*

Figure G-10 shows results from calculations with the new tunnel discretisation are compared to the discretisation used in SR-Can for two different L_{LR_TUN} (10.1 m and 93.5 m). To illustrate the importance of the discretisation of the tunnel, also a calculation with one single compartment is shown in the figure. In this calculation the compartment has the length of L. A finer discretisation of the tunnel gives later releases and this effect is more pronounced for longer pathways.

For a probabilistic calculation (6 824 realisations) the differences between the releases through Q3 for the two discretisations are minor, see Figure G-11. In this example the pinhole model was used and all input data was the same as used in the SR-Can assessment except for the ptb-files which were a preliminary delivery for SR-Site.

These comparisons show that the new method for discretisation is accurate to use in the growing pinhole calculations for SR-Site.

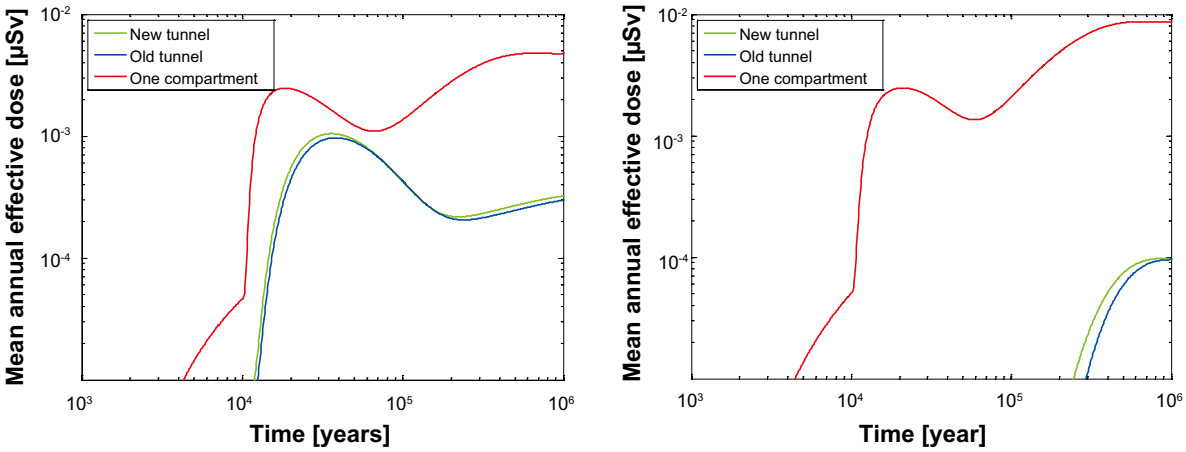

Figure G-10. *Comparison between the tunnel discretisation used in SR-Can and SR-Site for two different path lengths (10.1 m to the left and 93.5 m to the right). In addition results for a calculation with one single compartment are shown.*

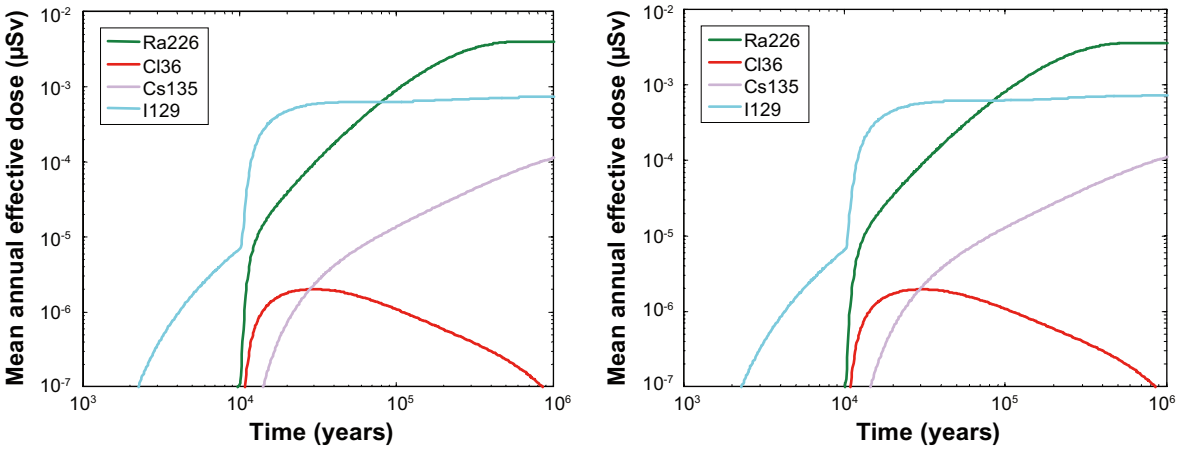

Figure G-11. *Probabilistic near-field releases from Q3 for the growing pinhole case. The new tunnel discretisation used in SR-Site to the left and the old discretisation used in SR-Can to the right.*

Appendix H

Transport parameters used in Section 6.4

This appendix has not been changed since the SR-Site assessment.

The near-field and far-field transport calculations were used to assess sensitivities to various modelling assumptions and parameter values and were initiated before SR-Site near-field parameters were finalised. Consequently, SR-Can or preliminary SR-Site values were used for some parameters.

H.1 Near-field transport parameters

SR-Can median values were used for near-field parameters. One important change, however, was made in the SR-Can values: the solubility limit for radium was reduced by a factor of 1 000 to account for co-precipitation with barium. In addition, the preliminary set of radionuclides used here includes some differences from the SR-Can and the final SR-Site sets: Ac-227 and Pb-210, which were not included in SR-Can, are included here; the radionuclides Am-242m, Pu-238, Cd-113m, Eu-152, H-3, Ho-166m, Mo-93, Nb-93m, Ni-63, Sm-151, and Sn-121m were not included in these sensitivity calculations but are in the final SR-Site set. The initial inventories for these radionuclides are relatively small and they are not expected to affect the sensitivities addressed here.

Preliminary SR-Site median values were used for inventories at 1 000 years after emplacement (the start of the transport calculation). Although there are some differences between these preliminary values and the final SR-Site inventories, these differences are relatively small and not expected to significantly affect the results shown here.

SR-Site median values were used for near-field geometries (Table G-1).

H.2 Far-field transport parameters

Preliminary SR-Site median values were used for far-field transport in granitic rock, backfilled tunnels, and buffer material (a few far-field pathways briefly pass through buffer material, which is why buffer parameters are needed in MARFA). The one exception is that a value of 3 m was used for matrix penetration depth (i.e., size of matrix region accessible by diffusion), in contrast to the SR-Site value of 12.5 m. Sensitivity to the assumed penetration depth was investigated and results for 3 m are identical to those of 12.5 m. Given the relatively rapid travel times for pathways that contribute to overall dose, a penetration depth of 3 m is essentially unlimited diffusion even for non-sorbing radionuclides. Thus, making the penetration depth even larger has little effect.

Equilibrium sorption partitioning coefficients (K_d values), porosities, and bulk densities are needed for the soil layers in modelling cases where sorption in near-surface soils is included. K_d values for organic and inorganic soils were taken from Nordén et al. (2010). For one rock type defined in the ConnectFlow ptv-file, the soil type could be organic or inorganic, depending on location. That layer was assigned the properties of inorganic material. All soils were assigned the porosity value 0.25 and the bulk density value of 2 000 kg/m^3.

Far-field transport parameters used in this study are summarised in Table H-2. The rock porosity is 0.0018 for all elements.

SR-Site values were used for landscape dose factors.

Table H-1. Near-field transport parameter values used in this sensitivity study for elements that were not included in SR-Can.

Element	Effective diffusivity Buffer (m^2/yr)	Effective diffusivity Backfill (m^2/yr)	Buffer K_d (m^3/kg)	Backfill K_d (m^3/kg)	Solubility Limit (mol/m^3)
Ac	4.43×10^{-3}	5.00×10^{-3}	5.15	5.15	none
Pb	4.44×10^{-3}	5.00×10^{-3}	49.3	49.6	1.3×10^{-6}

Table H-2. Far-field transport parameters used in this sensitivity study.

Element	Rock K_d (m^3/kg)	Rock Diffusivity (m^2/yr)	Buffer K_d (m^3/kg)	Backfill K_d (m^3/kg)	Inorganic Soil K_d (m^3/kg)	Organic Soil K_d (m^3/kg)
Ac	0.0150	6.61×10^{-7}	5.154	5.154	0	0
Am	0.0151	6.52×10^{-7}	25.497	25.522	2.6	2.5
C	0	6.61×10^{-7}	0	0	0	0
Cl	0	6.63×10^{-7}	0	0	4.4×10^{-4}	0.01
Cm	0.0147	6.63×10^{-7}	24.673	24.525	9.3	9.3
Cs	0.0004	6.57×10^{-7}	0.030	0.031	36	26
I	0	2.09×10^{-7}	0	0	7.1×10^{-3}	0.71
Nb	0.0204	6.63×10^{-7}	3.073	3.066	1.9	40
Ni	0.0011	6.61×10^{-7}	0.067	0.066	0.31	3
Np	0.0527	6.58×10^{-7}	37.979	37.124	0.02	0.81
Pa	0.0566	6.52×10^{-7}	3.160	3.076	1.4	2
Pb	0.0252	6.64×10^{-7}	49.354	49.643	7.7	43
Pd	0.0534	6.60×10^{-7}	4.968	5.192	0.14	0.18
Pu	0.0147	6.61×10^{-7}	39.162	39.088	0.74	0.74
Ra	0.0002	6.47×10^{-7}	0.001	0.001	2.5	2.5
Se	0.0003	2.08×10^{-7}	0	0	0.022	0.53
Sn	0.1596	6.60×10^{-7}	37.276	38.047	0.29	8
Sr	0	6.62×10^{-7}	0.001	0.001	0.32	0.12
Tc	0.0516	6.60×10^{-7}	38.841	37.276	6.0×10^{-5}	3.0×10^{-3}
Th	0.0521	6.61×10^{-7}	38.628	38.518	32	42
U	0.0535	6.51×10^{-7}	39.624	38.818	1.5	6.5
Zr	0.0214	6.56×10^{-7}	4.830	4.696	0.47	5.6

Appendix I

Colloid facilitated transport model

This appendix has not been changed since the SR-Site assessment.

Two limiting cases of interest for colloid-facilitated transport are identified based on the kinetics of radionuclide sorption onto colloids. In the first limiting case, the sorption kinetics for radionuclide sorption onto colloids is reversible and rapid compared to transport time scales of interest. In the second limiting case, radionuclides are assumed to sorb irreversibly onto colloids. For clay colloids generated by buffer erosion, the colloid type most likely to facilitate transport, sorption is understood to be reversible on the time scales of interest and therefore the reversible sorption model is used in SR-Site. Nevertheless, it is instructive to consider the hypothetical situation of irreversible sorption even though it was never used in SR-Site. Models for these two limiting cases are developed in this appendix.

I.1 Rapid reversible sorption onto colloids

To assess the possible role of rapid reversible sorption/desorption onto colloids in facilitating transport, the following assumptions are adopted: (i) equilibrium sorption of radionuclides onto mobile and immobile colloids, (ii) equilibrium sorption of colloids onto fracture surfaces, and (iii) colloid-free matrix pore space (conservative assumption, but also realistic for the small pore sizes of granitic rock). Although not strictly needed, an additional assumption of constant (in space) colloid concentration is used, consistent with the modelling cases of this report that involve colloid-facilitated transport.

The following concentrations are defined

C – radionuclide concentration in fracture water [mol/L^3]

C_m – radionuclide concentration in matrix pore space [mol/L^3]

S – concentration of radionuclides sorbed to mobile colloids [mol/L^3]

S^* – concentration of radionuclides sorbed to immobile colloids [mol/L^3]

m_c – colloid concentration in fracture water [M/L^3]

Mass balance equations for radionuclides in fractures, matrix, and on colloids are

$$\frac{\partial C}{\partial t} + TC = -\psi^{C\to S}(C,S) - \psi^{C\to S^*}(C,S^*) - \lambda C + \frac{D_e}{b}\frac{\partial C_m}{\partial z}\bigg|_{z=0} \qquad \text{I-1}$$

$$\theta R_m \frac{\partial C_m}{\partial t} = D_e \frac{\partial^2 C_m}{\partial z^2} - \lambda \theta R_m C_m \qquad \text{I-2}$$

$$\frac{\partial S}{\partial t} + TS = \psi^{C\to S}(C,S) - \psi^{S\to S^*}(S,S^*) - \lambda S \qquad \text{I-3}$$

$$\frac{\partial S^*}{\partial t} = \psi^{C\to S^*}(C,S^*) + \psi^{S\to S^*}(S,S^*) - \lambda S^* \qquad \text{I-4}$$

Where $T = v\frac{\partial}{\partial x} - D_l\frac{\partial^2}{\partial x^2}$ is the differential operator representing transport by advection and dispersion, θ is matrix porosity [-], D_e is effective diffusion coefficient [L^2/T], λ is the decay constant [1/T], R_m is matrix retardation factor, b is fracture half-aperture, v is velocity in the fracture, D_l is longitudinal dispersion/diffusion in fracture, z is the distance from the fracture in the direction perpendicular to the fracture, x is the distance along the fracture, and t is time. The ψ symbols are mass transfer functions representing the rate of mass transfer between various states (dissolved, sorbed to mobile colloids, sorbed to stationary colloids, etc.) per unit volume [mol L^{-3} T^{-1}]. An interface condition is also required $C_m(x, z = 0, t) = C(x, t)$.

The assumption of fast reversible attachment/detachment of colloids allows the S and S^* equations to be combined, resulting in the following system

$$\frac{\partial C}{\partial t} + TC = -\psi^{C\to S}(C,S) - \psi^{C\to S^*}(C,K_c'S) - \lambda C + \left.\frac{D_e}{b}\frac{\partial C_m}{\partial z}\right|_{z=0} \quad \text{I-5}$$

$$\theta R_m \frac{\partial C_m}{\partial t} = D_e \frac{\partial^2 C_m}{\partial z^2} - \lambda\theta R_m C_m \quad \text{I-6}$$

$$R_c \frac{\partial S}{\partial t} + TS = \psi^{C\to S}(C,S) + \psi^{C\to S^*}(C,K_c'S) - \lambda R_c S \quad \text{I-7}$$

Assuming instantaneous sorption of radionuclides onto colloids, the sorbed concentration can be written as where K_c is a mass-based partitioning coefficient [L^3/M] for radionuclide sorption onto colloids. Adding Equations I-5 and I-7 results in

$$1 + R_c m_c K_c)\frac{\partial C}{\partial t} + (1 + m_c K_c)TC = -\lambda(1 + R_c m_c K_c)C + \left.\frac{D_e}{b}\frac{\partial C_m}{\partial z}\right|_{z=0} \quad \text{I-8}$$

Which, upon dividing both sides by $1+m_cK_c$, gives the following system

$$R_{f,app}\frac{\partial C}{\partial t} + TC = -\lambda R_{f,app}C + \left.\frac{D_{e,app}}{b}\frac{\partial C_m}{\partial z}\right|_{z=0} \quad \text{I-9}$$

$$\theta R_{m,app}\frac{\partial C_m}{\partial t} = D_{e,app}\frac{\partial^2 C_m}{\partial z^2} - \lambda\theta R_{m,app}C_m \quad \text{I-10}$$

where

$$R_{f,app} \equiv \frac{1 + R_c m_c K_c}{1 + m_c K_c} \quad \text{I-11}$$

$$D_{e,app} \equiv \frac{D_e}{1 + m_c K_c} \quad \text{I-12}$$

and

$$R_{m,app} \equiv \frac{R_m}{1 + m_c K_c} \quad \text{I-13}$$

These equations have the same form as those solved by MARFA, but with apparent parameters that are dependent on the colloid concentrations, colloid retardation factor, and equilibrium partitioning coefficient for radionuclide sorption onto colloids.

For unlimited matrix diffusion, MARFA takes a single retention parameter for each radionuclide $\kappa = \sqrt{\theta D_e R_m}$. Thus, to model colloid-facilitated transport, D_e and R_m should be replaced by their apparent values. This is equivalent to using an apparent value for κ defined as

$$\kappa_{app} = \frac{\kappa}{1 + m_c K_c} \quad \text{I-14}$$

For limited matrix diffusion, the input values required by MARFA include κ and $\eta = \frac{\Delta}{D_e}$ where Δ [L] is the spatial extent of the diffusion zone adjacent to a fracture. Colloid-facilitated transport may be modelled by replacing η by its apparent value $\eta_{app} = \eta(1 + m_cK_c)$.

In summary, the effect of reversible/irreversible sorption to colloids may be represented in MARFA by replacing the transport parameter groups κ and η by apparent values. The ratio of the colloid-free parameters and the apparent values in the presence of colloids depends only on the colloid mass density m_c and the partitioning coefficient for sorption onto colloids K_c.

I.2 Irreversible sorption onto colloids

Clay colloids generated by buffer erosion are expected to be the most abundant colloid type in the repository system. Sorption onto clay colloids is understood to be reversible on the time scales of interest. Nevertheless, it is instructive to consider the hypothetical situation of irreversible sorption, at least for some fraction of the sorption sites. If radionuclides are irreversibly sorbed to colloids, the radionuclides will move with the colloids, which potentially have much lower interaction with the host rock. However, several processes help mitigate the potential effects of irreversible sorption. These mitigating processes include permanent filtration of the colloids, colloid retardation, the fact that permanent sorption onto bentonite would dramatically reduce near-field release, and limited availability of sorption sites on bentonite colloids. The last process is considered while pessimistically neglecting other mitigating processes.

A competitive Langmuir sorption model was used to assess the potential effect of irreversible sorption

$$\frac{\partial C_i}{\partial t} = -k_i C_i \left(S_{\max} - \sum_j S_j \right) - k_{desorp,i} S_i \qquad \text{I-15}$$

where S_i and C_i are the sorbed and aqueous concentration (mol/m^3) for radionuclide i; k_i and $k_{desorp,i}$ are the sorption and desorption rate constants; and S_{max} is the sorbed concentration when all available sites are occupied. This study is concerned with the situation $k_{desorp,i} = 0$. Making that substitution and using $S_i(t)=C_{0i}-C_i(t)$ where C_0 is the initial concentration yields

$$\frac{\partial C_i}{\partial t} = -k_i C_i \left(S_{\max} - \sum_j C_{0j} + \sum_j C_j \right) \qquad \text{I-16}$$

This study conservatively considers the forward sorption rates to be fast, so that the forward sorption process goes to completion within each time step of the COMP23 output. Thus, depending on the sign of the quantity $\left(S_{\max} - \sum_j C_{0j} \right)$, the process results in either a total transfer of radionuclides to the colloids or complete occupation of all sites with the remainder of radionuclides in solution. The system of equations above provides the partitioning of the available sorption sites among the various radionuclides.

The rate constants k_i are needed. Although these are assumed to be fast, $k_i \rightarrow ¥$, relative values of the rates are still needed. It is reasonable to assume the rate ratios are proportional to the equilibrium partitioning coefficients $\left. \frac{k_i}{k_j} \right|_{k_i, k_j \rightarrow \infty} = \frac{K_{d,i}}{K_{d,j}}$ where $K_{d,j}$ is the equilibrium partitioning coefficient for nuclide j.

Using 0.01 kg/m^3 for colloid concentration, and a site density of 7×10^{-2} mol/kg, S_{max} is calculated as 7×10^{-4} mol/m^3.

To get colloidal releases into the far field, the release history was discretised into 120 time steps, and the above system of ordinary differential equations (ODEs) was solved once for each time step and source location combination. Numerical solutions are required because the right side of Equation I-16 is non-linear in the concentration. The result of that calculation partitions the COMP23 output among the various colloid-associated species and dissolved species. The end time for the numerical solution was taken to be large enough to allow the sorption process to complete. To get initial concentrations, COMP23 output in units of mol/yr at each time step was divided by the QEQ parameter in units of m^3/yr provided the concentrations in units of mol/m^3. In the Q1 base case, 1 402 deposition holes have connected pathways to the biosphere. With the radionuclide source represented by 120 time steps and 1 402 source locations, approximately 168 000 solutions to the ODE system are required.

Appendix J

Safety assessment PSAR – Updated scoping calculations on the depletion of fracture calcite under fresh water infiltration at Forsmark

J.1 Introduction

The groundwaters at Forsmark, in the 100–700 m depth range, have a relatively homogeneous salinity (Laaksoharju et al. 2008): the samples with category 1 to 3 have a sum of cation concentrations ($\sum[M^{q+}]$) of 91 ± 4 mM and a sum of cationic charge ($\sum q[M^{q+}]$) of 119 ± 7 meq/L. Thus, at present the groundwaters are well above the limit of 8 meq/L, which is the safety function indicator criteria for chemically favourable conditions for the buffer and backfill. However, the PSAR assessment has to address the evolution of the salinity of groundwater during future periods of infiltration of fresh waters, for example during extended periods of temperate climate conditions, or during glacial periods. This appendix tries to provide insight into processes that may affect the cation concentration, with special focus on calcium, in meteoric waters infiltrating in fractures at Forsmark. The text focusses on the dissolution of fracture-filling calcite. Diffusion of salt from the rock matrix porewater to the fracture groundwater is discussed in another appendix of this report.

In the transport modelling report of SR-Site (SKB 2010d, Appendix B.8) scoping calculations were made of the rate of fracture infill calcite depletion. These calculations were based on a simple mass balance approach whereby calcite lining advective flow paths was postulated to dissolve under the influence of infiltrating low ionic strength glacial meltwater. In this appendix, the calculations from the SR-Site study are updated with more accurate values for the calcite fracture abundance and slightly different modelling assumptions concerning the composition of the infiltrating dilute water. Instead of the thermodynamic database (TDB) previously used by SKB (Duro et al. 2006), the more recent database, ThermoChimie_Phreeqc_eDH_v9b0, has been used in this study (Giffaut et al. 2014). The calcite equilibrium concentrations obtained with the ThermoChimie database are only slightly different to those presented before (5 % to 15 % lower).

In an extension to the work previously done, a simplified weathering model of rock matrix minerals is also examined in this study to ascertain if the rates of Ca-production are sufficient to at least partially offset the rate of fracture calcite depletion along recharge flowpaths. The model considers matrix diffusion, a kinetic rate of mineral weathering related to the measured BET surface area of intact rock, and the presence of a 10 cm thick alteration zone assumed to be completely depleted of its readily leachable Ca content.

J.2 Calculation of calcite depletion rates in a recharge path

J.2.1 Glacial meltwater infiltration

In SR Site, scoping calculations considered a dilute glacial groundwater composition calculated by Gimeno et al. (2008) with an ionic strength of 0.0489 mM and carbonate concentration corresponding to a CO_2 partial pressure of roughly 0.012 ppm (i.e. effectively zero). This was equilibrated with calcite to give an equilibrium concentration of Ca^{2+} of 1.3×10^{-4} M using the SKB TDB (1.1×10^{-4} M using Thermochimie).

Analysis of meltwater samples collected under the Greenland ice sheet have been published since SR-Site (Graly et al. 2014). The salinity (TDS, total dissolved solids) of these 17 samples of subglacial meltwaters is as follows: the minimum TDS is 0.006 g/L, max value = 0.12 g/L, median = 0.014 g/L, mean value = 0.030 g/L, standard deviation = 0.032 g/L. It can therefore not be ruled out that during the passage of the ice margin, when there is a lot of meltwater generated above the repository, the penetrating groundwater becomes very dilute, with TDS concentration lower than 0.005 g/L. However, the data also show that most samples have TDS> = 0.01 g/L (11 samples out of 17), and therefore it may be assumed that this value (TDS ≥ 0.01 g/L) applies for most of the glacial period.

PhreeqC calculations are performed here on the 17 samples of subglacial meltwaters. The results show that all meltwaters are under-saturated with respect to calcite, see Figure J-1. The calcium concentrations of these subglacial meltwaters are between 10^{-6} and 2.1×10^{-4} M. In the model presented in this section the calcium concentration of 1.1×10^{-4} M is used for calcite-equilibrium.

An illustration of the calcite depletion process is shown in Figure J-2 for a recharge flowpath from the surface.

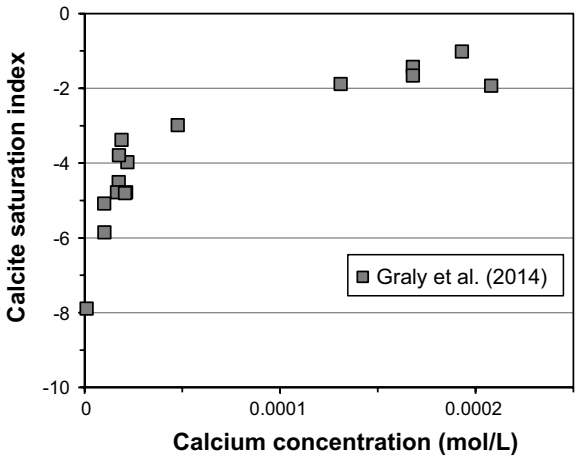

Figure J-1. *Calculated calcite saturation indices plotted against calcium concentrations for the subglacial meltwaters collected near Kangerlussuaq, Greenland (Graly et al. 2014).*

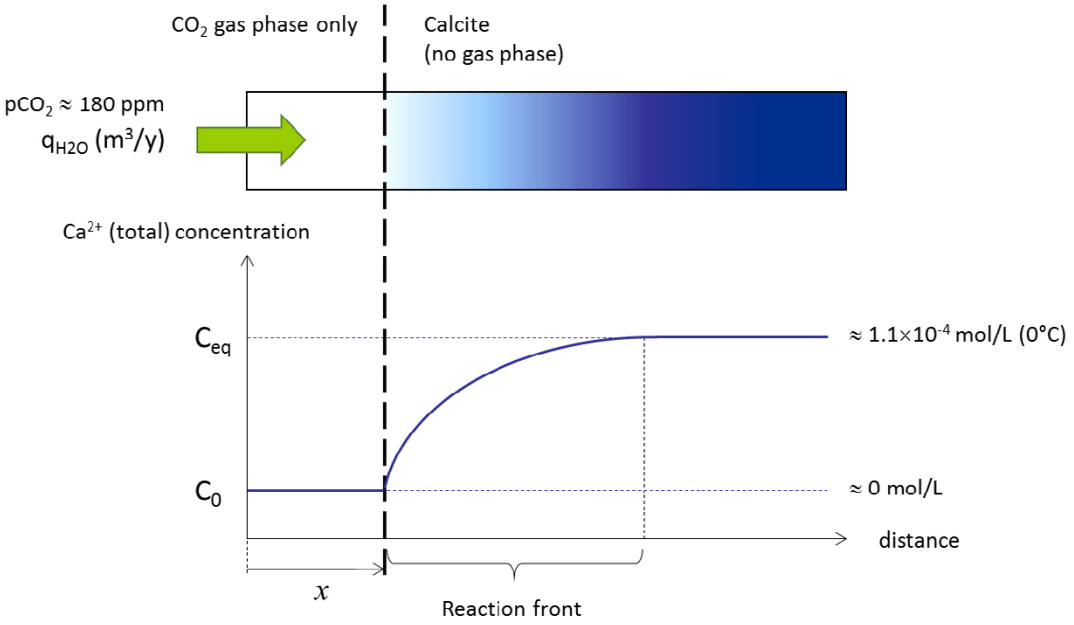

Figure J-2. *Conceptualisation of calcite depletion process for a flowpath where infiltrating dilute, glacial groundwater (with initial concentration, C_0) dissolves calcite. The dissolution products reach their equilibrium concentration (C_{eq}) over a distance determined by the kinetics of the dissolution reaction, reactive surface area, and advective travel time. The transient concentration region separating the initial and equilibrium states is referred to as the reaction front.*

The main reactions for calcite dissolution and pH buffering together with their equilibrium constants at 25 °C are:

$$CaCO_{3(s)} \; f \; Ca^{2+} + CO_3^{2-} \qquad K_{sp}^0 = 10^{-8.48} \tag{J-1}$$

$$H^+ + CO_3^{2-} \; f \; HCO_3^- \qquad K_{c1}^0 = 10^{10.33} \tag{J-2}$$

$$2H^+ + CO_3^{2-} \; f \; CO_{2(aq)} + H_2O \qquad K_{sp}^0 = 10^{16.68} \tag{J-3}$$

$$H_2O \; f \; H^+ + OH^- \qquad K_w^0 = 10^{-14} \tag{J-4}$$

If there is a gas phase present, we have an additional reaction for the dissolution of gaseous CO_2 in water:

$$CO_{2(g)} + H_2O \; f \; 2H^+ + CO_3^{2-} \qquad K_g^0 = 10^{-18.15} \tag{J-5}$$

The net rate of calcite dissolution, r_c (mmol/cm^{2}s) is given by Plummer et al. (1979) as:

$$r_c = k_1 \cdot \left[H^+\right] + k_2 \cdot K_{CO_2} \cdot pCO_2 + k_3 - k_4 \left[Ca^{2+}\right]\left[HCO_3^-\right] \tag{J-6}$$

At circumneutral to alkaline groundwater pH levels and low partial pressures of CO_2, however, the k_3 term dominates the forward reaction rate and the rate law can be simplified to the form:

$$r_c \approx k_3 \left(1 - \frac{\left[Ca^{2+}\right]\left[CO_3^{2-}\right]}{K_{sp}}\right) \tag{J-7}$$

Plummer et al. (1979) define the logarithm of the rate constant k_3 as:

$$\log_{10} k_3 = -5.86 - \frac{317}{\left(T + 273.15\right)} \tag{J-8}$$

Where, T is the temperature in °C. At 0 °C, the far-from equilibrium rate is then 9.54×10^{-7} mol/m^{2}s. For a simplified groundwater composition neglecting the minor contribution of carbonate complexation with electrolyte cations (Ca^{2+}, Na^+, etc.), the total carbonate concentration is given by:

$$\left[HCO_3^-\right]_{tot} = \left[CO_3^{2-}\right] + \left[HCO_3^-\right] + \left[CO_{2(aq)}\right] \tag{J-9}$$

From the equilibrium relations implied by reaction Equations J-2 and J-3, we can then write:

$$c_B = \left[CO_3^{2-}\right]_{tot} = \alpha \left[CO_3^{2-}\right] \tag{J-10}$$

Where the variable α is a non-linear function of local groundwater pH:

$$\alpha = 1 + K_{c1} \cdot 10^{-pH} + K_{c2} \cdot 10^{-2\,pH} \tag{J-11}$$

Since hydrolysis of the Ca^{2+} cation is negligible at normal groundwater pH levels, we also introduce the approximation:

$$c_A = \left[Ca^{2+}\right]_{tot} \approx \left[Ca^{2+}\right] \tag{J-12}$$

The pH can be estimated from a charge balance over the cationic and anionic charge of dissolved species which must sum to zero to achieve electroneutrality. Although an analytical solution is available it is much too complicated to be of practical use and it is far simpler to solve for the pH numerically by minimising the objective function, W for known c_A and c_B:

$$\Omega = 2c_A + 10^{-pH} + K_w \cdot 10^{pH} - c_B \left(\frac{2 + K_{c1} \cdot 10^{-pH}}{1 + K_{c1} \cdot 10^{-pH} + K_{c2} \cdot 10^{-2\,pH}}\right) = 0 \tag{J-13}$$

The rate equation can now be given in terms of the total concentrations of Ca^{2+} and CO_3^{2-} as:

$$r_c \approx k_3 \left(1 - \frac{c_A \left(c_{B0} + c_A\right)}{\alpha K_{sp}}\right) \tag{J-14}$$

Where, c_{B0} is the initial concentration of carbonate from equilibration of surface infiltrating water with the atmospheric partial pressure of CO_2. For a 1D advective flowpath through a rock fracture it can be assumed that the reactive calcite surface area is numerically equal to the flow-wetted surface area that is covered by calcite mineralisation regardless of thickness. For a packet of water travelling along the flowpath, the advective travel time of the water packet can be related to the reaction rate, r_c (mol/m^{2}s) by:

$$\frac{dc_A}{dt} = v\frac{dc_A}{dx} = \frac{\varphi_c}{\delta_t}\cdot r_c \tag{J-15}$$

Here, the constant j_c represents the fraction of the flow-wetted surface that is covered with calcite (~10 % as described in Crawford and Löfgren (2019), while d_t (m) is the average transport aperture of the recharge flowpath. Here, we note that the product of fluid velocity, v (m/y) and transport aperture can be obtained from the flow-related transport resistance, F (y/m) and recharge path length, L (m) using the relation:

$$\frac{1}{v\delta_t} = \frac{F}{2L} \tag{J-16}$$

Substituting the simplified rate expression, Equation J-14 into Equation J-15 then allows us to write:

$$\frac{dc_A}{dx} = k_f\left(1-\frac{c_A\left(c_{B0}+c_A\right)}{\alpha K_{sp}}\right) \tag{J-17}$$

Where,

$$k_f = \frac{F}{2L}\cdot\varphi_c\cdot k_3 \tag{J-18}$$

Equation J-17 is a variables separable equation that can be written in the form:

$$\int_0^{c_A}\frac{dc_A}{1-\dfrac{c_A\left(c_{B0}+c_A\right)}{\alpha K_{sp}}} = \int_0^x k_f dx \tag{J-19}$$

Since the variable α is a non-linear function of pH, which in turn depends on c_A, it is not possible to obtain an analytical expression for the integral on the left-hand side of Equation J-19 and this must be evaluated numerically. The value of α varies over several orders of magnitude from 4.83×10^5 at the pH of the inlet water (5.69) to approximately 2.3 at the equilibrium pH (10.46). The problem, however, can be simplified considerably by the observation that the value of α has the largest effect when the calcite reaction is close to equilibrium and has essentially no effect at lower pH levels where the forward rate of reaction is overwhelmingly dominant. If one assumes the minimum value of $\alpha \approx 2.3$ as a constant, Equation J-19 can be integrated analytically to obtain:

$$\frac{\alpha_* K_{sp}}{\sqrt{c_{B0}^2+4\alpha_* K_{sp}}}\cdot\ln\left(\frac{2\alpha_* K_{sp}-c_A\left(c_{B0}-\sqrt{c_{B0}^2+4\alpha_* K_{sp}}\right)}{2\alpha_* K_{sp}-c_A\left(c_{B0}+\sqrt{c_{B0}^2+4\alpha_* K_{sp}}\right)}\right) = k_f x \tag{J-20}$$

Here, we use the symbol α_* to denote the α-value assumed at the equilibrium pH (which is assumed constant) to distinguish it from the pH-dependent value of the α-parameter. This expression can be rearranged to give c_A (the Ca^{2+} concentration) explicitly:

$$c_A = \frac{2\alpha_* K_{sp}}{c_{B0}+\sqrt{c_{B0}^2+4\alpha_* K_{sp}}\coth\left(\dfrac{k_f x}{2\alpha_* K_{sp}}\cdot\sqrt{c_{B0}^2+4\alpha_* K_{sp}}\right)} \tag{J-21}$$

If the initial carbonate concentration in the infiltrating water is neglected, Equation J-21 simplifies further to:

$$c_A \approx \sqrt{\alpha_* K_{sp}}\tanh\left(\frac{k_f x}{\sqrt{\alpha_* K_{sp}}}\right) \tag{J-22}$$

If we are interested in estimating the distance required for the Ca^{2+} concentration to reach a fraction, c of its final equilibrium value, we can rearrange Equation J-22 to obtain:

$$x \approx \frac{\sqrt{\alpha_* K_{sp}}}{k_f} \cdot \tanh^{-1}(\chi) \qquad \text{(J-23)}$$

From Equation J-23, the required distance to achieve an equilibrium approach of 99.9 % (c = 0.999) is then calculated to be roughly 10 cm for a low range F value of 10^3 y/m, an advective travel time of 0.1 y, and recharge path length of 400 m (taking care that the units of the various parameters comprising k_f are consistent with the units of K_{sp}). Comparison of the numerically evaluated Equation J-17 with a full calculation of the kinetic dissolution profile using PhreeqC shows a very good agreement if allowance is made for the slightly different equilibrium state implied by the inclusion of aqueous phase activity coefficients (see Figure J-3). Furthermore, the estimate of the equilibration distance using Equation J-23 agrees exceptionally well with that calculated in the full numerical simulation and the PhreeqC calculations.

It should be noted that the width of the calcite dissolution front shown in Figure J-2 is exaggerated. Although we have not calculated this for other hydrodynamic conditions that those modelled above, it is likely to be very narrow, on the order of cm to dm at most due to the rapid dissolution and precipitation kinetics of calcite. The F value and advective travel time assumed in the calculation of the profiles shown in Figure J-3 are at the low end of what is deemed reasonable, however. Larger F values and longer advective travel times give raise to much shorter equilibration distances. Also note that in this model the meltwater is pre-equilibrated with a CO_2 containing gas phase of effectively infinite volume before the water enters the fracture and there it is equilibrated with calcite (as a closed system). This means there is no free gas phase along the recharge path even though the carbonate concentration in the water can be described in terms of a CO_2 partial pressure. Figure J-4 shows the PhreeqC-calculated equilibrium concentration of Ca^{2+} as a function of pCO_2 and temperature of the recharge water. In this conceptualisation, water enters the system at the surface initially in equilibrium with the assumed CO_2 gas partial pressure at 0 °C. The recharge water then then passes to a region with no free gas phase although with calcite present. The temperature of the water in this part of the flowpath increases in temperature as it flows to greater depth in the rock up to an assumed maximum of 15 °C.

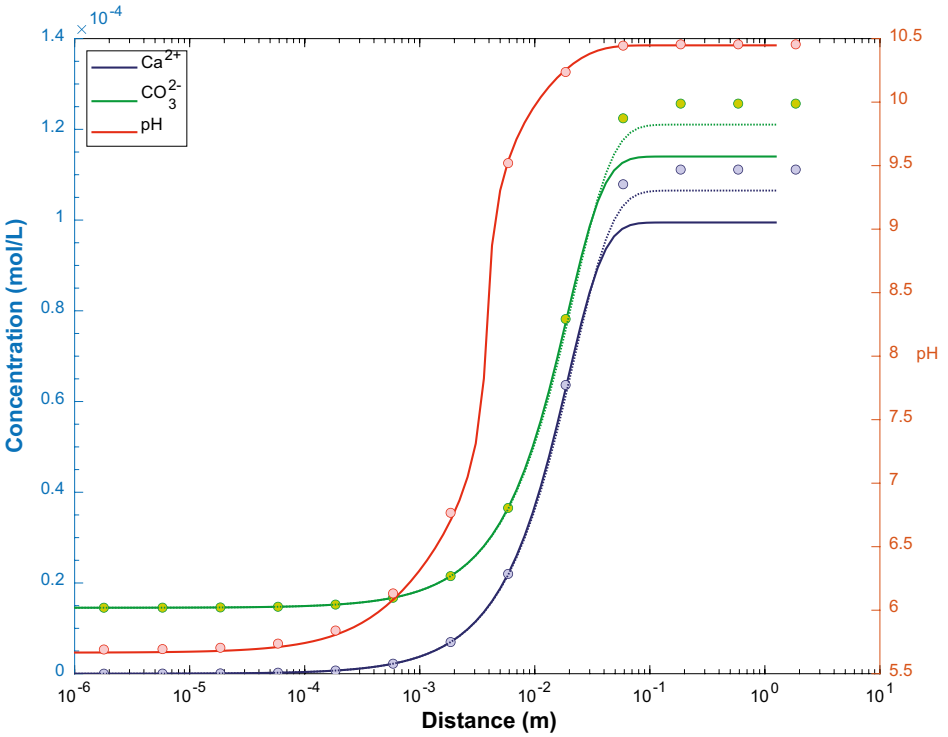

Figure J-3. *Reaction front for kinetic calcite dissolution ($F = 10^3$ y/m, $t_w = 0.1$ y, $L = 400$ m) calculated by PhreeqC (circular markers), as well as by numerical integration of equation using Matlab (lines), and using the approximate formula for Ca^{2+} concentration given by equation (broken lines). Slight differences in the final equilibrium concentrations are due to the neglection of activity corrections for the simplified (non-PhreeqC) cases.*

After a brief transient period, the rate at which the calcite dissolution front in the rock recedes from the surface is given by the (quasi-stationary-state) mass balance:

$$q\left(C_{eq}-C_0\right)=\left(\frac{W_c m_s}{M_w^{calcite}}\right)\frac{dx}{dt} \qquad \text{(J-24)}$$

In this equation dx/dt (m/y) is the rate of front movement, q (m^3/y) is the flowrate of inflowing water, W_c (m) is the flow channel width, m_s (g/m^2) is the mass of calcite per square meter of fracture, $M_w^{calcite}$ (g/mol) is the molecular weight of calcite, while C_0 and C_{eq} (mol/m^3) are the Ca^{2+} concentrations entering and at equilibrium downstream of the reaction front as illustrated in Figure J-2. Equation can be simply integrated to find the time, t_c (y) required to totally deplete the calcite content of a recharge flowpath associated with a specified flow-related transport resistance (F):

$$t_c=\left(\frac{m_s/M_w^{calcite}}{C_{eq}-C_0}\right)\cdot\frac{F}{2} \qquad \text{(J-25)}$$

In Crawford and Löfgren (2019), the calcite content of the fracture system at Forsmark has been re-evaluated from the raw data reported in SKB's Sicada database. From the statistics of calcite occurrence on fracture surfaces of borehole core samples associated with flowing features, Crawford and Löfgren (2019) estimate a specific volume of calcite of roughly 10.2 cm^3/m^2 of fracture area (the fracture area is half the flow-wetted surface which considers opposite faces of a fracture). The porosity of the fracture calcite is unknown although can be pessimistically assumed to lie in the range 30 %–70 % with a median value of 55 %. Based on this assumption, we can estimate a specific mass of 27.5 g/m^2 with an uncertainty range of (18.4–43.0 g/m^2).

The calculated equilibrium pCO_2 using PhreeqC on the data reported by Graly et al. (2014) is very sensitive to the pH value, which is difficult to measure in dilute un-buffered solutions. Excluding the sample with the lowest pH (5.8), the calculated equilibrium pCO_2 values for these sampled sub-glacial meltwaters are between 66 and 948 ppm. Assuming an inflowing water at 0 °C equilibrated with a fixed pCO_2 of 180 ppm and the equilibrium concentration of 1.11×10^{-4} mol/L for calcium from Figure J-4, the time to completely deplete from calcite a recharge flowpath is calculated and shown in Figure J-5. The selection of pCO_2 has only a marginal effect, as the value of C_{eq} is not very sensitive to this parameter (Figure J-4). As can be seen from the plot in Figure J-5, the best estimate time, t_c (y) required to fully deplete a flowpath of its calcite content is roughly numerically equal to 1.24 times the F value (y/m) for the used site-specific average conditions.

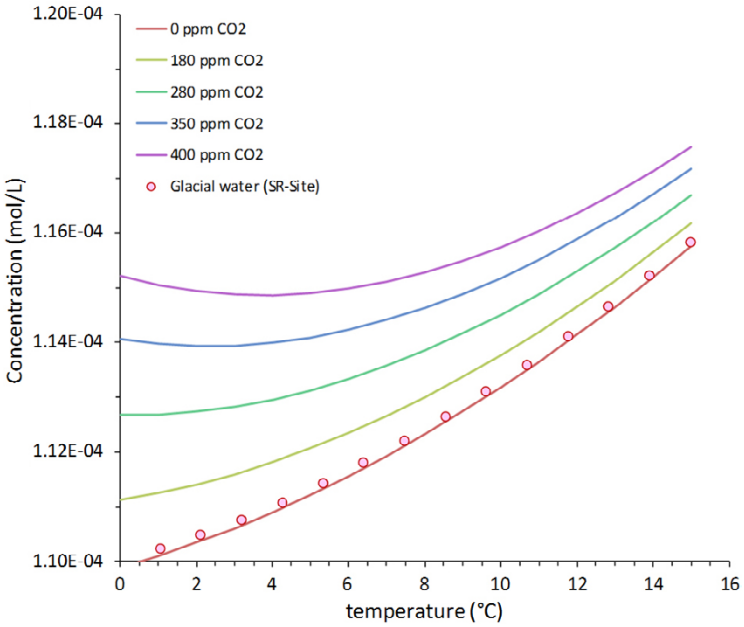

Figure J-4. *Concentration of Ca^{2+} in equilibrium with calcite as a function of temperature for water that has been pre-equilibrated at 0 °C with CO_2 gas of a fixed partial pressure corresponding to that specified in the legend text. The glacial water composition used previously in the SR-Site scoping calculations (SKB 2010d) is shown as circular markers.*

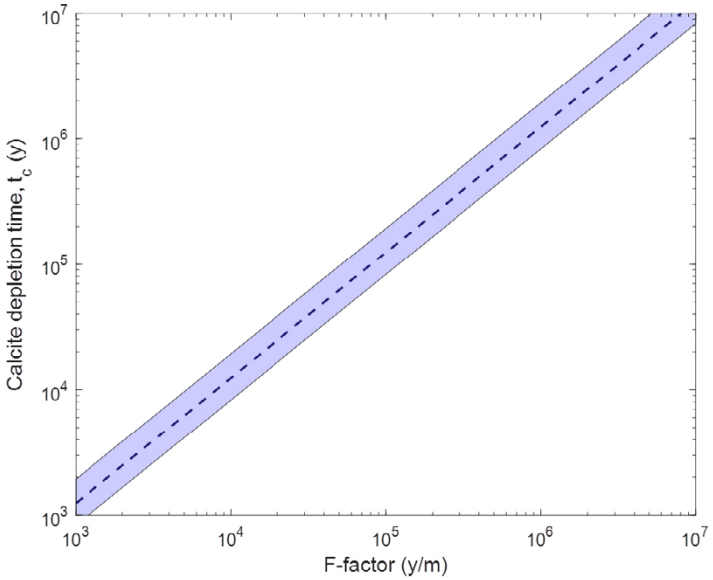

Figure J-5. *Time to deplete calcite from an advective flowpath as a function of F. Calculations assume a best estimate of the mass of calcite of 27.5 g/m² (min-max range 18.4-43.0 g/m²). The shaded region represents the minimum-maximum range and the broken line is the best estimate. Additional calcite buffering capacity may reside in stagnant zones of the fracture flanking the flow channel, although this has not been considered in the calculations.*

J.2.2 Infiltration of meteoric water during a temperate period

Influence of the regolith

During a temperate climate period, meteoric water will first percolate through the regolith at Forsmark. For such a situation it may be reasonable to expect that the infiltrating water is already equilibrated with calcite at a given fixed partial pressure of CO_2 at the inlet to the flowpath. This can be considered analogous to the situation depicted in Figure J-6 which might occur where calcite-containing glacial till is in contact with the atmosphere (i.e. where the till is considered to be an open system, with respect to the gas phase). Meteoric water passes from this zone downstream along the recharge path where the CO_2 containing gas phase is no longer present (closed system). As indicated in Figure J-6, the equilibrium concentration of Ca^{2+} in this case is nearly 6 times higher than that shown in Figure J-2. Evidence for this conceptual model, in terms of the chemical composition of superficial porewaters sampled at Forsmark is presented in the next section (Present composition of the infiltrating waters at Forsmark).

The PhreeqC-calculated equilibrium concentration of Ca^{2+} is shown in Figure J-7 as a function of temperature for an initial pCO_2 of 180 ppm in the inlet where the temperature of the recharge water is assumed to vary along the subsurface recharge flowpath. Under temperate climate conditions the partial pressure of CO_2 in soils is expected to be higher than in the atmosphere (≈407 ppm at present). As discussed in section Present composition of the infiltrating waters at Forsmark, the infiltrating meteoric waters are expected to have Ca^{2+} concentrations that correspond to quite high CO_2 contents in the regolith.

While there is calcite in the till to equilibrate the infiltrating waters, depletion of calcite is not to be expected in the flowpaths created by the fractures in the rock. In fact, if there is an increasing temperature gradient with depth in the rock, then calcite dissolved from the till will reprecipitate in small amounts along the flowpath due to the very slightly lower solubility at higher temperature. The quantity precipitated is very small, however, amounting to a few tenths of a percent of the equilibrium calcite concentration of each pore volume of water transported per C-degree of temperature increase (cf. the very shallow negative slope of the broken level curves shown in Figure J-7). Over time, however, a not entirely insignificant amount of calcite dissolved in the till will end up reprecipitated and redistributed along the flowpath at greater depth. If the calcite initially present in the till is eventually depleted, then Equation J-25 is appropriate for the estimation of the calcite-depletion time, and Figure J-4 indicates the equilibrium calcium concentration, rather than Figure J-7.

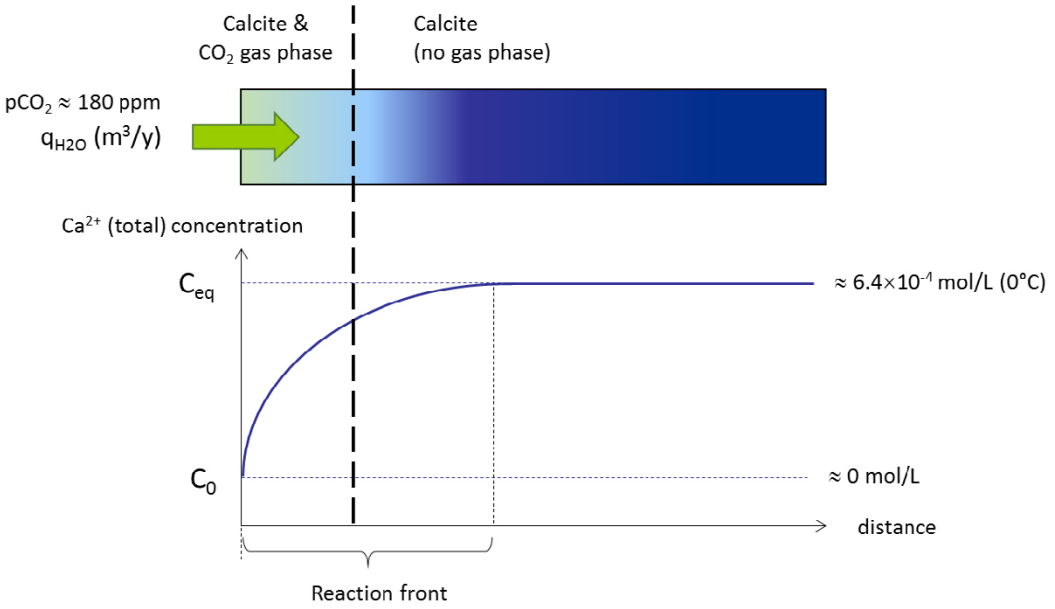

Figure J-6. *Conceptualisation of calcite depletion process for a flowpath where infiltrating dilute, glacial groundwater (with initial concentration, C_0) dissolves calcite. In this case, calcite is equilibrated with a fixed partial pressure of CO_2 already at the inlet to the system. This is analogous to the situation that might occur where glacial till containing calcite is in contact with the atmosphere (and can be assumed to be an open system).*

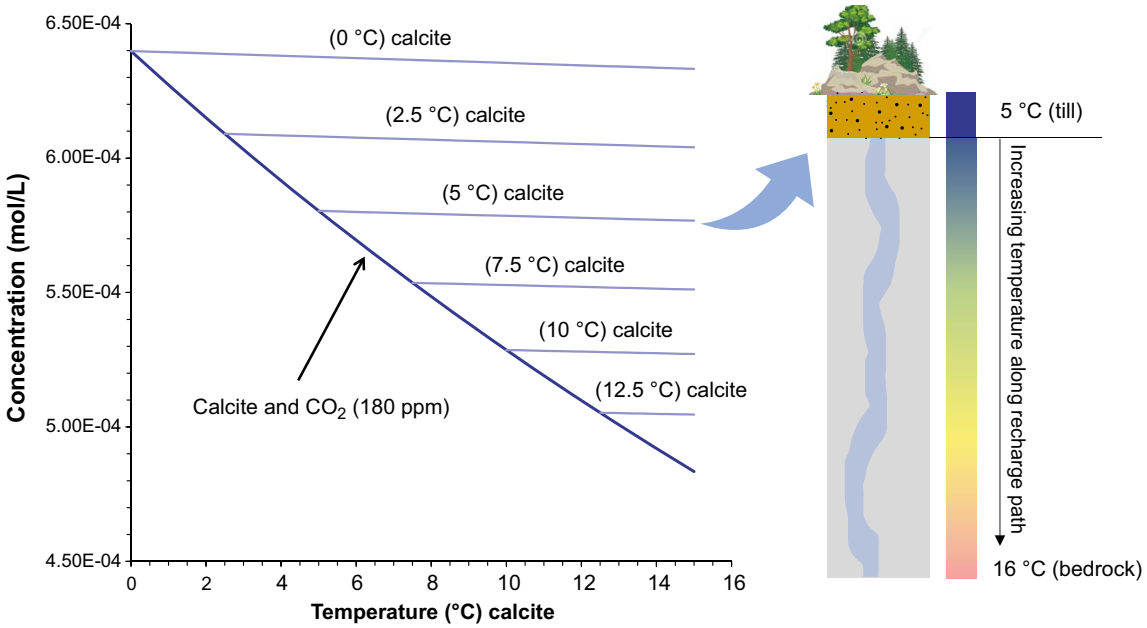

Figure J-7. *Concentration of Ca^{2+} in equilibrium with calcite as a function of temperature for water that has been pre-equilibrated at the same temperature with calcite and CO_2 gas of a fixed partial pressure of 180 ppm (unbroken curve). The unbroken curve describes the situation in the calcite containing till over a range of surface temperatures. Broken curves show the equilibrium for groundwater without a fixed CO_2 gas phase partial pressure starting at the surface at the (inlet water) temperature as indicated by the text annotation. Temperature values annotated on the level curves (broken lines) correspond to the temperature at the start of the flowpath and the lines show the trend for increasing temperature in the subsurface (indicated on the x-axis).*

Present composition of the infiltrating waters at Forsmark

Evidence on the chemical composition of present-day infiltrating waters at Forsmark may be found in the near surface groundwaters. The samples collected by SKB during the period 2002-07-18 to 2018-10-10 (Sicada 19_013) with elevations between −15 and +13 m a.s.l. are shortly described in this section.

An overview of the salinity and cationic charge of these near surface groundwaters may be seen in Figure J-8 and Figure J-9. A comparison with the category 1–3 deep groundwater data from Forsmark and Laxemar (Laaksoharju et al. 2008, 2009) is provided in Figure J-8. The figures show that the infiltrating waters at Forsmark have at present salinities ≈0.4 g/L or higher.

The calcite content in the regolith at Forsmark is relatively high (SKB 2008, Table 4-2), and this affects the composition of the porewaters, as calcite will partially dissolve when reacting with carbon dioxide in the overburden. Because the pCO_2 in soils vary widely, e.g. Amundson and Davidson (1990) it is not possible to assign an average partial pressure of CO_2 for the regolith in Forsmark. A lower limit to the equilibrium partial pressure of CO_2 in the regolith at Forsmark may be estimated by examining the values of alkalinity versus the corresponding calcium concentration and making a comparison with calculated curves at fixed pCO_2. Figure J-10 shows that the infiltrating meteoric waters are expected to have Ca^{2+} concentrations that correspond to quite high CO_2 contents in the regolith, larger than those corresponding to pCO_2 = 180 ppm used in the previous section (Influence of the regolith).

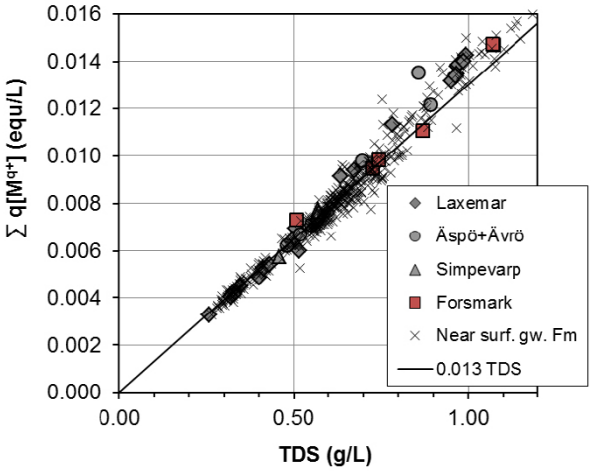

Figure J-8. *Values of $\sum q[M^{q+}]$ versus salinity (total dissolved solids, TDS) for the near surface groundwaters sampled at Forsmark. The data from the Forsmark and Oskarshamn areas (Laaksoharju et al. 2008, 2009) are shown for comparison. The correlation line for this salinity interval is also indicated.*

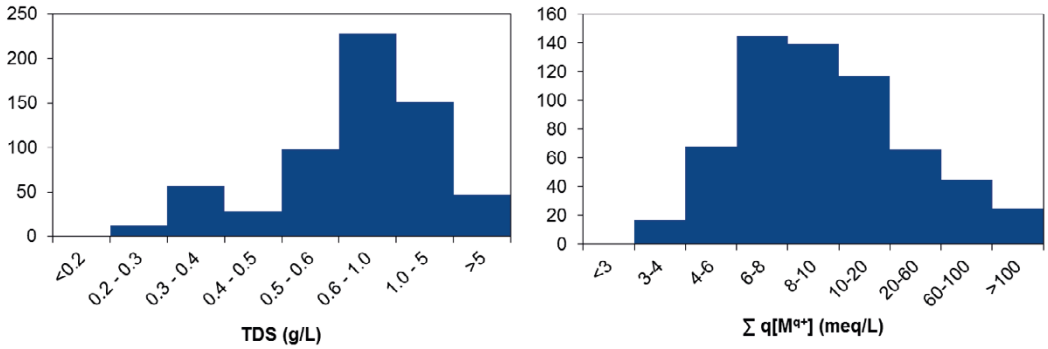

Figure J-9. *The distribution of TDS (total dissolved solids) and $\sum q[M^{q+}]$ for the near surface groundwaters sampled at Forsmark.*

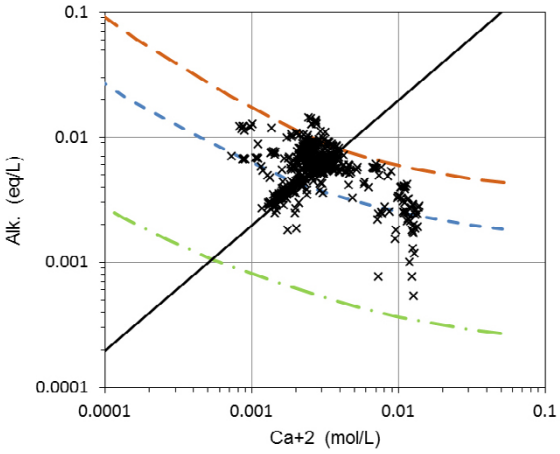

Figure J-10. *Sampled regolith porewaters (near surface groundwaters) from Forsmark (crosses). The curves correspond to the calculated alkalinity and Ca^{2+} concentration in equilibrium with calcite at 10 °C and at partial pressures of CO_2 gas of 180 ppm, 9000 ppm and 5 % (from bottom to top). The continuous line corresponds to the closed-system reaction: Calcite + CO_2 + H_2O = Ca^{2+} + 2 HCO_3^-.*

J.3 Effect of rock mineral weathering along a recharge path

J.3.1 Introduction

In an extension to the previous work, an analysis is made which attempts to estimate the rate at which Ca^{2+} (and other base cations) might be liberated from the rock matrix by weathering reactions coupled with matrix diffusion along recharge flowpaths. Although much simplified, this is a useful scoping calculation since if the rate of production of Ca^{2+} ions in the pore space of the rock matrix is sufficiently high, the depletion rate of fracture-filling calcite might be much less than what the previous analysis would suggest. It is also conceivable that the rate of weathering is sufficiently high that the calcite content of recharge paths is replenished as quickly as it is mobilised giving a net zero rate of depletion. Indeed, the weathering of Ca^{2+} from the same primary mineral phases comprising the rock coupled with precipitation with atmospheric (or, respiratory) CO_2 in the till is what leads to the continuous formation of calcite in the till in the first place.

The most volumetrically important rock type at Forsmark is metamorphosed, medium-grained granite to granodiorite (in this work, referred to as “metagranite”). The mineralogical composition of the rock (Sandström and Stephens 2009) is given in Table J-1 and shows a plagioclase content of roughly 33.8 % (vol.). Plagioclase is a group name for feldspar minerals with a variable Na and Ca content where the minerals albite ($NaAlSi_3O_8$) and anorthite ($CaAl_2Si_2O_8$) constitute end members. Albite is additionally divided into high-albite and low-albite triclinic crystal variants which differ slightly in unit cell volume (and equilibrium constant for dissolution). According to Stefansson (2001), the albite-high polymorph is a more disordered structure that results from heating (typically volcanic) whereas the more ordered albite-low structure is more commonly associated with deep metamorphic and plutonic rocks.

Table J-1. Mineralogical composition of metamorphosed, medium-grained granite to granodiorite (SKB rock code 101057) which is the volumetrically dominant rock type at the Forsmark site (Sandström and Stephens 2009).

	Median vol %	Range vol %	Inter-quartile range vol %
Quartz	34.6	19.0–46.4	32.4–39.0
K-feldspar	23.4	8.2–36.0	21.0–28.2
Plagioclase	33.8	24.0–52.0	30.6–36.4
Biotite	5.4	1.8–12.4	4.2–6.2

Based on whole rock geochemical analysis in Sandström and Stephens (2009) Forsmark metagranite is roughly 3.37 wt.% Na_2O and 1.47 wt% CaO. Taking into account the phosphate content of the rock (0.04 wt% P_2O_5) which can be presumed to be present as apatite ($Ca_5(PO_4)_3(F,OH)$) and assuming that the remainder is mostly representative of plagioclase, this suggests a predominantly oligoclase composition broadly consistent with $An_{30}Ab_{70}$ ($Ca_{0.3}Na_{0.7}Al_{1.3}Si_{2.7}O_8$).

A simplified analytical solution for the dissolution of oligoclase by weathering reactions and transport of Ca^{2+} in the recharge path is developed in next section.

J.3.2 Analytical model for Ca production along recharge flowpaths

Simplified derivation for a homogenous rock matrix

In the representation of oligoclase dissolution in this work, we assume that the system can be treated using a single component mass balance for dissolved Ca^{2+} where multicomponent interactions are neglected as well as precipitation-dissolution processes involving other minerals. This is, of course, an extremely simplified representation although should be sufficient to ascertain whether more detailed reactive transport simulation studies should be undertaken to study the phenomenon in more detail.

For a 1D flowpath with dispersion and matrix diffusion, the single component differential mass balance for the fracture flowpath and rock matrix are, respectively (symbols appearing in the equations of Section 19.3.2 are described in Table J-2):

$$\frac{\partial c_f}{\partial t} + v\frac{\partial c_f}{\partial x} - D_L\frac{\partial^2 c_f}{\partial x^2} = \frac{2}{\delta_t}\left(D_p\varepsilon_p\right)\frac{\partial c_p}{\partial z}\bigg|_{z=0} \tag{J-26}$$

$$\frac{\partial c_p}{\partial t} - D_p\frac{\partial^2 c_p}{\partial z^2} = k_+ A_m\left(1-\frac{c_p}{c_{eq}}\right) \tag{J-27}$$

The reaction rate of oligoclase (right-hand side of Equation J-27) is assumed to follow a simple TST-type (transition state theory) rate law (e.g. Steefel and Macquarie 1996). In its simplest form the dissolution rate (mol/m^{3}s) is given by the product of the far from equilibrium kinetic rate k_+ (mol/m^{2}s), the specific surface area of reacting mineral per volume of porewater A_m (m^2/m$^3_{H2O}$), and the driving force describing approach to equilibrium. In the present formulation, we approximate the approach to equilibrium as one minus the ratio of pore concentration c_p (mol/m^3) relative to the equilibrium concentration, c_{eq} (mol/m^3).

Here, we define the reactive surface area per unit volume of rock matrix porewater (m^2/m$^3_{H2O}$) as:

$$A_m = f_R\phi_m\left(\frac{1-\varepsilon_p}{\varepsilon_p}\right)\rho_s a_m \tag{J-28}$$

In order to simplify the mathematical description, we also introduce the following dimensionless variables for the fractional path length and dimensionless concentration in the fracture and rock matrix:

$$\theta = x/L \tag{J-29}$$

$$\chi_f = \frac{c_f - c_{eq}}{c_0 - c_{eq}} \tag{J-30}$$

$$\chi_p = \frac{c_p - c_{eq}}{c_0 - c_{eq}} \tag{J-31}$$

At steady-state, Equation J-27 can then be written as:

$$\frac{d^2\chi_p}{dz^2} = \left(\frac{k_+ A_m}{D_p c_{eq}}\right)\chi_p \tag{J-32}$$

Due to the ongoing dissolution of matrix mineral, a true steady state does not really exist as the porosity is (at least in principle) constantly evolving over time. Since the rate of change of the rock matrix porosity is very slow, however, it is reasonable to assume a quasi-stationary state for the transport problem. It should therefore be noted that when we use the term steady-state in this work we, in fact, mean quasi-stationary state.

Equation J-27 has the general solution:

$$\chi = \alpha_1 \exp\left(m_1 z\right) + \alpha_2 \exp\left(m_2 z\right) \tag{J-33}$$

Where α_1 and α_2 are constants, and m_1 and m_2 are the roots of the associated eigenvalue equation:

$$m^2 - \left(\frac{k_+ A_m}{D_p c_{eq}}\right) = 0 \tag{J-34}$$

Which has the following solutions:

$$m = \pm\sqrt{\frac{k_+ A_m}{D_p c_{eq}}} \tag{J-35}$$

For an unbounded rock matrix where the concentration at the fracture surface is equal to that in the flow channel ($\chi_p\big|_{z=0} = \chi_f$), we then can write:

$$\chi_p = \chi_f \exp\left(-z\sqrt{\frac{k_+ A_m}{D_p c_{eq}}}\right) \tag{J-36}$$

At the fracture surface ($z = 0$), the derivative of Equation J-36 is:

$$\left.\frac{d\chi_p}{dz}\right|_{z=0} = -\chi_f \sqrt{\frac{k_+ A_m}{D_p c_{eq}}} \tag{J-37}$$

The flux at the fracture surface can then be written as:

$$J_z = \left(D_p \varepsilon_p\right)\left.\frac{dc_p}{dz}\right|_{z=0} = -\chi_f D_p \varepsilon_p \sqrt{\frac{k_+ A_m}{D_p c_{eq}}} \tag{J-38}$$

At steady state and assuming the previously established definitions, we can write for the fracture (Equation J-26):

$$\frac{v}{L}\frac{d\chi_f}{d\theta} - \frac{D_L}{L^2}\frac{\partial^2 c_p}{\partial \theta^2} = \frac{2}{\delta_t}\left(D_p \varepsilon_p\right)\left.\frac{d\chi_p}{dz}\right|_{z=0} \tag{J-39}$$

Substituting the previously derived result for the matrix flux term (Equation J-38), gives:

$$\frac{1}{\mathrm{Pe}}\frac{\partial^2 \chi_f}{\partial \theta^2} - \frac{d\chi_f}{d\theta} - \mathrm{Da}_m \cdot \chi_f = 0 \tag{J-40}$$

Where,

$$\mathrm{Da}_m = F \cdot D_p \varepsilon_p \sqrt{\frac{k_+ A_m}{D_p c_{eq}}} \tag{J-41}$$

For a constant concentration boundary condition ($c_{f(0)} = c_{p(0)} = c_0$), we can write:

$$\chi_{f(0)} = 1 \tag{J-42}$$

The analytical solution to Equation J-40 subject to the boundary condition (Equation J-42) is:

$$\chi_f = \exp\left(\frac{\mathrm{Pe}}{2}\left(1 - a\right)\theta\right) \tag{J-43}$$

Where,

$$a = \sqrt{1 + \frac{4}{\mathrm{Pe}}\mathrm{Da}_m} \tag{J-44}$$

A similar solution has been given by Yang (2012) for the case of silica transport in a fracture bounded by an infinite medium. In this solution, however, the mineral constituting the fracture surface is also included as a source term. Adapting this description to the present system, the mass balance including the contribution of Ca^{2+} from dissolving oligoclase at the fracture surface can be written as:

$$\frac{\partial c_f}{\partial t} + v\frac{\partial c_f}{\partial x} - D_L\frac{\partial^2 c_f}{\partial x^2} = \frac{2}{\delta_t}\left(D_p\varepsilon_p\right)\frac{\partial c_p}{\partial z}\bigg|_{z=0} + \frac{2}{\delta_t}k_+ f_R\phi_m\left(1-\varepsilon_p\right)\left(1-\frac{c_f}{c_{eq}}\right) \tag{J-45}$$

Using the previously established dimensionless variables, we can then write for the steady state:

$$\frac{d\chi_f}{d\theta} - \frac{D_L}{vL}\frac{d^2\chi_f}{d\theta^2} = -\left(\frac{2}{v\delta_t}L\left(D_p\varepsilon_p\right)\sqrt{\frac{k_+A_m}{D_p c_{eq}}} + \frac{2}{v\delta_t}L\frac{k_+}{c_{eq}}f_R\phi_m\left(1-\varepsilon_p\right)\right)\chi_f \tag{J-46}$$

And thus:

$$\frac{1}{\mathrm{Pe}}\frac{\partial^2\chi_f}{\partial\theta^2} - \frac{d\chi_f}{d\theta} - \left(\mathrm{Da}_m + \mathrm{Da}_f\right)\cdot\ \chi_f = 0 \tag{J-47}$$

Where,

$$\mathrm{Da}_f = F\cdot\frac{k_+ f_R\phi_m}{c_{eq}}\left(1-\varepsilon_p\right) \tag{J-48}$$

The solution to Equation J-47 can then be obtained directly from Equation J-43, where the parameter a is now defined as:

$$a = \sqrt{1 + \frac{4}{\mathrm{Pe}}\left(\mathrm{Da}_m + \mathrm{Da}_f\right)} \tag{J-49}$$

Variant case for a homogenous rock matrix with an inert alteration layer

In this extended case, we consider the additional impact of an alteration zone where the oligoclase dissolution (Ca^{2+} production rate) is effectively zero. This might be the case for flowpaths which have been subject to considerable past hydrothermal alteration where the zone of alteration is depleted of its calcium content. We now have a discrete two-layer rock matrix described by the following mass balance equations:

$$\frac{\partial c_p}{\partial t} + D_{pa}\frac{\partial^2 c_p}{\partial z^2} = 0 \qquad 0 \le z < \delta_a \tag{J-50}$$

$$\frac{\partial c_p}{\partial t} + D_{pm}\frac{\partial^2 c_p}{\partial z^2} = k_+ A_m\left(1-\frac{c_p}{c_{eq}}\right) \qquad z \ge \delta_a \tag{J-51}$$

In terms of the previously established dimensionless variables, we can write for the steady state:

$$\frac{d^2\chi_p}{dz^2} = 0 \qquad 0 \le z < \delta_a \tag{J-52}$$

$$\frac{d^2\chi_p}{dz^2} = \left(\frac{k_+A_m}{D_{pm}c_{eq}}\right)\chi_p \qquad z \ge \delta_a \tag{J-53}$$

Equation J-52 and J-53 can be shown to have the solution:

$$\chi_p = \chi_f + \left(\chi_a - \chi_f\right)\frac{z}{\delta_a} \qquad 0 \le z < \delta_a \tag{J-54}$$

$$\chi_p = \chi_a \exp\left(-\left(z-\delta_a\right)\sqrt{\frac{k_+ A}{D_{pm}c_{eq}}}\right) \qquad z \ge \delta_a \tag{J-55}$$

Taking the derivatives of Equation J-54 and J-55 gives:

$$\frac{d\chi_p}{dz} = \frac{\chi_a - \chi_f}{\delta_a} \qquad 0 \le z < \delta_a \tag{J-56}$$

$$\frac{d\chi_p}{dz} = -\chi_a\sqrt{\frac{k_+ A_m}{D_p c_{eq}}}\exp\left(-\left(z-\delta_a\right)\sqrt{\frac{k_+ A_m}{D_p c_{eq}}}\right) \qquad z \ge \delta_a \tag{J-57}$$

The flux at the interface ($z = \delta_a$) between the two zones must be equal, thus:

$$J_z = D_{pa}\varepsilon_{pa}\left(\frac{\chi_a - \chi_f}{\delta_a}\right) = -D_{pm}\varepsilon_{pm}\chi_a\sqrt{\frac{k_+ A_m}{D_{pm}c_{eq}}} \tag{J-58}$$

Solving for c_a gives:

$$\chi_a = \chi_f \Bigg/ \left(1 + \delta_a\left(\frac{D_{pm}\varepsilon_{pm}}{D_{pa}\varepsilon_{pa}}\right)\sqrt{\frac{k_+ A_m}{D_{pm}c_{eq}}}\right) \tag{J-59}$$

We can then write for the flux at the fracture surface:

$$D_{pa}\varepsilon_{pa}\left.\frac{d\chi_p}{dz}\right|_{z=0} = -D_{pa}\varepsilon_{pa}\left(\frac{\left(\frac{D_{pm}\varepsilon_{pm}}{D_{pa}\varepsilon_{pa}}\right)\sqrt{\frac{k_+ A_m}{D_{pm}c_{eq}}}}{1+\delta_a\left(\frac{D_{pm}\varepsilon_{pm}}{D_{pa}\varepsilon_{pa}}\right)\sqrt{\frac{k_+ A_m}{D_{pm}c_{eq}}}}\right)\chi_f \tag{J-60}$$

Noting that there is no surface production of Ca^{2+} in this formulation, we can write for the fracture flowpath:

$$\frac{d\chi_f}{d\theta} - \frac{D_L}{vL}\frac{d^2\chi_f}{d\theta^2} = -\left(\frac{2}{v\delta_t}L\left(D_{pa}\varepsilon_{pa}\right)\cdot\frac{\left(\frac{D_{pm}\varepsilon_{pm}}{D_{pa}\varepsilon_{pa}}\right)\sqrt{\frac{k_+ A_m}{D_{pm}c_{eq}}}}{1+\delta_a\left(\frac{D_{pm}\varepsilon_{pm}}{D_{pa}\varepsilon_{pa}}\right)\sqrt{\frac{k_+ A_m}{D_{pm}c_{eq}}}}\right)\chi_f \tag{J-61}$$

And thus:

$$\frac{1}{\mathrm{Pe}}\frac{\partial^2\chi_f}{\partial\theta^2} - \frac{d\chi_f}{d\theta} - \mathrm{Da}_m^* \cdot \chi_f = 0 \tag{J-62}$$

Where,

$$\mathrm{Da}_m^* = F \cdot D_{pm}\varepsilon_{pm}\frac{\sqrt{\frac{k_+ A_m}{D_{pm}c_{eq}}}}{1+\delta_a\left(\frac{D_{pm}\varepsilon_{pm}}{D_{pa}\varepsilon_{pa}}\right)\sqrt{\frac{k_+ A_m}{D_{pm}c_{eq}}}} \tag{J-63}$$

For a constant concentration boundary condition, the general solution to Equation J-62 is the same as given previously, although with adjusted definition of Da_m:

$$\chi_f = \exp\left(\frac{\mathrm{Pe}}{2}(1-a)\theta \right) \tag{J-64}$$

Where,

$$a = \sqrt{1+\frac{4}{\mathrm{Pe}}\mathrm{Da}_m^*} \tag{J-65}$$

J.3.3 Application to the rock at Forsmark

Assuming that the dissolution and transport of Ca^{2+} can be treated as a single component mass balance (a very rough approximation) without any multicomponent interactions and dissolution-precipitation processes of secondary minerals, the analytical solution for Ca^{2+} concentration along the recharge path can be given as (previous Equation J-64):

$$\frac{c_f - c_{eq}}{c_0 - c_{eq}} = \exp\left(\frac{\mathrm{Pe}}{2}(1-a)\theta \right) \tag{J-66}$$

Where, the dimensionless variable q is the fractional flowpath length for a specified flowpath flow-related transport resistance, F (y/m):

$$\theta = x/L \tag{J-67}$$

The parameter a is defined as (previous Equation J-65):

$$a = \sqrt{1+\frac{4}{\mathrm{Pe}}\mathrm{Da}_m^*} \tag{J-68}$$

Where the Damköhler number for the coupled reaction diffusion problem is given by (previous Equation J-63):

$$\mathrm{Da}_m^* = F \cdot D_{pm}\varepsilon_{pm} \frac{\sqrt{\frac{k_+ A_m}{D_{pm}c_{eq}}}}{1+\delta_a\left(\frac{D_{pm}\varepsilon_{pm}}{D_{pa}\varepsilon_{pa}}\right)\sqrt{\frac{k_+ A_m}{D_{pm}c_{eq}}}} \tag{J-69}$$

In the limit of zero dispersion ($\mathrm{Pe} \approx \infty$), the analytical solution simplifies to:

$$\frac{c_f - c_{eq}}{c - c_{eq}} = \exp\left(-Da_m^* \cdot \theta\right) \tag{J-70}$$

In this formulation we consider advective flow with hydrodynamic dispersion as well as matrix diffusion of Ca^{2+} produced by weathering reactions in the rock matrix. Furthermore, to increase realism we assume that the rock matrix flanking the recharge path has undergone some period of hydrothermal alteration and has been depleted of readily leachable Ca-content. The thickness of the assumed alteration zone is given by the constant d_a (m) in Equation J-69.

As can be readily appreciated from Equations J-66 and J-69, it is necessary to specify the equilibrium concentration of the dissolving Ca^{2+}. Given the well-constrained total geochemistry and mineralogy of the rock matrix, this is surprisingly difficult to specify owing to the slow reaction rates of silicate minerals and the fact that it is challenging to identify a set of secondary minerals that are consistent with observations of weathering in low temperature natural systems. The difficulty is compounded by the fact that alkali and plagioclase feldspar minerals are typically solid solutions of variable composition and do not necessarily undergo congruent dissolution in a fashion that is easy to represent accurately in thermodynamic models.

The equilibrium concentration appears in the analytical solution both on the left-hand side of Equation J-66 (which describes the approach to equilibrium) as well as in the definition of the Damköhler number, Da_m^*. As can be readily appreciated from the form of Equation J-66 (or, more easily Equation J-70 for no hydrodynamic dispersion), the higher the equilibrium concentration, the longer the flowpath distance

required for the concentration to approach the equilibrium value. Since this is one of the more uncertain variables in the analysis, a range of possible values have been considered in this work.

Although it is feasible to calculate a nominal solubility product for the oligoclase dissolution reaction using the procedure described by Arnorsson and Stefansson (1999), this was beyond the scope of the present work. Instead, PhreeqC calculations have been made assuming simultaneous partial equilibrium of anorthite (An) and albite (Ab) in an attempt to bound the value of the equilibrium concentration of Ca^{2+} in the rock matrix. In these calculations, the concentration of silica (H_4SiO_4) and aluminium (Al^{3+}) are assumed fixed by simultaneous equilibrium with quartz and kaolinite. This may not give exactly the same results as a calculation for oligoclase, although should be similar order of magnitude for this initial scoping work. The results of the PhreeqC calculations are shown in Figure J-11 where the target saturation index of anorthite (and albite where appropriate) has been varied in a range.

Three different variants have been considered in the calculations: one case without albite, and also two cases considering the simultaneous partial equilibrium of the different polymorphs of albite (low albite and high albite). Some additional cases using solubility products taken from Stefansson (2001) are also shown in Figure J-11 for anorthite with and without albite-high as well as an Oligoclase with the composition $An_{29}Ab_{71}$ ($Ca_{0.29}Na_{0.71}Al_{1.29}Si_{2.71}O_8$) which is not far off the presumed composition of Forsmark oligoclase. The results using the Stefansson (2001) data, however, should be seen as being only indicative since the solubility products may not be fully consistent with the Thermochimie v9.0b TDB as can be appreciated by the slight offset of calculated values for anorthite and anorthite-albite combinations.

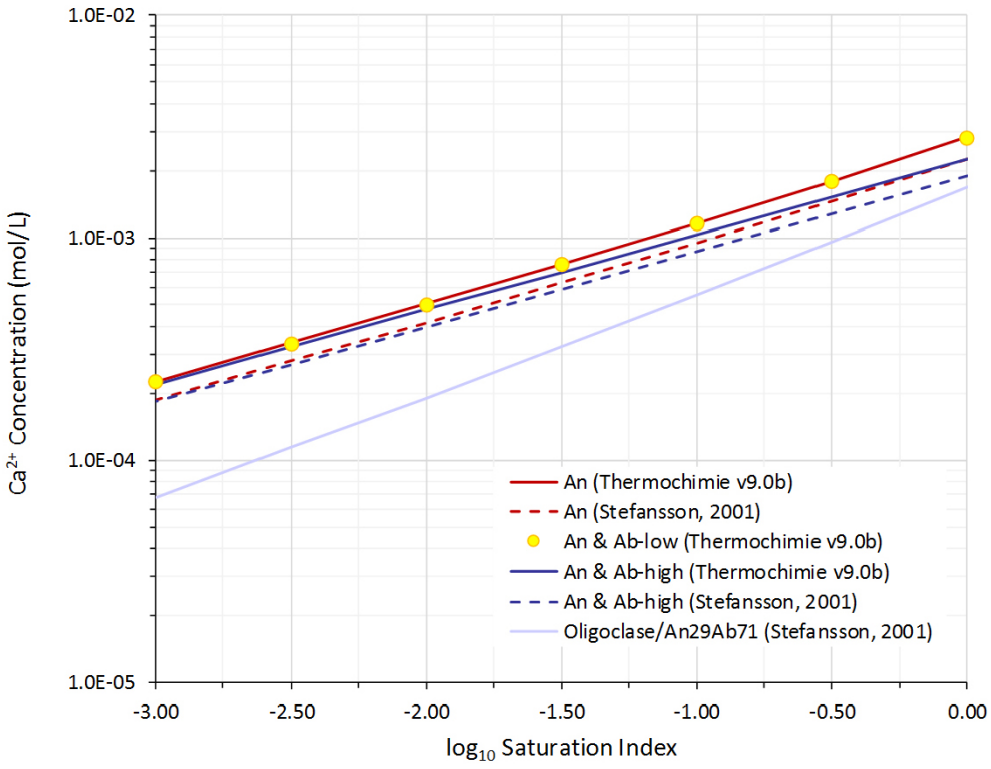

Figure J-11. *"Equilibrium" concentration of Ca^{2+} calculated using PhreeqC for Anorthite (An) at 0 °C with, and without, high- and low-albite (Ab) polymorphs. Different assumptions concerning the equilibrium state of oligoclase have been approximated by considering a range of effective saturation indices for anorthite (and albite where relevant) to simulate a partial equilibrium. The light blue line shows the Ca^{2+} concentration for Oligoclase partial equilibrium with composition $An_{29}Ab_{71}$ ($Ca_{0.29}Na_{0.71}Al_{1.29}Si_{2.71}O_8$) calculated using the solubility product given by Stefansson (2001) and different saturation states for the oligoclase. This solubility product, however, may not be fully consistent with the ThermoChimie TDB so is only shown for context (as can be appreciated from the comparison cases for Anorthite and Albite indicated by broken lines with solubility products also taken from Stefansson (2001). In all cases, the concentration of silica (H_4SiO_4) and aluminium (Al^{3+}) are assumed fixed by simultaneous equilibrium with quartz and kaolinite.*

As can be seen from the calculation results shown in Figure J-11, the presence or absence of albite has very little effect on the equilibrium concentration of Ca^{2+}. The only impact is by way of a small ionic strength effect on the solubility of anorthite (since high albite is more soluble than low albite). It can be noted that the presence or absence K-feldspar (microcline) or calcite has no impact on the calculated equilibrium. Based on the PhreeqC simulation results, we have assumed Ca^{2+} equilibrium concentrations in the range 3×10^{-4} mol/L to 3×10^{-3} mol/L as being an approximately representative range for the scoping calculations of Ca transport.

For the far-from-equilibrium kinetic rate of oligoclase dissolution, k_+ (mol/m^{2}s) two cases have been considered; a moderately slow kinetic rate of 10^{-14} mol/m^{2}s and a very slow kinetic rate of 10^{-16} mol/m^{2}s. Although faster kinetic rates are possible, these have not been considered since they may not be conservative for the intact rock under in-situ conditions. It can be noted that the kinetic rate range of 10^{-14} to 10^{-16} mol/m^{2}s is at the low end of values reported in the literature (e.g. Brantley and Olsen 2014).

It is assumed in this work that the reactive surface area is approximately equal to 1 % of the BET surface area of Oligoclase also assuming that the oligoclase fraction of the rock has a specific surface area fraction in proportion to its volume fraction (33.8 %) in the rock. The bulk BET surface area of the rock is assumed to be 0.018 m^2/g based on the whole core measurements reported by André et al. (2008). This would appear to be a relatively conservative assumption.

For the alteration layer and unaltered matrix, we have assumed material properties (porosity and pore diffusivity) as compiled in Crawford and Löfgren (2019) for typical Forsmark transport classes, see Table J-2. Although the alteration layer thickness in Crawford and Löfgren (2019) is estimated to be on the order of 1 cm, a thickness of 10 cm has been assumed in this work to exaggerate the impact of the alteration layer.

Table J-2. Parameter values used in scoping calculations in this work.

Parameter (units)	Value	Description
A_0 (m^2/g)	0.018	BET surface area of intact rock matrix
f_R (-)	0.01	"Reactive" fraction of BET surface area (conservatively asumed value)
ρ_s (kg/m^3)	2657	Average crystallographic density (non-porous) of rock
ϕ (-)	0.338	Plagioclase volume fraction
D_w (m^2/s)	3.604×10^{-10}	Free diffusivity of Ca^{2+} at 0 °C and infinite dilution
ε_{pm} (-)	1.8×10^{-3}	Transport porosity of unaltered rock matrix
F_{fm} (-)	2.1×10^{-5}	Formation factor for the rock matrix
D_{pm} (m^2/s)	4.205×10^{-12}	Pore diffusivity of rock matrix
ε_{ps} (-)	0.01	Transport porosity of alteration zone
F_{fs} (-)	5×10^{-4}	Formation factor for the alteration zone
D_{ps} (m^2/s)	1.802×10^{-11}	Pore diffusivity of alteration zone
c_0 (mol/L)	0	Inlet concentration of Ca^{2+}
c_{eq} (mol/L)	3×10^{-4}–3×10^{-3}	"Equilibrium" concentration of Ca^{2+} (Oligoclase dissolution)
δ_a (m)	0.1	Assumed thickness of alteration zone
L (m)	450	Recharge flowpath length
F (y/m)	10^4	Recharge flowpath flow-related transport resistance
Pe (-)	10	Péclet number for hydrodynamic dispersion
k_+ (mol/m^{2}s)	10^{-16}–10^{-14}	Far from equilibrium kinetic rate of oligoclase dissolution

Using Equation J-66 to J-69 and the parameter values given in Table J-2, calculations have been made of the production of Ca^{2+} in the rock matrix, out-diffusion and transport along a recharge path with an assumed low-range F value (10^4 y/m). The results of the calculations are shown in Figure J-12 ($k_+ = 10^{-14}$ mol/m^{2}s) and Figure J-13 ($k_+ = 10^{-16}$ mol/m^{2}s).

Interestingly, the presence of a 10 cm alteration zone depleted of its easily leachable Ca-content seems to have only a minor effect on the transport of Ca provided the effective diffusivity of the alteration zone is at least 10–100 times that of the unaltered rock matrix. For the case considered in Figure J-12 and Figure J-13, the effective diffusivity ratio is roughly 24. If the alteration zone has an effective diffusivity roughly the same order of magnitude as the unaltered rock matrix then the dampening effect on Ca-production can be considerable. A sensitivity case is shown in Figure J-14 where the alteration zone is assumed to have the same effective diffusivity as the unaltered rock matrix.

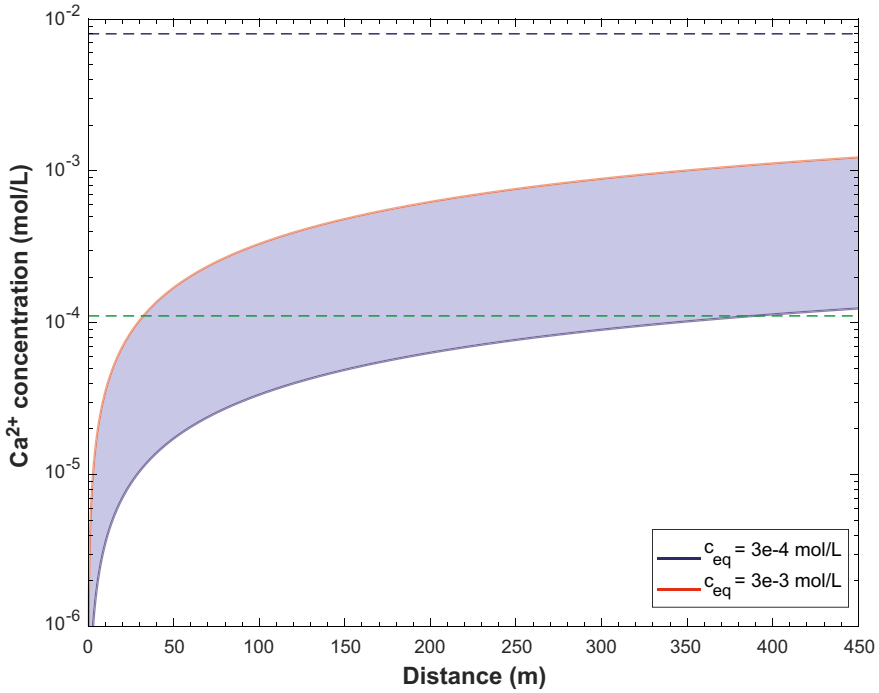

Figure J-12. *Ca-transport along a recharge path with production in the rock matrix from oligoclase weathering reactions assuming a flowpath F value of 10^4 y/m and kinetic rate constant $k_+ = 10^{-14}$ (mol/m^{2}s). Other model parameters are set to values as defined in Table J-2. The horizontal broken green line indicates the equilibrium concentration calculated previously for calcite at 0 °C while the broken blue line indicates the critical concentration level of 8 meq/L for buffer stability (Posiva SKB 2017).*

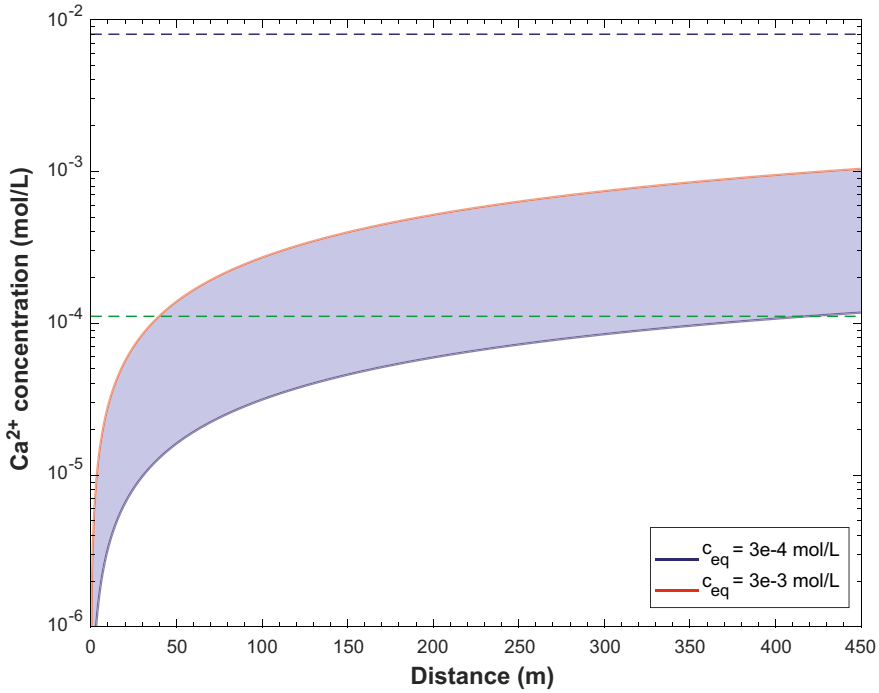

Figure J-13. *Ca-transport along a recharge path with production in the rock matrix from oligoclase weathering reactions assuming a flowpath F value of 10^4 y/m and kinetic rate constant $k_+ = 10^{-16}$ (mol/m^{2}s). Other model parameters are set to values as defined in Table J-2. The horizontal broken green line indicates the equilibrium concentration calculated previously for calcite at 0 °C while the broken blue line indicates the critical concentration level of 8 meq/L for buffer stability (Posiva SKB 2017).*

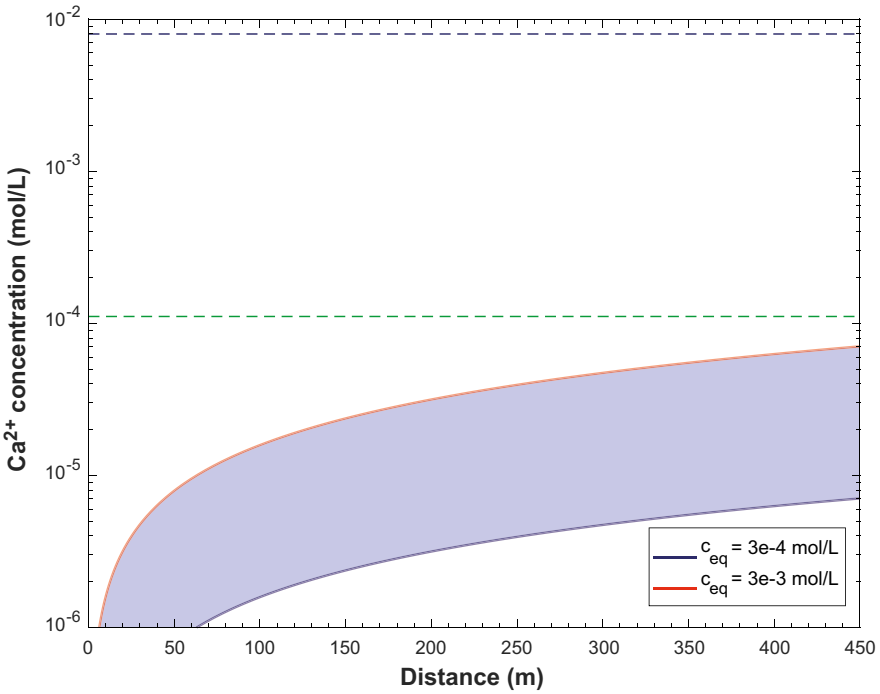

Figure J-14. *Ca-transport along a recharge path with production in the rock matrix from oligoclase weathering reactions assuming a flowpath F value of 10^4 y/m and kinetic rate constant $k_+ = 10^{-14}$ (mol/m^{2}s). Other model parameters are set to values as defined in Table J-2 except for the effective diffusivity of the alteration zone which is assumed to be identical to the unaltered rock matrix. The horizontal broken green line indicates the equilibrium concentration calculated previously for calcite at 0 °C while the broken blue line indicates the critical concentration level of 8 meq/L for buffer stability (Posiva SKB 2017).*

J.4 Discussion and conclusions

From the scoping calculations made in Section 19.2, we conclude that the calcite content of average recharge paths at the Forsmark site is sufficient to withstand many thousand years of sustained high-flow without being fully depleted, even if the inflowing water is glacial meltwater. In the scoping calculations, the best estimate time (y) for calcite depletion given the various underlying assumptions is roughly in numerical parity with (~125 % of) the F value. A recharge flowpath with an F value of 10^4 y/m will therefore take slightly more than 10 ky to fully deplete of its calcite content. Since the quantitative statistics of fracture mineral abundance at Forsmark as compiled by Eklund and Mattson (2009) are volumetrically based, it is necessary to make assumptions about the porosity of the observed fracture coatings. In the calculations made in this work a range of fracture coating porosities in the range 0.3–0.7 is assumed giving a calcite specific mass on the order of 18.4–43.0 g/m^2 of nominal fracture area. It is likely that this assumed range is overly generous and lower porosities are quite possible which would imply greater specific mass of calcite and even longer depletion times. The occurrence at present of calcite in the regolith at Forsmark is expected to prevent the depletion of calcite in the rock fractures and possibly even contribute to a very slight positive mass balance of calcite at lower depths along recharge paths if there is a non-negligible increasing temperature gradient with depth.

In the extended analysis presented in Section 19.3, the rate of Ca-production by weathering reactions in the rock matrix and out-diffusion into the main recharge path appears to be sufficiently large to at least partially, if not completely offset the flushing of calcite from the recharge path. This conclusion, however, is based on a simple comparison of the amount of Ca mobilised from upstream calcite dissolution with the amount produced by mineral (oligoclase) weathering. If the Ca^{2+} produced by the weathering mechanism precipitates with a significant fraction of the in-transported carbonate, the depletion of calcite can be potentially arrested. A more detailed analysis including the de-novo precipitation of calcite would require more detailed reactive transport modelling that was beyond the scope of the present work.

Although the calculations only consider transport of Ca^{2+}, it is also possible that the simultaneous production of Na^{+} ions from oligoclase dissolution together with the effect of matrix out-diffusion of higher salinity water from the rock matrix could keep salinity levels at depth above the critical level of $\sum q[M^{q+}] = 8$ meq/L for a longer period of time than that predicted by invoking matrix diffusion of higher salinity water only. Although the scoping calculations presented in this work are extremely simplified, they use parameter values that seem highly conservative with regard to material properties and surface area normalised reaction rates. At the very least, the calculations do not seem to rule out the possibility of a significant contribution to the groundwater ionic strength at depth from ongoing weathering of oligoclase (and other rock matrix minerals not considered in the calculations).

Appendix K

Safety assessment PSAR – Updated calculations on penetration of dilute water

K.1 Implementation

In Joyce et al. (2010), calculations for use in SR-Site on penetration of dilute water are presented. The analytical solution used is based on transport along one-dimensional recharge paths in the discrete fracture network model used in the hydrogeological simulations of SR-Site. In the analytical solution, diffusion from the stagnant water in the matrix to the flowing water channel is considered; specifically, an infiltration of fresh water with zero concentration is assumed, while the matrix initially is loaded with water with a non-zero concentration (assuming equilibrium between fracture and matrix water prior to the infiltration of fresh water). Moreover, the matrix extent is assumed infinite in the analytical solution based on the Complementary Error Function, but in order to account for the effect of a finite matrix, also a solution based on assuming advection to be sufficiently slow to allow equilibrium transport conditions to apply, a retardation factor for the advance of the mixing front is derived. The time for penetration of dilute water is then estimated using the smaller value provided by these two solutions.

In PSAR, a number of the simplifying assumptions in the above approach are relaxed. First, scoping calculations indicate that the use of the equilibrium transport conditions assumption is very conservative; hence, a solution which explicitly incorporates a finite matrix is preferable. Second, the assumption of dilute water having zero concentration is also overly conservative, and third, the conceptual model of transport along one-dimensional flow paths interacting only with the surrounding matrix is likely conservative. In reality, flow paths will encounter fracture intersections where mixing may occur, and there will also be an interaction between the flowing water in the channels and the stagnant water (in the fractures) between the flow channels. Finally, in SR-Site the criterion for the water concentration implying buffer erosion was not strictly applied in the temperate phase calculations (a safety factor of approximately three was applied).

With the above considerations in mind, a solution is derived based on the results in Mahmoudzadeh et al. (2013). In their work, injection of a non-zero concentration water into a system with initially zero concentration water in both matrix and channel is considered. In this appendix, a solution is obtained for a model simlar to Mahmoudzadeh et al. (2013), but for the case of constant inlet concentration of C_{in}, and constant initial concentration of C_0 within all regions.

The solution in Mahmoudzadeh et al. (2013) incorporates the effect of a finite matrix and stagnant water zones of finite extent next to the flow channel and provides the concentration of a non-decaying solute through a flow channel. It also accounts for diffusion into the finite rock matrices from the stagnant zones. Figure K-1 illustrates a conceptual picture of the model (Mahmoudzadeh et al. 2013). Flow is taking place through a rectangular channel of width $2W_f$ and aperture $2b_f$. The water velocity, u, is assumed to be uniform across the flow channel, and complete mixing is assumed. The stagnant water zone next to the flow channel is conceptualized as a rectangular cuboid with the same length as the flow channel but different aperture $2b_s$ and width $2W_s$. Transport along the fracture is controlled by advection, and solute can diffuse directly from the flow channel into the adjacent rock matrix. Solute may also first diffuse into the stagnant water zone and then from there into the rock matrix adjacent to it. Although in Figure K-1 diffusion in both the stagnant water zone and the rock matrix is shown only in the up and left directions, the model also considers diffusion in opposite directions. In addition, linear equilibrium sorption onto both the fracture surface and the rock matrix is included.

Using the 1-D approach, as was done by Hodgkinson and Maul (1988), the system shown in Figure K-1 can be split into four subsystems, for which the equations of continuity describing solute transport processes can be formulated individually. This approach essentially takes a 3-D system as an assemblage of 1-D subsystems, in which solute transport is assumed to take place only in one direction. The exchange of solute between the subsystems are, then, described as a sink or source located at the interface, to couple the 1-D transport equations automatically. The following sections present the system of equations describing solute transport in each subsystem.

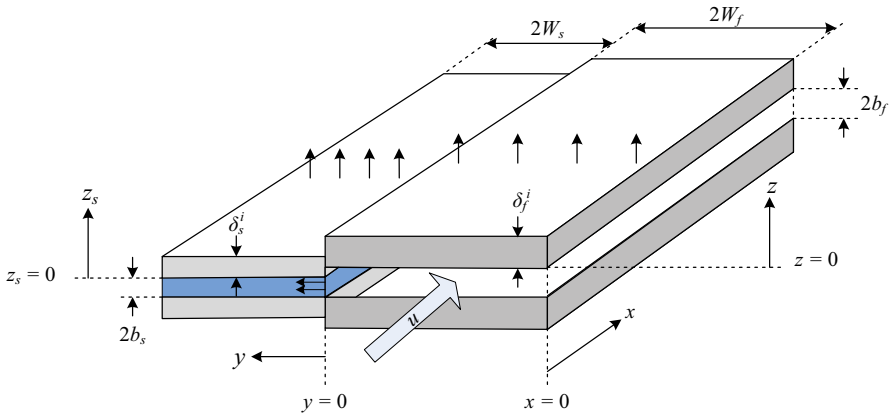

Figure K-1. *Flow in a channel in fractured rock where solutes diffuse into stagnant water zones as well as into the rock matrices in both positive and negative directions (Mahmoudzadeh et al. 2013).*

K.1.1 Solute transport through the flow channel

The 1-D transport equation for the aqueous concentration in the flow channel, C_f, is of the form,

$$R_f \frac{\partial C_f}{\partial t} = -u\frac{\partial C_f}{\partial x} + \frac{b_s}{b_f}\frac{D_s}{W_f}\frac{\partial C_s}{\partial y}\Big|_{y=0} + \frac{D_{ef}}{b_f}\frac{\partial C_{pf}}{\partial z}\Big|_{z=0} \quad \text{(K-1)}$$

where x is distance along the flow direction. y and z are the coordinates into the stagnant water zone and into the rock matrix adjacent to the flow channel, respectively, and both are perpendicular to the channel. A complete list of symbols and units is given in Table K-1.

The initial condition is,

$$C_f(x, 0) = C_0 \quad \text{(K-2)}$$

and the boundary condition at the inlet is given by,

$$C_f(0, t) = C_{in} \quad \text{(K-3)}$$

The first term at the right-hand side of Equation (K-1) describes the advection, while the last two terms describe the diffusion at the interfaces between the flow channel and the stagnant water zone and between the flow channel and the rock matrix adjacent to it, respectively.

K.1.2 Solute transport in the stagnant water zone

Assuming that the diffusion in the direction parallel to the flow is negligible, the transport equation for the solute concentration in the stagnant water zone, C_s, is given by,

$$R_s \frac{\partial C_s}{\partial t} = D_s \frac{\partial^2 C_s}{\partial y^2} + \frac{D_{es}}{b_s}\frac{\partial C_{ps}}{\partial z_s}\Big|_{z_s=0} \quad \text{(K-4)}$$

where z_s is the coordinate into the rock matrix adjacent to the stagnant water zone and is perpendicular to the interface between the stagnant water zone and the adjacent rock matrix. The last term at the right-hand side of Equation (K-4) describes diffusion at the interface between the stagnant water zone and the rock matrix adjacent to it.

The initial condition is,

$$C_s(y, 0) = C_0 \quad \text{(K-5)}$$

and the boundary conditions are given by,

$$C_s(0, t) = C_f \quad \text{(K-6)}$$

and

$$\frac{\partial C_s}{\partial y}\Big|_{y=2W_s} = 0 \quad \text{(K-7)}$$

The processes of solute transport in the flow channel and in the stagnant water zone are coupled through Equation (K-6), which describes the continuity of solute concentration.

K.1.3 Solute transport in the rock matrix adjacent to the flow channel

Accounting for diffusion and linear equilibrium sorption, the 1-D transport equation for the solute concentration in the pore water of the rock matrix adjacent to the flow channel, C_{pf}, is,

$$\frac{\partial C_{pf}}{\partial t} = D_{af} \frac{\partial^2 C_{pf}}{\partial z^2} \tag{K-8}$$

where the apparent diffusivity is defined as,

$$D_{af} = \frac{D_{ef}}{R_{pf} \varepsilon_{pf}} \tag{K-9}$$

The initial condition is,

$$C_{pf}(z, 0) = C_0 \tag{K-10}$$

and the boundary conditions are given by,

$$C_{pf}(0, t) = C_f \tag{K-11}$$

and

$$\left.\frac{\partial C_{pf}}{\partial z}\right|_{z=\delta_f} = 0 \tag{K-12}$$

The processes of solute transport in the flow channel and in the adjacent rock matrix are coupled through Equation (K-11), which describes the continuity of the solute concentration at the interface between the flow channel and the rock matrix adjacent to it.

K.1.4 Solute transport in the rock matrix adjacent to the stagnant water zone

Similar to Equation (K-8), the 1-D transport equation for the aqueous concentration in the pore water of the rock matrix adjacent to the stagnant water zone, C_{ps}, can be written as,

$$\frac{\partial C_{ps}}{\partial t} = D_{as} \frac{\partial^2 C_{ps}}{\partial z_s^2} \tag{K-13}$$

the apparent diffusivity D_{as} has the same definition as D_{af} in Equation (K-9), except for changing the subscripts from *f* to *s*.

The initial condition is,

$$C_{ps}(z, 0) = C_0 \tag{K-14}$$

and the boundary conditions are given by,

$$C_{ps}(0, t) = C_s \tag{K-15}$$

and

$$\left.\frac{\partial C_{ps}}{\partial z_s}\right|_{z_s=\delta_s} = 0 \tag{K-16}$$

Equation (K-15) describes the continuity of the aqueous concentration of the solute at the interface between the stagnant water zone and the adjacent rock matrix. It couples the behaviour of solute transport in the two subsystems.

Table K-1. Nomenclauture.

Symbol	Definition (unit)	Symbol	Definition (unit)
b_f	Half aperture of the flow channel (L)	s	Laplace transform variable (T^{-1})
b_s	Half aperture of the stagnant water zone (L)	t	Time (T)
C_0	Initial concentration in fracture and matrix waters (ML^{-3})	u	Groundwater velocity (LT^{-1})
C_f	Concentration in the flow channel (ML^{-3})	w_f	Half width of the flow channel (L)
C_{in}	Concentration of injected water (ML^{-3})	w_s	Half width of the stagnant water zone (L)
C_{pf}	Pore water concentration in the rock matrix adjacent to the flow channel (ML^{-3})	x	Distance along the flow direction (L)
C_{ps}	Pore water concentration in the rock matrix adjacent to the stagnant water zone (ML^{-3})	y	Distance into the stagnant water zone (L)
C_s	Concentration in the stagnant water zone (ML^{-3})	z	Distance into the rock matrix adjacent to the flow channel
D_{af}	Apparent diffusivity in the rock matrix adjacent to the flow channel (L^2T^{-1})	z_s	Distance into the rock matrix adjacent to the stagnant water zone
D_{as}	Apparent diffusivity in the rock matrix adjacent to stagnant water zone (L^2T^{-1})	δ_f	Thickness of the rock matrix adjacent to the flow channel (L)
D_{ef}	Effective diffusivity in the rock matrix adjacent to the flow channel (L^2T^{-1})	δ_s	Thickness of the rock matrix adjacent to the stagnant water zone (L)
D_{es}	Effective diffusivity in the rock matrix adjacent to the stagnant water zone (L^2T^{-1})	ε_{pf}	Porosity of the rock matrix adjacent to the flow channel (-)
D_s	Diffusivity in the water in the stagnant water zone (L^2T^{-1})	ε_{ps}	Porosity of the rock matrix adjacent to the stagnant water zone (-)
F_f	Ratio of the flow-wetted surface of the flow channel to the volumetric water flow rate (TL^{-1})	τ_f	Characteristic time of advection (-)
F_s	Ratio of the stagnant-water-wetted surface to the diffusion conductance of the stagnant water zone (TL^{-1})	τ_{Df}	Characteristic time of diffusion through the rock matrix adjacent to the flow channel (-)
MPG_f	Material property group of the rock matrix adjacent to the flow channel ($LT^{-1/2}$)	τ_{Ds}	Characteristic time of diffusion through the rock matrix adjacent to the stagnant water zone (-)
MPG_s	Material property group of the rock matrix adjacent to the stagnant water zone ($LT^{-1/2}$)	τ_s	Characteristic time of diffusion through the stagnant water zone (-)
N	Ratio between the diffusion rate into the stagnant water zone and the mass flow rate through the channel (-)	**Sub-scripts**	
R_f	Surface retardation coefficient in the flow channel (-)	f	Refers to the flow channel
R_{pf}	Retardation coefficient of the rock matrix adjacent to the flow channel (-)	s	Refers to the stagnant water zone
R_{ps}	Retardation coefficient of the rock matrix adjacent to the stagnant water zone (-)	pf	Refers to the rock matrix adjacent to the flow channel
R_s	Surface retardation coefficient in the stagnant water zone (-)	ps	Refers to the rock matrix adjacent to the stagnant water zone

K.1.5 Solution in the Laplace domain

By introducing a simple change of variable in order to have a zero initial condition in all regions, the equations governing solute transport in the four subsystems can be most easily solved by applying the Laplace transformation (Watson 1981). It removes the time variable, leaving a system of ordinary differential equations, the solutions of which yield the transform of the concentrations as a function of the space variables. The general procedure for solving the Laplace-transformed equations in four subsystems have been described in Mahmoudzadeh et al. (2013). Due to the high similarity between

the governing equations in the present work and the ones given in Mahmoudzadeh et al. (2013), the detailed steps to get the Laplace-transformed concentrations are not repeated here. Instead, the final solution describing the Laplace-transformed concentration in the flow channel is presented as,

$$\bar{C}_f(x,s) = \frac{C_0}{s} + \frac{C_{in}-C_0}{s} exp\left(-\Omega_f - N\sqrt{\Omega_s}\tanh\left(2\sqrt{\Omega_s}\right)\right) \quad \text{(K-17)}$$

with

$$\Omega_f = R_f\tau_f s + \mathrm{F}_f\mathrm{P}_f\sqrt{s} \quad \text{(K-18)}$$

and

$$\Omega_s = R_s\tau_s s + \mathrm{F}_s\mathrm{P}_s\sqrt{s} \quad \text{(K-19)}$$

where the overbar denotes the Laplace transformed quantities and s is the Laplace transform variable. In Equations (K-18) and (K-19), P_f and P_s are defined,respectively, as

$$\mathrm{P}_f = \mathrm{MPG}_f\tanh(\sqrt{\tau_{Df}s}) \quad \text{(K-20)}$$

and

$$\mathrm{P}_s = \mathrm{MPG}_s\tanh(\sqrt{\tau_{Ds}s}) \quad \text{(K-21)}$$

where four characteristic parameters MPG_f, MPG_s, τ_{Df} and τ_{Ds} have been defined. A complete list of characteristic parameters used in Mahmoudzadeh et al. (2013) is given in Table K-2 together with their definition and physical significance.

For the case of fresh water inlet (C_{in} = 0), the solution given in Equation (K-17) will be,

$$\bar{C}_f(x,s) = \frac{C_0}{s}\left\{1 - exp\left(-\Omega_f - N\sqrt{\Omega_s}\tanh\left(2\sqrt{\Omega_s}\right)\right)\right\} \quad \text{(K-22)}$$

Table K-2. Characteristic parameters.

Definition	Physical significance
$\mathrm{MPG}_f = \sqrt{D_{ef}R_{pf}\varepsilon_{pf}}$	Material property group for the rock matrix adjacent to the flow channel.
$\mathrm{MPG}_s = \sqrt{D_{es}R_{ps}\varepsilon_{ps}}$	Material property group for the rock matrix adjacent to the stagnant water zone.
$F_f = \frac{x}{ub_f}$	Flow-related transport resistance.
$F_s = \frac{{W_s}^2}{D_s b_s}$	The ratio of the wetted surface of the rock matrix adjacent to the stagnant water zone to the diffusion conductance of the stagnant water zone. It describes the competition between diffusion into the stagnant water zone and diffusion from the water into the adjacent rock matrix. A large value of the F_s–ratio indicates that a large amount of solute diffusing from the flow channel into the stagnant water zone can quickly diffuse into the adjacent rock matrix.
$\tau_f = \frac{x}{u}$	Advective travel time.
$\tau_s = \frac{{W_s}^2}{D_s}$	Characteristic time for solute diffusion into the stagnant water zone.
$\tau_{Df} = \frac{{\delta_f}^2}{D_{af}}$	Characteristic time for solute diffusion through the rock matrix adjacent to the flow channel.
$\tau_{Ds} = \frac{{\delta_s}^2}{D_{as}}$	Characteristic time for solute diffusion through the rock matrix adjacent to the flow channel.
$N = \frac{D_s x b_s / W_s}{u b_f W_f}$	The ratio between the characteristic rate of diffusion into the stagnant water zone and the characteristic rate of advection through the flow channel. It quantifies the fraction of solute that can depart from the flow channel into the stagnant water zone. A high value of the N–ratio indicates that the stagnant water zone has a large capacity to capture the solute passing by and then deliver it from there into the adjacent rock matrix.

The simulations in the next section are performed by implementing Equation (K-17) in Matlab where a numerical inversion of the Laplace solution into real space is performed. It should be noted that the solution is applied on multiple recharge pathways with specific values of F_f and τ_f for each pathway. By calculating concentration through each pathway, it can then be estimated how many canisters may be affected by infiltration of dilute groundwater from ground surface during temperate or glacial conditions.

K.2 Application

Two cases are considered here; these are the Temperate and Glacial periods of SR-Site as also used in PSAR. The assumptions on initial water concentration in the bedrock for the two climate periods are described in SKB (2011, Sections 9.3.6 and 9.4.6, respectively), as well as in Appendix F of Joyce et al. (2010). Except the new parameters introduced here, other values such as advective travel times and flow related transport resistances are motivated in Appendix F of Joyce et al. (2010).

K.2.1 Temperate case

The matrix and fracture water salinity are assumed at equilibrium at the start of the simulations (C_0 =10 g/L). Along the flow paths, it is assumed that solutes diffuse into/out of the matrix water. Furthermore, diffusion into the stagnant water zones in the fracture plane is accounted for. The solutes can also diffuse into/out of the matrix water adjacent to the stagnant water zones.

Here, the question posed is how many canisters may be affected by infiltration of dilute groundwater from ground surface during conditions characterized by temperate climate conditions. Two salinity criteria for buffer erosion, which represents the dilute conditions with potential for buffer erosion to occur are used; these are 0.3 g/L (SR-Site value) and 0.6 g/L (PSAR value). The input data are provided in Table K-3; flow-related transport resistances and advective travel times for backward particle tracking of 663 deposition hole positions are based on the simulations provided in Appendix F of Joyce et al. (2010) for temperate conditions.

By applying the inverse Laplace transform of Equation (K-17), the outlet concentrations for 663 pathways are calculated. Accordingly, the fraction of the total of 6919 deposition holes that experience dilute water is calculated and shown in Figure K-2 to Figure K-6 for different inlet boundary conditions and different values for α, where $\alpha = C/C_0$.

Table K-3. Input data for sensitivity cases.

$\delta_f = \delta_s$	Half-size of matrix blocks	12.5 m
$\varepsilon_{pf} = \varepsilon_{ps}$	Matrix porosity	3.7×10^{-3}
$D_{ef} = D_{es}$	Effective diffusivity in the rock matrix	4×10^{-14} m^2/s (1.26×10^{-6} m^2/y)
D_s	Diffusivity in stagnant water zone	1×10^{-9} m^2/s (0.0315 m^2/y)
$2W_s$	Half-distance between flow channels	0, 0.2, 2, 10 m
C_{in}	Concentration of injected water	0, 0.1, 0.2, 0.4 g/L
C_0	Concentration of initial fracture and matrix waters	10 g/L
W_f	Half-width of flow channel	0.1, 1 m

K.2.2 Glacial case

For the glacial case, the matrix and fracture water salinity are at equilibrium at the start of the simulations with a concentration of C_0 = 3 g/L. Two cases representing different phases of glacial climate conditions are considered. First, a case where the ice front is located above the repository is considered (Glacial II), and second a case where the site is completely covered by an ice sheet (Glacial V) is considered. For both these cases the concentration of the infiltrating water is set to zero, representing glacial melt water. The input data are provided in Table K-4; flow-related transport resistances and advective travel times are based on the simulations provided in Appendix F of Joyce et al. (2010) for 983 and 589 backward positions for glacial II and V conditions, respectively.

By applying the inverse Laplace transform of Equation (K-17), the outlet concentrations for 983 and 589 pathways are calcualted for glacial II and V conditions, respectively. Accordingly, the fraction of the total of 6919 deposition holes that experience dilute water are shown in Figure K-7 and Figure K-8 for the cases with an ice front above the repository (Glacial II) and the case with an ice sheet covering the site (Glacial V) for both α = 10 % and α = 20 % where $\alpha = C/C_0$. These α values correspond to the concentration being reduced from the initial 3 g/L to the value corresponding to onset of erosion (0.3 g/L in SR-Site, and 0.6 g/L in PSAR).

Table K-4. Input data.

$\delta_f = \delta_s$	Half-size of matrix blocks	12.5 m
$\varepsilon_{pf} = \varepsilon_{ps}$	Matrix porosity	3.7×10^{-3}
$D_{ef} = D_{es}$	Effective diffusivity	4×10^{-14} m^2/s (1.26×10^{-6} m^2/y)
D_s	Diffusivity in stagnant water zone	1×10^{-9} m^2/s (0.0315 m^2/y)
$2W_s$	Half-distance between flow channels	0, 0.2, 2, 10 m
C_{in}	Concentration of injected water	0 g/L
C_0	Concentration of initial fracture and matrix waters	3 g/L
W_f	Half-width of flow channel	1 m

K.3 Results

K.3.1 Temperate case

The results are shown in Figure K-2 through Figure K-6 below. In Figure K-2 to Figure K-5, the top figure displays the case of a narrow channel (W_f = 0.1 m) and the bottom figure a wider channel (W_f = 1.0 m). Figure K-6 presents the case propagated within PSAR. Furthermore, in each figure, four stagnant water channels widths, including the case without stagnant water, are illustrated in order to show the sensitivity to this parameter. Two different time periods are indicated by the vertical lines; 10 000 years and 60 000 years. These two times represent the assumed duration of temperate climate conditions, see SKB (2011) for details. It is noted that for the case without stagnant water, the width of the flow channel is arbitrary; i.e., this parameter does not appear in the solution for concentration through the flow channel.

Figure K-2 represents a case which is close to the case of Joyce et al. (2010) in that infiltrating water has zero concentration, and a concentration ratio of 10 % is considered. Changes to the case of Joyce et al. (2010) are the inclusion of the effects of a finite matrix in a single model, and the variants with inclusion of stagnant water next to the flow channel. It is here observed that an increasing stagnant water width implies a lower number of canister deposition hole positions being subject to dilute conditions; however, the narrowest stagnant water width shown implies only a small reduction relative to the case without stagnant water. Furthermore, a narrower flow channel width implies fewer dilute positions relative to the case with a wider flowing channel. This latter phenomenon is consistent with traditional matrix diffusion where a smaller aperture yields stronger matrix diffusion effects.

Figure K-3 represents identical conditions to Figure K-2 except that a concentration ratio of 3 % is considered. Relative to the results in Figure K-2, this case obviously leads to a lower number of deposition hole positions experiencing dilute conditions.

Figure K-4 and Figure K-5 additionally assume the infiltrating water having concentrations of 0.1 g/L and 0.2 g/L, respectively. As argued in Appendix J, an infiltrating water concentration of up to 0.4 g/L can be defended. However, infiltrating water with a concentration equal to or higher than the value 0.3 g/L, corresponding to the limit value for erosion used in SR-Site, is for obvious reasons not of interest in the assessment if a concentration ratio of α = 3 % is used.

Figure K-6 presents the PSAR case where the infiltrating water has a concentration of 0.4 g/L, and the threshold concentration for onset of erosion is set to 0.6 g/L. Here, only the case with a flowing channel width of 1.0 m is used. It is noted that this case is more favourable than the case in Figure K-2 (which in turn is very similar to the SR-Site case).

It should be noted that results are shown for a time longer than the typical time frame for assessment of post-closure safety. This is solely done in order to provide a better view of the curves based on the mathematical solutions. Furthermore, it can be seen that all the simulations in Figure K-2 through Figure K-6 have the same plateau value of about 0.096; this value is related to the number of deposition holes, i.e., 663 positions out of total 6 919 holes, considered for the temperate simulations based on Appendix F of Joyce et al. (2010). This obviously also implies that all considered deposition holes finally will reach the dilute concentration considering constant inlet concentration; however, the positions without stagnant water zones will reach the limit value earlier than the ones with stagnant water zones.

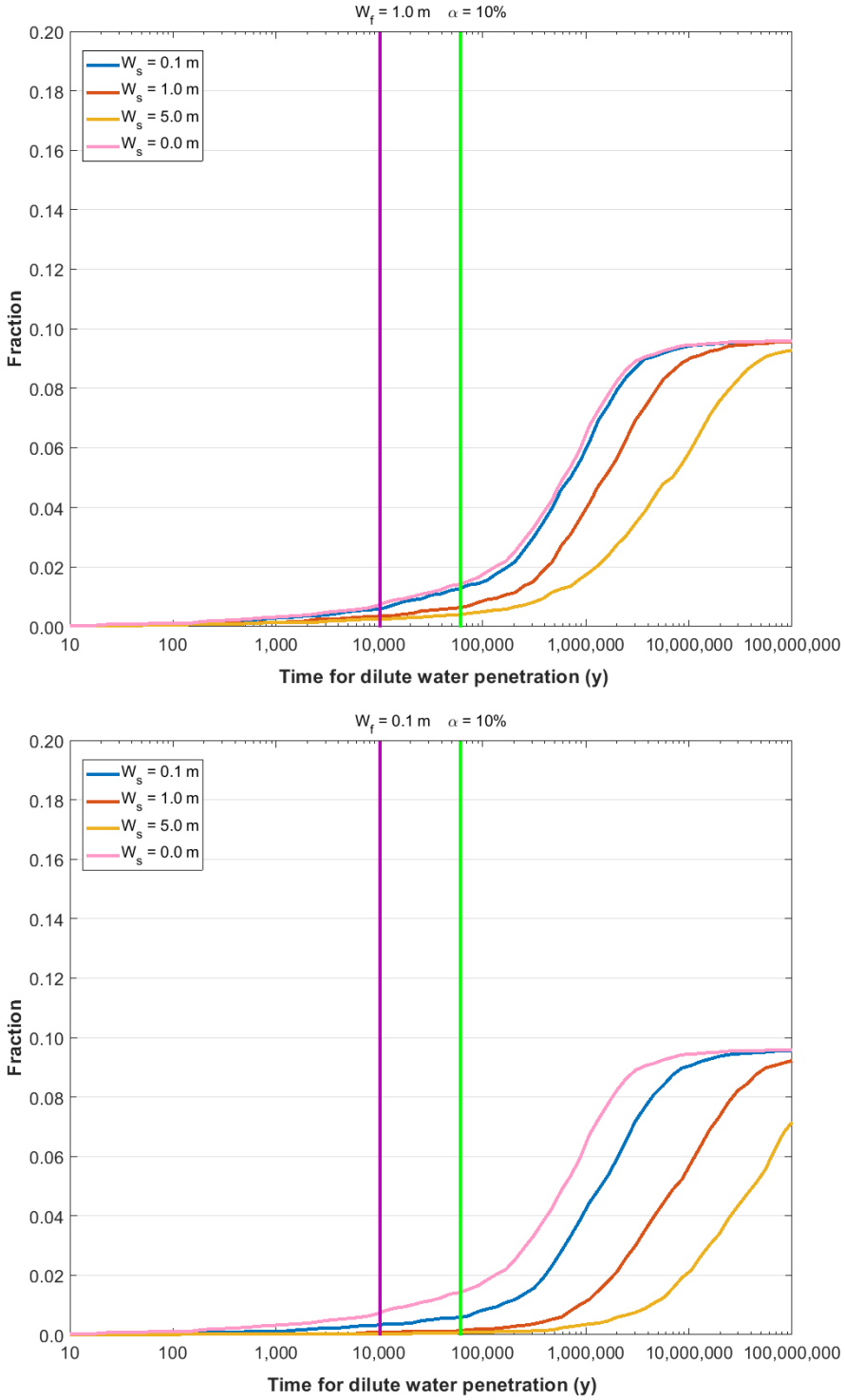

Figure K-2. *Temporal distribution for all deposition hole positions to obtain ten percent of the initial water salinity concentration for (up) a W_f = 1 m and (down) a W_f = 0.1 m. The green line represents "Base case~10 000 y", and the purple line represents "Global warming~60 000 y". Inlet concentration is C_{in} = 0 g/L.*

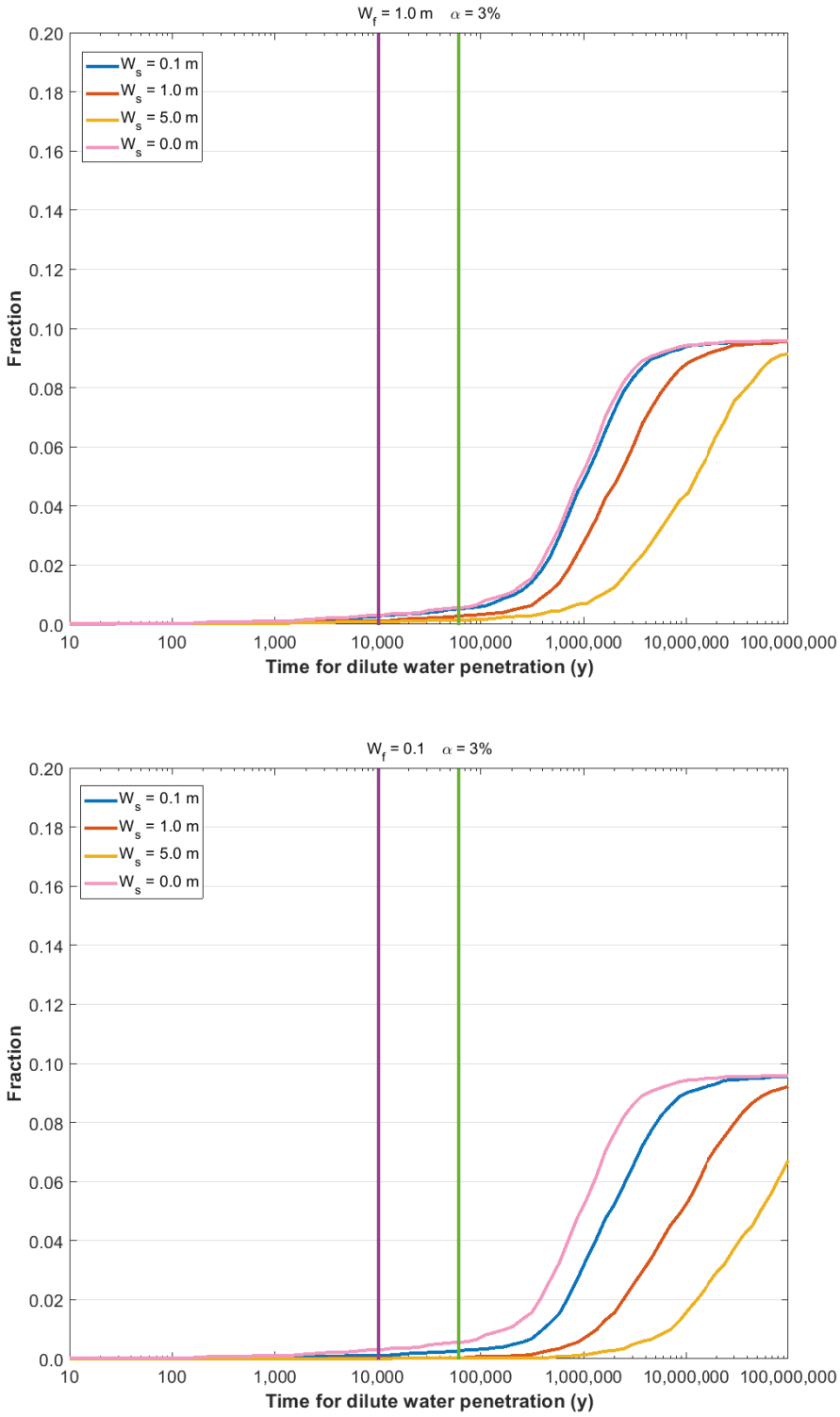

Figure K-3. *Temporal distribution for all deposition hole positions to obtain three percent of the initial water salinity concentration for (up) a W_f = 1 m and (down) a W_f = 0.1 m. The green line represents "Base case~10 000 y", and the purple line represents "Global warming~60 000 y". Inlet concentration is C_{in} = 0 g/L.*

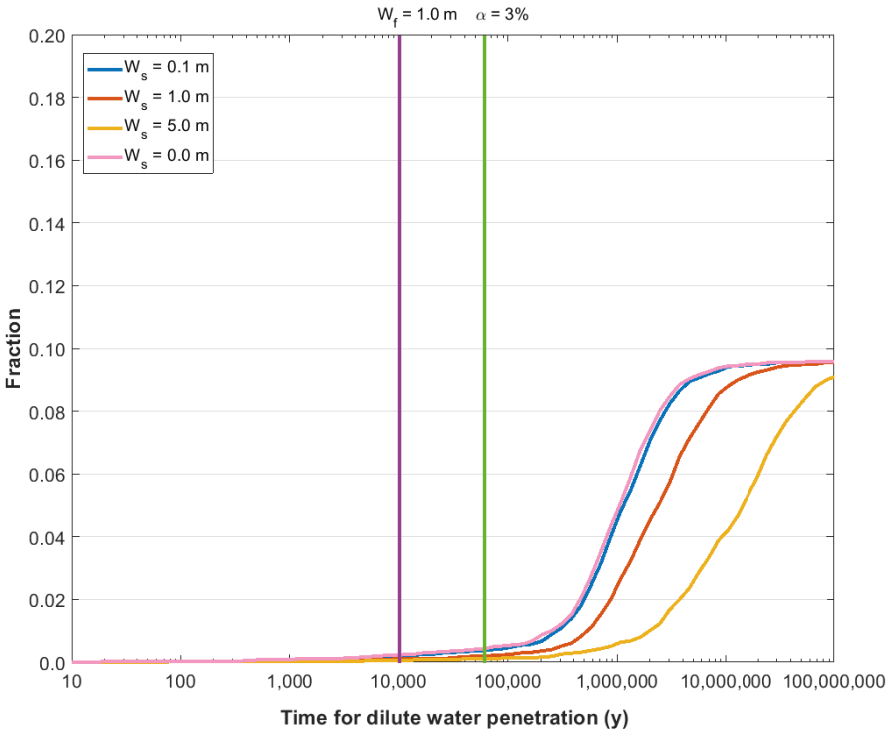

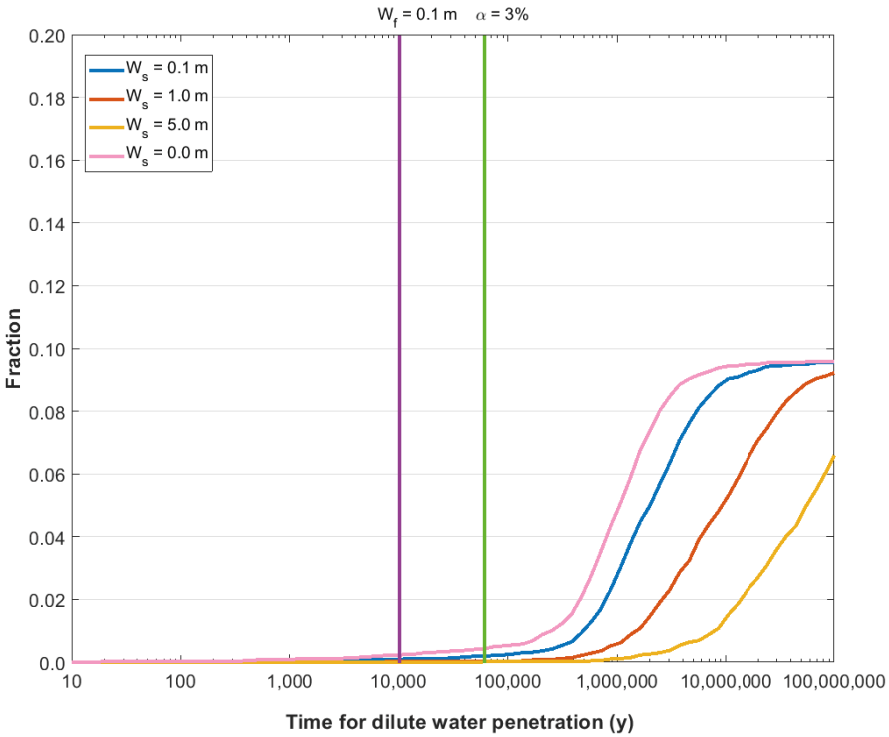

Figure K-4. *Temporal distribution for all deposition hole positions to obtain three percent of the initial water salinity concentration for (up) a W_f = 1 m and (down) a W_f = 0.1 m. The green line represents "Base case~10 000 y", and the purple line represents "Global warming~60 000 y". Inlet concentration is C_{in} = 0.1 g/L.*

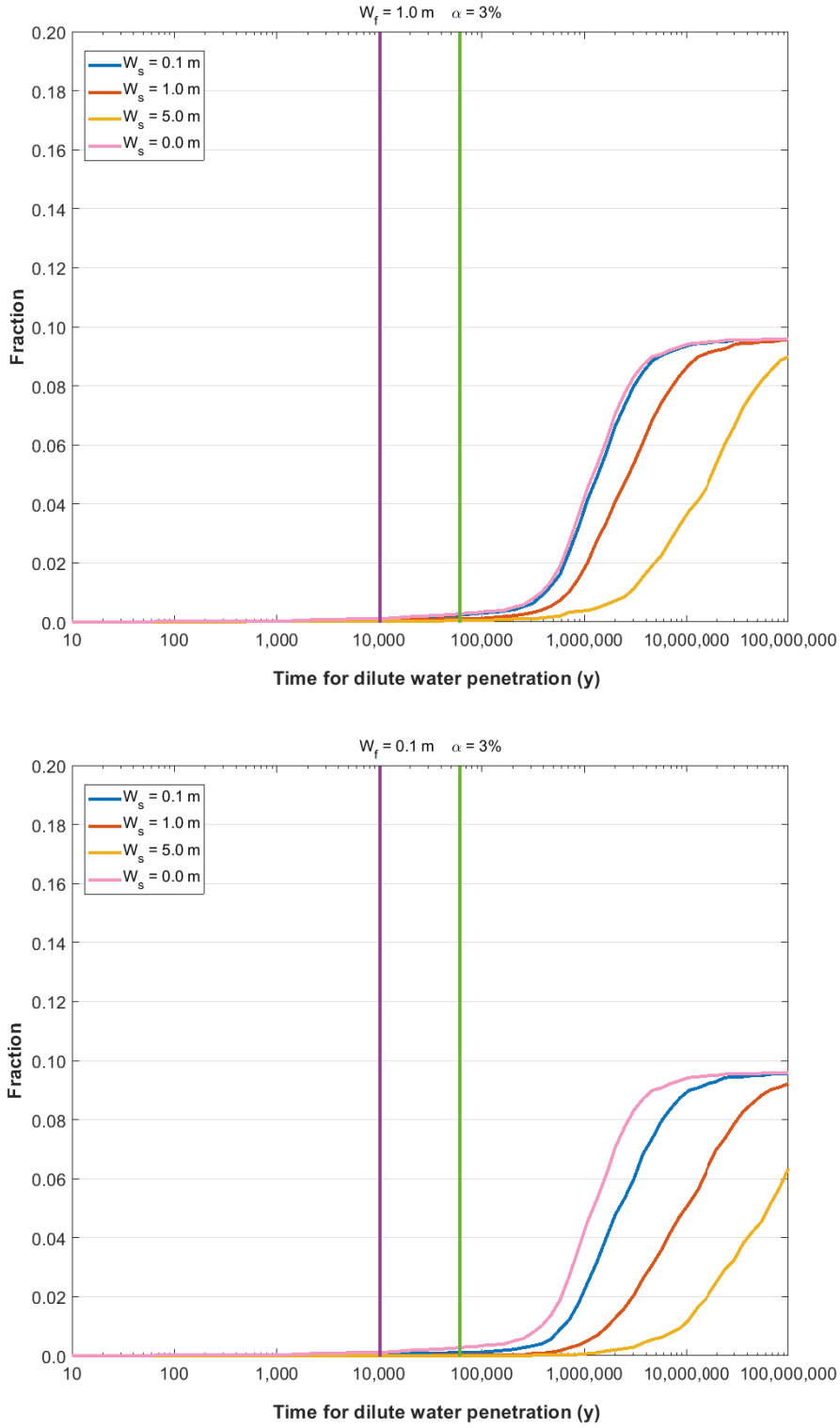

Figure K-5. *Temporal distribution for all deposition hole positions to obtain three percent of the initial water salinity concentration for (up) a W_f = 1 m and (down) a W_f = 0.1 m. The green line represents "Base case~10 000 y", and the purple line represents "Global warming~60 000 y". Inlet concentration is C_{in} = 0.2 g/L.*

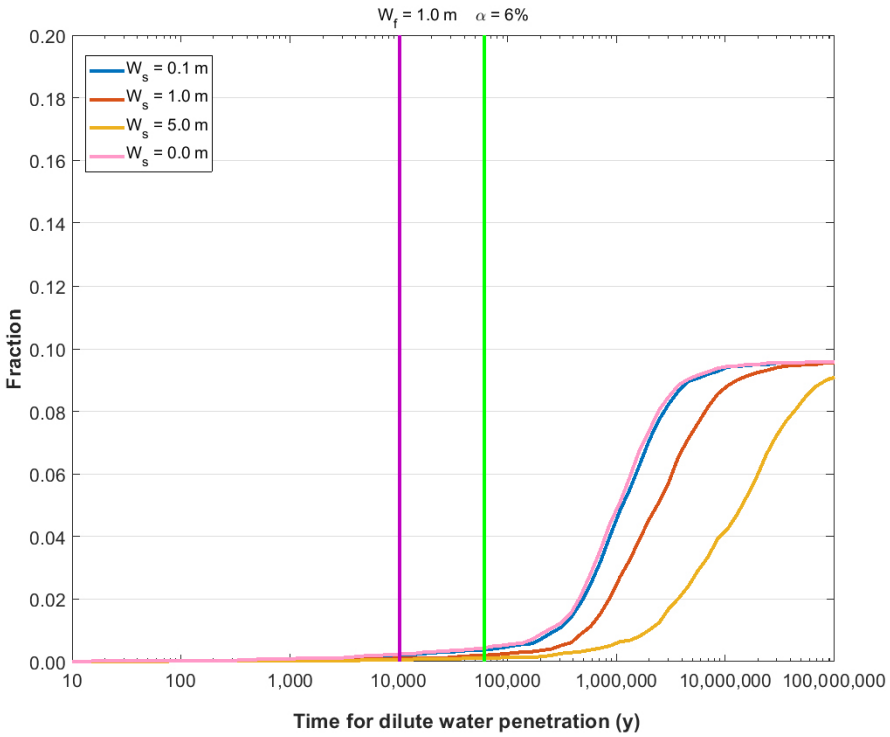

Figure K-6. *Temporal distribution for all deposition hole positions to obtain six percent of the initial water salinity concentration for W_f = 1 m. The green line represents "Base case~10 000 y", and the purple line represents "Global warming~60 000 y". Inlet concentration is C_{in} = 0.4 g/L.*

K.3.2 Glacial case

The results are shown in Figure K-7 and Figure K-8 below. Only the case of a wider channel (W_f = 1.0 m) is shown. In each figure, four stagnant water channels widths, including the case of no stagnant water, are illustrated in order to show the sensitivity to this parameter. Figure K-7 presents the case of an ice sheet located above the repository. Here two time durations are indicated by the vertical lines; 20 years representing a glacial retreat situation, and 100 years representing a glacial advance situation, respectively. Figure K-8 presents the case of the site being covered by an ice sheet. The two time durations shown represent a 20 000 year and 100 000 year-ice-sheet coverage, respectively. Motivation for the different times assumed for duration of the various glacial climate conditions are found in SKB (2011). In both Figure K-7 and Figure K-8, the upper plots are for the case α=10 % (corresponding to SR-Site), while the lower plots are for the case α=20 % (corresponding to PSAR).

What is observed in the upper plot Figure K-7 is that a value of W_s=0 or 0.1 m results in a number of deposition hole locations being subject to dilute water close to the values presented in Joyce et al. (2010). However, increasing the width of the stagnant zone results in a decrease of the number of affected positions. Changing the concentration ratio to α=20 %, the fraction of positions experiencing dilute conditions increases as seen in the lower plot of Figure K-7.

The corresponding results in the upper plot of Figure K-8 yield a somewhat lower ratio of deposition holes experiencing dilute conditions relative to the results presented in Joyce et al. (2010). However, the same sensitivities are observed here with respect to stagnant water zone width and concentration ratio (α value); thus, for the higher concentration ratio, the results are close to those of Joyce et al. (2010).

It should be noted that, similar to the temperate case, results are shown for a time longer than the typical time frame for assessment of post-closure safety. This is solely done in order to provide a better view of the curves based on the mathematical solutions.Furthermore, it can be seen that the simulations in Figure K-7 through Figure K-8 have plateau values of about 0.14 and 0.085, respectively; these values are related to the number of deposition holes, i.e., 983 and 589 positions out of total 6 919 deposition

holes, considered for the glacial simulations based on Appendix F of Joyce et al. (2010). This obviously also implies that all considered deposition holes finally will reach the dilute concentration considering constant inlet concentration; however, the positions without stagnant water zones will reach the limit value earlier than the ones with stagnant water zones.

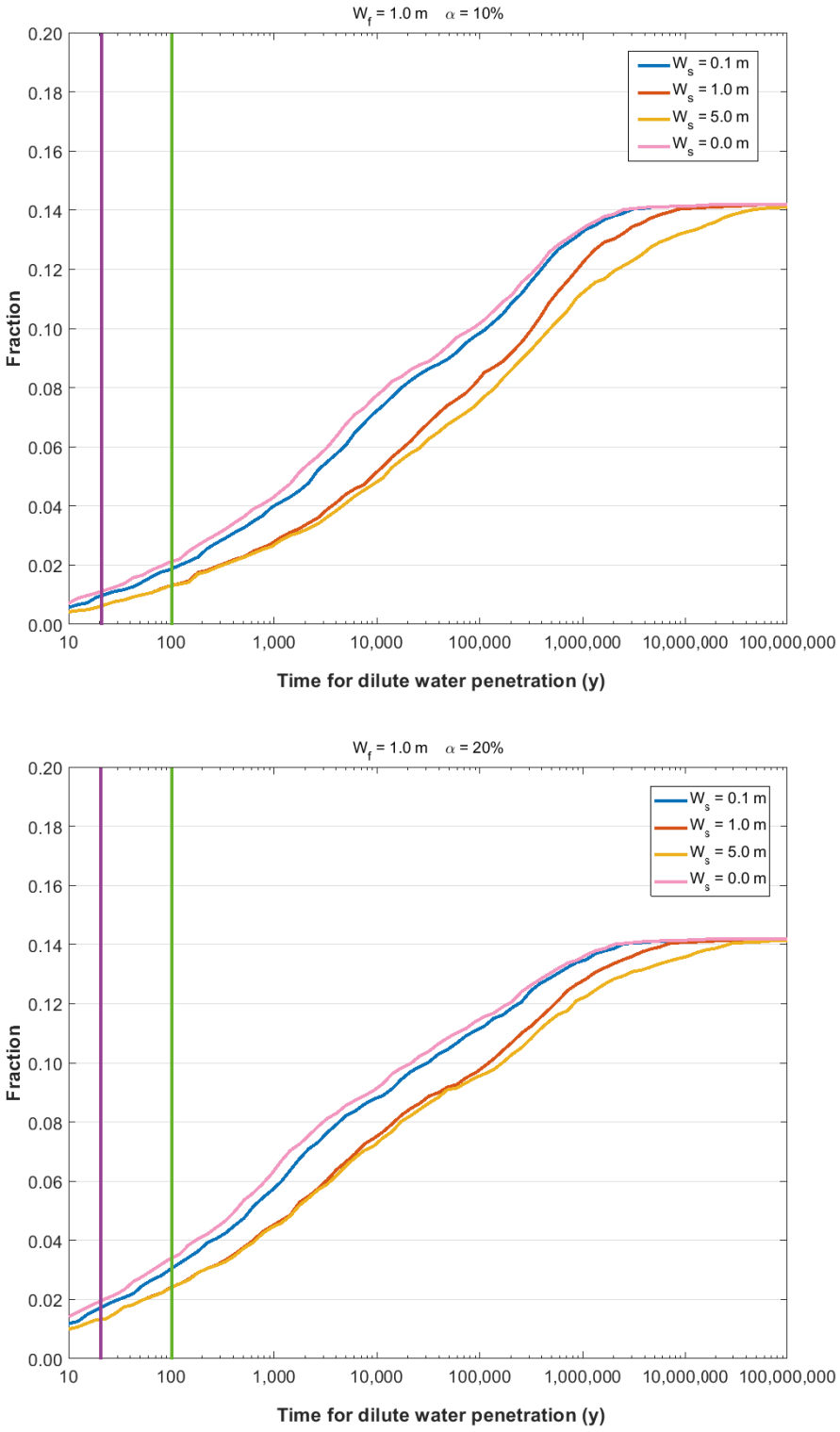

Figure K-7. *Temporal distribution for all deposition hole positions to obtain ten (upper plot) and twenty (lower plot) percent of the initial water salinity concentration under Glacial II conditions. The green line represents "Advance~100 y", and the purple line represents "Retreat~20 y".*

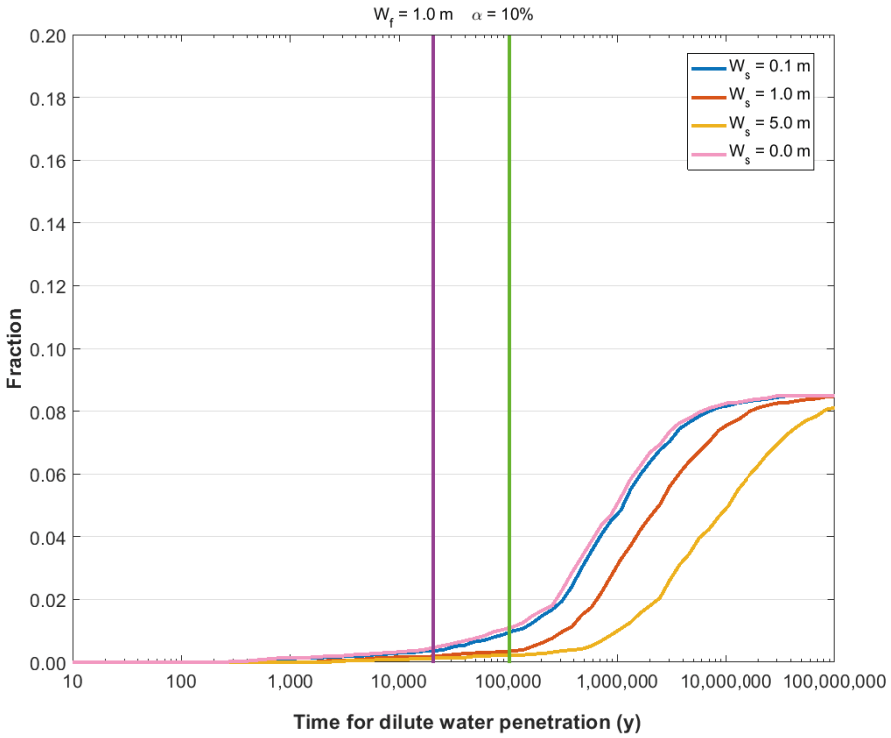

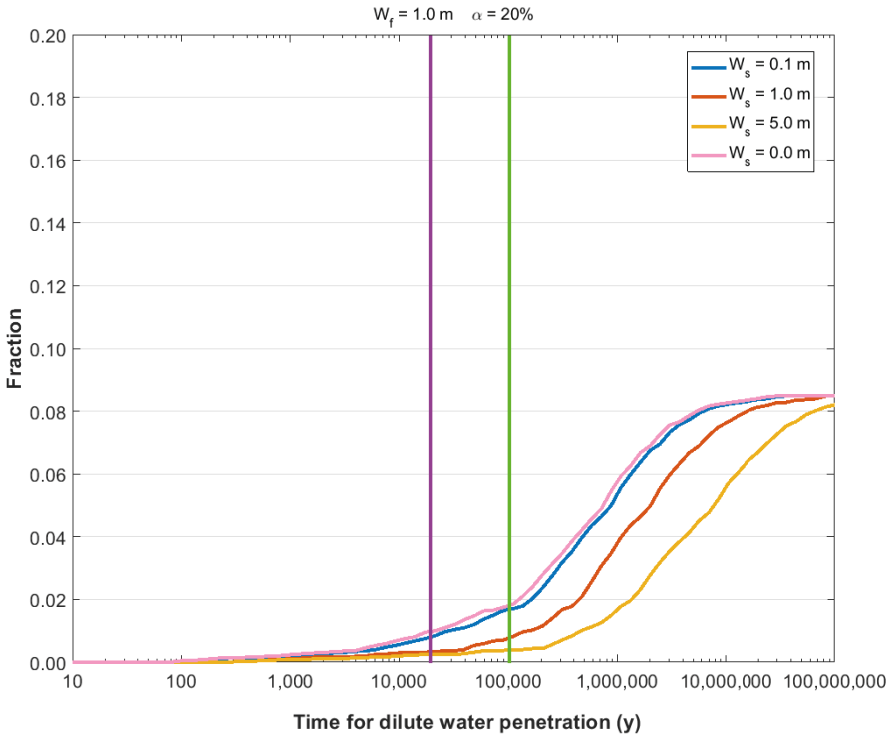

Figure K-8. *Temporal distribution for all deposition hole positions to obtain ten (upper plot) and twenty (lower plot) percent of the initial water salinity concentration under Glacial V conditions. The green line represents "Ice sheet~100 000 y", and the purple line represents "Ice sheet~20 000 y".*

K.3.3 Summary of results

Below, the results are tabulated for each figure above. Specifically, the fraction of deposition hole positions subject to dilute conditions for each of the time durations considered are shown.

Table K-5. Fraction of affected canisters for W_f = 1.0 m in Figure K-2 (C_0 = 10 g/L, C_{in} = 0 g/L, α = 10 %).

Time (y)	W_s = 0.0 m	W_s = 0.1 m	W_s = 1.0 m	W_s = 5.0 m
10 000	0.0075	0.0061	0.0035	0.0025
60 000	0.0142	0.0127	0.0064	0.0039

Table K-6. Fraction of affected canisters for W_f = 0.1 m in Figure K-2 (C_0 = 10 g/L, C_{in} = 0 g/L, α = 10 %).

Time (y)	W_s = 0.0 m	W_s = 0.1 m	W_s = 1.0 m	W_s = 5.0 m
10 000	0.0075	0.0034	7.2265e-04	2.8906e-04
60 000	0.0142	0.0058	0.0013	7.2265e-04

Table K-7. Fraction of affected canisters for W_f = 1.0 m in Figure K-3 (C_0 = 10 g/L, C_{in} = 0 g/L, α = 3 %).

Time (y)	W_s = 0.0 m	W_s = 0.1 m	W_s = 1.0 m	W_s = 5.0 m
10 000	0.0032	0.0028	0.0012	8.6718e-04
60 000	0.0056	0.0052	0.0027	0.0014

Table K-8. Fraction of affected canisters for W_f = 0.1 m in Figure K-3 (C_0 = 10 g/L, C_{in} = 0 g/L, α = 3 %).

Time (y)	W_s = 0.0 m	W_s = 0.1 m	W_s = 1.0 m	W_s = 5.0 m
10 000	0.0032	0.0012	1.4453e-04	0
60 000	0.0056	0.0026	2.8906e-04	1.4453e-04

Table K-9. Fraction of affected canisters for W_f = 1.0 m in Figure K-4 (C_0 = 10 g/L, C_{in} = 0.1 g/L, α = 3 %).

Time (y)	W_s = 0.0 m	W_s = 0.1 m	W_s = 1.0 m	W_s = 5.0 m
10 000	0.0023	0.0020	0.0010	5.7812e-04
60 000	0.0042	0.0038	0.0019	0.0010

Table K-10. Fraction of affected canisters for W_f = 0.1 m in Figure K-4 (C_0 = 10 g/L, C_{in} = 0.1 g/L, α = 3 %).

Time (y)	W_s = 0.0 m	W_s = 0.1 m	W_s = 1.0 m	W_s = 5.0 m
10 000	0.0023	9.3944e-04	1.4453e-04	0
60 000	0.0042	0.0019	1.4453e-04	1.4453e-04

Table K-11. Fraction of affected canisters for W_f = 1.0 m in Figure K-5 (C_0 = 10 g/L, C_{in} = 0.2 g/L, α = 3 %).

Time (y)	W_s = 0.0 m	W_s = 0.1 m	W_s = 1.0 m	W_s = 5.0 m
10 000	0.0012	0.0012	2.8906e-04	2.8906e-04
60 000	0.0027	0.0023	0.0012	5.7812e-04

Table K-12. Fraction of affected canisters for W_f = 0.1 m in Figure K-5 (C_0 = 10 g/L, C_{in} = 0.2 g/L, α = 3 %).

Time (y)	W_s = 0.0 m	W_s = 0.1 m	W_s = 1.0 m	W_s = 5.0 m
10 000	0.0012	2.8906e-04	0	0
60 000	0.0027	0.0012	1.4453e-04	0

Table K-13. Fraction of affected canisters for W_f = 1.0 m in Figure K-6 (C_0 = 10 g/L, C_{in} = 0.4 g/L, α = 6 %).

Time (y)	W_s = 0.0 m	W_s = 0.1 m	W_s = 1.0 m	W_s = 5.0 m
10 000	0.0024	0.0020	0.0011	5.7812e-04
60 000	0.0043	0.0038	0.0020	0.0010

Table K-14. Fraction of affected canisters for W_f = 1.0 m in Figure K-7 (C_0 = 3 g/L, C_{in} = 0 g/L, α = 10 %).

Time (y)	W_s = 0.0 m	W_s = 0.1 m	W_s = 1.0 m	W_s = 5.0 m
20	0.0111	0.0096	0.0061	0.0061
100	0.0212	0.0187	0.0131	0.0131

Table K-15. Fraction of affected canisters for W_f = 1.0 m in Figure K-7 (C_0 = 3 g/L, C_{in} = 0 g/L, α = 20 %).

Time (y)	W_s = 0.0 m	W_s = 0.1 m	W_s = 1.0 m	W_s = 5.0 m
20	0.0195	0.0173	0.0133	0.0133
100	0.0340	0.0305	0.0242	0.0240

Table K-16. Fraction of affected canisters for W_f = 1.0 m in Figure K-8 (C_0 = 3 g/L, C_{in} = 0 g/L, α = 10 %).

Time (y)	W_s = 0.0 m	W_s = 0.1 m	W_s = 1.0 m	W_s = 5.0 m
20 000	0.0046	0.0036	0.0018	0.0013
100 000	0.0108	0.0094	0.0035	0.0022

Table K-17. Fraction of affected canisters for W_f = 1.0 m in Figure K-8 (C_0 = 3 g/L, C_{in} = 0 g/L, α = 20 %).

Time (y)	W_s = 0.0 m	W_s = 0.1 m	W_s = 1.0 m	W_s = 5.0 m
20 000	0.0099	0.0082	0.0033	0.0025
100 000	0.0180	0.0168	0.0077	0.0039

K.4 Verification

K.4.1 Verification against a case with an infinite matrix only (modified SR-Site case)

First, a comparison (verification) of the new solution presented here is made against the solution presented in Joyce et al. (2010). However, in this comparison, the solution of Joyce et al. (2010) is modified such that only the infinite matrix part based on the Complementary Error Function is included (and thus the approximate solution to include the effect of a finite matrix is ignored).

Thus, in this verification, the Laplace transformed solution is compared against the analytical solution for the case where there is no stagnant water zone in the fracture plane, i.e., $W_s = 0$. The rock matrix is considered to have an infinite thickness, which is equivalent to the case when we have zero concentration at infinity of the rock matrix.

First, a comparison of temperate phase conditions is made. The input data used are given in Table K-18 and the results are shown in Figure K-9.

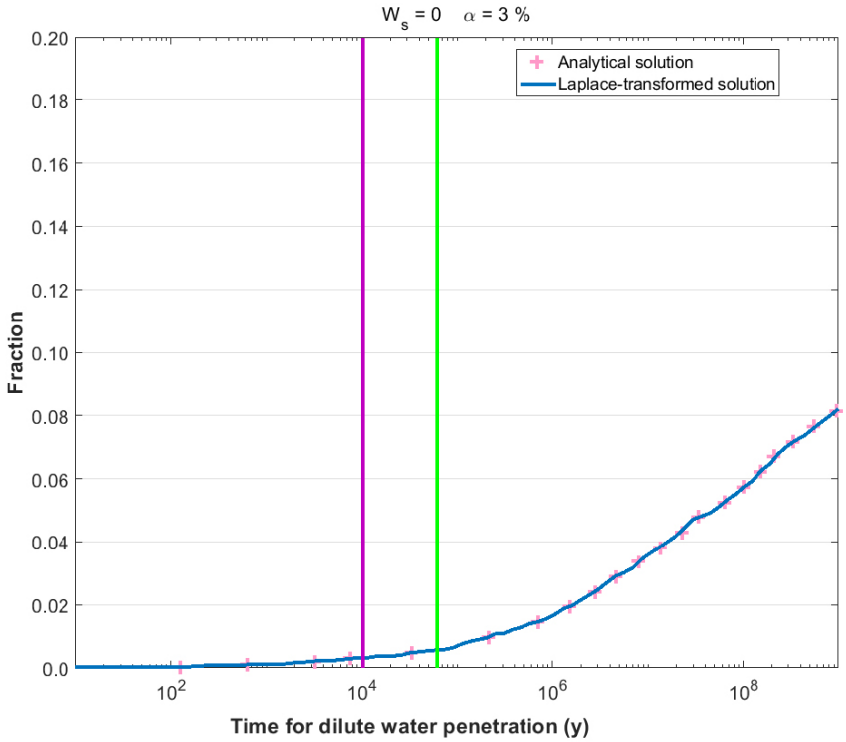

Figure K-9. *Comparison with analytical solution: Temperate condition for the case with no stagnant water zone and infinite rock matrix. The green line represents "Base case~10 000 y", and the purple line represents "Global warming~60 000 y". Inlet concentration is C_{in} = 0 g/L. Analytical solution refers to the complementary error function solution, whereas Laplace-transformed solution refers to the solution presented in this appendix.*

Table K-18. Input data.

ε_{pf}	3.7×10^{-3}
D_{ef}	4×10^{-14} m²/s (1.26×10^{-6} m²/y)
C_{in}	0 g/L
C_0	10 g/L
α	0.03

Second, a comparison is made against the glacial cases (Glacial II and V); the input data are given in Table K-19, and results are shown in Figure K-10 (Glacial II) and Figure K-11 (Glacial V), respectively.

Table K-19. Input data.

ε_{pf}	3.7×10^{-3}
D_{ef}	4×10^{-14} m²/s (1.26×10^{-6} m²/y)
C_{in}	0 g/L
C_0	3 g/L
α	0.03

It is noted that the two solutions match perfectly for all three cases considered, and hence the new solution can be assumed verified for the case of an infinite matrix and no stagnant water channels.

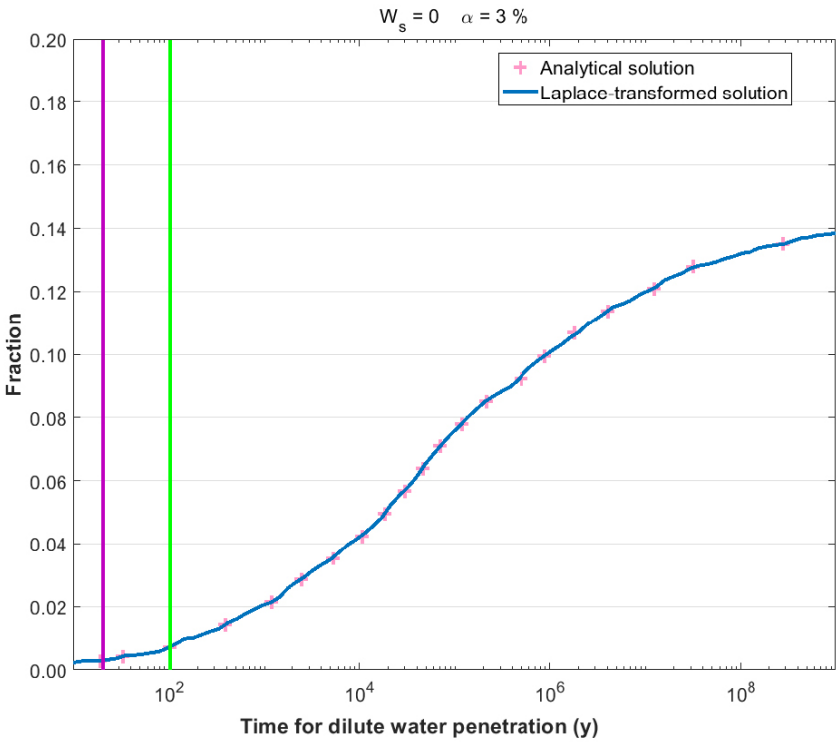

Figure K-10. *Comparison with analytical solution: Glacial II condition for the case with no stagnant water zone and infinite rock matrix. The green line represents "Advance~100 y", and the purple line represents "Retreat~20 y". Analytical solution refers to the complementary error function solution, whereas Laplace-transformed solution refers to the solution presented in this appendix.*

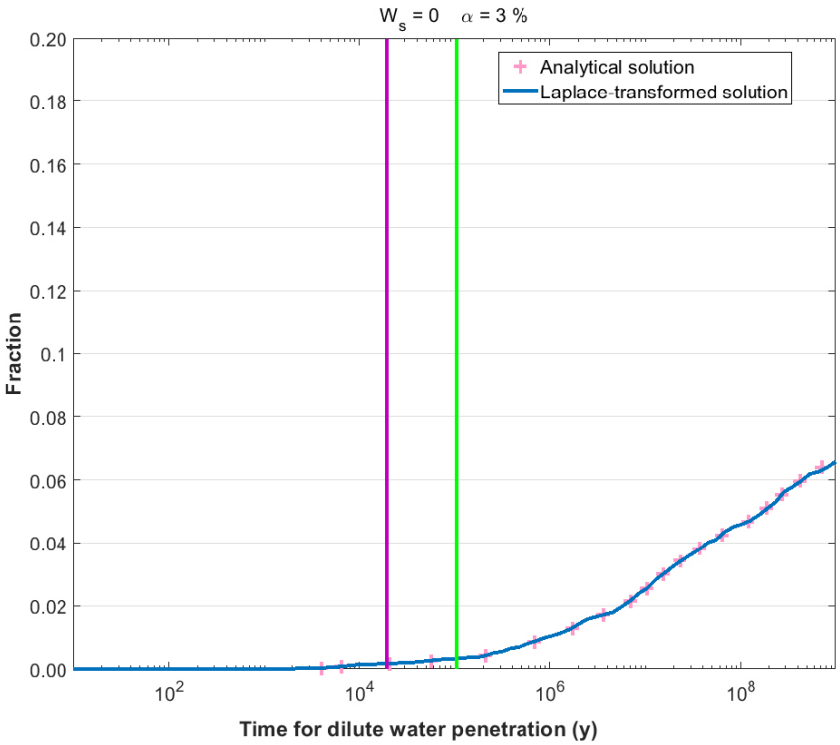

Figure K-11. *Comparison with analytical solution: Glacial V condition for the case with no stagnant water zone and infinite rock matrix. The green line represents "Ice sheet~100 000 y", and the purple line represents "Ice sheet~20 000 y". Analytical solution refers to the complementary error function solution, whereas Laplace-transformed solution refers to the solution presented in this appendix.*

K.4.2 Verification against a case with stagnant channels and with finite/infinite matrix (Trinchero et al. 2020)

In a recent paper by Trinchero et al. (2020), the radionuclide transport code MARFA is extended to account for diffusion into stagnant zones and subsequent matrix diffusion from the stagnant zones. The functionality is implemented using a conditional sampling scheme of retention times, see Trinchero et al. (2020) for details. The paper by Trinchero et al. (2020) presents two test cases where the new particle-based functionality in MARFA is verified against analytical solutions. The analytical solution used in the first test case is equivalent to the solution by Mahmoudzadeh et al. (2013), but expressed differently. Thus, a comparison of the solution presented here, based directly on Mahmoudzadeh et al. (2013), against the solutions presented in Trinchero et al. (2020) constitutes a proper verification.

Two cases are considered; first, a case with an infinite matrix, and second a case with a finite matrix with a depth of 5 m. The input data for both cases are given in Table K-20.

Table K-20. Input data.

$\delta_f = \delta_s$	Half-size of matrix blocks	∞, 5 m
$\varepsilon_{pf} = \varepsilon_{ps}$	Matrix porosity	1.8×10^{-3}
$D_{ef} = D_{es}$	Effective diffusivity	6.3×10^{-7} m²/y
D_s	Diffusivity in stagnant water zone	6.3×10^{-2} m²/y
$2W_s$	Half-distance between flow channels	3 m
C_0	Concentration of initial fracture and matrix waters	0 g/L
W_f	Half-width of flow channel	0.1 m

For zero initial condition, i.e. $C_0 = 0$, and a point-source boundary, i.e. $C_f(0, t) = c\delta(t)$, the Laplace-transformed solution given in Equation (K-17) will be,

$$\bar{C}_f(x, s) = c\, exp\left(-\Omega_f - N\sqrt{\Omega_s}\tanh\left(2\sqrt{\Omega_s}\right)\right) \qquad \text{(K-23)}$$

which is consistent with the solution given in Mahmoudzadeh et al. (2013) for the same case. Here, the inlet boundary concentration is defined as $c\delta(t)$, where $\delta(t)$ is the Dirac delta function and c is not a concentration but a quantity with units of $ML^{-3}T$ and is the ratio between the mass injected instantaneously and the volumetric flow rate through the channel. It is noted that the breakthrough curves are expressed in terms of normalized mass flux; thus, the input concentration c can be defined as arbitrary.

In Figure K-12 the case with an infinite matrix is shown and results of the current model are compared against the particle-based method of MARFA and analytical solution presented in Trinchero et al. (2020). The validation is considered successful and confirms that the coding of the current solution is indeed correct (since solutions “New” and “Full” are equivalent).

In Figure K-13 the corresponding case with a finite matrix is presented. Here only a comparison against MARFA is made. The fit is good, even if not as excellent as for the case with a finite matrix. The discrepancy is believed to be due to numerical imprecision in the MARFA solution; specifically, the small discrepancies observed are likely related to the look-up tables used in MARFA for the limited diffusion case (for the specific case considered, we are close to the minimum range used in the look-up table, which is also where discretisation is coarser). Still, the verification is considered successful such that the new solution presented here can be applied with confidence in PSAR simulations.

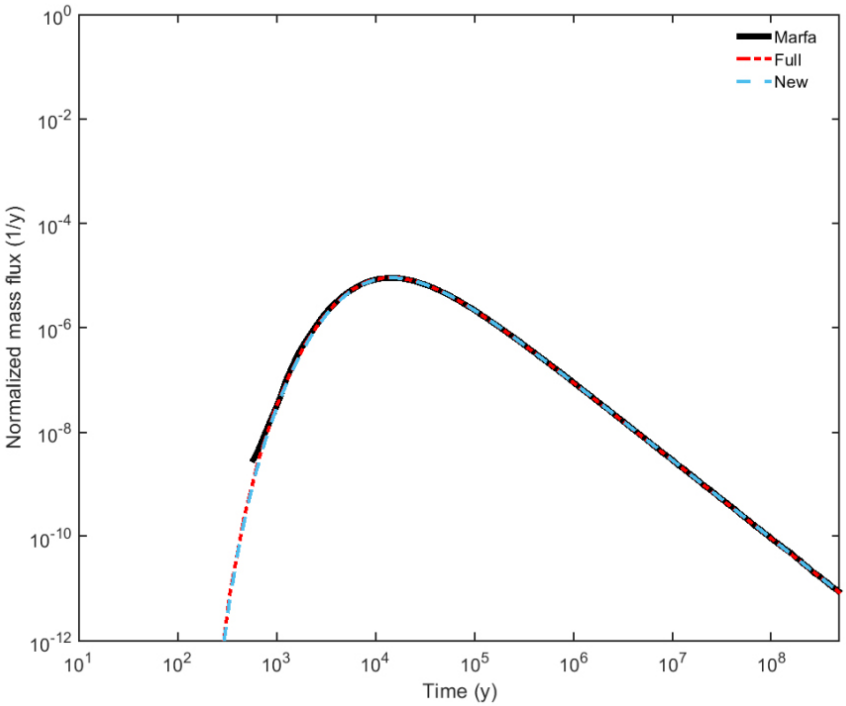

Figure K-12. *Infinite matrix and stagnant water zones; comparison of current solution (New) against results of Trinchero et al. (2020) with particle based method (Marfa) and analytical solution (Full).*

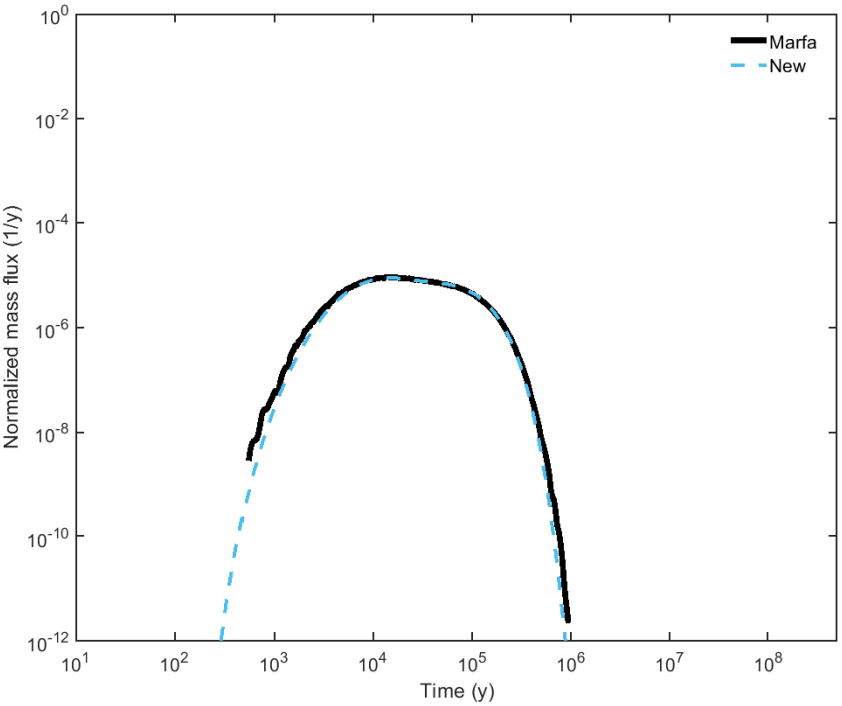

Figure K-13. *Finite matrix and stagnant water zones; comparison of current solution (New) against results of Trinchero et al. (2020) with particle based method (Marfa).*

Appendix L

Safety assessment PSAR – Input data

In this appendix, the input data used in the PSAR radionuclide transport calculations are given. Emphasis is put on data where changes are made compared with SR-Site.

L.1 Input data updated since the SR-Site

The updated input data in the PSAR comprise a combination of new data deliveries and corrections made to erroneous data identified in SR-Site:

- Updated radionuclide inventory, instant release fractions and corrosion release fractions, (Sections L.2, L.3 and L.4).
- Addition of a specific corrosion time for Ag-108m (Section L.5).
- Updated half-lives of radionuclides (Section L.6).
- Addition of input data for Rn-222 as it is included separately in the PSAR calculations.
- Addition of landscape dose conversion factors for new radionuclides and for radionuclides for which LDFs were not reported in SR-Site (Section L.15).
- QA-related issues identified in the SR-Site (Section 3.7.3):
  - The correlation groups for the sorption partitioning coefficient of rock are corrected to correspond with the final version of the **Data report** (Section L.12).
  - The inventory of Ag-108m is automatically corrected since the whole radionuclide inventory is updated (Section L.2).
  - The probabilistic distributions for the porosity of the buffer bentonite are corrected to correspond with the final version of the **Data report** (Section L.11).
  - Erroneous correlations between probabilistic input data are corrected (Section 3.7.3).
  - Corrected solubility limits. An error for plutonium made in the Simple Functions calculations (Grivé et al. 2010) was corrected in Appendix F already in SR-Site and now these corrections are also made in the input data to the radionuclide transport calculations (Section L.8).
- Systematic input data generation. All input data are treated as described in the **Data report** with the number of significant digits as given in the **Data report**.
- Updated input data specific for the corrosion scenario – the SR-Site erosion/corrosion model is updated in the PSAR (now including sedimentation). This entails changes of input data regarding canister failures, i.e. number of failures and data for the deposition holes where the canister fails, i.e. time of failure, rock transport resistance, advective travel time and advective flow through the deposition hole (Section L.17).

L.2 Radionuclide inventory

The data presented here represent the radionuclide inventory of an average canister for a selection of radionuclides expected in year 2045, at the time for shutdown of the last nuclear power plant. The inventory of an average canister is obtained by dividing the total inventory expected at the time for shutdown by the estimated total number of canisters, which is 5 689. The radionuclide inventory data used in the PSAR are specified in Section 3.1 of the **Data report** and listed in Table L-1.

Since the initial inventory is specified for the year 2045, which is before repository closure and earlier than the start time of the radionuclide transport calculations, the inventory at year 2045 was recalculated, through decay chain calculations, to the following two later times, see also Table L-2:

- Year 2070 – corresponding to repository closure (used only in the Shear load – Early failure case).
- Year 3070 – corresponding to 1 000 years after repository closure, which is used as the starting point in time for the radionuclide release in all remaining PSAR radionuclide transport calculation cases. 1 000 years is the time between canister failure and the establishement of a continous water pathway from the fuel to the exterior of the canister (**Data report**, Section 4.2).

When performing the recalculations of the initial inventory to later times, all original radionuclides from the data delivery in Table L-1 were kept throughout the calculation. Then, as a post-process, the radionuclides not included in the radionuclide transport calculations were removed by including their inventory in those of their daughters, see Table L-1 and Table L-2.

Table L-1. Inventory in mol per average canister at year 2045 (Data report, Section 3.1). The radionuclides marked with (*) are not explicitly included in the PSAR radionuclide transport calculations, but their inventories are included in those of theirprogeny nuclides. Update of Table E-1 in this report.

Radionuclide	Inventory [mol/canister]	Inventory included in radionuclide	Chain
Ac-227	1.85E−09		
Ag-108m	1.60E−01		
Am-241	8.98E+00		
Am-242 (*)	9.37E−08	Pu-242	4n+2
Am-242m	7.25E−03		
Am-243	1.60E+00		
C-14	4.99E−02		
Cd-113m	3.40E−04		
Cl-36	8.64E−03		
Cm-242 (*)	1.89E−05	U-234	4n+2
Cm-243 (*)	1.84E−03	Pu-239	4n+3
Cm-244 (*)	1.56E−01	Pu-240	4n
Cm-245	2.42E−02		
Cm-246	3.50E−03		
Cs-135	6.45E+00		
Cs-137	1.01E+01		
Eu-152	9.44E−05		
H-3	7.25E−03		
Ho-166m	7.49E−04		
I-129	3.08E+00		
Mo-93	8.81E−04		
Nb-93m	7.75E−02		
Nb-94	3.25E−01		
Ni-59	2.25E+00		
Ni-63	3.18E−01		
Np-237	4.75E+00		
Np-238	1.34E−09	Excluded	4n+2
Np-239 (*)	1.39E−06	Pu-239	4n+3
Pa-231	4.71E−06		
Pa-233 (*)	1.64E−07	U-233	4n+1
Pa-234m (*)	3.98E−12	U-234	4n+2
Pb-210	1.13E−10		
Pd-107	5.74E+00		
Pu-238	1.53E+00		
Pu-239	4.08E+01		
Pu-240	2.35E+01		
Pu-241 (*)	1.97E+00	Am-241	4n+1
Pu-242	6.66E+00		
Ra-226	2.74E−08		
Rn-222	-		
Se-79	1.67E−01		
Sm-151	1.47E−01		
Sn-121m	2.77E−03		
Sn-126	8.97E−01		
Sr-90	6.21E+00		
Tc-99	1.99E+01		
Th-229	1.34E−08		
Th-230	1.64E−04		
Th-232	4.39E−05		
Th-234 (*)	1.20E−07	U-234	4n+2
U-233	1.17E−04		
U-234	1.76E+00		

Radionuclide	Inventory [mol/canister]	Inventory included in radionuclide	Chain
U-235	4.21E+01		
U-236	3.93E+01		
U-237 (*)	6.10E−08	Np-237	4n+1
U-238	8.11E+03		
Zr-93	2.13E+01		

Table L-2. Inventory in average canister used in the PSAR radionuclide transport calculations. Update of Table E-1 in this report.

Radionuclide	Inventory in average canister [mol/canister]	
	Calculated, year 2070 (0 yrs)	Calculated, year 3070 (1 000 yrs)
Ac-227	2.77E−09	3.05E−08
Ag-108m	1.54E−01	3.17E−02
Am-241	1.06E+01	2.14E+00
Am-242m	6.41E−03	4.70E−05
Am-243	1.60E+00	1.45E+00
C-14	4.97E−02	4.41E−02
Cd-113m	9.95E−05	4.45E−26
Cl-36	8.64E−03	8.62E−03
Cm-245	2.42E−02	2.23E−02
Cm-246	3.49E−03	3.02E−03
Cs-135	6.45E+00	6.45E+00
Cs-137	5.68E+00	5.67E−10
Eu-152	2.64E−05	1.94E−27
H-3	1.77E−03	5.95E−28
Ho-166m	7.38E−04	4.14E−04
I-129	3.08E+00	3.08E+00
Mo-93	8.77E−04	7.38E−04
Nb-93m	2.67E−02	2.28E−04
Nb-94	3.25E−01	3.14E−01
Ni-59	2.25E+00	2.23E+00
Ni-63	2.68E−01	2.80E−04
Np-237	5.13E+00	1.36E+01
Pa-231	5.74E−06	4.72E−05
Pb-210	4.60E−10	4.73E−07
Pd-107	5.74E+00	5.74E+00
Pu-238	1.26E+00	5.34E−04
Pu-239	4.08E+01	3.98E+01
Pu-240	2.36E+01	2.12E+01
Pu-242	6.66E+00	6.65E+00
Ra-226	7.95E−08	3.62E−05
Rn-222	0.00E+00	0.00E+00
Se-79	1.67E−01	1.67E−01
Sm-151	1.21E−01	5.53E−05
Sn-121m	1.87E−03	2.59E−10
Sn-126	8.97E−01	8.94E−01
Sr-90	3.40E+00	1.20E−10
Tc-99	1.99E+01	1.98E+01
Th-229	2.82E−08	6.86E−06
Th-230	2.98E−04	9.08E−03
Th-232	7.30E−05	1.27E−03
U-233	1.57E−04	3.51E−03
U-234	2.03E+00	3.29E+00
U-235	4.21E+01	4.33E+01
U-236	3.94E+01	4.17E+01
U-238	8.11E+03	8.11E+03
Zr-93	2.13E+01	2.13E+01

L.3 Instant release fraction of inventory, IRF

The instant release fraction, IRF, represents the fraction of the total radionuclide inventory that is modelled to be instantly released to the interior of the canister, upon contact with water. Depending on radionuclide, in terms of the data used as input to probabilistic radionuclide transport calculations, the IRF is modelled using either a normal distribution, a double triangular distribution in normal space with values for lower limit, best estimate, and upper limit or a single point value, see Table L-3. The IRF data are calculated for an average canister based on 5 869 canisters. The IRF data used in the PSAR are specified in Section 3.2 of the **Data report** and listed in Table L-3.

The IRFs of the radionuclides in group 1 (see Table L-3), i.e. Cl-36, Cs-135, Cs-137 and I-129, together with Se-79, are assumed to be correlated (**Data report**, Section 3.2). The IRFs for all other radionuclides are uncorrelated. For all radionuclides of the selected inventory that are not displayed in Table L-3, the IRF is insignificant and set equal to zero.

Table L-3. Instant release fractions of inventory, IRF, used in the PSAR (Data report, Section 3.2).

		Normal distribution		Double triangular distribution		
Radionuclide	**Group**	**μ**	**σ**	**Lower limit**	**Best estimate**	**Upper limit**
Cl-36	1	0.078	0.066			
Cs-135		0.026	0.022			
Cs-137		0.026	0.022			
I-129		0.026	0.022			
H-3 (*)	2				1.0	
Pd-107				0	0.002	0.01
Se-79		0.0039	0.0033			
Sn-126				0	0.00030	0.001
Sr-90				0	0.0025	0.01
Tc-99				0	0.002	0.01
Mo-93	3			4.0E-03	4.8E-03	6.2E-03
Nb-93m				3.7E-04	4.7E-04	2.5E-02
Nb-94				4.3E-04	5.4E-04	2.9E-02
Ni-59				4.4E-03	5.4E-03	5.8E-03
Ni-63				4.4E-03	5.6E-03	6.0E-03
Zr-93				1.4E-05	1.7E-05	2.1E-05
Ag-108m	4			3.0E-05	3.0E-04	6.0E-04
C-14				9.1E-02	9.2E-02	9.3E-02
Cd-113m (*)					1.0	
Sn-121m				7.6E-05	4.8E-04	1.1E-03

(*) Single point value used

L.4 Corrosion release fraction of inventory, CRF

The corrosion release fraction, CRF, represents the inventory fraction that is modelled to be released on a relatively short time scale, as a result of corrosion of construction material upon contact with water. In the probabilistic radionuclide transport calculations, the CRF is modelled using double triangular distributions in the normal space with values for lower limit, best estimate, and upper limit, using two significant digits, according to Table L-4. The CRF data are calculated for an average canister based on 5 869 canisters. For the PSAR, Ag-108m is assumed to be part of the CRF rather than the IRF, due to new experimental data. It was decided to model Ag-108m with a CRF-value of 1.0 (together with a small IRF) but with a different (slower) corrosion time compared with other elements. The CRF data used in the PSAR are specified in Section 3.2 of the **Data report** and listed in Table L-4. The CRFs are uncorrelated for all radionuclides and for all radionuclides of the selected inventory that are not displayed in Table L-4, the CRFs are insignificant and set equal to zero. In the radionuclide transport calculations, if the sum of CRF and IRF is larger than 1, the CRF fraction is calculated as 1-IRF.

Table L-4. Corrosion release fractions of inventory, CRF, used in the PSAR (Data report, Section 3.2).

	Double triangular distribution		
Radionuclide	**Lower limit**	**Best estimate**	**Upper limit**
Ag-108m		1.0	
C-14	0.44	0.49	0.53
Cl-36	0.011	0.020	0.072
Mo-93	0.72	0.97	0.99
Nb-93m	0.77	1.0	1.0
Nb-94	0.79	1.0	1.0
Ni-59	0.82	0.99	0.99
Ni-63	0.79	0.99	0.99
Se-79	0.0	0.00039	0.0013
Sn-121m	0.000021	0.029	0.043
Tc-99	0.000037	0.00036	0.0012
U-233	0.22	0.44	0.55
Zr-93	0.084	0.11	0.13

L.5 Corrosion time, t_{corr}

The corrosion time, t_{corr}, is the time over which the construction material fully corrodes. The corrosion times used in the PSAR are specified in Section 3.2 of the **Data report** and listed in Table L-5. Thus, for the corrosion time used in the probabilistic radionuclide transport calculations, a triangular distribution is suggested in the $\log_{10}$-space with lower limit, best estimate, and upper limit. In the PSAR, the corrosion time is assumed to be different for Ag-108m compared to other elements, with a best estimate of the corrosion time equal to 5.9×10^7 years. The recommended distribution is triangular in the $\log_{10}$-space ranging from 5.9×10^6 to 5.9×10^8 years. The slow release rate of Ag-108m is based on experiments performed on irradiated control rods containing mostly Ag, but also some In and Cd. The experiments were performed in a reducing environment mimicking that expected in a failed copper canister (**Fuel and canister process report**). As the corrosion rate is assumed to be uniform, the corrosion release rate for each radionuclide is calculated by taking the product of the CRF and total inventory and dividing it by the corrosion time.

Table L-5. Corrosion time distribution values for all CRF radionuclides, as used in the PSAR (Data report, Section 3.2).

	Triangular distribution, $\log_{10}$-space		
Radionuclide	**Lower limit [years]**	**Best estimate [years]**	**Upper limit [years]**
Ag-108m	5.9E+06	5.9E+07	5.9E+08
C-14	1.0E+02	1.0E+03	1.0E+04
Cl-36	1.0E+02	1.0E+03	1.0E+04
Mo-93	1.0E+02	1.0E+03	1.0E+04
Nb-93m	1.0E+02	1.0E+03	1.0E+04
Nb-94	1.0E+02	1.0E+03	1.0E+04
Ni-59	1.0E+02	1.0E+03	1.0E+04
Ni-63	1.0E+02	1.0E+03	1.0E+04
Se-79	1.0E+02	1.0E+03	1.0E+04
Sn-121m	1.0E+02	1.0E+03	1.0E+04
Tc-99	1.0E+02	1.0E+03	1.0E+04
U-233	1.0E+02	1.0E+03	1.0E+04
Zr-93	1.0E+02	1.0E+03	1.0E+04

L.6 Half-lives of radionuclides

The half-lives used in the PSAR are specified in Section 3.1 of the **Data report**. All the data in Table 3-5 of the **Data report**, except for Se-79, are recommended for use in modelling. In addition, the half-life and specific activity Rn-222 is relevant for radionuclide transport calculations, even if it is not significant for the initial radionuclide inventory. For Rn-222 and Se-79, the half-lives in Table 3-6 of the **Data report** are recommended for use in modelling. The half-lives used in the PSAR are listed in Table L-6.

Table L-6. Half-live values of radionuclides, used in the PSAR (Data report, Section 3.1).

Radionuclide	Half-life [years]
Ac-227	2.18E+01
Ag-108m	4.39E+02
Am-241	4.33E+02
Am-242m	1.41E+02
Am-243	7.37E+03
C-14	5.71E+03
Cd-113m	1.41E+01
Cl-36	3.01E+05
Cm-245	8.52E+03
Cm-246	4.77E+03
Cs-135	2.30E+06
Cs-137	3.01E+01
Eu-152	1.36E+01
H-3	1.23E+01
Ho-166m	1.20E+03
I-129	1.57E+07
Mo-93	4.00E+03
Nb-93m	1.62E+01
Nb-94	2.03E+04
Ni-59	7.60E+04
Ni-63	1.01E+02
Np-237	2.15E+06
Pa-231	3.28E+04
Pb-210	2.22E+01
Pd-107	6.50E+06
Pu-238	8.79E+01
Pu-239	2.41E+04
Pu-240	6.56E+03
Pu-242	3.74E+05
Ra-226	1.60E+03
Rn-222	1.05E-02
Se-79	3.27E+05
Sm-151	9.01E+01
Sn-121m	4.39E+01
Sn-126	2.30E+05
Sr-90	2.88E+01
Tc-99	2.11E+05
Th-229	7.35E+03
Th-230	7.55E+04
Th-232	1.41E+10
U-233	1.59E+05
U-234	2.46E+05
U-235	7.04E+08
U-236	2.34E+07
U-238	4.47E+09
Zr-93	1.53E+06

L.7 Fuel dissolution rate

The fuel dissolution rate specifies the rate by which the fuel matrix dissolves or becomes otherwise altered, as a consequence of groundwater coming in contact with the fuel in case of canister failure. The fuel dissolution rate recommended for use in the in the probabilistic radionuclide transport calculations in the PSAR is the same as that for SR-Site, see Table L-7 (**Data report**, Section 3.3). A dissolution rate with a triangular probability density function in the log10-space is suggested and is suggested not to vary in time.

For modelling dissolution of irregular fuel types containing failed fuel and spent fuel residues, the data in Table L-8 is used (**Data report**, Section 3.3).

Table L-7. Fuel dissolution rate values, used in the PSAR (Data report, Section 3.3).

Case	Lower limit [yr^{-1}]	Best estimate [yr^{-1}]	Upper limit [yr^{-1}]
Regular fuel	1.0E−08	1.0E−07	1.0E−06

Table L-8. Fuel dissolution rate values, used for modelling irregular fuel types in the PSAR (Data report, Section 3.3).

Case	Best estimate [yr^{-1}]
Failed fuel	2.9E−04
Fuel residues	1.0E−03

L.8 Solubility data

In case of canister failure, groundwater will enter the void inside the canister and come into contact with the spent fuel and metal parts inside the canister. As a result, radionuclides will be released into this water as dissolved species. If the concentrations of the dissolved species get high enough, radionuclides will precipitate as solid phases. The solubility of the precipitated phases will determine the maximum concentration of a radioelement inside the canister. These concentrations are used as the source term for the radionuclide transport calculations.

In SR-Site, incorrect values of the solubility limits for plutonium were used. The values for plutonium were too high because of an incorrect value for the associated error in an equilibrium constant used in the calculations. For the PSAR, this error has been corrected, see Table L-9, and updated solubility values are used in the radionuclide transport calculations. Elements not included in solubility calculations (i.e. Ac, C, Ca, Cd, Cl, Cs, Eu, H, I, Mo and Rn) are added to the solubility input data and defined as having no solubility limit, in the model represented with a sufficiently high value (1×10^{17} mol/m^3) that solubility limits never have an impact in the modelling.

The complete solubility data set is too large to present here. For details about the solubility calculations, see Appendix F. Note that the figures in Appendix F have been corrected with respect to the incorrect plutonium equilibrium constant already in SR-Site.

Table L-9. Corrected solubility data for plutonium, used in the PSAR (Model summary report, Section 3.20).

Species	Reaction	$logK^0$	$\Delta logK^0$
$Pu(CO_3)_3^{3-}$	$Pu^{3+} + 3CO_3^{2-} = Pu(CO_3)_3^{3-}$	16.40	1.40

L.9 Sorption partitioning coefficient of buffer and backfill, K_d

In the probabilistic radionuclide transport calculations, the sorption partitioning coefficient of buffer and backfill is modelled using triangular distributions in the $\log_{10}$-space with values for lower limit, best estimate, and upper limit, together with correlations. The recommended data are based on data for highly saline porewater (HSPW), corresponding to highly saline groundwaters. For the buffer, data for the clay material Deponit Ca-N is used. For the backfill, data for the clay material Milos Backfill is used. For all elements except for Cs, Ra and Sr, the same K_d values apply for both buffer and backfill. Ag is assumed to be non-sorbing. For all non-sorbing elements ($K_d = 0$), no correlation is needed. For the remaining elements, the correlation group for the buffer and backfill is specified, while the correlation group is omitted for the elements without any correlation with other elements. The sorption partitioning coefficient data for the buffer and backfill used in the PSAR are specified in Section 5.3 of the **Data report** and listed in Table L-10 (buffer) and Table L-11 (backfill), respectively.

Table L-10. Sorption partitioning coefficient values of the buffer, used in the PSAR. Values in $\log_{10}$-space (Data report, Section 5.3).

Element	Lower limit [m^3/kg]	Best estimate [m^3/kg]	Upper limit [m^3/kg]	Correlation group
Ac	−0.70	0.70	2.15	3
Ag	0	0	0	
Am	0.60	1.38	2.18	3
C	0	0	0	
Cd	−2.70	−1.15	0.48	2
Cl	0	0	0	
Cm	0.60	1.38	2.18	3
Cs	−2.32	−1.54	−0.77	1
Eu	−0.30	0.70	1.76	3
H	0	0	0	
Ho	−0.30	0.70	1.76	3
I	0	0	0	
Mo	0	0	0	
Nb	−0.70	0.48	1.65	
Ni	−2.00	−1.15	−0.10	2
Np	0.30	1.60	2.85	4
Pa	−0.70	0.48	1.65	
Pb	0.85	1.66	2.46	2
Pd	−0.52	0.70	1.88	
Pu	0.30	1.60	2.85	4
Ra	−3.74	−2.96	−2.18	1
Se	0	0	0	
Sm	−0.30	0.70	1.76	3
Sn	0.15	1.60	3.05	4
Sr	−3.74	−2.96	−2.18	1
Tc	0.15	1.60	3.05	4
Th	0.60	1.60	2.65	4
U	0.36	1.60	2.85	4
Zr	−0.70	0.70	2.13	4

Table L-11. Sorption partitioning coefficient values of the backfill, used in the PSAR. Values in log_{10}-space (Data report, Section 5.3).

Element	Lower limit [m^3/kg]	Best estimate [m^3/kg]	Upper limit [m^3/kg]	Correlation group
Ac	−0.70	0.70	2.15	3
Ag	0	0	0	
Am	0.60	1.38	2.18	3
C	0	0	0	
Cd	−2.70	−1.15	0.48	2
Cl	0	0	0	
Cm	0.60	1.38	2.18	3
Cs	−2.30	−1.52	−0.74	1
Eu	−0.30	0.70	1.76	3
H	0	0	0	
Ho	−0.30	0.70	1.76	3
I	0	0	0	
Mo	0	0	0	
Nb	−0.70	0.48	1.65	
Ni	−2.00	−1.15	−0.10	2
Np	0.30	1.60	2.85	4
Pa	−0.70	0.48	1.65	
Pb	0.85	1.66	2.46	2
Pd	−0.52	0.70	1.88	
Pu	0.30	1.60	2.85	4
Ra	−3.72	−2.96	−2.17	1
Se	0	0	0	
Sm	−0.30	0.70	1.76	3
Sn	0.15	1.60	3.05	4
Sr	−3.72	−2.96	−2.17	1
Tc	0.15	1.60	3.05	4
Th	0.60	1.60	2.65	4
U	0.36	1.60	2.85	4
Zr	−0.70	0.70	2.13	4

L.10 Effective diffusivity of buffer and backfill, D_e

The approach taken for the effective diffusivity of buffer and backfill is to sort the different elements into three categories: anions (Cl, I, Mo and Se); cations and non-charged species (except Cs); and Cs. In the probabilistic radionuclide transport calculations, a triangular distribution is used for cations and non-charged species (except Cs). For anions, a double triangular distribution is used, while for Cs, a right triangular distribution is used. All distributions are in the log10-space and data for all elements are correlated. The effective diffusivity data for the buffer and backfill used in the PSAR are specified in Section 5.3 of the **Data report** and listed in Table L-12 (buffer) and Table L-13 (backfill), respectively.

Table L-12. Effective diffusivity values of buffer, used in the PSAR. Values in log_{10}-space (Data report, Section 5.3).

Element	Lower limit [m^2/s]	Best estimate [m^2/s]	Upper limit [m^2/s]	Correlation group
Cations and non-charged species	−10.03	−9.85	−9.68	1
Anions	−12.22	−10.96	−10.22	1
Cs	−10.02	−9.38	−9.38	1

Table L-13. Effective diffusivity values of backfill, used in the PSAR. Values in log_{10}-space (Data report, Section 5.3).

Element	Lower limit [m^2/s]	Best estimate [m^2/s]	Upper limit [m^2/s]	Correlation group
Cations and non-charged species	−9.96	−9.80	−9.62	1
Anions	−12.00	−10.92	−10.15	1
Cs	−9.96	−9.32	−9.32	1

L.11 Diffusion-available porosity of buffer and backfill, ε

The approach taken for the diffusion available porosity of buffer and backfill is to sort the different elements into two categories: anions (Cl, I, Mo and Se); and, cations and non-charged species. In the probabilistic radionuclide transport calculations, a triangular distribution is used for cations and non-charged species. For anions, a double triangular distribution is used. Both distributions are in the normal space and data for all elements are correlated. The diffusion available porosity data for the buffer and backfill used in the PSAR are specified in Section 5.3 of the **Data report** and listed in Table L-14 (buffer) and Table L-15 (backfill), respectively.

Table L-14. Diffusion-available porosity values of buffer, used in the PSAR. Values in the normal space (Data report, Section 5.3).

Element	Lower limit [%]	Best estimate [%]	Upper limit [%]	Correlation group
Cations and non-charged species	41.0	43.5	46.0	1
Anion	12.4	17.4	24.1	1

Table L-15. Diffusion-available porosity values of backfill, used in the PSAR. Values in normal space (Data report, Section 5.3).

Element	Lower limit [%]	Best estimate [%]	Upper limit [%]	Correlation group
Cations and non-charged species	44.0	46.0	48.0	1
Anions	13.1	18.4	25.6	1

L.12 Sorption partitioning coefficient of rock, K_d

The sorption partitioning coefficient data are given in the form of log-normal distributions, characterised by a mean (μ) and standard deviation (σ), which implicitly includes the combined impact of uncertainty as well as spatial and temporal variability. The median of the log-transformed K_d uncertainty is taken to be the best estimate value for deterministic calculations. For probabilistic calculations, the log-normal distributions are sampled uniformly between the 2.5 % and 97.5 % percentiles (i.e. the distribution is truncated). K_d data of the same correlation group (1 or 2) should be correlated according to Table L-16. The sorption partitioning coefficient data for the rock used in the PSAR are specified in Section 6.8 of the **Data report** and listed in Table L-16.

Table L-16. Sorption partitioning coefficient values of rock, used in the PSAR. Values in log_{10}-space (Data report, Section 6.8).

Element	μ_{10} [m^3/kg]	σ_{10} [m^3/kg]	Correlation group
Ac	−1.83	0.72	2
Ag	−3.46	0.51	1
Am	−1.83	0.72	2
C	-	-	
Cd	−2.96	0.65	1
Cl	-	-	
Cm	−1.83	0.72	2
Cs	−3.46	0.51	1
Eu	−1.83	0.72	2
H	-	-	
Ho	−1.83	0.72	2
I	-	-	
Mo	-	-	
Nb	−1.70	0.64	2
Ni	−2.96	0.65	1
Np	−1.28	0.65	2
Pa	−1.23	0.48	2
Pb	−1.60	0.56	2
Pd	−1.28	0.83	2
Pu	−1.83	0.72	2
Ra	−3.62	0.41	1
Se	−3.53	0.55	
Sm	−1.83	0.72	2
Sn	−0.80	0.28	2
Sr	−5.47	0.99	1
Tc	−1.28	0.65	2
Th	−1.28	0.65	2
U	−1.28	0.65	2
Zr	−1.67	0.35	2

L.13 Effective diffusivity of rock, D_e

The approach taken for the effective diffusivity of rock is to sort the different elements into two categories: anions (Cl, I, Mo and Se); and, cations and non-charged species. In the probabilistic radionuclide transport calculations, normal distributions in log_{10}-space are used for all elements. Data for all elements are correlated. The effective diffusivity data for the rock used in the PSAR are specified in Section 6.8 of the **Data report** and listed in Table L-17.

Table L-17. Effective diffusivity values of rock, used in the PSAR. Values in log_{10}-space (Data report, Section 6.8).

Element	μ [m^2/s]	σ [m^2/s]	Correlation group
Cations and non-charged species	−13.7	0.25	1
Anions	−14.2	0.25	1

L.14 Diffusion-available porosity of rock, ε

For the diffusion available porosity, the fraction of the connected pore space that is available for solutes is close to unity, for anions, cations, and non-charged species. Therefore, the suggested flow path averaged diffusion available in situ porosity is 0.18 % for all solutes. The uncertainty associated with this single point value is so small that no range is suggested. The diffusion available porosity data for the rock used in the PSAR are specified in Section 6.8 of the **Data report** and listed in Table L-18.

Table L-18. Diffusion-available porosity values of rock, used in the PSAR. Values in normal space (Data report, Section 6.8).

Element	ε [-] (flow path averaged)
Cations and non-charged species	0.0018
Anions	0.0018

L.15 Landscape dose conversion factors, LDF

Landscape dose conversion factors, LDFs, are used to calculate dose to humans from the radionuclide activity release to the biosphere. In SR-Site, Rn-222 and Po-210 were not included in the radionuclide transport calculations but need to be accounted for in the PSAR. Therefore, an LDF value has been added for Rn-222 (see Table L-19). For Po-210, this is accomplished by assuming secular equilibrium between Pb-210 and Po-210 and adding the LDF for Po-210 to Pb-210 as (see [(a)] in Table L-19),

$$\mathrm{LDF(Pb\text{-}210) = LDF(Pb\text{-}210) + LDF(Po\text{-}210) = 5.07 \times 10^{-12} + 8.86 \times 10^{-12} = 1.39 \times 10^{-11}}$$

Hence, only Pb-210 values are presented in the reported PSAR results (Chapter 7 and Appendix M) but this then includes the contribution of Po-210.

In addition, the SR-Site data delivery did not provide LDFs for the radionuclides Am-242m, Pu-238, Cd-113m, Eu-152, H-3, Mo-93, Nb-93m and Sn-121m (see [(c)] in Table L-19). In SR-Site and in the PSAR, these radionuclides are assigned the value of the radionuclide with the highest LDF, i.e. Se-79. The values for the remaining radionuclides are unchanged since SR-Site. The LDF-values used in the PSAR for both deterministic and probabilistic calculations are specified in Section 7.2 of the **Data report** and listed in Table L-19.

L.16 Deterministic input data

The deterministic input data set consists of median values from the probabilistic input data sets of 6916 iterations, see Table L-20 and Table L-21. These parameter values are the same in all deterministic PSAR calculation cases.

For the transport parameters (U0, QEQ, FLEN, TW, F, TRAPP, LR_TUN and TR_TUN), used in the deterministic shear load and pinhole cases in the PSAR, data from the semi-correlated base case are used. This data have not changed since SR-Site and are given in Section 3.7.2 in Table 3-5 and Table 3-6, for the near-field and the far-field respectively.

For the corrosion scenario, the transport parameters change with the hydrogeological case and the results from the erosion/corrosion model. The parameters used in the deterministic calculations are always those associated with the earliest failure time, see Table L-22.

The LDF-values used for both deterministic and probabilistic calculations are given in Table L-19.

Table L-19. Basic landscape dose factors, LDF, used in the PSAR. Update of Table 3-7 in this report (Data report, Section 7.2).

Radionuclide	LDF [Sv/yr per Bq/yr]
Ac-227	8.00E−12
Ag-108m	7.05E−13
Am-241	1.46E−12
Am-242m [c]	1.21E−09
Am-243	1.53E−12
C-14	5.44E−12
Ca-41	9.90E−14
Cd-113m [c]	1.21E−09
Cl-36	5.84E−13
Cm-244	8.74E−13
Cm-245	1.58E−12
Cm-246	1.55E−12
Cs-135	3.96E−14
Cs-137	1.20E−13
Eu-152 [c]	1.21E−09
H-3 [c]	1.21E−09
Ho-166m	5.90E−14
I-129	6.46E−10
Mo-93 [c]	1.21E−09
Nb-93m [c]	1.21E−09
Nb-94	4.00E−12
Ni-59	7.39E−14
Ni-63	1.21E−15
Np-237	4.83E−11
Pa-231	8.10E−12
Pb-210 [a]	1.39E−11
Pd-107	6.73E−15
Po-210	8.86E−12
Pu-238 [c]	1.21E−09
Pu-239	1.94E−12
Pu-240	1.88E−12
Pu-242	1.89E−12
Ra-226	3.75E−12
Rn-222 [b]	5.20E−14
Se-79	1.21E−09
Sm-151	7.16E−16
Sn-121m [c]	1.21E−09
Sn-126	2.47E−11
Sr-90	2.19E−13
Tc-99	8.98E−13
Th-229	3.61E−12
Th-230	1.31E−11
Th-232	1.72E−12
U-233	2.50E−12
U-234	3.62E−12
U-235	2.76E−12
U-236	1.85E−12
U-238	1.85E−12
Zr-93	2.77E−14

[a] Includes contribution from Pb-210

[b] 5.10E−14 in the **Data report**.

[c] Assigned the value of the radionuclide with the highest LDF, i.e. the value for Se-79.

Table L-20. Median values of D_e, K_d and ε used in the deterministic calculations in the PSAR. ε rock is not in the table since it is constant 1.80×10^{-3} (-), for all nuclides. Update of Table 3-3 in this report.

Radionuclide	De buffer [m³/yr]	De backfill [m³/yr]	De rock [m³/yr]	K_d buffer [m³/kg]	K_d backfill [m³/kg]	K_d rock [m³/kg]	ε buffer [-]	ε backfill [-]
Ac-227	4.41E−03	5.09E−03	6.30E−07	5.16E+00	5.16E+00	1.48E−02	0.43	0.46
Ag-108m	4.41E−03	5.09E−03	6.30E−07	0.00E+00	0.00E+00	3.47E−04	0.44	0.46
Am-241	4.41E−03	5.09E−03	6.30E−07	2.43E+01	2.43E+01	1.48E−02	0.44	0.46
Am-242m	4.41E−03	5.09E−03	6.30E−07	2.43E+01	2.43E+01	1.48E−02	0.44	0.46
Am-243	4.41E−03	5.09E−03	6.30E−07	2.43E+01	2.43E+01	1.48E−02	0.44	0.46
C-14	4.41E−03	5.09E−03	6.30E−07	0.00E+00	0.00E+00	0.00E+00	0.44	0.46
Cd-113m	4.41E−03	5.09E−03	6.30E−07	7.37E−02	7.37E−02	1.10E−03	0.44	0.46
Cl-36	3.47E−04	3.79E−04	1.99E−07	0.00E+00	0.00E+00	0.00E+00	0.17	0.18
Cm-245	4.41E−03	5.09E−03	6.30E−07	2.43E+01	2.43E+01	1.48E−02	0.43	0.46
Cm-246	4.41E−03	5.09E−03	6.30E−07	2.43E+01	2.43E+01	1.48E−02	0.43	0.46
Cs-135	8.58E−03	9.84E−03	6.30E−07	2.88E−02	3.00E−02	3.47E−04	0.43	0.46
Cs-137	8.58E−03	9.84E−03	6.30E−07	2.88E−02	3.00E−02	3.47E−04	0.43	0.46
Eu-152	4.41E−03	5.09E−03	6.30E−07	5.17E+00	5.17E+00	1.48E−02	0.43	0.46
H-3	4.41E−03	5.09E−03	6.30E−07	0.00E+00	0.00E+00	0.00E+00	0.43	0.46
Ho-166m	4.41E−03	5.09E−03	6.30E−07	5.17E+00	5.17E+00	1.48E−02	0.44	0.46
I-129	3.47E−04	3.79E−04	1.99E−07	0.00E+00	0.00E+00	0.00E+00	0.17	0.18
Mo-93	3.47E−04	3.79E−04	1.99E−07	0.00E+00	0.00E+00	0.00E+00	0.17	0.18
Nb-93m	4.41E−03	5.09E−03	6.30E−07	3.00E+00	3.00E+00	2.00E−02	0.43	0.46
Nb-94	4.41E−03	5.09E−03	6.30E−07	3.00E+00	3.00E+00	2.00E−02	0.43	0.46
Ni-59	4.41E−03	5.09E−03	6.30E−07	7.94E−02	7.94E−02	1.10E−03	0.44	0.46
Ni-63	4.41E−03	5.09E−03	6.30E−07	7.94E−02	7.94E−02	1.10E−03	0.44	0.46
Np-237	4.41E−03	5.09E−03	6.30E−07	3.87E+01	3.87E+01	5.25E−02	0.43	0.46
Pa-231	4.41E−03	5.09E−03	6.30E−07	3.00E+00	3.00E+00	5.89E−02	0.43	0.46
Pb-210	4.41E−03	5.09E−03	6.30E−07	4.54E+01	4.54E+01	2.51E−02	0.44	0.46
Pd-107	4.41E−03	5.09E−03	6.30E−07	4.87E+00	4.87E+00	5.25E−02	0.43	0.46
Pu-238	4.41E−03	5.09E−03	6.30E−07	3.87E+01	3.87E+01	1.48E−02	0.43	0.46
Pu-239	4.41E−03	5.09E−03	6.30E−07	3.87E+01	3.87E+01	1.48E−02	0.43	0.46
Pu-240	4.41E−03	5.09E−03	6.30E−07	3.87E+01	3.87E+01	1.48E−02	0.43	0.46
Pu-242	4.41E−03	5.09E−03	6.30E−07	3.87E+01	3.87E+01	1.48E−02	0.43	0.46
Ra-226	4.41E−03	5.09E−03	6.30E−07	1.10E−03	1.12E−03	2.40E−04	0.43	0.46
Rn-222	4.41E−03	5.09E−03	6.30E−07	0.00E+00	0.00E+00	0.00E+00	0.43	0.46
Se-79	3.47E−04	3.79E−04	1.99E−07	0.00E+00	0.00E+00	2.95E−04	0.17	0.18
Sm-151	4.41E−03	5.09E−03	6.30E−07	5.17E+00	5.17E+00	1.48E−02	0.44	0.46
Sn-121m	4.41E−03	5.09E−03	6.30E−07	3.97E+01	3.97E+01	1.58E−01	0.44	0.46
Sn-126	4.41E−03	5.09E−03	6.30E−07	3.97E+01	3.97E+01	1.58E−01	0.44	0.46
Sr-90	4.41E−03	5.09E−03	6.30E−07	1.09E−03	1.12E−03	3.39E−06	0.43	0.46
Tc-99	4.41E−03	5.09E−03	6.30E−07	3.97E+01	3.97E+01	5.25E−02	0.44	0.46
Th-229	4.41E−03	5.09E−03	6.30E−07	4.10E+01	4.10E+01	5.25E−02	0.43	0.46
Th-230	4.41E−03	5.09E−03	6.30E−07	4.10E+01	4.10E+01	5.25E−02	0.43	0.46
Th-232	4.41E−03	5.09E−03	6.30E−07	4.10E+01	4.10E+01	5.25E−02	0.43	0.46
U-233	4.41E−03	5.09E−03	6.30E−07	4.01E+01	4.01E+01	5.25E−02	0.43	0.46
U-234	4.41E−03	5.09E−03	6.30E−07	4.01E+01	4.01E+01	5.25E−02	0.43	0.46
U-235	4.41E−03	5.09E−03	6.30E−07	4.01E+01	4.01E+01	5.25E−02	0.43	0.46
U-236	4.41E−03	5.09E−03	6.30E−07	4.01E+01	4.01E+01	5.25E−02	0.43	0.46
U-238	4.41E−03	5.09E−03	6.30E−07	4.01E+01	4.01E+01	5.25E−02	0.43	0.46
Zr-93	4.41E−03	5.09E−03	6.30E−07	5.09E+00	5.09E+00	2.14E−02	0.44	0.46

Table L-21. Median values of solubilities, CSOL, (temperate conditions, See Appendix F), IRF and CRF used in the deterministic calculations in the PSAR. If IRF+CRF is greater than one, CRF is set to 1-IRF. A solubility of 1.00×10^{17} corresponds to an unlimited solubility. The mean values of IRF are used when calculating the peak annual doses from the pulse releases from the IRF. Update of Table 3-4 in this report.

Radionuclide	CSOL [mol/dm^3]	IRF [-]	IRF mean [-]	CRF [-]
Ac-227	1.00E+17	0.00E+00	-	0.00E+00
Ag-108m	2.03E−06	3.00E−04	3.05E−04	1.00E+00
Am-241	1.30E−06	0.00E+00	-	0.00E+00
Am-242m	1.30E−06	0.00E+00	-	0.00E+00
Am-243	1.30E−06	0.00E+00	-	0.00E+00
C-14	1.00E+17	9.20E−02	-	4.90E−01
Cd-113m	1.00E+17	1.00E+00	-	0.00E+00
Cl-36	1.00E+17	8.79E−02	9.29E−02	2.00E−02
Cm-245	1.40E−06	0.00E+00	-	0.00E+00
Cm-246	1.40E−06	0.00E+00	-	0.00E+00
Cs-135	1.00E+17	2.93E−02	3.10E−02	0.00E+00
Cs-137	1.00E+17	2.93E−02	-	0.00E+00
Eu-152	1.00E+17	0.00E+00	-	0.00E+00
H-3	1.00E+17	1.00E+00	-	0.00E+00
Ho-166m	2.24E−06	0.00E+00	-	0.00E+00
I-129	1.00E+17	2.93E−02	3.10E−02	0.00E+00
Mo-93	1.00E+17	4.80E−03	-	9.70E−01
Nb-93m	4.82E−05	4.66E−04	-	1.00E+00
Nb-94	4.82E−05	5.44E−04	5.24E−03	1.00E+00
Ni-59	2.01E−04	5.40E−03	5.30E−03	9.90E−01
Ni-63	2.01E−04	5.60E−03	-	9.90E−01
Np-237	1.28E−09	0.00E+00	-	0.00E+00
Pa-231	3.19E−07	0.00E+00	-	0.00E+00
Pb-210	7.59E−07	0.00E+00	-	0.00E+00
Pd-107	3.99E−06	2.00E−03	-	0.00E+00
Pu-238	1.73E−06	0.00E+00	-	0.00E+00
Pu-239	1.73E−06	0.00E+00	-	0.00E+00
Pu-240	1.73E−06	0.00E+00	-	0.00E+00
Pu-242	1.73E−06	0.00E+00	-	0.00E+00
Ra-226	2.54E−06	0.00E+00	-	0.00E+00
Rn-222	1.00E+17	0.00E+00	-	0.00E+00
Se-79	6.15E−09	4.39E−03	4.64E−03	3.90E−04
Sm-151	7.09E−08	0.00E+00	-	0.00E+00
Sn-121m	9.82E−08	4.80E−04	-	2.90E−02
Sn-126	9.82E−08	3.00E−04	3.68E−04	0.00E+00
Sr-90	1.27E−03	2.50E−03	-	0.00E+00
Tc-99	4.44E−09	2.00E−03	3.01E−03	3.60E−04
Th-229	5.21E−09	0.00E+00	-	0.00E+00
Th-230	5.21E−09	0.00E+00	-	0.00E+00
Th-232	5.21E−09	0.00E+00	-	0.00E+00
U-233	9.86E−10	0.00E+00	-	4.40E−01
U-234	9.86E−10	0.00E+00	-	0.00E+00
U-235	9.86E−10	0.00E+00	-	0.00E+00
U-236	9.86E−10	0.00E+00	-	0.00E+00
U-238	9.86E−10	0.00E+00	-	0.00E+00
Zr-93	1.80E−08	1.70E−05	-	1.10E−01

L.17 Input data specific for the corrosion scenario

For the deterministic calculations of the corrosion scenario, the hydraulic and transport properties used are those associated to the earliest failure time calculated with the erosion/corrosion model for the PSAR (Hedin 2021b); these parameters are summarised in Table L-22.

For the probabilistic calculation of the central corrosion case, failure times and geosphere transport data from the ten realisations of the semi-correlated hydrogeological model for the 45 failed canisters are used, see Table L-23. The corresponding data for the five other corrosion cases are given in Hedin (2021a).

The earlier failure time in the PSAR is due to changes in the SR-Site erosion/corrosion model (update (**Post-closure safety report**, Section 10.3.13) and adjustment of an error (SKB 2013b, Hedin 2013)).

Table L-22. Data for the deposition holes where the first canister fails, used in the deterministic calculations of the corrosion scenario in the PSAR. Update of Table 4-2 in this report.

Hydrogeological model; Erosion/corrosion model	Time of failure [yr]	Rock transport resistance, F [yr/m]	Advective travel time, t_w [yr]	Advective flow through deposition hole, q [m^3/yr]
Semi-correlated; PSAR	93 141	53 660	6	0.733
Uncorrelated; PSAR	107 331	1 020 000	53	0.443
Fully correlated; PSAR	91 846	45 600	12	0.626
Semi-correlated; Initial advection	62 295	53 660	6	0.733
Uncorrelated; Initial advection	78 377	93 310	20	0.463
Fully correlated; Initial advection	67 397	45 600	12	0.626

Table L-23. Data for deposition holes where canisters fail due to corrosion for the ten realisations of the semi-correlated hydrogeological model, used in the PSAR. Sorted by ascending time of failure. Update of Table 4-3 in this report.

Time of failure [yr]	Rock transport resistance, F [yr/m]	Advective travel time, t_w [yr]	Advective flow through deposition hole, q [m^3/yr]
93 141	53 660	6	0.733
104 258	564 900	61	0.557
133 209	26 260	7	0.358
138 269	642 100	78	0.316
157 065	87 820	14	0.251
189 603	89 910	17	0.144
201 991	818 600	38	0.148
257 760	33 970	16	0.082
279 586	38 170	14	0.095
282 096	2 184 000	124	0.083
295 392	157 900	19	0.086
330 436	155 100	19	0.075
359 529	163 400	29	0.067
434 114	116 600	241	0.050
483 428	471 800	31	0.048
520 082	211 100	20	0.044
610 704	1 710 000	99	0.033
643 104	11 330	20	0.035
644 233	53 660	6	0.733
682 570	53 660	6	0.733
730 547	61 400	18	0.032
735 973	3 845,000	91	0.033
736 241	53 660	6	0.733
736 615	564 900	61	0.557
766 438	39 850	17	0.038
773 367	53 660	6	0.733
780 605	564 900	61	0.557
787 053	9 083 000	601	0.026
797 090	53 660	6	0.733
814 624	2 008 000	135	0.024
842 191	564 900	61	0.557
884 470	354 500	144	0.025
884 791	564 900	61	0.557
891 523	328 400	135	0.025
897 656	50 020	35	0.023
897 656	42 330	20	0.023
912 012	564 900	61	0.557
921 373	26 260	7	0.358
921 895	30 620	19	0.024
924 279	1 456 000	43	0.026
939 691	558 800	232	0.023
953 504	1 505 000	152	0.020
953 822	4 054 000	336	0.021
976 202	26 260	7	0.358
976 911	642 100	78	0.316

Appendix M

Safety assessment PSAR – Comparison of PSAR and SR-Site results

The transport models for the near and far field are identical to those used in SR-Site. Also, most of the calculated cases are the same as those in SR-Site and the input data to most cases are nearly identical. Therefore, the approach to accounting for radionuclide transport in the PSAR has been to calculate all cases related to compliance with all appropriate updates, whereas most of the cases used for illustrative and completeness purposes have not been recalculated.

In this appendix it is investigated whether the conclusions drawn from the results of the SR-Site radionuclide transport calulations, as shown in Chapters 4–6, are still valid with the adopted changes of input data. The analysis is performed in two steps.

The first step is a recalculation of calculations performed in the SR-Site assessment and can be seen as a quality assurance step, i.e. that input data, codes etc are still producing the same results as in the SR-Site assessment. The results of these calculations are shown in this appendix and the conformity between the curves from the original calculations in SR-Site, shown in Chapters 4–6, and the recalculated SR-Site calculations in this appendix is evaluated.

The second step is calculations with updated input data for the PSAR. The updated input data are described in the previous appendix. The results from these calculations are shown in this appendix and the differences between these and the results from the SR-Site are evaluated.

M.1 Performed calculations

M.1.1 Corrosion scenario

In the canister failure due to corrosion scenario (briefly called the corrosion scenario) canisters fail as a result of enhanced corrosion due to advective conditions in the deposition hole following the loss of buffer through erosion. For this failure mode, both the canister and buffer are bypassed, and the rock retention is small since substantial copper corrosion after buffer erosion only occurs in deposition holes with high flow rates, which in general are associated with flow paths to the surface of low geosphere retention. Since SR-Site, sedimentation has been added to the erosion/corrosion model (**Post-closure safety report**, Section 10.3.11) and adjustment has been made of an error in the model (SKB 2013b, Hedin 2013). The mean number of failed canisters is an outcome of the corrosion calculations (**Post-closure safety report**, Section 12.6.2).

The calculations performed for the canister failure due to corrosion scenario are described in Sections 4.1 to 4.3. The calculation cases performed for this scenario are summarised in Figure 4-1, and in Table M-1 it is shown which of them are, in the present Appendix, first recalculated and then calculated with the PSAR input data. Table M-1 also gives the sections were the results are described.

M.1.2 Shear load scenario

In the canister failure due to shear load scenario (briefly called the shear load scenario) a canister fails as a result of secondary rock movements induced by a large earthquake. For this failure mode, the canister is bypassed, the thickness of the buffer is reduced, and the rock retention is insignificant. The calculations performed for the canister failure due to shear load scenario are described in Sections 5.1 to 5.2 and 5.5. The calculations cases performed for the shear load scenario are summarised in Table M-2.

Table M-1. Summary of calculation cases performed for the canister failure due to corrosion scenario with reference to the section where the results are described.

Calculation case	SR-Site	Recalculated SR-Site and PSAR
Central corrosion case, deterministic caluclations	4.4.1	M.2.1
Central corrosion case, probabilistic calculations	4.4.2	M.2.2
Corrosion, Semi-correlated hydrogeological model – Disregarding thorium sorption in the near field, deterministic calculations	4.5.1	-
Corrosion, Semi-correlated hydrogeological model – Disregarding thorium sorption in the near field, probabilistic calcualtions	4.5.1	M.3
Corrosion, Semi-correlated hydrogeological model – Including solubility limits in the near field, deterministic calculation	4.5.2	-
Corrosion, Semi-correlated hydrogeological model – Including solubility limits in the near field, probabilistic calculations	4.5.2	M.5
Other alternative corrosion cases based on the semi-correlated hydrogeological DFN model	4.5.3–4.5.8	-
Corrosion, Semi-correlated hydrogeological model – Initial advection, deterministic calculations	4.5.9	M.5.1
Corrosion, Semi-correlated hydrogeological model – Initial advection, probabilistic calculations	4.5.9	M.5.2
Corrosion, Uncorrelated hydrogeological model – Base case transport assuptions, deterministic calculations	4.6.1	M.6.1
Corrosion, Uncorrelated hydrogeological model – Base case transport assuptions, probabilistic calculations	4.6.1	M.6.2
Corrosion, Uncorrelated hydrogeological model – Initial advection, deterministic calculations	4.6.2	M.7.1
Corrosion, Uncorrelated hydrogeological model – Initial advection, probabilistic calculations	4.6.2	M.7.2
Corrosion, Fully correlated hydrogeological model – Base case transport assumptions, deterministic calculations	4.7.1	M.8.1
Corrosion, Fully correlated hydrogeological model – Base case transport assumptions, probabilistic calculations	4.7.1	M.8.2
Corrosion, Fully correlated hydrogeological model – Initial advection, deteministic calculations	4.7.2	M.9.1
Corrosion, Fully correlated hydrogeological model – Initial advection, probabilistic calculations	4.7.2	M.9.2

Table M-2. Summary of calculation cases performed for the shear load scenario with reference to where the results are described.

	SR-Site	Recalculated SR-Site and PSAR
Shear load, Postulated failure of one canister at 100 000 years, deterministic calculations	5.2.1	M.11.1
Shear load, Postulated failure of one canister at 100 000 years, probabilistic calculations	5.2.1	M.11.2
Shear load, Failure during the period 1 000 years to one million years, probabilistic calculations	5.2.2	M.12.1
Shear load, Failure during the period 1 000 years to one million years, probabilistic calculations, disregarding co-precipitation of radium and barium	5.2.2	M.12.2
Shear load, Early failure, probabilistic calculations	5.2.3	M.13.1
Combination of shear load and buffer advection, probabilistic calculations	5.2.4	M.14.1

M.1.3 The growing pinhole failure

A hypothetical, postulated failure mode where an initial defect in the form of a penetrating pinhole in the copper shell grows over time into a larger defect is analysed. The calculations performed for this failure mode are described in Section 6.3. The calculations cases performed for the pinehole failure are summarised in Table M-3.

Table M-3. Summary of calculation cases performed for the pinhole failure with reference to the section where the results are described.

	SR-Site	Recalculated SR-Site and PSAR
Pinhole, Base case, including the effect of spalling, deterministic calculations	6.3.1	M.16.1
Pinhole, Base case, including the effect of spalling, probabilistic calculations	6.3.1	M.16.2
Pinhole, Disregarding the effect of spalling, deterministic calcualtions	6.3.2	M.17.1
Pinhole, Disregarding the effect of spalling, probabilistic calcualtions	6.3.2	M.17.2
Other pinhole cases	6.3.3–6.3.4	-

M.2 Central corrosion case (semi-correlated hydrogeological model)

M.2.1 Deterministic calculations

Hydrogeological case:	Semi-correlated, ten realisations
Erosion/corrosion model:	SR-Site model, PSAR model
Failure time:	114 485 years (SR-Site), 93 141 years (PSAR)
Number of failed canisters:	1
Solubility limits:	No
Thorium sorption in near field:	Yes (modelled as low solubility limit)
Number of realisations:	1
Number of nuclides:	37 (SR-Site), 38 (PSAR)

A deterministic calculation of the central corrosion case is performed for a canister taken from the realisation with the earliest failure time of the analysed realisations with corresponding geosphere transport data, i.e. data used to calculate the corrosion time are from the same hydrogeological calculation as the geosphere transport data (see Table 4-2 for the SR-Site and Table L-22 for the PSAR). The earliest failure time is obtained for the same realisation in the SR-Site and the PSAR, hence the geosphere transport data are the same. The earlier failure time in the PSAR is due to changes in the erosion/corrosion model since SR-Site. This case is further described in Section 4.4.1. The contributions from the instantly released fraction, IRF, are handled as described in Section 4.1.3.

Table M-4 shows peak annual doses from the pulse releases from the instantly released fraction, IRF. The IRF inventory (inventory multiplied with IRF) at 100 000 years has been multiplied by the pulse LDF-values given in Table L-19. The higher peak annual doses calcultated in the PSAR are mainly due to increased inventory. The lower peak annual doses for Ni-59 and Nb-94 are due to decreased IRF-values.

The dose equivalent releases from the near field and far field are shown in Figure M-1 and Figure M-2, respectively. Comparison between the curves from the recalculated SR-Site calculations and the original calculations in the SR-Site, Figure 4-2 and 4-3, shows that they are almost identical.

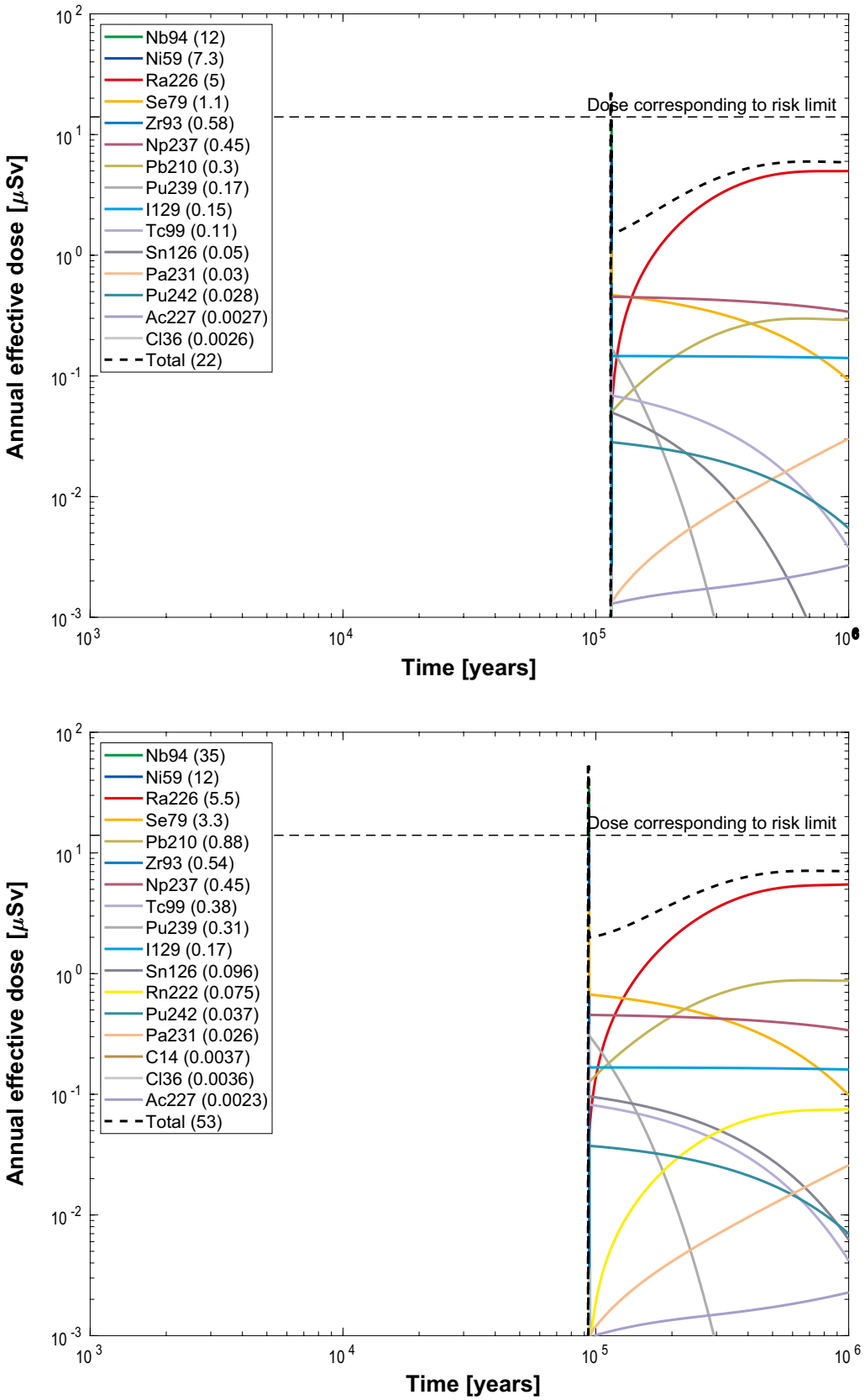

Figure M-1. *Near-field dose equivalent release for a deterministic calculation of the central corrosion case. The legend is sorted by peak (in the one-million year period) of the annual effective dose. The values in brackets are peak dose in units of μSv. The curves for Nb-94 and Ni-59 are hidden under the curve showing the total dose equivalent release.* ***Top:*** *SR-Site.* ***Bottom:*** *PSAR.*

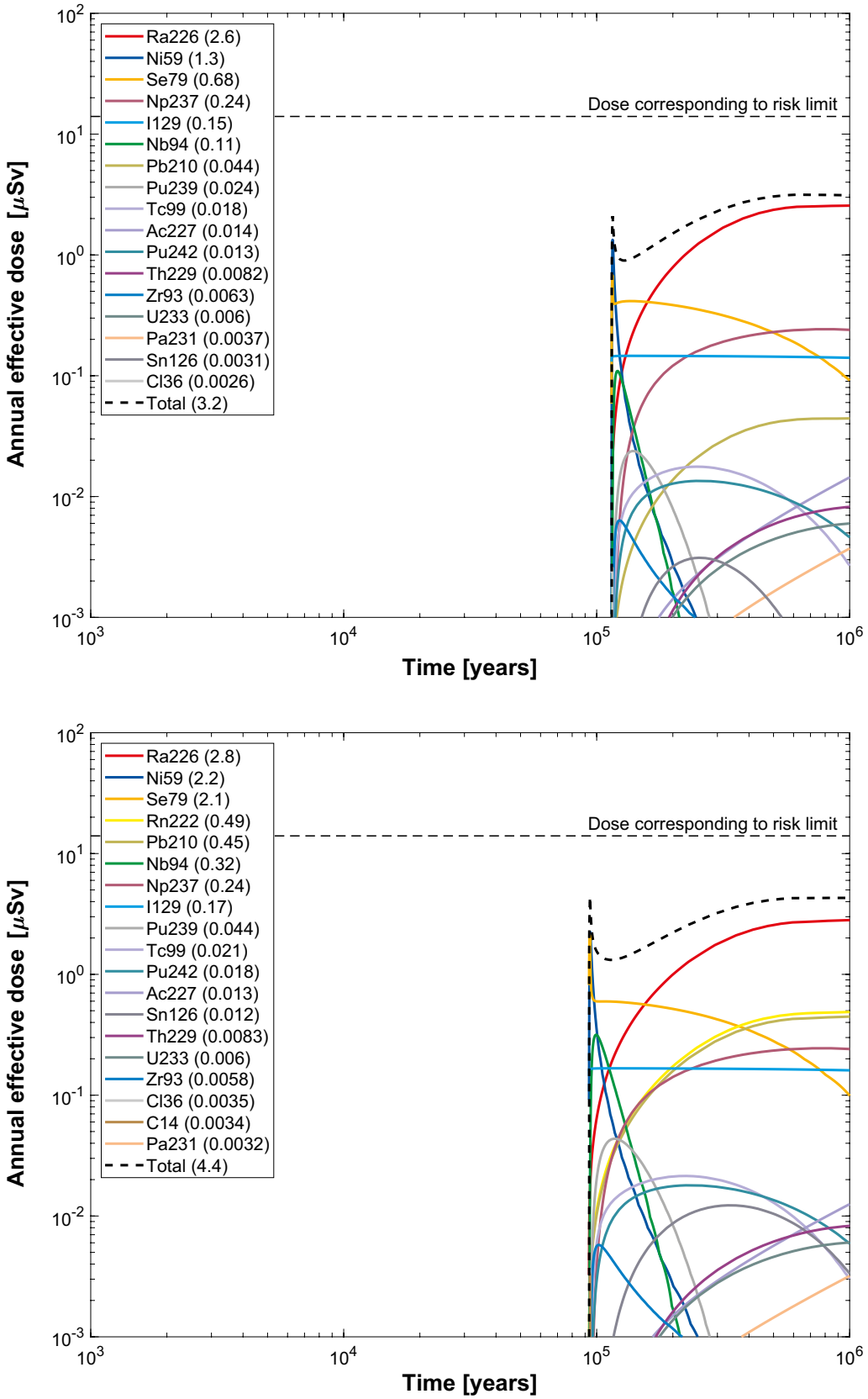

Figure M-2. *Far-field annual effective dose for a deterministic calculation of the central corrosion case. The legend is sorted by peak (in the one-million year period) of the annual effective dose. The values in brackets are peak dose in units of μSv.* ***Top:*** *SR-Site.* ***Bottom:*** *PSAR.*

Comparison between the SR-Site and the PSAR for the near-field shows an increase of the release of Nb-94, this increase is due to the earlier failure in combination with the relatively short half-life for Nb-94. However, the dose equivalent release from the near field is dominated by Tc-99 (as IRF-pulse). The differences are small for the far field release and the doses caused by releases from the far field are still dominated by I-129 (as IRF-pulse) initially and in the longer term by Ra-226. Including Rn-222 separately in the calculations and adding the LDF-value for Po-210 to Pb-210 results in visible changes for Rn-222 and Pb-210, however not markedly influencing the total dose.

Table M-4. Peak annual dose from the pulse releases from the instantly released fraction, IRF. The dose is calculated at 100 000 years.

Nuclide	Peak annual dose (μSv) (SR-Site)	Peak annual dose (μSv) (PSAR)
I-129	3.82	4.5
Se-79	1.72	2.5
Cs-135	0.21	0.20
Cl-36	0.12	0.12
Nb-94	0.026	0.012
Sn-126	0.019	0.032
Ni-59	0.012	0.008
Tc-99	6.81[a)]	7.6[a)]

[a)] The peak annual dose for Tc-99 is only valid for the near field.

M.2.2 Probabilistic calculations

Hydrogeological case:	Semi-correlated, ten realisations
Erosion/corrosion model:	SR-Site model, PSAR model
Failure time:	SR-Site: 56 times according to Table 4-3.
	PSAR: 45 times according to Table L-23.
Mean number of failed canisters:	0.12 (SR-Site), 0.094 (PSAR)
Solubility limits:	No
Thorium sorption in near field:	Yes (modelled as low solubility limit)
Number of realisations:	50 per canister failure time
Number of nuclides:	37 (SR-Site), 38 (PSAR)

A probabilistic calculation of the central corrosion case is performed with failure times and geosphere transport data from the ten realisations of the semi-correlated hydrogeological model (see Table 4-3 for the SR-Site and Table L-23 for the PSAR). This case is further described in Section 4.4.1. The contributions from the instantly released fraction, IRF, are handled as described in Section 4.1.3.

The results for the IRF presented in Section 4.4.2 are judged to be sufficient to conclude that their contribution is negligible also in this case.

The dose equivalent releases from the near field and far field are shown in Figure M-3 and Figure M-4, respectively. Comparison between the curves from the recalculated SR-Site calculations and the original calculations in SR-Site, Figure 4-4 and 4-5, shows some minor differences for the near field, for some radionuclides with negligible contributions, but the curves for the far field are very similar.

Comparison between the SR-Site and the PSAR shows the total dose caused by releases from the far field is very similar, even though the details as to when and how high the peaks are, especially for the near field, differ due to the changes in the erosion/corrosion model. Including Rn-222 separately in the calculations and adding the LDF-value for Po-210 to Pb-210 results in visible changes for Rn-222 and Pb-210, however not markedly influencing the total dose.

Also, the statistics (discussed in Section 4.4.2) for the far-field release shown in Figure M-5 show that the recalculated SR-Site results as well as the PSAR results are very similar to the SR-Site results. The minor differences are due to the differences described in the previous two paragraphs.

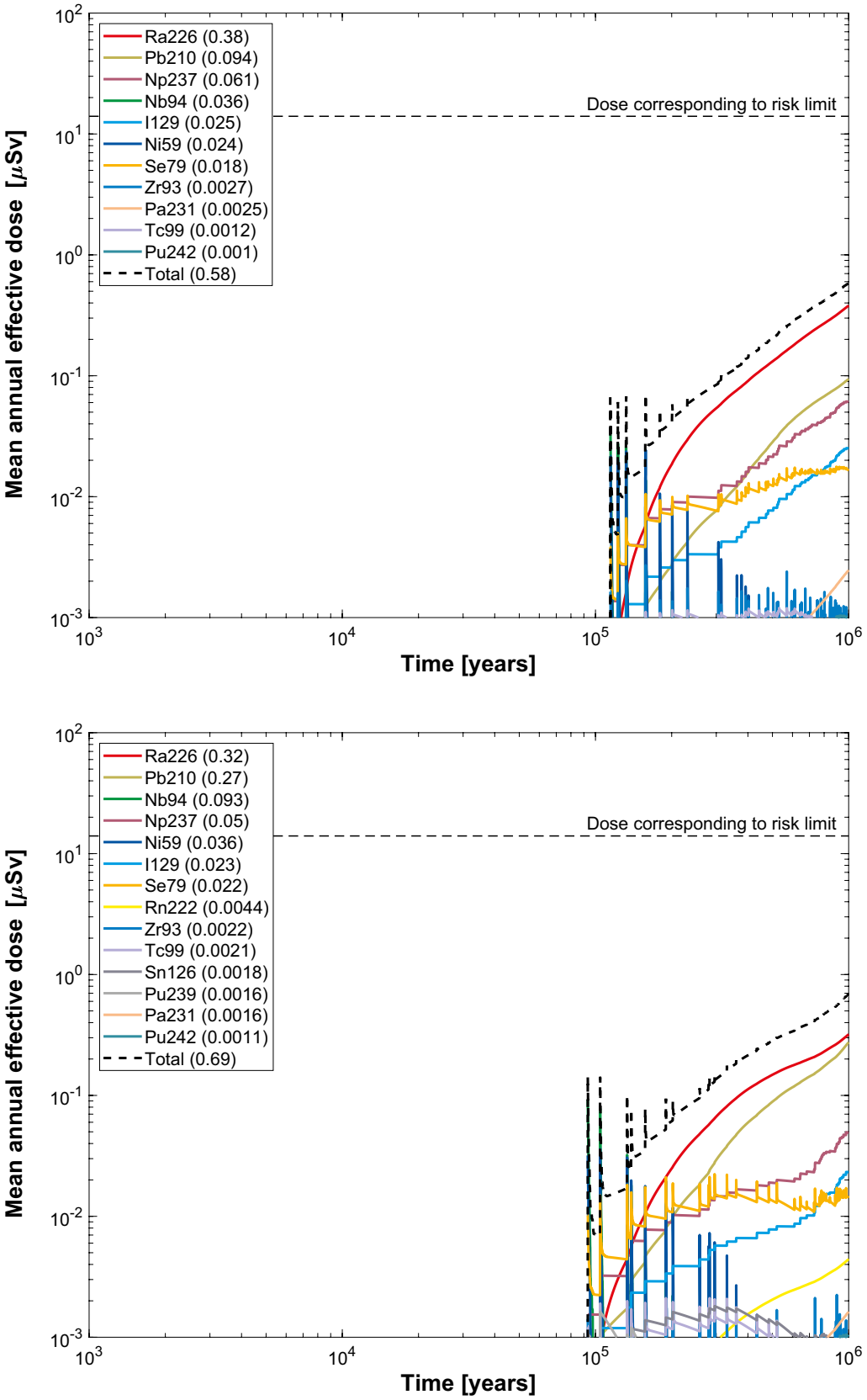

Figure M-3. *Near-field dose equivalent release for a probabilistic calculation of the central corrosion case. The mean number of failed canisters is 0.12 in the SR-Site and 0.094 in the PSAR. The legend is sorted by peak (in the one-million year period) of the mean annual effective dose. The values in brackets are peak dose in units of μSv.* ***Top:*** *SR-Site.* ***Bottom:*** *PSAR.*

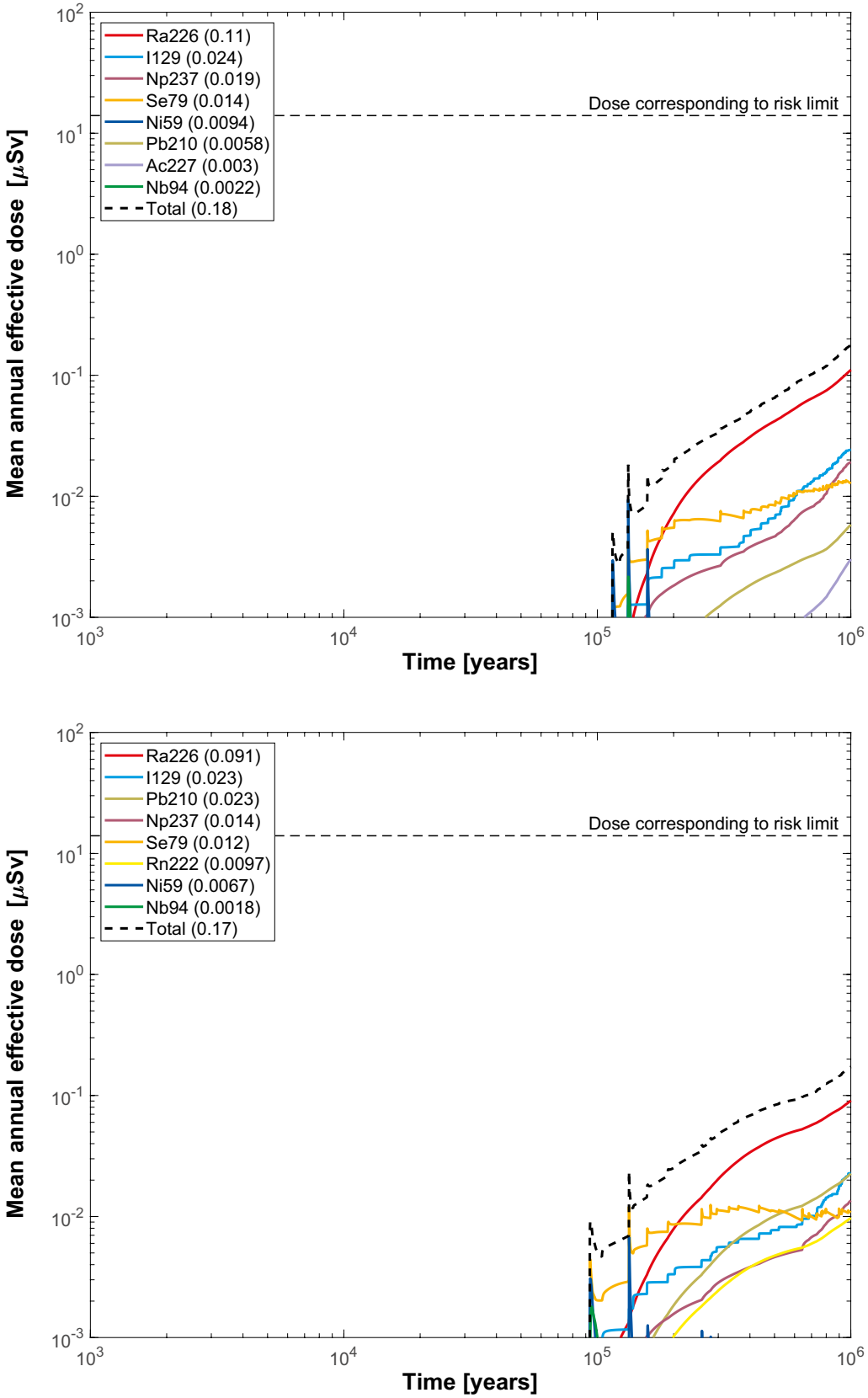

Figure M-4. *Far-field mean annual effective dose for a probabilistic calculation of the central corrosion case. The legend is sorted by peak (in the one-million year period) of the mean annual effective dose. The values in brackets are peak dose in units of μSv.* ***Top:*** *SR-Site.* ***Bottom:*** *PSAR.*

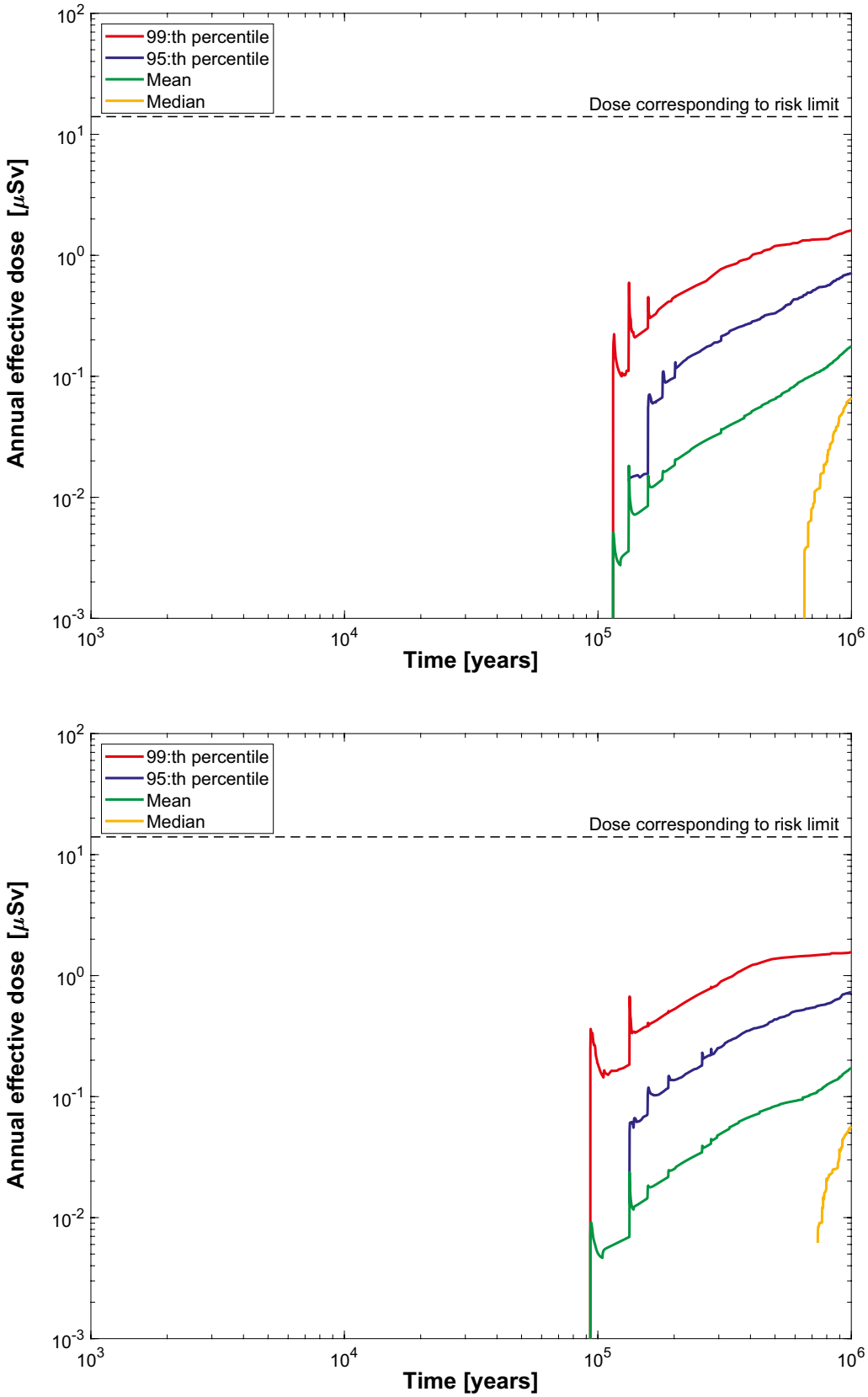

Figure M-5. *Far-field annual effective dose (mean, median, 95th and 99th percentiles) for the probabilistic calculation of the central corrosion case.* ***Top:*** *SR-Site.* ***Bottom:*** *PSAR.*

M.3 Corrosion, Semi-correlated hydrogeological model – Disregarding thorium sorption in the near field

Hydrogeological case:	Semi-correlated, ten realisations
Erosion/corrosion model:	SR-Site model, PSAR model
Failure time:	SR-Site: 56 times according to Table 4-3. PSAR: 45 times according to Table L-23.
Mean number of failed canisters:	0.12 (SR-Site), 0.094 (PSAR)
Solubility limits:	No
Thorium sorption in near field:	No
Number of realisations:	50 per canister failure time
Number of nuclides:	37 (SR-Site), 38 (PSAR)

A probabilistic calculation of the the semi-correlated case with all data equal to the central corrosion case except that the sorption of thorium is disregarded to assess the sensitivity of the release of primarily Ra-226 due to alternative transport conditions for thorium. This case is further described in Section 4.5.1. The contributions from the instantly released fraction, IRF, are treated as described in Section 4.1.3.

The results for the IRF presented in Section 4.4.2 are judged to be sufficient to conclude that their contribution is negligible also in this case.

The dose equivalent releases from the near field and far field are shown in Figure M-6 and Figure M-7, respectively. Comparison between the curves from the recalculated SR-Site calculations and the original calculations in SR-Site, Figure 4-14 and 4-15, shows some minor differences for the near field, but the curves for the far field are very similar.

Comparison between SR-Site and the PSAR shows the total dose caused by releases from the far field is very similar, even though the details in when and how high the peaks are, especially for the near field, differs due to the changes in the erosion/corrosion model. Including Rn-222 separately in the calculations and adding the LDF-value for Po-210 to Pb-210 results in visible changes for Rn-222 and Pb-210, however not markedly influencing the total dose.

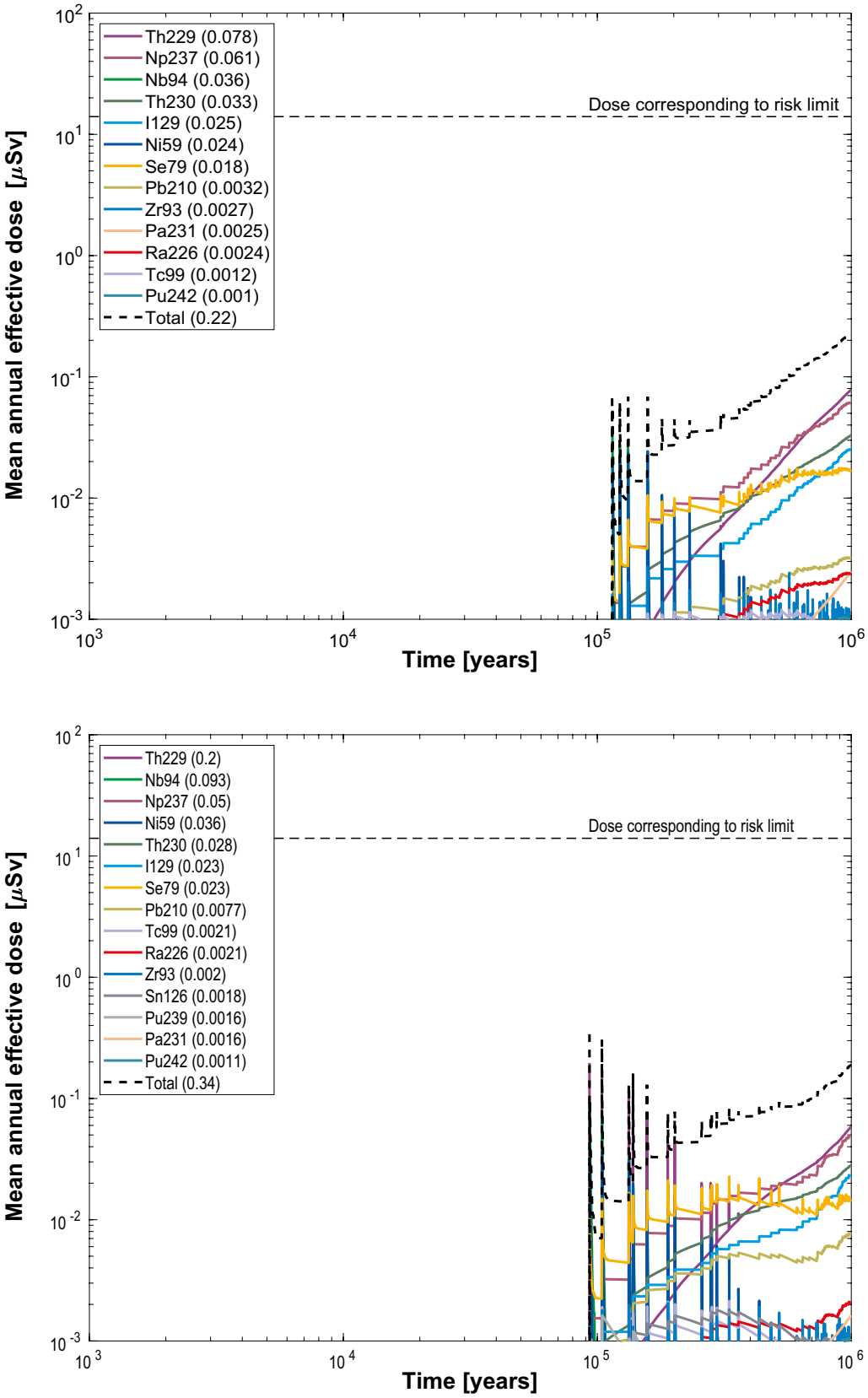

Figure M-6. *Near-field dose equivalent release for the probabilistic central corrosion case, disregarding thorium sorption in the near field. The legend is sorted by peak (in the one-million year period) of the mean annual effective dose. The values in brackets are peak dose in units of μSv.* ***Top:*** *SR-Site.* ***Bottom:*** *PSAR.*

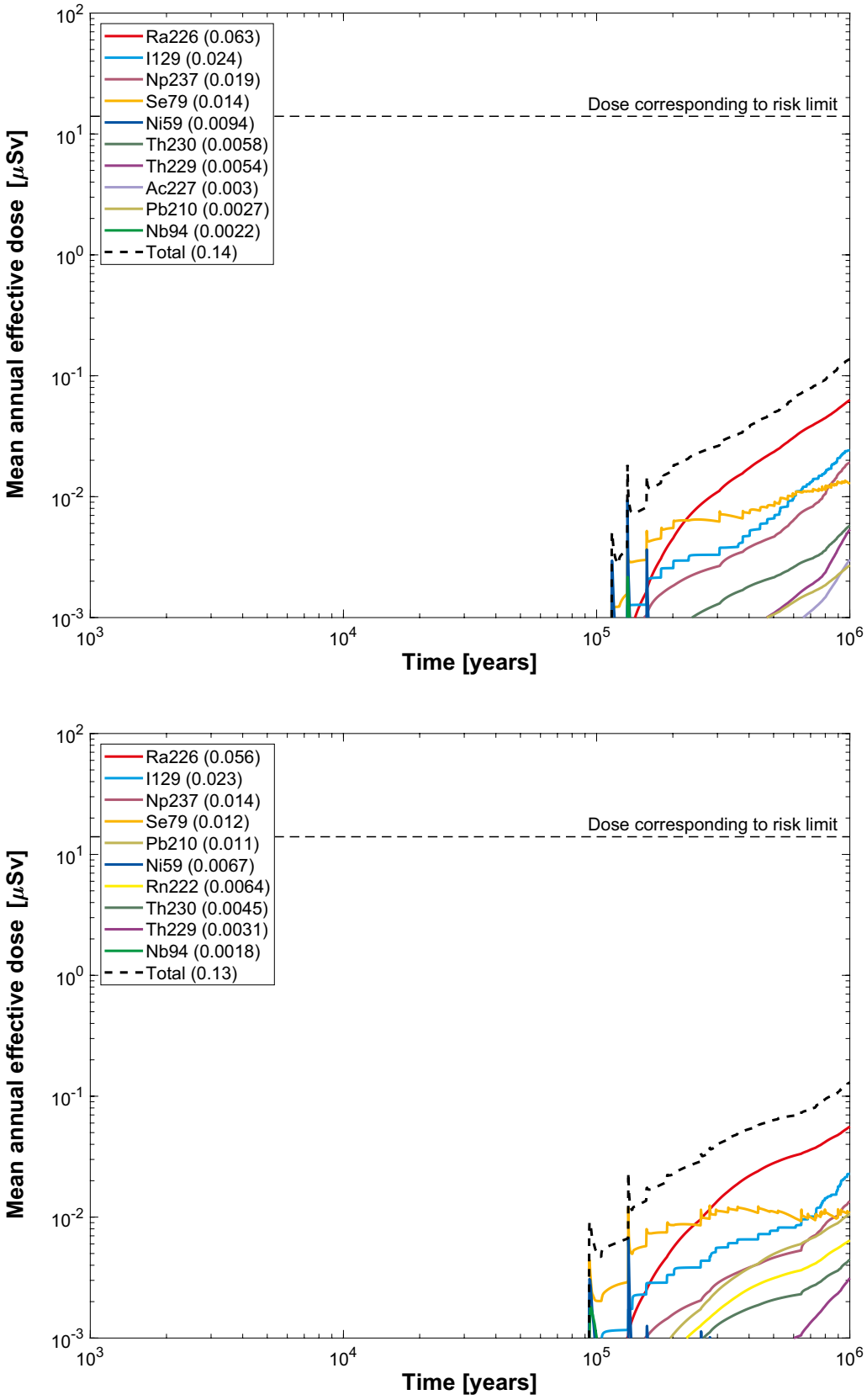

Figure M-7. *Far-field mean annual effective dose for the probabilistic central corrosion case, disregarding thorium sorption in the near field. The legend is sorted by peak (in the one-million year period) of the mean annual effective dose. The values in brackets are peak dose in units of μSv.* ***Top:*** *SR-Site.* ***Bottom:*** *PSAR.*

M.4 Corrosion, Semi-correlated hydrogeological model – Including solubility limits in the near field

Hydrogeological case:	Semi-correlated, ten realisations
Erosion/corrosion model:	SR-Site model, PSAR model
Failure time:	SR-Site: 56 times according to Table 4-3. PSAR: 45 times according to Table L-23.
Mean number of failed canisters:	0.12 (SR-Site), 0.094 (PSAR)
Solubility limits:	Yes
Thorium sorption in near field:	Yes (modelled as low solubility limit)
Number of realisations:	50 per canister failure time
Number of nuclides:	37 (SR-Site), 38 (PSAR)

A probabilistic calculation of the the semi-correlated case with all data equal to the central corrosion case except that solubility limits are included in the near field. This case is further described in Section 4.5.2. The contributions from the instantly released fraction, IRF, are treated as described in Section 4.1.3.

The results for the IRF presented in Section 4.4.2 are judged to be sufficient to conclude that their contribution is negligible also in this case.

The dose equivalent releases from the near field and far field are shown in Figure M-8 and Figure M-9, respectively. Comparison between the curves from the recalculated SR-Site calculations and the original calculations in SR-Site, Figure 4-18 and 4-19, shows some minor differences for the near field, but the curves for the far field are very similar.

Comparison between the SR-Site and the PSAR shows the total dose caused by releases from the far field is very similar, even though the details as to when and how high the peaks are differ due to the changes in the erosion/corrosion model. Including Rn-222 separately in the calculations and adding the LDF-value for Po-210 to Pb-210 results in visible changes for Rn-222 and Pb-210, however not markedly influencing the total dose.

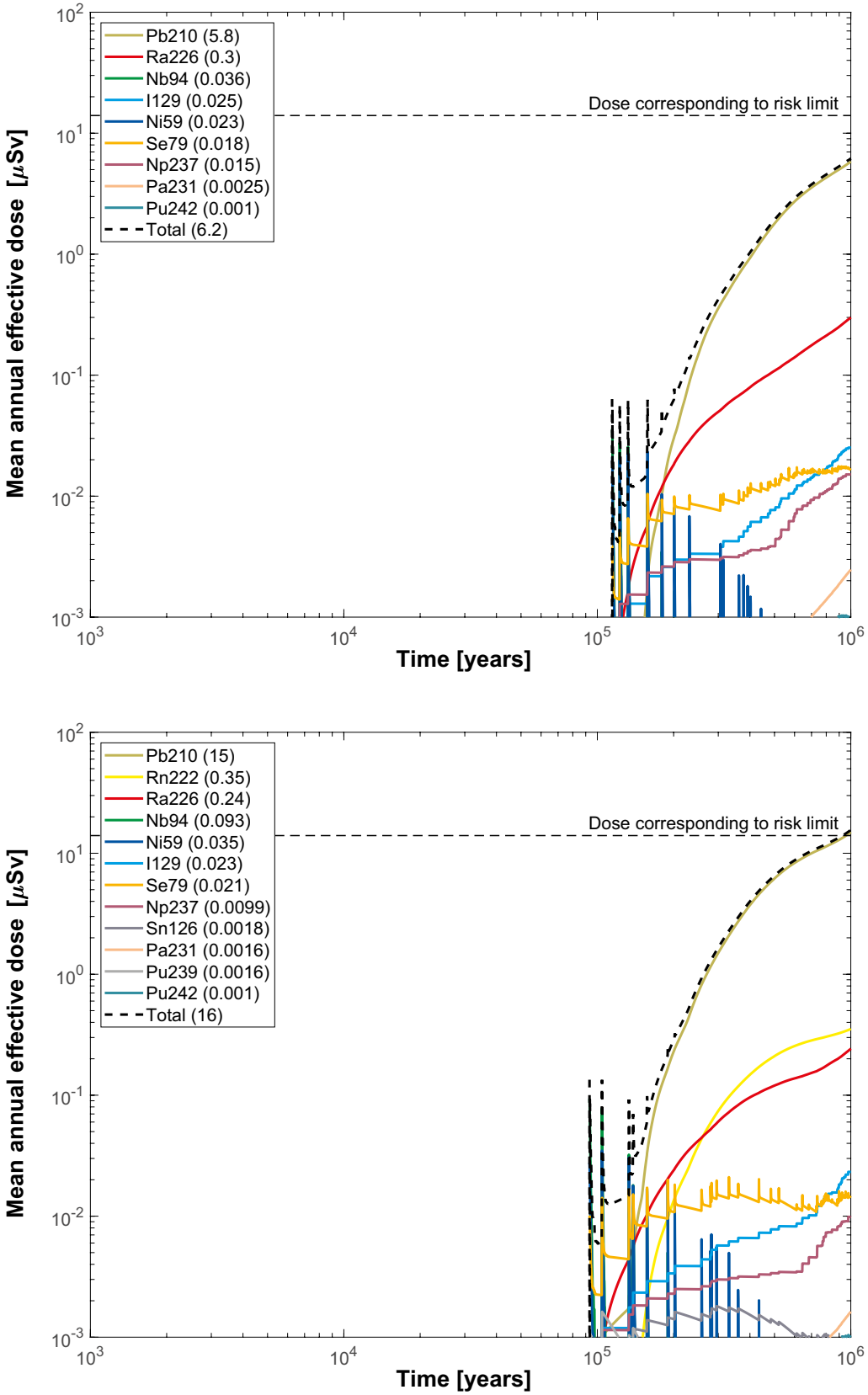

Figure M-8. *Near-field dose equivalent release for the probabilistic central corrosion case, including solubility limits in the near field. The legend is sorted by peak (in the one-million year period) of the mean annual effective dose. The values in brackets are peak dose in units of μSv.* ***Top:*** *SR-Site.* ***Bottom:*** *PSAR.*

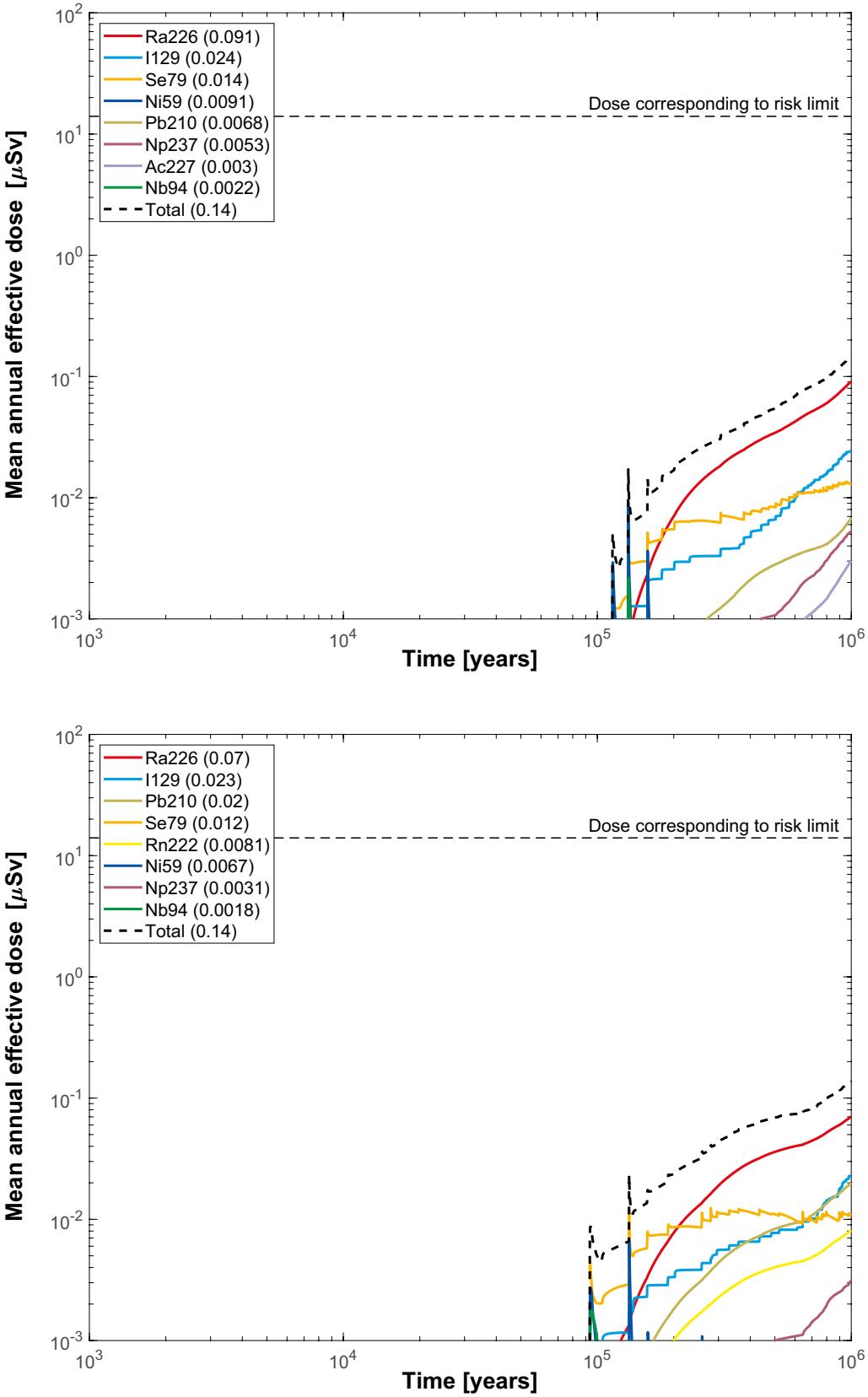

Figure M-9. *Far-field mean annual effective dose for the probabilistic central corrosion case, including solubility limits in the near field. The legend is sorted by peak (in the one-million year period) of the mean annual effective dose. The values in brackets are peak dose in units of μSv.* ***Top:*** *SR-Site.* ***Bottom:*** *PSAR.*

M.5 Corrosion, Semi-correlated hydrogeological model – Initial advection

M.5.1 Deterministic calculations

Hydrogeological case:	Semi-correlated, ten realisations
Erosion/corrosion model:	Initial advection
Failure time:	44 049 years (SR-Site), 62 295 years (PSAR)
Number of failed canisters:	1
Solubility limits:	No
Thorium sorption in near field:	Yes (modelled as low solubility limit)
Number of realisations:	1
Number of nuclides:	37 (SR-Site), 38 (PSAR)

A deterministic calculation of the semi-correlated case with initial advection is performed for a canister taken from the realisation with the earliest failure time of the analysed realisations with corresponding geosphere transport data, i.e. data used to calculate the corrosion time are from the same hydrogeological calculation as the geosphere transport data (see Table 4-2 for SR-Site and Table L-22 for the PSAR). The earliest failure time is obtained for the same realisation in SR-Site and the PSAR, hence the geosphere transport data are the same. The changed failure time is due to an update in the erosion/corrosion model since SR-Site. This calculation case is described in more detail in Section 4.5.9. This case is further described in Section 4.4.1. The contributions from the instantly released fraction, IRF, are treated as described in Section 4.1.3 and 22.2.1.

The dose equivalent releases from the near field and far field are shown in Figure M-10 and Figure M-11, respectively. Note that the peaks in Figure M-10 reach outside the figure (doses larger than 100 μSv) but the real maximum doses are given in brackets in the figure legend. Comparison between the curves from the recalculated SR-Site calculations and the original calculations in SR-Site, Figure 4-28 and 4-29, shows that they are very similar.

Comparison between the SR-Site and the PSAR for the near-field shows a decrease of the release of Nb-94, this decrease is due to the later failure in combination with the relatively short half-life for Nb-94. The differences are small for the far field release and the doses caused by releases from the far field are still dominated by I-129 (as IRF-pulse, see Table M-4) initially and thereafter by Ni-59, Nb-94, Se-79 and in the longer term by Ra-226.

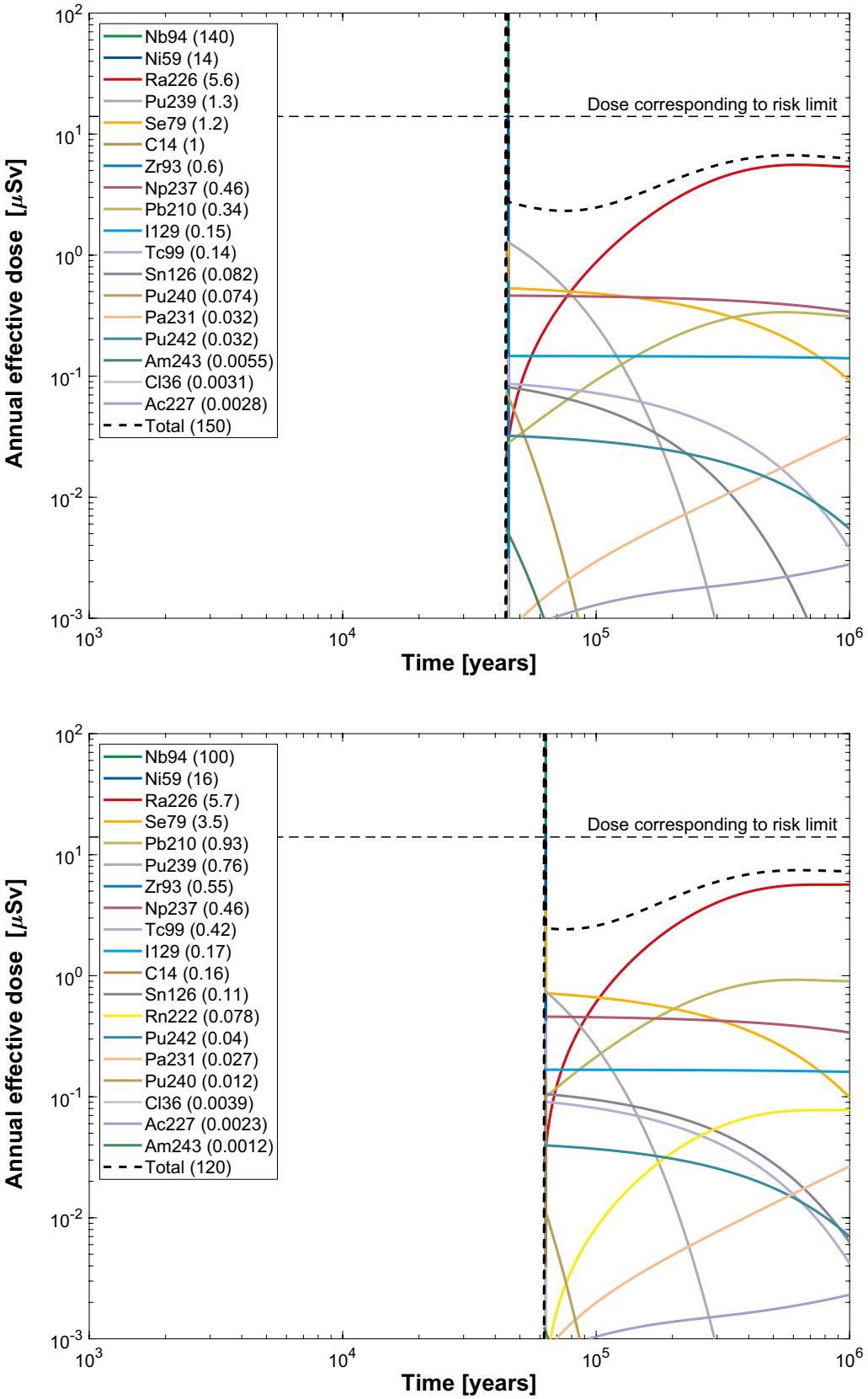

Figure M-10. *Near-field dose equivalent release for a deterministic calculation of the central corrosion case, with initial advection in the erosion/corrosion model. The legend is sorted by peak (in the one-million year period) of the annual effective dose. The values in brackets are peak dose in units of μSv. Note that the dose equivalent release for Nb-94 reaches outside the figure (doses larger than 100 μSv) but the real maximum doses are given in brackets in the figure legend.* ***Top:*** *SR-Site.* ***Bottom:*** *PSAR.*

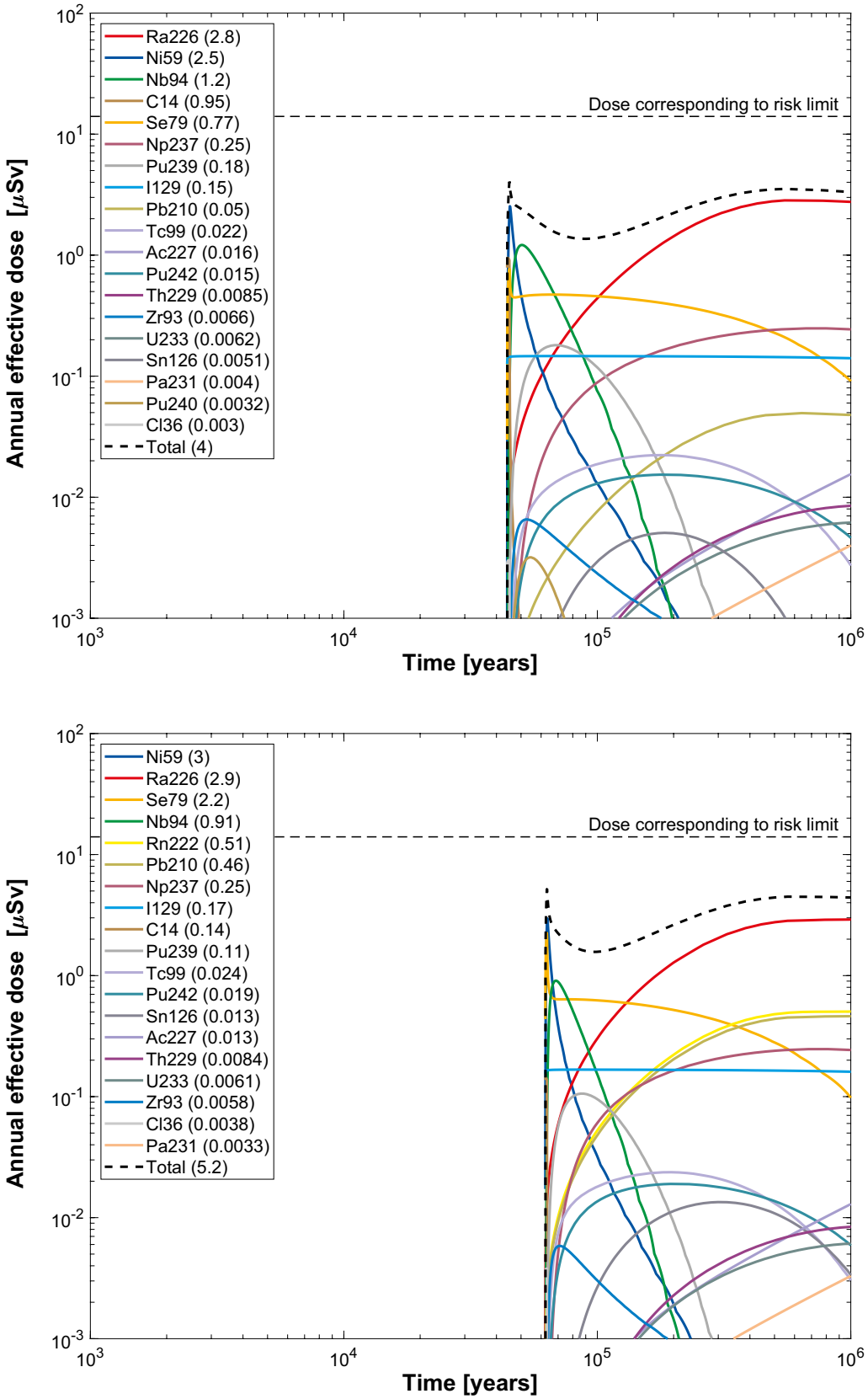

Figure M-11. *Far-field annual effective dose for a deterministic calculation of the central corrosion case, with initial advection in the erosion/corrosion model. The legend is sorted by peak (in the one-million year period) of the annual effective dose. The values in brackets are peak dose in units of μSv.* ***Top:*** *SR-Site.* ***Bottom:*** *PSAR.*

M.5.2 Probabilistic calculations

Hydrogeological case:	Semi-correlated, ten realisations
Erosion/corrosion model:	Initial advection
Failure time:	84 times (SR-Site), 60 times (PSAR) according to the erosion/corrosion calculations
Mean number of failed canisters:	0.17 (SR-Site), 0.12 (PSAR)
Solubility limits:	No
Thorium sorption in near field:	Yes (modelled as low solubility limit)
Number of realisations:	50 per canister failure time
Number of nuclides:	37 (SR-Site), 38 (PSAR)

A probabilistic calculation of the semi-correlated case with initial advection is performed with failure times and geosphere transport data from the ten realisations of the semi-correlated model (see Table 3-8) and failure times from the erosion/corrosion calculations with initial advection (see Table 3-8 for the SR-Site and Section L.17 for the PSAR). This case is further described in Section 4.5.9. The contributions from the instantly released fraction, IRF, are treated as described in Section 4.1.3.

The results for the IRF presented in Section 4.4.2 are judged to be sufficient to conclude that their contribution is negligible also in this case.

The contributions from the instantly released fraction of nuclides, IRF, are not included in the calculations except for Tc-99. Tc-99 is, however, not included in the figures showing results for the near field, but in the figures for the far field.

The dose equivalent releases from the near field and far field are shown in Figure M-12 and Figure M-13, respectively. Comparison between the curves from the recalculated SR-Site calculations and the original calculations in SR-Site, Figure 4-30 and 4-31, shows some minor differences for the near field, the peaks are somewhat higher especially for some radionuclides with negligible contribution, but the curves for the far field are very similar.

Comparison between SR-Site and the PSAR shows the total dose caused by releases from the far field is very similar, eventough the details in when and how high the peaks are, especially for the near field, differs due to the changes in the erosion/corrosion model. Including Rn-222 separately in the calculations and adding the LDF-value for Po-210 to Pb-210 results in visible changes for Rn-222 and Pb-210, however not markedly influencing the total dose.

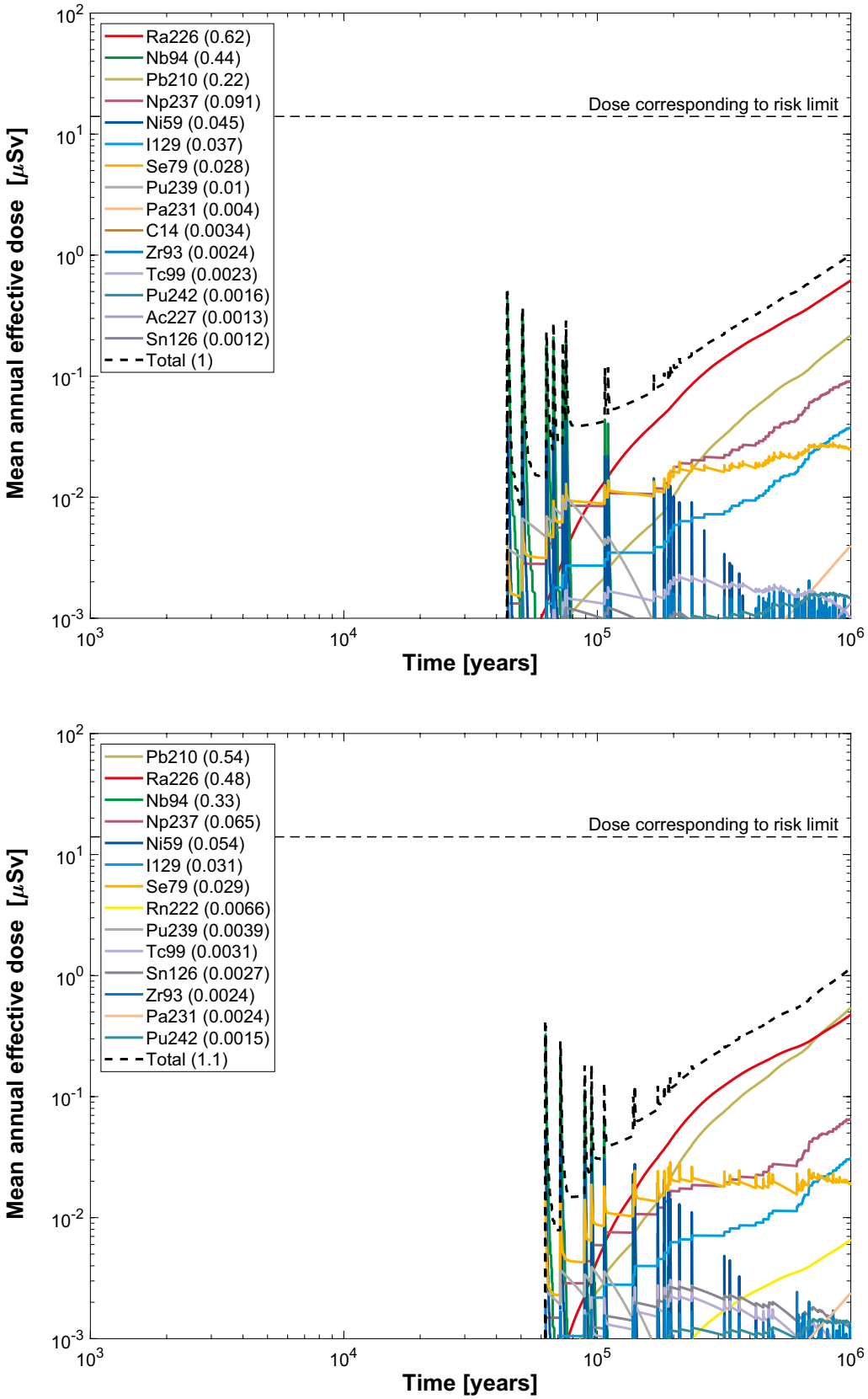

Figure M-12. *Near-field dose equivalent release for a probabilistic calculation of the central corrosion case, with initial advection in the erosion/corrosion model. The legend is sorted by peak (in the one-million year period) of the mean annual effective dose. The values in brackets are peak dose in units of μSv.* ***Top:*** *SR-Site.* ***Bottom:*** *PSAR.*

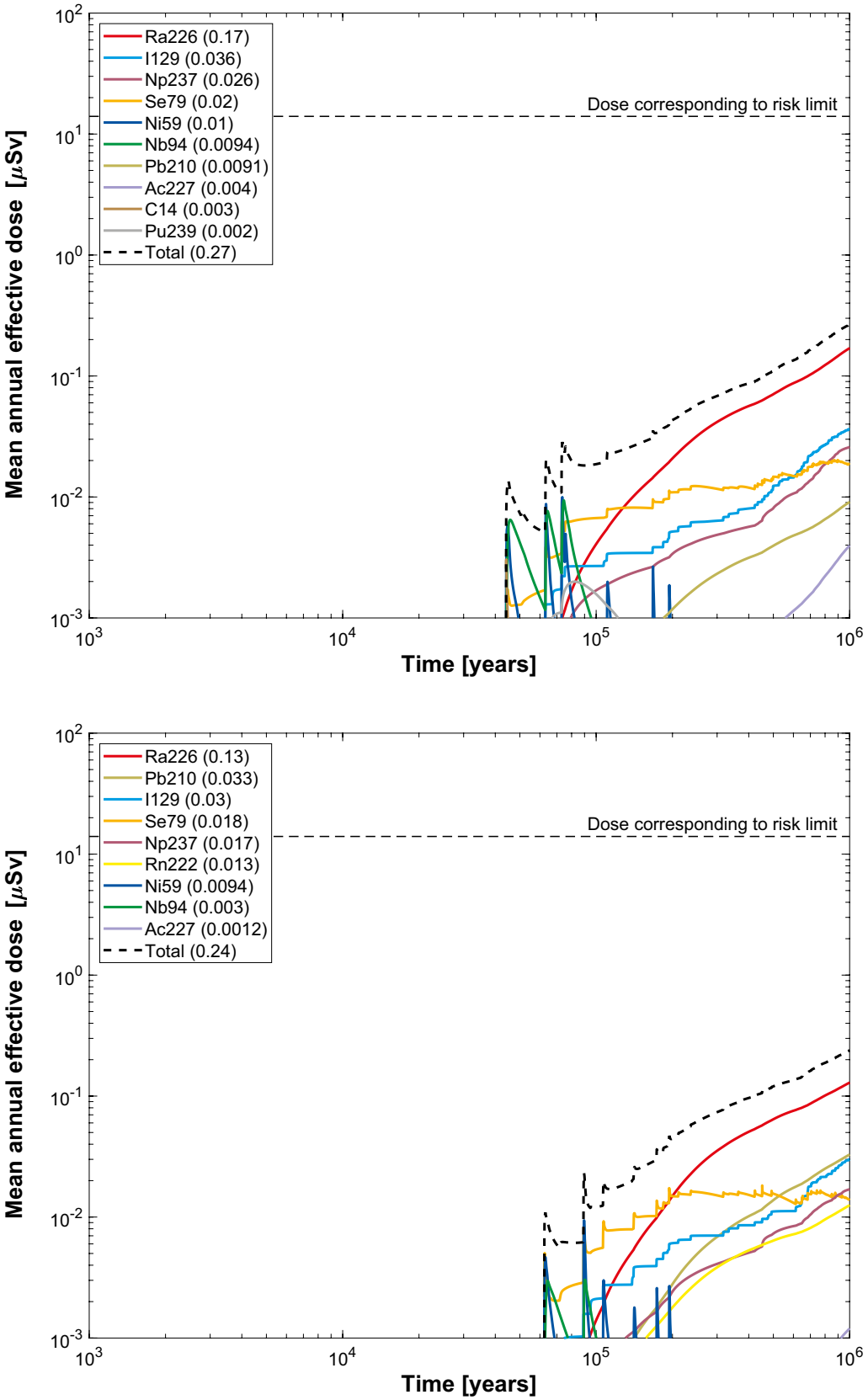

Figure M-13. *Far-field mean annual effective dose for a probabilistic calculation of the central corrosion case, with initial advection in the erosion/corrosion model. The legend is sorted by peak (in the one-million year period) of the mean annual effective dose. The values in brackets are peak dose in units of μSv.* ***Top:*** *SR-Site.* ***Bottom:*** *PSAR.*

M.6 Corrosion, Uncorrelated hydrogeological model – Base case transport assuptions

M.6.1 Deterministic calculations

Hydrogeological case:	Uncorrelated, five realisations
Erosion/corrosion model:	SR-Site model, PSAR model
Failure time:	97 815 years (SR-Site), 107 331 years (PSAR)
Number of failed canisters:	1
Solubility limits:	No
Thorium sorption in near field:	Yes (modelled as low solubility limit)
Number of realisations:	1
Number of nuclides:	37 (SR-Site), 38 (PSAR)

A deterministic calculation of the uncorrelated case is performed for a canister taken from the realisation with the earliest failure time of the analysed realisations with corresponding geosphere transport data, i.e. data used to calculate the corrosion time are from the same hydrogeological calculation as the geosphere transport data (see Table 4-2 for the SR-Site and Table L-22 for the PSAR). This case is further described in Section 4.6.1. The contributions from the instantly released fraction, IRF, are treated as described in Section 4.1.3 and 22.2.1.

Figure M-14 and Figure M-15 show the deterministic near-field and far-field dose equivalent releases, respectively. Comparison between the curves from the recalculated SR-Site calculations and the original calculations in SR-Site, Figure 4-32 and 4-33, shows that they are almost identical.

Comparison between SR-Site and the PSAR shows visible differences for the far field release, but the total dose is are still dominated by the IRF-pulse (I-129 and Se-79, see Table M-4) and in the longer term by I-129 and Se-79. The low releases of for example Ra-226 from the far field is an effect of the high F values for the analysed realisation in both SR-Site and the PSAR. The F value is lower in the calculation for the PSAR (1 020 000 yr/m) than for SR-Site (5 757 000 yr/m) resulting in less retention in the geosphere and thereby a higher release from the far field. This is markedly seen for Se-79, which does not decay to the same degree as in SR-Site.

In the SR-Site assessment the realisation leading to the shortest failure time was erroneously included, despite the fact that it should have been filtered out since the hydrogeological calculations did not yield a meaningful result for the deposition position in question. Corrected SR-Site input data are judged to give very similar results to the PSAR.

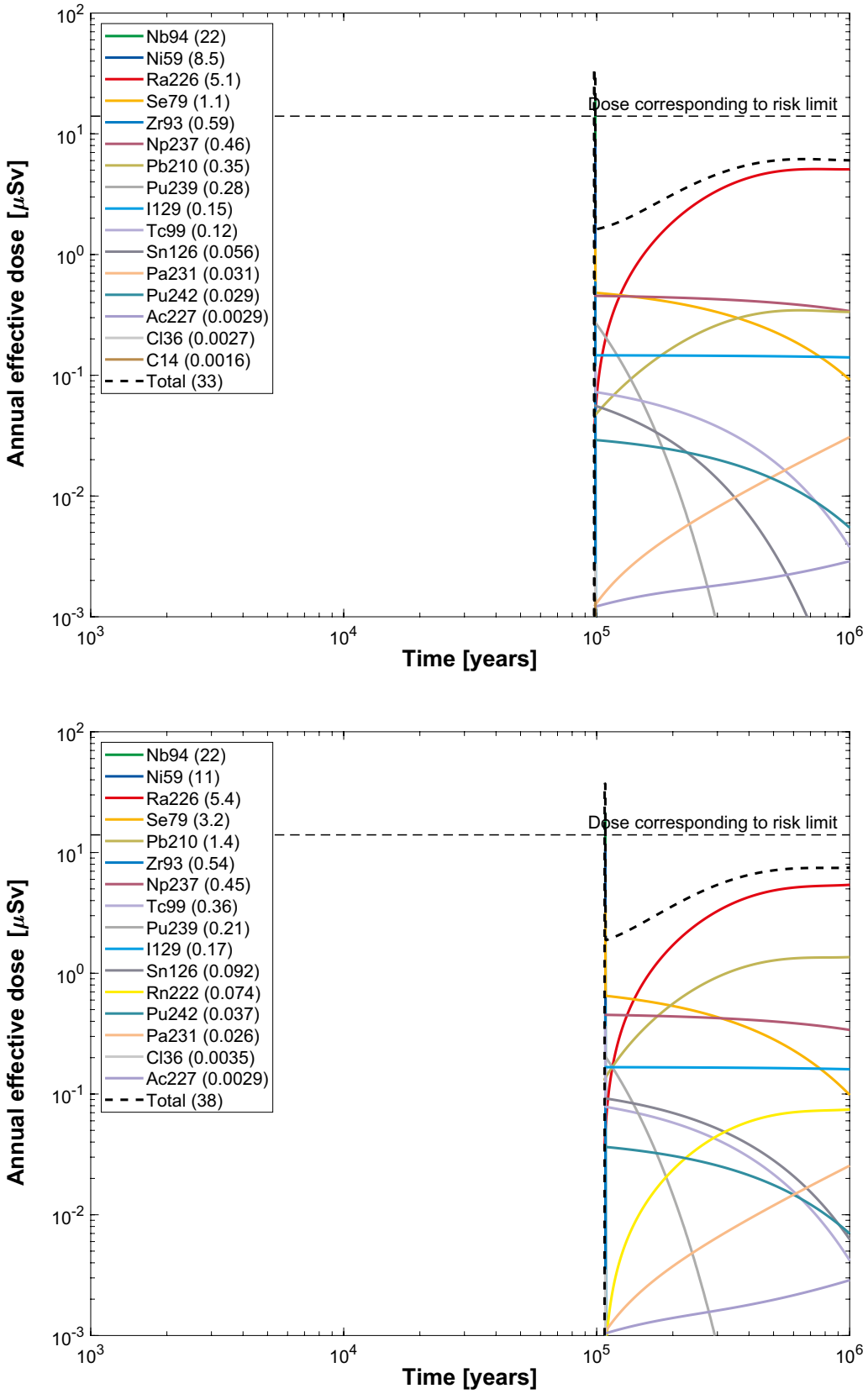

Figure M-14. *Near-field dose equivalent release for a deterministic calculation of the corrosion scenario, with hydrogeological data from the uncorrelated model. The legend is sorted by peak (in the one-million year period) of the annual effective dose. The values in brackets are peak dose in units of μSv.* ***Top:*** *SR-Site.* ***Bottom:*** *PSAR.*

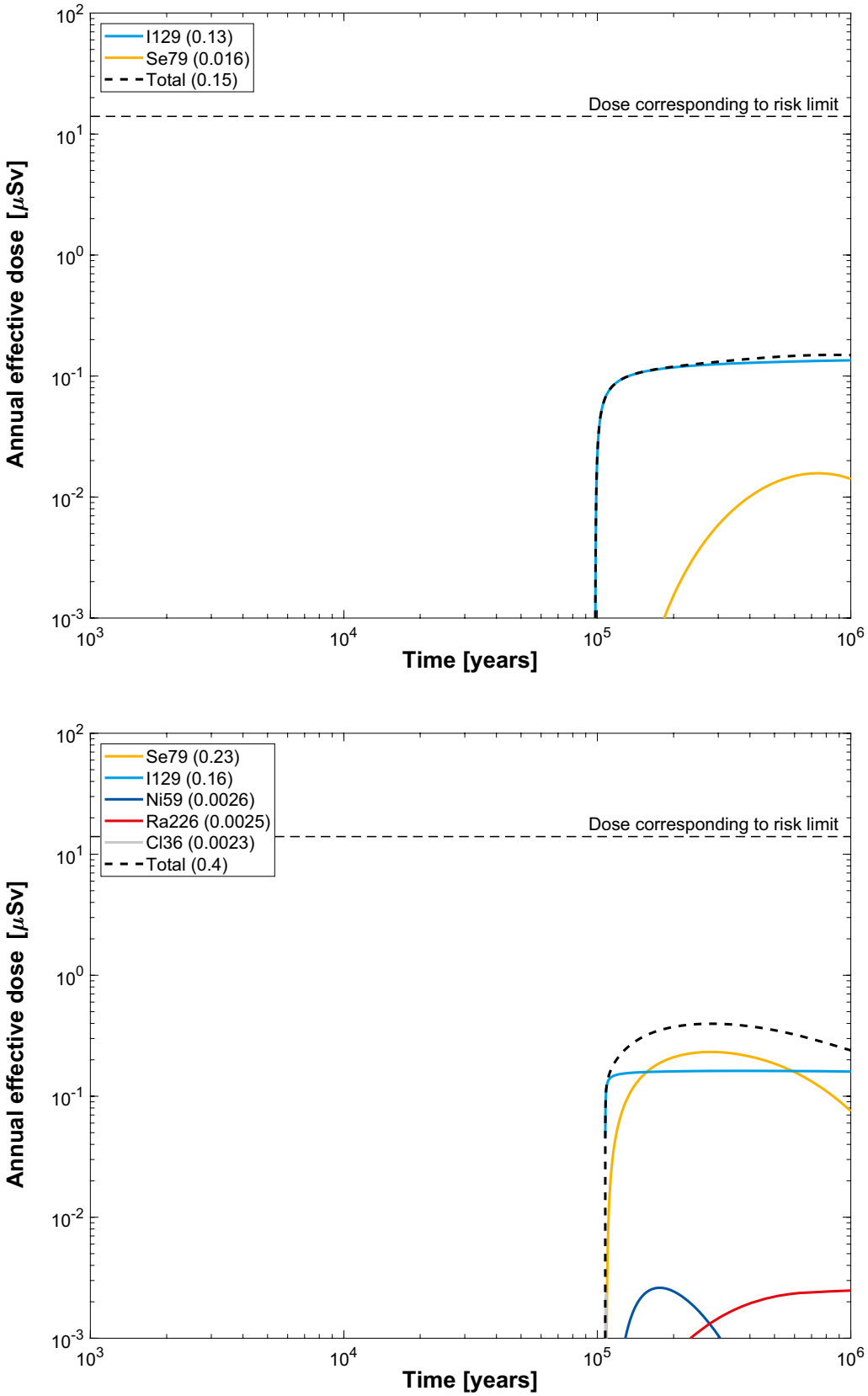

Figure M-15. *Far-field annual effective dose for a deterministic calculation of the corrosion scenario, with hydrogeological data from the uncorrelated model. The legend is sorted by peak (in the one-million year period) of the annual effective dose. The values in brackets are peak dose in units of μSv.* ***Top:*** *SR-Site.* ***Bottom:*** *PSAR.*

M.6.2 Probabilistic calculations

Hydrogeological case:	Uncorrelated, five realisations
Erosion/corrosion model:	SR-Site model, PSAR model
Failure time:	154 times (SR-Site), 143 times (PSAR) according to the erosion/corrosion calculations
Mean number of failed canisters:	0.65 (SR-Site), 0.60 (PSAR)
Solubility limits:	No
Thorium sorption in near field:	Yes (modelled as low solubility limit)
Number of realisations:	50 per canister failure time
Number of nuclides:	37 (SR-Site), 38 (PSAR)

A probabilistic calculation is performed with geosphere transport data from the five realisations of the uncorrelated model (see Table 3-8) and failure times from the erosion/corrosion calculations (see Table 3-8 for SR-Site and Section L.17 for the PSAR). This case is further described in Section 4.6.1. The contributions from the instantly released fraction, IRF, are treated as described in Section 4.1.3.

The results for the IRF presented in Section 4.4.2 are judged to be sufficient to conclude that their contribution is negligible also in this case.

Figure M-16 and Figure M-17 show the near-field and far-field dose equivalent releases, respectively. Comparison between the curves from the recalculated SR-Site calculations and the original calculations in SR-Site, Figure 4-34 and 4-35, shows some minor differences for a few radionuclides with negligible contribution, but the total dose from both the far field and near field are very similar.

Comparison between SR-Site and the PSAR shows the total dose caused by releases from the far field is very similar, eventough the details as to when and how high the peaks are, especially for the near field, differ due to the changes in the erosion/corrosion model. Including Rn-222 separately in the calculations and adding the LDF-value for Po-210 to Pb-210 results in visible changes for Rn-222 and Pb-210, and somewhat higher maxmimum dose.

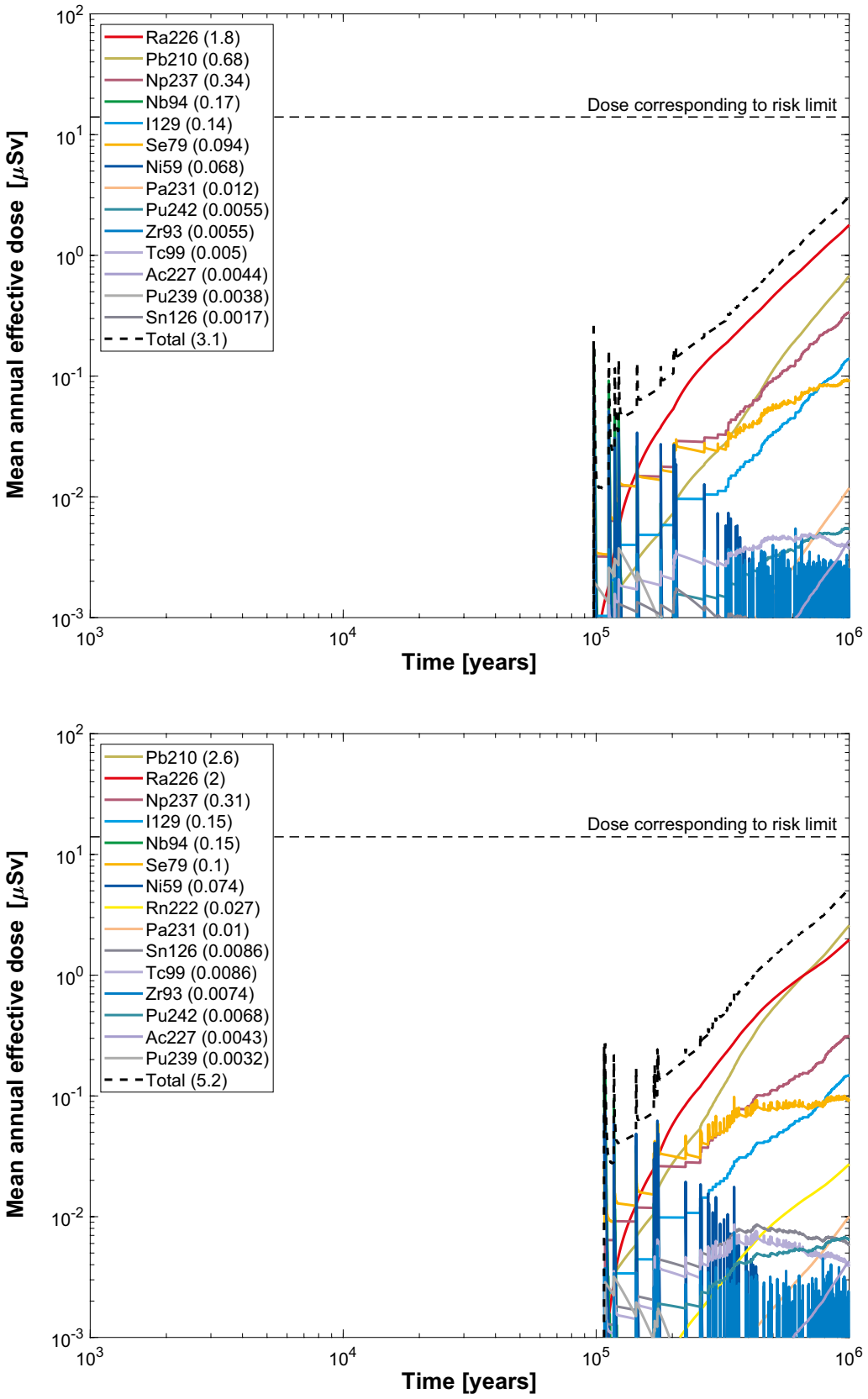

Figure M-16. *Near-field dose equivalent release for the probabilistic calculation of the corrosion scenario, with hydrogeological data from the uncorrelated model. The legend is sorted by peak (in the one-million year period) of the mean annual effective dose. The values in brackets are peak dose in units of μSv.* ***Top:*** *SR-Site.* ***Bottom:*** *PSAR.*

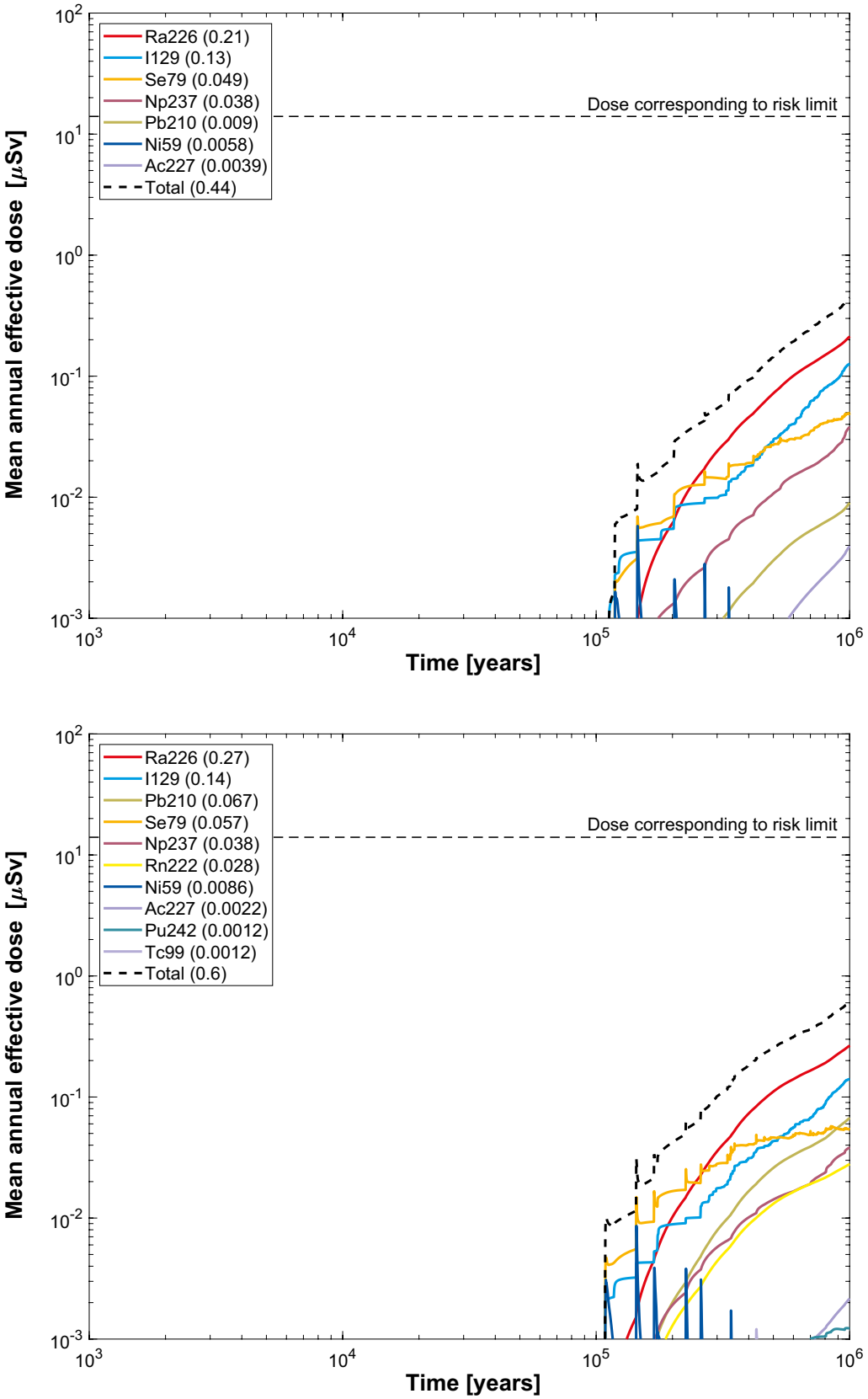

Figure M-17. *Far-field mean annual effective dose for the probabilistic calculation of the corrosion scenario, with hydrogeological data from the uncorrelated model. The legend is sorted by peak (in the one-million year period) of the mean annual effective dose. The values in brackets are peak dose in units of μSv.* ***Top:*** *SR-Site.* ***Bottom:*** *PSAR.*

M.7 Corrosion, Uncorrelated hydrogeological model – Initial advection

M.7.1 Deterministic calculations

Hydrogeological case:	Uncorrelated, five realisations
Erosion/corrosion model:	Initial advection
Failure time:	47 107 years (SR-Site), 78 377 years (PSAR)
Number of failed canisters:	1
Solubility limits:	No
Thorium sorption in near field:	Yes (modelled as low solubility limit)
Number of realisations:	1
Number of nuclides:	37 (SR-Site), 38 (PSAR)

A deterministic calculation of the uncorrelated case with initial advection is performed for a canister taken from the realisation with the earliest failure time of the analysed realisations with corresponding geosphere transport data (see Table 4-2 for SR-Site and Table L-22 for the PSAR), i.e. data used to calculate the corrosion time are from the same hydrogeological calculation as the geosphere transport data. This case is further described in Section 4.6.2. The contributions from the instantly released fraction, IRF, are treated as described in Section 4.1.3 and 22.2.1.

The dose equivalent releases from the near field and far field are shown in Figure M-18 and Figure M-19, respectively. Note that the peaks in Figure M-18 reach outside the figure (doses larger than 100 μSv) but the real maximum doses are given in brackets in the figure legend. Comparison between the curves from the recalculated SR-Site calculations and the original calculations in SR-Site, Figure 4-36 and 4-37, shows that they are almost identical.

Comparison between SR-Site and the PSAR for the near-field shows a decrease of the release of Nb-94, this decrease is due to the later failure in combination with the relatively short half-life for Nb-94. However, the dose equivalent release from the near field is dominated by Tc-99 (as IRF-pulse, see Table M-4). The differences are visibly large for the far field release. The differences are mainly due to less favourable geosphere transport data for the single realisation used in the deterministic calculation. For example, the F value is higher in SR-Site (5 757 000 yr/m) than in the PSAR (93 310 yr/m). In the SR-Site assessment the realisation leading to the shortest failure time was erroneously included, despite the fact that it should have been filtered out since the hydrogeological calculations did not yield a meaningful result for the deposition position in question. Corrected SR-Site input data are judged to give very similar results as the PSAR. The maximum total dose is dominated by I-129 (as IRF-pulse, see Table M-4).

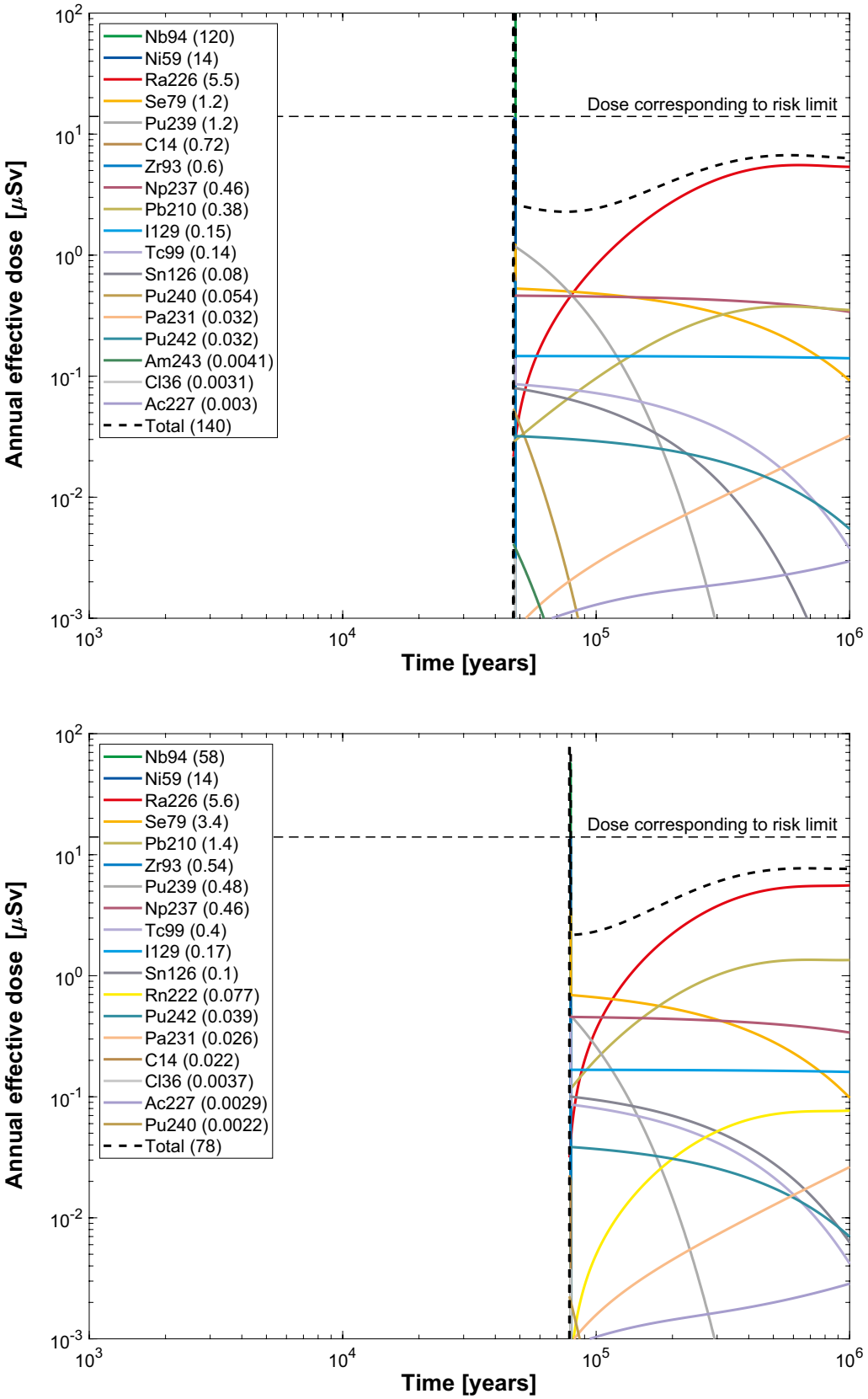

Figure M-18. *Near-field dose equivalent release for a deterministic calculation of the corrosion scenario, with hydrogeological data from the uncorrelated model and initial advection in the erosion/corrosion model. The legend is sorted by peak (in the one-million year period) of the annual effective dose. The values in brackets are peak dose in units of μSv. Note that the dose equivalent release for Nb-94 reach outside the figure (doses larger than 100 μSv) but the real maximum doses are given in brackets in the figure legend.* ***Top:*** *SR-Site.* ***Bottom:*** *PSAR.*

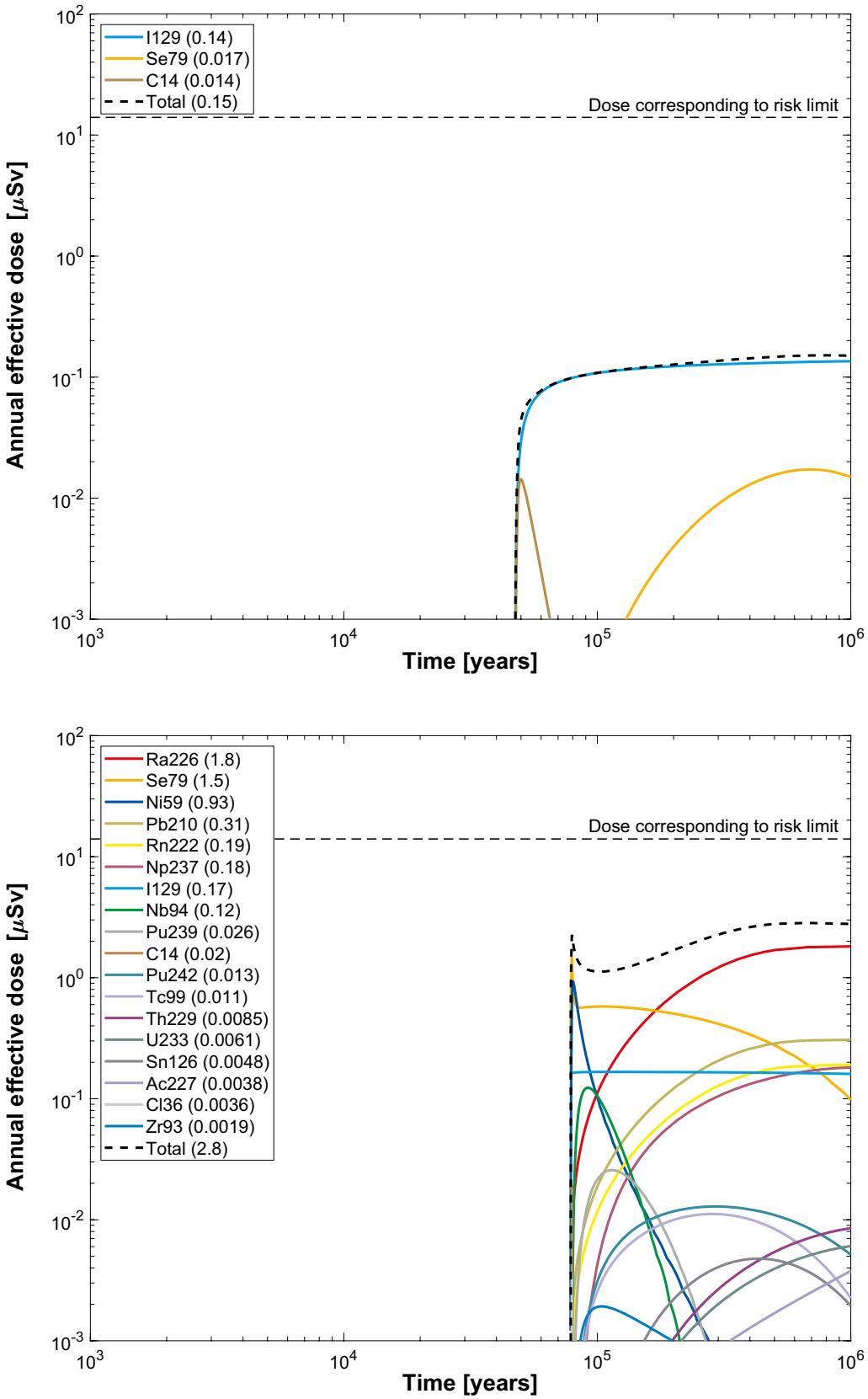

Figure M-19. *Far-field annual effective dose for a deterministic calculation of the corrosion scenario, with hydrogeological data from the uncorrelated model and initial advection in the erosion/corrosion model. The legend is sorted by peak (in the one-million year period) of the annual effective dose. The values in brackets are peak dose in units of μSv.* ***Top:*** *SR-Site.* ***Bottom:*** *PSAR.*

M.7.2 Probabilistic calculations

Hydrogeological case:	Uncorrelated, five realisations
Erosion/corrosion model:	Initial advection
Failure time:	289 times (SR-Site), 211 times (PSAR) according to the erosion/corrosion calculations
Mean number of failed canisters:	1.22 (SR-Site), 0.89 (PSAR)
Solubility limits:	No
Thorium sorption in near field:	Yes (modelled as low solubility limit)
Number of realisations:	50 per canister failure time
Number of nuclides:	37 (SR-Site), 38 (PSAR)

A probabilistic calculation of the uncorrelated case with initial advection is performed with failure times (see Table 3-8 for the SR-Site and Section L.17 for the PSAR) and geosphere transport data from the five realisations of the uncorrelated model (see Table 3-8). This case is further described in Section 4.6.2. The contributions from the instantly released fraction, IRF, are treated as described in Section 4.1.3.

The results for the IRF presented in Section 4.4.2 are judged to be sufficient to conclude that their contribution is negligible also in this case.

The dose equivalent releases from the near field and far field are shown in Figure M-20 and Figure M-21, respectively. Comparison between the curves from the recalculated SR-Site calculations and the original calculations in SR-Site, Figure 4-38 and 4-39, shows some minor differences for the near field, the peaks are somewhat higher especially for some radionuclides with negligible contribution, but the curves for the far field are very similar.

Comparison between SR-Site and the PSAR shows differences in the details as to when and how high the peaks are, especially for the near field, due to the changes in the erosion/corrosion model. Including Rn-222 separately in the calculations and adding the LDF-value for Po-210 to Pb-210 results in visible changes for Rn-222 and Pb-210, especially in that Pb-210 dominates the dose from the near field. However, the influence on the far field release is less and the overall result for the far field is very similar.

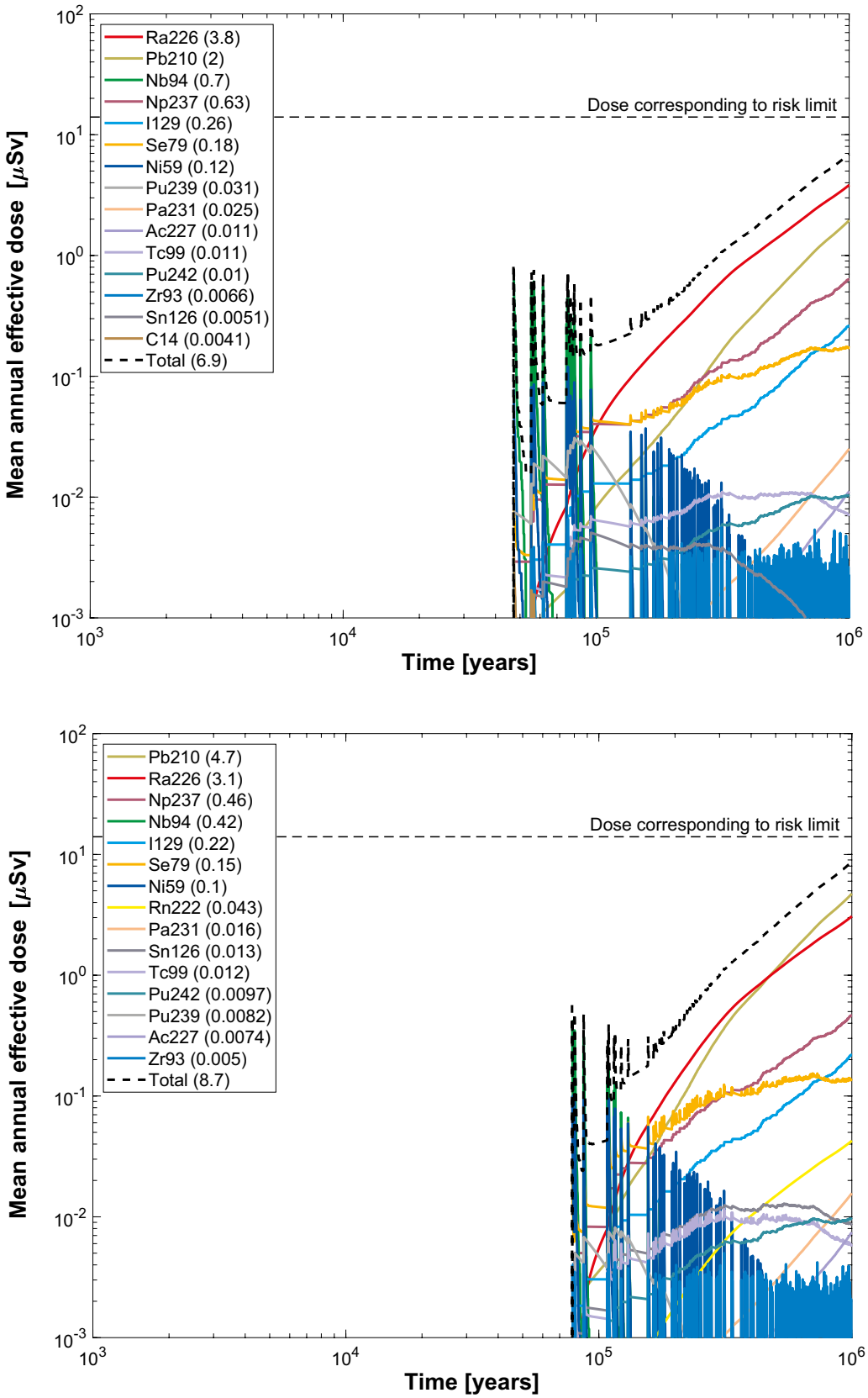

Figure M-20. *Near-field dose equivalent release for the probabilistic calculation of the corrosion scenario, with hydrogeological data from the uncorrelated model and initial advection in the erosion/corrosion model. The legend is sorted by peak (in the one-million year period) of the mean annual effective dose. The values in brackets are peak dose in units of μSv.* ***Top:*** *SR-Site.* ***Bottom:*** *PSAR.*

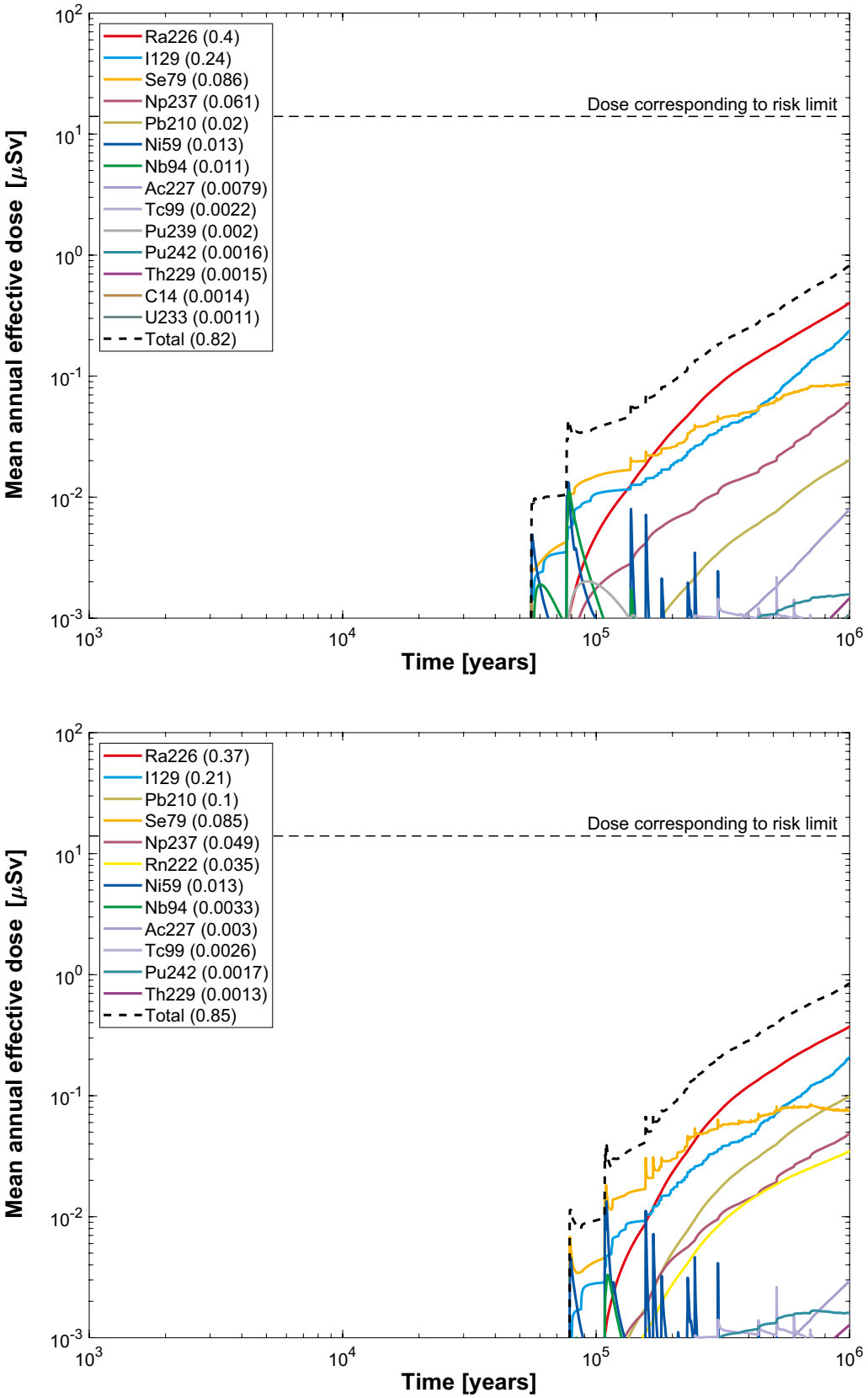

Figure M-21. *Far-field mean annual effective dose for the probabilistic calculation of the corrosion scenario, with hydrogeological data from the uncorrelated model and initial advection in the erosion/corrosion model. The legend is sorted by peak (in the one-million year period) of the mean annual effective dose. The values in brackets are peak dose in units of μSv.* ***Top:*** *SR-Site.* ***Bottom:*** *PSAR.*

M.8 Corrosion, Fully correlated hydrogeological model – Base case transport assumptions

M.8.1 Deterministic calculations

Hydrogeological case:	Fully correlated, five realisations
Erosion/corrosion model:	SR-Site model, PSAR model
Failure time:	99 700 years (SR-Site), 91 846 (PSAR)
Number of failed canisters:	1
Solubility limits:	No
Thorium sorption in near field:	Yes (modelled as low solubility limit)
Number of realisations:	1
Number of nuclides:	37 (SR-Site), 38 (PSAR)

A deterministic calculation of the fully correlated case is performed for a canister taken from the realisation with the earliest failure time of the analysed realisations with corresponding geosphere transport data, i.e. data used to calculate the corrosion time are from the same hydrogeological calculation as the geosphere transport data (see Table 4-2 for SR-Site and Table L-22 for the PSAR). The earliest failure time is obtained for the same realisation in SR-Site and the PSAR, hence the geosphere transport data are the same. This case is further described in Section 4.7.1. The contributions from the instantly released fraction, IRF, are treated as described in Section 4.1.3 and 22.2.1.

Figure M-22 and Figure M-23 show the deterministic near-field and far-field dose equivalent releases, respectively. Comparison between the curves from the recalculated SR-Site calculations and the original calculations in SR-Site, Figure 4-40 and 4-41, shows that they are almost identical.

Comparison between the SR-Site and the PSAR shows small differences, but the total dose is still dominated by the IRF-pulse from I-129 (see Table M-4) and in the long term by Ra-226. Including Rn-222 separately in the calculations and adding the LDF-value for Po-210 to Pb-210 results in visible changes for Rn-222 and Pb-210, especially in that Pb-210 contributes more to the total dose in the longer term even though the dose is still totally dominated by Ra-226.

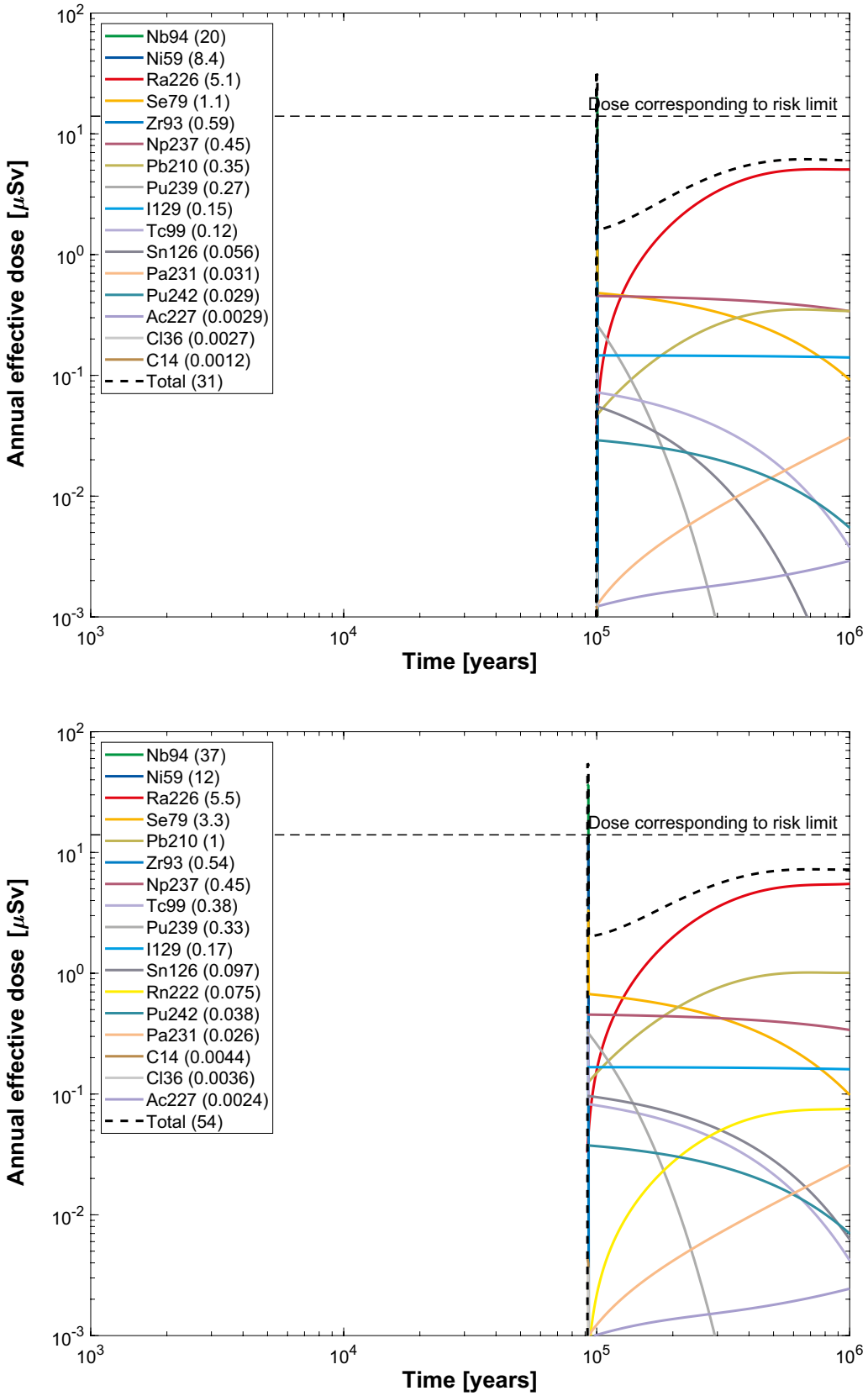

Figure M-22. *Near-field dose equivalent release for a deterministic calculation of the corrosion scenario, with hydrogeological data from the fully correlated model. The legend is sorted by peak (in the one-million year period) of the annual effective dose. The values in brackets are peak dose in units of μSv.* ***Top:*** *SR-Site.* ***Bottom:*** *PSAR.*

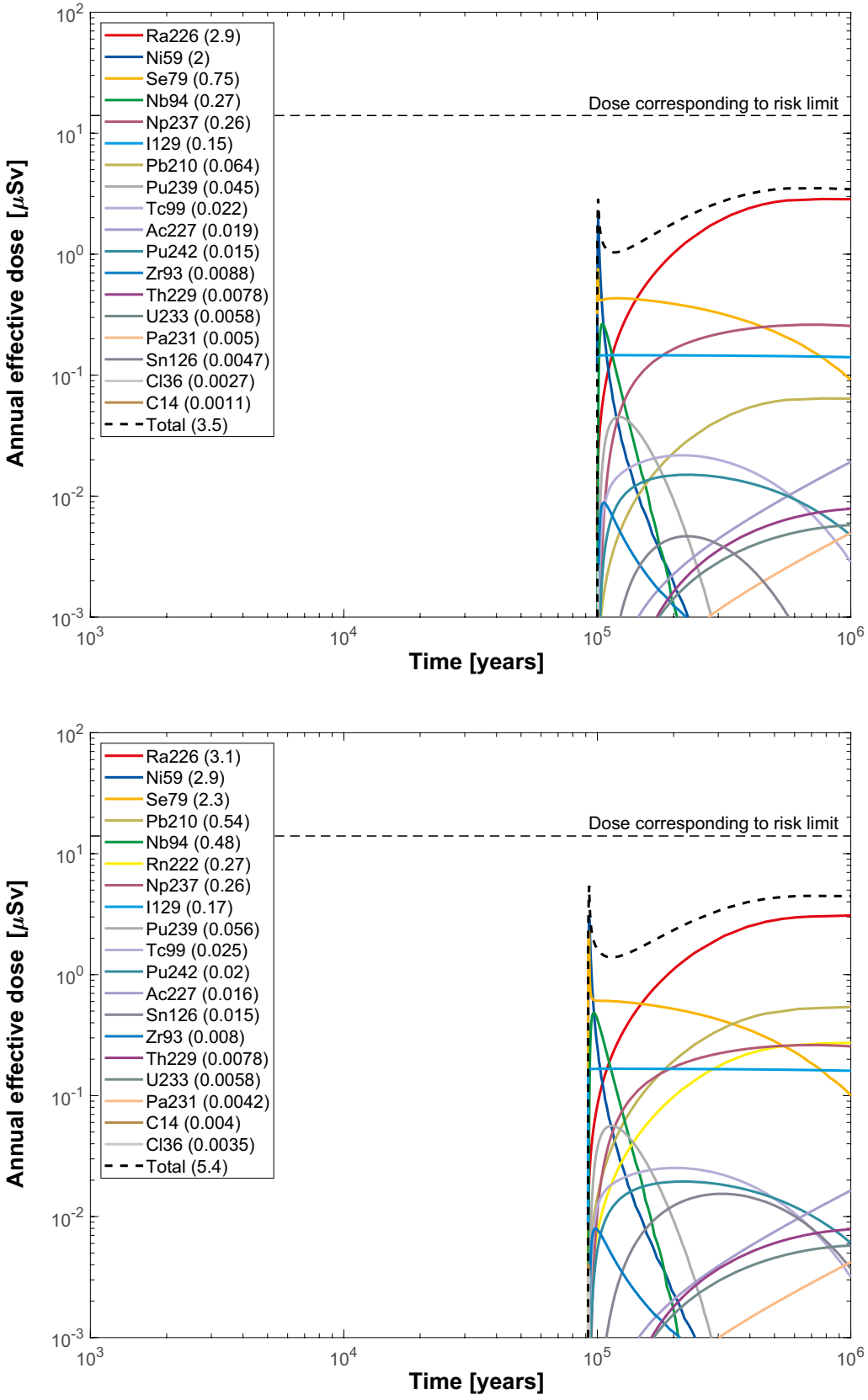

Figure M-23. *Far-field annual effective dose for a deterministic calculation of the corrosion scenario, with hydrogeological data from the fully correlated model. The legend is sorted by peak (in the one-million year period) of the annual effective dose. The values in brackets are peak dose in units of μSv.* ***Top:*** *SR-Site.* ***Bottom:*** *PSAR.*

M.8.2 Probabilistic calculations

Hydrogeological case:	Fully correlated, five realisations
Erosion/corrosion model:	SR-Site model
Failure time:	132 times (SR-Site), 123 times (PSAR) according to the erosion/corrosion calculations
Mean number of failed canisters:	0.57 (SR-Site), 0.53 (PSAR)
Solubility limits:	No
Thorium sorption in near field:	Yes (modelled as low solubility limit)
Number of realisations:	50 per canister failure time
Number of nuclides:	37 (SR-Site), 38 (PSAR)

A probabilistic calculation of the fully correlated case was performed with failure times and geosphere transport data from the five realisations of the uncorrelated model ((see Table 3-8) and the erosion/corrosion calculations (see Table 3-8 for SR-Site and Section L.17 for the PSAR). This case is further described in Section 4.7.1. The contributions from the instantly released fraction, IRF, are treated as described in Section 4.1.3.

The results for the IRF presented in Section 4.4.2 are judged to be sufficient to conclude that their contribution is negligible also in this case.

Figure M-24 and Figure M-25 show the near-field and far-field dose equivalent releases, respectively. Comparison between the curves from the recalculated SR-Site calculations and the original calculations in SR-Site, Figure 4-42 and 4-43, shows some minor differences, for some radionuclides with negligible contribution, but the total dose from both the far field and near field are very similar.

Comparison between SR-Site and the PSAR shows the total dose caused by releases from the far field is very similar, eventough the details as to when and how high the peaks are, especially for the near field, differ due to the changes in the erosion/corrosion model.

Including Rn-222 separately in the calculations and adding the LDF-value for Po-210 to Pb-210 results in visible changes for Rn-222 and Pb-210. In addition, a few single radionuclides contribute to a somewhat higher maxmimum dose.

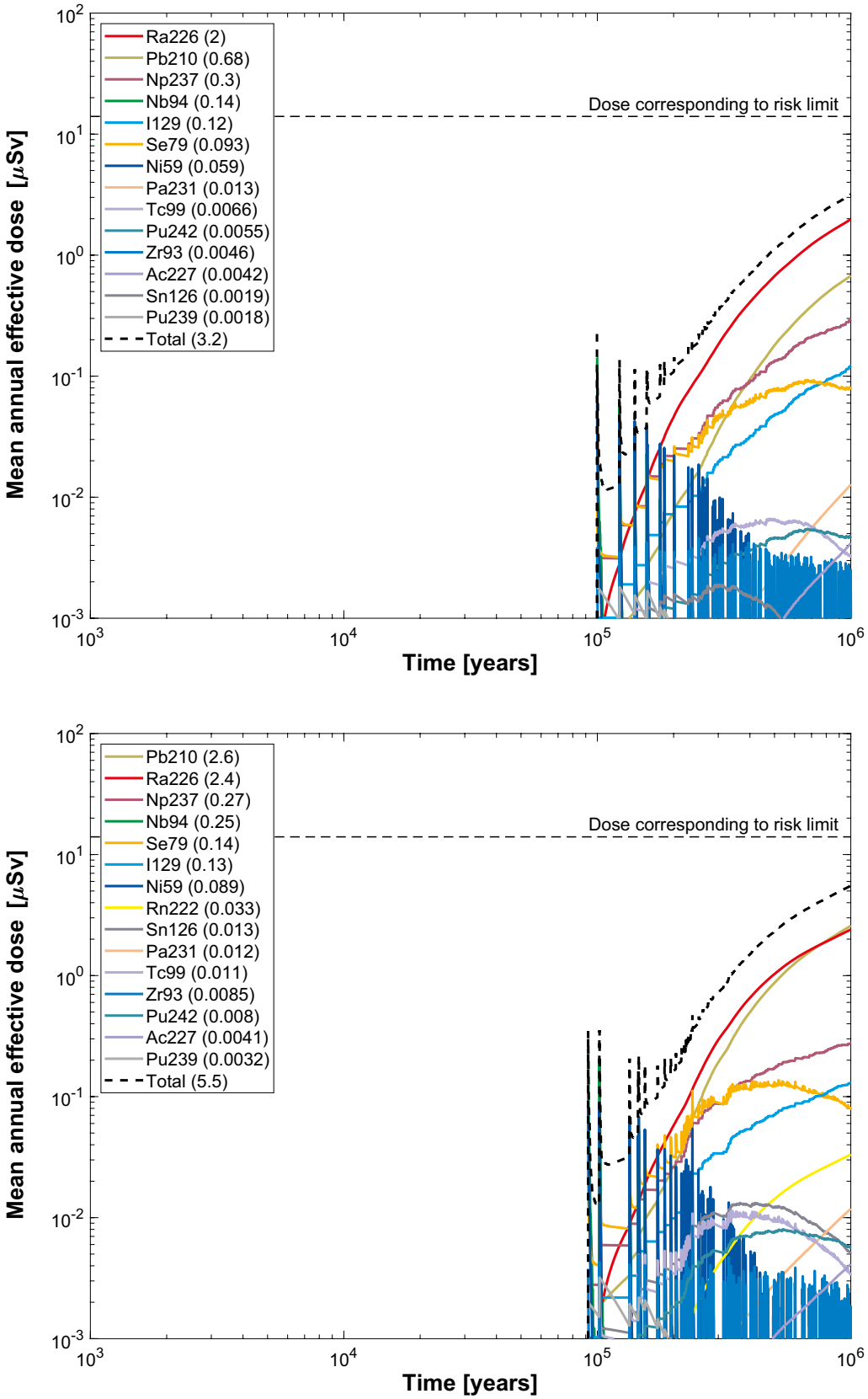

Figure M-24. *Near-field dose equivalent release for the probabilistic calculation of the corrosion scenario, with hydrogeological data from the fully correlated model. The legend is sorted by peak (in the one-million year period) of the mean annual effective dose. The values in brackets are peak dose in units of μSv.*
Top: *SR-Site.* ***Bottom:*** *PSAR.*

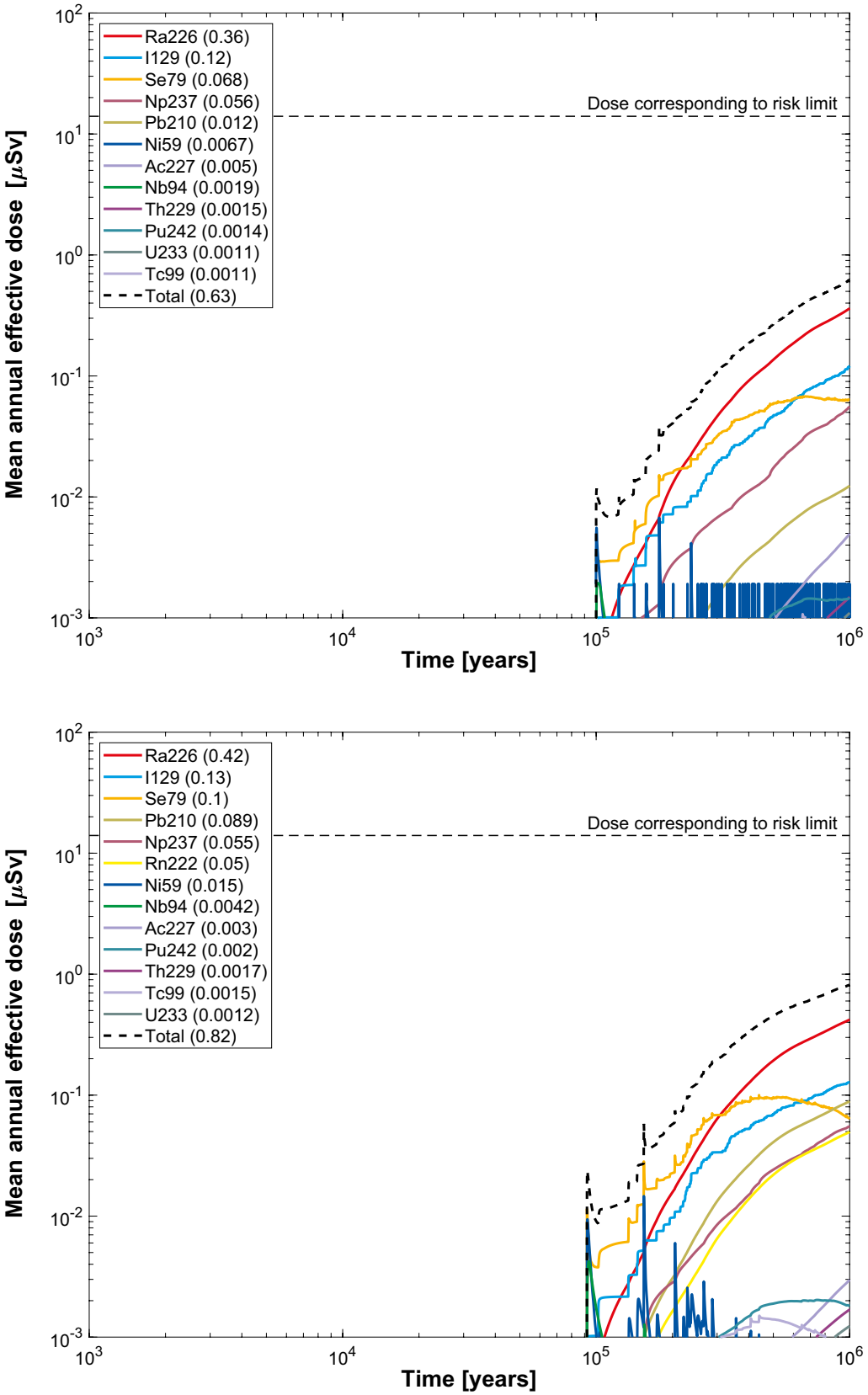

Figure M-25. *Far-field mean annual effective dose for the probabilistic calculation of the corrosion scenario, with hydrogeological data from the fully correlated model. The legend is sorted by peak (in the one-million year period) of the mean annual effective dose. The values in brackets are peak dose in units of μSv.*
Top: *SR-Site.* ***Bottom:*** *PSAR.*

M.9 Corrosion, Fully correlated hydrogeological model – Initial advection

M.9.1 Deterministic calculations

Hydrogeological case:	Fully correlated, five realisations
Erosion/corrosion model:	Initial advection
Failure time:	47 657 years (SR-Site), 67 397 (PSAR)
Number of failed canisters:	1
Solubility limits:	No
Thorium sorption in near field:	Yes (modelled as low solubility limit)
Number of realisations:	1
Number of nuclides:	37 (SR-Site), 38 (PSAR)

A deterministic calculation of the fully correlated case with initial advection is performed for a canister taken from the realisation with the earliest failure time of the analysed realisations with corresponding geosphere transport data, i.e. data used to calculate the corrosion time are from the same hydrogeological calculation as the geosphere transport data The earliest failure time is obtained for the same realisation in SR-Site and the PSAR, hence the geosphere transport data are the same. The later failure time in the PSAR is due to changes in the erosion/corrosion model since SR-Site. This case is further described in Section 4.7.2. The contributions from the instantly released fraction, IRF, are treated as described in Section 4.1.3 and 22.2.1.

Figure M-26 and Figure M-27 show the deterministic near-field and far-field dose equivalent releases, respectively. Note that the peaks in Figure M-26 reach outside the figure (doses larger than 100 μSv) but the real maximum doses are given in brackets in the figure legend. Comparison between the curves from the recalculated SR-Site calculations and the original calculations in SR-Site, Figure 4-44 and 4-45, shows that they are almost identical.

Comparison between SR-Site and the PSAR shows small differences, but the total dose is still dominated by the IRF-pulse from I-129 (see Table M-4) and in the longer term by Ra-226. Including Rn-222 separately in the calculations and adding the LDF-value for Po-210 to Pb-210 results in visible changes for Rn-222 and Pb-210, especially in that Pb-210 contributes more to the total dose in the longer term even though the dose is still totally dominated by Ra-226.

Comparison between SR-Site and the PSAR for the near-field shows a decrease of the release of Nb-94, this decrease is due to the later failure in combination with the relatively short half-life for Nb-94. The differences are small for the far field release and the doses caused by releases from the far field are still dominated by the IRF-pulse from I-129 (see Table M-4) and thereafter by Ni-59, Nb-94, Se-79 and in the longer term by Ra-226.

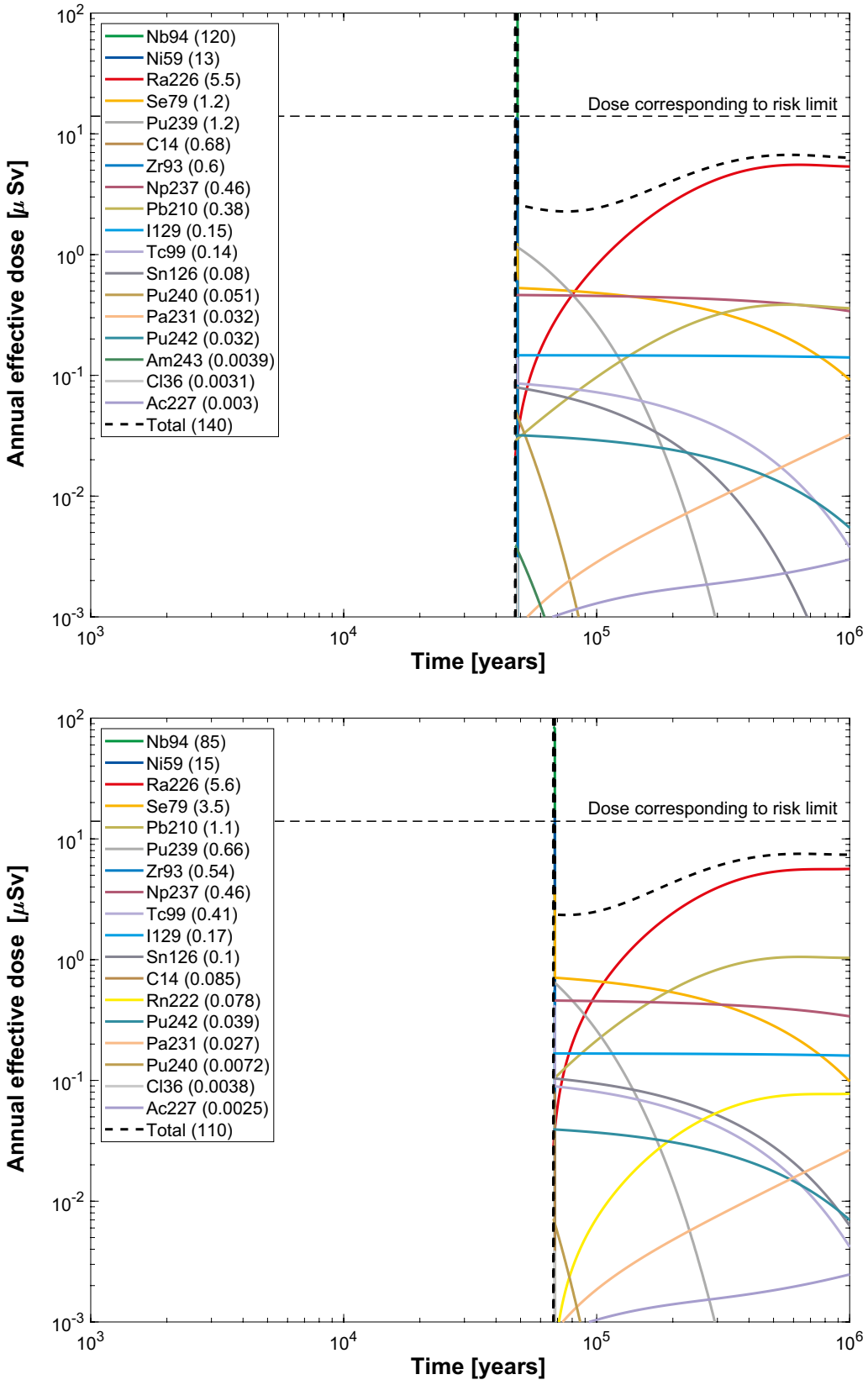

Figure M-26. *Near-field dose equivalent release for a deterministic calculation of the corrosion scenario, with hydrogeological data from the fully correlated model and initial advection in the erosion/corrosion model. The legend is sorted by peak (in the one-million year period) of the annual effective dose. The values in brackets are peak dose in units of μSv. Note that the peaks in reach outside the figure (doses larger than 100 μSv) but the real maximum doses are given in brackets in the figure legend.* ***Top:*** *SR-Site.* ***Bottom:*** *PSAR.*

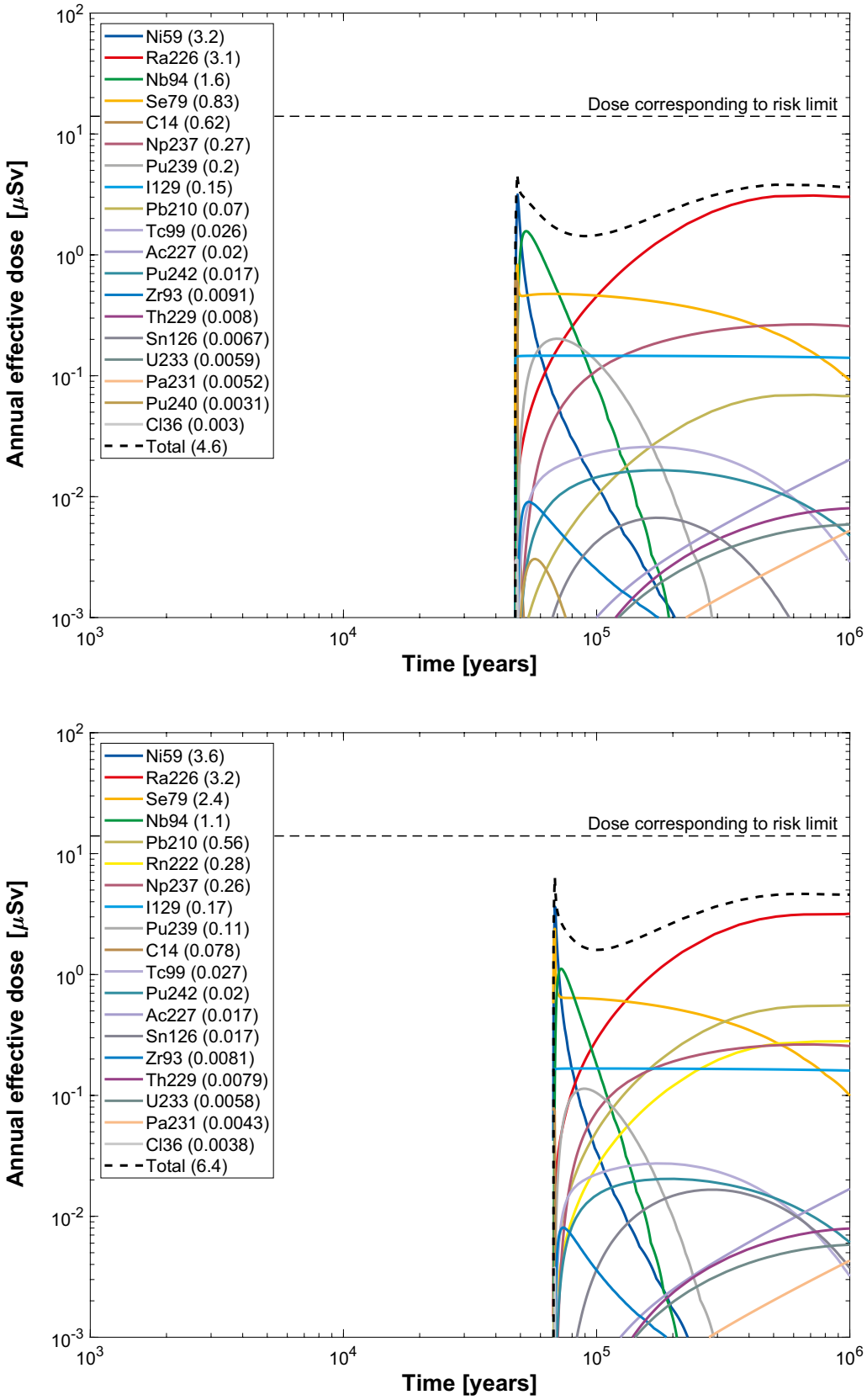

Figure M-27. *Far-field annual effective dose for a deterministic calculation of the corrosion scenario, with hydrogeological data from the fully correlated model and initial advection in the erosion/corrosion model. The legend is sorted by peak (in the one-million year period) of the annual effective dose. The values in brackets are peak dose in units of μSv.* ***Top:*** *SR-Site.* ***Bottom:*** *PSAR.*

M.9.2 Probabilistic calculations

Hydrogeological case:	Fully correlated, five realisations
Erosion/corrosion model:	Initial advection
Failure time:	200 times (SR-Site), 163 (PSAR) according to the erosion/corrosion calculations
Mean number of failed canisters:	0.86 (SR-Site), 0.70 (PSAR)
Solubility limits:	No
Thorium sorption in near field:	Yes (modelled as low solubility limit)
Number of realisations:	50 per canister failure time
Number of nuclides:	37 (SR-Site), 38 (PSAR)

A probabilistic calculation of the fully correlated case with initial advection was performed with failure times and geosphere transport data from the five realisations of the uncorrelated model (see Table 3-8) and the erosion/corrosion calculations (see Table 3-8 for SR-Site and Section L.17 for the PSAR). This case is further described in Section 4.7.2. The contributions from the instantly released fraction, IRF, are treated as described in Section 4.1.3.

The results for the IRF presented in Section 4.4.2 are judged to be sufficient to conclude that their contribution is negligible also in this case.

The dose equivalent releases from the near field and far field are shown in Figure M-28 and Figure M-29, respectively. Comparison between the curves from the recalculated SR-Site calculations and the original calculations in SR-Site, Figure 4-46 and 4-47, shows some minor differences in that the peaks are somewhat higher for some radionuclides with negligible contribution. This is especially noted for for Ni-59 in the far-field and the constant low level of the peaks in the longer term indicate a numerical problem. However, the total dose for the far field is very similar.

Comparison between SR-Site and the PSAR shows differences in the details as to when and how high the peaks are, especially for the near field, due to the changes in the erosion/corrosion model. Including Rn-222 separately in the calculations and adding the LDF-value for Po-210 to Pb-210 results in visible changes for Rn-222 and Pb-210, especially in that Pb-210 dominates the dose from the near field at long times. However, the influence on the far field release is less and the overall result for the far field is very similar.

M.10 Summary of the corrosion scenario

Figure M-30 and Figure M-31 shows the total dose equivalent releases for cases calculated probabilistically for the corrosion scenario for the near field and far field, respectively. The corresponding figures for the original SR-Site calculations are Figure 4-58 and 4-59. In the previous sections it has been concluded that the results from original and recalculated SR-Site cases are almost identical.

Comparison between SR-Site and the PSAR shows differences in the details as to when and how high the peaks are, especially for the near field, due to the changes in the erosion/corrosion model since SR-Site. Generally, the doses from the far field are almost the same but slightly higher in the PSAR. The conclusions from SR-Site, as described in Section 4.11, are therefore still valid. The differences are minor and of no concern for the safety of the repository.

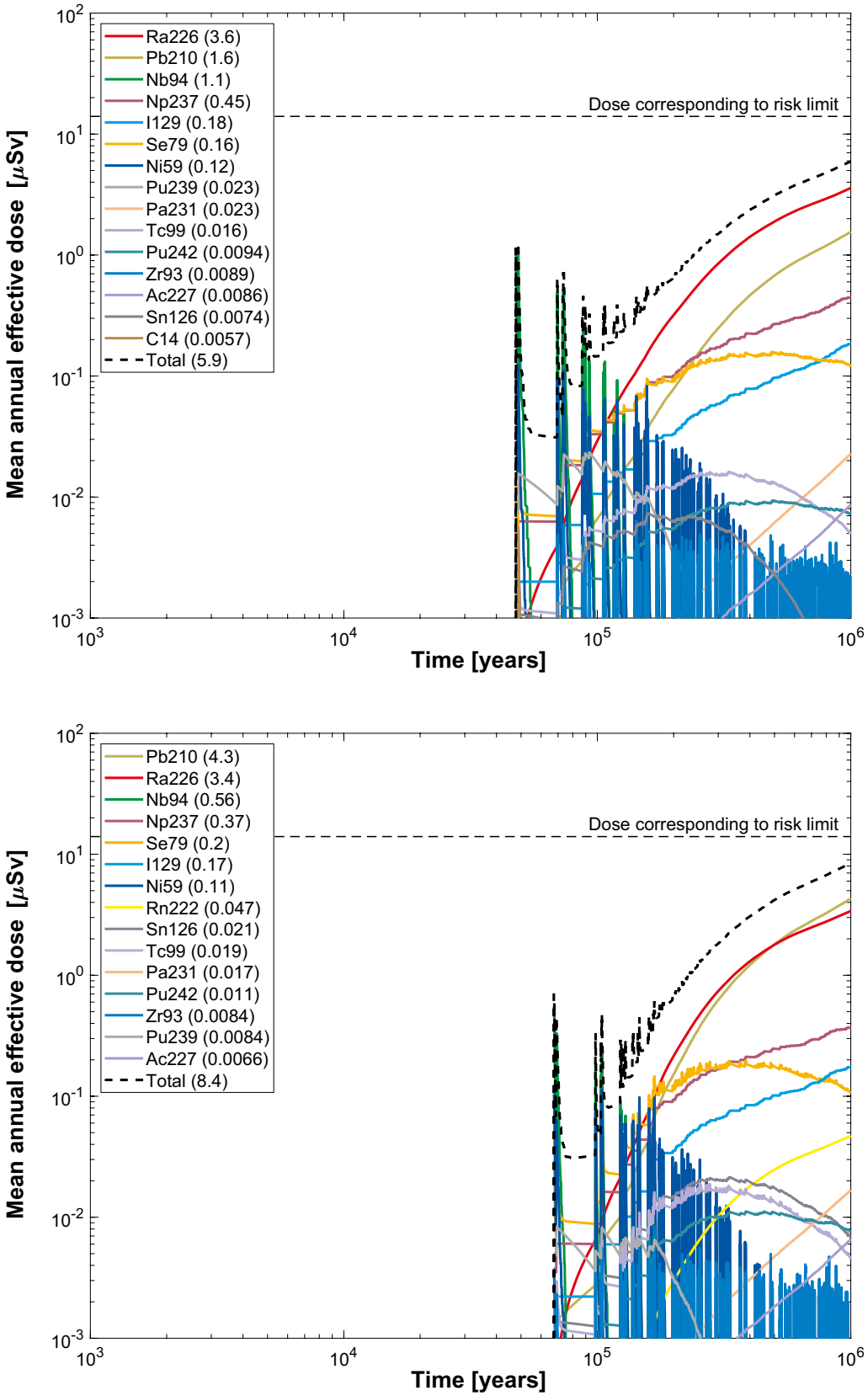

Figure M-28. *Near-field dose equivalent release for the probabilistic calculation of the corrosion scenario, with hydrogeological data from the fully correlated model and initial advection in the erosion/corrosion model. The legend is sorted by peak (in the one-million year period) of the mean annual effective dose. The values in brackets are peak dose in units of μSv.* ***Top:*** *SR-Site.* ***Bottom:*** *PSAR.*

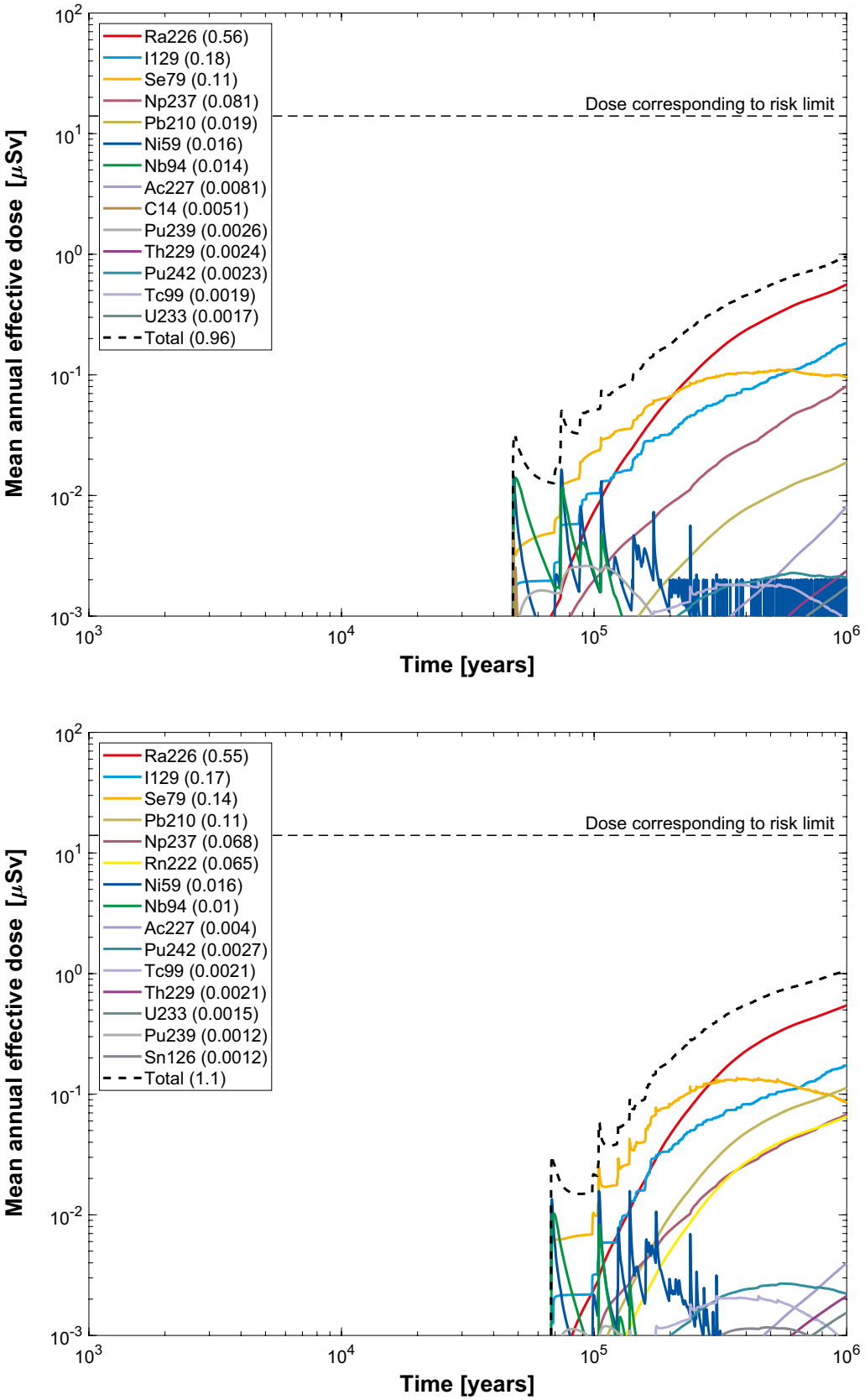

Figure M-29. *Far-field mean annual effective dose for the probabilistic calculation of the corrosion scenario, with hydrogeological data from the fully correlated model and initial advection in the corrosion model. The legend is sorted by peak (in the one-million year period) of the mean annual effective dose. The values in brackets are peak dose in units of μSv.* ***Top:*** *SR-Site.* ***Bottom:*** *PSAR.*

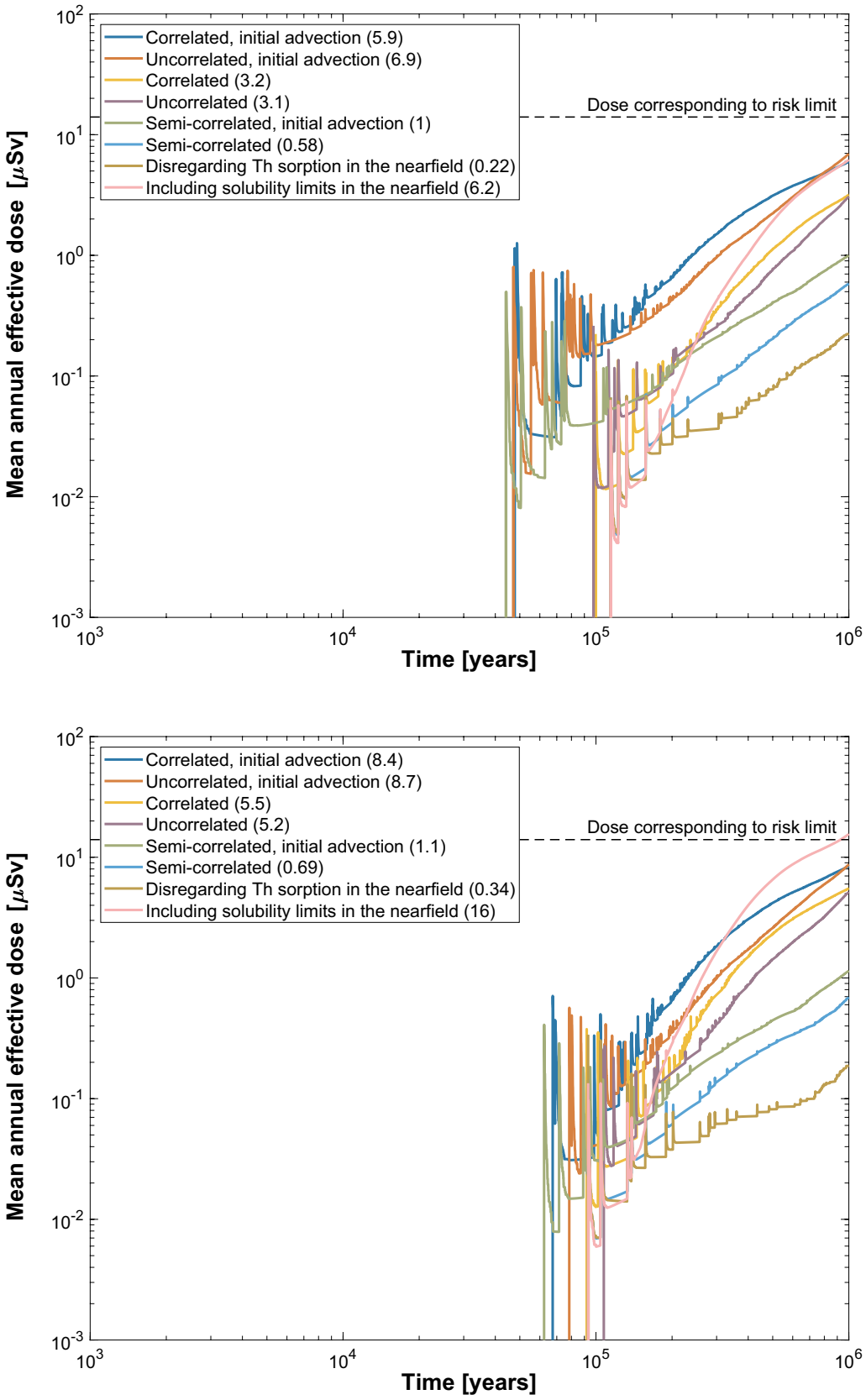

Figure M-30. *Summary of near-field mean annual effective dose equivalent release for all probabilistic calculations performed for the corrosion scenario. The peak doses are given in parentheses in μSv.* ***Top:*** *SR-Site.* ***Bottom:*** *PSAR.*

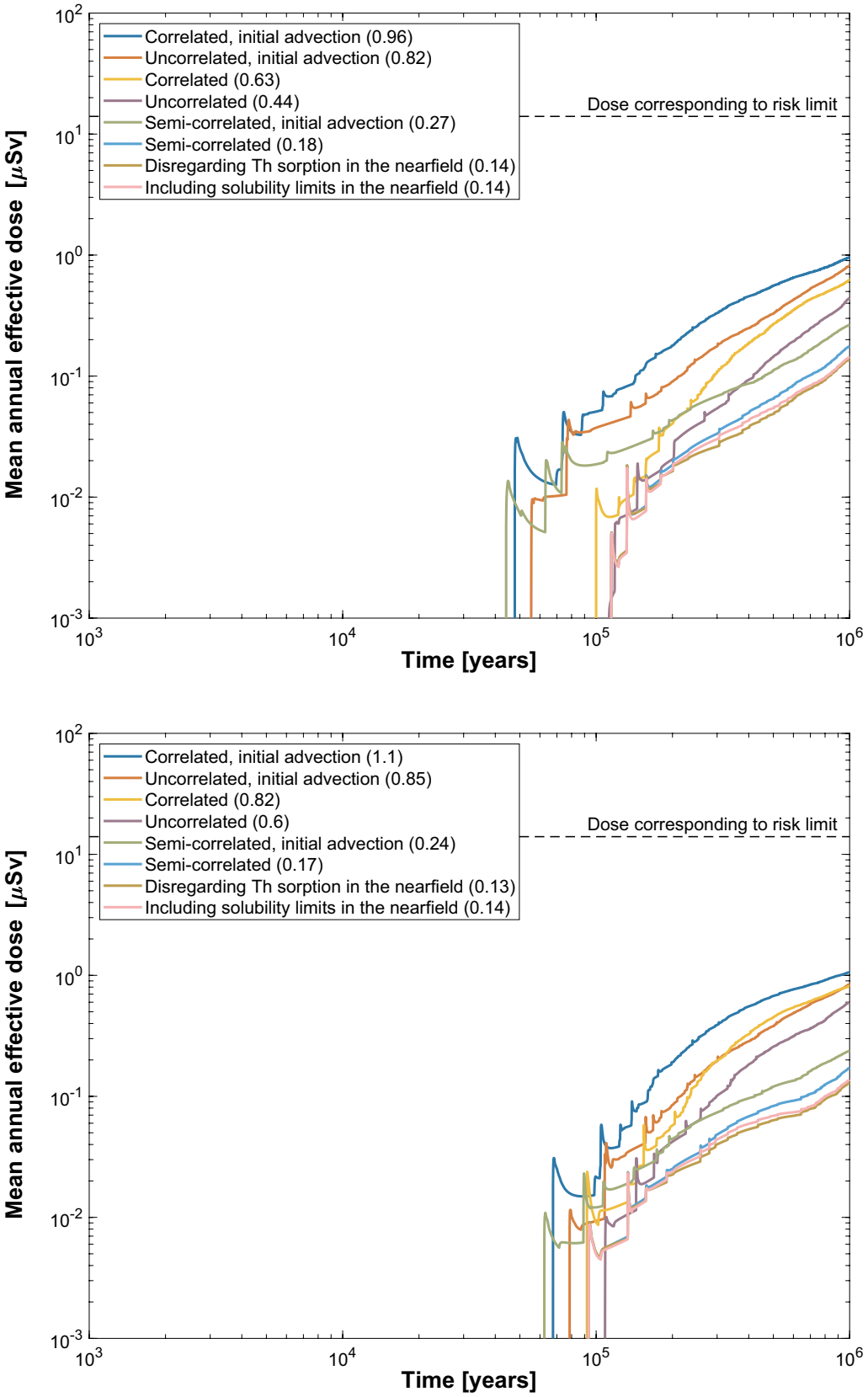

Figure M-31. *Summary of far-field mean annual effective dose equivalent release for all probabilistic calculations performed for the corrosion scenario. The peak doses are given in parentheses in μSv.* ***Top:*** *SR-Site.* ***Bottom:*** *PSAR.*

M.11 Shear load, Postulated failure of one canister at 100 000 years

M.11.1 Deterministic calculations

Failure time:	100 000 years
Number of failed canisters:	1 (postulated)
Solubility limits:	Yes
Number of realisations:	1
Number of nuclides:	45 (SR-Site), 46 (PSAR)

A deterministic calculation of the shear load case is performed for a postulated failure of one canister at 100 000 years. No retention in the geosphere occurs and hence the release calculated for the near field is also valid for the far field. The contributions from the instantly released fraction of nuclides, IRF, are not included in the calculations. The contributions from the instantly released fraction, IRF, are treated as described in Section 4.1.3 and M.2.1.

Figure M-32 shows the deterministic far-field dose equivalent release. Comparison between the curves from the recalculated SR-Site calculations and the original calculations in SR-Site, Figure 5-1, shows that they are almost identical.

Comparison between SR-Site and the PSAR shows some small differences, but the total dose is still initially dominated by I-129 (as IRF-pulse, see Table M-4) and Ni-59 and in the longer term by Ra-226. The increase in the dose from Ra-226 is explained by the erranous solubility limits used in the calculations in SR-Site (SKB 2010d, Section 3.7.3). The shape of the curve for Se-79 with a plateau is due to the fact that the solubility limit is reached, the changed level of the plateau is due to the corrected solubility limits while the longer duration is due to the increased corrosion release fraction, CRF.

M.11.2 Probabilistic calculations

Failure time:	100 000 years
Number of failed canisters:	1 (postulated)
Solubility limits:	Yes
Number of realisations:	1 000 (SR-Site), 6 916 (PSAR)
Number of nuclides:	37 (SR-Site), 38 (PSAR)

A probabilistic calculation of the shear load case is performed for a postulated failure time at 100 000 years. The postulated number of failed canisters is 1. The contributions from the instantly released fraction of nuclides, IRF, are not included in the calculations. Table M-4 show the peak annual doses from the pulse releases from the instantly released fraction, IRF. No retention in the geosphere occurs and hence the release calculated for the near field is also valid for the far field.

Figure M-33 shows the probabilistic far-field dose equivalent release. Comparison between the curves from the recalculated SR-Site calculations and the original calculations in SR-Site, Figure 5-2, shows that they are almost identical.

Comparison between SR-Site and the PSAR shows some small differences, but the total dose is still initially dominated by I-129 (as IRF-pulse 4,5 µSv) and Ni-59 and in the longer term by Ra-226.

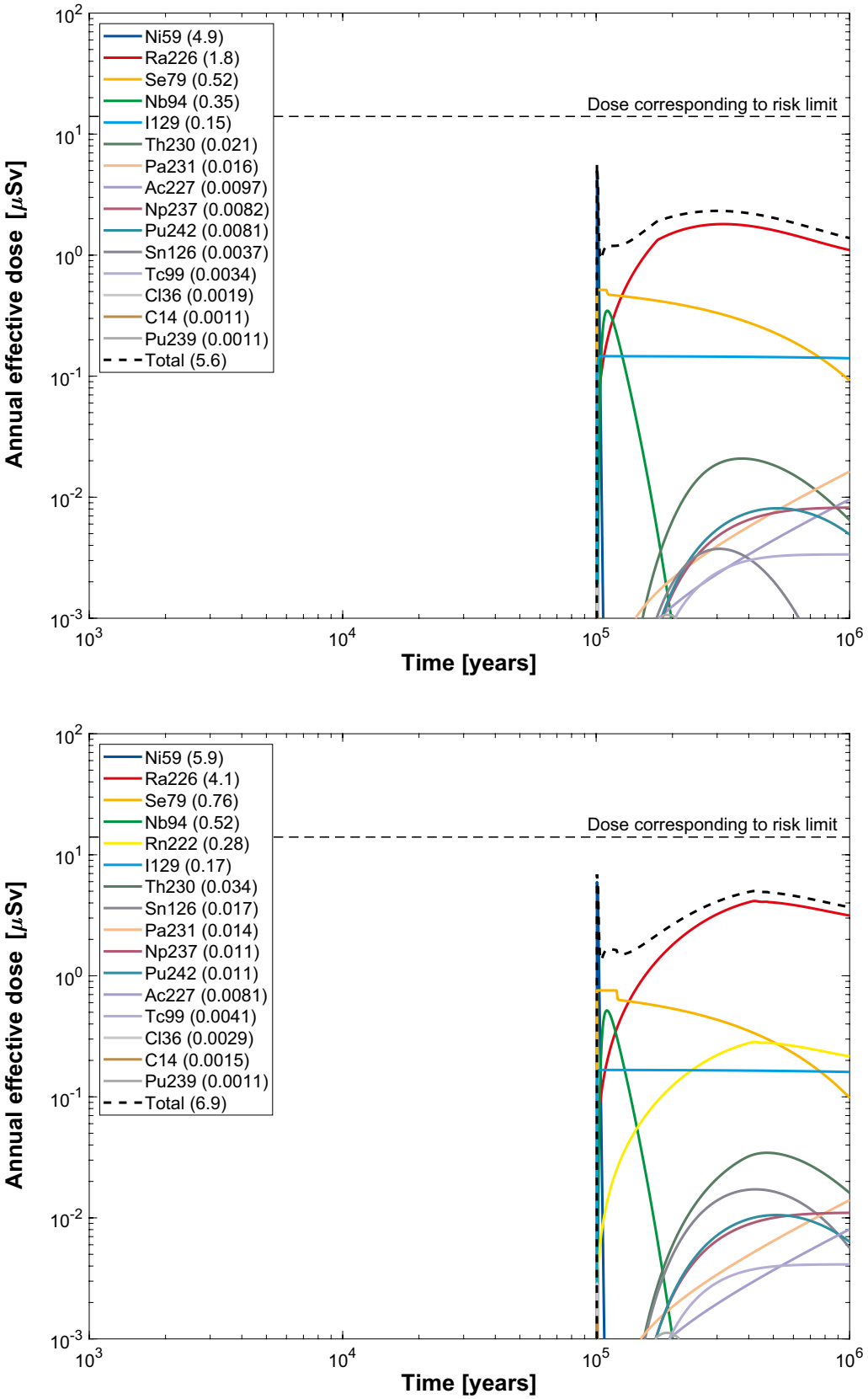

Figure M-32. *Far-field annual effective dose for a deterministic calculation of the shear load scenario, with a postulated failure of one canister at 100 000 years. The legend is sorted by peak (in the one-million year period) of the annual effective dose. The values in brackets are peak dose in units of μSv.* ***Top:*** *SR-Site.* ***Bottom:*** *PSAR.*

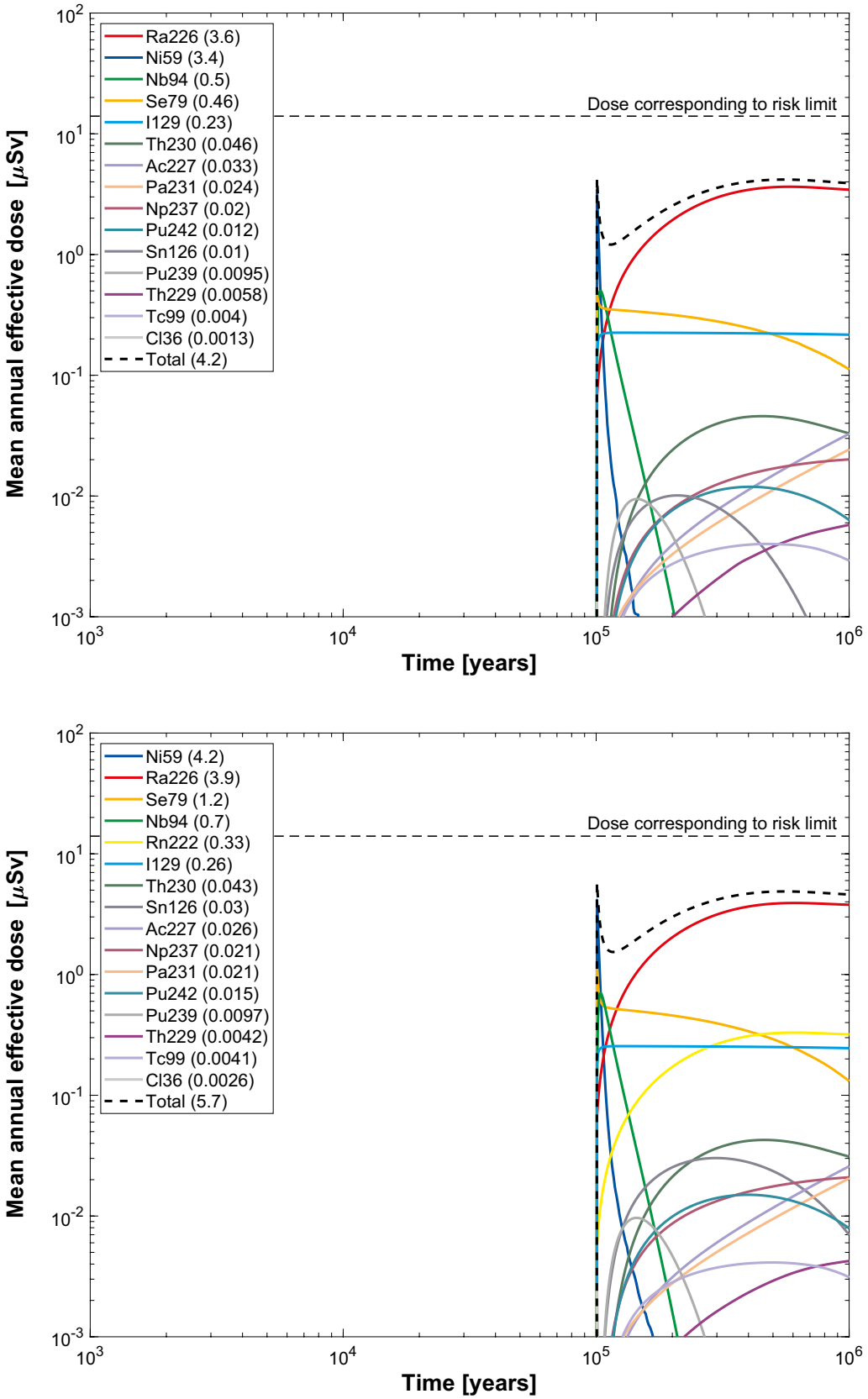

Figure M-33. *Far-field mean annual effective dose for the probabilistic calculation of the shear load scenario, with a postulated failure of one canister at 100 000 years. The legend is sorted by peak (in the one-million year period) of the mean annual effective dose. The values in brackets are peak dose in units of μSv.* ***Top:*** *SR-Site.* ***Bottom:*** *PSAR.*

M.12 Shear load, Failure during the period 1 000 years to one million years

M.12.1 Probabilistic calculations

Failure time:	1 000 to one million years
Mean number of failed canisters:	0.079
Solubility limits:	Yes
Number of realisations:	6 916
Number of nuclides:	37 (SR-Site), 38 (PSAR)

A probabilistic calculation of the shear load case is performed with failure during the period 1 000 years to one million years. The mean number of failed canisters is 0.079 (Section 10.4.5 in both SKB (2011) and the **Post-closure safety report**). The contributions from the instantly released fraction of nuclides, IRF, are not included in the calculations, except for Tc-99, which is included. The contribution from the IRF is judged to be negligible based on the low probability for this scenario and the low contribution shown in the central corrosion case in Section 4.4.2. The influence is also shown to be small at early failure times, see 5.2.3. No retention in the geosphere occurs and hence the release calculated for the near field is also valid for the far field.

Figure M-34 shows the far-field dose equivalent releases. Comparison between the curves from the recalculated SR-Site calculations and the original calculations in SR-Site, Figure 5-3, shows that they are almost identical. A small difference can be noted for C-14, which is somewhat lower in the recalculation.

Comparison between SR-Site and the PSAR shows slightly higher doses for many radionuclides, but overall the difference is small. Two additional radionuclides are visible in the figure; Rn-222 which is not included in the SR-Site calculations and Ni-59, which has an increased inventory.

M.12.2 Probabilistic calculations, disregarding co-precipitation of radium and barium

Failure time:	1 000 to one million years
Mean number of failed canisters:	0.079
Solubility limits:	Yes, disregarding co-precipitation of radium and barium
Number of realisations:	6 916
Number of nuclides:	37 (SR-Site), 38 (PSAR)

This case is the same as the previous, except that co-precipitation of radium and barium is disregarded. This case is further described in Section 5.2.2.

Figure M-35 shows the far-field dose equivalent releases. Comparison between the curves from the recalculated SR-Site calculations and the original calculations in SR-Site, Figure 5-5, shows that they are almost identical.

Comparison between SR-Site and the PSAR shows slightly higher doses for many radionuclides, but overall the difference is small. The overall conclusion that disregarding co-precipitation led to an increase of the release of Ra-226 by only a factor of about 1.5 remains. Rn-222, the progeny of Ra-226, is equally affected.

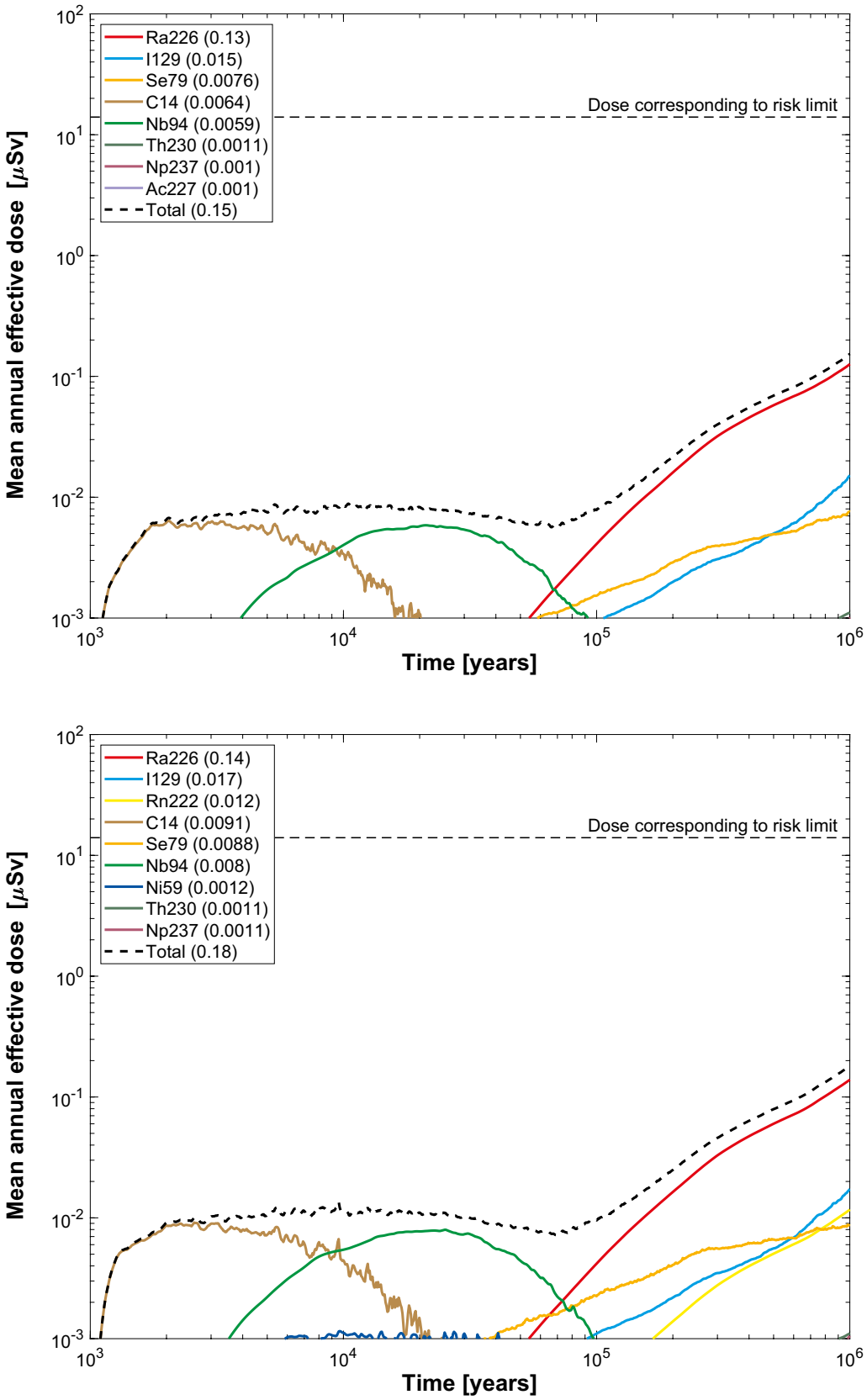

Figure M-34. *Far-field mean annual effective dose for the probabilistic calculation of the shear load scenario, with failure during the period 1 000 years to one million years. The legend is sorted by peak (in the one-million year period) of the mean annual effective dose. The values in brackets are peak dose in units of μSv.* ***Top:*** *SR-Site.* ***Bottom****: PSAR.*

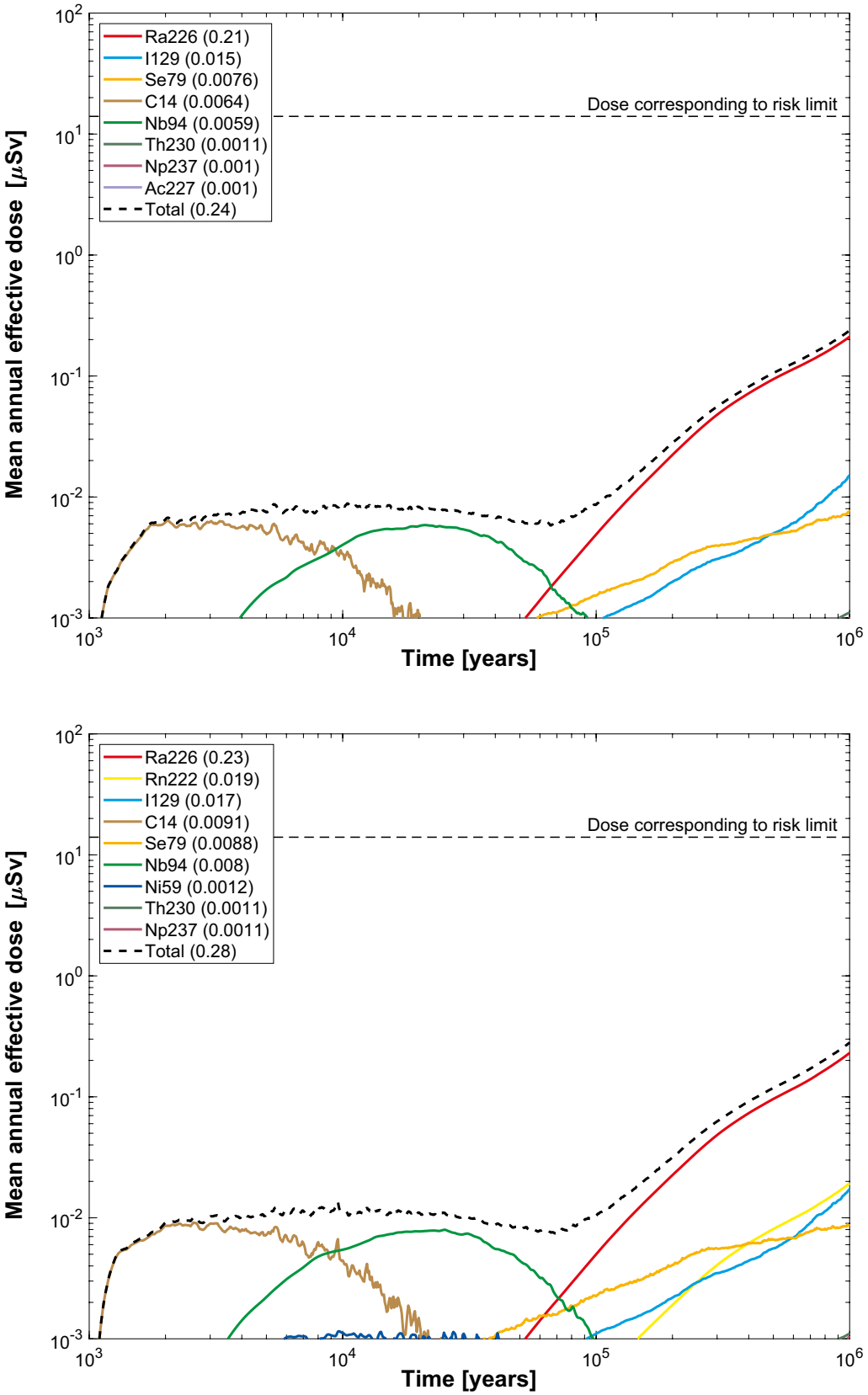

Figure M-35. *Far-field mean annual effective dose for the probabilistic calculation of the shear load scenario, with failure during the period 1 000 years to one million years, disregarding co-precipitation of radium and barium. The legend is sorted by peak (in the one-million year period) of the mean annual effective dose. The values in brackets are peak dose in units of μSv.* ***Top:*** *SR-Site.* ***Bottom:*** *PSAR.*

M.13 Shear load, Early failure

M.13.1 Probabilistic calculations

Failure time:	0–10 000 years
Mean number of failed canisters:	2.4×10^{-8}/year
Solubility limits:	Yes
Number of realisations:	6 916
Number of nuclides:	45 (SR-Site), 46 (PSAR)

A more detailed calculation of the shear load scenario for the initial 10 000 years was done to facilitate comparison with the results for the one million year time frame presented above. The mean number of failed canisters is 2.4×10^{-8}/year (Section 10.4.5 in both SKB (2011) and the **Post-closure safety report**). In this case, the results from COMP23 were used as input to the dynamic biosphere modelling instead of using the basic LDF values as in all other cases. This case is further described in Section 5.2.3.

Figure M-36 shows the far-field dose equivalent releases. Comparison between the curves from the recalculated SR-Site calculations and the original calculations in SR-Site, Figure 5-6, shows that they are almost identical.

The total dose is dominated by relatively rapid variations in C-14 dose. The C-14 dose is dominated by exposure through consumption of fish and the variations are caused by changes in the landscape due to changes in relative sea-level affecting the occurrence of lakes in the vicinity of the site. Beyond a few thousand years, the landscape is relatively unaffected by further changes in relative sea-level.

Comparison between SR-Site and the PSAR shows that some radionuclides with low doses are below the limit of the y-axis in the PSAR. Note that the scale in this figure differs from most of the other figures. The total dose is about the same and very low (almost four orders of magnitude lower than that corresponding to the regulatory risk limit).

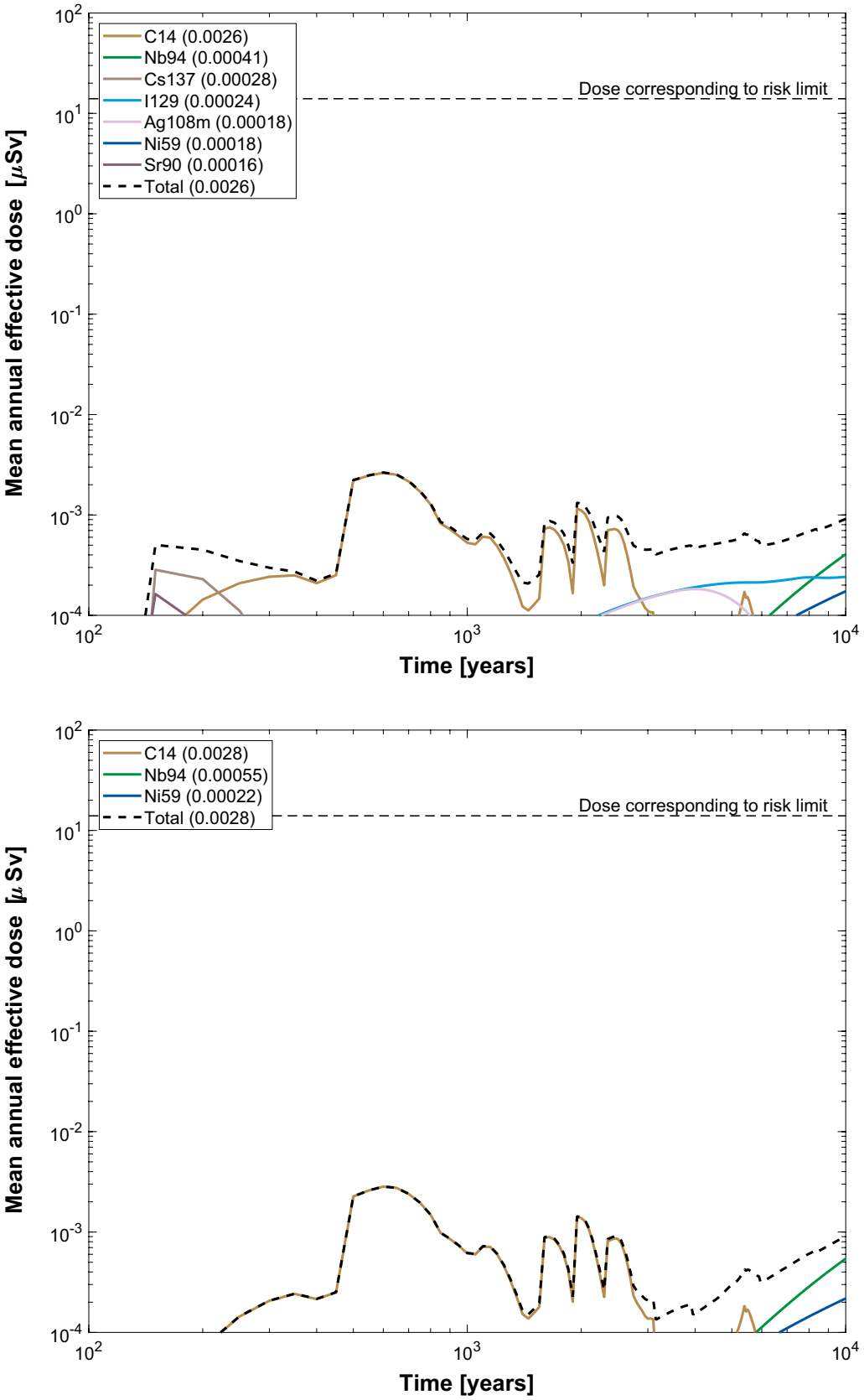

Figure M-36. *Far-field mean annual effective dose for the probabilistic calculation of the shear load scenario, with failure during the period up to 10 000 years. The legend is sorted by peak (in the one-million year period) of the mean annual effective dose. The values in brackets are peak dose in units of μSv.* ***Top:*** *SR-Site.* ***Bottom:*** *PSAR.*

M.14 Combination of shear load and buffer advection

M.14.1 Probabilistic calculations

Failure time:	1 000 to one million years
Mean number of failed canisters:	0.079
Solubility limits:	No
Thorium sorption in near field:	Yes (modelled as low solubility limit)
Number of realisations:	6 916
Number of nuclides:	37 (SR-Site), 38 (PSAR)

In this case the combination of the shear load and the buffer advection scenarios is addressed and the consequences of a shear failure followed by buffer erosion is considered. This case is further described in Section 5.2.4.

Figure M-37 shows the far-field dose equivalent releases. Comparison between the curves from the recalculated SR-Site calculations and the original calculations in SR-Site, Figure 5-7, shows that they are almost identical.

Comparison between SR-Site and the PSAR shows small differences. The maximum dose is slightly higher mainly due to a higher contribution from Pb-210 as a consequence of adding the LDF-value for Po-210 to Pb-210 in the PSAR calculations.

M.15 Summary of the shear load scenario

Figure M-38 shows a summary of the far-field dose equivalent releases for all cases for the shear load scenario described in the previous sections. It should be noted that these cases are not directly comparable since they do not have the same probability and the biosphere is not treated equally. In the previous sections it has been concluded that the results from original and recalculated SR-Site are almost identical.

Comparison between SR-Site and the PSAR shows small differences that are discussed in previous sections. Although the differences are very small it could be noted that all maximum doses are slightly higher for all cases in the PSAR. The conclusions from the SR-Site, as described in Section 5.5, are therefore still valid. The differences are minor and of no concern for the safety of the repository and hence the results from SR-Site are verified to be valid also for the PSAR.

The two cases that are propagated to the risk calculation are the early failure case and the failure during the period 1 000 years to one million years case. It is seen that the early failure peak dose has it maximum of 0.0028 μSv after about 600 years. For later failure the peak dose of 0.18 μSv occurs at one million years and is about two orders of magnitude below the dose corresponding to the regulatory risk limit, 14 μSv.

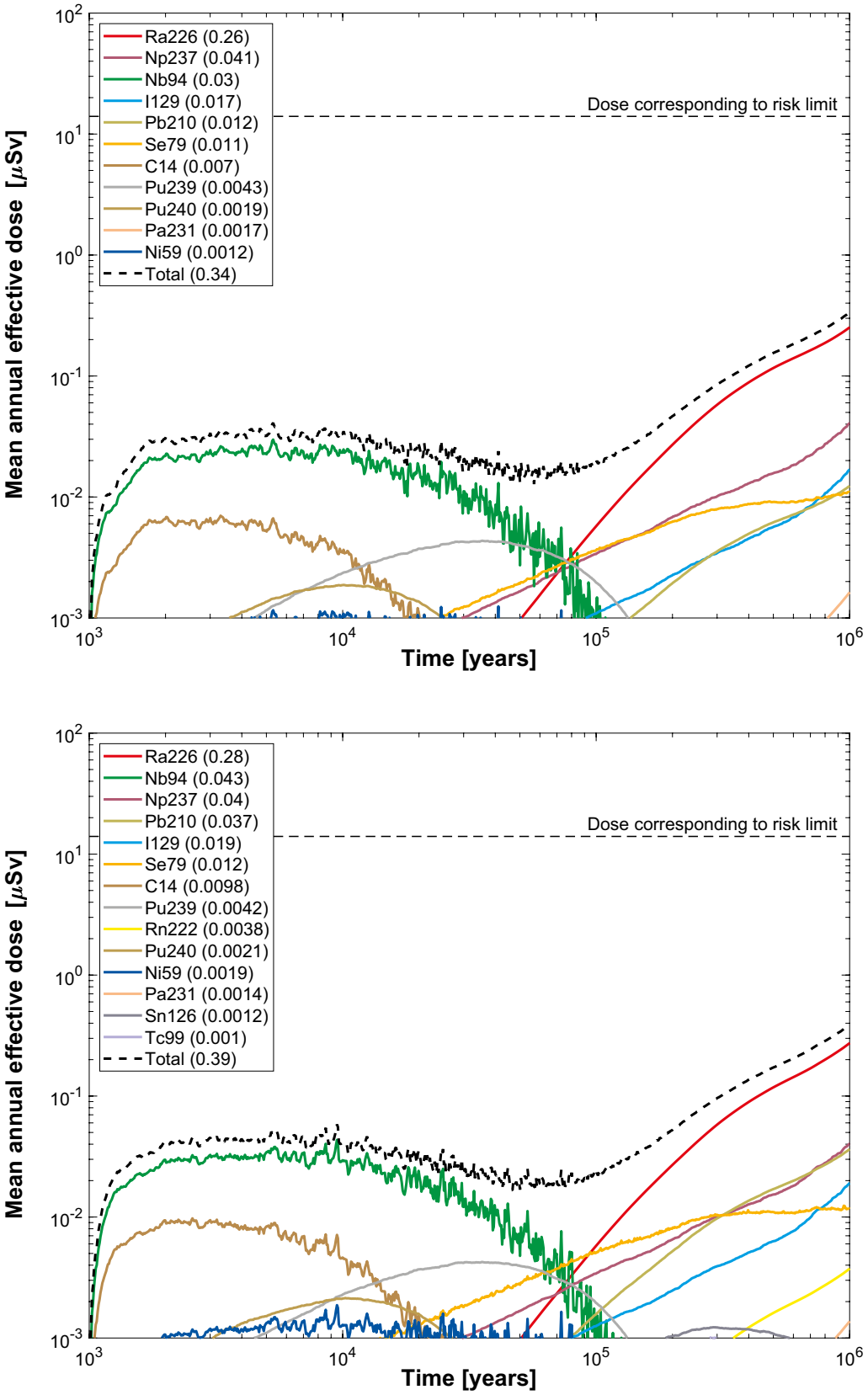

Figure M-37. *Far-field mean annual effective dose for a probabilistic calculation of the shear load scenario, with advective conditions in the deposition hole, failure during the period between 1 000 years and one million years. The legend is sorted by peak (in the one-million year period) of the mean annual effective dose. The values in brackets are peak dose in units of μSv.* ***Top:*** *SR-Site.* ***Bottom:*** *PSAR.*

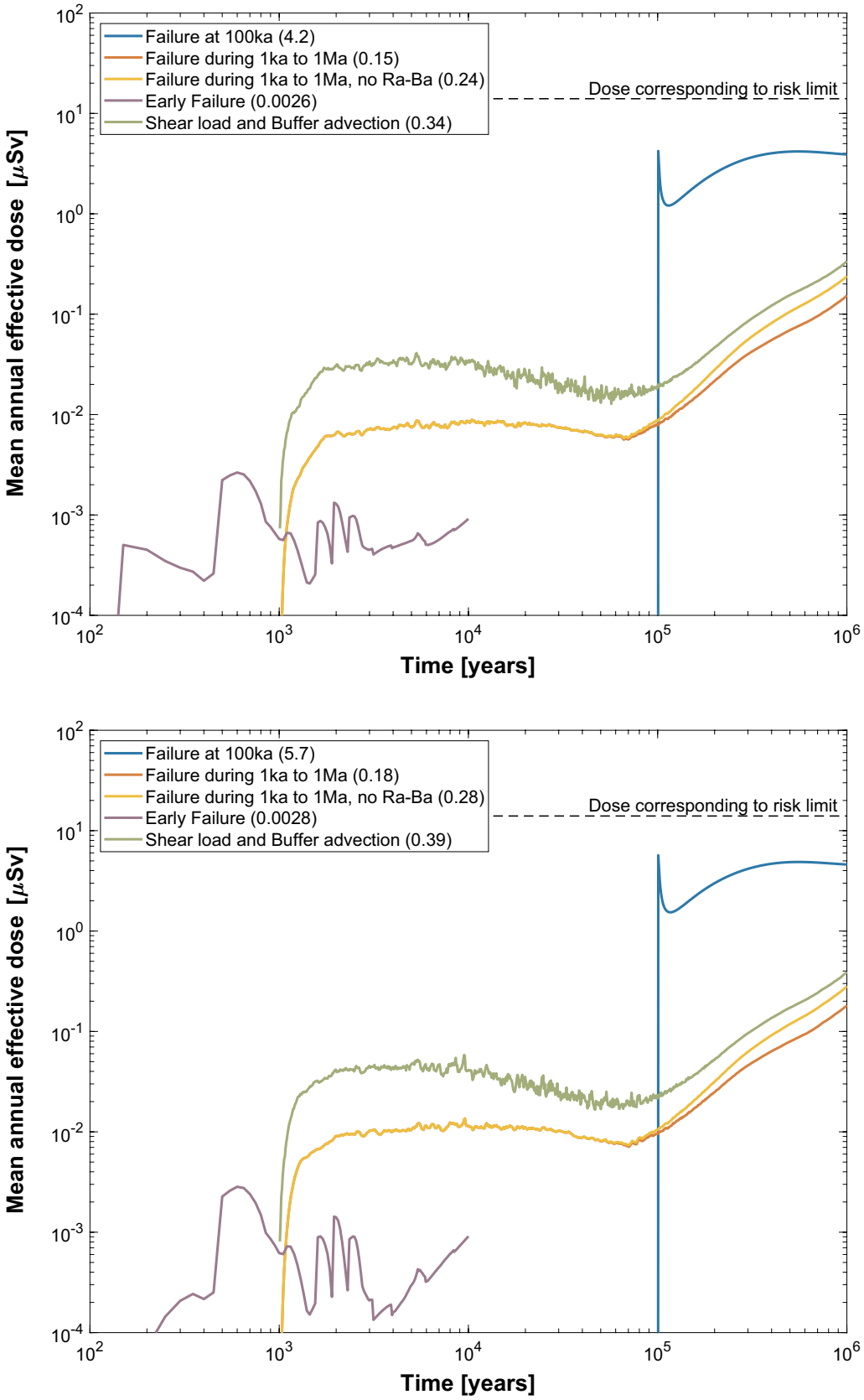

Figure M-38. *Summary of far-field mean annual effective dose equivalent release for all probabilistic calculations for the shear load scenario. The peak doses are given in parentheses in μSv.* ***Top:*** *SR-Site.* ***Bottom:*** *PSAR.*

M.16 Pinhole, Base case, including the effect of spalling

M.16.1 Deterministic calculations

Hydrogeological case:	Semi-correlated, base case
Failure time:	0 and 10 000 years
Number of failed canisters:	1
Solubility limits:	Yes
Spalling:	Yes
Number of realisations:	1
Number of nuclides:	37 (SR-Site), 38 (PSAR)

A deterministic calculation of the hypothetical pinhole failure mode including the effect of spalling was performed for a canister with an initial penetrating pinhole that grows to a large hole after 10 000 years. This case is further described in Section 6.3.1.

Figure M-39 shows the deterministic near-field dose equivalent releases. Figure M-40 shows the same near-field dose equivalent releases decomposed into Q1, Q2 and Q3. Comparison between the curves from the recalculated SR-Site calculations and the original calculations in SR-Site, Figure 6-11 and 6-12, shows that they are almost identical.

Figure M-41 shows the far-field dose equivalent releases and Figure M-40 shows the releases decomposed into Q1, Q2 and Q3. Comparison between the curves from the recalculated SR-Site calculaions and the original calculations in SR-Site, Figure 6-13 and 6-14, shows that they are almost identical.

The maximum dose from the near field is higher in the PSAR than in SR-Site. The maximum dose is dominated by C-14 and I-129, both having a higher inventory in the PSAR. In the longer term the most visible changes are for Ra-226 and Rn-222. The increase in the dose from Ra-226 is mainly caused by corrected solubilities as described in Section L.8. This has been verified by performing an extra calculation with data for the PSAR except for the solubilities that were from SR-Site. Rn-222 was not included separately in SR-Site. The dose from the far field is, however, almost the same in the PSAR as in SR-Site.

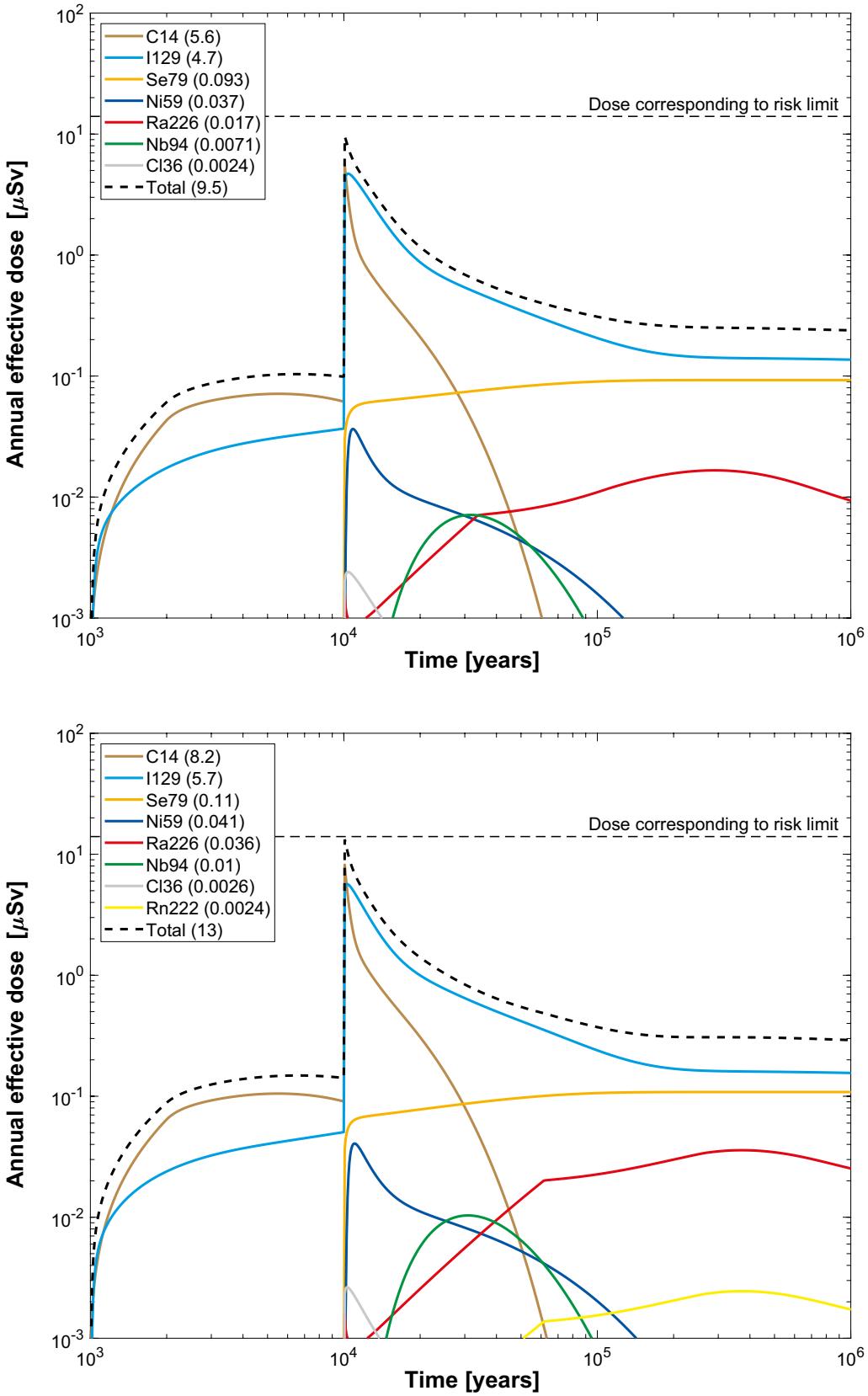

Figure M-39. *Near-field dose equivalent release for a deterministic calculation of the pinhole case, including the effect of spalling. Summed doses for all release paths (Q1+Q2+Q3). The legend is sorted by peak (in the one-million year period) of the annual effective dose. The values in brackets are peak dose in units of μSv.* ***Top:*** *SR-Site.* ***Bottom:*** *PSAR.*

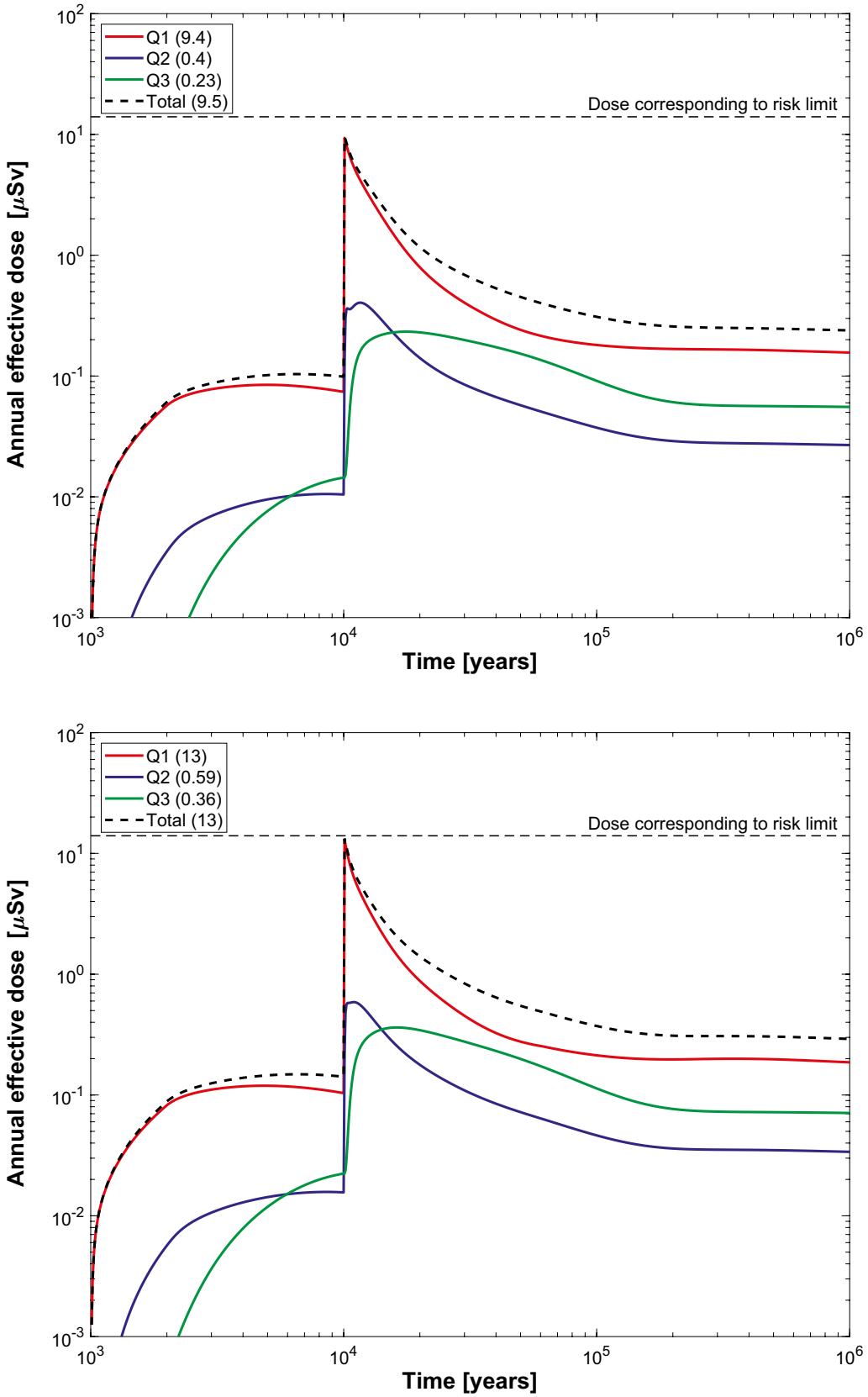

Figure M-40. *Near-field dose equivalent release for a deterministic calculation of the pinhole case, including the effect of spalling. Doses decomposed into Q1, Q2 and Q3. The legend is sorted by peak (in the one-million year period) of the annual effective dose. The values in brackets are peak dose in units of μSv.* ***Top:*** *SR-Site.* ***Bottom:*** *PSAR.*

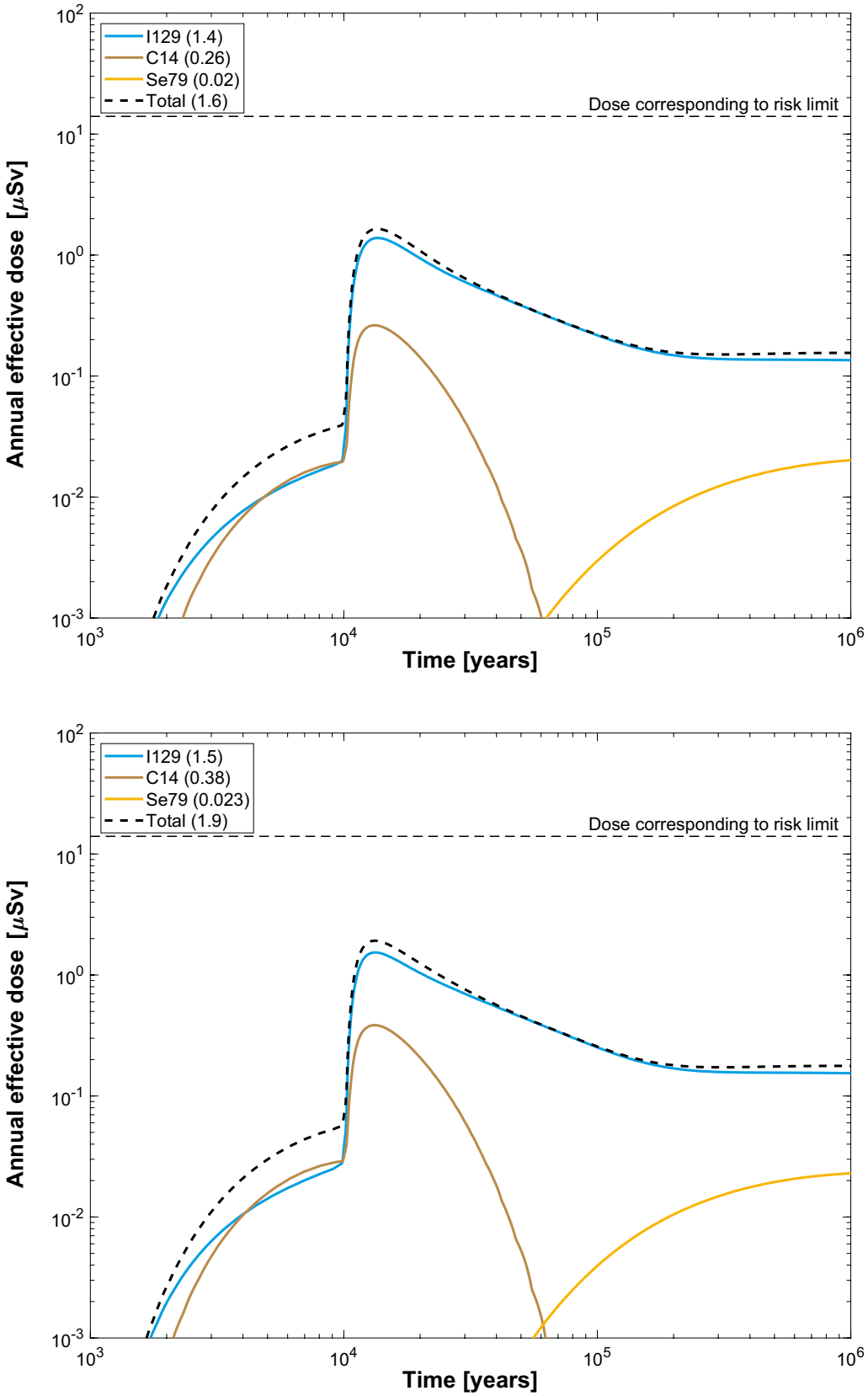

Figure M-41. *Far-field annual effective dose for a deterministic calculation of the pinhole case, including the effect of spalling. Summed doses for all release paths (Q1+Q2+Q3). The legend is sorted by peak (in the one-million year period) of the annual effective dose. The values in brackets are peak dose in units of μSv.* ***Top:*** *SR-Site.* ***Bottom:*** *PSAR.*

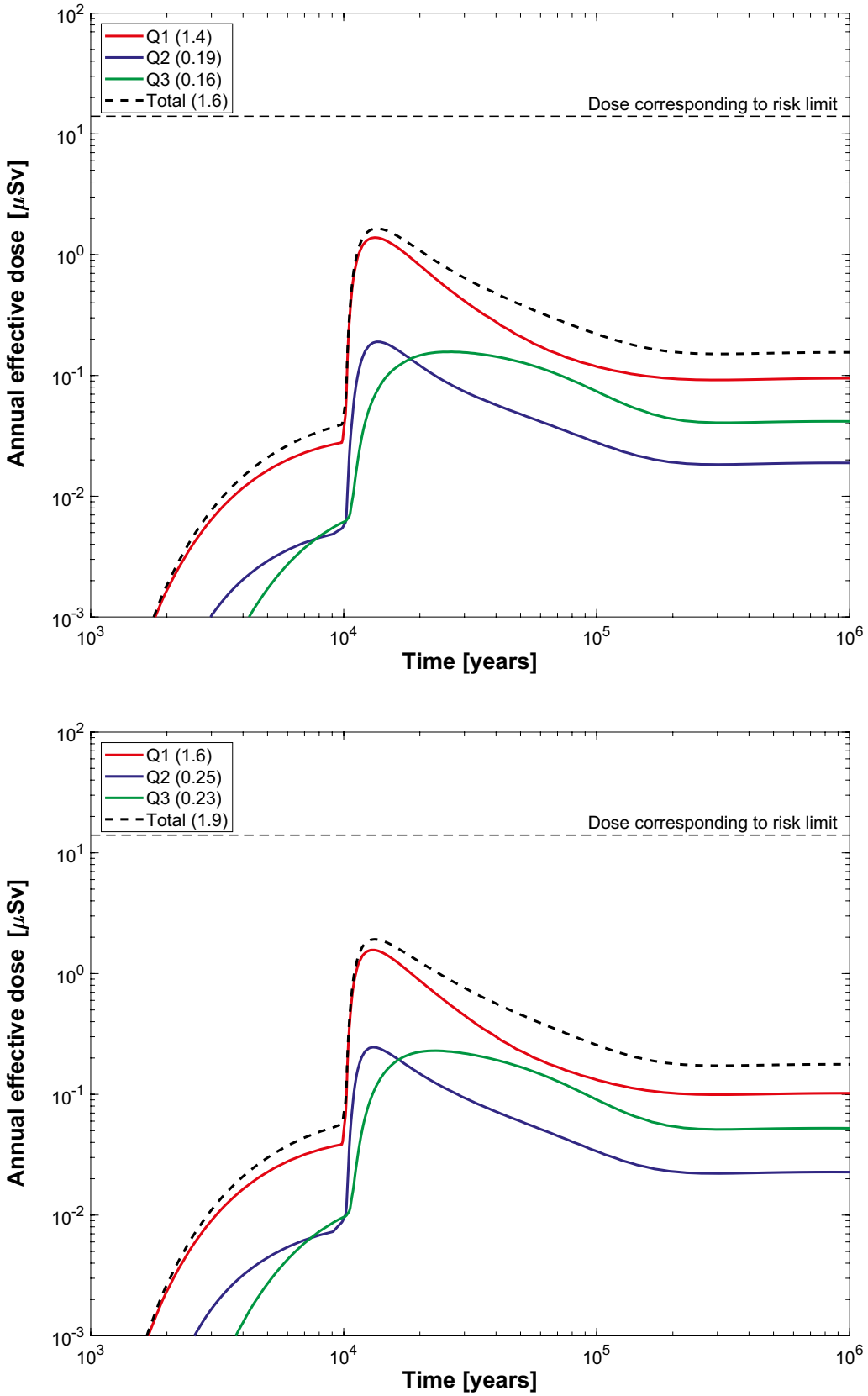

Figure M-42. *Far-field annual effective dose for a deterministic calculation of the pinhole case, including the effect of spalling. Doses decomposed into Q1, Q2 and Q3. The legend is sorted by peak (in the one-million year period) of the annual effective dose. The values in brackets are peak dose in units of μSv.* ***Top:*** *SR-Site.* ***Bottom:*** *PSAR.*

M.16.2 Probabilistic calculations

Hydrogeological case:	Semi-correlated, base case
Failure time:	0 and 10 000 years
Number of failed canisters:	1
Solubility limits:	Yes
Spalling:	Yes
Number of realisations:	6 916
Number of nuclides:	37 (SR-Site), 38 (PSAR)

A probabilistic calculation of the hypothetical pinhole failure mode including the effect of spalling was performed for one canister with an initial penetrating pinhole that grows to a large hole after 10 000 years. This case is further described in Section 6.3.1.

Figure M-43 shows the near-field dose equivalent releases for the pinhole case including the effect of spalling and Figure M-44 shows the same releases decomposed into Q1, Q2 and Q3. Comparison between the curves from the recalculated SR-Site calculaions and the original calculations in SR-Site, Figure 6-15 and 6-16, shows that they are almost identical. A small decrease for Ra-226 could be noted, but its contribution to the total dose is negligible. The maximum dose from the near field is higher in the PSAR than in SR-Site. The maximum dose is dominated by C-14 and I-129, both having a higher inventory in the PSAR. In the longer term the most visible changes are the occurrence of Rn-222, that is included separately in the PSAR but not in SR-Site.

Figure M-45 shows the corresponding far-field dose equivalent releases and Figure M-46 shows the same releases decomposed into Q1, Q2 and Q3. Comparison between the curves from the recalculated SR-Site calculaions and the original calculations in the SR-Site, Figure 6-17 and 6-18, shows that they are almost identical. As for the near field, a small decrease for Ra-226 could be noted, but its contribution to the total dose is negligible. The increase in the inventory in the PSAR of both C-14 and I-129 gives slightly higher maximum release also from the far field.

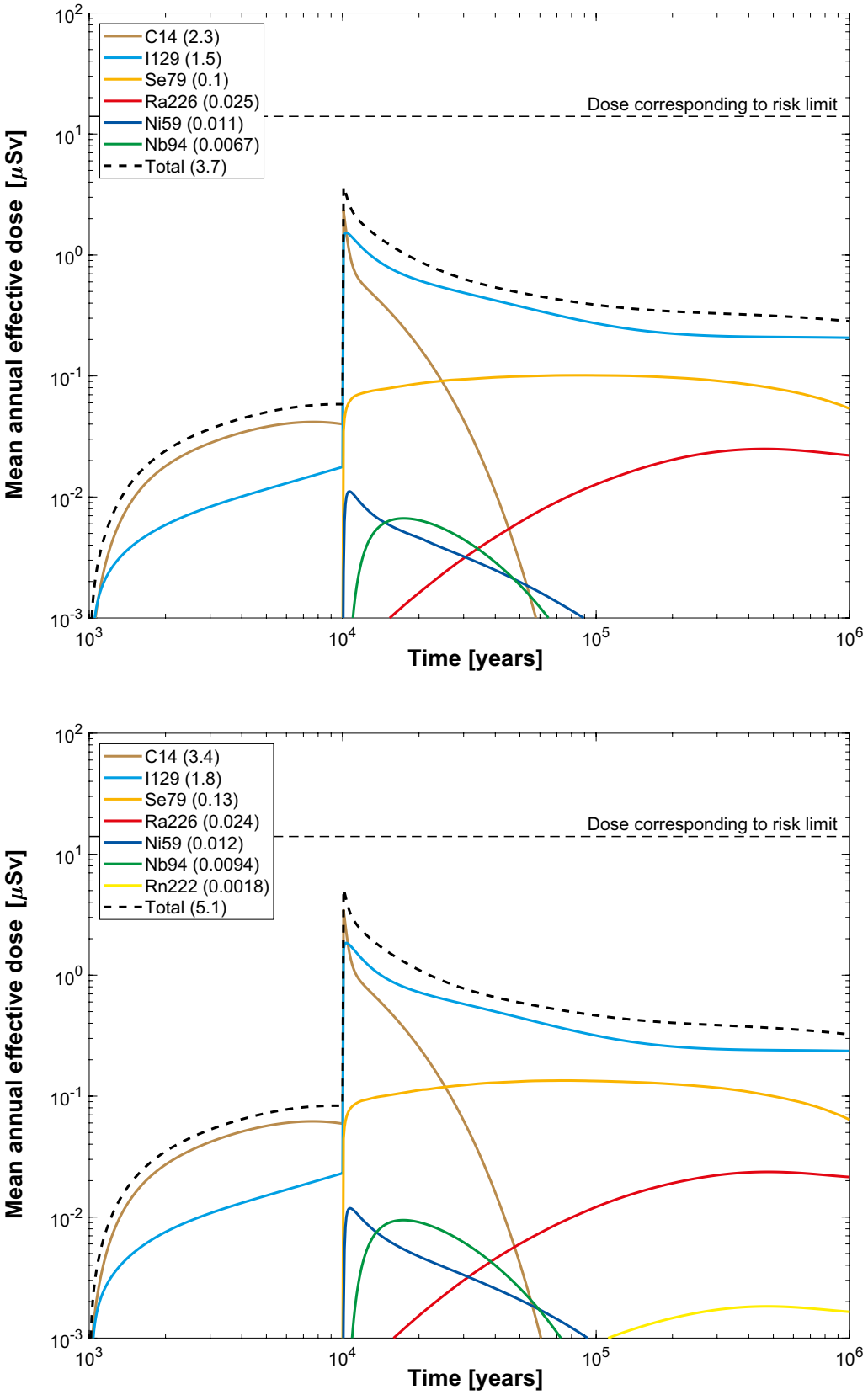

Figure M-43. *Near-field dose equivalent release for the probabilistic calculation of the pinhole case, including the effect of spalling. Summed doses for all release paths (Q1+Q2+Q3). The legend is sorted by peak (in the one-million year period) of the mean annual effective dose. The values in brackets are peak dose in units of μSv.* ***Top:*** *SR-Site.* ***Bottom:*** *PSAR.*

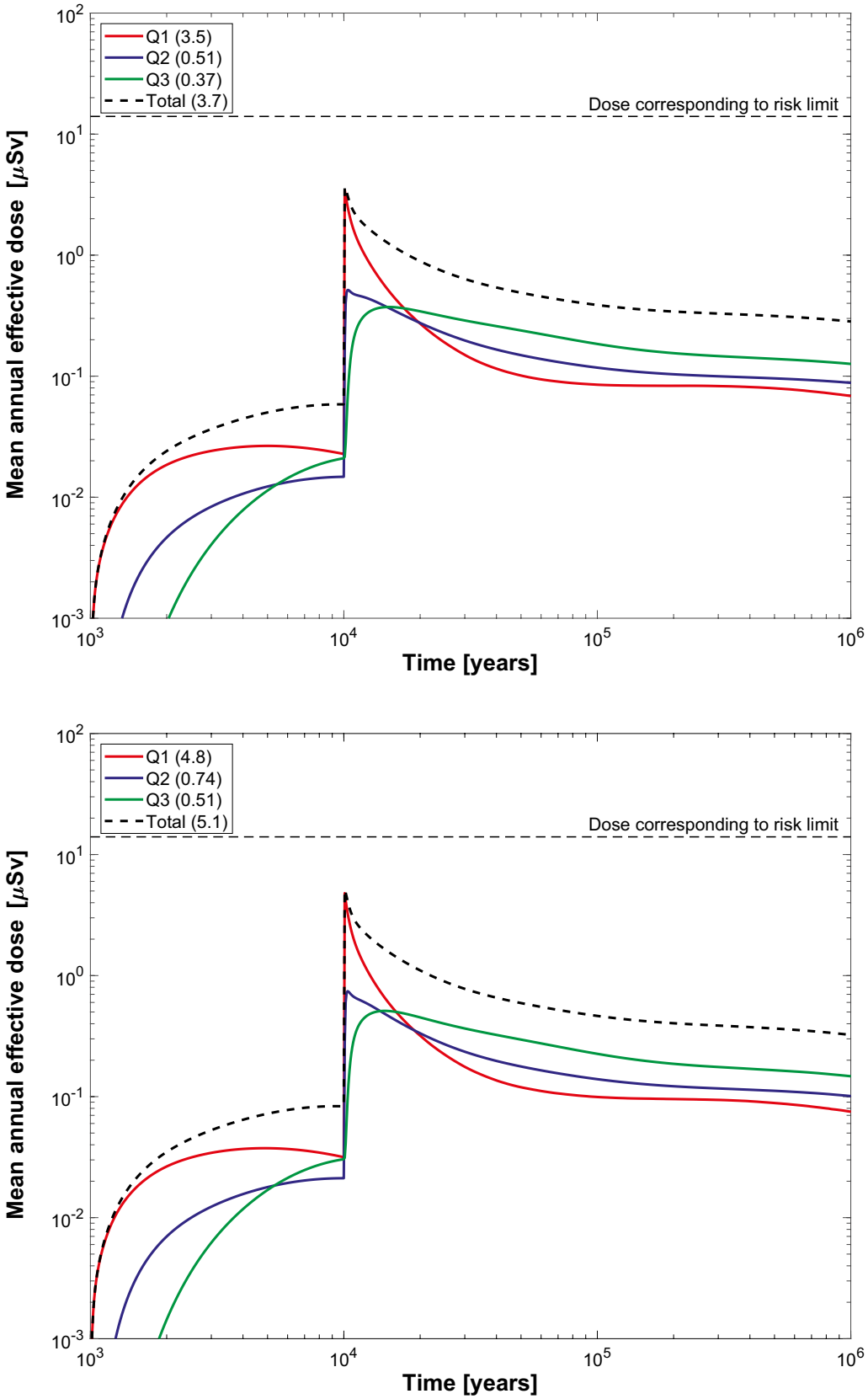

Figure M-44. *Near-field dose equivalent release for the probabilistic calculation of the pinhole case, including the effect of spalling. Doses decomposed into Q1, Q2 and Q3. The legend is sorted by peak (in the one-million year period) of the mean annual effective dose. The values in brackets are peak dose in units of μSv.* ***Top:*** *SR-Site.* ***Bottom:*** *PSAR.*

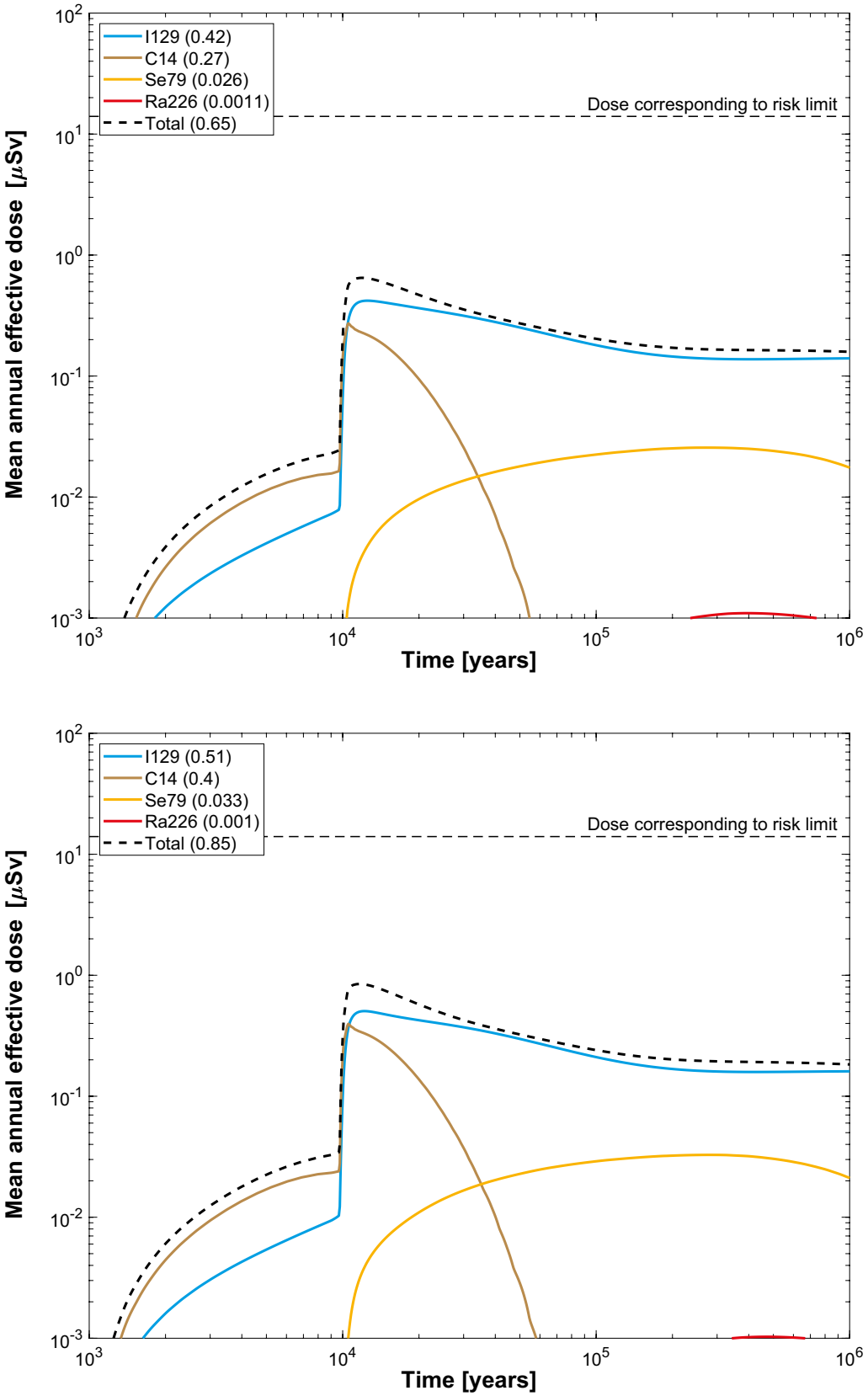

Figure M-45. *Far-field mean annual effective dose for the probabilistic calculation of the pinhole case, including the effect of spalling. Summed doses for all release paths (Q1+Q2+Q3). The legend is sorted by peak (in the one-million year period) of the mean annual effective dose. The values in brackets are peak dose in units of μSv.* ***Top:*** *SR-Site.* ***Bottom:*** *PSAR.*

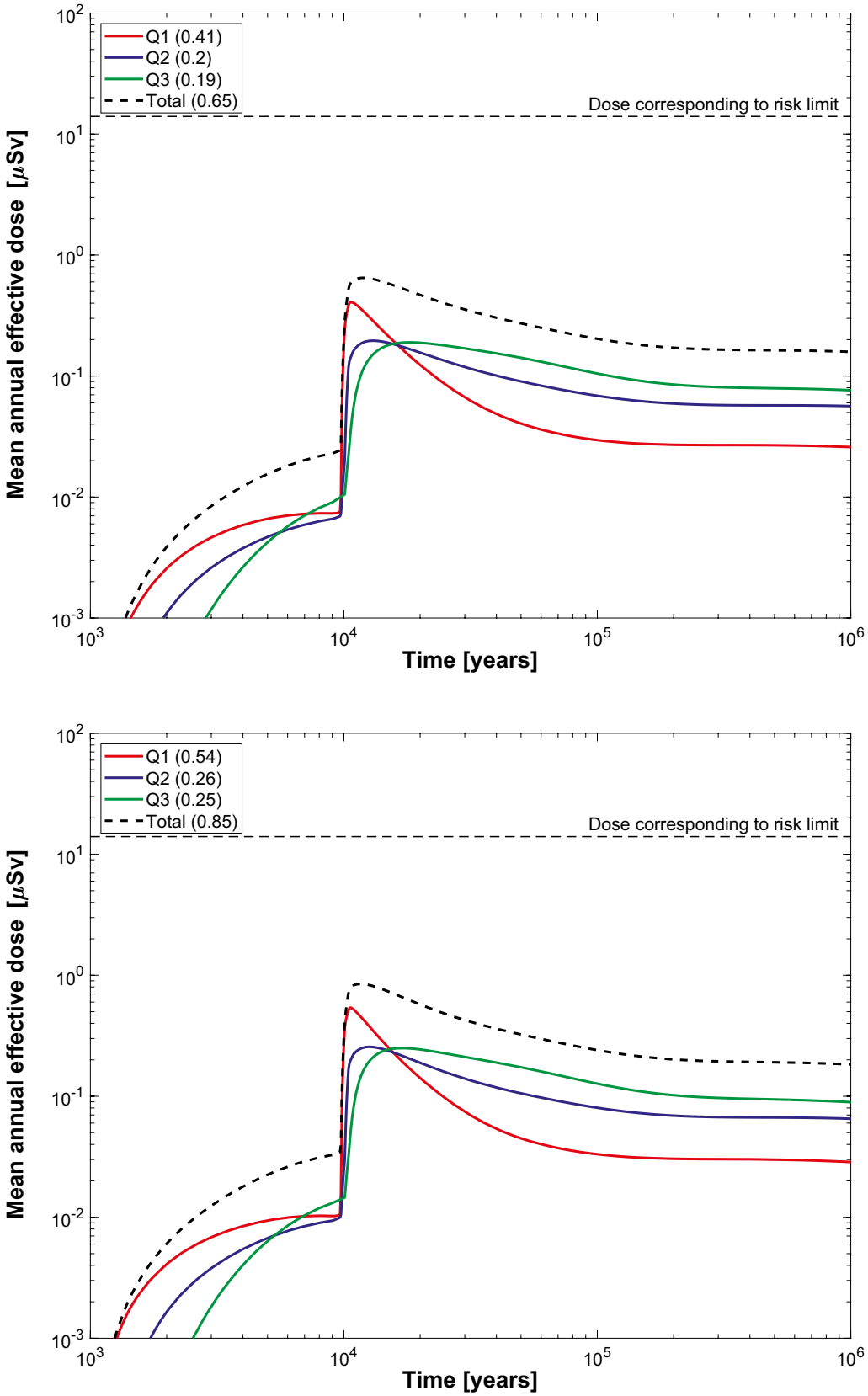

Figure M-46. *Far-field mean annual effective dose for the probabilistic calculation of the pinhole case, including the effect of spalling. Doses decomposed into Q1, Q2 and Q3. The legend is sorted by peak (in the one-million year period) of the mean annual effective dose. The values in brackets are peak dose in units of μSv.* ***Top:*** *SR-Site.* ***Bottom:*** *PSAR.*

M.17 Pinhole, Disregarding the effect of spalling

M.17.1 Deterministic calculations

Hydrogeological case:	Semi-correlated, base case
Failure time:	0 and 10 000 years
Number of failed canisters:	1
Solubility limits:	Yes
Spalling:	No
Number of realisations:	1
Number of nuclides:	37 (SR-Site), 38 (PSAR)

A deterministic calculation of the hypothetical pinhole failure mode disregarding the effect of spalling was performed for a canister with an initial penetrating pinhole that grows to a large hole after 10 000 years. This case is further described in Section 6.3.2.

Figure M-47 shows the deterministic near-field dose equivalent releases and Figure M-48 shows the releases decomposed into Q1, Q2 and Q3. Comparison between the curves from the recalculated SR-Site calculaions and the original calculations in SR-Site, Figure 6-19 and 6-20, shows that they are almost identical.

Figure M-49 shows the far-field dose equivalent releases and Figure M-50 shows the same releases decomposed into Q1, Q2 and Q3. Comparison between the curves from the recalculated SR-Site calculations and the original calculations in SR-Site, Figure 6-21 and 6-22, shows that they are almost identical.

The maximum dose from the near field is higher in the PSAR than in SR-Site. The maximum dose is dominated by C-14 and I-129, both having a higher inventory in the PSAR. In the longer term the most visible changes are for Ra-226. The increase in the dose from Ra-226 is mainly caused by corrected solubilities as described in Section L.8. The dose from the far field is, however, almost the same in the PSAR as in SR-Site.

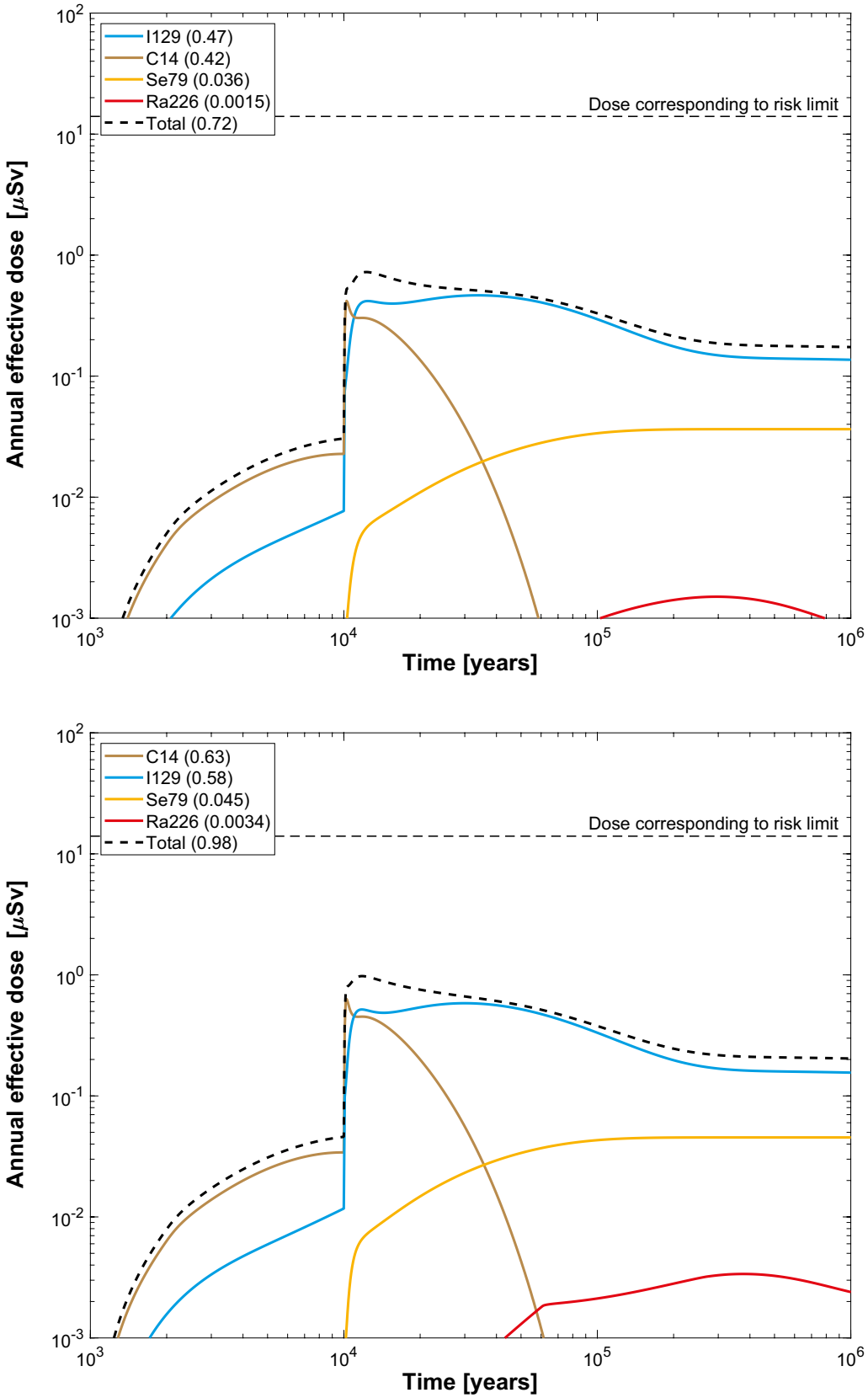

Figure M-47. *Near-field dose equivalent release for a deterministic calculation of the pinhole case, disregarding the effect of spalling. Summed doses for all release paths (Q1+Q2+Q3). The legend is sorted by peak (in the one-million year period) of the annual effective dose. The values in brackets are peak dose in units of μSv.* ***Top:*** *SR-Site.* ***Bottom:*** *PSAR.*

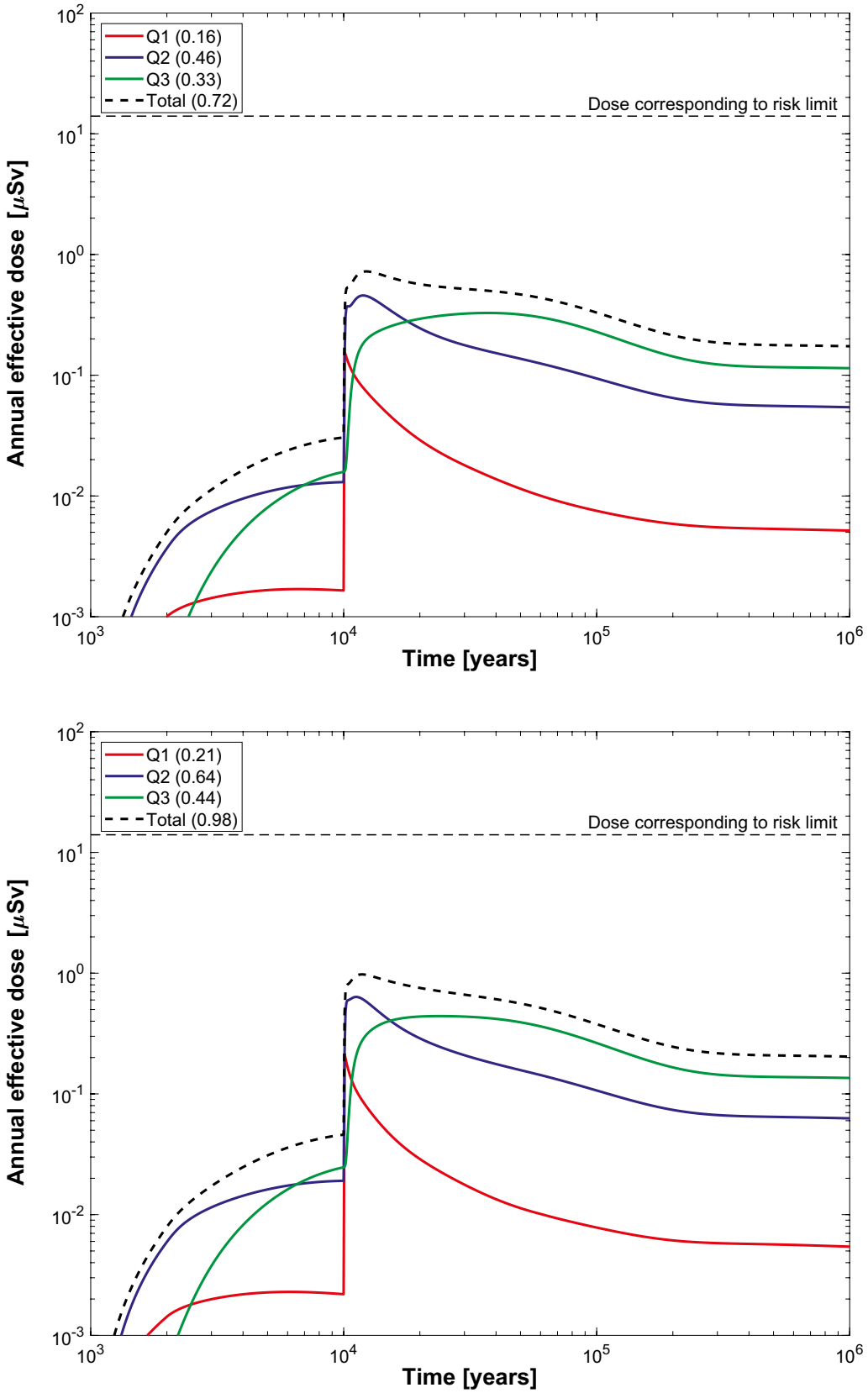

Figure M-48. *Near-field dose equivalent release for a deterministic calculation of the pinhole case, disregarding the effect of spalling. Doses decomposed into Q1, Q2 and Q3. The legend is sorted by peak (in the one-million year period) of the annual effective dose. The values in brackets are peak dose in units of μSv.* ***Top:*** *SR-Site.* ***Bottom:*** *PSAR.*

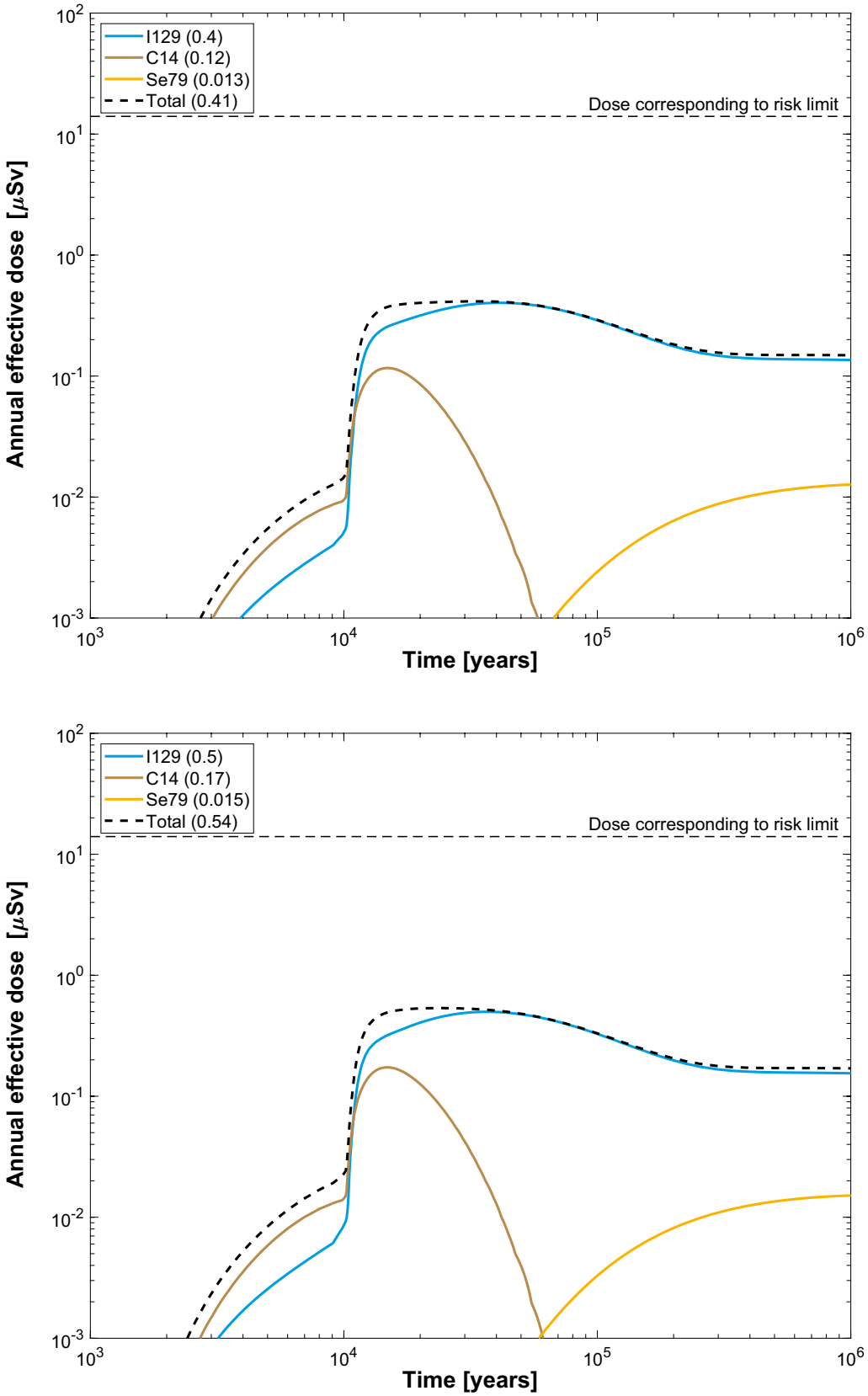

Figure M-49. *Far-field annual effective dose for a deterministic calculation of the pinhole case, disregarding the effect of spalling. Summed doses for all release paths (Q1+Q2+Q3). The legend is sorted by peak (in the one-million year period) of the annual effective dose. The values in brackets are peak dose in units of μSv.* ***Top:*** *SR-Site.* ***Bottom:*** *PSAR.*

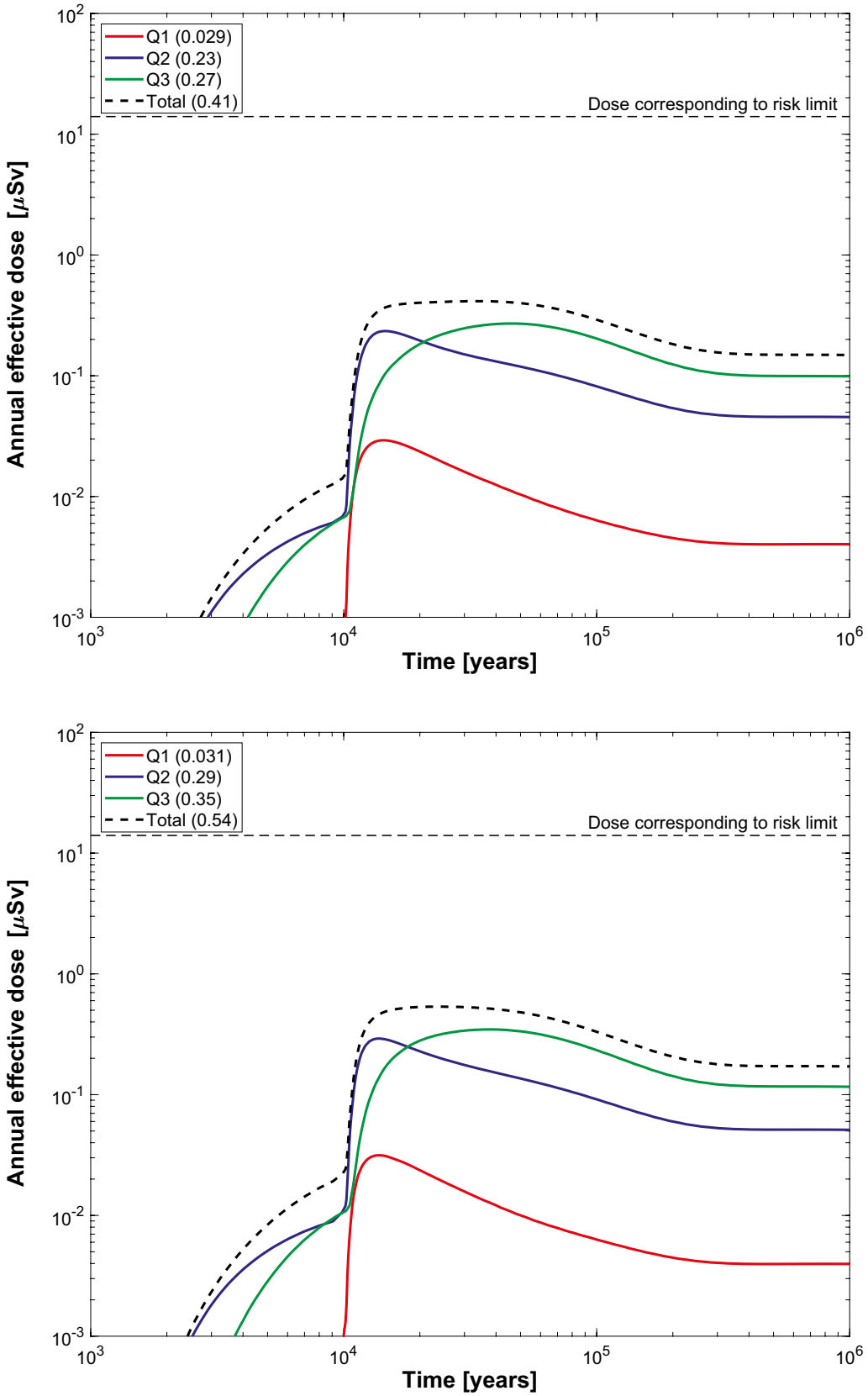

Figure M-50. *Far-field annual effective dose for a deterministic calculation of the pinhole case, disregarding the effect of spalling. Doses decomposed into Q1, Q2 and Q3. The legend is sorted by peak (in the one-million year period) of the annual effective dose. The values in brackets are peak dose in units of μSv.* ***Top:*** *SR-Site.* ***Bottom:*** *PSAR.*

M.17.2 Probabilistic calculations

Hydrogeological case:	Semi-correlated, base case
Failure time:	0 and 10 000 years
Number of failed canisters:	1
Solubility limits:	Yes
Spalling:	No
Number of realisations:	6 916
Number of nuclides:	37 (SR-Site), 38 (PSAR)

A probabilistic calculation of the hypothetical pinhole failure mode disregarding the effect of spalling was performed for one canister with an initial penetrating pinhole that grows to a large hole after 10 000 years. This case is further described in Section 6.3.2.

Figure M-51 shows the near-field dose equivalent and Figure M-52 shows the releases decomposed into Q1, Q2 and Q3. Comparison between the curves from the recalculated SR-Site calculations and the original calculations in SR-Site, Figure 6-23 and 6-24, shows that they are almost identical. The maximum dose from the near field is higher in the PSAR than in SR-Site. The maximum dose is dominated by C-14 and I-129, both having a higher inventory in the PSAR.

Figure M-53 shows the far-field dose equivalent releases and Figure M-54 shows the releases decomposed into Q1, Q2 and Q3. Comparison between the curves from the recalculated SR-Site calculations and the original calculations in SR-Site, Figure 6-25 and 6-26, shows that they are almost identical. The maximum dose is somewhat higher in the PSAR than in SR-Site. The maximum dose is dominated by C-14 and I-129, both having a slightly higher inventory in the PSAR.

M.18 Summary of the growing pinhole failure

Figure M-55 shows the total dose equivalent releases for the far field for cases calculated probabilistically for the growing pinhole failure. The corresponding results for the original SR-Site calculations are given in Figure 6-40. In the previous sections it has been concluded that recalculation of the SR-Site cases gives almost identical results.

Comparison between SR-Site and the PSAR shows small differences that are discussed in previous sections. The maximum dose is somewhat higher in the PSAR than in SR-Site. The maximum dose is dominated by C-14 and I-129, both having a slightly higher inventory in the PSAR. The conclusions from SR-Site, as described in Section 6.3.5, are therefore still valid. The differences are minor and of no concern for the safety of the repository and hence the results from the SR-Site are verified to be valid also for the PSAR.

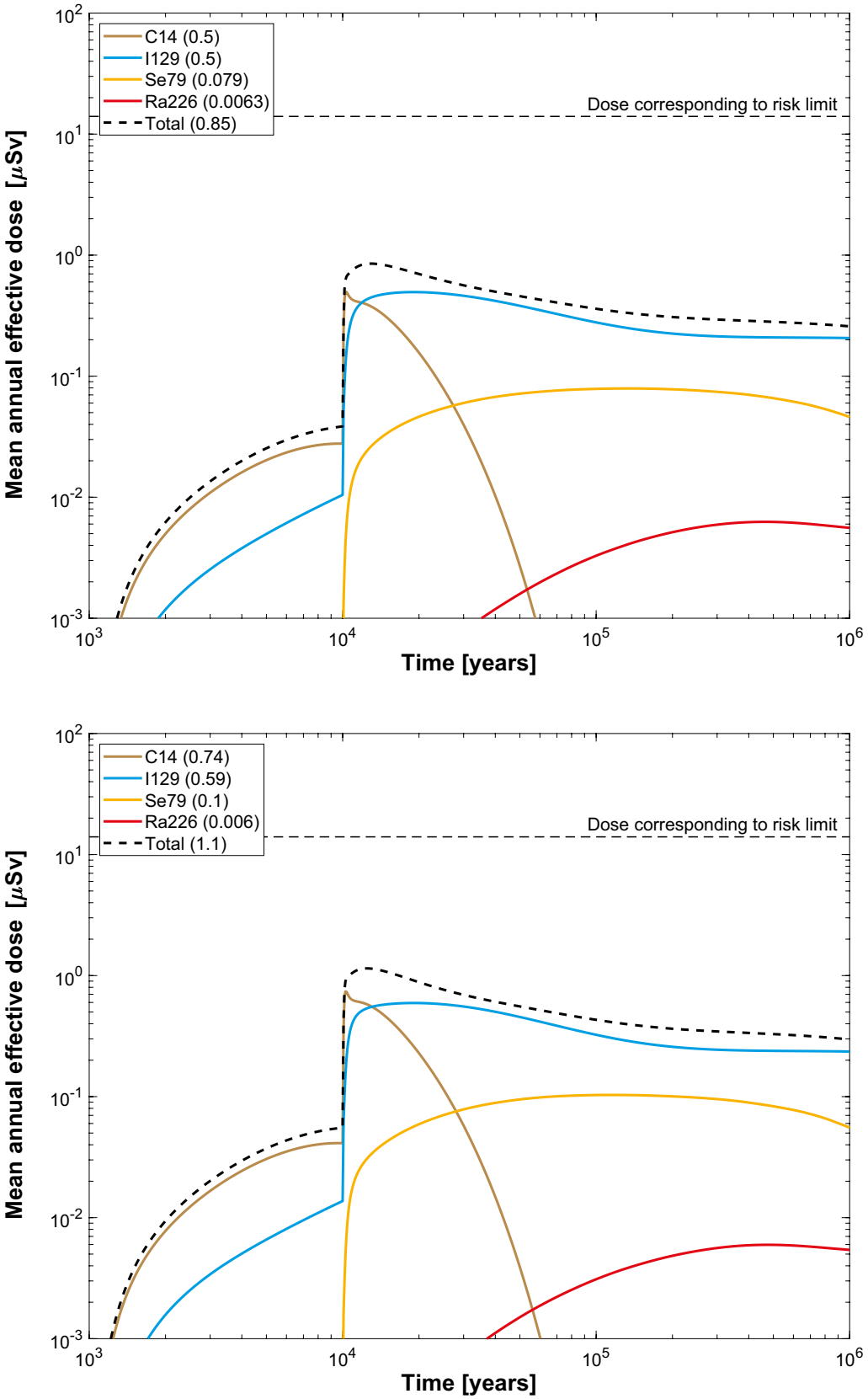

Figure M-51. *Near-field dose equivalent release for the probabilistic calculation of the pinhole case, disregarding the effect of spalling. Summed doses for all release paths (Q1+Q2+Q3). The legend is sorted by peak (in the one-million year period) of the mean annual effective dose. The values in brackets are peak dose in units of μSv.* ***Top:*** *SR-Site.* ***Bottom:*** *PSAR.*

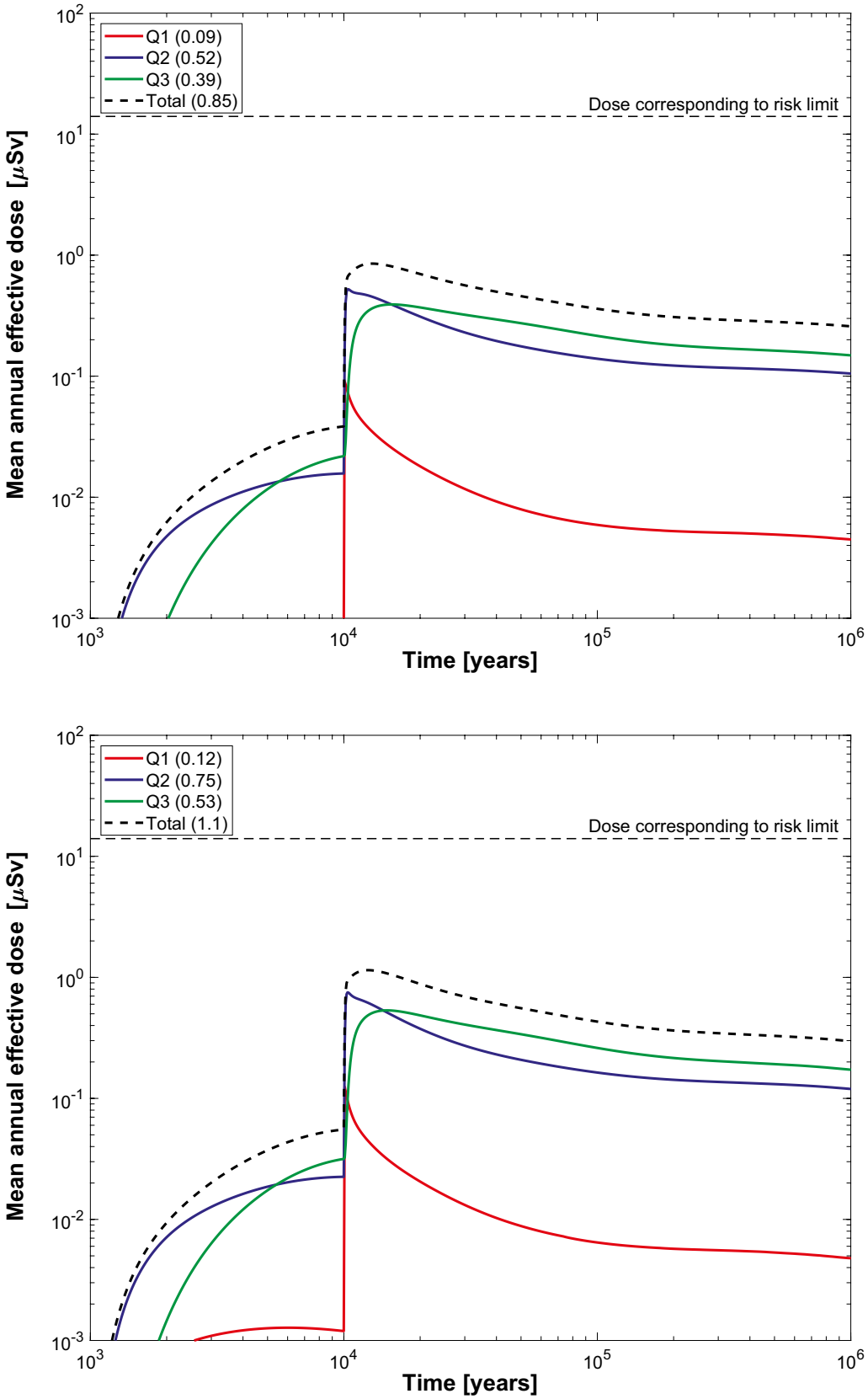

Figure M-52. *Near-field dose equivalent release for the probabilistic calculation of the pinhole case, disregarding the effect of spalling. Doses decomposed into Q1, Q2 and Q3. The legend is sorted by peak (in the one-million year period) of the mean annual effective dose. The values in brackets are peak dose in units of μSv.* ***Top:*** *SR-Site.* ***Bottom:*** *PSAR.*

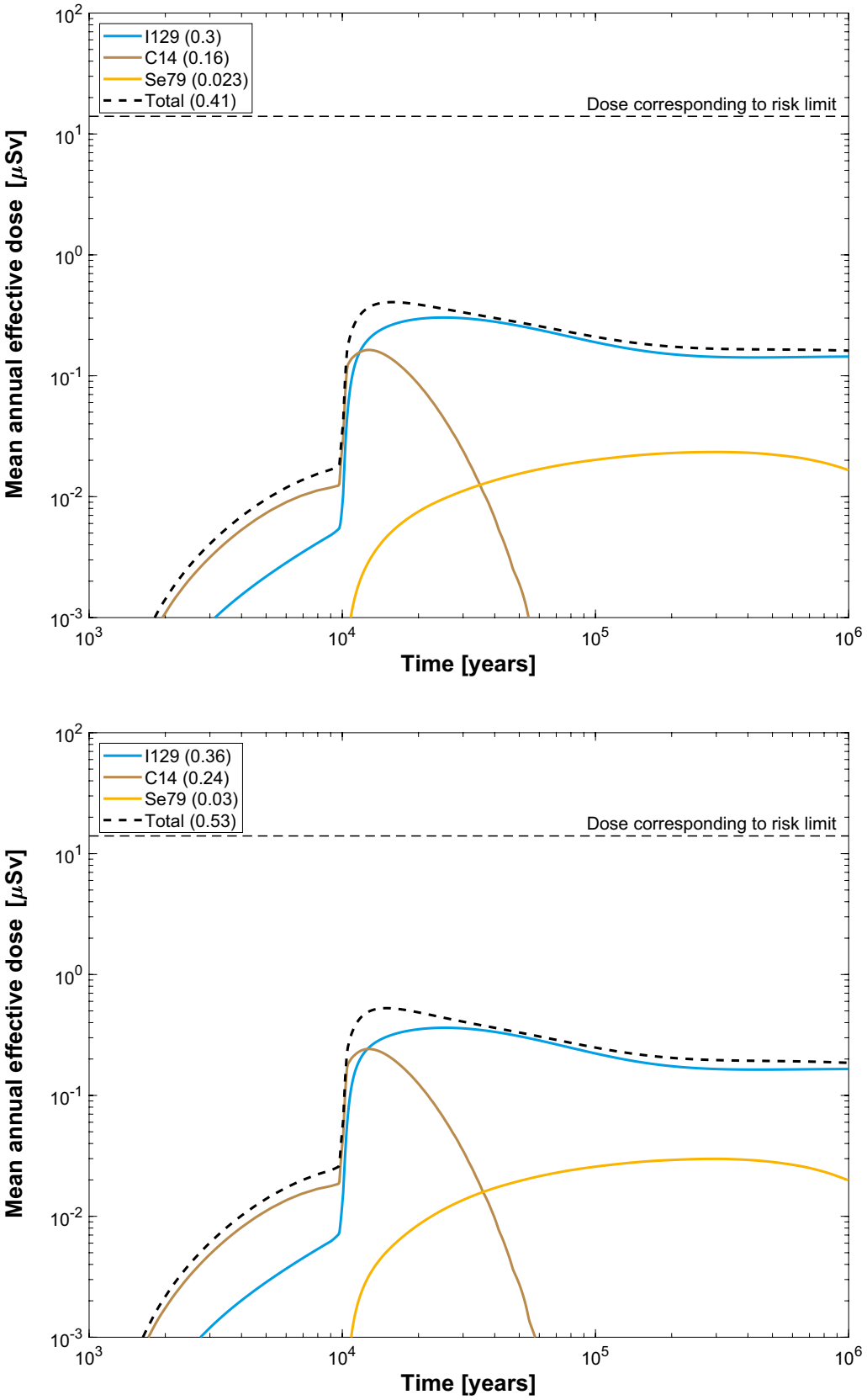

Figure M-53. *Far-field mean annual effective dose for the probabilistic calculation of the pinhole case, disregarding the effect of spalling. Summed doses for all release paths (Q1+Q2+Q3). The legend is sorted by peak (in the one-million year period) of the mean annual effective dose. The values in brackets are peak dose in units of μSv.* ***Top:*** *SR-Site.* ***Bottom:*** *PSAR.*

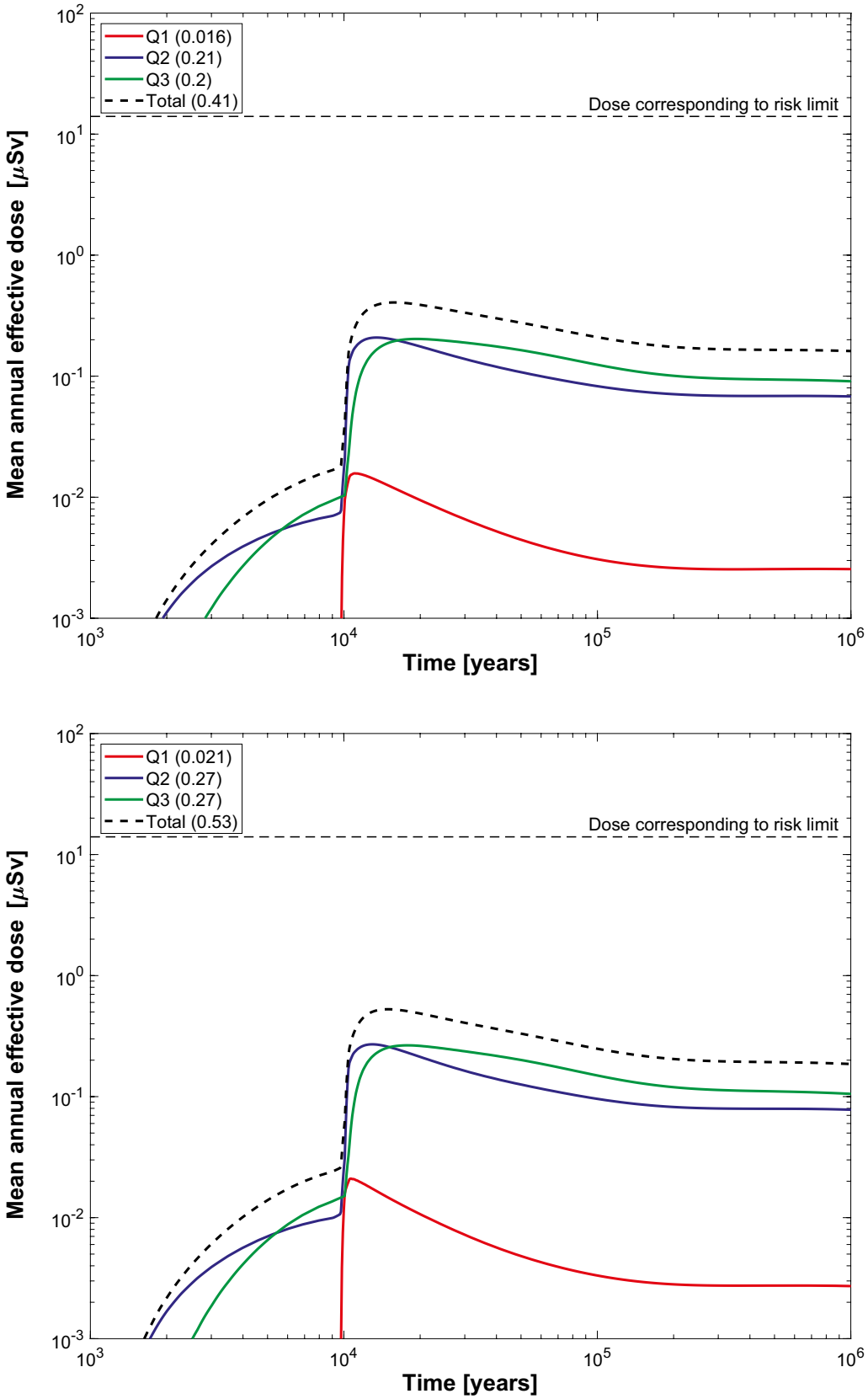

Figure M-54. *Far-field mean annual effective dose for the probabilistic calculation of the pinhole case, disregarding the effect of spalling. Doses decomposed into Q1, Q2 and Q3. The legend is sorted by peak (in the one-million year period) of the mean annual effective dose. The values in brackets are peak dose in units of μSv.* ***Top:*** *SR-Site.* ***Bottom:*** *PSAR.*

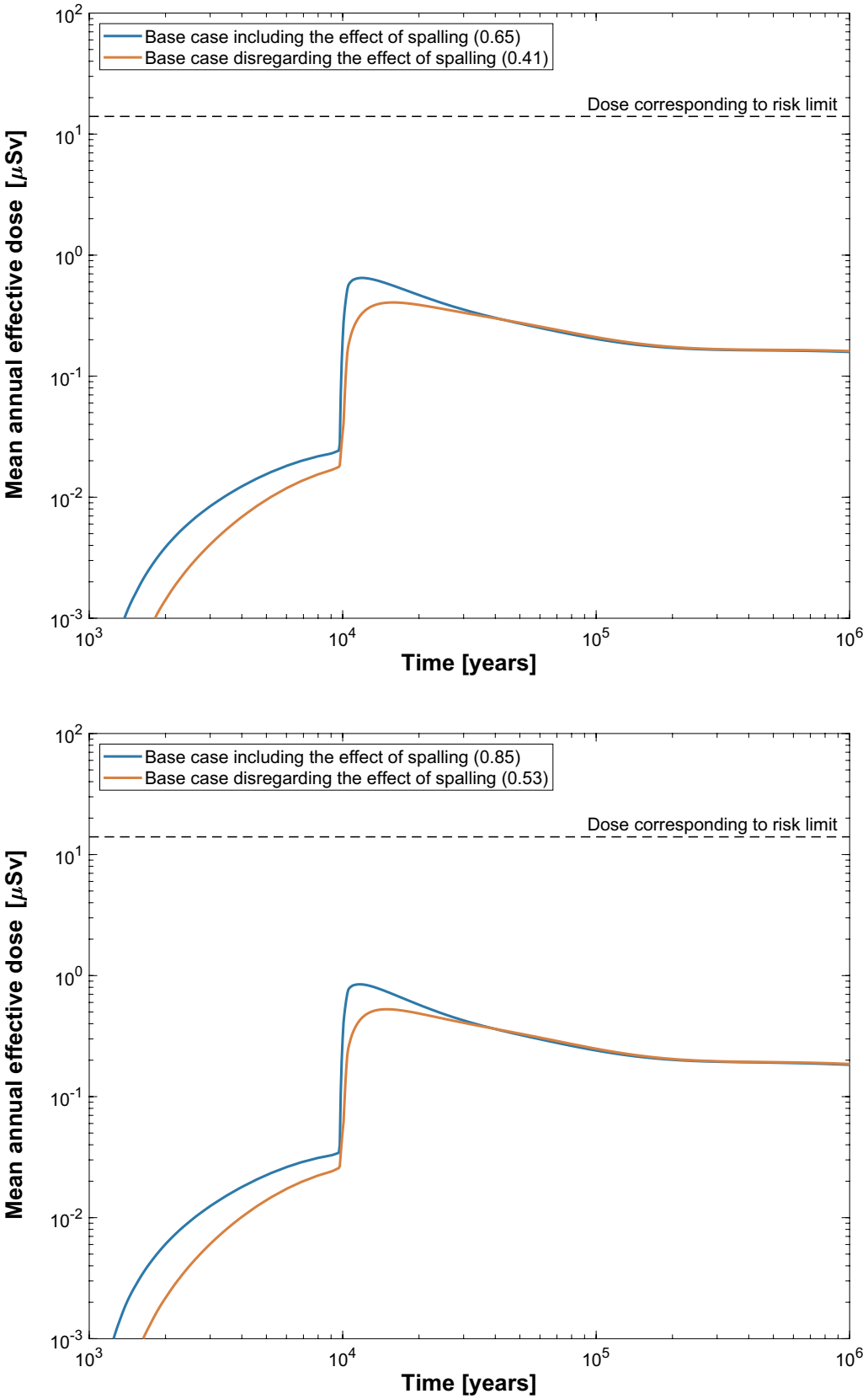

Figure M-55. *Summary of far-field mean annual effective dose equivalent release for all probabilistic calculations performed for the growing pinhole failure scenario. The peak doses are given in parentheses in μSv.* ***Top:*** *SR-Site.* ***Bottom:*** *PSAR.*

Arkitektkopia AB, Bromma, 2023

SKB is responsible for managing spent nuclear fuel and radioactive waste produced by the Swedish nuclear power plants such that man and the environment are protected in the near and distant future.

skb.se